

AN ABSTRACT OF THE DISSERTATION OF

Andrew W. Strahler for the degree of Doctor of Philosophy in Civil Engineering presented on June 3, 2016.

Title: An Experimental and Numerical Investigation of Tall Mechanically Stabilized Earth Walls.

Abstract approved:

Armin W. Stuedlein

The implementation and construction of Mechanically Stabilized Earth (MSE) walls has undergone substantial expansions in recent years, owing to its relatively low cost, ease of construction, and high efficiency compared to conventional retaining methods. As a result, MSE walls are being constructed to greater heights with complex features (e.g. multiple tiers, equivalent batter angles, close reinforcement spacing) even though impacts on wall response associated with these characteristics are not well understood. Available methods to predict wall responses are limited to empirical databases of single tiered walls less than 20 m and designers are left to complex finite element modelling to estimate the behavior of tall walls (walls with heights greater than 20 m). The current study aims to provide practitioners with a better understanding of the working stress behavior of tall MSE walls during and after construction through the use of a calibrated numerical model

that incorporates pressure dependent soil, panel-soil interaction, non-linear soil reinforcement interaction, facing rigidity, foundation stiffness, and compaction stresses.

First, an extensive laboratory investigation is conducted to characterize the plane strain and three dimensional stress-strain and stress-dilatancy response of a well-graded gravelly soil. Laboratory pullout tests are performed to characterize the influence of reinforcement spacing on load-displacement response. Results from the high quality laboratory investigations are used to calibrate specific numerical elements in FLAC (e.g. reinforcement-soil interface, facing-soil interface, soil constitutive response) incorporating pressure dependent constitutive responses. A numerical model representing a 46 m tall MSE wall is developed in FLAC, incorporating calibrated element parameters. Measurements made during the construction of a 46 m tall MSE wall are used to establish those factors within the model that most accurately simulate the observed wall performance. Results from a geometric parametric study conducted to assess the influence of boundary conditions on wall response are presented, focusing on impacts associated with tier height, tier offset, and wall height. The synthesis of the results from the geometric parametric study are used to establish a more thorough understanding of wall response, with specific emphasis on wall displacements and reinforcement strains.

© Copyright by Andrew W. Strahler

June 3, 2016

All Rights Reserved

An Experimental and Numerical Investigation of Tall Mechanically Stabilized Earth Walls

by

Andrew W. Strahler

A DISSERTATION

submitted to

Oregon State University

in partial fulfillment of
the requirements for the
degree of

Doctor of Philosophy

Presented June 3, 2016
Commencement June 2017

Doctor of Philosophy dissertation of Andrew W. Strahler presented on June 3, 2016.

APPROVED:

Major Professor, representing Civil Engineering

Head of the School of Civil and Construction Engineering

Dean of the Graduate School

I understand that my dissertation will become part of the permanent collection of Oregon State University libraries. My signature below authorizes release of my dissertation to any reader upon request.

Andrew W. Strahler, Author

ACKNOWLEDGEMENTS

I would like to first and foremost thank my graduate advisor, Professor Armin Stuedlein for his guidance, support, and strength throughout my time here at Oregon State University (OSU). This document is the culmination of three and a half years of effort and would not have been possible without him. He has been an effective mentor and I will carry the lessons I have learned from him for years to come. I am also very grateful for the support and comments provided by my graduate thesis committee: Professors Pedro Arduino, Matt Evans, Brady Gibbons, and Ben Leschinsky. Your thoughtful comments, suggestions, and overall advice proved to be extremely helpful throughout this process. I would also like to extend my sincerest thank you to the late Dr. Jerry Yamamuro and his family for providing funding during this research.

To the many, many friends and colleagues that I have had the pleasure of getting to know over the almost six years I have spent here at OSU, I can express nothing but appreciation and gratitude for your endless support. Specifically, I would like to mention Mr. Paul Barker, Mr. Trevor Carey, Mr. John Martin and his Family, Dr. Tadesse Meskele, Dr. Debora Piemonti, and Dr. Seth Reddy. Without all of the encouragement, free meals, and tomfoolery that you have afforded me, my time here at OSU would have been far less enjoyable, and possibly more productive. Finally, I would like to thank my amazing parents for the ceaseless love and guidance that you have given me over these years. Without it I would never have finished this document.

Thank you all. - Dr. Drew

TABLE OF CONTENTS

	<u>Page</u>
Chapter 1: Introduction	1
1.1 Statement of Problem	1
1.2 Purpose and Scope.....	2
1.3 Outline	3
Chapter 2: Literature Review	7
2.1 Introduction	7
2.2 Seattle Tacoma International Airport MSE Walls	8
2.3 Behavior of Well-graded Gravelly Soils	10
2.3.1. Effect of Particle Size, Shape and Gradation.....	11
2.3.2. Stress-Dilatancy of Granular soils	13
2.3.3. Effect of Intermediate Principal Stress	17
2.4 Reinforcement-Soil Structure Interaction	22
2.4.1. Direct Shear Interface Frictional Responses.....	23
2.4.2. Pullout Resistance and Apparent Friction Coefficient.....	25
2.5 Discussion regarding MSE Wall Design Methods.....	30
2.5.1. Effects of Tier Height and Offset.....	30
2.5.2. Rigidity of the Front Facing.....	32
2.5.3. Curvature in the Mohr Failure Envelope	33
2.5.4. Global and Local Reinforcement Stiffness	34
2.5.5. Displacement Estimation Methods	38
2.6 Numerical Modeling of Steel MSE Walls.....	42
2.7 Summary of Literature Review	44
2.7.1. Summary	44
2.7.2. Outstanding Problems and Issues	45

TABLE OF CONTENTS (Continued)

	<u>Page</u>
Chapter 3: Research Objectives and Program.....	47
3.1. Research Objectives	47
3.2. Research Program.....	48
Chapter 4: Stress-Strain Response and Dilatancy of Sandy Gravel in Triaxial Compression and Plane Strain	50
4.1 Abstract	51
4.2 Introduction	52
4.3 Experimental Program and Soil Description.....	54
4.3.1. Laboratory Testing Program and Criteria	54
4.4 Axysymmetric Isotropically Consolidated Drained (AICD) Response	58
4.5 Quasi- K_0 consolidated pure shear Plane Strain (PSK ₀ CD) response	65
4.5.1. Quasi- K_0 Consolidation Behavior.....	65
4.5.2. Stiffness of Kanaskat Gravel	70
4.5.3. Strain Compatibility and Shear Band Formation.....	71
4.5.4. Effect of Intermediate Stresses and Strains	74
4.6 Discussion of the Stress-Dilatancy behavior of Kanaskat gravel.....	80
4.7 Summary and Conclusion	84
4.8 List of References.....	86
Chapter 5: Three-Dimensional Stress-Strain Response and Stress-Dilatancy of Well-graded Gravel.....	95
5.1 Abstract	96
5.2 Introduction	97
5.3 Soil Description and Experimental Program.....	98

TABLE OF CONTENTS (Continued)

	<u>Page</u>
5.4 3-D True-triaxial response of Kanaskat Gravel	101
5.4.1. Shear Modulus of Kanaskat Gravel	105
5.4.2. Strain Compatibility and Shear Band Formation.....	109
5.4.3. Pressure Dependent Behavior of Kanaskat Gravel at Failure.....	111
5.5 Discussion of the 3-D Response of Kanaskat gravel	115
5.5.1. Stress-Dilatancy Response.....	115
5.5.2. Assessment and Calibration of Three-Dimensional Failure Criteria.....	117
5.6 Summary and Conclusion	121
5.7 Acknowledgments	123
5.8 References	124
Chapter 6: Frictional Resistance of Closely-Spaced Steel MSE Wall Reinforcement Strips	130
6.1 Abstract	131
6.2 Introduction	133
6.3 Apparent Frictional Resistance	135
6.4 Experimental Program.....	137
6.4.1. Characterization of Soil Backfill	137
6.4.2. Single Strip Pullout Apparatus.....	139
6.4.3. Multi-Strip Pullout Apparatus.....	143
6.4.4. Specimen Preparation	145
6.4.5. Effect of Boundary Conditions	147

TABLE OF CONTENTS (Continued)

	<u>Page</u>
6.5 Soil Reinforcement-Interaction of Isolated and Closely-Spaced Strips	149
6.5.1. Frictional Response of Isolated, Single Reinforcement Strips	149
6.5.2. Frictional Response of Fully-confined Reinforcements Strips	151
6.5.3. Pullout Response at Working Stresses.....	154
6.5.4. Ultimate Pullout Resistance of Isolated Single Strips	156
6.5.5. Effect of Spacing on Ultimate Pullout Resistance of Fully-Confined Strips....	158
6.5.6. Apparent Friction Coefficient for Ribbed Steel Strips in Kanaskat Gravel.....	159
6.5.7. Discussion and Potential Design Implications.....	165
6.6 Concluding Remarks	167
6.7 Acknowledgements	168
6.8 References	169
Chapter 7: Calibration and Numerical simulations of Tall Steel Strip-Reinforced MSE Wall	175
7.1 Abstract	176
7.2 Introduction	177
7.3 Critical Aspects of The Validation Case History	179
7.4 Calibration of Element Specific Constitutive Models.....	182
7.4.1. General Approach	182
7.4.2. Subsurface Soil Properties	185
7.4.3. Element Parameter Updating Routines	187
7.4.4. Reinforced and Retained Soil Properties	187
7.4.5. Panel Beam Elements and Bearing Pad Response.....	191
7.4.6. Concrete-Soil Interface	194
7.4.7. Soil-Reinforcement Strip Interface and Spacing Effects	197

TABLE OF CONTENTS (Continued)

	<u>Page</u>
7.5 Model Validation and Parametric Evaluation of the West MSE Wall.....	201
7.5.1. Measured Responses and the Baseline Model.....	202
7.5.2. Influence of Compaction Stresses.....	205
7.5.3. Influence of Retained Embankment Stiffness.....	206
7.5.4. Influence of Reinforced Fill and Strip Interface Stiffness.....	210
7.5.5. Simulation of Construction Sequencing using the Representative MSE Wall Model Analysis.....	213
7.6 Geometric Parametric Study.....	219
7.6.1. Wall Deformations.....	223
7.6.2. Reinforcement Strains.....	229
7.7 Concluding Remarks.....	233
7.8 Acknowledgements.....	235
7.9 References.....	236
Chapter 8: Summary, Conclusions, and Proposed Future Work.....	242
8.1 Summary.....	242
8.2 Summary and Conclusions.....	244
8.2.1. Stress-Strain Response and Dilatancy of Sandy Gravel in Triaxial Compression and Plane Strain.....	244
8.2.2. Three –Dimensional Stress-Strain Response and Stress-Dilatancy of Well- Graded graded Gravel.....	245
8.2.3. Frictional Resistance of Closely-Spaced Steel MSE Wall Reinforcement Strips.....	246
8.2.4. Numerical Modelling of Tall MSE walls.....	248
8.3 Proposed Future Work.....	249
Complete List of References.....	250

LIST OF APPENDICES

<u>Appendix</u>	<u>Page</u>
Appendix A: Results from PSK ₀ CD tests.....	270
Appendix B: Results from TC, TE, and SS tests	278
Appendix C: Design of the Multi-strip Pullout Box.....	290
Part 1: Design Calculations and Procedures	291
Part 2: Shop Drawings and 3D renderings.....	314
Part 3: Supplemental Appendix for Chapter 5.....	338
Appendix D: Load-Displacement Response from Multi-Strip Pullout Tests	341
Appendix E: FISH and C++ Codes used To Update mean Effective Stress and Element Parameters in Numerical Simulations.....	353
E.1 C++ UDM - Modified Chsoil.....	354
E.2 FISH CODE - Strip Interface Stiffness	367
E.3 FISH Code - Soil-Panel Interface.....	367
E.4 FISH Code - Bearing Pad Modulus.....	369
Appendix F: Plots from the Geometric Parametric Study of Tall MSE walls.....	371

LIST OF FIGURES

	<u>Page</u>
Figure 2.1. Aerial view of the STIA third runway and the north and west MSE walls (after Stuedlein et al. 2010).	8
Figure 2.2. Cross section of the tall STIA MSE walls showing primary instrumented sections of the (a) west wall and (b) north wall (from Stuedlein et al. 2012).....	9
Figure 2.3. Changes in frictional angle due to the effect of the intermediate principal stress by reference: (a) Bishop (1966); (b) Lade and Duncan (1973), Reades and Green (1976); (c) Green (1971), Lade and Duncan (1973); (d) Ergun (1981), Haruyama (1981); (e) Sutherland and Mesdary (1969), Ramamurthy and Rowat (1973); (f) Shankariah and Ramamurthy (1980), (adapted from Sayao and Vaid 1996).....	18
Figure 2.4. Comparison of the Matsuoka-Nakai (M-C), Lade-Duncan (L-D), and Mohr-Coulomb (M-C) failure yield surfaces in the deviatoric plane (Davis and Selvadurai 2002).	21
Figure 2.5. Stress transfer mechanisms for ribbed steel strips (Mitchell and Christopher et al. 1990a and 1990b).....	24
Figure 2.6. Testing techniques and boundary conditions presented in the literature (after Larson 1992).	27
Figure 2.7. Frictional resistance during pullout tests with different front facing friction conditions (adapted from Palmeira 1987).....	28
Figure 2.8. Apparent friction coefficient versus effective vertical stress data originally used to calibrate the pullout design procedure.	29
Figure 2.9. Representative observed and predicted tensile reinforcement strain in the west STIA MSE wall showing the (a) accumulation of strain during construction, (b) method used to differentiate initial installation effect from overburden placement (adapted from Stuedlein et al. 2010b).....	36
Figure 2.10. Effect of local reinforcement stiffness on the strain rate uptake observed in the west STIA MSE wall (after Stuedlein et al. 2010)	37
Figure 2.11. Observed and predicted peak reinforcement loads for the completed West MSE wall (H = 45.7 m, surcharge) (after Stuedlein et al. 2012).	38
Figure 2.12. First order approximation of lateral displacements at the end of construction (after Mitchell and Christopher 1990a and b).....	40
Figure 2.13. Comparison between deformational responses from numerical simulations and analytical methods for geo-synthetically reinforced walls as a function of the reinforcement stiffness and the soil-wall interface coefficient (after Rowe and Ho 1998).	41

LIST OF FIGURES (Continued)

	<u>Page</u>
Figure 2.14. Comparison between deformational responses from numerical simulations and analytical methods for geo-synthetically reinforced walls as a function of the backfill friction angle and interface coefficient (after Rowe and Ho 1998).....	41
Figure 4.1. Grain size distributions of a sandy gravel: (a) sample and representative (target) distributions and (b) example distribution presenting particle shape.	56
Figure 4.2. Changes in relative density due to consolidation as a function of confining pressure for AICD and PSK ₀ CD tests on Kanaskat Gravel; Note: AC = After Consolidation, BC = Before Consolidation.	58
Figure 4.3. Principal effective stress ratio and volumetric strain response of Kanaskat gravel developed from AICD triaxial tests.	60
Figure 4.4. Effective friction and dilation angles at failure as a function normalized mean effective stress for AICD and PSK ₀ CD tests. Note: shaded points were removed from the PSK ₀ CD trends due to boundary condition effects at low confining stresses.	61
Figure 4.5. Evolution of void ratios during shear for (a) AICD and (b) PSK ₀ CD tests on Kanaskat gravel; e_c , e_f , and e_{cs} correspond to the void ratio at consolidation, failure, and the critical state, respectfully.	63
Figure 4.6. State paths during shearing of the AICD stress path tests as a function of mean effective stress with indicators showing the state parameters following consolidation and at failure. Data for $p'_c = 10$ kPa omitted.	64
Figure 4.7. Ratio of stress invariants and volumetric strain as function of engineering shear strain for the PSK ₀ CD stress paths.	67
Figure 4.8. PSK ₀ CD stress paths of a sandy gravel in q-p' space with markers indicating the formation of shear bands and deviations from continuum response.....	67
Figure 4.9. PSK ₀ CD specimen response during consolidation and shearing: (a) deviatoric stress-strain response, (b) volumetric strain calculated using LVDTs in principal directions, and (c) volumetric strain measured using burette observations.	69
Figure 4.10. Initial tangent shear modulus computed at 0.05% shear strain and plotted versus p'/p_{ref}	71
Figure 4.11. Progression of facing bladder displacements for $p'_c = 114$ kPa. Inset: major principal (i.e., 1a and 1b) and minor principal faces (3a and 3b).	73
Figure 4.12. Progression of the intermediate deviatoric stress ratio during shearing in the PSK ₀ CD stress path.	76

LIST OF FIGURES (Continued)

	<u>Page</u>
Figure 4.13. Development of intermediate principal stresses for the PSK ₀ CD consolidation and shearing stress paths.....	77
Figure 4.14. Stress-dilatancy behavior of Kanaskat gravel: (a) comparison of effective friction and dilation angle at failure and (b) comparison of observations to Bolton's approximation as a function of mean effective confining stress.	82
Figure 5.1. Stress paths for true triaxial tests at $p'_c \approx 100$ kPa, projected onto the deviatoric plane and bounded by the Matsuoka-Nakai failure criterion.....	103
Figure 5.2. Variation of the ratio of stress invariants and volumetric strain with engineering shear strain for: (a) TC, (b) SS, and (c) TE stress paths.	104
Figure 5.3. Variation in the secant shear modulus at (a) $\gamma_s = 0.05\%$ and (b) 50% of peak q with normalized mean effective stress at failure in SS, TC, TE, and PSK ₀ stress paths.	107
Figure 5.4. Variation of (a) initial shear modulus and (b) shear modulus at 50% shear stress with b and confining pressure.....	108
Figure 5.5. Principal face displacements versus shearing strain for a true-triaxial test conducted at $p'_c = 102$ kPa in the SS stress path where A and C are σ'_1 and σ'_3 , respectively; Note: inset depicts the face location for each principal displacement. ...	110
Figure 5.6. Responses of Kanaskat gravel at failure measured in PSK ₀ , TE, SS, TC, and AICD stress paths as a function of normalized mean effective stress: (a) Friction and (b) Dilation angles.	113
Figure 5.7. Stress dilatancy response of Kanaskat gravel in three dimensional stress paths.	117
Figure 5.8. Material parameter fitting coefficients for L-D and M-N failure criterion; Note: gray data points were omitted due to influences of low stresses at the boundary conditions.....	119
Figure 5.9. Variation of measured ϕ'_f for each p'_c as a function of b plotted alongside the fitted true triaxial L-D and M-N failure criterion.	121
Figure 6.1. Friction and dilation angles at failure for Kanaskat gravel in AICD and PSK ₀ CD stress paths as a function of normalized mean effective confining pressure (data from Strahler et al. 2015).....	139
Figure 6.2. Single strip pullout testing apparatus.	140

LIST OF FIGURES (Continued)

	<u>Page</u>
Figure 6.3. Stiffened steel face with 101 mm openings and slotted neoprene rubber membrane providing a soft boundary condition for the (a) single- and (b) multi-strip pullout apparatus.....	141
Figure 6.4. Multiple strip pullout test apparatus.	144
Figure 6.5. Cross section of the multi-strip pullout box with strip designations (reinforcement spacing of 305 mm shown).	145
Figure 6.6. Influence of embedment length on the maximum pullout force of ribbed steel strips in Kanaskat gravel, $\sigma'_v = 100$ kPa.....	148
Figure 6.7. Apparent load versus strip displacement curve (a) at small displacements showing the initial non-slip resistance and (b) over full range of displacements for test 200-2.....	150
Figure 6.8. Typical load displacement behavior of the multiple strip pullout apparatus: (a), (c), (e) at small displacements and (b), (d), (f) over full range of displacements for test 100A-66 (Note: See Figure 4 for strip locations).....	152
Figure 6.9. Secant stiffness at 5 mm of displacement as a function of normalized spacing ratio and vertical effective stress for (a) isolated and (b) fully-confined reinforcement strips (Note: DNA = Density Not Available).	155
Figure 6.10. Peak apparent strip loads for (a) the single strip apparatus and (b) fully confined center strips adjusted for length differences and boundary condition effects. (Note: DNA = Density not available).....	157
Figure 6.11. Fitted models for (a) single and multi-strip pullout tests presented here using Kanaskat gravel and (b) tests available in the literature. Note: NM1 and NM1LB correspond to New Model 1 and its lower bound, respectively, reported by Miyata and Bathurst (2012a).....	161
Figure 7.1. West MSE wall cross-section showing instrumentation locations.....	180
Figure 7.2. Mesh used for 2D FLAC simulations of the STIA West MSE wall.	184
Figure 7.3. Comparison of observed triaxial test data and calibrated <i>Chsoil</i> constitutive model responses: (a) and (b) variation of deviatoric stress with axial strain, and (c) and (d) variation of volumetric strain with axial strain.	190
Figure 7.4. Comparison of the fitted, bilinear bearing pad stress-strain responses I to data reported by Neely and Tan (2010) and Choufani et al. (2011).....	193

LIST OF FIGURES (Continued)

	<u>Page</u>
Figure 7.5. Comparison of sand-concrete interface response reported by Gomez to calibrated interface model used in the numerical simulations: (a) variation of shear stress with interface displacement, and (b) variation of vertical displacement with interface displacement (Note: $k_n = 1000 \text{ MN/m/m}$).	196
Figure 7.6. Comparison of calibrated and measured pullout resistance of ribbed steel strips in dense Kanaskat gravel at $\sigma'_v =$ (a) 50 kPa, (b) 100 kPa, and (c) 200 kPa.	199
Figure 7.7. Influence of compaction stresses on (a) lateral and (b) vertical panel displacement, (c) peak axial strip strains measured at EOC, (d) lateral and (e) vertical inclinometer displacement measured at completion of Tier 4.	204
Figure 7.8. Influence of retained embankment stiffness on (a) lateral and (b) vertical panel displacement, (c) peak axial strip strains measured at EOC, (d) lateral and (e) vertical inclinometer displacement measured at completion of Tier 4.	207
Figure 7.9. Accumulated shear strain increments at EOC in the dense Mohr embankment fill numerical model.	208
Figure 7.10. Accumulated shear strain increments at EOC in the dense <i>Chsoil</i> embankment fill numerical model.	209
Figure 7.11. Influence of reinforcement interface and reinforced fill stiffness on (a) lateral and (b) vertical panel displacement, (c) peak axial strip strains measured at EOC, (d) lateral and (e) vertical inclinometer displacement measured at completion of Tier 4.	212
Figure 7.12. Influence of reinforcement interface and reinforced fill stiffness on (a) lateral and (b) vertical panel displacement, (c) peak axial strip strains, (d) lateral and (e) vertical inclinometer displacement measured at various times during construction. ...	214
Figure 7.13. Measured and representative axial strain distributions along reinforcements at instrumented elevations (a through g) during completion of different stages of construction.	217
Figure 7.14. Variations in normalized vertical stresses at completion of different stages in the representative West MSE wall model (Note: a smoothing function with 2 m interval was used to reduce scatter).	219
Figure 7.15. Variation in (a) normalized local stiffness and (b) horizontal spacing in the generic model. (Note: $S_v = 0.50 \text{ m}$).	222
Figure 7.16. Test designation based on wall geometry and reinforcement spacing distribution.	222
Figure 7.17. Normalized face settlement for a 6 tiered 50 m tall wall with (a) flexible, (b) medium stiff, and (c) stiff reinforcement distributions for various batter angles.	224

LIST OF FIGURES (Continued)

	<u>Page</u>
Figure 7.18. Normalized lateral face displacement for a 6 tiered 50 m tall wall with (a) flexible, (b) medium stiff, and (c) stiff reinforcement distributions as a function of batter angle.....	225
Figure 7.19. Normalized peak lateral displacement versus wall batter angle for (a and b) 20 m and (c and d) 50 m tall wall simulations with 4 and 6 tiers.	227
Figure 7.20. Normalized peak face settlement versus wall batter angle for (a, b, c) 20 m and (d, e, f) 50 m tall wall simulations with 4 and 6 tiers.....	228
Figure 7.21. Peak reinforcement strain for (a) 4 and (b) 6 tiered 50 m tall walls with flexible strip distributions.	230
Figure 7.22. Location of peak strain corrected for batter angle effects for (a) 4 and (b) 6 tiered 50 m tall flexible walls (Note: data has been smoothed using a 2 m interval)...	231
Figure 7.23. Normalized reinforcement strain parameter versus wall batter angle for (a and b) 20 m and (c and d) 50 m tall wall simulations with 4 and 6 tiers.....	233
Figure A.1. Results from PSK ₀ CD test at $p'_o = 28$ kPa on Kanaskat grave1: (a) stress path, (b) deviatoric stress versus shear strain, (c) deviatoric stress versus normal strain in principal stress directions, (d) friction angle versus shear strain, (e) burette volumetric strain measurement, (f) normalized 3-D stress path. (Note: white marker denotes failure).....	271
Figure A.2. Results from PSK ₀ CD test at $p'_o = 63$ kPa on Kanaskat grave1: (a) stress path, (b) deviatoric stress versus shear strain, (c) deviatoric stress versus normal strain in principal stress directions, (d) friction angle versus shear strain, (e) burette volumetric strain measurement, (f) normalized 3-D stress path. (Note: white marker denotes failure).....	272
Figure A.3. Results from PSK ₀ CD test at $p'_o = 86$ kPa on Kanaskat grave1: (a) stress path, (b) deviatoric stress versus shear strain, (c) deviatoric stress versus normal strain in principal stress directions, (d) friction angle versus shear strain, (e) burette volumetric strain measurement, (f) normalized 3-D stress path. (Note: white marker denotes failure).....	273
Figure A.4. Results from PSK ₀ CD test at $p'_o = 114$ kPa on Kanaskat grave1: (a) stress path, (b) deviatoric stress versus shear strain, (c) deviatoric stress versus normal strain in principal stress directions, (d) friction angle versus shear strain, (e) burette volumetric strain measurement, (f) normalized 3-D stress path. (Note: white marker denotes failure).....	274

LIST OF FIGURES (Continued)

	<u>Page</u>
Figure A.5. Results from PSK ₀ CD test at $p'_o = 147$ kPa on Kanaskat gravel: (a) stress path, (b) deviatoric stress versus shear strain, (c) deviatoric stress versus normal strain in principal stress directions, (d) friction angle versus shear strain, (e) burette volumetric strain measurement, (f) normalized 3-D stress path. (Note: white marker denotes failure).....	275
Figure A.6. Results from PSK ₀ CD test at $p'_o = 172$ kPa on Kanaskat gravel: (a) stress path, (b) deviatoric stress versus shear strain, (c) deviatoric stress versus normal strain in principal stress directions, (d) friction angle versus shear strain, (e) burette volumetric strain measurement, (f) normalized 3-D stress path. (Note: white marker denotes failure).....	276
Figure A.7. Three dimensional stress path responses for all PSK ₀ CD tests compared to the Mohr-Coulomb (in grey) and Matsuoka Nakai (in black) failure surfaces. (Note: white marker denotes failure)	277
Figure B.1. Results from SS test at $p'_c = 49$ kPa on Kanaskat gravel: (a) stress path, (b) deviatoric stress versus shear strain, (c) deviatoric stress versus normal strain in principal stress directions, (d) friction angle versus shear strain, (e) burette volumetric strain measurement, (f) normalized 3-D stress path. (Note: white marker denotes failure.).....	279
Figure B.2. Results from SS test at $p'_o = 54$ kPa on Kanaskat gravel: (a) stress path, (b) deviatoric stress versus shear strain, (c) deviatoric stress versus normal strain in principal stress directions, (d) friction angle versus shear strain, (e) burette volumetric strain measurement, (f) normalized 3-D stress path. (Note: white marker denotes failure.).....	280
Figure B.3. Results from SS test at $p'_o = 101$ kPa on Kanaskat gravel: (a) stress path, (b) deviatoric stress versus shear strain, (c) deviatoric stress versus normal strain in principal stress directions, (d) friction angle versus shear strain, (e) burette volumetric strain measurement, (f) normalized 3-D stress path. (Note: white marker denotes failure.).....	281
Figure B.4. Results from SS test at $p'_o = 204$ kPa on Kanaskat gravel: (a) stress path, (b) deviatoric stress versus shear strain, (c) deviatoric stress versus normal strain in principal stress directions, (d) friction angle versus shear strain, (e) burette volumetric strain measurement, (f) normalized 3-D stress path. (Note: white marker denotes failure.).....	282
Figure B.5. Results from TC test at $p'_o = 46$ kPa on Kanaskat gravel: (a) stress path, (b) deviatoric stress versus shear strain, (c) deviatoric stress versus normal strain in principal stress directions, (d) friction angle versus shear strain, (e) burette volumetric strain measurement, (f) normalized 3-D stress path. (Note: white marker denotes failure.).....	283

LIST OF FIGURES (Continued)

	<u>Page</u>
Figure B.6. Results from TC test at $p'_o = 106$ kPa on Kanaskat grave1: (a) stress path, (b) deviatoric stress versus shear strain, (c) deviatoric stress versus normal strain in principal stress directions, (d) friction angle versus shear strain, (e) burette volumetric strain measurement, (f) normalized 3-D stress path. (Note: white marker denotes failure.).....	284
Figure B.7. Results from TC test at $p'_o = 201$ kPa on Kanaskat grave1: (a) stress path, (b) deviatoric stress versus shear strain, (c) deviatoric stress versus normal strain in principal stress directions, (d) friction angle versus shear strain, (e) burette volumetric strain measurement, (f) normalized 3-D stress path. (Note: white marker denotes failure.).....	285
Figure B.8. Results from TE test at $p'_o = 52$ kPa on Kanaskat grave1: (a) stress path, (b) deviatoric stress versus shear strain, (c) deviatoric stress versus normal strain in principal stress directions, (d) friction angle versus shear strain, (e) burette volumetric strain measurement, (f) normalized 3-D stress path. (Note: white marker denotes failure.).....	286
Figure B.9. Results from TE test at $p'_o = 98$ kPa on Kanaskat grave1: (a) stress path, (b) deviatoric stress versus shear strain, (c) deviatoric stress versus normal strain in principal stress directions, (d) friction angle versus shear strain, (e) burette volumetric strain measurement, (f) normalized 3-D stress path. (Note: white marker denotes failure.).....	287
Figure B.10. Results from TE test at $p'_o = 202$ kPa on Kanaskat grave1: (a) stress path, (b) deviatoric stress versus shear strain, (c) deviatoric stress versus normal strain in principal stress directions, (d) friction angle versus shear strain, (e) burette volumetric strain measurement, (f) normalized 3-D stress path. (Note: white marker denotes failure.).....	288
Figure B.11. Results from TE test at $p'_o = 200$ kPa on Kanaskat grave1: (a) stress path, (b) deviatoric stress versus shear strain, (c) deviatoric stress versus normal strain in principal stress directions, (d) friction angle versus shear strain, (e) burette volumetric strain measurement, (f) normalized 3-D stress path. (Note: white marker denotes failure.).....	289
Figure B.5.S1. Stiffened steel face with 101 mm openings and slotted neoprene rubber membrane providing a soft boundary condition for the (a) single- and (b) multi-strip pullout apparatus.....	339
Figure B.5.S2. Interchangeable steel plates that represent different reinforcement spacing (Note: 101 mm opening maintained in each plate).....	340
Figure D.1. Multi-strip pullout test results for 100A-44: (a) strips 1-3, (b) strips 4-6, (c) strips 7-9, (c) strips 1-9 at small displacements.....	342

LIST OF FIGURES (Continued)

	<u>Page</u>
Figure D.2. Multi-strip pullout test results for 30A-66: (a) strips 1-3, (b) strips 4-6, (c) strips 7-9, (c) strips 1-9 at small displacements.	343
Figure D.3. Multi-strip pullout test results for 100B-66: (a) strips 1-3, (b) strips 4-6, (c) strips 7-9, (c) strips 1-9 at small displacements.	344
Figure D.4. Multi-strip pullout test results for 200A-66: (a) strips 1-3, (b) strips 4-6, (c) strips 7-9, (c) strips 1-9 at small displacements.	345
Figure D.5. Multi-strip pullout test results for 100A-88: (a) strips 1-3, (b) strips 4-6, (c) strips 7-9, (c) strips 1-9 at small displacements.	346
Figure D.6. Multi-strip pullout test results for 100A-1010: (a) strips 1-3, (b) strips 4-6, (c) strips 7-9, (c) strips 1-9 at small displacements.	347
Figure D.7. Multi-strip pullout test results for 100B-1010: (a) strips 1-3, (b) strips 4-6, (c) strips 7-9, (c) strips 1-9 at small displacements.	348
Figure D.8. Multi-strip pullout test results for 30A-1212: (a) strips 1-3, (b) strips 4-6, (c) strips 7-9, (c) strips 1-9 at small displacements.	349
Figure D.9. Multi-strip pullout test results for 100A-1212: (a) strips 1-3, (b) strips 4-6, (c) strips 7-9, (c) strips 1-9 at small displacements.	350
Figure D.10. Multi-strip pullout test results for 200A-1212: (a) strips 1-3, (b) strips 4-6, (c) strips 7-9, (c) strips 1-9 at small displacements.	351
Figure D.11. Multi-strip pullout test results for 100A-2424: (a) strips 1-3, (b) strips 4-6, (c) strips 7-9, (c) strips 1-9 at small displacements.	352
Figure F.1. FLAC model results showing shear strains for F – 1T – 0% - 20H.	372
Figure F.2. FLAC model results showing shear strains for F – 1T – 0% - 50H.	372
Figure F.3. FLAC model results showing shear strains for F – 4T – 2% - 20H.	373
Figure F.4. FLAC model results showing shear strains for F – 4T – 2% - 50H.	373
Figure F.5. FLAC model results showing shear strains for F – 4T – 4% - 20H.	374
Figure F.6. FLAC model results showing shear strains for F – 4T – 4% - 50H.	374
Figure F.7. FLAC model results showing shear strains for F – 4T – 8% - 20H.	375
Figure F.8. FLAC model results showing shear strains for F – 4T – 8% - 50H.	375

LIST OF FIGURES (Continued)

	<u>Page</u>
Figure F.9. FLAC model results showing shear strains for F – 6T – 2% - 20H.....	376
Figure F.10. FLAC model results showing shear strains for F – 6T – 2% - 50H.....	376
Figure F.11. FLAC model results showing shear strains for F – 6T – 4% - 20H.....	377
Figure F.12. FLAC model results showing shear strains for F – 6T – 4% - 50H.....	377
Figure F.13. FLAC model results showing shear strains for F – 6T – 8% - 20H.....	378
Figure F.14. FLAC model results showing shear strains for F – 6T – 8% - 50H.....	378
Figure F.15. FLAC model results showing shear strains for F – 6T – 12% - 50H.....	379
Figure F.16. FLAC model results showing shear strains for M – 1T – 0% - 20H.	380
Figure F.17. FLAC model results showing shear strains for M – 1T – 0% - 50H.	380
Figure F.18. FLAC model results showing shear strains for M – 4T – 2% - 20H.	381
Figure F.19. FLAC model results showing shear strains for M – 4T – 2% - 50H.	381
Figure F.20. FLAC model results showing shear strains for M – 4T – 4% - 20H.	382
Figure F.21. FLAC model results showing shear strains for M – 4T – 4% - 50H.	382
Figure F.22. FLAC model results showing shear strains for M – 4T – 8% - 20H.	383
Figure F.23. FLAC model results showing shear strains for M – 4T – 8% - 50H.	383
Figure F.24. FLAC model results showing shear strains for M – 6T – 2% - 20H.	384
Figure F.25. FLAC model results showing shear strains for M – 6T – 2% - 50H.	384
Figure F.26. FLAC model results showing shear strains for M – 6T – 4% - 20H.	385
Figure F.27. FLAC model results showing shear strains for M – 6T – 4% - 50H.	385
Figure F.28. FLAC model results showing shear strains for M – 6T – 8% - 20H.	386
Figure F.29. FLAC model results showing shear strains for M – 6T – 8% - 50H.	386
Figure F.30. FLAC model results showing shear strains for M – 6T – 12% - 50H.	387
Figure F.31. FLAC model results showing shear strains for S – 1T – 0% - 20H.....	388
Figure F.32. FLAC model results showing shear strains for S – 1T – 0% - 50H.....	388

LIST OF FIGURES (Continued)

	<u>Page</u>
Figure F.33. FLAC model results showing shear strains for S – 4T – 2% - 20H.....	389
Figure F.34. FLAC model results showing shear strains for S – 4T – 2% - 50H.....	389
Figure F.35. FLAC model results showing shear strains for S – 4T – 4% - 20H.....	390
Figure F.36. FLAC model results showing shear strains for S – 4T – 4% - 50H.....	390
Figure F.37. FLAC model results showing shear strains for S – 4T – 8% - 20H.....	391
Figure F.38. FLAC model results showing shear strains for S – 4T – 8% - 50H.....	391
Figure F.39. FLAC model results showing shear strains for S – 6T – 2% - 20H.....	392
Figure F.40. FLAC model results showing shear strains for S – 6T – 2% - 50H.....	392
Figure F.41. FLAC model results showing shear strains for S – 6T – 4% - 20H.....	393
Figure F.42. FLAC model results showing shear strains for S – 6T – 4% - 50H.....	393
Figure F.43. FLAC model results showing shear strains for S – 6T – 8% - 20H.....	394
Figure F.44. FLAC model results showing shear strains for S – 6T – 8% - 50H.....	394
Figure F.45. FLAC model results showing shear strains for S – 6T – 12% - 50H.....	395

LIST OF TABLES

	<u>Page</u>
Table 2.1. Summary of numerically modeled inextensible MSE walls.....	42
Table 4.1 Characteristic soil properties of Kanaskat gravel.	55
Table 4.2. Overview of the laboratory testing program and relevant results.....	57
Table 5.1. Summary of testing results for Kanaskat gravel in various stress paths.....	100
Table 5.2. Summary of friction angle fitting parameters in different stress paths; Note: AICD – p'_f fitting values can be used to represent the TC response.	113
Table 6.1. Summary of isolated and fully confined pullout test results.	142
Table 6.2. Summary of fitted AASHTO and New Model 1 (NM1) fitting parameters for Kanaskat gravel.....	163
Table 7.1. Summary of Mohr-Coulomb soil properties.....	186
Table 7.2. Summary of <i>Chsoil</i> constitutive model properties.	190
Table 7.3. Summary of beam element modelling parameters.	193
Table 7.4. Summary of calibrated interface modelling parameters.	197
Table 7.5. Summary of FLAC strip interface element properties.....	200
Table 7.6. Element-level parametric study of the simulated West MSE wall performance. Note: baseline model parameters indicated by bold text.	202
Table 7.7. Summary of geometric parametric study.....	220
Table 7.8. Number of tiers and tier offsets evaluated in the geometric parametric study and equivalent batter angles.	220

CHAPTER 1: INTRODUCTION

1.1 STATEMENT OF PROBLEM

Reinforced soil is a composite construction material where reinforcements with tensile capacity are placed within compacted soil fill to strengthen the retaining structure. Since the initial development of reinforced soil in the modern era by Henri Vidal (1969), this composite material has been used to construct retaining walls, bridge abutments, foundations, and support highways, railways, airports, and coastal infrastructure with great success. Civil engineers have a strong interest in the use of reinforced earth due to its ease of construction, range of applications, and relatively low cost. Mechanically Stabilized Earth (MSE) walls represent a specific application of reinforced earth where alternating layers of compacted soil and reinforcement are placed to form of a retaining wall. With increasing populations and subsequently increasing right-of-way constraints, MSE walls are being constructed to greater heights, with non-linear geometries, multiple tiers and closer reinforcement spacing. Since the first application of the reinforced in the United States in 1972, more than 9 million square feet of MSE walls have been constructed (Alzamora and Barrows 2007) with the tallest in the Western Hemisphere constructed to 46 meters in height as part of the Seattle-Tacoma International Airport (STIA) third runway project (Stuedlein et al. 2010a).

Despite the proliferation of MSE walls and their construction to increasing heights, our understanding of the working stress behavior and MSE wall performance is primarily based on empirical evidence from MSE walls with heights less than 20 meters (Allen and Bathurst 2015). Stuedlein et al. (2010a, 2010b) noted that some prediction methods for estimating wall performance ignore fundamental design components such as soil dilation and

reinforcement stiffness, and thus produce poor approximations and thereby result in increased design factors of safety and reduced efficiency. New methods that better represent the fundamental composite response and performance of MSE walls are required to ensure that tall walls can be designed not just safely, but efficiently.

1.2 PURPOSE AND SCOPE

The main purpose of this study is to improve the fundamental understanding of MSE wall behavior with a specific emphasis on tall walls. The research presented here focuses on backfill material, reinforcements, and measurements observed during construction of STIA MSE walls discussed by Stuedlein et al. (2007, 2010a, and 2010b) owing to its value as a well-documented case history with which to understand component and global response of tall walls. The experimental portion of this research focuses on extending classical behavior that was formulated based on uniformly distributed sands to well graded granular materials. It is typically assumed that well-graded granular soils behave similar to uniformly distributed soil which may not be true. This is accomplished by characterizing the well graded-sandy gravel backfill material (termed Kanaskat gravel) used in the construction of the STIA tall MSE walls and its interaction with steel strip reinforcements. A large scale true-triaxial apparatus was used to determine the plane strain and triaxial stress-strain responses of Kanaskat gravel.

The soil-reinforcement interaction between Kanaskat gravel and the ribbed steel reinforcing strips used in the STIA MSE walls was characterized using a series of large scale pullout tests. The baseline response of the ribbed steel strips was established using a single

strip pullout test box. Very little work has been conducted studying effects on the reinforcement behavior associated with closely spaced reinforcements. The impact of reinforcement spacing on the baseline resistance was characterized using a multi-strip pullout box which tested nine strips in unison. Results from the laboratory experiments will be used to calibrate element-specific constitutive responses for use in numerical models in the explicit finite difference program FLAC. These numerical models which will be used to model the STIA MSE walls for the purpose of calibration to the performance observed during and just after construction. The framework established in the development of the STIA MSE numerical models will be used to conduct a parametric study to develop a fundamental understanding of tall MSE walls. Finally, the results from the parametric study will be aggregated and evaluated to develop new and/or modify current design methods that may be used for planning new tall MSE walls.

1.3 OUTLINE

The work presented here provides the details of this research, which is focused on increasing the fundamental understanding of MSE wall behavior with a specific emphasis on tall walls. Chapter 2 provides a detailed discussion of the available literature pertinent to the study of steel reinforced MSE walls, and addresses various aspects such as stress-dilatancy behavior of granular soils considerations for the design of MSE walls, available MSE wall design methods, and previously reported MSE wall numerical models. The chapter summarizes the gaps in the engineering knowledge of MSE walls.

Chapter 3 presents the objectives of this study and the research program undertaken to increase the fundamental understanding of steel strip-reinforced MSE walls.

Chapter 4 presents the details of the laboratory program used to characterize the stress-dilatancy behavior of well-graded Kanaskat gravel in the triaxial and plane strain stress paths. Characterization of the triaxial compression strength was performed using large isotropically consolidated drained axisymmetrical compression tests over a large range of confining pressures. The plane strain strength was assessed using a large cubical true-triaxial device that employs flexible bladders to apply principal effective stresses. Results from laboratory tests on the well graded gravel are compared against estimates of stiffness, strength, and stress-dilatancy responses provided by commonly used theoretical relationships developed based on uniformly graded soils.

Chapter 5 presents results from a laboratory investigation into the 3-D strength and stress-dilatancy response of Kanaskat gravel. Characterization of stiffness, strength, and stress-dilatancy soil behavior in triaxial compression, simple shear and, triaxial extension was performed using the same large cubical true-triaxial device discussed in Chapter 4. Results from the laboratory investigation are compared against stress-dilatancy theories and used to calibrate two 3-D failure criterion.

Chapter 6 presents the experimental program developed to characterize the soil-reinforcement interaction between ribbed steel strip reinforcements and Kanaskat gravel. Two pullout test boxes are discussed with emphasis given to a unique soft front facing boundary condition that mitigates passive pressures at the face and allows the measurement and interpretation of the true response of the reinforcement strip. A discussion regarding the

impact of the front facing boundary condition on the reinforcement load displacement response is provided. A baseline resistance model is established using results from a single strip pullout box and a multi-strip pullout apparatus is designed and constructed to investigate the influence of reinforcement density on the interface behavior. Results from the multi-strip test will provide practitioners guidance on reinforcement spacing when designing tall MSE walls.

Chapter 7 presents numerical modelling work that focuses on the behavior of tall MSE walls. Results from experimental investigations performed in Chapters 4, 5, and 6 are used to calibrate element specific pressure dependent numerical models in FLAC. A numerical model, representative of the west STIA MSE wall that incorporates the pressure dependent response into specific elements is validated against measurements taken during wall construction. The representative model is then subjected to a parametric study to assess the influence of specific factors such as soil stiffness, wall geometry, and soil-reinforcement stiffness on global wall behavior. Results from the parametric study are compared against current design methods to evaluate the applicability of these approaches to tall walls.

The anticipated conclusions of the proposed dissertation are summarized in Chapter 8 where the findings-to-date and anticipated conclusions are presented along with areas for future research. A complete list of references is provided in Chapter 9. Appendices A and B provide stress-strain-volumetric responses from laboratory tests conducted in plane strain, triaxial compression, simple shear, and triaxial compression stress paths in the large cubical true-triaxial device. Appendix C provides calculations and figures that facilitated the design of the multi-strip pullout test apparatus. Appendix D presents the multi-strip pullout test

results. Plots pertaining to the parametric study conducted in Chapter 7 are provided in Appendix F.

CHAPTER 2: LITERATURE REVIEW

2.1 INTRODUCTION

Mechanically stabilized earth walls are retaining walls that utilize reinforced earth technology to facilitate a steep grade transition. Prior to the pioneering work of Henri Vidal (1969) in reinforced earth over 50 years ago, rigid structural retaining walls built with concrete and steel were the predominant method of soil retention (Alzamora and Barrows 2007). Concrete gravity retaining walls are often selected for small grade transitions but costs of construction increase exponentially as the height increases (Berg et al. 2009a and 2009b). In the U.S. the use of MSE walls has increased greatly since its first application in California in 1972 due its ease of construction and flexibility. Historically, MSE walls have been used in roadway embankments, bridge abutments, and airport runways where right-of-way (ROW) is limited. The performance of MSE walls is primarily dependent on the interaction between the soil and the reinforcing material where vertical pressures are transferred to the reinforcement through shear stresses at the interface. As a result, MSE wall behavior is much more complex than concrete gravity retaining walls and highly dependent on the behavior of the reinforcement and backfill which is more prominent in taller MSE walls due to increases in confining stresses. This complexity has given rise to increased application of numerical modeling methods to determine the fundamental behavior and validate current design methods of MSE walls.

This chapter provides an overview of granular soil mechanics and a discussion is provided regarding the effect it has on MSE wall behavior. This is followed by a discussion focusing on the specifics of soil-structure interaction occurring at the reinforcement-soil

interface. Next, aspects of design methods that are pertinent to tall walls are discussed in detail. Lastly, a discussion regarding numerical modeling methods available in the literature are presented.

2.2 SEATTLE TACOMA INTERNATIONAL AIRPORT MSE WALLS

The large majority of research presented here will use data gathered from two tall MSE walls constructed as part of the Seattle Tacoma International Airport (STIA) third runway project. The walls were constructed to facilitate the grade raising for the third runway which are presented in Figure 2.1. The north MSE wall defines the northern boundary of the runway which is approximately 350 meters long and has a reinforced zone of 25.9 meters high with an exposed height of 23.6 meters. The wall consists of two tiers, with a 2.4 meter setback near mid-height. The 436 meter long west MSE wall has four tiers with 2.4 meter offsets. The tallest section has a 45.7 meter reinforced zone with an exposed height of 41.9 meters. A $2H:1V$ soil embankment slope with a crest height of 4.5 meters exists at the top of the wall. The ground slope behind the crest is at negative 3% to allow for drainage.



Figure 2.1. Aerial view of the STIA third runway and the north and west MSE walls (after Stuedlein et al. 2010).

The critical nature of the structure prompted designers to install strain gages on the reinforcement, inclinometers in the reinforced backfill, and digital monitoring points (DMP) on the wall face at the tallest sections to observe wall behavior. Cross sections of the two walls are presented in Figure 2.2, depicting instrument locations.

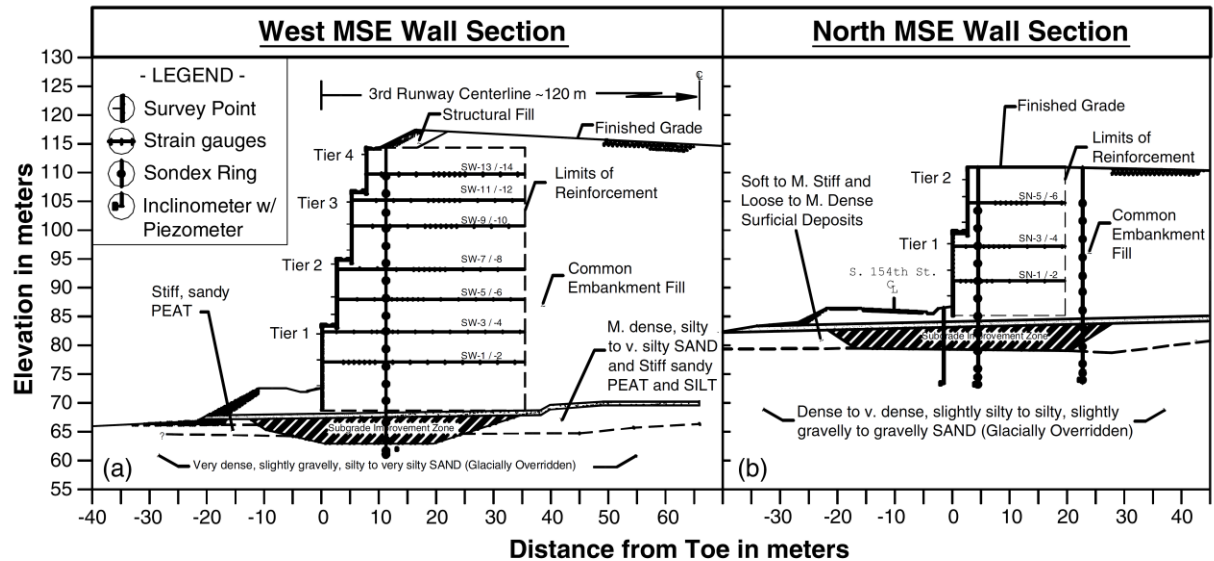


Figure 2.2. Cross section of the tall STIA MSE walls showing primary instrumented sections of the (a) west wall and (b) north wall (from Stuedlein et al. 2012).

Subsurface investigations below the footprint of the STIA MSE walls indicated the presence of 3-4 meters of soft peat with some loose to medium dense silty sand, underlain by glacially overridden dense to very dense, slightly gravelly, silty to very silty sand. The unsuitable subgrade was excavated to a depth of 4 meters and replaced with clean sandy gravel and gravelly sand. The reinforced backfill material was a well-graded gravelly sand that met specific gradational criteria that is more restrictive than the AASHTO recommendations. Reinforcement material consisted of ribbed steel strips with lengths that were evaluated on a tier-by-tier basis but were not less than 70 percent of the wall height.

Vertical reinforcement strip spacing ranged from 0.24 meters at the base of the wall to 0.78 meters. Horizontal reinforcement strip spacing ranged from 0.14 to 0.74 meters. A further discussion regarding the design and construction of the STIA MSE walls is provided in Stuedlein et al. (2010a).

2.3 BEHAVIOR OF WELL-GRADED GRAVELLY SOILS

The fundamental behavior of MSE walls is heavily influenced by the behavior of the reinforced backfill. Design guidelines typically specify well-graded granular soils that meet gradational criteria and minimum strength requirements usually characterized by conventional triaxial compression (CTC) and/or direct shear (DS) tests. However, MSE wall behavior is considered to behave in a two-dimensional fashion where the soil behavior is better approximated by plane strain (PS) tests where the available frictional strength is increased resulting increases in the intermediate principal stress.

True triaxial (TT) tests have been used extensively to characterize the behavior of granular soils incorporating the presence of a larger intermediate principal stress. Principal stresses in TT tests are typically controlled, allowing for the establishment of generalized three-dimensional soil responses that can be used to represent various loading conditions, including plane strain (Evans and Frost 2010). The majority of laboratory investigations that establish fundamental soil responses are performed primarily using uniformly distributed, poorly graded, sands with maximum particle sizes ranging from 0.15 to 5 mm (e.g. Bolton 1986, Colliat-Dangus et al. 1988). However, soils used in MSE walls are typically well-graded with maximum particle sizes as large as 101 mm (Berg et al. 2009a and b) which are not well represented by laboratory soils. Nonetheless, theories developed based on uniformly

distributed particles are used in practice to predict soil behavior. The following section discusses fundamental soil behavior that is pertinent to MSE wall behavior with specific emphases on the influence of soil particle characteristics, flow behavior, the intermediate principal stress, and soil anisotropy on the frictional strength of granular soils.

2.3.1. EFFECT OF PARTICLE SIZE, SHAPE AND GRADATION

A large quantity of research available in the literature focuses on small uniformly graded sands that can be mathematically simulated as uniform spheres (e.g. Rowe 1962, Cornforth 1964, Barden et al. 1969, Rawat and Ramamurthy 1976, Green 1975, Ramamurthy and Tokhi 1981, Colliat-Dangus et al. 1988, and Lade and Bopp 2005). Granular soils encountered in real design scenarios are typically not well represented by spherical uniform granular material. A summary of results from CTC on uniform quartz and Ottawa sands performed by Koerner (1970) determined that peak frictional angles increase with angularity and density; however reductions in the friction angle were observed with increases in the particle size. Similarly, results from CTC on uniform Leighton Buzzard sand and glass beads performed by Kirkpatrick (1965) also observed reductions in friction angle with increases in angularity, in contradiction to Kolbuszewski and Frederick (1963). Kirkpatrick (1965) conducted triaxial tests with different coefficient of uniformities, C_u , values to assess changes in the frictional response resulting from gradational differences of uniform sands and determined that the comparison is complicated by changes in the limiting porosity. As a result, a simple comparison between tests with different gradations is difficult.

More recently, a large database of uniform sands, established by Cho et al. (2006) determined that the behavior of the soil at critical state is dependent on the particle roundness

and an empirical relationship was fitted to the database. A large portion of research in the literature focuses on the behavior of uniformly graded rockfill material with large particle diameters ($d_{50} > 10$ mm). Tests on these soils exhibit large quantities of particle breakage which influences the behavioral response (Marsal 1967, Fumagalli 1969, Marachi et al. 1972, Charles and Watt 1980, Thiers and Donovan 1981, Indraratna et al. 1993, Honkanadavar and Sharma 2014, Xiao et al 2014). Similar to uniform sand the available literature on rockfill materials suggests that increases in particle size reduce the peak friction angle. As a result, the behavior of uniformly distributed particles is relatively similar for given angularities and mineral content.

The behavior of uniform soils has been well documented; however the stress-strain strength and volumetric behavior of well-graded soils ($C_u > 20$) is less understood and the available literature is limited. The first tests on well-graded gravelly river deposited ($d_{50} = 1.5$ to 9 mm, $C_u = 6.25$ to 10) and quarried soils ($d_{50} = 10, 19.1$ mm, $C_u \approx 270, 85$) performed by Holtz and Gibbs (1956) suggested that increases in the gravel content and particle angularity resulted in increases in shear strength. Al-Hussaini (1983) performed triaxial compression, extension and plane strain tests on crushed basalt with different gradations and median particle sizes ($d_{50} \approx 3.2$ to 38.1 mm, $C_u = 3.31$ to 11.6) at high confining stresses and concluded that compressibility decreases with increases in C_u , the strength is not influence by the stress path during consolidation, and the strength is similar in triaxial compression and extension. Additionally, observed shear strengths in plane strain were higher than those in triaxial compression or extension. Large scale triaxial compression tests on coarse fluvial soils ($d_{50} = 8.5$ to 37 mm, $c_u = 0.3$ to 3.84) performed by Verdugo and de la Hoz (2006) show that at low confining stresses the measured friction angle in triaxial compression approaches

70 degrees and there is little effect on the peak strength when the parallel gradation technique is used. Large scale triaxial tests performed by Zhao et al. (2013) on well-graded gravelly colluvial soils ($d_{50} = 0.015$ to 3.5 mm, $C_u = 0.42$ to greater than 200) to determine the effect of coarse content on the compressibility and shear strength under low confining pressures ($\sigma'_c < 25$ kPa) showed that the critical or constant volume friction angle is a function of the mean and maximum particle diameter and the quantity of the fines content.

Laboratory investigations on well graded gravelly soils presented in the literature is limited to triaxial compression tests, low confining stresses, or compressibility tests. As a result, an extensive investigation into the behavior of well graded gravelly soils over a wide range of confining pressures is warranted.

2.3.2. *STRESS-DILATANCY OF GRANULAR SOILS*

Typical constitutive model frameworks use associative flow behavior to bound the attainable state of stress and regulate the mechanisms that control plastic deformation (Roscoe et al. 1958, Schofield and Wroth 1968, Wood 1990). In granular soils, the most commonly used flow rule was developed by Rowe (1962) for uniform spherical particles where plastic deformations stem from dilation and inter-particle sliding (Taylor 1948). Dilation is the global representation of particles being forced to move around each other during shearing. Many investigators (e.g., Penman 1953, Bishop 1954, Newland and Allely 1957, Poorooshasb and Roscoe 1961, Rowe 1962, Rowe et al. 1964) have attempted to develop a theoretical understanding of the components and the inter-particle behavior during shearing. Lee and Seed (1967) separated the available strength of soil into three components: (1) dilatancy, (2) particle reorientation, and (3) sliding friction effects.

The strength and dilatancy of soils received a significant amount of focus in the 1960's pioneered by the early work of Taylor (1948). Since then two schools of thought have developed by Rowe (1964) and Poorooshasb and Roscoe (1961), differences being associated with treatment of non-elastic volume changes. Subsequently, Rowe's stress dilatancy theory has become a widely used form of predicting flow behavior of soils due to its ability to capture plastic volume changes. Rowe (1962, 1969) and Rowe et al. (1964) used the minimum energy principal to develop a saw-tooth model for plane strain and axisymmetric testing where the possible failure plane is modified based on the quantity of dilatancy (De Josselin de Jong 1976). The theory was developed assuming uniform spherical particles in a generalization of the Coulomb-Rankine expression for a friction angle that has been corrected for dilatancy effects, ϕ'_{fr} , and assumed associated flow behavior (i.e. the peak friction angle occurs at the same axial strain as the peak dilation angle). The major principal effective stress ratio, defined as the ratio of the major principal stress, σ'_1 , to the minor principal stress, σ'_3 , given by Rowe's theory in compression is given by:

$$\frac{\sigma'_1}{\sigma'_3} = KD \quad (2.1)$$

where K is equal to $\tan^2(45 + \phi'_{fr}/2)$, D is the dilatancy factor and is equal to $(1 + d\varepsilon_v/d\varepsilon_1)_f$, and subscript f denotes quantities at failure. Based on Rowe's stress-dilatancy theory, Horne (1965) found that the maximum value for D is limited to two, indicating that the mobilized dilation angle, ψ_m , is limited to 19.5 degrees given by (Rowe 1969):

$$\psi_m = \sin^{-1} \left(\frac{\sin(\phi'_m) - \sin(\phi'_{cv})}{1 - \sin(\phi'_p) \sin(\phi'_{cv})} \right) \quad (2.2)$$

and the constant volume friction angle, ϕ'_{cv} , is defined as:

$$\phi'_{cv} = \sin^{-1} \left(\frac{\sin(\phi'_p) - \sin(\psi_p)}{1 - \sin(\phi'_p) \sin(\psi_p)} \right) \quad (2.3)$$

where ϕ'_p and ψ_p are the friction and dilation angles measured at peak principal effective stress ratio. The dilation angle during shear is given by (e.g., Frydman et al. 2007):

$$\sin(\psi) = - \frac{d\varepsilon_v}{|d\gamma_s|} = - \frac{d\varepsilon_1 + kd\varepsilon_3}{d\varepsilon_1 - kd\varepsilon_3} = - \frac{d\varepsilon_v / d\varepsilon_1}{2 - d\varepsilon_v / d\varepsilon_1} \quad (2.4)$$

where k is equal to one for plane strain and two for triaxial compression, $d\gamma_s$ is the change in shear strain, $d\varepsilon_v$ is change in volumetric strain, $d\varepsilon_1$ is the major principal strain and $d\varepsilon_3$ is the minor principal strain.

An empirical approach to estimate the stress-dilatancy behavior of uniform sands was developed by Bolton (1986) using a database of 17 uniform sands and a relative dilatancy index, I_R :

$$I_R = D_R \left[Q - \ln \left(\frac{P'}{P'_{ref}} \right) \right] - R \quad (2.5)$$

where p'_{ref} is a reference mean effective stress (typically equal to 1 kPa), D_R is the relative density in decimal form, and empirical fitting coefficients Q and R equal 10 and 1, respectively. The statistical regression for the dilatational friction component:

$$\phi'_p - \phi'_{cv} = A_{\psi,PS} I_R = A_{\psi,TC} I_R \quad (2.6)$$

and $A_{\psi,PS} = 5$, $A_{\psi,TC} = 3$, and subscripts PS and TC denote plane strain and triaxial compression, respectively. The rate of dilation at failure may be approximated by (Bolton 1986):

$$\left(- \frac{d\varepsilon_v}{d\varepsilon_1} \right)_f = B_v I_R \quad (2.7)$$

where $B_v = 0.3$ for PS and TC. Bolton (1987) presented data on Toyoura sand to show that Bolton's (1986) empirical relationship over-predicts the ψ_p at low mean effective stresses ($p' < 150$ kPa). Bolton (1987) attributed the resulting error to increases in the ϕ'_{cv} with reductions in σ'_3 , and proposed improved empirical correlations as a function of p' . Salgado et al. (2000) and Chakraborty and Salgado (2010) analyzed the results of previous studies on Toyoura sand to determine Bolton's fitting parameters at low mean effective stresses and found that Q empirically reduces with decreases in σ'_3 below 50 kPa. The use of Bolton's (1986) stress dilatancy approximation to estimate the dilatational response of well-graded

granular materials is done with little providence given to the assumptions used in developing Rowe's (1969) theory.

2.3.3. EFFECT OF INTERMEDIATE PRINCIPAL STRESS

In typical design practice, frictional strengths resulting from CTC tests are assumed to be valid for a wide range of in-situ loading conditions even though it has been well documented that stress-strain volumetric response is dependent on the three-dimensional loading path (Kjellman 1936, Bardet 1997). Kjellman (1936) conducted the first true triaxial tests on uniform sand which emphasized the importance of the intermediate principal stress. Since then, devices that control and quantify stresses in the intermediate direction have proliferated (Arthur 1988). Several investigators (Bishop 1966, Sutherland and Mesdary 1969, Green 1971, Lade and Duncan 1973, Ramamurthy and Rowat 1973, Matsuoka and Nakai 1974, Shankariah and Ramamurthy 1980, Ergun 1981, Haruyama 1981) have shown that incorporation of σ'_2 affects the available shearing resistance.

It is convenient to summarize the effect of the intermediate stress using an effective intermediate deviatoric stress ratio, b , where:

$$b = \frac{(\sigma'_2 - \sigma'_3)}{(\sigma'_1 - \sigma'_3)} \quad (2.8)$$

The magnitude of b is stress path dependent (Habib 1953) and bounded between zero (i.e., CTC) and unity (i.e., CTE). Discussions provided by Bishop (1966) regarding CTC, CTE, and PS tests conducted by Cornforth (1961) on loose and dense Ham river sand ($d_{50} = 0.25$ mm, $C_u = 2.07$) suggested that no increase in the friction angle is observed as the b -value

increases from zero to unity. Conversely, a large number of investigators (e.g. Lade and Duncan 1973, Ramamurthy and Rowat 1973, Reades and Green 1976, Shankariah and Ramamurthy 1980) have shown that increasing the intermediate principal stress increases the measured resistance. Figure 2.3 presents a summary of methods that capture the frictional responses of uniform sands resulting from changes in the intermediate principal stress. In general, increases in the intermediate stress increase the effective friction angle at failure, ϕ' , up to a b -value of 0.4. Increases beyond this value seem to produce different frictional responses depending on the material and the testing device (Sayao and Vaid 1996).

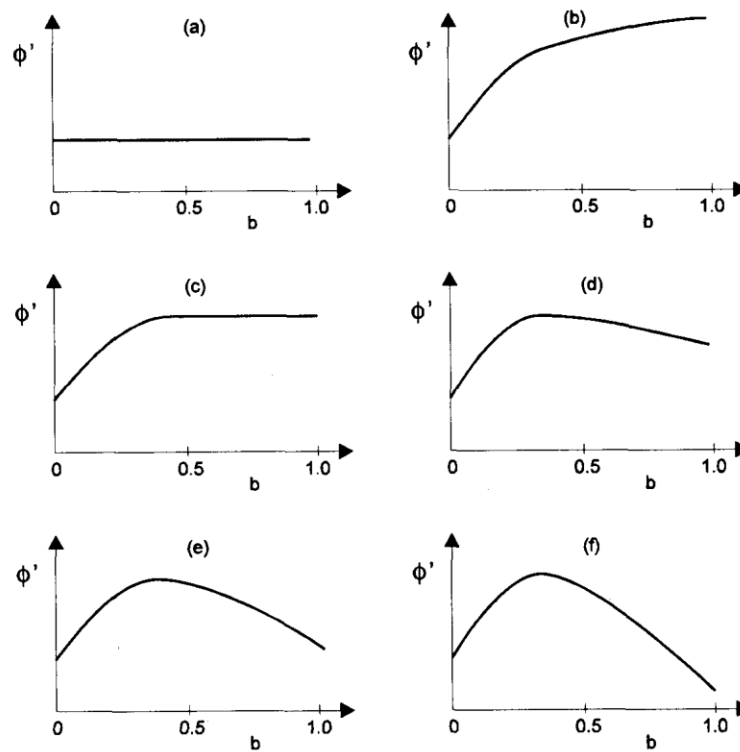


Figure 2.3. Changes in frictional angle due to the effect of the intermediate principal stress by reference: (a) Bishop (1966); (b) Lade and Duncan (1973), Reades and Green (1976); (c) Green (1971), Lade and Duncan (1973); (d) Ergun (1981), Haruyama (1981); (e) Sutherland and Mesdary (1969), Ramamurthy and Rowat (1973); (f) Shankariah and Ramamurthy (1980), (adapted from Sayao and Vaid 1996).

Figure 2.3 is a simplified representation of a three dimensional failure criterion which is better visualized in a three dimensional stress space which is presented in Figure 2.4. The Mohr-Coulomb failure criterion (M-C) developed by Coulomb (1773) was developed specifically for soils and is represented in terms of stresses by:

$$\tau = \sigma' \tan(\phi') + c \quad (2.9)$$

where τ is the shear stress, and c is the apparent cohesion component, typically negligible in granular soils, and:

$$\sin(\phi') = \frac{\sigma'_1 - \sigma'_3}{\sigma'_1 + \sigma'_3} \quad (2.10)$$

Although Equation (2.10) is a simple and widely used relationship to calculate the effective friction angle, it does not incorporate the effect of the intermediate principal stress (Mesdary et al. 1970).

The Matsuoka Nakai (M-N) failure surface, presented in Figure 2.4 in the deviatoric stress plane, was initially validated using triaxial compression, extension, and plane strain tests on loose uniform Toyoura ($d_{50} = 0.16$ mm, $C_u = 1.46$) and Ottawa ($d_{50} = 0.21$ mm, $C_u = 2.09$) sands. In terms of a deviatoric stress space, the M-N failure criterion is expressed as (Bardet 1997, Leroueil and Hight 2003):

$$K = \sqrt{\frac{J_1 J_2 - 9 J_3}{9 J_3}} = \frac{I_1 I_2}{I_3} = \frac{9 - \sin^2(\phi')}{1 - \sin^2(\phi')} \quad (2.11)$$

where K is equal to a constant, I_1 , I_2 , and I_3 are the first, second, and third effective stress invariants, and J_1 , J_2 , and J_3 are the first, second, and third effective deviatoric stress invariants. The Lade and Duncan (1975) failure criterion (L-D) also presented in Figure 2.4, was initially developed in principal stress space using cubical triaxial tests and ring torsion shear tests conducted by Lade and Duncan (1973) on loose and dense Monterey No. 0 sand ($d_{50} = 0.43$ mm, $C_u = 1.53$). The L-D failure criterion was validated by tests conducted on uniform Ottawa sand (Ko and Scott 1968) dense uniform River Welland Sand (Procter and Barden 1969) and dense uniform Ham River sand (Green and Bishop 1969) and can be expressed as:

$$\kappa = \frac{I_1^3}{I_3} = \frac{[3 - \sin(\phi')]^3}{[1 - \sin(\phi')] \cos(\phi')^2} \quad (2.12)$$

where κ is a constant. Good agreement has been found between cubical triaxial tests on poorly graded Chiba gravel ($d_{50} = 6.6$ mm, $C_u = 1.6$) and the L-D failure surface (Biggerstaff 2010).

The PS frictional strength can be determined from a soil specific three-dimensional failure criterion given that typical PS b values range from 0.20 and 0.40 depending on sample density and anisotropy (e.g., Green 1971, Reades and Green 1976, and Peters et al. 1988). However, unless the material is uniform laboratory sand, a series of expensive TT or PS tests are required to calibrate the three-dimensional failure criterion. Practitioners often rely on empirically or semi-empirically based methods to estimate PS response of granular soils based on DS or CTC tests.

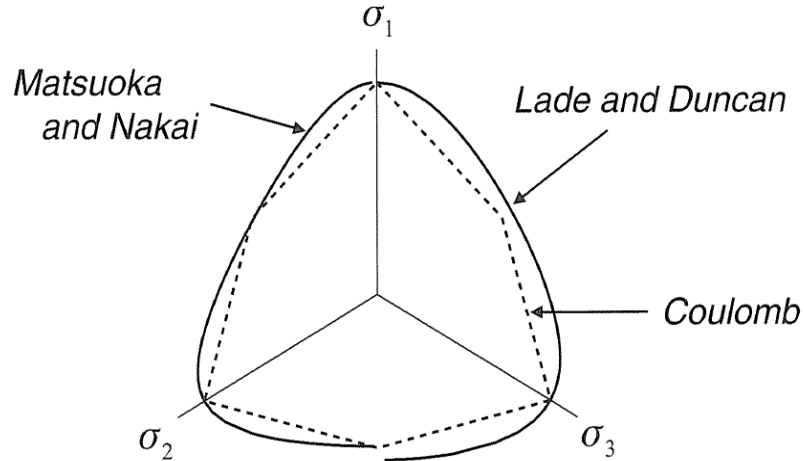


Figure 2.4. Comparison of the Matsuoka-Nakai (M-C), Lade-Duncan (L-D), and Mohr-Coulomb (M-C) failure yield surfaces in the deviatoric plane (Davis and Selvadurai 2002).

Rowe (1969) used Equation (2.1) in conjunction with Mohr's circles of stresses and strains and direct shear tests on Mersey River sand ($d_{50} = 0.5$ mm, $C_u \approx 1.6$) to develop a simple yet fundamental relationship between the DS friction angle, ϕ'_{ds} , and PS friction angle, ϕ'_{ps} , which is given by:

$$\tan \phi'_{ds} = \sin \phi'_{ps} \cos \phi'_{cv,ds} \quad (2.13)$$

where $\phi'_{cv,ds}$ is the constant volume friction in direct shear. Jewell and Wroth (1978) conducted direct shear tests on Leighton buzzard sand ($d_{50} = 0.9$ mm, $C_u = 1.2$) providing additional evidence to the validity of Equation (2.13) and suggested if $\phi'_{cv,ds}$ is not available it could be replaced with a safety factor of 0.8 based on typical values of $\phi'_{cv,ds}$ for uniform sands.

Lade and Lee (1976) proposed an empirical relationship to convert CTC friction angles, ϕ'_{ctc} , to PS friction angles which is given by:

$$\text{If } \phi'_{ctc} > 34^\circ \quad \phi'_{ps} = 1.5\phi'_{ctc} - 17 \quad (2.14a)$$

$$\text{If } \phi'_{ctc} \leq 34^\circ \quad \phi'_{ps} = \phi'_{ctc} \quad (2.14b)$$

Good agreement was found by Lee (2000) between Equation (2.14)(2.14a) and measured PS friction angles for sands with angular grains at low confining stresses but produced poor estimates for rounded grain Ottawa sand at similar pressures.

The available literature on the influence of the intermediate principal stress on granular soil response has focused on uniformly graded sands which are not physically representative of typical soils used in MSE walls. As a result, in order to accurately predict MSE wall behavior, additional studies focusing on the PS behavior of well-graded gravelly soils should be conducted to assess the accuracy of the theoretical, semi-empirical, and empirical methods used to predict its response.

2.4 REINFORCEMENT-SOIL STRUCTURE INTERACTION

Some of the earliest MSE walls constructed used smooth steel strips as a reinforcing material. It is widely accepted that the load-displacement behavior of reinforcements in a soil mass is dictated by the soil-structure interaction. Consequently, the behavior of MSE walls is strongly dependent on the soil-reinforcement interface characteristics which are usually characterized using single strip pullout tests or direct shear interface testing (Vidal 1969, Lee et al. 1973, Chang and Forsyth 1977).

2.4.1. DIRECT SHEAR INTERFACE FRICTIONAL RESPONSES

Shear stresses at the interface of smooth steel strips develop solely due to friction between the soil and surface of the reinforcement (Lee 1978). Early applications of direct shear interface tests were used to determine conservative estimates of an interface friction angle, δ , for smooth planar reinforcements (Potyondy 1961, Uesugi and Kishida 1986). More recent laboratory investigations on the soil-structure interface response (Frost et al. 1999, Hebeler 2004) have indicated that there are two modes of shearing at the interface: (1) particle slippage along the structures surface and (2) shearing within the adjacent granular material. Slippage along the surface of the structure is expected to occur under conditions where the surface is smooth compared to the particle size, the normal stress is small enough that particles do not embed in the surface, and the surface is hard enough that abrasive wear is negligible during sliding. When these conditions are satisfied the expected zone of failed soil (i.e. shear band thickness) has been shown to be on the order 1 to 2 D_{50} from the interface (Frost et al. 2004). Generally, larger shear bands form in the adjacent soil when these conditions do not exist. For example, studies on geosynthetic reinforcement-soil interface behavior by Dove and Frost (1999) indicate that the frictional response is a combination of adhesion and plowing, dependent on the material stiffness. There are little studies that investigate the rubber-interface behavior of neoprene materials.

The increasing popularity and demand for taller MSE walls have prompted designers to use closely spaced reinforcements and prompted the Reinforced Earth Company (ReCO) to develop steel reinforcements with trapezoidal ribs that increase the roughness of the soil-reinforcement interface and subsequently the pullout resistance. A theoretical stress transfer mechanism is presented in Figure 2.5 where the total shearing resistance is a combination of

frictional sliding along the smooth parts of the interface and passive resistance at the rib locations (Christopher et al. 1990a and 1990b). However, direct shear interface tests conducted by Irsyam and Hryciw (1991) and Hryciw and Irsyam (1993) on Ottawa 20-30 and Glazier Way 20-30 sands with varying rib geometries have shown that the quantity of passive resistance is dictated by the shape and spacing of the rib. Results from this investigation indicate that square ribs, or ribs with 90 degree asperity angles, were able to form passive failure surfaces and were most efficient when the rib spacing was 10 to 13 times the asperity height. The results also showed that trapezoidally shaped ribs do not produce enough resistance in the soil to form passive log spiral failure surfaces and should be treated as rough reinforcements (Uesugi 1986).

Similarly, a systematic experimental investigation on soil-metal interface behavior conducted by Dove and Jarrett (2002) has indicated that this behavior is controlled by the rib dimensions, spacing, and mean particle diameter. Dove and Jarrett (2002) showed that peak interface efficiency occurs when the height of the rib and the rib spacing are approximately equal to the mean particle diameter, and one to three times the mean particle diameter, respectively.

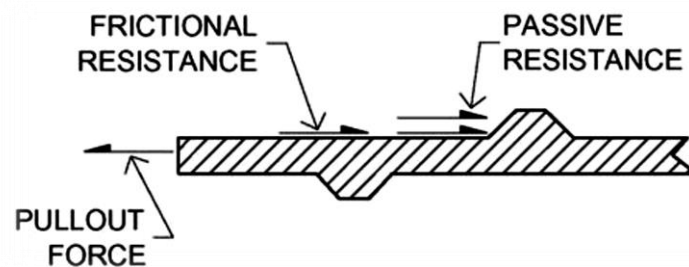


Figure 2.5. Stress transfer mechanisms for ribbed steel strips (Mitchell and Christopher et al. 1990a and 1990b).

Additionally, ribs with asperity angles greater than 50 degrees will likely form passive failure surfaces whereas asperity angles less than this allow grains to traverse over the rib and produces volume changes and an interface strength less than the frictional strength of the soil. As a result, the expected zone of influence that forms in the adjacent soil is a function of the mean particle diameter, and roughness of the reinforcement.

As MSE walls are being constructed to greater and greater heights, reinforcement spacing values are becoming smaller and smaller to accommodate the increases in vertical confining stress. The most common types of steel strip reinforcing used in tall MSE walls have non-uniform spacing patterns with similar rib geometry to that tested by Hryciw and Irsyam (1993). The reported shear band thickness at failure of the trapezoidally ribbed specimen is on the order of $6d_{50}$, however, the results of numerical direct shear tests conducted by Wang et al. (2007) indicated that observable shear strains develop as far as $25 D_{50}$ from the interface. As the need for smaller reinforcement spacing increases, the potential for overlapping stress behavior and frictional interference between reinforcing strips becomes more of a design concern even though very little work has been done to study this behavior.

2.4.2. PULLOUT RESISTANCE AND APPARENT FRICTION COEFFICIENT

Pullout tests are often performed to determine the reinforcement-soil interface characteristics and because they overcome some of the drawbacks associated with direct shear tests (e.g. stress concentrations at the edges, small range of displacements, small sample size). As a result, comparisons between direct shear soil-grout interface tests and soil nail pullout tests indicated that pullout tests produce higher peak unit frictional resistances (Chu and Yin 2005). Early pullout tests conducted by Alimi et al. (1978) and Schlosser and Elias

(1978) used smooth and ribbed single strips in uniform sands to quantify the interface behavior based on the load-displacement response. Several investigators (Chang et al. 1974, Schlosser and Guilloux 1979, Ingold 1983, Rowe et al. 1985, Palmeira 1987, Juran and Christopher 1989) have adopted different pullout tests techniques (Figure 2.6) to minimize the effect of boundary conditions on the load-displacement response.

However, Palmeira and Milligan (1989) assessed the effect of boundary conditions by performing a series of medium and large scale pullout tests on grid reinforcements and found that the load displacement response is greatly influenced by the front facing boundary conditions. Results from a series of pullout tests with different front face frictional characteristics presented in Figure 2.7 show that increasing the front face interface friction angle, μ , produced much larger peak responses. Palmeira and Milligan (1989) concluded that developing passive pressures increase the normal stress near the front wall face and suggested that this effect could be minimized by reducing μ . However, to date there is no standardized method that completely mitigates the effect of passive pressures at the front face on the pullout load-displacement response.

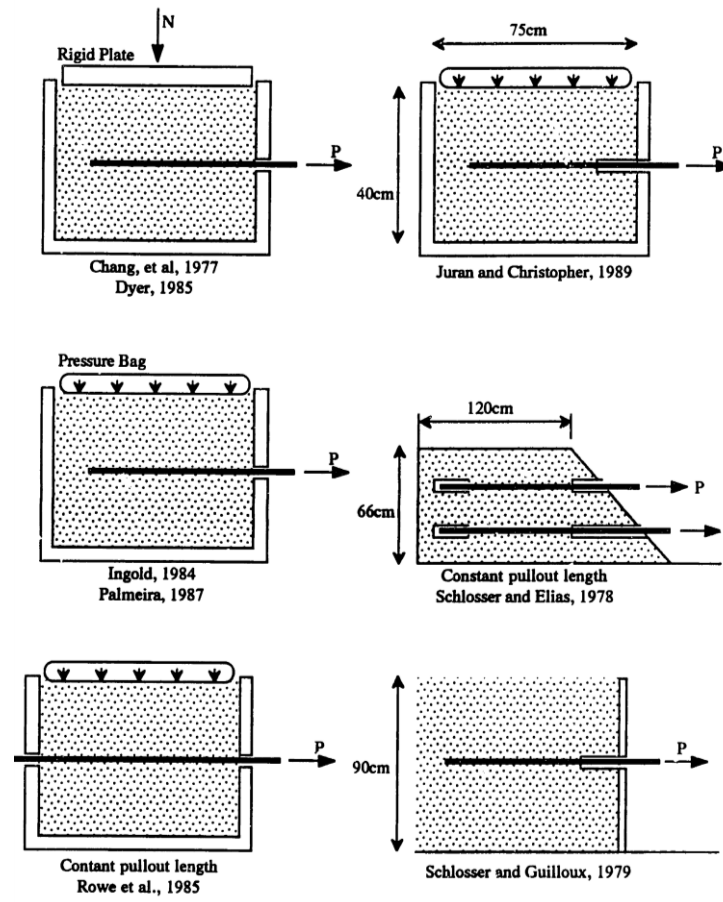


Figure 2.6. Testing techniques and boundary conditions presented in the literature (after Larson 1992).

The parametric study conducted by Schlosser and Elias (1978) concluded that three fundamental factors affecting the load displacement behavior are the effective overburden stress, backfill density, and reinforcement surface characteristics. Alimi et al. (1978) and Schlosser and Elias (1978) established a design parameter that captured the peak pullout response of a reinforcement material. The apparent friction coefficient, f^* , (e.g. friction bearing interaction factor or unit frictional resistance) determined from pullout load displacement data and is given by:

$$f^* = \frac{P_{max}}{\sigma_v A_s} \quad (2.15)$$

where P_{max} is the maximum load observed during the pullout test. Observations from pullout tests showed that increases in the overburden stress reduced the measured f^* which Schlosser and Elias (1978) attributed to dilatancy effects.

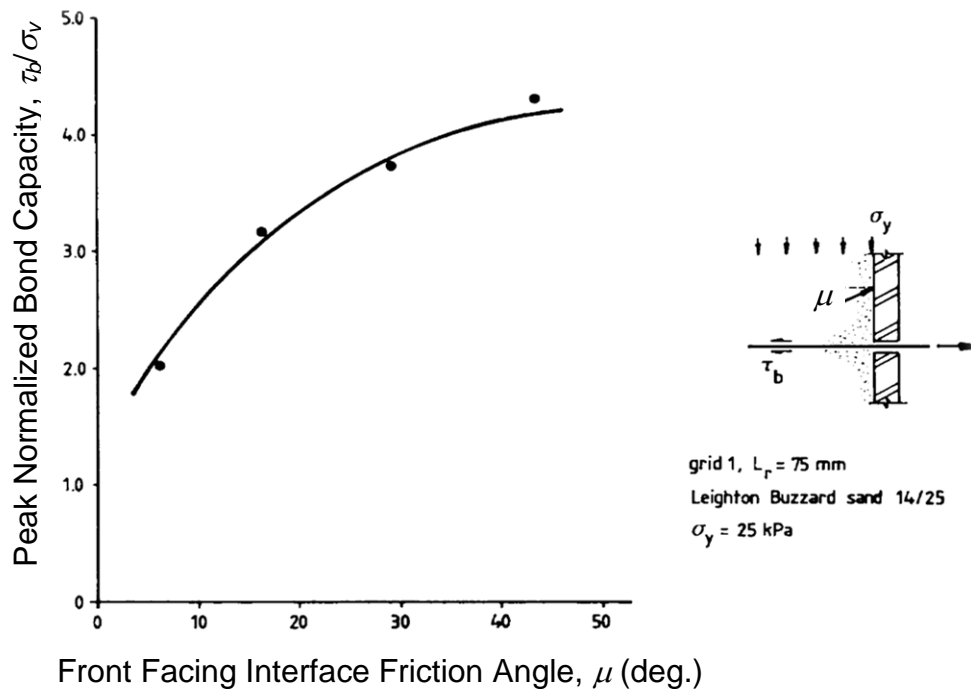


Figure 2.7. Frictional resistance during pullout tests with different front facing friction conditions (adapted from Palmeira 1987).

The majority of pullout tests on metallic strip reinforcements presented in the literature are performed using uniformly graded sands and smooth planar reinforcements (Schlosser and Elias 1978, Guilloux et al. 1979, Abramento and Whittle 1995, Lee 2005) even though MSE walls are typically constructed with well-graded soils. Results from the few studies

that do perform single strip pullout tests on well-graded granular materials (McKittrick 1978, Boyd 1993, Jayawickrama 2014) are presented in Figure 2.8. However, these results do not give consideration given to front face boundary condition effects. As a result, the extensive investigation of ribbed steel strips provided by Jayawickrama (2014) could not determine any relationship between strip length and f^* which indicates that the measured responses could be artificially altered by passive pressures forming at the front face (Palmeira and Milligan 1987).

Variability in the apparent friction coefficient is associated with difference in soil gradation, particle shapes, and testing apparatuses as described previously. Investigators rarely accompany basic soil characteristic information (e.g. particle gradations and angularity) with pullout testing information and the effect of these variables is not quantifiable using available literature. Additionally, all previously reported pullout tests use single reinforcement strips that are not able to capture changes in the steel strip reinforcement response stemming from reinforcement density.

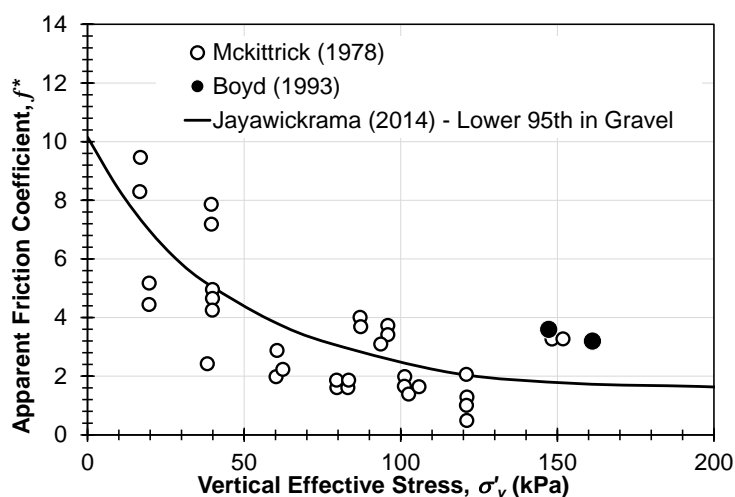


Figure 2.8. Apparent friction coefficient versus effective vertical stress data originally used to calibrate the pullout design procedure.

2.5 DISCUSSION REGARDING MSE WALL DESIGN METHODS

Several methods are available to engineers to predict required reinforcement strength, spacing, and length in order to ensure the stability of MSE walls. These methods include the Coherent Gravity method (Schlosser, 1978; Juran and Schlosser, 1978; Schlosser and Segrestin, 1979), the FHWA Structure Stiffness method (Christopher et al., 1990a and 1990b; Christopher, 1993), the Ehrlich and Mitchell (1994) method, the Simplified method (Elias and Christopher, 1996; Allen et al., 2001, Elias et al., 2001) and the K-Stiffness method (Allen et al., 2004). Differences between the methods include the type of friction angle specified in the design procedures (plane strain or triaxial/direct shear), consideration of imposed vertical stresses (geostatic with or without overturning stress), consideration of reinforcement density, and consideration of compaction stress. However, most of these design methods are empirically calibrated using walls that are less than 20 meters in height. Detailed discussions regarding MSE wall design methods are provided by Elias et al. (2001), AASHTO (2010), Berg et al. (2009), Washington State Department of Transportation (2012), and Walters (2013). As a result, extension of current design procedures to tall multi-tiered MSE walls requires careful consideration of specific wall components. The following section discusses available literature regarding pertinent design components that effect the behavior of tall steel strip reinforced multi-tiered MSE walls.

2.5.1. EFFECTS OF TIER HEIGHT AND OFFSET

Reinforcement tensile loads in vertical MSE walls generally increase with increases in wall height and are often mitigated by separating the wall facing into smaller tiers and reducing the reinforcement spacing. The use of offset tiers has prompted design guidelines

where internal reinforcement loads are estimated using limit equilibrium and lateral earth pressure methods, depending on wall batter angle. The increasing need for multi-tiered MSE walls has prompted investigators to perform studies using limit equilibrium methods that have been extended to design charts to estimate required reinforcement lengths and tensile forces (Wright 2005). Additional studies (e.g. Leshchinsky and Han 2004, Mohamed et al. 2014) have assessed the validity of assumptions made in multi-tier MSE wall design, however, these investigations have generally been limited to two or three tiered geosynthetically reinforced walls. General results from these studies indicate that increasing the tier offset distance reduces tensile loads in the reinforcement accordingly (Leshchinsky and Han 2004).

Multi-tiered MSE walls are often designed assuming an equivalent batter angle, especially if the offset distances are relatively small. The Federal Highway Administration (FHWA) specifies that multi-tier MSE walls with equivalent batter angles less than 70 degrees be treated as reinforced slopes and designed using limit equilibrium methods. Conversely, MSE walls with equivalent batter angles greater than 70 degrees are to be designed using lateral earth pressure approaches. However, limit equilibrium methods generally assume uniform mobilization of resistance along reinforcements (Wright 2005) which is in contrast with tensile stress measurements of reinforcement loads in MSE walls (Damians et al. 2014). The assumptions used in lateral earth pressure methods are significantly different from those used in limit equilibrium approaches even though no fundamental differences between reinforced slopes and MSE walls have been acknowledged. The development of new design methods could overcome the limitations associated with current design assumptions, thus producing more efficient and fundamentally sound methods.

2.5.2. *RIGIDITY OF THE FRONT FACING*

Of the lateral earth pressure methods, the Coherent Gravity and Ehrlich and Mitchell methods consider increases in vertical stresses due to an assumed rigid body behavior of the reinforced soil mass using overturning stresses. The developers of the Coherent Gravity and Ehrlich and Mitchell methods (Schlosser 1978, Juran and Schlosser 1978, Schlosser and Segrestin 1979, Ehrlich and Mitchell 1994) assumed that soil reinforced with steel strips led to a relatively rigid, coherent mass that acted monolithically, similar to concrete gravity structures. Accordingly, they selected the method developed by Meyerhof (1953) for determining vertical pressure and subsequently reinforcement load increases, which is based on eccentrically loaded footings. However, Allen et al. (2001) collected a series of total stress cell measurements to evaluate the effect of overturning stress and found that although increases in the vertical stress were observed, they were only slightly effected by the assumption of rigidity. Discussion provided by Stuedlein et al. (2012) regarding the tall STIA MSE walls suggested that this behavior is not surprising given their inherent flexible nature, even at tight reinforcement spacing. The assumption of a rigid reinforced structure may not be valid for use with MSE walls but the effects are considered to be small in comparison to other key factors (e.g. confining stress, soil friction angle, and reinforcement spacing) (Bathurst et al. 2008).

The largest increases in vertical stresses were observed nearest to the wall face which Allen et al. (2001) attributed to down drag forces initially observed by Christopher (1993). Down drag forces at the front facing are caused by outward displacements of the stabilized earth mass, compaction of the retained earth mass, compression of the retained earth mass under the self-weight of the soil, and differential settlement of the soil foundation (Damians

et al. 2013). Methods of estimating down-drag forces in steel strip reinforced MSE walls have been limited to numerical simulations due to the complex nature of their formation and dependency on the facing stiffness. In segmental panel systems commonly used in MSE walls, bearing pads installed at the horizontal joints maintain sufficient spacing between panels to mitigate spalling and cracking while still allowing vertical loads to be carried through the entire height of the wall (Neely and Tan 2010). Estimating vertical loads and subsequently vertical deformations in the panel facing are difficult using limit equilibrium methods because down forces are primarily attributed to differential settlement between the backfill soil, facing, and complex interactions at the reinforcement connections. However, numerical modelling has shown that down drag forces can be twice the self-weight of the concrete facing (Damians et al. 2014) and can alter the deformation profile of the retained soil mass (Rowe and Ho 1998). This behavior is likely to be amplified in tall walls where vertical down drag forces are increased

2.5.3. CURVATURE IN THE MOHR FAILURE ENVELOPE

The behavior of the reinforced backfill is controlled by the relative density, gradation, surface characteristics, and the strength of the particle as discussed in Chapter 2. It is generally accepted that increases in the confining stress produces reductions in the friction angle as the tendency for soil to dilate is reduced (Duncan et al. 1980). However, current MSE wall design methods use a failure envelop that does not consider this behavior. The assumption of a linear failure surface may be adequate for typical walls where confining stresses are small. In fact, the database established by Allen et al. (2001 and 2004) that were used to calibrate the Simplified and K-stiffness methods and assess the accuracy of the

Coherent Gravity method is limited to wall heights of 18 meters which corresponds to confining stresses of 78 kPa. Conversely, the estimated confining stress at the base of the wall, including the slope fill surcharge, is approximately 221 kPa. Considering the potential change in the friction angle for a well graded limestone material over this range in pressures could be as high as 10 degrees (Duncan et al. 2007) use of a single value of effective friction angle in the calculation of reference active lateral earth pressures may not be appropriate.

2.5.4. GLOBAL AND LOCAL REINFORCEMENT STIFFNESS

An alternative method to mitigating high reinforcement loads is to reduce the vertical and horizontal reinforcement spacing. Changes in reinforcement spacing are often incorporated into design procedures using local and global stiffness parameters that have been recognized as one of the most important parameters in typical MSE wall design (Christopher et al. 1990a, and 199b, Ehrlich and Mitchell 1994, Neely 1995, Allen et al. 2004). However, the Simplified and Coherent Gravity methods do not consider reinforcement stiffness. Conversely, the K-stiffness and Ehrlich and Mitchell methods directly incorporate the reinforcement stiffness. The local stiffness parameter for strip reinforcements is given by:

$$S_{local} = \frac{EA_s}{S_v S_h} = \frac{J}{S_v} \quad (2.16)$$

where E is the Young's modulus of the reinforcement, A_s is the area of the strip, J is the reinforcement stiffness, S_v and S_h are the vertical and horizontal reinforcement spacing, respectively. The global reinforcement stiffness represents an average local stiffness value and is given by:

$$S_{global} = \frac{EA_s}{\left(\frac{H}{n_s}\right) S_{v,ave}} = \frac{J_{ave}}{\left(\frac{H}{n_s}\right)} \quad (2.17)$$

where subscript *ave* represents an average value over the wall height and n_s is the total number of strip layers over the entire wall height. Typical global wall stiffness values are dependent on wall height but generally range from 18 to 120 MPa (Bathurst et al. 2009). Reported local stiffness values in the STIA MSE walls, were as large as 450 MPa due to the reduced horizontal and vertical spacing required to accommodate increased confining stresses.

Stuedlein et al. (2010b) presented reinforcement strain performance data during construction of the STIA MSE walls which is presented in Figure 2.9(a and b). Figure 2.9b indicates that the strain accumulation in reinforcing strips can be represented by a bilinear trend. Stuedlein et al. (2010b) attributed this behavior to initial take-up effects and compaction induced stresses. The average amount of estimated fill required to overcome compaction and initial installation effects was 1.52 meters. Plotted in Figure 2.9(a) are the predicted strains based on four currently used design methods. The K-Stiffness and Ehrlich and Mitchell methods explicitly take into account changes in the local reinforcement stiffness, and provide the best estimates of the measured strain response. The Coherent Gravity and Simplified methods do not consider local reinforcement and consistently under-predict the tensile strain for the duration of wall construction.

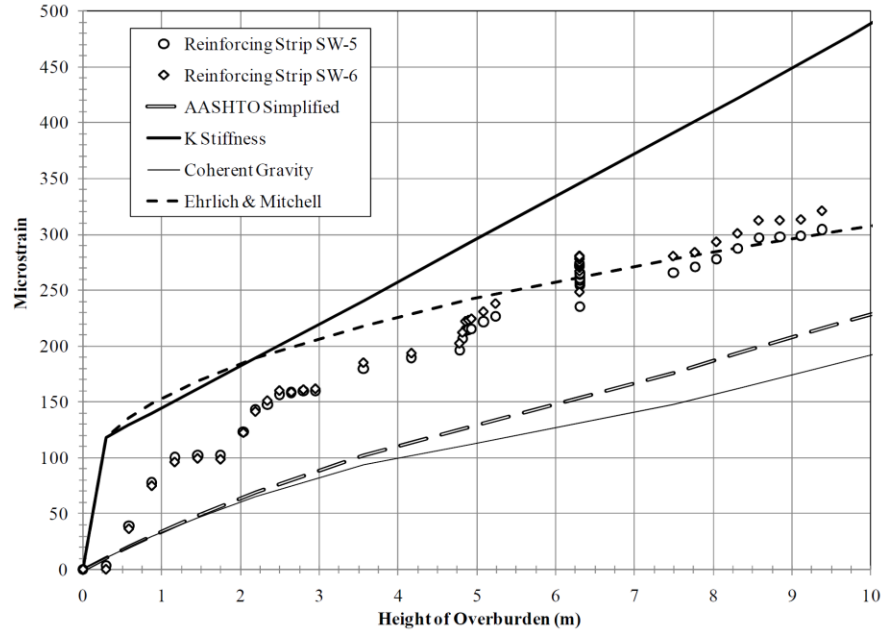


Figure 2.9. Representative observed and predicted tensile reinforcement strain in the west STIA MSE wall showing the (a) accumulation of strain during construction, (b) method used to differentiate initial installation effect from overburden placement (adapted from Stuedlein et al. 2010b).

The strain rate of accumulation corresponding to the initial uptake strain and strain caused by overburden stresses was aggregated for the 20 instrumented reinforcing strips in the west STIA wall and plotted against the local reinforcement stiffness in Figure 2.10. The rate of strain accumulation during placement and compaction of the first lifts of fill indicates that reinforcement stiffness has a moderate role in the initial uptake of strain and the majority of the variability in Figure 2.10 is associated with difference in local stiffness from elevation to elevation.

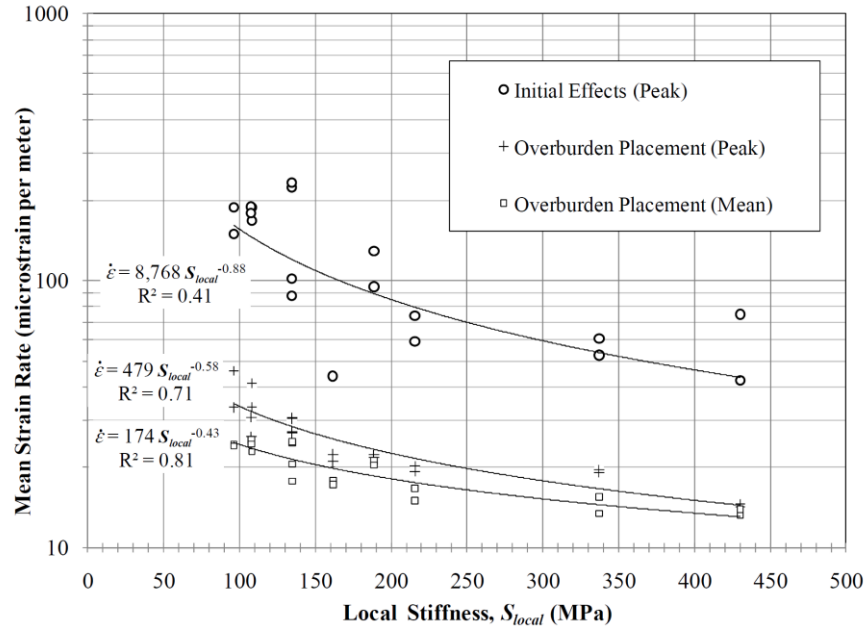


Figure 2.10. Effect of local reinforcement stiffness on the strain rate uptake observed in the west STIA MSE wall (after Stuedlein et al. 2010)

Reinforcement loads recorded just after completion of the west STIA MSE wall are presented in Figure 2.11. When inferred reinforcement loads are compared to the loads predicted by the Coherent Gravity method, a marked increase in reinforcement loads below an elevation of 90 meters is observable. Stuedlein et al. (2012) hypothesized that this behavior was not a result of overturning stresses in the soil mass but is likely attributed to increases in stress concentrations as a result increased local reinforcement stiffness, especially considering the exceptionally high local stiffness values. However, none of the design methods to date are able to capture the increased loading stemming from increases in local stiffness which becomes a design concern in tall walls when closely spaced reinforcements are required due to increased confining stresses.

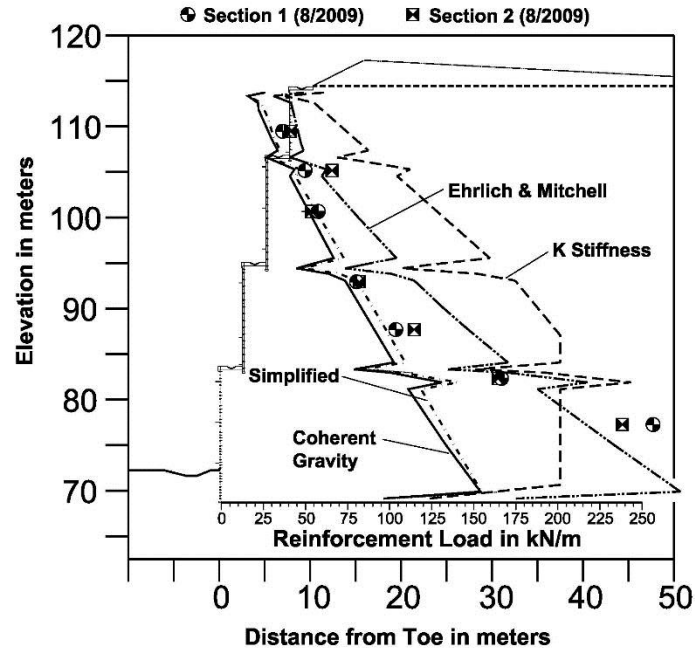


Figure 2.11. Observed and predicted peak reinforcement loads for the completed West MSE wall (H = 45.7 m, surcharge) (after Stuedlein et al. 2012).

2.5.5. DISPLACEMENT ESTIMATION METHODS

Lateral deformations in MSE walls primarily occur during construction where the major influencing factors are compaction forces, reinforcement stiffness, length of reinforcement, condition of the facing connection, front facing deformation behavior, and soil behavior. The estimation of lateral deformations to date has focused on geo-synthetically reinforced MSE walls and is predominantly accomplished using numerical models. Early estimates of the deformation behavior of MSE walls reinforced with various reinforcement types were accomplished using the FEM program SSCOMP and indicated that lateral wall displacements were qualitatively reasonable (Collin 1986, Adib 1988, Jaber 1989, Schmertman et al. 1989).

However, the first method that could be applied to generic MSE walls was developed by Jewell and Milligan (1989) using a Rankine analyses to determine vertical and lateral

deflections of geo-synthetically reinforced structures with ideal and truncated reinforcement lengths. Responses from numerical models conducted by Rowe and Ho (1998) indicated that the approach developed by Jewell and Milligan (1989) adequately predicts displacements at the wall face of geo-synthetically reinforced MSE walls as presented in Figure 2.13. Chew et al. (1990) developed a method based on results from numerical studies of a 6.3 meter tall bar mat reinforced soil mass has been adopted by the FHWA (Berg et al. 2009a and b) to represent a first order estimate of lateral displacement. The method was modified by Mitchell and Christopher (1990a and b) and is presented in Figure 2.12 where the relative lateral deformation, δ_R , is a function of the normalized wall reinforcement length, L/H , and the maximum expected lateral deformation, δ_{max} , is a function of the extensibility of the reinforcements. Christopher (1993) combined Figure 2.12 with full scale field tests of 6.3 meter tall walls reinforced with inextensible and extensible materials to develop logarithmic approximation which is given by:

$$\delta_{max} = \delta_R \left(\frac{H}{75 \log (S_{global})} \right) \quad (2.18)$$

where S_{global} is the global reinforcement stiffness in kips/ft².

A parametric study was performed using the plane strain FEM program AFENA varying the wall height, local reinforcement stiffness, soil-concrete interface characteristics, and backfill friction angles performed by Rowe and Ho (1998) on geo-synthetically reinforced single tier walls was used to assess lateral deformation behavior. Good agreement was found between results from the numerical models and the method proposed by Jewell and Milligan

(1989) as depicted in Figure 2.13 and Figure 2.14. However, validation against measured responses of real MSE walls was not provided and the use of Figure 2.13 and Figure 2.14 may not be appropriate for design. Similarly, the methods presented here are predominantly based on single tier geo-synthetically reinforced MSE walls with heights of 6.3 meters and provide the basis of the current methods used to estimate wall deformations in practice which are not valid in tall multi-tiered walls.

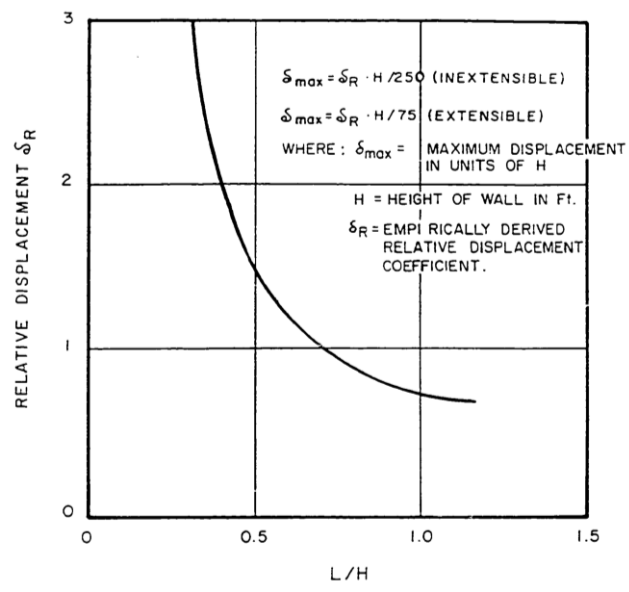


Figure 2.12. First order approximation of lateral displacements at the end of construction (after Mitchell and Christopher 1990a and b).

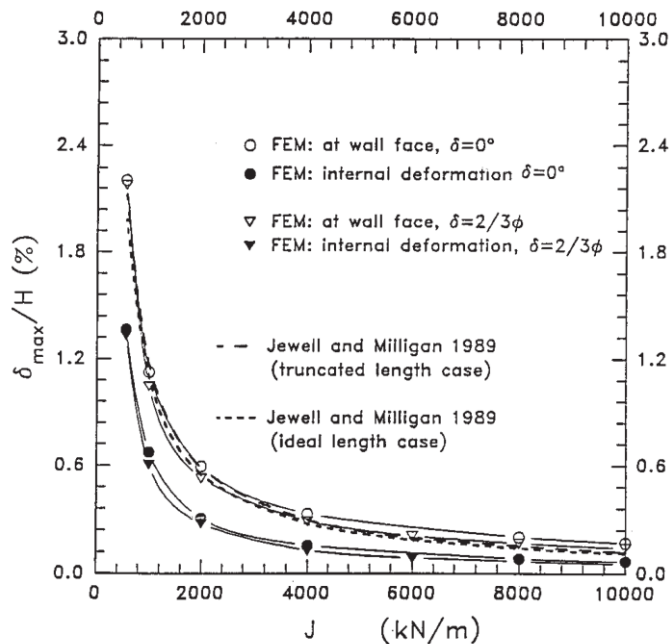


Figure 2.13. Comparison between deformational responses from numerical simulations and analytical methods for geo-synthetically reinforced walls as a function of the reinforcement stiffness and the soil-wall interface coefficient (after Rowe and Ho 1998).

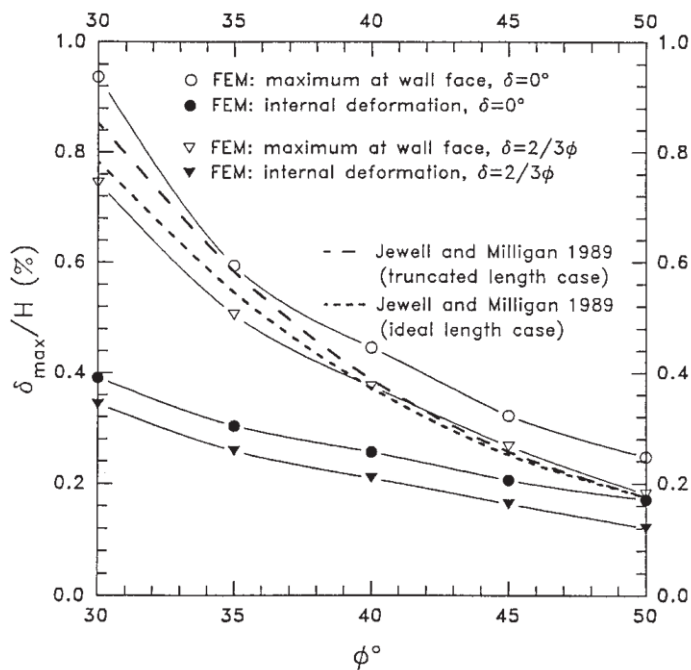


Figure 2.14. Comparison between deformational responses from numerical simulations and analytical methods for geo-synthetically reinforced walls as a function of the backfill friction angle and interface coefficient (after Rowe and Ho 1998).

2.6 NUMERICAL MODELING OF STEEL MSE WALLS

Finite-element and finite-difference methods (FEM and FDM, respectively), have been used by researchers to aid in the evaluation of MSE walls. However, very few studies have been verified against extensively instrumented and monitored full-scale walls (Huang et al. 2010) and even fewer numerical studies have been conducted using walls reinforced with inextensible materials. To date, the number of numerical models calibrated using extensible reinforcements are numerous, whereas a summary of the models with inextensible materials is on the order of eight, only four of which use steel strips; a summary which is provided in Table 2.1.

Table 2.1. Summary of numerically modeled inextensible MSE walls.

Reference	FEM/FDM Program	Wall Height (m)	Reinforcement Type
Adib et al. (1990)	SSCOMP (Seed 1983)	6	GG/WG/SS/WWM
Al-Hussaini and Johnson (1978)	2D FEM Code (Clough and Duncan 1969)	3.6	SS
Chang and Forsyth (1977)	SSCOMP (Seed 1983)	10	SS
Chew et al. (1990)	SSCOMP (Seed 1983)	6.1	WWM
Damians et al. (2013)	2D PLAXIS	16.7	SS
Damians et al. (2014)	2D PLAXIS	3.6, 6, 9	GG/WWM
Hatami and Bathurst (2006)	FLAC	3.6	GG/WG/WWM

Note: GG = Geogrid, WG = Woven Geotextile, SS = Steel Strips, WWM = Welded Wire Mesh

Adib (1990) and Christopher (1990) used the FEM program SSCOMP developed by Seed (1983) to compare the location and distribution of the maximum tensile load and found relatively good agreement. Chang and Forsyth (1977) compared predicted and measured tensile reinforcement loads in a 10 m tall wall using a FEM program established by Romstad et al. (1976) and also found good agreement between the tensile reinforcement loads. Al-

Hussaini and Johnson (1978) used a plane strain FEM code originally developed by Clough and Duncan (1969) to determine the effect of the fixity condition at the toe of the wall and it was concluded that a fixed toe condition produced more accurate estimates of facing deformations whereas a free condition produced better agreements with tensile strains in the reinforcement. Comparisons of measured and predicted wall deformations have shown that although the displacement estimates are qualitatively accurate they are quantitatively insufficient (Collin 1986, Adib 1988, Jaber 1989, Christopher 1993).

More recently, a two dimensional PLAXIS program was used to model a 16.7 meter tall steel-strip reinforced Minnow Creek wall initially presented by Runser (1999) and Runser et al. (2001) to determine the effect of the vertical facing loads on the behavior of steel reinforced MSE walls (Damians et al. 2013). It was concluded by Damians et al. (2013) that estimation of the vertical facing loads cannot be predicted using limit equilibrium methods due to complex deformation behavior; however, numerical methods provide guidance on selecting the quantity and compressibility of bearing pads to reduce vertical compression loads while maintaining acceptable gap between facing panels. Physical test walls constructed by Damians et al. (2014) with uniform rounded beach sand (RMC sand) backfill material and simulated using PLAXIS assessed the predictability of wall displacements, tensile forces, vertical and horizontal toe forces, and constitutive model non-linearity. Good agreement was found between measured and predicted toe boundary forces and reinforcement tension loads regardless of the constitutive model linearity. However lateral displacement estimate are only qualitatively sufficient, similar to results reported by Christopher (1993).

Generally, results from properly calibrated numerical models have provided sufficiently accurate estimates of the tensile force distributions along the reinforcing strip, horizontal stresses at the wall face and vertical down drag forces in the facing. However, predictions of wall displacements are highly dependent on the soil constitutive model and only qualitatively accurate estimates have been accomplished as a result. Nonetheless, FEM software packages can be a powerful tool for steel-reinforced soil wall structures.

2.7 SUMMARY OF LITERATURE REVIEW

2.7.1. SUMMARY

The literature review presented herein discussed: (1) basics of reinforced earth and its role in MSE walls, (2) brief overview of the STIA MSE walls followed by three fundamental properties of soil mechanics that can alter the behavior of well-graded granular soils that are commonly used in MSE walls, (3) methods commonly used to quantify soil-reinforcement interaction and the current available data used to establish this behavior for MSE wall design, (4) the effect of specific geometrical components on MSE wall behavior, (5) reinforced soil rigidity and its implications on design, (6) incorporation of a curved Mohr-Coulomb failure envelope into design methods, (7) changes in observed behavior attributed to reductions in the global and local reinforcement stiffness, (8) current methods used to estimate lateral wall displacements, and (9) numerical models that have been conducted on steel strip reinforced MSE walls. Particular attention was given to well-graded granular soil behavior and prediction methods used for estimating reinforcement loads in tall ribbed steel strip MSE walls.

2.7.2. *OUTSTANDING PROBLEMS AND ISSUES*

Base on the discussion presented herein the following list of concerns have been identified, and should be addressed in order to advance the state of the art in the investigation and evaluation of deep foundations:

1. The study of the stress-strain response of well-graded gravelly soils to date consist of in-situ direct shear tests, limited ranges in confining pressure, or extremely large angular weak rock fill that exhibits extensive particle breakage. Large scale triaxial tests to determine stress-strain soil response if Kanaskat gravel could provide insight into behavioral difference between well-graded and uniformly graded soils;
2. Available literature discussing the influence of the intermediate principal stress on granular soil response has focused on uniformly graded sands which are not physically representative of typical soils used in MSE walls. Large scale cubical true-triaxial devices are capable of performing experimental investigations into this behavior.
3. The vast majority of literature studying the soil-reinforcement interface behavior focuses on quantifying interface strength characteristics in an isolated condition with little consideration given to potential frictional interference stemming from adjacent reinforcements. Characterization of responses from single and multi-strip pullout tests representing isolated and confined behaviors could provide sufficient evidence for determining the frictional interference of closely spaced reinforcements.
4. Assumptions used in designing reinforced slopes and MSE walls are quite dissimilar even though no fundamental difference has been acknowledged. A more thorough

- understanding of reinforced earth will aid in the formulation of new methods of design with more theoretically robust assumptions.
5. The behavior of MSE walls is dependent on the rigidity of the front facing and incorporation of the effect of facing stiffness should yield a more fundamental understanding of MSE wall behavior.
 6. Considering the potential change in the friction angle for a well graded limestone material over pressure ranges observed in tall MSE walls the use of a single value of effective friction angle in the calculation of reference active lateral earth pressures may not be appropriate. The development of new methods that incorporate this response will produce more accurate results.
 7. Increased reinforcement loads observed in the tall STIA MSE walls indicate that our present understanding of MSE wall behavior may be inadequate and behavior associated with high local stiffness values needs to be investigated.
 8. Numerical models have been used to predict satisfactory estimates of physical results (e.g. reinforcement loads, horizontal earth pressures) but struggles to predict lateral wall deformations with sufficient accuracy that is strongly dependent on the backfill soil constitutive model.

CHAPTER 3: RESEARCH OBJECTIVES AND PROGRAM

3.1. RESEARCH OBJECTIVES

The primary focus of this study is to develop a better understanding of the components that comprise a reinforced soil mass, their performance in tall MSE walls, and the contribution of these components to the overall behavior of the reinforced soil system. To fully understand tall MSE wall performance, this study focused on several objectives, including the characterization of soil stiffness, strength, and stress-dilatancy, soil-strip interaction, calibration of numerical models for the various wall components, and a parametric study of these pertinent variables. The intent of this study is not to focus on any specific wall, but add to the general knowledge of tall MSE wall design and performance. The specific objectives of this study include:

1. Characterization of the three dimensional stress-strain response of a relatively unstudied well-graded gravelly backfill soil;
2. Determination of the stress-dependent soil-reinforcement interaction, if any, to quantify the potential effect of frictional interference between closely spaced reinforcements.
3. Synthesize experimental work for forward modeling.
4. Study the effect of design variables such as reinforced and retained soil stiffness, frictional interference between closely spaced reinforcements, gradients in reinforcement density and corresponding frictional interference, tier offsets and

equivalent batter angle, and wall height on MSE wall displacements and strain distributions in the reinforcements.

3.2. RESEARCH PROGRAM

The research program conducted to accomplish the objectives include:

1. Perform drained axisymmetrical isotropically consolidated tests (AICD) at various effective confining stresses on wall backfill material to determine the stress-strength-volumetric behavior of a well-graded gravelly soil.
2. Perform a series of tests in a true triaxial apparatus using various stress paths and effective confining stresses to determine the stress-dependent three dimensional constitutive behavior of the backfill material;
3. Design and construct a pullout test apparatus that allows the pullout testing of multiple reinforcement strips at various spacing;
4. Perform a series of laboratory multi-strip pullout tests at various normal effective stresses on the reinforced backfill and steel ribbed strips to characterize the frictional interference behavior between strips;
5. Combine previous work conducted on single strip pullout tests to develop load-displacement and unit frictional resistance models that account for frictional interference of closely spaced reinforcements;
6. Calibrate a numerical soil constitutive model in FLAC using the three-dimensional stress-strain response of the backfill soil determined from testing;

7. Calibrate soil-reinforcement interface model for the single and multiple strip tests using FLAC and develop a soil-concrete wall panel interface model based on direct shear interface testing, and;
8. Calibrate a representative tall MSE wall model in the finite difference program FLAC and conduct parametric studies in FLAC at working stress conditions.

**CHAPTER 4: STRESS-STRAIN RESPONSE AND DILATANCY OF
SANDY GRAVEL IN TRIAXIAL COMPRESSION AND PLANE
STRAIN**

Andrew Strahler, EIT, Armin W. Stuedlein, PhD, P.E., and Pedro W. Arduino, PhD, P.E.

Journal of Geotechnical and Geoenvironmental Engineering

Volume 142, Issue 4

DOI: 10.1061/(ASCE)GT.1943-5606.0001435

1801 Alexander Bell Drive

Reston, VA 20191-4400

*Updated with Strahler et al. (2016), Errata for “Stress-Strain Response and Dilatancy of
Sandy Gravel in Triaxial Compression and Plane Strain.”*

4.1 ABSTRACT

The strength and stress-dilatancy of uniform sands has been studied extensively in geotechnical investigations, and practitioners can draw on a wealth of previously reported data for the estimation of their volumetric response. However, the suitability of accepted stress-dilatancy theory and empiricism has not been evaluated for well-graded gravelly soils. Axisymmetric, isotropically consolidated drained compression and pure shear, plane strain quasi- K_0 consolidated drained tests were performed on well-graded Kanaskat gravel using confining pressures ranging over three orders of magnitude to determine its stiffness, strength, and stress-dilatancy response. The plane strain stiffness, strength, and stress-dilatancy of Kanaskat gravel is observed from tests performed using a large cubical true-triaxial device with flexible bladders. The observed response is interpreted with a view of experimental boundary conditions and their effects, such as the development of multiple shear bands within specimens and their impact on the volumetric response. The observed plane strain friction, and dilation angles of well-graded sandy gravel soils commonly used in practice are significantly higher than those measured in the triaxial compression stress path. Existing empirical and modified stress-dilatancy expressions proposed for low confining pressures under-estimate the observed dilation response, however, another common empirical approach appears to adequately capture the dilatancy. The data reported herein should help practitioners estimate plane strain behavior of sandy gravel mixtures.

4.2 INTRODUCTION

Soil dilatancy was initially investigated by Reynolds (1885) and has since been recognized to control critical aspects of soil behavior at working stresses. Although the stability of slopes or shallow foundations, geotechnical structures that lie in proximity to free surfaces, are less affected by soil dilation (Zienciewicz et al. 1975), the serviceability of highly confined geotechnical elements such as tunnels and deep foundations is greatly impacted by soil dilatancy (Houlsby 1991). Rowe (1962) and Poorooshasb and Roscoe (1961) presented two stress-dilatancy relationships for granular soils based on laboratory investigations on Fort Peck sand by Taylor (1948) using assumed uniform particle sizes and packing. Building on Rowe's work, a significant body of literature has been developed on the stress-dilatancy behavior of uniform sands (Cornforth 1964, Lee and Seed 1967, Rowe 1969, Tatsuoka 1976, Bolton 1986, Chu 1994, Schanz and Vermeer 1996, Panda and Ghosh 2000, Hanna 2001, Wan and Guo 2004, Chakraborty and Salgado 2010). A widely used, empirical stress-dilatancy relationship developed by Bolton (1986) and focused on the strength parameters of uniform sands yielded:

$$\phi'_f = \phi'_{cv} + a \psi_f \quad (4.1)$$

where ϕ'_f is the friction angle at failure, ϕ'_{cv} is the friction angle at a constant volume condition, and coefficient a varies based on soil type and stress path. The dilation angle at failure, ψ_f , in Equation (1) is defined by:

$$\sin \psi_f = \frac{-(d\varepsilon_v/d\varepsilon_1)_f}{2 - (d\varepsilon_v/d\varepsilon_1)_f} \quad (4.2)$$

where $d\varepsilon_v$ and $d\varepsilon_1$ are changes in the volumetric and axial strains during shearing, and subscript f denotes failure. Although the various theories and empirical relationships work well in many cases, they are based on stress-dilatancy relations developed assuming uniform particle packing which have not been validated against the response of well-graded granular soils. The study of the stress-strain response of well-graded gravelly soils to date consists of in-situ direct shear tests, limited ranges in confining pressure, or large, angular, and weak rock fill that exhibit extensive particle breakage (Holtz and Gibbs 1956, Marsal 1967, Skermer and Hillis 1970, Marachi et al. 1972, Charles and Watts 1980, Matsuoka and Liu 1998, Matsuoka et al. 2001, Zhao et al. 2013, Xiao et al. 2014). The aim of this study is to characterize the uniaxial and plane strain behavior of Kanaskat gravel, a rounded to sub-rounded well-graded sandy gravel used to construct several tall mechanically stabilized earth (MSE) walls in SeaTac, WA, described by Stuedlein et al. (2007, 2010, 2012). A series of large, axisymmetric, isotropically-consolidated drained triaxial compression (AICD) and cubical, pure shear, quasi- K_0 consolidated drained plane strain (PS K_0 CD) tests were conducted on Kanaskat gravel to study the influence of stress path on its stiffness, strength, and stress-dilatancy response. This paper first details the comprehensive laboratory testing program that was used to investigate the stress-strain response of Kanaskat gravel. The stress-strain-strength and volume change behavior observed in large axisymmetric triaxial tests over a wide range of confining stresses is provided as a baseline response. Then, the highly frictional stress-strain-strength and volume change response of quasi- K_0 consolidated plain strain pure shear tests are described, in consideration of complex boundary conditions

and shear band formation. Comparisons of the stress-strain-strength response of cubical, pure shear, plane strain and simple shear specimens to axisymmetric, isotropically-consolidated triaxial compression tests indicate that the strength and stiffness of this well-graded soil in plane strain are larger than expected. Additional comparisons to three dimensional failure criteria that incorporate the intermediate principal stress are made and show that the Matsuoka-Nakai failure criterion underestimates the strength, but that the Lade-Duncan failure criterion sufficiently estimates the strength of Kanaskat gravel. The stress-dilatancy response of Kanaskat gravel is compared to Bolton's (1986, 1987) empirical relationships and shows that some, but not all, simple expressions may be used to estimate the dilatancy of a well-graded granular soil.

4.3 EXPERIMENTAL PROGRAM AND SOIL DESCRIPTION

4.3.1. LABORATORY TESTING PROGRAM AND CRITERIA

The soil investigated in this study was placed and compacted similar to reinforced fill within MSE walls that were constructed as part of the SeaTac International Airport (STIA) third runway expansion project described by Stuedlein et al. (2007, 2010, and 2012). Sourced from a quarry in Kanaskat, Washington and selected based on specified limits put forth by the designers, the sandy gravel soil characteristics tested in accordance with ASTM (2006, 2009) standards are presented in Table 4.1. Its gradation, representing an average of six samples from a large stockpile, is presented in Figure 4.1 along with the project-specified gradation limits. The roundness and sphericity of Kanaskat gravel was quantified following Krumbein and Sloss (1963); based on the classification system proposed by Powers (1953), Kanaskat gravel is characterized as rounded to sub-rounded. The mineral content of

Kanaskat gravel was evaluated using X-ray diffraction, and indicated that the composition primarily consists of quartz with some potassium feldspar and hornblende which have mineral surface friction angles ranging from 22 to 35 degrees, 36 to 38 degrees, and 31 degrees, respectively (Terzaghi et al. 1996).

Table 4.1 Characteristic soil properties of Kanaskat gravel.

D_{10} (mm)	D_{50} (mm)	C_u	C_c	e_{min}	e_{max}	$\gamma_{d,max}$ (kN/m ³)	w_{opt} (%)
0.22	6	46	0.4	0.182	0.365	22.4	6.4

The research presented in this study focused on the stresses and states representative of tall MSE walls (i.e., fills). As a result, consolidation stresses, presented in Table 4.2, for the AICD and PSK₀CD tests were selected based on mean effective consolidation pressures, p'_c , representative of conditions in a tall MSE wall, and tests were conducted at the post consolidation relative density to simulate void ratio changes expected during wall construction. The AICD and PSK₀CD tests were conducted to assess the effects of confining pressure and stress path on the strength and dilation of Kanaskat gravel, and to provide a benchmark for interpretation of experiments on the performance of closely-spaced reinforcement strips not described here. Mean effective stresses at consolidation for each stress path, presented in Table 4.2, used for the AICD tests ranged from 10 to 1,000 kPa to study the stress-strain-strength response over a wide range in stresses using a conventional stress path, whereas p'_c ranged from 28 to 172 kPa for the less common PSK₀CD tests owing to experimental limitations.

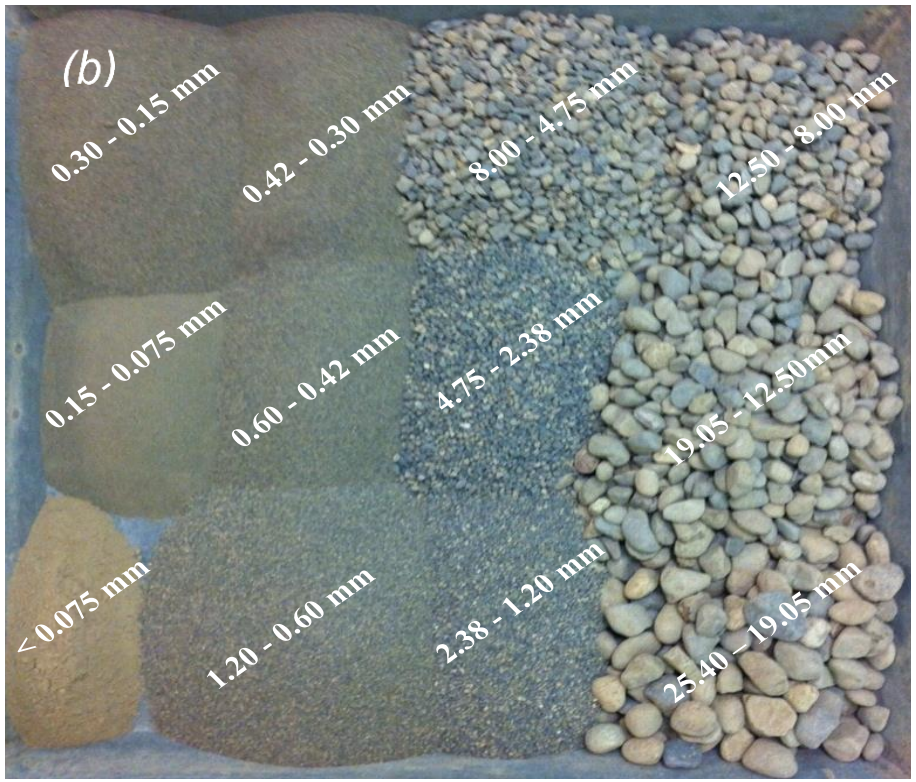
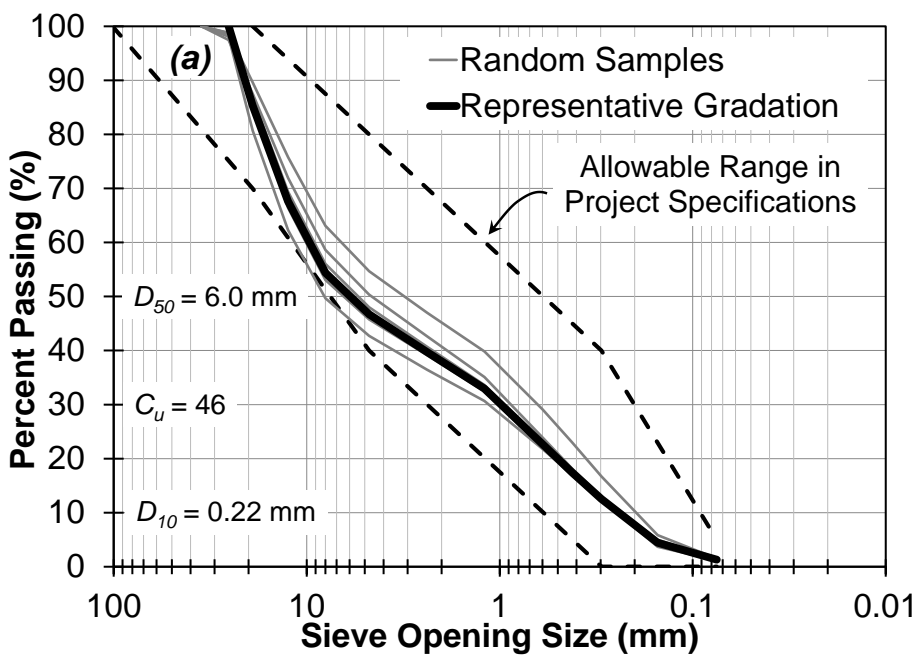


Figure 4.1. Grain size distributions of a sandy gravel: (a) sample and representative (target) distributions and (b) example distribution presenting particle shape.

Table 4.2. Overview of the laboratory testing program and relevant results.

Stress Path	Mean Effective Consolidation Stress, p'_c (kPa)	Significant Void Ratios ^a				Friction Angle at Failure, ϕ'_f (deg)	Dilation Angle at Failure, ψ_f (deg)
		e_{bc}	e_{ac}	e_f	e_{cs}		
AICD	10	0.250	0.249	0.256	0.276	54.1	22.6
	20	0.248	0.246	0.253	0.275	51.5	18.7
	50	0.248	0.242	0.248	0.264	48.7	14.7
	100	0.250	0.241	0.247	0.260	45.2	11.2
	250	0.248	0.231	0.235	0.245	43.6	8.7
	500	0.248	0.231	0.228	0.235	42.9	4.2
	1000	0.246	0.227	0.222	0.227	41.6	2.0
PSK ₀ CD	28	0.246	0.246	0.251	N/A	64.6	29.8
	63	0.243	0.242	0.246	N/A	65.4	23.8
	86	0.244	0.240	0.247	N/A	62.5	19.2
	114	0.245	0.237	0.246	N/A	62.6	19.8
	142	0.247	0.237	0.245	N/A	56.8	18.1
	172	0.242	0.234	0.242	N/A	57.0	15.8

AICD = Axisymmetrical Isotropically Consolidated Drained.

PSK₀CD = Plane Strain Quasi- K_0 Consolidated Drained.

^a bc = before consolidation, ac = after consolidation, f = at failure, cs = critical state.

Specifications at the STIA third runway project required that the reinforced fill be compacted to 92% of the maximum Modified Proctor (ASTM 2006) dry unit weight, $\gamma_{d,max}$, with corresponding optimum moisture content, w_{opt} , at \pm two percent (Stuedlein et al. 2010). For Kanaskat gravel, $\gamma_{d,max} = 22.4 \text{ kN/m}^3$ at $w_{opt} = 6.4 \%$ as shown in Table 4.1. In consideration of project specifications, each test specimen was compacted to a target $\gamma_d = 21.3 \text{ kN/m}^3$, corresponding to a relative density of 65 %; deviations of $\pm 2.5 \%$ in actual relative density were allowed. Details for AICD specimen preparation are described by Walters (2013). Most of the triaxial compression tests were compacted slightly below the target relative density of 65 % with the lowest value being 63 % and the highest being 66 %. Similarly, initial relative densities for the PSK₀CD tests ranged from 64 to 67 %. Relative density

changes that occur during consolidation are presented in Figure 4.2 as a function of p'_c normalized by a reference pressure, $p_{ref} = 101.3$ kPa, which shows that although the sample was initially compacted to $D_r \approx 65$ %, D_r as high as 76 % were observed before the onset of shearing.

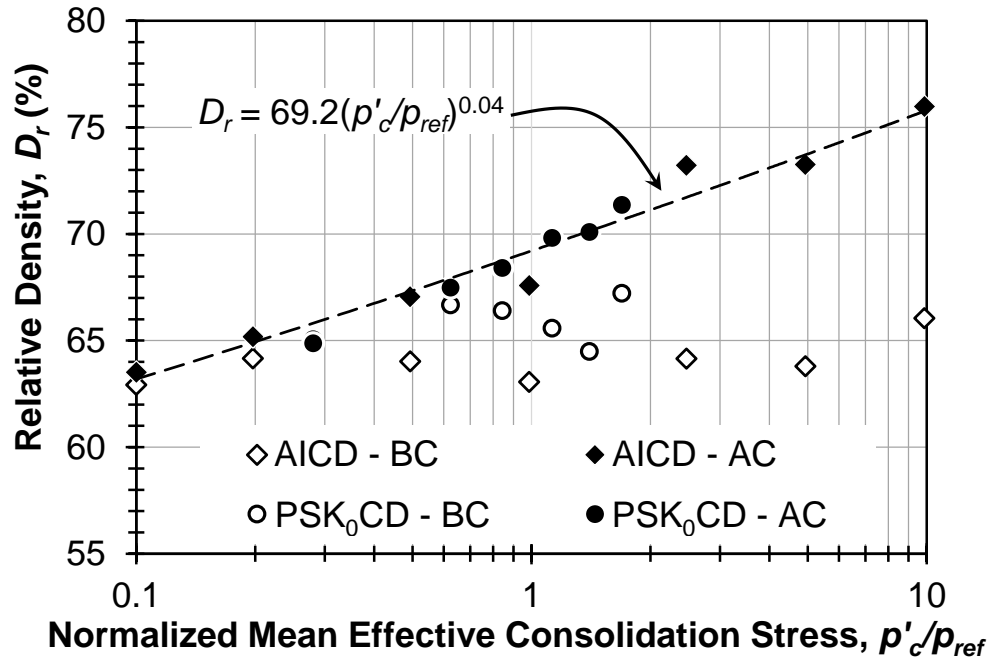


Figure 4.2. Changes in relative density due to consolidation as a function of confining pressure for AICD and PSK₀CD tests on Kanaskat Gravel; Note: AC = After Consolidation, BC = Before Consolidation.

4.4 AXYSYMMETRIC ISOTROPICALLY CONSOLIDATED DRAINED (AICD) RESPONSE

Seven cylindrical AICD specimens (diameter = 152 mm, height = 305 mm) were sheared at 0.05 %/min to provide a baseline stress-strain-strength and volumetric response of Kanaskat gravel for comparison to the plane strain stress path. In order to directly compare

results of different stress paths, intermediate principal stresses were incorporated by adopting the three dimensional form of the deviatoric stress, q , which is given by:

$$q = \sqrt{3J_2} \quad (4.3)$$

where J_2 is the second stress invariant. Similarly, the mean effective stress, p' , defined as:

$$p' = \frac{(\sigma'_1 + \sigma'_2 + \sigma'_3)}{3} \quad (4.4)$$

was adopted, where σ'_1 , σ'_2 , and σ'_3 are the major, intermediate, and minor principal effective stress, respectively. Figure 4.3 presents the AICD responses of specimens in terms of the stress invariant ratio, $\eta = q/p'$, as a function of engineering shear strain, γ_s , calculated using the three-dimensional form given by:

$$\gamma_s = \sqrt{\frac{4}{3}J''_2} \quad (4.5)$$

where J''_2 is the second invariant of the deviatoric strain tensor. Generally, increases in confining stress results in reductions in peak η , increases in shear strain to failure, and the suppression of dilation.

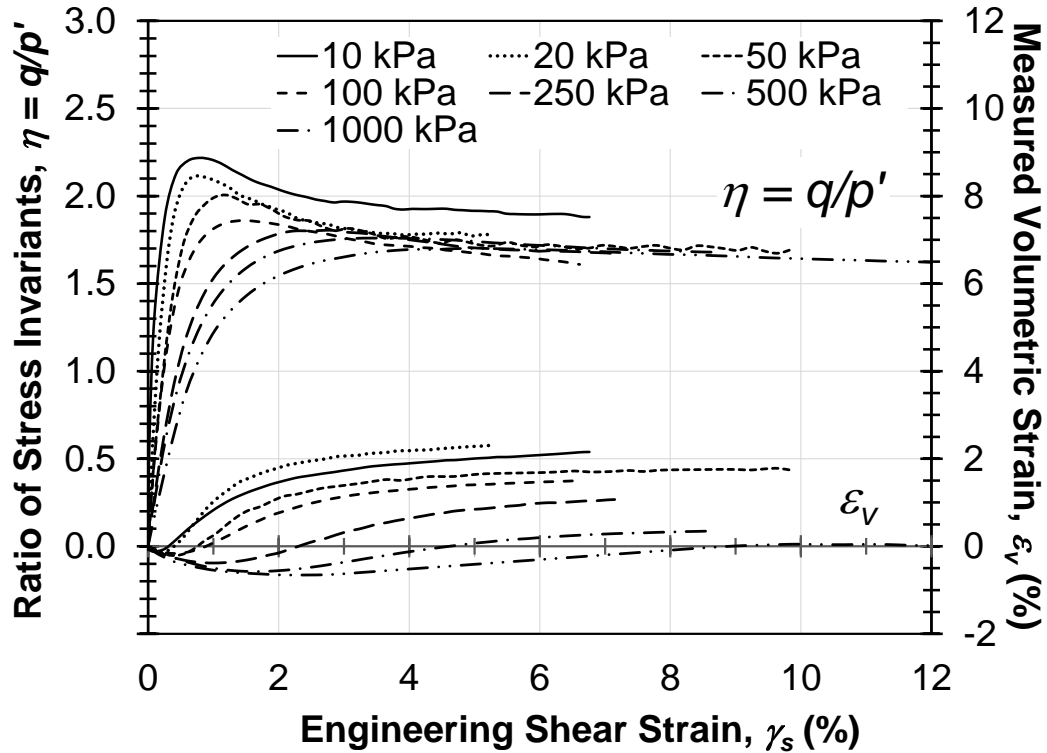


Figure 4.3. Principal effective stress ratio and volumetric strain response of Kanaskat gravel developed from AICD triaxial tests.

Figure 4.4 presents AICD friction and dilation angles at failure, $\phi'_{f,AICD}$ and $\psi_{f,AICD}$, respectively, where failure in the AICD stress path is defined at the peak stress invariant ratio. The AICD friction angles at failure range from 54 to 42 degrees and were corrected for the geostatic stress gradient in the sample by adding the average (i.e., midpoint) geostatic vertical stress, approximately 7 kPa to the major principal stress, σ'_1 . The largest change in the friction angle as a result of the pressure gradient in the sample was approximately 1 degree at the lowest confining pressure test. The friction angles are fitted using a log-linear relationship and deviations from this trend correspond to differences between the initial relative densities of specimens. The corresponding dilation angles for the AICD tests ranged from 2 to 23 degrees as presented in Figure 4.4.

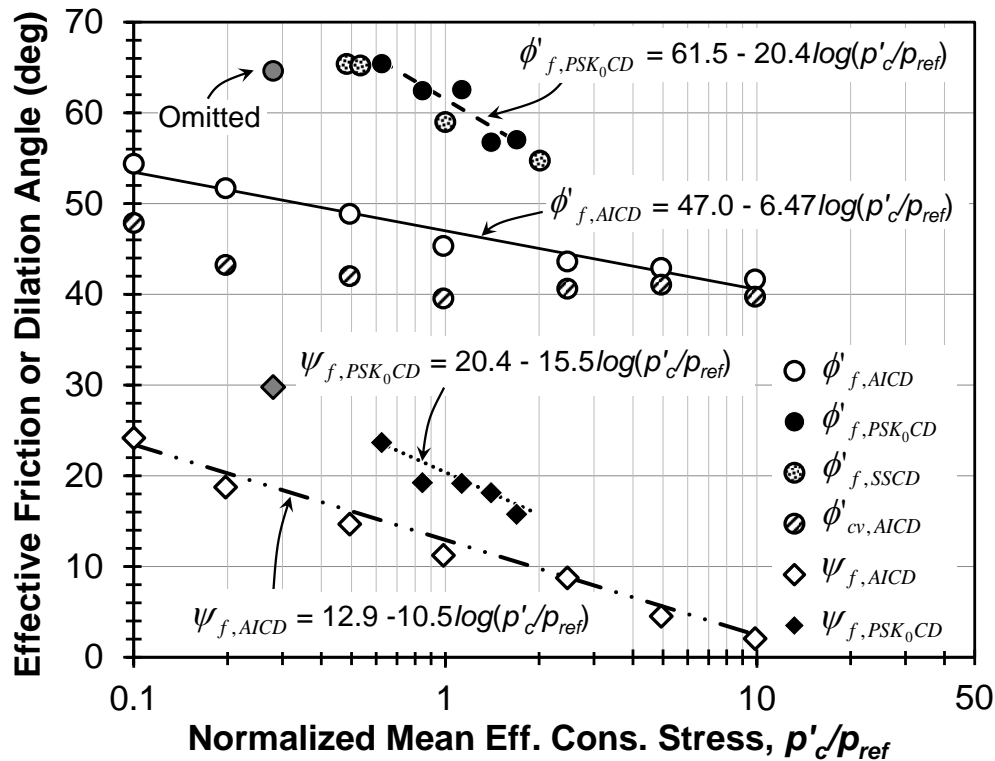


Figure 4.4. Effective friction and dilation angles at failure as a function normalized mean effective stress for AICD and PSK₀CD tests. Note: shaded points were removed from the PSK₀CD trends due to boundary condition effects at low confining stresses.

Void ratio paths, presented in Figure 4.5, indicate the change in the global void ratio during shearing in the AICD and PSK₀CD stress paths. Markers in Figure 4.5 indicate the void ratio at consolidation, e_c , at failure, e_f , and at the critical state, e_{cs} . The observed void ratio paths during shearing in the AICD stress path show that all specimens initially contracted and then expanded towards the critical state with significant changes in p' . Conversely, no contraction was observed in the void ratio path in the PSK₀CD stress path indicating that the specimen dilated until failure with only slight increases in p' . Owing to its fundamental correlation to geotechnical performance measures (Been and Jefferies 1985), it is of interest to understand the evolution of the state parameter, $\Psi = e - e_{cs}$, of Kanaskat

gravel during shear. However, this can only be observed for the AICD specimens due to the inability to observe the critical state response in the PSK_0CD tests, as discussed subsequently. Figure 4.6 provides state paths for the AICD specimens during shearing, with markers showing the state parameter at consolidation, Ψ_c , and at failure, Ψ_f and where negative state parameters indicate a dense state. Owing to its well-graded nature, the change in void ratio required to achieve the critical state is much smaller than that observed for uniform sands (e.g., Been and Jefferies 1985; Been et al. 1991) over the same range in p'_c . The state paths indicate that the magnitude of contraction is much greater at higher confining pressures, and that Kanaskat gravel begins and ends shearing at the critical state for $p'_c = 1$ MPa and $D_r = 65\%$.

Tests in the AICD stress path were sheared to different quantities of strain and some of them may not have reached a true critical state. However, comparison of trends presented Figures 4.5 and 4.6 suggests that all tests were sheared sufficiently to reach a representative constant volume state and further shearing would not have changed the results significantly. As a result, the observed stress-strain response at larger strains and void ratio evolution was used to estimate the constant volume or critical state of the soil. Constant volume friction angles (quantified at the end

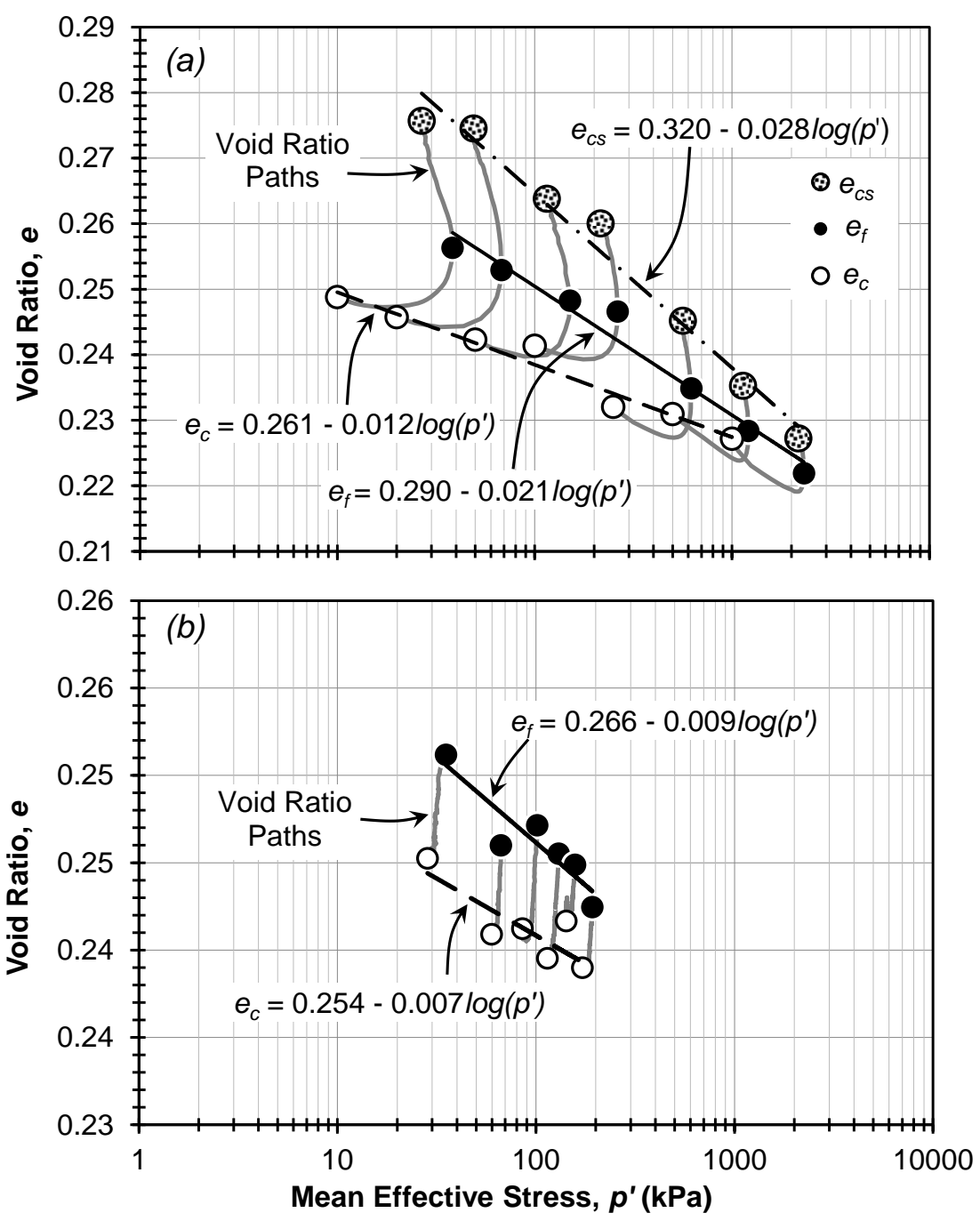


Figure 4.5. Evolution of void ratios during shear for (a) AICD and (b) PSK₀CD tests on Kanaskat gravel; e_c , e_f , and e_{cs} correspond to the void ratio at consolidation, failure, and the critical state, respectively.

of each test), ϕ'_{cv} , presented in Figure 4.4 appear to reduce slightly with increases in confining pressure. An average ϕ'_{cv} of 40 degrees is consistent with a 41 degree constant volume friction angle reported by Zhao et al. (2013) for a gravelly sand with similar gradation characteristics ($D_{50} = 3.0$ mm, $D_{max} = 10$ mm , $C_u = 14.3$) tested in a triaxial compression stress path at low confining pressures.

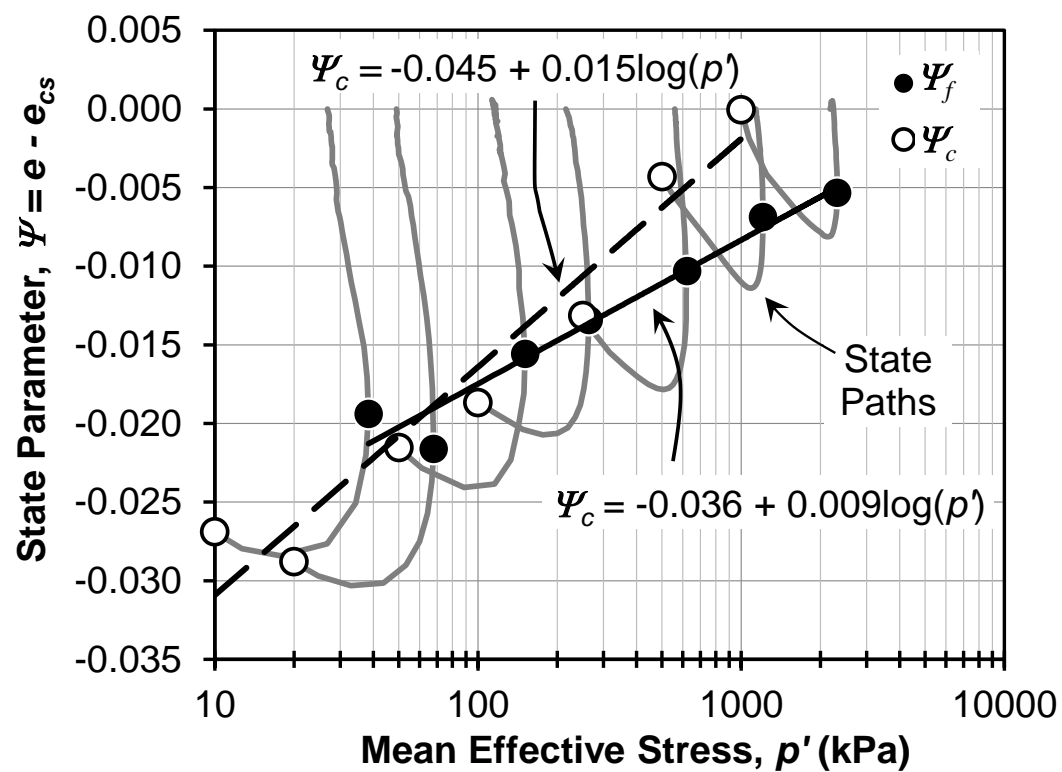


Figure 4.6. State paths during shearing of the AICD stress path tests as a function of mean effective stress with indicators showing the state parameters following consolidation and at failure. Data for $p'_c = 10$ kPa omitted.

4.5 QUASI- K_0 CONSOLIDATED PURE SHEAR PLANE STRAIN (PSK $_0$ CD) RESPONSE

The cubical true triaxial apparatus (TTA) described by Hoopes (2007), Choi et al. (2008) and Biggerstaff (2010) allowed testing of Kanaskat gravel due to its internal dimensions, equal to 240 mm in each direction. The stress-controlled TTA is able to measure the intermediate principal stress using load cells, but is unable to capture softening responses due to its use of flexible membranes (Arthur 1988, Choi et al. 2008). Hence, the deviatoric stress-strain and volumetric strain response deviates from that observed in the AICD test series. Additionally, the geometry and boundary conditions of the TTA alters the development of shear bands and strain compatibility during shearing. This results in the development of a quasi- K_0 consolidation mechanism that impacts the stress-strain and volumetric responses of Kanaskat gravel. Efforts to interpret the response of Kanaskat gravel with regard to these experimental conditions are explained below.

4.5.1. QUASI- K_0 CONSOLIDATION BEHAVIOR

True K_0 consolidation requires one dimensional strain (Terzaghi et al. 1996); consolidation of specimens in the TTA and similar devices (Wanatowski and Chu 2008) results in strains in both the σ'_1 and σ'_2 directions and produces a quasi- K_0 consolidation stress path. Consolidation in the TTA device was accomplished by applying an increase in σ'_1 and σ'_2 while applying a constant minor principal effective stress equal to the backpressure. This was done to prevent the rubber membrane and specimen from separating from the load cells and influencing control of σ'_3 . The resulting stress path during consolidation, presented in Figures 4.7 and 4.8, produced shear stresses in the specimen prior

to failure and as a result, slight differences in the compaction protocol, boundary conditions, and relative density likely affected the consolidation stress path. For example, the shallowest consolidation line (corresponding to $p'_c = 172$ kPa) is indicative of a slightly higher D_r . Additionally, compressive strains on the order of 0.05 % in the σ'_3 direction occurred due to compliance associated with strains in the intermediate load cells, which produce a non-zero intermediate strain, ε_2 , during consolidation. However, results from PS tests performed by Marachi et al. (1981) indicate that small magnitudes of ε_2 do not appreciably affect the plane strain behavior of soil; therefore, ε_2 was not considered to affect the strength of specimens presented herein.

The deviatoric stress and volumetric strain response of the PSK₀CD test specimens are shown in Figure 4.9. Figure 4.9a shows that the specimens did not exhibit strain softening following failure, in marked contrast to the AICD test specimens, owing to the stress-controlled test protocol. Note that the plotted deviatoric response includes shearing incurred during consolidation. The volumetric response of Kanaskat gravel in the TTA was independently measured using both linear voltage displacement transducers (LVDTs) centered behind the rubber bladders and a burette with a differential pressure transducer. The LVDTs were used to calculate shear strains from the principal displacement of a cubical soil element. However, volumetric burette readings more accurately represent the soil behavior of the entire sample and were used to estimate the average volumetric response.

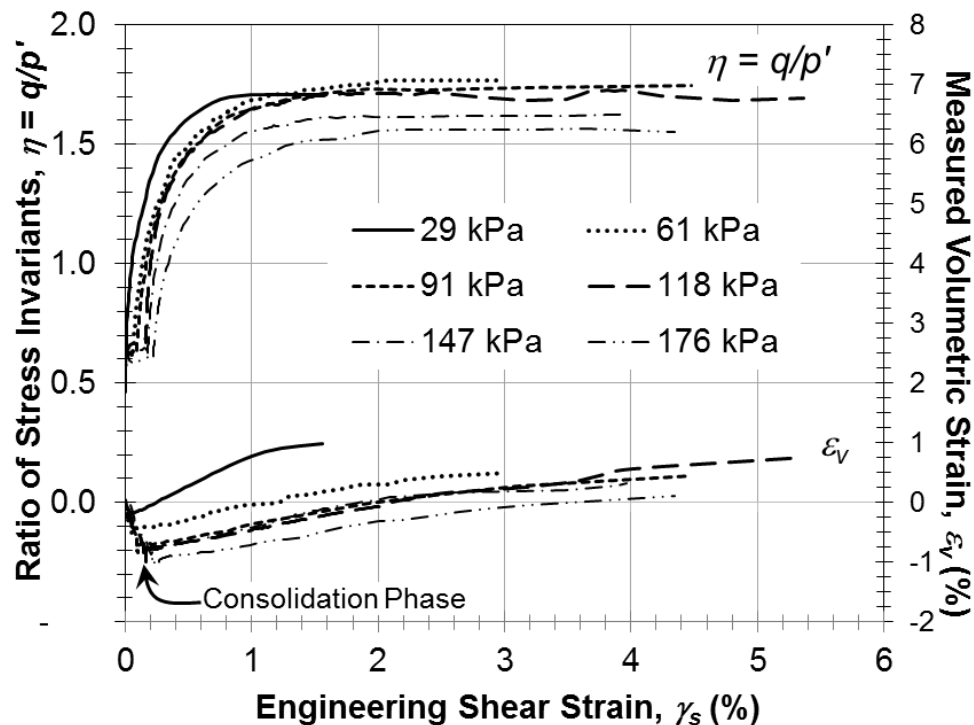


Figure 4.7. Ratio of stress invariants and volumetric strain as function of engineering shear strain for the PSK₀CD stress paths.

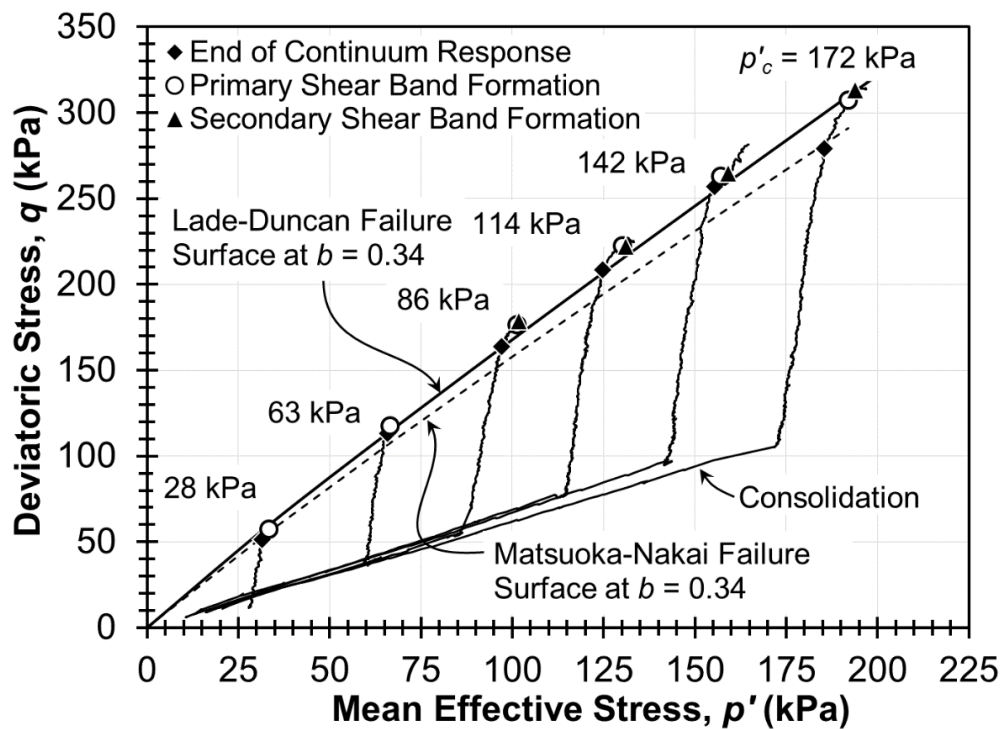


Figure 4.8. PSK₀CD stress paths of a sandy gravel in q - p' space with markers indicating the formation of shear bands and deviations from continuum response.

Two assessments of volumetric strain, presented in Figure 4.9b and 4.9c, were made: those that were calculated using the trace of the principal strain vector as described by Choi et al. (2008) and those measured using the burette. Choi et al. (2008) showed that the bladder deformation pattern in the TTA was fairly uniform, even at higher displacements, for tests on uniform granular soils and in the absence of shear bands. Figure 4.9 indicates that the calculated volumetric strains (Figure 4.9b) deviate significantly from the measured volumetric strains (Figure 4.9c) as shearing progresses. Owing to the potential development of shear bands in specimens of Kanaskat gravel, the assessment of dilatancy required careful interpretation of the volumetric and principal strains, as described further below.

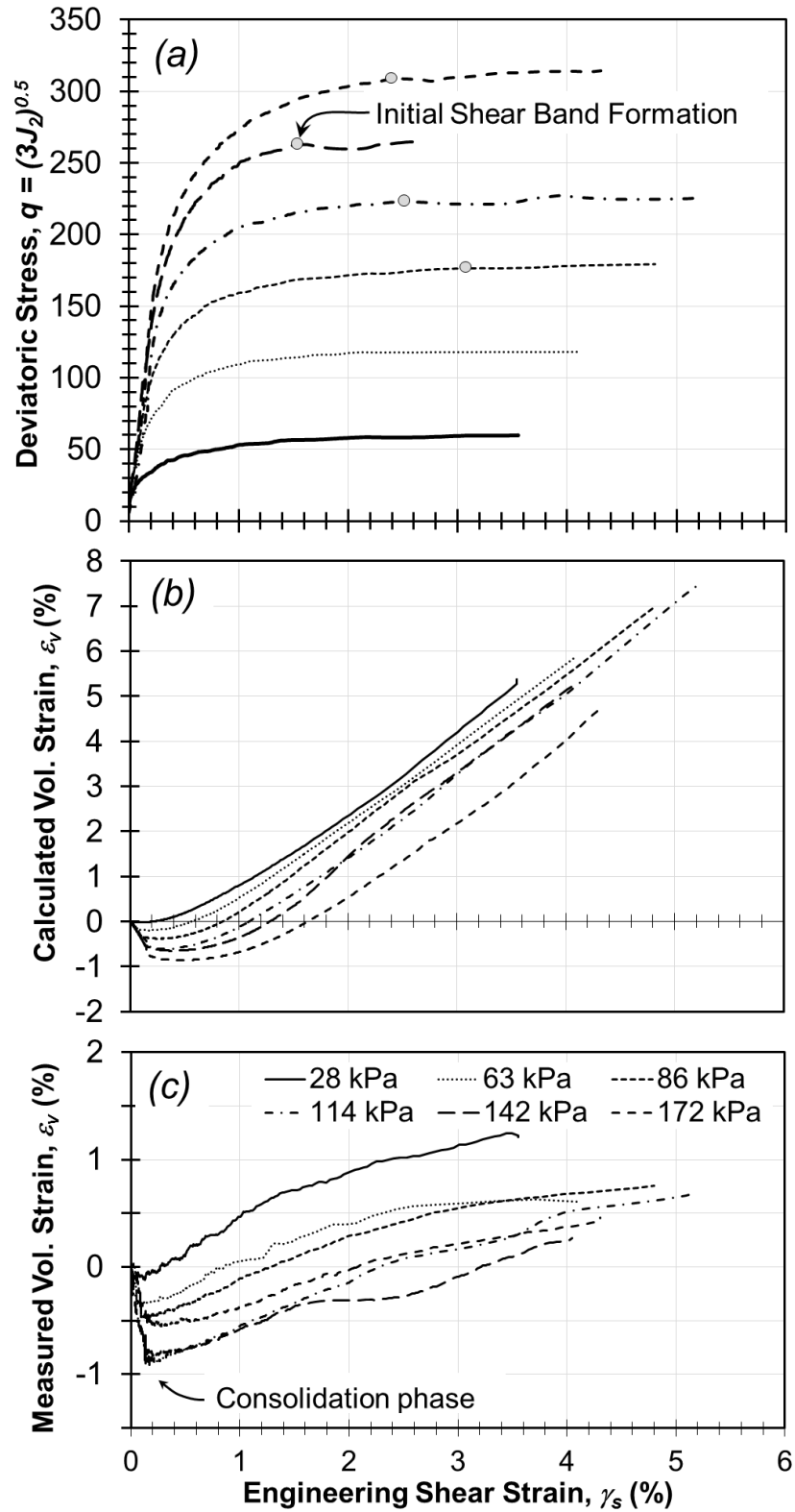


Figure 4.9. PSK₀CD specimen response during consolidation and shearing: (a) deviatoric stress-strain response, (b) volumetric strain calculated using LVDTs in principal directions, and (c) volumetric strain measured using burette observations.

4.5.2. STIFFNESS OF KANASKAT GRAVEL

The stiffness of the AICD and PSK_0CD tests on Kanaskat gravel may be represented using a secant shear modulus, G , presented in Figure 4.10 as a function of p'_c/p_{ref} . The secant shear modulus in the AICD stress path, G_{AICD} , was calculated at a post-consolidation shear strain of 0.05% assuming that the volumetric and shear strains were decoupled; for this case, $G_{AICD} = \Delta q / (3\Delta\gamma_s)$ where Δq is the change in deviatoric stress and $\Delta\gamma_s$ is the change in the shear strain (Wood 1990). The computed G_{AICD} ranged between 9 MPa at a p'_c of 10 kPa and 70 MPa at a p'_c of 1 MPa. The fitted power law exponent, equal to 0.56, is consistent with those reported in the literature (Schanz and Vermeer 1998). The initial tangent shear modulus corresponding to the PSK_0CD stress path, G_{PSK_0CD} , was calculated using the same approach as in the AICD stress path and ranged from 37 to 92 MPa for p'_c of 28 to 172 kPa. These are lower than those measured in the AICD stress path which is not consistent with plane strain shear moduli reported by Hatami and Bathurst (2005). The unique K_0 stress path allows for the estimation of shear modulus near the end of the consolidation phase where G_{PSK_0CD} were calculated at $\gamma_s = 0.05\%$ prior to the onset of shear. Shear moduli calculated at the end of consolidation presented in Figure E3 are similar to those measured at the onset of shearing, confirming that the soil behavior is independent of stress path and therefore represent soil response within the UW-TTA testing apparatus. The low G_{PSK_0CD} are attributed to small amounts of ε_2 strains stemming from displacements in the load cells in the intermediate direction. During consolidation, measured ε_2 are characterized as being 0.03% on average with observed maximum and minimum of 0.06% and 0.02%, respectively. Therefore, ε_2 strains that develop within the UW-TTA system are not considered small enough to accurately represent this condition for small strain measurements. As a result,

G_{PSK_0CD} presented here and in the paper are largely influenced by compliance in the testing apparatus and do not represent soil response.

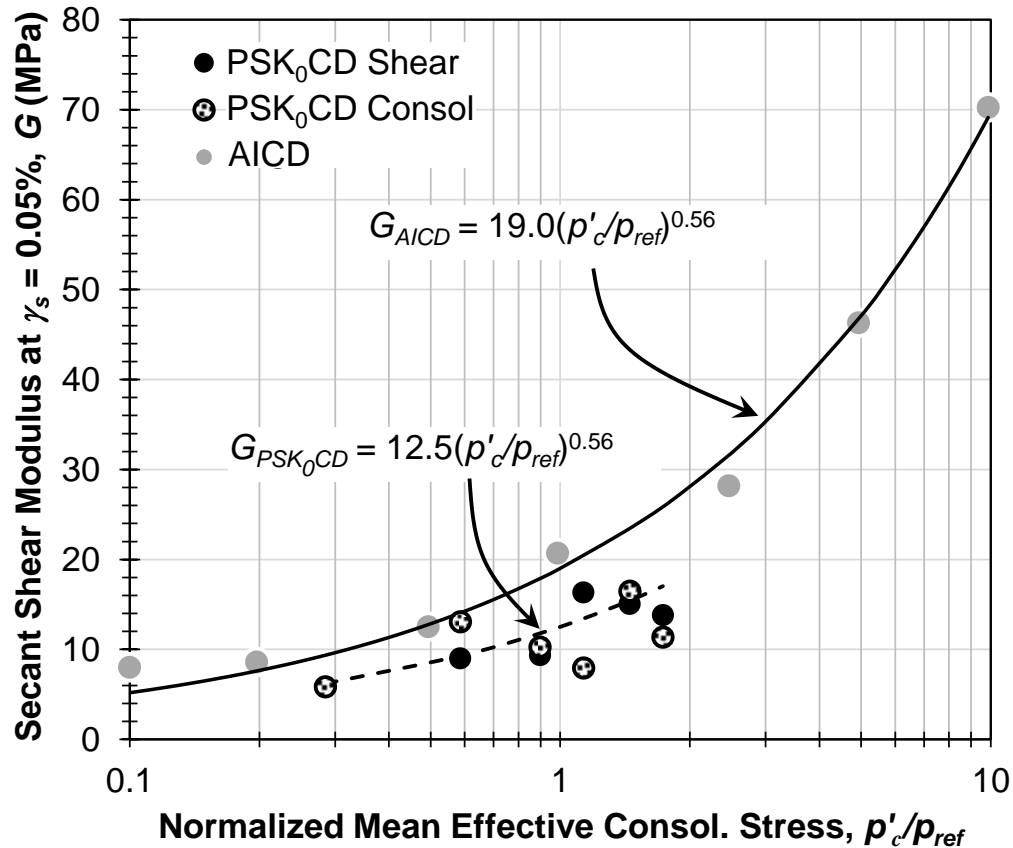


Figure 4.10. Initial tangent shear modulus computed at 0.05% shear strain and plotted versus p'_c/p_{ref} .

4.5.3. STRAIN COMPATIBILITY AND SHEAR BAND FORMATION

The predominant failure mechanism in typical prismoidal PS tests (i.e., with aspect ratios of 2:1) is the formation of a single well-defined shear band (e.g., Lee 1970, Evans and Frost 2010), typically evident by strain softening. The stress-controlled protocol required by the TTA did not allow for the observation of constant volume behavior, resulting in PSK₀CD responses (Figures 4.7, 4.9a) that do not reduce to a critical state like AICD specimens

(Figure 4.3). However, the measured volumetric and principal displacement measurements and fluctuations in the deviatoric response provided indications that shear bands formed during shear. The calculated volumetric strain (Figure 4.9b) initially follows the measured volumetric response but deviates significantly after about one percent shear strain which suggests that the specimen transitions from a continuum to bifurcation response (Bardet 1991). After bifurcation, the measured volumetric response of the soil is primarily dependent on the soil in the shearing zone which has essentially reached a constant volume state. Shear banding of cubical specimens is evident in Figure 4.9b for those portions of the measured volumetric strain measurements that exhibit shear strains with little to no change in volumetric strain. The test conducted at $p'_c = 142$ kPa exhibits the most apparent development of a shear band, occurring at approximately $\gamma_s = 1.7$ %. The formation of shear bands within cubical specimens impacted the deformations observed at the flexible bladders, resulting in the inability to adequately measure rigid block sliding during bifurcation.

Figure 4.11 presents the principal displacement measurements, δ , for a PSK₀CD test at a $p'_c = 114$ kPa as a function of γ_s . The displacements in the major principal directions are positive, indicating compression, whereas displacements in the minor principal direction are negative and indicate extension. Significant deviations between measurements in the minor principal direction are observed at approximately $\gamma_s = 1.75$ %, indicating that face [3a] begins translating whereas face [3b] ceases to displace. At approximately $\gamma_s = 3.5$ %, the behavior reverses and face [3a] stops and face [3b] starts to displace, suggesting that the cubical sample developed two shear bands. Shapiro and Yamamuro (2003), Abelev and Lade 2003, and Lade and Abelev 2003 showed that at least two shear bands can develop in cubical devices as a result of the geometrical constraints of the device that intersect the top or bottom

of a cubical specimen without significantly altering the measured peak friction angles. Considering the geometry of the TTA, shear bands can hypothetically daylight at the center of the top or bottom (i.e., major) faces of the cube as shown in Figure 4.11 inset. However, due to limitations of the testing device, no methods were used to obtain the actual angle of inclination of the specimens; therefore, the schematic in Figure 4.11 represents an estimated or hypothetical geometry.

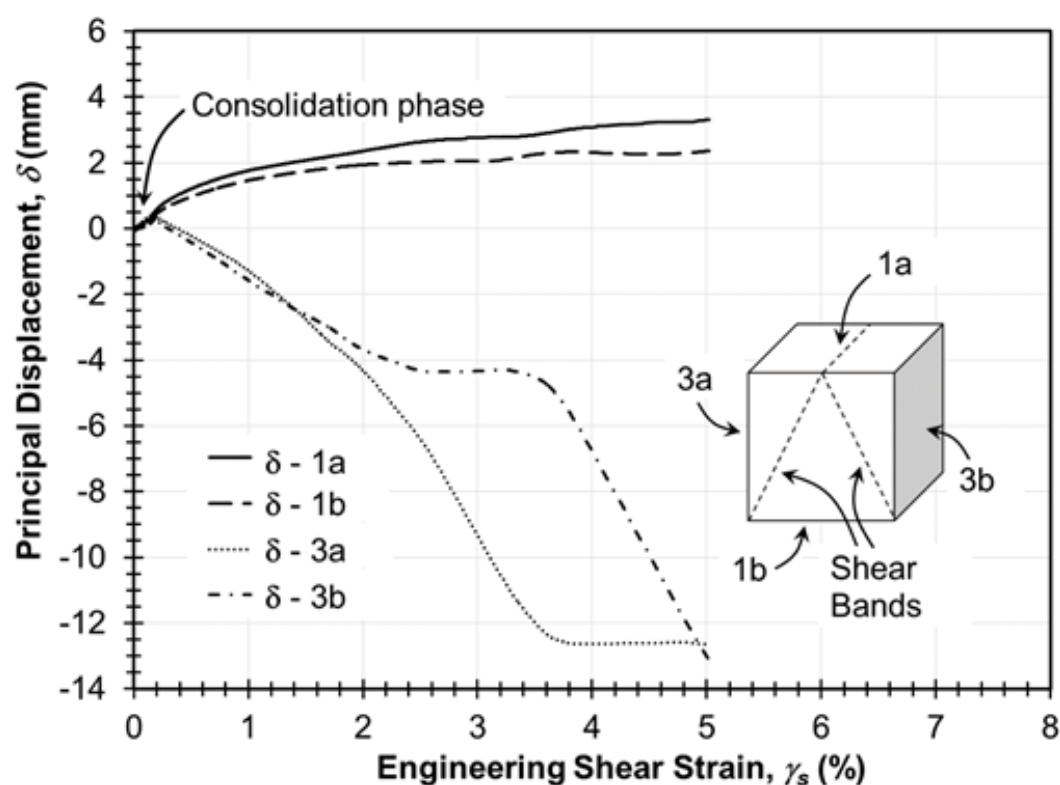


Figure 4.11. Progression of facing bladder displacements for $p'_c = 114$ kPa. Inset: major principal (i.e., 1a and 1b) and minor principal faces (3a and 3b).

The measured change in specimen volume is therefore associated with shearing along these zones and the corresponding dilation angle can be approximated using Equation (4.2) and the measured volumetric response just prior to the onset of initial shear banding. The resulting ψ_{f,PSK_0CD} presented in Figure 4.4 are on average 2.2 times greater than $\psi_{f,AICD}$ and

reduce from 24 to 16 degrees over the range of confining stresses investigated. Although large, the measured PSK₀CD dilation angles are similar in magnitude to those resulting from cubical true triaxial tests on Santa Monica beach sand at effective confining stresses of 50 kPa reported by Lade and Abelev (2003). Lade and Abelev (2003) showed that dilation angles of uniform sands in the plane strain stress path can be on the order of 70% larger than those measured in triaxial compression. Here, the observed PSK₀CD dilation angles on well-graded sandy gravel are approximately 60% larger than those resulting from the AICD stress path.

4.5.4. *EFFECT OF INTERMEDIATE STRESSES AND STRAINS*

Figure 4.8 presents the PSK₀CD stress path to failure and describes key milestones in specimen response during shearing. The end-of-continuum response was defined by the onset of deviation in the principal displacements along the minor principal directions (Figure 4.11), and corresponded to the initiation of shear banding. During shearing, σ'_1 and σ'_2 were uniformly increased and decreased at 1.5 kPa/min, respectively, to produce an applied near-constant p' stress path. As shown in Figure 4.8, a constant p' stress path was not achieved during shear, owing to increases in stresses in the restrained direction.

The intermediate differential stress ratio, b , is used to define the stress state in relation to triaxial compression (TC) and extension (TE) stress paths, where:

$$b = \frac{\sigma'_2 - \sigma'_3}{\sigma'_1 - \sigma'_3} \quad (4.6)$$

The magnitude of b is stress path-dependent and bounded between zero (i.e., TC) and one (i.e., TE), respectively. Green (1971), Reades and Green (1976), Tatsuoka et al. (1986) and Peters et al. (1988) have shown that the strength of soil in plane strain ($b \approx 0.3$) or other intermediate stress states is larger than that for triaxial compression stress paths. On average, PSK₀CD specimens of Kanaskat gravel at failure exhibited $b = 0.34$, similar to the typical range of 0.2 to 0.4, depending on sample density, anisotropy, and testing device, for PS specimens (e.g., Green 1971, Reades and Green 1976, and Peters et al. 1988). Failure was defined as the stress invariant ratio that corresponds to the formation of the initial shear band.

Figure 4.12 presents the progression of b during shearing for the PSK₀CD test specimens. Initially, b is approximately equal to one as a result of the quasi- K_0 consolidation stress path. Upon initiation of shear, b drops rapidly to zero indicating the rotation of the minor principal stresses, whereupon the restrained direction becomes σ'_2 . Figure 4.13 presents the evolution of stresses measured in the restrained direction during consolidation and shearing; markers indicate the initiation of shear (i.e., end-of-consolidation) and the rotation of σ'_2 and σ'_3 . During consolidation, σ'_2 increases in a near-linear manner with increases in p'_c . However, during shearing, σ'_2 decreases while σ'_3 increases until these principal stresses rotate, after which the restrained direction serves to host the intermediate principal effective stress. Thereafter, σ'_2 increases with rapid straining to failure and subsequent increases in the mean effective stress, producing the stress path presented in Figure 4.8. Phusing et al. (2015) conducted true-triaxial DEM simulations with varying and constant b to determine that the shape and location of the yield surface is independent of the stress path, and therefore, the yield surface identified herein is considered insensitive to the selected stress path.

Figure 4.4 presents the PSK_0CD friction angles at failure for Kanaskat gravel which were computed by finding the intersection of the three dimensional stress path with the Mohr Coulomb (M-C) failure criterion:

$$\phi' = \sin^{-1} \left(\frac{\frac{q}{\sqrt{3}} \sin \left(\theta_L + \frac{1}{3} \pi \right)}{p' + \frac{q}{\sqrt{9}} \cos \left(\theta_L + \frac{1}{3} \pi \right)} \right) \quad (4.7)$$

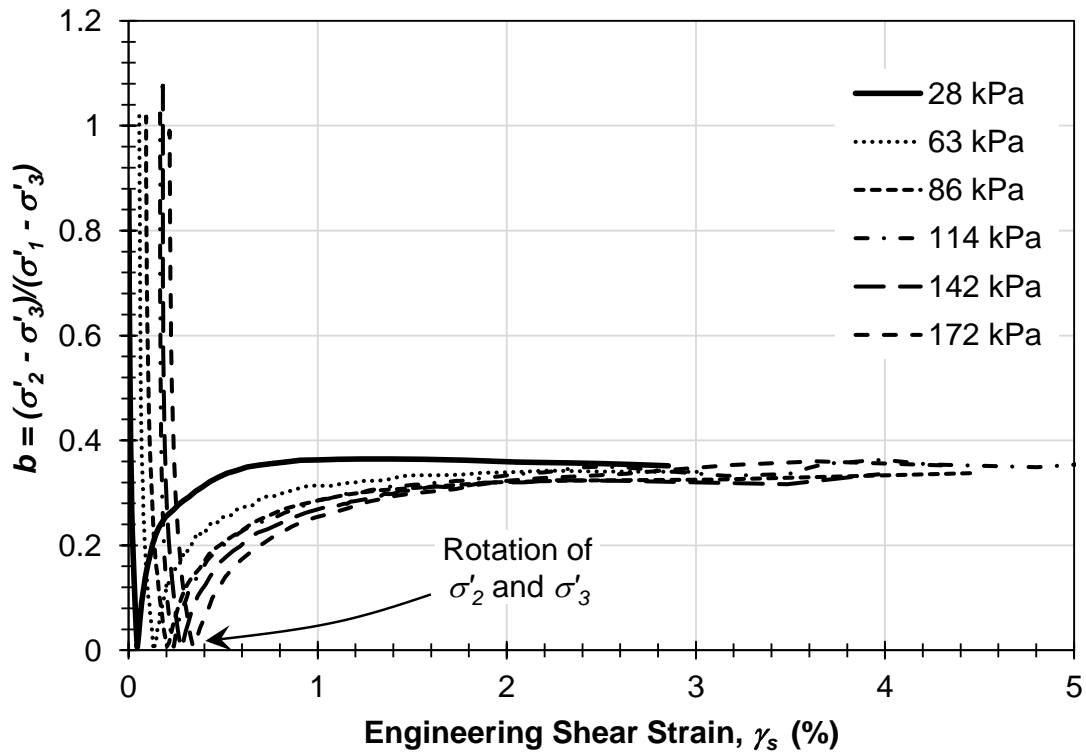


Figure 4.12. Progression of the intermediate deviatoric stress ratio during shearing in the PSK_0CD stress path.

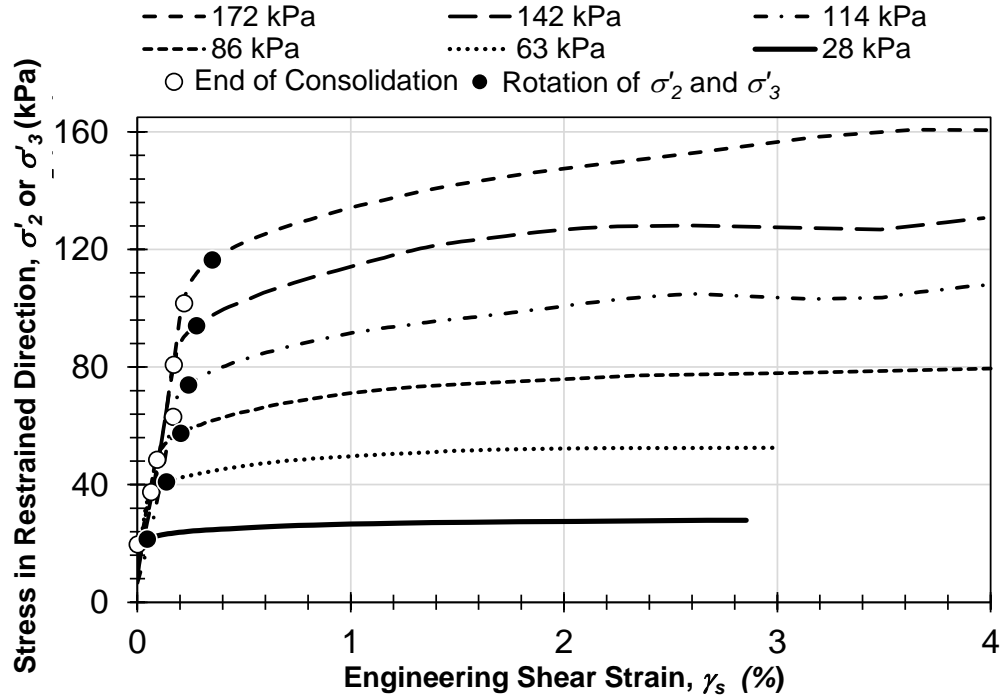


Figure 4.13. Development of intermediate principal stresses for the PSK₀CD consolidation and shearing stress paths.

where θ_L is the lode angle, defined as the angle between the failure point on the three dimensional surface and the major principal stress direction. The lode angle is related to b by (Suzuki and Yanagisawa 2006):

$$\theta_L = \tan^{-1} \left(\frac{\sqrt{3}b}{2-b} \right) \quad (4.8)$$

The log-linear trend shown in Figure 4 did not include the PSK₀CD test at $p'_c = 28$ kPa due to the exaggerated boundary condition effects associated with the flexible membranes at such low confining pressures.

Friction angles for Kanaskat gravel in plane strain, presented in Figure 4.4, have been corrected for geostatic stresses (i.e., 5 kPa) similar to the AICD tests and are approximately

33% larger than those resulting from AICD stress paths. This is larger than that expected given the typical magnitudes reported for plane strain (Jewell and Wroth 1987; Kulhawy and Mayne 1990), which are generally 10 to 20% larger than in triaxial compression. However, typical ranges were developed on the experimental basis of uniformly-graded soils with lower AICD friction angles. Koerner (1970) and Mitchell and Soga (2005) suggest that greater shear resistance in well-graded soils is associated with a greater degree of fabric anisotropy, the presence of larger particles in the soil matrix, and lower void ratios which produce a greater number of frictional contacts. As a result, the measured frictional responses of well-graded materials will be subject to the influence of stress path effects, relative density, and changes in p' that are not readily apparent in Figure 4.7. The large magnitude of the measured friction angles prompted additional cubical triaxial testing to verify the measured plane strain response. Friction angles measured for the simple shear consolidated drained (SSCD) stress path tests on Kanaskat gravel using the TTA are shown in Figure 4.4. The σ'_2 was not allowed to change in the SSCD tests; thus, compared to the PSK₀CD friction angles, the SSCD friction angles are slightly smaller. However, they are of similar magnitude and trend as the plane strain friction angles.

Additionally, comparisons between measured PSK₀CD responses, and calibrated three-dimensional failure criteria can be used to assess the validity of the larger peak response in consideration of σ'_2 . The Matsuoka-Nakai (M-N) or Lade-Duncan (L-D) criteria (Matsuoka et al. 1974, Lade and Duncan 1973), presented in Figure 4.8 indicate that the increase in peak strength can be sufficiently predicted by well-established three-dimensional failure criteria. The M-N failure surface calibrated to the AICD data is presented in Figure 4.8 at $b = 0.34$.

The plotted M-N failure criterion fitting parameter, ξ , was best represented using bi-linear functions of p'_c normalized by p_{ref} :

$$\begin{aligned} \xi &= 0.96 \left(\frac{p'_c}{p_{ref}} \right)^{-0.134} && \text{for } \frac{p'_c}{p_{ref}} < 1; \\ \xi &= 0.96 \left(\frac{p'_c}{p_{ref}} \right)^{-0.059} && \text{for } \frac{p'_c}{p_{ref}} \geq 1; \end{aligned} \quad (4.9)$$

and produced lower deviatoric stresses at a given mean effective stress than those measured. However, the observed curvature of the trend is similar to the fitted trend. The L-D failure criterion requires the fitting of coefficient κ , which was calibrated to the TC stress path using the AICD data and was also best-represented using bi-linear functions of p'_c/p_{ref} for Kanaskat gravel:

$$\begin{aligned} \kappa &= 83.8 \left(\frac{p'_c}{p_{ref}} \right)^{-0.278} && \text{for } \frac{p'_c}{p_{ref}} < 1; \\ \kappa &= 84.0 \left(\frac{p'_c}{p_{ref}} \right)^{-0.095} && \text{for } \frac{p'_c}{p_{ref}} \geq 1; \end{aligned} \quad (4.10)$$

The L-D failure criterion satisfactorily estimates the deviatoric stress of PSK₀CD specimens at failure. The PSK₀CD strength predicted using the L-D failure criterion fitted to the AICD specimens, in concert with comparison to SSCD friction angles, suggests that the observed

PSK₀CD friction angles appropriately represent the highly frictional behavior of Kanaskat gravel in plane strain.

4.6 DISCUSSION OF THE STRESS-DILATANCY BEHAVIOR OF KANASKAT GRAVEL

Bolton (1986) proposed an empirical approach to Rowe's (1962, 1964, and 1969) stress-dilatancy theory using a database of 17 uniform sands to capture the effect of the rate of dilation, relative density, and mean effective stress with the relative dilatancy index, I_R :

$$I_R = D_r \left[Q - \ln \left(\frac{p_f'}{p_{refB}} \right) \right] - R \quad (4.11)$$

where p_{refB} is a reference pressure typically equal to 1 kPa, D_r is the relative density in decimal form, and Q and R are fitting coefficients equal to 10 and 1, respectively. The statistical regression for the dilatation component of strength was found equal to:

$$\phi_f' - \phi_{cv}' = A_{\psi,PS} I_R = A_{\psi,TC} I_R \quad (4.12)$$

where $\phi_f' - \phi_{cv}'$ is a measure of dilatancy, $A_{\psi,PS} = 5$, $A_{\psi,TC} = 3$, , and the subscripts PS and TC denote plane strain and triaxial compression, respectively. In a response to Tatsuoka (1987), Bolton (1987) presented data on uniform Toyoura sand to show that Equation (4.11) overpredicts $\phi_f' - \phi_{cv}'$ at low mean effective stresses ($p' < 150$ kPa). Bolton (1987) attributed the resulting error to an apparent increase in ϕ_{cv}' at low to very low σ'_3 , and proposed improved

empirical correlations as a function of p' . More recently, Salgado et al. (2000) and Chakraborty and Salgado (2010) confirmed that Bolton's Q decreases with a decrease in σ'_3 below approximately 200 kPa for Toyoura Sand which was also attributed to changes in ϕ'_{cv} .

Equation (4.11) is a formulation of Equation (4.1) in which the a coefficient was empirically derived by Bolton (1986) to be equal to 0.8 in plane strain and 0.48 in triaxial compression. Figure 4.14(a) presents the variation of $\phi'_{f,AICD}$ and ϕ'_{f,PSK_0CD} with ψ_f along with estimates provided by Equation (4.11). The fitted linear trends presented in Figure 4.14(a) were established by assuming that ϕ'_{cv} was equal to a constant 40 degrees in the PSK₀CD and AICD stress paths. The resulting fitting coefficient a for use with Equation (4.1) is equal to 1.08 and 0.58 for Kanaskat gravel in PSK₀CD and AICD stress paths, respectively.

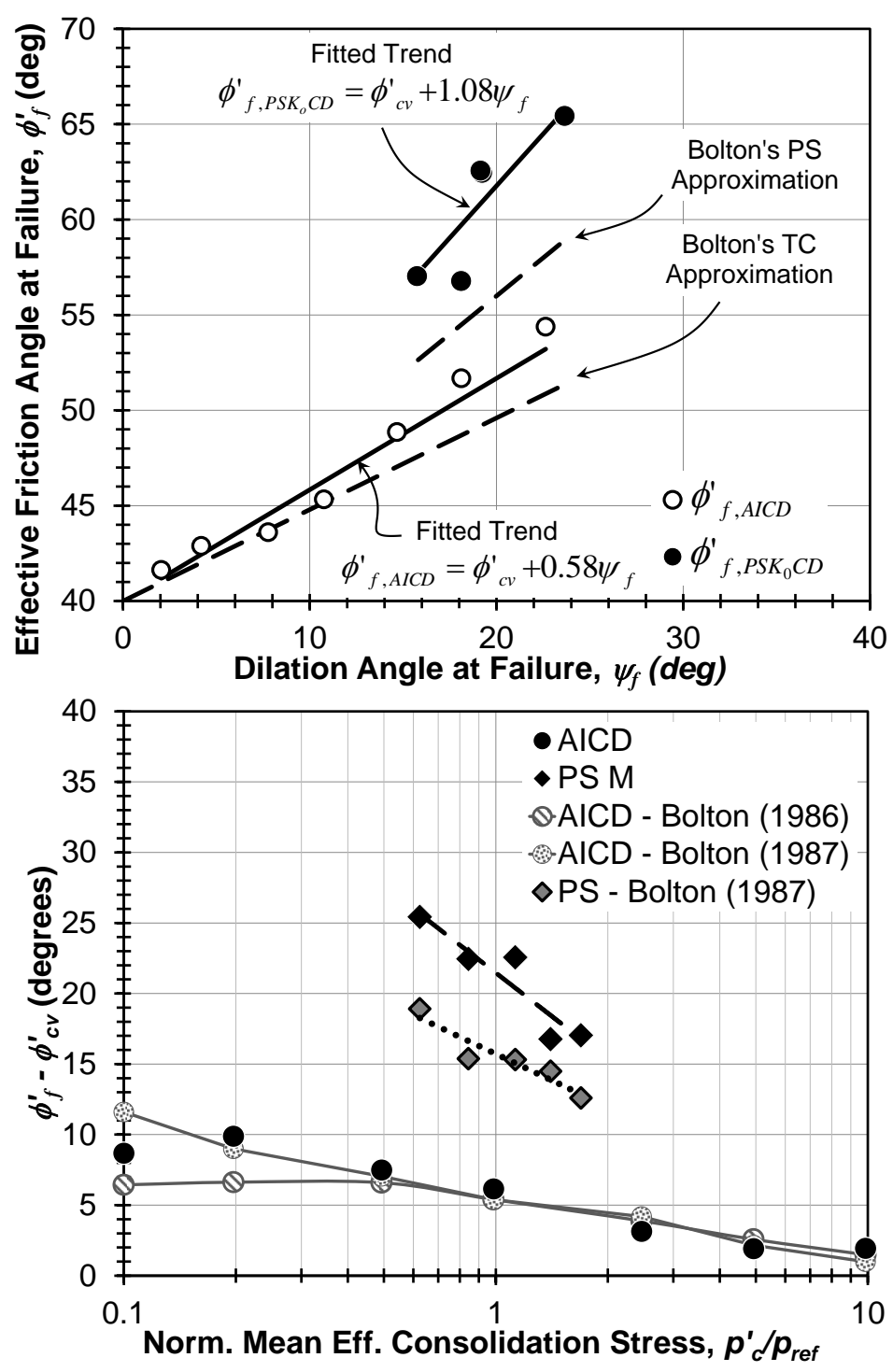


Figure 4.14. Stress-dilatancy behavior of Kanaskat gravel: (a) comparison of effective friction and dilation angle at failure and (b) comparison of observations to Bolton's approximation as a function of mean effective confining stress.

Figure 4.14(b) compares measured $\phi'_f - \phi'_{cv}$ as a function of p'/p_{ref} to that approximated by Bolton's (1986) original and modified (Bolton 1987) empirical expressions. Individually measured $\phi'_{cv,AICD}$ were used to compute the $\phi'_f - \phi'_{cv}$ values for the AICD stress path shown in Figure 4.14. The effective constant volume friction angle for the PSK₀CD specimens could not be observed, as described previously (refer to Figure 4.9). However, experimental work by Lee (1970) suggests that ϕ'_{cv} is equivalent for plane strain and triaxial compression at high confining pressures. Therefore, the average PSK₀CD constant volume friction angle equal to 40 degrees was used in order to calculate $\phi'_f - \phi'_{cv}$ for the PSK₀CD stress path, based on measured $\phi'_{cv,AICD}$.

Although some differences are noted, there is relatively good agreement between the observed and predicted response of Bolton's (1986) original triaxial compression stress path approximation. However, Bolton's (1987) modified approximation does not adequately capture the trend in $\phi'_f - \phi'_{cv}$ for Kanaskat gravel at low mean effective pressures and for the AICD specimens. This response is attributed to the presence of stronger particles and the larger number of particle contacts in the well-graded soil matrix that dominate the frictional characteristics at lower pressures. Differences in the trends of the measured and predicted PSK₀CD data indicated that Bolton's (1986) approximation of plane strain strength at failure underestimates the quantity of dilation by approximately 30%. Thus, it appears that Bolton's (1986) approximation of Rowe's stress-dilatancy theory may not be a estimate of the stress-dilation response of well-graded gravelly soils in both TC and PS stress paths. This suggests that Bolton's fitting a coefficient in the plane strain stress path should be increased to 1.08 in order for use in practice.

4.7 SUMMARY AND CONCLUSION

Geotechnical engineers often use stress-dilatancy theories and approximations that are developed based on uniform sands, however, very little information of this kind exists for well-graded gravelly soils. Pertinent questions regarding the stiffness, strength, and volumetric response of these soils in plane strain remain to be answered. To reduce the evident gap in information, an experimental program was conducted to study the stiffness, strength, and stress-dilatancy of well-graded Kanaskat gravel using axisymmetric, isotropically consolidated drained (AICD) triaxial and cubical pure shear quasi- K_0 consolidated drained (PSK₀CD) plane strain tests over a wide range of confining stresses. Results from the testing program indicate that the stress-dilatancy behavior of Kanaskat gravel differs from that of uniform sands. However the theories developed based on uniform soils can be used to satisfactorily estimate the soil response under typical working stresses.

The secant shear stiffness of PSK₀CD specimens were approximately 35% less than that measured in AICD specimens, which indicates that the presence of intermediate strains has a significant effect on the pre-failure response of sandy gravel soils. Additionally, the plane strain friction and dilation angles of Kanaskat gravel at failure are significantly greater than for AICD specimens sheared in triaxial compression, on the order of 33 and 120% larger, respectively. The PSK₀CD response at failure was compared to drained consolidated simple shear tests and three dimensional failure criteria fitted to AICD specimens and that incorporate the effect of the intermediate principal stress. The Matsuoka-Nakai failure criterion was found to under-predict the observed failure envelope, whereas the Lade-Duncan failure criterion was found to adequately predict the measured PSK₀CD response at failure. Geometrical constraints imposed by the cubical triaxial device impacted the measured

volumetric response and inhibited free shear band formation. As a result, two incipient shear bands formed in the TTA requiring careful interpretation of volumetric responses for estimation of the dilation angle. Comparisons between Bolton's (1986, 1987) approximation of Rowe's (1969) stress-dilatancy theory indicate that in general, the modified approximation does not appear appropriate for low confining stresses. Bolton's (1986) original correlation appeared applicable to the well-graded gravelly soils in the triaxial compression stress path over the range in pressures investigated. Bolton's (1986) correlation was found to under estimate dilation in well-graded gravelly soils and new coefficients are recommended for use in practice. The data reported here should help those requiring accurate estimates of the stiffness, strength, and stress-dilatancy of well-graded sandy gravel and improve their confidence in selected design parameters.

4.8 LIST OF REFERENCES

- Abelev, A. V., and Lade, P. V. (2003). Effects of cross-anisotropy on three-dimensional behavior of sand. I: Stress-strain behavior and shear banding. *Journal of Engineering Mechanics*, 129(2), pp. 160–166.
- Arthur, J.R.F. and Assadi, A. (1977). Ruptured Sand Sheared in Plane Strain. *Proceedings, Ninth International Conference on Soil Mechanics and Foundation Engineering*, Tokyo, 1, pp.19-22.
- Arthur, J.R.F. (1988) Cubical Devices: Versatility and Constraints. *Advanced Triaxial Testing of Soil and Rock, ASTM 977*, Robert T. Donaghe, Ronald C. Chaney, and Marshal L. Silver, Eds., American Society of Testing Materials, Philadelphia, pp. 743-765.
- Alshibli, K.A., Batiste, S.N., and Sture, S. (2003). Strain Localization in Sand: Plane Strain versus Triaxial Compression. *Journal of Geotechnical and Geoenvironmental Engineering*, 129(6), pp. 483-494.
- Bardet, J.P. (1991). Orientation of shear bands in frictional soils. *Journal of Engineering Mechanics*, 117(7), 1466-1485.
- Biggerstaff, D.C. (2010). Analysis of the effects of the Intermediate Principal Stress on the Behavior of Gravel with a 9.5 inch True Triaxial Apparatus. *MS Thesis*, University of Washington, Seattle, WA.
- Bishop, A.W. (1954). Correspondence on “Shear characteristics of a saturated silt, measured in triaxial compression.” *Géotechnique*, 4(1), pp. 43-45.
- Black, D.K., and Lee, K.L. (1973). Saturating laboratory samples by back pressure. *Journal of the Soil Mechanics and Foundation Division, ASCE*, 99(1), 75-93.

- Bolton, M.D. (1986). The strength and dilatancy of sands. *Géotechnique*, 36(1), 65-78.
- Bolton, M.D. (1987). "Closure of 'The strength and dilatancy of sands' by Tatsuoka, F. *Géotechnique*, 37(2), 219-226.
- Chakraborty, T. and Salgado, R. (2010). Dilatancy and Shear Strength of Sand at Low Confining Pressures. *Journal of Geotechnical and Geoenvironmental Engineering*, 136(3), pp. 527-532.
- Chang, C.S. and Yin, Z.Y. (2010). Modeling Stress-Dilatancy for Sand under Compression and Extension Loading Conditions. *Journal of Engineering Mechanics*, 136(6), pp. 777-786.
- Charles, J.A. and Watts, K.S. (1980). The influence of confining pressure on the shear strength of compacted rockfill. *Géotechnique*, 30(4), pp. 353-367.
- Choi, C., Arduino, P., and Harney, M.D. (2008). Development of a True Triaxial Apparatus for Sands and Gravels. *Geotechnical Testing Journal*, 31(1), pp. 1-13.
- Chu, J. (1994). Study on the stress-dilatancy behavior of sand by strain path testing. *Proc. Pre-failure Deformation of Geomaterials*, Shibuya, Malachi and Miura, Eds., Rotterdam, pp. 365-370.
- Colliat-Dangus, J.L., Desrues, J., and Foray, P. 1988. Triaxial testing of granular soil under elevated cell pressure. *Advanced triaxial testing of soil and rock*. Edited by R.T. Donaghe, R.C. Chaney, and M.L. Silver. American Society for Testing and Materials, Special Technical Publication STP 977, pp. 290–310.
- Cornforth, D.H. (1964). Some experiments on the influence of strain conditions on the strength of sands. *Géotechnique*, 14(2), pp.143-167.

- De Josselin de Jong, G. (1976). Rowe's stress-dilatancy relation based on friction. *Géotechnique*, 26(3), pp. 527-534.
- Evans, T.M., and Frost, J.D. (2010). Multi-scale investigation of shear bands in sand: Physical and numerical experiments. *International Journal for Numerical and Analytical Methods in Geomechanics*, 34(15), pp. 1634-1650.
- Finn, W.D.L., Wade, N.H., and Lee, K.L. (1967). Volume changes in triaxial and plane strain tests. *Journal of the Soil Mechanics and Foundation Division, ASCE*, 93(SM6), pp. 297-308.
- Frydman, S., Talesnick, M., Nawatha, H., and Schwartz, K. (2007). Stress-dilation of undisturbed sand samples in drained and undrained triaxial shear. *Soils and Foundations*, 47(1), pp. 27-32.
- Green, G.E. (1971). Strength and deformation of sand measured in an independent stress control cell. *Stress-strain behavior of soils. Proc. Roscoe Memorial Symposium*, pp. 285-323.
- Hanna, A. (2001). Determination of plane-strain shear strength of sand from the results of triaxial tests. *Canadian Geotechnical Journal*, 38(6), pp.1231-1240.
- Holtz, W.G. and Gibbs, J. (1956). Triaxial shear tests on pervious gravelly soils. *Journal of Soil Mech. Found. Div. ASCE*, 82(1), pp. 1-22.
- Hoopes, O.T. (2007). Experimental Study with a 9.5-in. True-Triaxial Apparatus: Phase Transformation Surface Mapping and PID Strain-Control. *MS Thesis*, University of Washington, Seattle, WA.

- Horne, M.R. (1965). The behavior of an assembly of rotund, rigid, cohesionless Particles. *Proc. Of the Royal Society of London. Series A, Mathematical and Physical Sciences*, 286(1404), pp. 79-97.
- Houlsby, G.T. (1991). How the dilatancy of soils affects their behavior. Invited Theme Lecture, *Proceedings of the Tenth European Conference on Soil Mechanics and Foundation Engineering*, Florence, May 27-30, 4, pp. 1189-1202.
- Jewell, R.A., and Wroth, C.P. (1987). Direct Shear Tests on Reinforced Sand. *Géotechnique*, 37(1), pp. 53-68.
- Krumbein, W. C. and Sloss, L. L. (1963). *Stratigraphy and sedimentation*, 2nd Ed., Freeman and Company, San Francisco.
- Kulhawy, F.H., and Mayne, P.W. (1990). *Manual on Estimating Soil Properties for Foundations*, Final Report, Project 1493-6, EL-6800, Electric Power Research Institute, Palo Alto, CA.
- Lade, P. V., and Abelev, A. V. (2003). Effects of cross anisotropy on three-dimensional behavior of sand. II: Volume change behavior and failure. *Journal of Engineering Mechanics*, 129(2), pp. 167–174.
- Lade, P.V. and Duncan, J.M. (1973). Cubical triaxial tests on cohesionless soils. *Journal of Soil Mechanics and Foundations Division*, 99(SM10), 793-812.
- Lee, K.L. (1970) Comparison of plane strain and triaxial tests on sand. *Journal of the Soil Mechanics and Foundation Division*, 96(SM3), pp. 901-923.
- Lee, K.L. and Seed, H.B. (1967). Drained Strength Characteristics of Sands. *Journal of the Soil Mechanics and Foundation Division*, November, 93(SM6), pp. 117-141.

- Maqbool, S. and Koseki, J. (2007). Large-Scale Plane Strain Compression Tests on Compacted Gravel. *Pakistan Journal of Engineering and Applied Science*, 1, pp. 40-60.
- Marachi, N.D., Chan, C.K., and Seed, H.B. (1972). Evaluation of properties of rockfill materials. *Journal of Soil Mechanics and Foundations Division ASCE*, 98(SM1), pp. 95-114.
- Marachi, N., Duncan, J.M., Chan, C.K., and Seed, H.B. (1981). Plain-Strain Testing of Sand. *Laboratory Shear Strength of Soil, ASTM STP 740*. R.N. Young and F.C. Townsend, Eds., pp. 294-302.
- Marsal, R.J. (1967). Large scale testing of rockfill materials. *Journal of Soil Mechanics and Foundations Division ASCE*, 93(SM2), pp. 27-44.
- Matsuoka, H. and Nakai, T. (1974). Stress-Deformation and Strength Characteristics of Soil under Three Different Principal Stresses. *Proc. JSCE*, Vol. 232, pp. 59-70.
- Matsuoka, H., Hoshikawa, T., and Ueno, K. (1990). A general failure criterion and stress-strain relation for granular materials to metals. *Soils and Foundations*, 30(2), pp.119-127.
- Matsuoka, H. and Liu, S. (1998). Simplified direct shear test on granular materials and its application to rockfill materials. *Soils and Foundations*, 38(4), pp. 275-284.
- Matsuoka, H., Liu, S., Sun, D., and Nishikata, U. (2001). Development of a new in situ direct shear test. *Geotechnical Testing Journal*, 24(1), pp. 92-101.
- Mitchell, J.K., and Soga, K. (2005). *Fundamentals of Soil Behavior*, John Wiley and Sons, Inc., New York.
- Newland, P.L. and Allely, B.H. (1957). Volume Changes in Drained Triaxial Tests on Granular Materials. *Géotechnique*, 7(1), pp. 17-34.

- Panda, B.C. and Ghosh, A.K. (2000). Influence of Grain Size Distribution on Dilatancy of Sand. *Journal of the Institution of Engineers*, 81(2), pp. 68-70.
- Penman, A.D.M. (1953). Shear characteristics of a saturated silt. *Géotechnique*, 3(8), pp. 312-328.
- Peters, J.F., Lade, P.V., and Bro, A. (1988). Shear Band Formation in Triaxial and Plane Strain Tests. *Advanced Triaxial Testing of Soil and Rock*, Donaghe, R.T., Chaney, R.C., and Silver, M.L., Eds., ASTM, Philadelphia, pp. 604-627.
- Poorooshasb, H.B. and Roscoe, K.H. (1961). The correlation of the results of shear tests with varying degrees of dilatation. *Proc. 5th International Conference on Soil Mechanics*, 1, pp. 297-304.
- Powers, M.C. (1953). A New Roundness Scale for Sedimentary Particles. *Journal of Sedimentary Petrology*, 23(2), pp. 117-119.
- Ramamurthy, T. and Tokhi, V.K. (1981). Relation of Triaxial and Plane Strain Strengths. *Proc. of the International Conference on Soil Mechanics and Foundation Engineering*, 1, pp. 755-758.
- Reades, D.W. and Green, G.E. (1976). Independent stress control and triaxial extension tests on sand. *Géotechnique*, 26(4), pp. 551-576.
- Reynolds, O. (1885). The Dilating of Media Composed of Rigid Particles in Contact. *Philosophical Magazine*. December.
- Rowe, P.W. (1962). The Stress-dilatancy Relations for static Equilibrium of an Assembly of Particles in Contact. *Proc. R. Soc.*, 269A, pp. 500-527.

- Rowe, P.W. (1969). The relation between the shear strength of sands in triaxial compression, plane strain, and direct shear. *Géotechnique*, 19(1), pp. 75-86.
- Rowe, P.W., Barden, L., and Lee, I.K. (1964) Energy Components during the Triaxial Cell and Direct Shear Tests. *Géotechnique*, 14(3), September.
- Russell, A., and Khalili, N. (2005). A bounding surface plasticity model for sands exhibiting particle crushing. *Canadian Geotechnical Journal*, 41, pp. 1179-1192.
- Salgado, R., Bandini, P., and Karim, A. (2000). Shear Strength and Stiffness of Silty Sand. *Journal of Geotechnical and Geoenvironmental Engineering*, 126(5), pp. 451-462.
- Schanz, T. and Vermeer, P.A. (1996). Angles of friction and dilatancy of sand. *Géotechnique*, 46(1), pp. 145-151.
- Shapiro, S. and Yamamuro, J.A. (2003). Effects of Silt on Three-Dimensional Stress-Strain Behavior of Loose Sand. *Journal of Geotechnical and Geoenvironmental Engineering*, 129(1), pp. 1-11.
- Skemmer, N. A. and Hillis, S. F. (1970). Gradation and shear characteristics of four cohesionless soils. *Canadian Geotechnical Journal*, 7, pp. 62-68.
- Stuedlein, A. W., Mikkelsen, P. E., and Bailey, M. J. (2007). Instrumentation and performance of the third runway north MSE wall at Seattle-Tacoma international airport. *7th International Symposium on Field Measurements in Geomechanics, FMGM 2007, September 24, 2007 - September 27, 2007*, Geotechnical Special Publication, American Society of Civil Engineers, 26.

- Stuedlein, A. W., Bailey, M. J., Lindquist, D. D., Sankey, J., and Neely, W. (2010). Design and Performance of a 46-m-High MSE Wall. *Journal of Geotechnical and Geoenvironmental Engineering*, 136(6), 786–796.
- Stuedlein, A. W., Allen, T. M., Holtz, R. D., and Christopher, B. R. (2012). Assessment of Reinforcement Strains in Very Tall Mechanically Stabilized Earth Walls. *Journal of Geotechnical and Geoenvironmental Engineering*, 138(3), 345–356.
- Suzuki, K and Yanagisawa, E. (2006). “Principal Deviatoric Strain Increment Ratios for Sand Having Inherent Transverse Isotropy.” *ASCE International Journal of Geomechanics*, Sept/Oct 2006, 356-366.
- Tatsuoka, F. (1976). Stress-dilatancy relations of anisotropic sands in three dimensional stress condition. *Soils and Foundations*, 19(2), pp. 1-18.
- Tatsuoka, F., Sakamoto, M., and Kawamura, T. (1986). Strength and deformation characteristics of sand in plane strain compression at extremely low pressures. *Soils and Foundations*, 26(1), pp. 65-84.
- Tatsuoka, F. (1987). “Discussion of ‘The strength and dilatancy of sands’ by Bolton, 1986.” *Géotechnique*, 37(2), 219–226.
- Terzaghi, K., Peck, R.B., and Mesri, G. (1996). *Soil in engineering practice*, 3rd Edn. London: Wiley.
- Taylor, D.W. (1948). *Fundamentals of Soil Mechanics*. New York: J. Wiley and Sons.
- Vardoulakis, I. (1980). Shear band inclination and shear modulus of sand in biaxial tests. *Int. Journal for Numerical and Analytical Methods in Geomechanics*, 4, 103-119.

- Walters, J.J. (2013). Characterization of reinforced fill soil, soil-reinforcement interaction and global stability of very tall MSE walls. *MS Thesis*, Oregon State University, Corvallis, OR.
- Wan, R.G. and Guo, P.J. (2004). Stress-dilatancy and fabric dependencies on sand behavior. *Journal of Engineering Mechanics*. 130(6), pp. 635-645.
- Wanatowski, D. and Chu, J. (2008). Stress-Strain Behavior of a Granular Fill Measured by a New Plane-Strain Apparatus. *Geotechnical Testing Journal*, 29(2), pp. 1-9.
- Wood, D.M., and Maeda, K. (2008). Changing grading of soil: effect on critical states. *Acta Geotechnica*, 3(1), pp. 3-14.
- Xiao, Y., Liu, H., Chen, Y., and Jiang, J. (2014). Strength and deformation of rockfill material based on large-scale triaxial compression tests. I: Influences of Density and Pressure. *Journal of Geotechnical and Geoenvironmental Engineering*, 10.1061/(ASCE)GT.1943-5606.0001176, 04014070.
- Zhao, H.F., Zhang, L.M., and Chang, D.S. (2013). Behavior of Coarse Widely Graded Soils under Low Confining Pressures. *Journal Geotechnical and Geoenvironmental Engineering*, 139(1), pp. 35-48.
- Zienciewicz, O.C. Humpheson, C. and Lewis, R.W. (1975). Associated and Non-Associated Visco-Plasticity and Plasticity in Soil Mechanics, *Géotechnique*, Vol. 25, 4, pp. 671-689.

**CHAPTER 5: THREE-DIMENSIONAL STRESS-STRAIN
RESPONSE AND STRESS-DILATANCY OF WELL-GRADED
GRAVEL**

Andrew Strahler, EIT, Armin W. Stuedlein, PhD, P.E., and Pedro W. Arduino, PhD, P.E.

Journal of Engineering Mechanics

1801 Alexander Bell Drive

Reston, VA 20191-4400

To Be Submitted

5.1 ABSTRACT

The three dimensional (3-D) stress-strain response of uniform sands has been the primary focus of laboratory investigations, generally due to limitations of laboratory devices. However, the applicability of stress-dilatancy theories and 3-D stiffness, strength, and volumetric responses have not been evaluated for well-graded fill soils commonly used in design. A series of drained true-triaxial tests at three levels of confining stress on specimens of well-graded Kanaskat gravel were conducted to address pertinent questions regarding this behavior. Constant mean effective stress paths during shearing corresponded to triaxial compression (TC), simple shear (SS), and triaxial extension (TE). Results plane strain quasi- K_0 consolidated (PSK₀) stress paths on the same material are incorporated and the general behavior suggest that 3-D stress-dilatancy and frictional responses differ from that of uniform soils. The secant shear modulus at an initial stage of shearing was found to be stress path dependent with TC specimens being the highest. However, the stiffness at a more advanced stage of shearing was found to be relatively independent of stress path and fitted power laws presented adequately capture pressure-dependent stiffness. Friction and dilation angles at failure are interpreted with respect to experimental boundary conditions and are significantly higher than those measured in the TC stress path. However, properly calibrated stress-dilatancy theories and 3-D failure criterion are sufficiently capable of capturing this behavior. Fitting parameters are provided for a commonly used stress-dilatancy approximation and two 3-D dimensional failure criterion for the soil investigated here. The data presented here should help those seeking to estimate the 3-D response of a well-graded gravelly soil.

5.2 INTRODUCTION

The influence of the intermediate principal stress on the response of uniform laboratory sands and uniform rock fill material has been the focus of much research (Kjellman 1936, Green G. E. 1972, Lade and Duncan 1973, Lade 1978, Yamada and Ishihara 1983, Matsuoka et al. 2002, Lade and Abelev 2003, Abelev and Lade 2003, Shapiro and Yamamuro 2003, Choi et al. 2008, Xiao et al. 2014, and Xiao et al. 2015). However, axisymmetrical, isotropically- (AICD) and plane strain, K_0 -consolidated drained (PSK₀) tests conducted to establish a benchmark for a well-graded gravelly soil, described by Strahler et al. (2015), indicated that the strength and dilatancy in these stress paths were greater than those produced by uniform granular soils and could be used to improve design efficiency. Even less is known about the true triaxial compression, true triaxial extension, and simple shear stress path responses of well-graded gravelly soils. The experimental work presented here expands upon the work reported by Strahler et al. (2015). A true triaxial apparatus (TTA) was used to conduct a series of consolidated drained constant mean effective stress path tests to assess the influence of the stress path on the stiffness, strength, and stress-dilatancy response of well-graded gravelly soil. First, the comprehensive experimental program used to investigate the three dimensional (3-D) stress-strain response of Kanaskat gravel is described and the baseline AICD and PSK₀ stress-strain and volumetric responses are reviewed. Then, the selected, three-dimensional stress paths and corresponding stress-strain and volumetric responses within the large University of Washington (UW) TTA is presented. Comparisons of the stress-strain-strength response of cubical, simple shear (SS), triaxial compression (TC), and triaxial extension (TE) specimens to plane strain and axisymmetric, isotropically consolidated triaxial compression tests indicate the strength and dilatancy of this

well-graded soil are larger than implied by experimental work on uniformly-graded soils. The stress-dilatancy response of Kanaskat gravel outside TC and TE stress paths is generally under-predicted by Bolton's (1986) approximation. Comparisons between fitted Matsuoka-Nakai (M-N) and Lade-Duncan (L-D) three-dimensional failure criteria indicate that the L-D failure criterion most accurately represents the response at failure and fitted coefficients are provided for both failure criteria. The paper concludes with a discussion regarding the influence of the stress path on dilatancy.

5.3 SOIL DESCRIPTION AND EXPERIMENTAL PROGRAM

The well-graded sandy gravel used in this research comprised the reinforced fill material in the tall MSE walls constructed for the SeaTac International Airport (STIA) third runway expansion project described by Stuedlein et al. (2007, 2010a, 2010b, and 2012). The sub-rounded sandy gravel used in this study is characterized with a D_{10} , D_{50} , D_{max} , and C_u equal to 0.22 mm, 6.0 mm, 25.4 mm, and 46, respectively. The mineral content primarily consists of quartz with some potassium feldspar and hornblende. Minimum and maximum void ratios determined using ASTM D4253 (2006) were equal to 0.182 and 0.365, respectively. The maximum dry unit weight, $\gamma_{d,max}$, and corresponding optimum moisture content, w_{opt} , established from Modified Proctors (ASTM D1557, 2012) are 22.4 kN/m³ and 6.4 percent, respectively. In consideration of the STIA project specifications, each test specimen was compacted to a target $\gamma_d = 21.3$ kN/m³, corresponding to a relative density, D_R , of 65 percent; deviations of ± 2.5 percent in actual relative density were allowed. Baseline AICD and PSK₀ strength tests reported by Strahler et al. (2015) indicated that the well-graded gravel has a constant volume friction angle, ϕ'_{cv} , of approximately 40°, and AICD effective friction angles

at failure, $\phi'_{f,AICD}$, ranging from 54 to 42° for confining pressures of 10 to 1,000 kPa. Friction angles measured in the PSK_0 stress path, $\phi'_{f,PSK0}$, were approximately 30% greater than those measured in the AICD stress path and were as high as 68 degrees. Refer to Strahler et al. (2015) for additional details on this experimental work.

A series of true triaxial tests were performed on specimens of well-graded sandy gravel within the cubical UW-TTA to assess the effects of confining pressure and stress path on the strength and dilation of a well-graded gravelly soil. The UW-TTA device was first implemented by Anderson (1993), and has since undergone modifications to improve its capability and accuracy (Choi et al. 2008, Biggerstaff 2010, and Strahler et al. 2015). The UW-TTA consists of a stress-controlled flexible boundary system with specimens having side lengths of 240 mm, and is considered sufficiently large enough to accommodate the maximum particle size of the Kanaskat gravel (ASTM 2011). A more detailed discussion regarding the development and application of the UW-TTA is provided by Choi et al. (2008).

Specimens were compacted in lifts to achieve a relative density of $65\% \pm 2.5\%$ to correspond to the specifications implemented by Strahler et al. (2015). After compaction, specimens were isotropically consolidated until the target mean effective stress, p'_c , was reached. Limitations such as the maximum available pressure and minimum allowable back pressure required that p'_c range between approximately 45 to 200 kPa (Table 5.1). All tests were performed such that a constant mean effective stress was maintained during shearing. This was accomplished by increasing the major principal stress and simultaneously reducing or maintaining the intermediate and minor principal stresses. Constant intermediate principal stress ratios, or b , were maintained during shearing in this manner.

Table 5.1. Summary of testing results for Kanaskat gravel in various stress paths.

Stress Path	b -value	p'_c (kPa)	p'_f (kPa)	ϕ'_f (deg)	ψ_f (deg)	D_R (%)	G_{50} (MPa)	G_{in} (MPa)	E_{50}^* (MPa)
TC	0.03	46	46	64	32	65.6	9	23	25
	0.00	106	106	52	15	63.7	20	33	50
	0.01	201	201	47	13	63.7	26	44	64
TE	1.00	52	52	62	30	63.7	9	14	50
	1.00	100	100	49	20	64.5	15	21	68
	0.98	202	202	53	17	64.5	26	37	109
	0.98	200	200	52	23	66.7	25	38	98
SS	0.53	49	49	64	33	62.6	11	19	37
	0.51	54	55	64	33	63.1	9	21	29
	0.54	101	101	59	19	62.3	18	31	57
	0.51	204	204	55	16	66.1	23	37	75
PSK ₀	0.35	29	34	63	30	65.0	4	5	23
	0.35	59	67	65	24	66.7	4	10	22
	0.34	91	102	62	19	66.4	7	13	32
	0.34	115	133	62	19	65.6	11	21	32
	0.36	147	164	57	18	64.5	10	19	40
	0.34	176	194	55	16	67.2	11	17	42
AICD	0.00	10	38	54	23	62.9	7	8	13
	0.00	20	68	52	18	64.2	8	9	19
	0.00	50	151	49	15	64.0	12	13	29
	0.00	100	263	45	11	63.1	20	21	46
	0.00	250	623	44	8	64.2	28	28	70
	0.00	500	1209	43	4	63.8	45	46	114
	0.00	1000	2314	42	2	66.0	69	70	174

*Calculated ignoring σ'_2

5.4 3-D TRUE-TRIAxIAL RESPONSE OF KANASKAT GRAVEL

The three-dimensional framework used to compare the soil response in each stress path was presented by Choi et al. (2008) and Strahler et al. (2015), where the deviatoric stress, q , is given by:

$$q = \sqrt{3J_2} \quad (5.1)$$

where J_2 is the second invariant of the effective stress tensor. Engineering shear strains on the deviatoric plane are given by:

$$\gamma_s = \sqrt{\frac{4}{3}J''_2} \quad (5.2)$$

where J''_2 is the second invariant of the deviatoric strain tensor. The stress paths are represented in terms of an intermediate principal stress ratio, more commonly referred to as b , given by:

$$b = \frac{\sigma'_2 - \sigma'_3}{\sigma'_1 - \sigma'_3} \quad (5.3)$$

where σ'_1 , σ'_2 , and σ'_3 are the minor, intermediate, and major principal stresses, respectively. The intermediate principal stress ratio ranges from zero for conventional TC tests, to one for conventional TE tests, whereas SS tests produce a b equal to 0.5. The intermediate principal

stress ratio for PSK_0 tests of Kanaskat gravel was determined equal to 0.34 (Strahler et al. 2015).

Figure 5.1 presents representative TE, TC, and SS constant mean effective stress paths projected on to the deviatoric plane in specimens that were consolidated to $p'_c \approx 100$ kPa. In general the TE, TC, and SS stress paths start at a hydrostatic stress condition where $\sigma'_1 = \sigma'_2 = \sigma'_3$, and progress consistently towards failure. Figure 5.1 includes a representative PSK_0 stress path sheared at a $p'_c = 91$ kPa presented by Strahler et al. (2015). The PSK_0 stress path was consolidated in a quasi- K_0 consolidation phase where σ'_1 and σ'_2 were increased uniformly, while σ'_3 remained constant. This stress path was selected due to the limitations of the UW-TTA, resulting in shear stresses during the consolidation phase that are observed in the initial phase of the PSK_0 stress path (Figure 5.1). Shearing in the PSK_0 stress path was accomplished by applying a constant mean effective stress path similar to in the SS stress path where σ'_1 is increased at the same rate as σ'_2 is reduced. A more thorough discussion regarding the PSK_0 stress path and its effects on soil behavior is provided by Strahler et al. (2015). Differences between the SS and PSK_0 stress path during shearing are attributed to differences in the intermediate boundary condition; a constant applied σ'_2 was set for the SS stress path, whereas σ'_2 was measured at the intended $\varepsilon_2 = 0$ boundary for the PSK_0 stress path. The observed curvature in the PSK_0 stress path is attributed to increases in σ'_2 during shearing, resulting in slight differences in the 3-D stress path. The markers in Figure 5.1 indicate failure, and compare reasonably to the 3-D failure criterion proposed by Matsuoka et al. (1990).

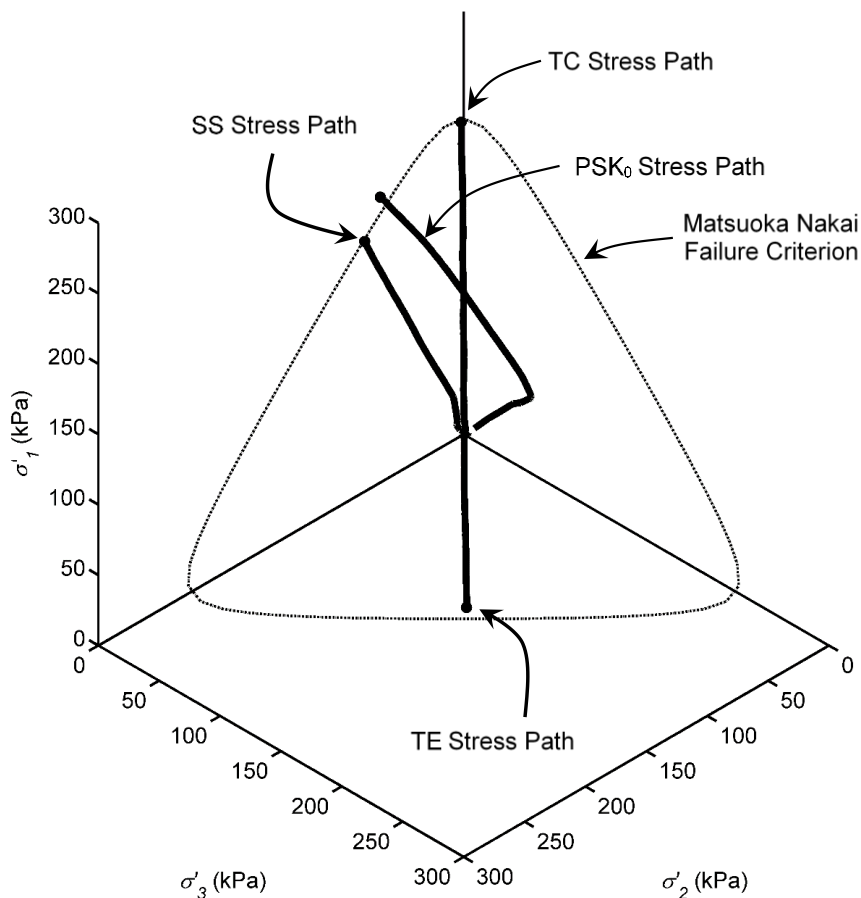


Figure 5.1. Stress paths for true triaxial tests at $p'_c \approx 100$ kPa, projected onto the deviatoric plane and bounded by the Matsuoka-Nakai failure criterion.

The variation in the ratio of stress invariants, $\eta = q/p'$ with γ_s is presented in Figure 5.2 for the TC, TE, and SS tests on Kanaskat gravel and for p'_c ranging from 49 to 204 kPa. In general, η increased over the entire strain range for each test, which is in marked contrast with typical strain-controlled testing devices in which softening can be observed. This behavior is a result of the stress-controlled testing protocol of the UW-TTA and complicates the determination at which point the specimen has failed, discussed in greater

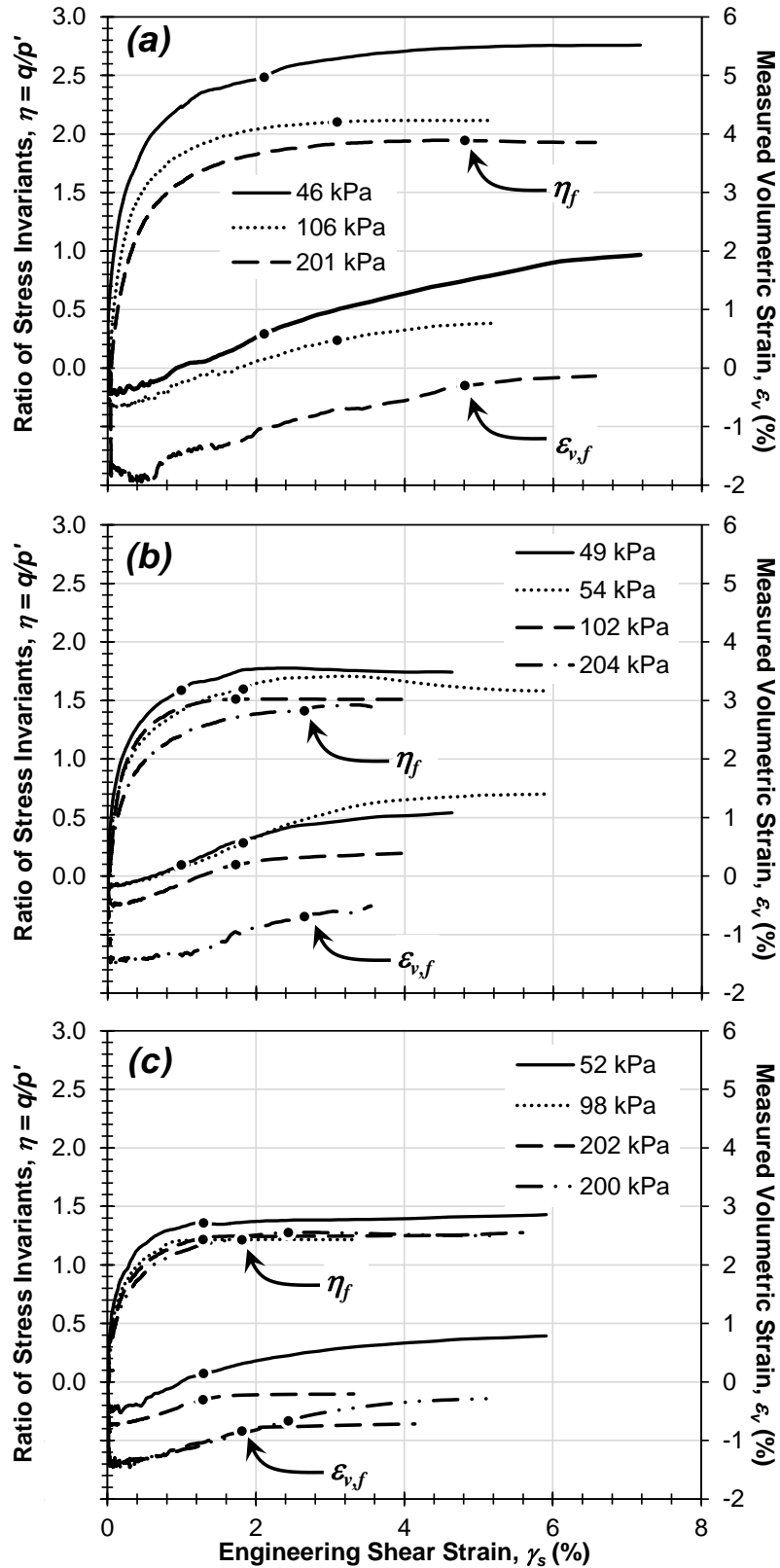


Figure 5.2. Variation of the ratio of stress invariants and volumetric strain with engineering shear strain for: (a) TC, (b) SS, and (c) TE stress paths.

detail subsequently. Observed η can generally be characterized as being greatest in the TC stress path (Figure 5.2a) and the least in the TE stress path (Figure 5.2b). The volumetric response of Kanaskat gravel in the TTA was independently measured using linear voltage displacement transducers (LVDTs) centered behind the rubber bladders and a burette with a differential pressure transducer. The LVDTs were used to calculate shear strains from the principal face displacements of a cubical soil element. However, volumetric burette readings more accurately represent the behavior of the entire sample and are presented in Figure 5.2. Similar to the η response, the volume of the sample increases during shearing indicating the specimen continuously dilates, and there was no contraction observed due to the stress-controlled nature of the device. Observed changes in the volumetric strain, ε_v , can generally be characterized as greatest in the TC stress path (Figure 5.2a) and the least in the TE stress path (Figure 5.2b). The interpretation of the response of Kanaskat gravel with regard to these experimental conditions are described below.

5.4.1. *SHEAR MODULUS OF KANASKAT GRAVEL*

Little experimental work has been performed to observe the variation in stiffness of granular materials with stress path. Prior investigations have been limited to cubical true-triaxial tests conducted by Abelev and Lade (2003) on Santa Monica Beach Sand, where the secant Young's modulus, E_s , was reported to increase with increases in b . To assess the change in stiffness with change in stress path and b , the secant shear modulus, $G = \Delta q / (3\Delta\gamma_s)$ where Δq is the change in deviatoric stress and $\Delta\gamma_s$ is the change in the shearing strain (Wood 1990), was measured at initial and advanced stages of shearing. The initial secant shear modulus may be determined by fitting a hyperbola to the stress-strain data, which can reduce

error associated with observed seating effects. The Kondner (1963) hyperbolic relationship was modified to incorporate the initial shear modulus which is given by:

$$q = \frac{3\gamma_s}{\left(\frac{1}{G_{in}} + \frac{3\gamma_s}{q_f} \right)} \quad (5.4)$$

where G_{in} is the initial secant shear modulus and q_f is the fitted deviatoric stress at failure. The secant shear modulus may also be computed at a strain at 50% of the deviatoric stress at failure, defined here as G_{50} . Figure 5.3 presents variations in the secant shear modulus at different strain levels for each stress path as a function of normalized mean effective consolidation pressure, p'_c/p_{ref} , where p_{ref} was set equal to atmospheric pressure ($p_{ref} = 101.3$ kPa). It is important to note that the PSK₀ stress path tests have been included in Figure 5.3, but are considered to be influenced by the development of intermediate strains that developed during shearing, resulting in a smaller stiffness (Strahler et al. 2015).

In general, the pressure-dependent nature of G_{50} and G_{in} are sufficiently captured using fitted power laws. The power law exponent was maintained equal to 0.56 during fitting, as it should theoretically be material specific and independent of stress path (Schanz and Vermeer 1998, Strahler et al. 2015). The theoretical framework established in Equations (5.1) and (5.2) incorporates the intermediate principal stress into the calculation of deviatoric stresses and strains. As a result, the measured shear modulus should theoretically be independent of stress path. However, it is apparent that stress path effects are somewhat significant at small strains (Figure 5.3). Figure 5.4 presents G_{in} and G_{50} in each stress paths at different confining pressures. Although some scatter is observed,

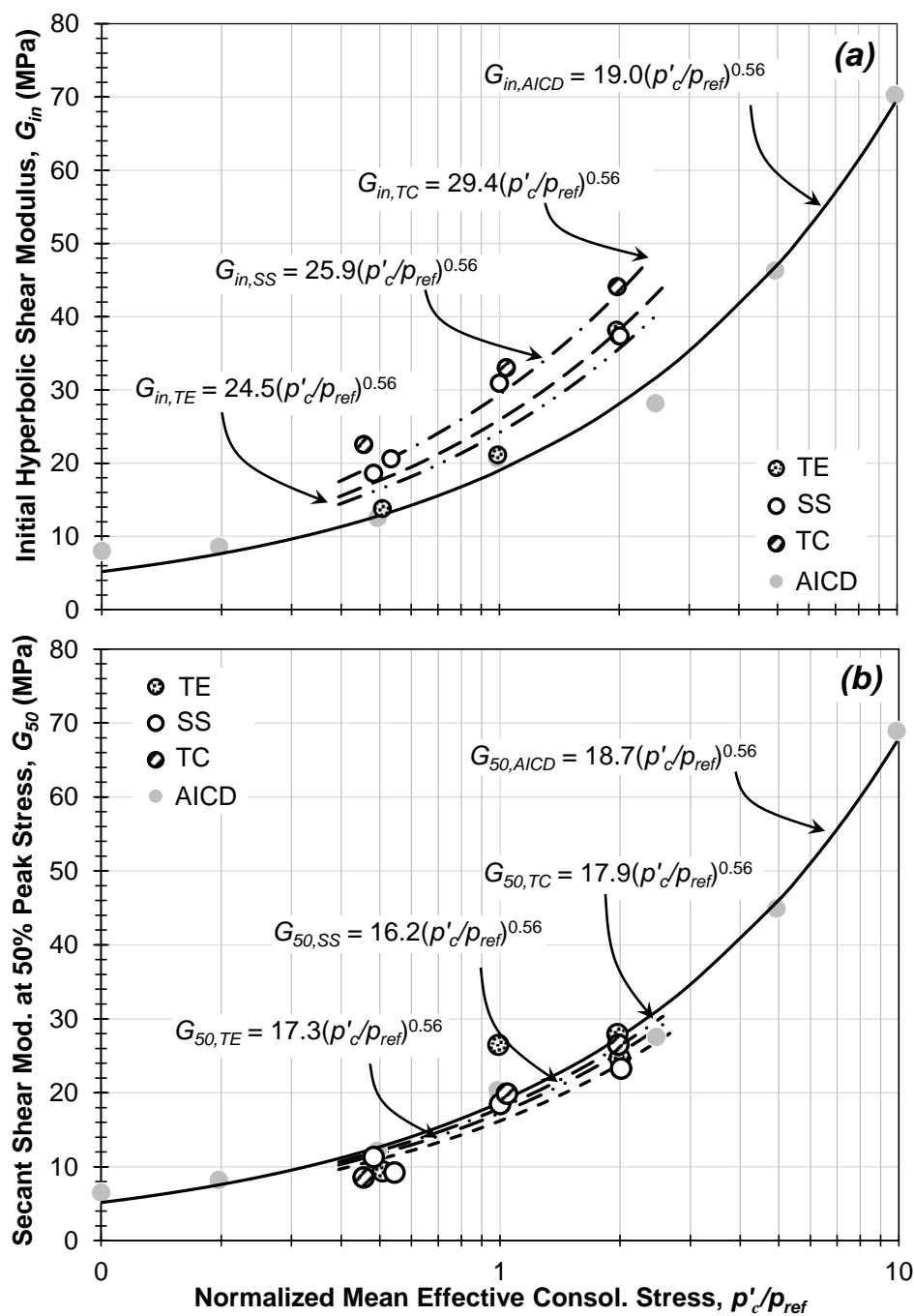


Figure 5.3. Variation in the secant shear modulus at (a) $\gamma_s = 0.05\%$ and (b) 50% of peak q with normalized mean effective stress at failure in SS, TC, TE, and PSK₀ stress paths.

Figure 5.4(a) suggests that G_{50} is relatively independent of stress path at confining pressures investigated here, with the exception of 100 kPa where slight reductions occur with increases in b . This same behavior was observed G_{in} (Figure 5.4b) and was relatively independent of p'_c . The response reported in Figure 5.4(b) indicates that G_{in} reduces linearly with increase in b and the TE stress path ($b = 0$) is, on average, 30% less than the TC stress path.

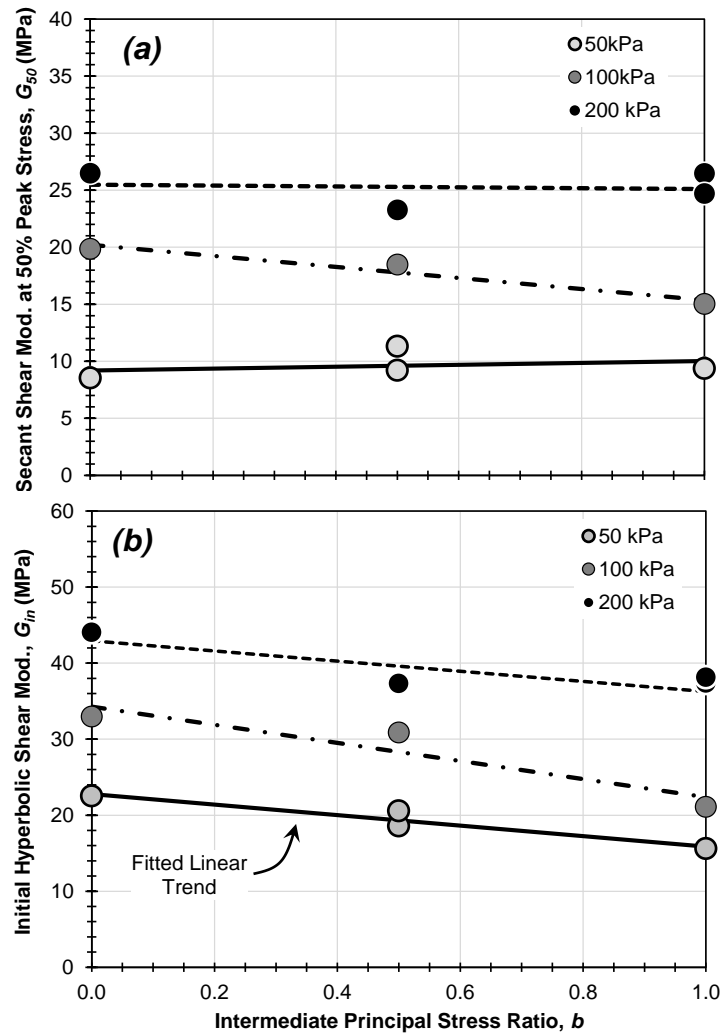


Figure 5.4. Variation of (a) initial shear modulus and (b) shear modulus at 50% shear stress with b and confining pressure.

5.4.2. STRAIN COMPATIBILITY AND SHEAR BAND FORMATION

Observations on the behavior of uniform soils under 3-D stress conditions has indicated that the shape of the failure surface is influenced by the presence of shear bands (Wang and Lade 2001, Abelev and Lade 2003, Lade and Abelev 2003). These studies have suggested that failure is caused by shear banding in the hardening phase (pre-peak) for b ranging from 0.18 to 0.85; outside of this range, failure has been observed to occur in the softening phase (post-peak). The stress-controlled nature of the TTA did not allow for softening to occur (Figure 5.2), producing a response that does not reduce to a constant volume condition like strain-controlled tests. This complicated the determination of the point at which specimens are considered to have failed and did not allow observation of critical state responses. However, the measured volumetric strains, principal displacement measurements, and variations in the deviatoric responses provided indications of shear band formation.

The formation of two shear bands was inferred based on the principal displacement measurements and volumetric responses for the PSK_0 stress paths presented by Strahler et al. (2015). In the TC, TE, and SS stress path tests presented here, strains in the intermediate principal direction were not restrained and the observed response of principal displacement measurements indicated the presence of more than two shear bands. Such behavior has been observed by Desrues et al. (2002), Shapiro and Yamamuro (2003), Abelev and Lade (2003), Lade and Abelev (2003), and Lade et al. (2008), and has been attributed to geometrical constraints imposed by the cubical devices used. As a result, specimens discussed here are considered to have failed at the first indications of shear banding, determined from principal face displacement measurements, δ . Figure 5.5 presents δ for a

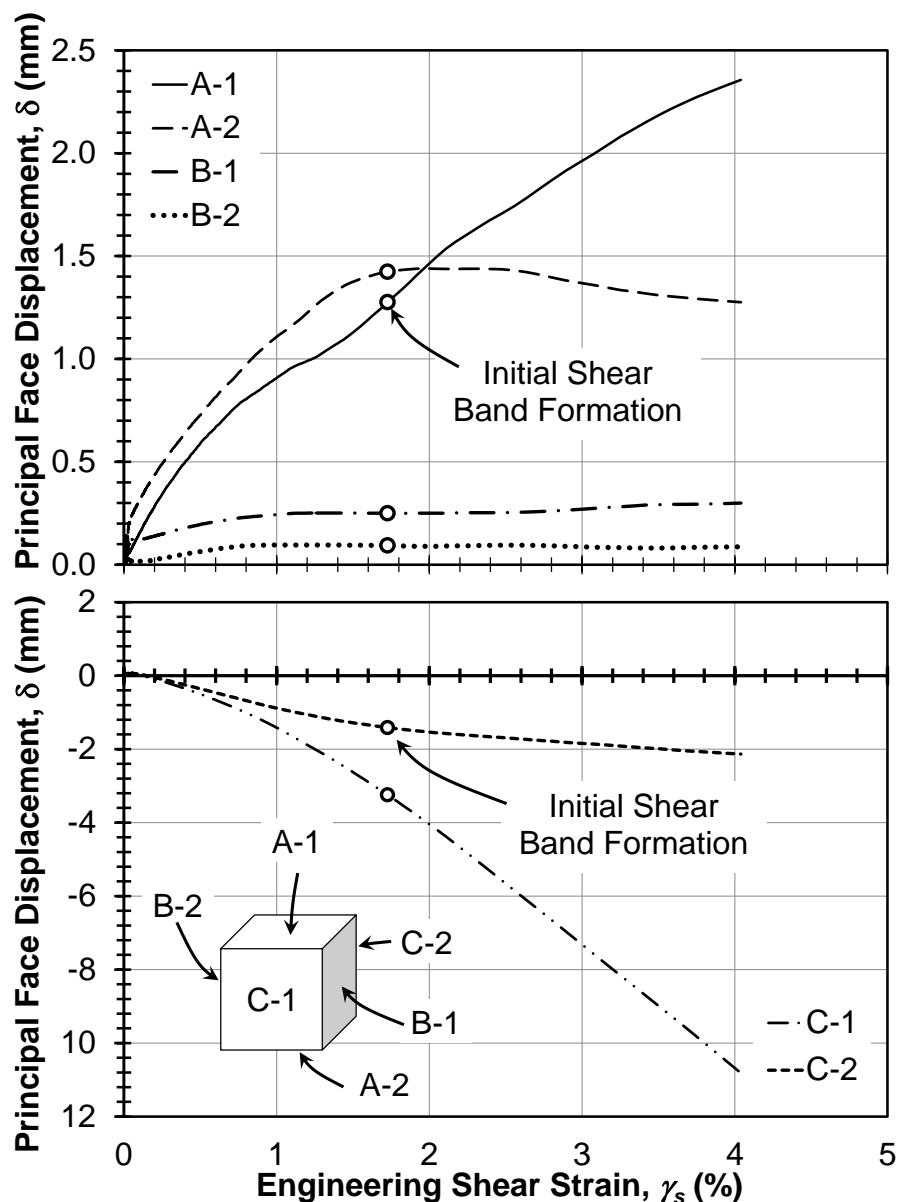


Figure 5.5. Principal face displacements versus shearing strain for a true-triaxial test conducted at $p'_c = 102$ kPa in the SS stress path where A and C are σ'_1 and σ'_3 , respectively; Note: inset depicts the face location for each principal displacement.

SS stress path test at $p'_c = 102$ kPa. The inset presented in Figure 5.5 depicts corresponding locations of each principal face displacement where A and C correspond to σ'_1 and σ'_3 , respectively. Prior to approximately 1% of shearing strain, principal face displacements increased and decreased at the same rates, suggesting that the specimen has undergone

uniform deformation in each principal direction. As shearing strains increased above 1%, each face began to displace differentially, indicating a bifurcation response consistent with the presence of shear bands. Face A-2 notably ceased displacing at a shear strain of approximately 1.7%, whereas displacements in Face A-1 and C-2 continue developing. The comparison of Figure 5 with 2b shows the corresponding transition in volumetric behavior at $\gamma_s = 1.7\%$, suggesting a fundamental change in the specimen response. This behavior is considered to represent the formation of the initial shear band in the SS specimen and as indicated by the marker in Figure 5.2. A similar response observed in PSK_0 specimens is described in detail by Strahler et al. (2015).

5.4.3. *PRESSURE DEPENDENT BEHAVIOR OF KANASKAT GRAVEL AT FAILURE*

The effects of confining pressure on the 3-D response of uniform granular soils has been well investigated (e.g. Lee and Seed 1967, Alshibli 2003, Wanatowski and Chu 2008). However, some work on well-graded soils indicate that the influence of p'_c is greater than that observed in uniform soils (Strahler et al. 2015). Figure 5.6 presents friction angles measured at failure, ϕ'_f , versus normalized mean effective stress at failure, p'_f/p_{ref} , in each stress path for Kanaskat gravel, computed by determining the intersection of the three dimensional stress path with the Mohr Coulomb (M-C) failure criterion (Choi, 2004):

$$\phi' = \sin^{-1} \left(\frac{\frac{q}{\sqrt{3}} \sin \left(\theta_L + \frac{1}{3} \pi \right)}{p' + \frac{q}{\sqrt{9}} \cos \left(\theta_L + \frac{1}{3} \pi \right)} \right) \quad (5.5)$$

where θ_L is the lode angle, defined as the angle between the failure point on the three dimensional surface and the major principal stress direction. The lode angle is related to b by (Suzuki and Yanagisawa 2006):

$$\theta_L = \tan^{-1} \left(\frac{\sqrt{3}b}{2-b} \right) \quad (5.6)$$

It is important to note that $p'_c \approx p'_f$, in the constant mean effective stress path however, p'_f tends to be 2 to 3 times greater than p'_c in the AICD stress path. To make direct comparisons at consistent mean effective stresses, two trends are provided for $\phi'_{f,AICD}$ in Figure 5.6(a), one in which Equation (5.7) is fitted using p'_c and one using p'_f . Observed friction angles ranged from 65 to 42 degrees in PSK₀ and AICD stress paths, and are generally bracketed by the TC, SS, and TE stress paths over the range of pressures tested here. The constant mean effective stress path selected required that σ'_2 in tests at low p'_c tended to approach zero at failure, and small deviations in σ'_2 stemming from measurement error resulted in large changes in ϕ'_f . This testing protocol had a significant influence on measured friction angles at low confining stresses resulting in some scatter (typically ± 3 deg.) that is observed Figure 5.6. However, comparisons with data from other true triaxial tests (e.g., Lade et al. 2008) suggest that the scatter is inherent in tests in which shear bands develop. The log-linear relationship used to establish the trends presented in Figure 5.6(a) is given by:

$$\phi'_f = \phi'_0 - \Delta \phi' \log \left(\frac{p'_c}{p_{ref}} \text{ or } \frac{p'_f}{p_{ref}} \right) \quad (5.7)$$

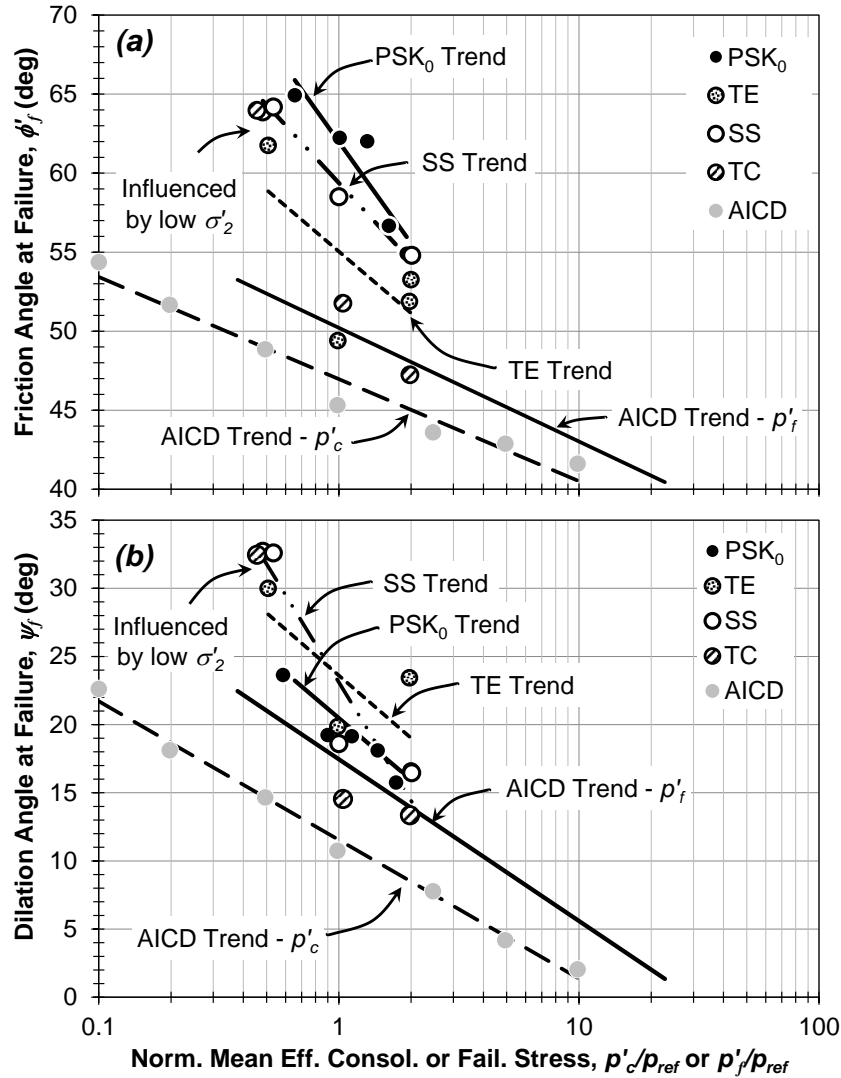


Figure 5.6. Responses of Kanaskat gravel at failure measured in PSK₀, TE, SS, TC, and AICD stress paths as a function of normalized mean effective stress: (a) Friction and (b) Dilation angles.

Table 5.2. Summary of friction angle fitting parameters in different stress paths; Note: AICD - p'_f fitting values can be used to represent the TC response.

Stress Path	ϕ'_0 (deg)	$\Delta\phi'$ (deg)
AICD - p'_c	47.0	6.5
AICD - p'_f	50.2	7.2
PSK ₀	62.0	21.3
TE	55.0	13.0
SS	59.4	16.4

where the fitting coefficients ϕ'_0 and $\Delta\phi'$ are the measured friction angle when p'/p_{ref} or p'_f/p_{ref} equal to one and the change in friction angle over one log cycle of normalized mean effective stress, respectively. Fitting coefficients for the trend in each stress path are provided in Table 5.2. No trend is presented for the TC stress path due to the large ϕ'_f measured at low confining stresses. However, measured ϕ'_f in the TC stress path at p'_f of 100 and 200 kPa can be sufficiently approximated by the AICD trend plotted at p'_f . The calculation of the dilation angle in AICD and PS stress paths is given by (Lade and Wang 2001):

$$\sin \psi = \frac{-(d\varepsilon_v/d\varepsilon_1)}{2 - (d\varepsilon_v/d\varepsilon_1)} \quad (5.8)$$

where $d\varepsilon_v$ and $d\varepsilon_1$ equal the volumetric and major principal strain increments, respectively. However, this formulation is derived without consideration of non-zero or coincident intermediate principal strains (i.e. $\varepsilon_2 \neq \varepsilon_3$ or 0) which are typically assumed in the AICD and PS stress paths. The definition of the dilation angle used here is given by (Houlsby 1991):

$$\sin \psi = \frac{d\varepsilon_1 + d\varepsilon_2 + d\varepsilon_3}{d\varepsilon_1 - d\varepsilon_3} = \frac{d\varepsilon_v}{d\gamma_s} \quad (5.9)$$

where $d\varepsilon_3$, and $d\gamma_s$ are changes in the minor principal and shear strain, respectively. Figure 5.6(b) presents ψ_f versus p'_c/p_{ref} and p'_f/p_{ref} in a similar manner as friction angles discussed previously. Scatter in TC, SS, TE, and PSK₀ stress paths ψ_f is more prevalent than in ϕ'_f , ranging from 33 to 14 degrees at p'_f of 50 and 204 kPa, respectively. Similar to measured ϕ'_f , large ψ_f were observed in lower confining stresses where σ'_3 approached zero and allowed larger volumetric strains than would be restrained at higher stresses. Although the data is limited and includes scatter, the trends presented in Figure 5.6 indicate that these dilation angles are generally larger than those measured in the AICD stress path.

5.5 DISCUSSION OF THE 3-D RESPONSE OF KANASKAT GRAVEL

5.5.1. STRESS-DILATANCY RESPONSE

The test program described in this study has shed new light on the stress-dilatancy response of granular soils. In contrast to the significant body of work reported for uniformly-graded soils in the TC and PS stress paths (Cornforth 1964, Lee and Seed 1967, Rowe 1969, Tatsuoka 1976, Bolton 1986, Chu 1994, Schanz and Vermeer 1996, Panda and Ghosh 2000, Hanna 2001, Wan and Guo 2004, Chakraborty and Salgado 2010), the true-triaxial tests conducted by Strahler et al. (2015) indicated that a reliance on previously reported work under-estimated the influence of the intermediate principal stress on dilatancy. The stress-dilatancy response of granular soils in stress paths other than TC and PS has been limited to investigations on uniformly-graded rock fill material, which exhibit particle breakage (Xiao et al. 2014a, Xiao et al. 2014b, Xiao et al. 2015). Figure 5.7 presents the results from TC, TE, SS, PSK₀, and AICD stress paths within the framework of Bolton's stress dilatancy

approximation. Trends in the data, presented in Figure 5.7, were fit using Bolton's (1986) approximation of Rowe's (1969) stress dilatancy theory:

$$\phi'_f = a \psi_f + \phi'_{cv} \quad (5.10)$$

where a is a fitting parameter (Chakraborty and Salgado 2010). No trend is presented for the TC stress path due to the large ϕ'_f at low confining pressures discussed previously. However, its stress-dilatancy behavior is similar to the AICD trend plotted at lower ψ_f . Although significant scatter is observed, the data is generally bracketed by the AICD and PSK₀ stress paths with a ranging from 0.58 to 1.06, respectively.

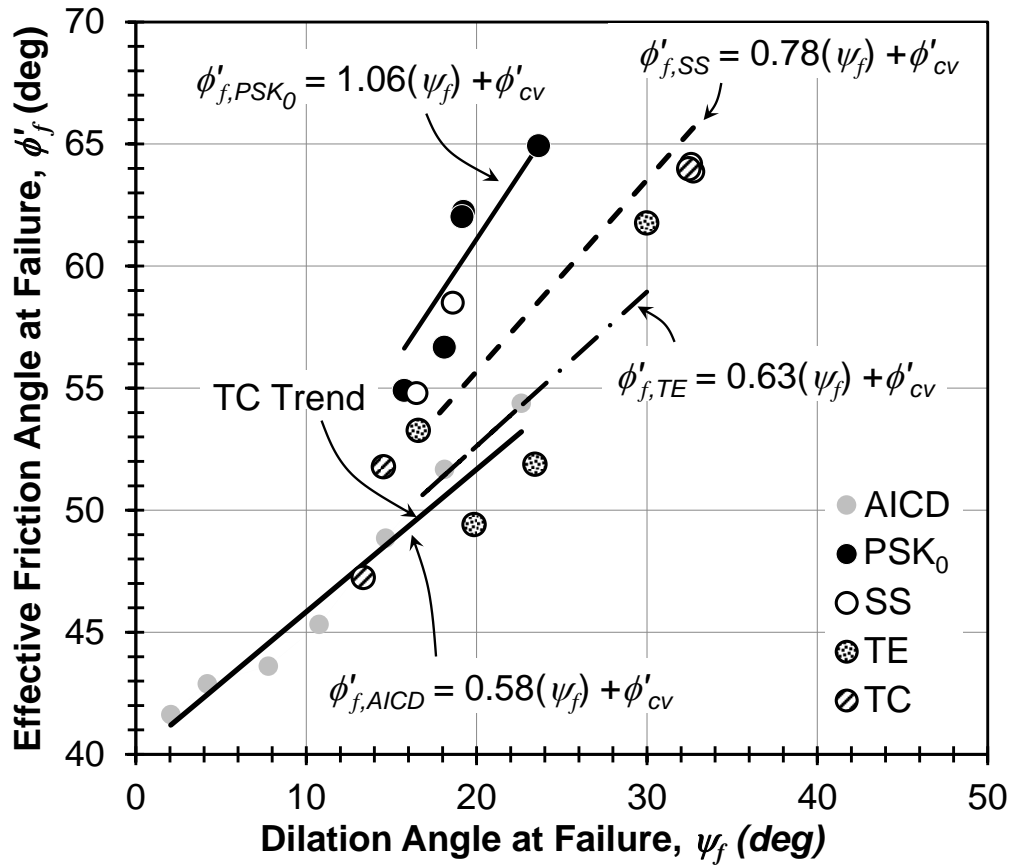


Figure 5.7. Stress dilatancy response of Kanaskat gravel in three dimensional stress paths.

5.5.2. ASSESSMENT AND CALIBRATION OF THREE-DIMENSIONAL FAILURE

CRITERIA

A well-formulated 3-D failure criterion describes the general response of soil at failure as a function of stress invariants. Two 3-D failure criteria originally formulated by Lade and Duncan (1975) and Matsuoka et al. (1990) have been developed based on true triaxial tests on uniformly-graded soils. The Lade-Duncan (L-D) failure criterion is expressed in terms of the first, I_1 , and third stress invariants, I_3 , given by Lade et al. (2008):

$$\left(\frac{I_1^3}{I_3} - 27 \right) \left(\frac{I_1}{p_{ref}} \right)^m = \kappa_1 \quad (5.11)$$

where κ_1 and m are the fitting coefficients that describe the shape and pressure dependency of the failure surface. The Matsuoka-Nakai (M-N) failure criterion was originally presented without the incorporation of the pressure-dependent nature of granular soils. A version of the M-N failure criterion that incorporates the same approach adopted by the L-D failure criterion used here is given by:

$$\sqrt{\frac{I_1 I_2 - 9}{I_3}} \left(\frac{I_1}{p_{ref}} \right)^n = \xi_1 \quad (5.12)$$

where ξ_1 and n are M-N fitting coefficients describing shape and pressure dependency and I_2 is the second stress invariant. Figure 5.8 presents the M-N and L-D fitting coefficients, ξ and η versus the normalized stress ratio p_{ref}/I_1 in a log-log plot where ξ_1 and η_1 represent the fitted intercept when $p_{ref}/I_1 = 1$ and m and n represent the slope of the ordinary least squares regression-based trend. For comparison, the AICD and PSK_0 responses reported by Strahler et al. (2015) are also shown in Figure 5.8. Trends developed from all of the data (i.e. global trend) are compared to those developed from the true triaxial data only (i.e. true triaxial trend). The true triaxial test conducted at $p'_c = 46$ kPa was omitted from the data set, due to the influence of the low pressure boundary conditions on the fitting coefficients. The resulting trends presented in Figure 5.8 sufficiently capture the pressure dependent nature of

Kanaskat gravel, however, the global model more accurately represents the response over a large range of pressures.

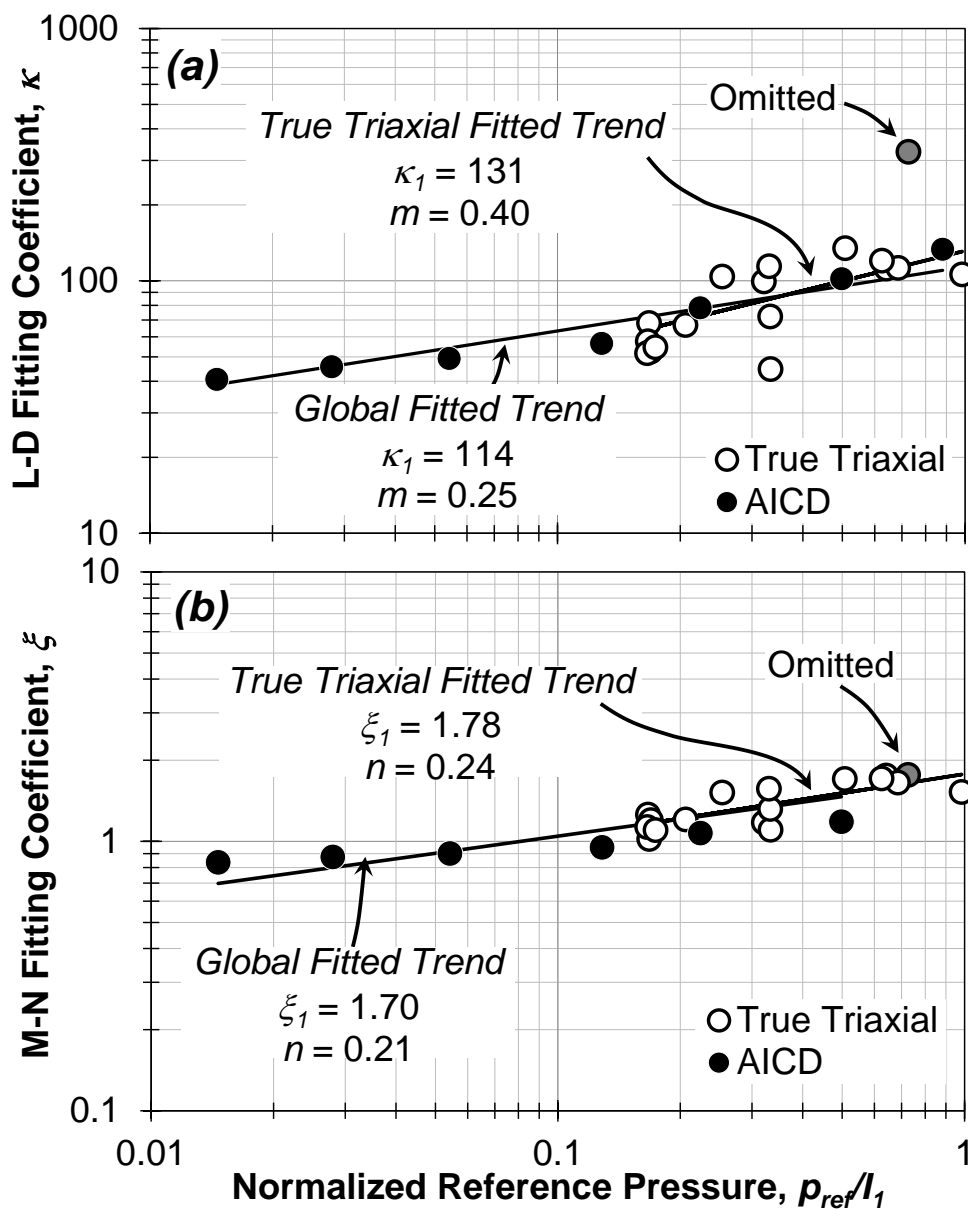


Figure 5.8. Material parameter fitting coefficients for L-D and M-N failure criterion; Note: gray data points were omitted due to influences of low stresses at the boundary conditions.

Figure 5.9 compares the ϕ'_f computed using the globally fit L-D and M-N failure criteria to those measured from the true triaxial tests. The lowest friction angle generally corresponded to the TC stress path and increased to a peak value in the PSK₀ stress path. In general, the L-D and M-N failure criterion adequately capture the ϕ'_f behavior over the range of b and consolidation pressures evaluated herein. However, the L-D failure criterion appears to more accurately capture the observed trend in the TC and TE stress paths. The L-D fitting coefficients for the true triaxial trend presented here, at $\kappa_I = 148$ and $m = 0.45$, are ~330% greater than those reported for specimens of Santa Monica beach sand by Lade et al. (2008) with relative densities of 30% greater than tested here. The larger coefficients are considered to be the result of differences in soil gradations. The slope of the L-D and M-N global trends ($m = 0.26$, $n = 0.25$) are lower than those in the true triaxial fitting ($m = 0.45$, $n = 0.21$) indicating that incorporation of the AICD tests reduces the influence of confining pressure on the failure surface. As a result, the true triaxial trends should not be used when p'_f is expected to fall outside the range of pressures tested here ($50 < p'_c < 200$ kPa). The global model has been fitted to much larger ranges of stress conditions (p'_f between 40 and 2300 kPa) and can be used to represent the 3-D response of a well-graded gravelly sand over this range.

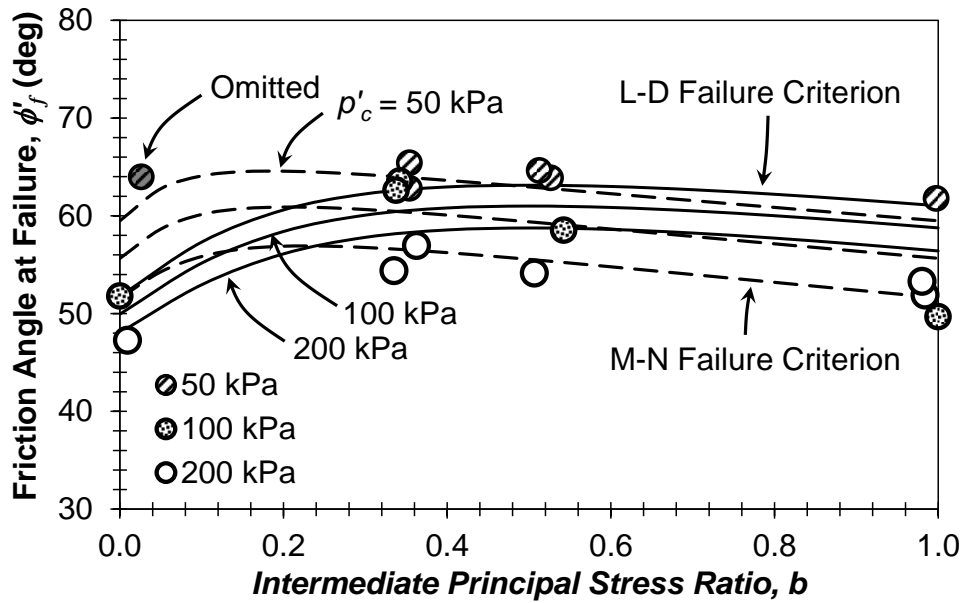


Figure 5.9. Variation of measured ϕ'_f for each p'_c as a function of b plotted alongside the fitted true triaxial L-D and M-N failure criterion.

5.6 SUMMARY AND CONCLUSION

The three dimensional stress-strain response of granular soils has predominantly focused on uniformly-graded sands. However, the 3-D behavior of these soils do not accurately model well-graded fill soils commonly used in construction. Pertinent questions regarding the stiffness, strength, and stress-dilatancy were investigated through a series of drained true-triaxial tests on specimens of well-graded Kanaskat gravel. Tests were conducted on the triaxial compression (TC), simple shear (SS), and triaxial extension (TE) constant mean effective stress paths at three different confining stresses. The results from the laboratory investigation suggest that the three dimensional stress-dilatancy and frictional responses differs from that of uniform soils. However, the theories developed based on uniformly graded soils can sufficiently estimate this soil response, once properly calibrated.

The secant shear modulus at an initial stage of shearing was found to be dependent on stress path; TC specimens produced a shear modulus 30% larger than TE specimens, on average. However, the stiffness at larger strains was found to be relatively independent of stress path and the fitted power laws adequately capture the pressure-dependent stiffness. Geometrical limitations of the cubical true triaxial device restricted the formation of free shear bands and did not allow development of a constant volume response. The development of multiple shear bands was inferred from deviations in principal face displacements in the cubical device and failure was defined as the onset of the initial shear band. Some scatter was observed in the frictional and dilational responses at failure, however, fitted log-linear trends sufficiently capture the observed pressure-dependent soil behavior. The friction and dilation angles at failure were observed to be as high as 33% larger in the SS and PS stress paths than in TC, greater than expected for uniform granular soils based on previously reported experimental data. A properly calibrated stress-dilatancy theory and two pressure-dependent 3-D failure criteria are adequately able to capture this behavior. New parameters for Bolton's (1986) stress dilatancy approximation can be used to approximate the 3-D stress dilatancy response of Kanaskat gravel, which allows estimation of greater dilatancy than implied for uniformly-graded soils. A modified, pressure-dependent version of the Matsuoka-Nakai failure criterion is used to incorporate the stress dependent nature of granular soils. However, the Lade Duncan failure criterion was found to most accurately capture the measured responses at failure and fitting parameters are presented for its use in forward modeling.

This work presents a first exploration of 3-D stress path effects on stiffness, strength, and stress-dilatancy of well-graded soil materials. Further work is required to establish

meaningful relationships between the angularity and the coefficient of uniformity of soil on the magnitude of stress path dependency of stiffness, strength, and dilatancy.

5.7 ACKNOWLEDGMENTS

The material presented herein was supported by the National Science Foundation through Grant Number CMMI 1100903 under Program Director Dr. Richard Fragaszy, and is greatly appreciated. Any opinions, findings, and conclusions expressed in this study are those of the writers and do not necessarily reflect the views of the National Science Foundation. The donation of Kanskat gravel from the Watson Asphalt Paving Company, Inc., of Redmond, WA is gratefully appreciated. The authors thank Dr. Matthew Evans of Oregon State University for helpful discussions of this work.

5.8 REFERENCES

- Abelev, A. V., and Lade, P. V. (2003). Effects of cross-anisotropy on three-dimensional behavior of sand. I: Stress-strain behavior and shear banding. *Journal of Engineering Mechanics*, 129(2), pp. 160–166.
- Alshibli, K.A., Batiste, S.N., and Sture, S. (2003). “Strain Localization in Sand: Plane Strain versus Triaxial Compression.” *Journal of Geotechnical and Geoenvironmental Engineering*, 129(6), pp. 483-494.
- ASTM. (2012). “Standard Test Methods for Laboratory Compaction Characteristics of Soil Using Modified Effort (56,000 ft-lbf/ft³ (2,700 kN-m/m³)).” *ASTM D1557-12*. , West Conshohocken, PA.
- ASTM. (2006). “Test methods for minimum index density and unit weight of soils and calculation of relative density.” *ASTM D4254-06*, West Conshohocken, PA.
- ASTM. (2011). “Test Method for Consolidated Drained Triaxial Compression Test for Soils. Standard”, *ASTM D71881-11*, West Conshohocken, PA.
- Biggerstaff, D.C. (2010). Analysis of the effects of the Intermediate Principal Stress on the Behavior of Gravel with a 9.5 inch True Triaxial Apparatus. *MS Thesis*, University of Washington, Seattle, WA.
- Bolton, M.D. (1986). “The strength and dilatancy of sands.” *Géotechnique*. 36(1), 65-78.
- Bolton, M.D. (1987). “Closure of ‘The strength and dilatancy of sands’ by Tatsuoka, F. *Géotechnique*, 37(2), 219-226.

- Chakraborty, T. and Salgado, R. (2010). "Dilatancy and Shear Strength of Sand at Low Confining Pressures." *Journal of Geotechnical and Geoenvironmental Engineering*, 136(3), pp. 527-532.
- Choi, C. H. (2004). "Physical and mathematical modeling of coarse-grained soils." *Ph.D. thesis*, Univ. of Washington, Seattle.
- Choi, C., Arduino, P., and Harney, M.D. (2008). "Development of a True Triaxial Apparatus for Sands and Gravels." *Geotechnical Testing Journal*, 31(1), pp. 1-13.
- Chu, J. (1994). "Study on the stress-dilatancy behavior of sand by strain path testing." *Proc. Pre-failure Deformation of Geomaterials*, Shibuya, Malachi and Miura, Eds., Rotterdam, pp. 365-370.
- Cornforth, D.H. (1964). "Some experiments on the influence of strain conditions on the strength of sands." *Géotechnique*, 14(2), pp.143-167.
- Desrues, J., & Chambon, R. (2002). "Shear band analysis and shear moduli calibration." *International Journal of Solids and Structures*, 39(13), pp. 3757-3776.
- Duncan, J., Byrne, P., Womg, K. and Mabry, P., (1980). "Strength, Stress-Strain and Bulk Modulus Parameters for Finite Element Analyses of Stresses and Movements in Soil Masses" *Report No. UCB/GT/80-01*, University of California, Berkeley.
- Green, G. E., (1972), "Strength and Deformation of Sand Measured in an Independent Stress Control Cell." *Proceedings of the Roscoe Memorial Symposium: Stress Strain Behaviour of Soils*, R. H. G. Parry, Ed., G.T. Foulis & Co. Ltd., Oxfordshire, England, pp 752.
- Hanna, A. (2001). "Determination of plane-strain shear strength of sand from the results of triaxial tests." *Canadian Geotechnical Journal*, 38(6), pp.1231-1240.

- Houlsby, G.T. (1991). "How the dilatancy of soils affects their behavior. Invited Theme Lecture", *Proceedings of the Tenth European Conference on Soil Mechanics and Foundation Engineering*, Florence, May 27-30, 4, pp. 1189-1202.
- Kjellman, W., (1936). Report on an Apparatus for Consummate Investigation of the Mechanical Properties of Soils, *Proceedings of the First International Conference on Soil Mechanics and Foundation Engineering*, Vol. 2, A. Casagrande, P. C. Rutledge, and J. D. Watson, Ed., Harvard University, Cambridge, MA, pp. 16–20.
- Lade, P. V., and Abelev, A. V. (2003). "Effects of cross anisotropy on three-dimensional behavior of sand. II: Volume change behavior and failure." *Journal of Engineering Mechanics*, 129(2), pp. 167–174.
- Lade, P.V. and Duncan, J.M. (1973). "Cubical triaxial tests on cohesionless soils." *Journal of Soil Mechanics and Foundations Division*, 99(SM10), 793-812.
- Lade, P. V., and Duncan, J. M. (1975). "Elastoplastic stress-strain theory for cohesionless soil." *Journal of the Geotechnical Engineering Division*, 101(10), pp. 1037-1053.
- Lade, P. V., and Wang, Q. (2001). "Analysis of shear banding in true triaxial tests on sand." *Journal of Engineering Mechanics*, 127(8), pp. 762-768.
- Lade, P. V. (2008). "Failure criterion for cross-anisotropic soils." *Journal of Geotechnical and Geoenvironmental engineering*, 134(1), pp. 117-124.
- Lade, P. V., (1978). "Cubical Triaxial Apparatus for Soil Testing." *Geotechnical Testing Journal*, Vol. 1, No. 2, pp. 93–101.
- Lee, K.L. and Seed, H.B. (1967). "Drained Strength Characteristics of Sands." *Journal of the Soil Mechanics and Foundation Division*, November, 93(SM6), pp. 117-141.

- Matsuoka, H., Hoshikawa, T., and Ueno, K. (1990). "A general failure criterion and stress-strain relation for granular materials to metals." *Soils and Foundations*, 30(2), pp.119-127.
- Matsuoka, H., Sun, D., Kogane, A., Fukuzawa, N., and Ichihara, W. (2002). "Stress-Strain Behaviour of Unsaturated Soil in True Triaxial Tests." *Canadian Geotechnical Journal*, 39(3), pp. 608–619.
- Panda, B.C. and Ghosh, A.K. (2000). "Influence of Grain Size Distribution on Dilatancy of Sand." *Journal of the Institution of Engineers*, 81(2), pp. 68-70.
- Rowe, P.W. (1969). "The relation between the shear strength of sands in triaxial compression, plane strain, and direct shear." *Géotechnique*, 19(1), pp. 75-86.
- Schanz, T. and Vermeer, P.A. (1998). "On the stiffness of sands. Special issue on Pre-failure Deformation Behaviour of Geomaterials." *Géotechnique*, pp. 383-387.
- Shapiro, S. and Yamamuro, J.A. (2003). "Effects of Silt on Three-Dimensional Stress-Strain Behavior of Loose Sand." *Journal of Geotechnical and Geoenvironmental Engineering*, 129(1), pp. 1-11.
- Strahler, A., Stuedlein, A. W., and Arduino, P. (2015). "Stress-Strain Response and Dilatancy of Sandy Gravel in Triaxial Compression and Plane Strain." *Journal of Geotechnical and Geoenvironmental Engineering*. 10.1061/(ASCE)GT.1943-5606.0001435, 04015098.
- Stuedlein, A. W., Mikkelsen, P. E., and Bailey, M. J. (2007). "Instrumentation and performance of the third runway north MSE wall at Seattle-Tacoma international airport." *7th International Symposium on Field Measurements in Geomechanics, FMGM 2007*,

September 24, 2007 - September 27, 2007, Geotechnical Special Publication, American Society of Civil Engineers, 26.

Stuedlein, A. W., Bailey, M. J., Lindquist, D. D., Sankey, J., and Neely, W. (2010a). "Design and Performance of a 46-m-High MSE Wall." *Journal of Geotechnical and Geoenvironmental Engineering*, 136(6), pp. 786–796.

Stuedlein, A.W., Allen, T., Holtz, R., and Christopher, B. (2010b). "Factors affecting the development of MSE wall reinforcement strain." *ER2010: Earth Retention Conference. 3*, ASCE, Reston, VA, pp. 502–511.

Stuedlein, A. W., Allen, T. M., Holtz, R. D., and Christopher, B. R. (2012). "Assessment of Reinforcement Strains in Very Tall Mechanically Stabilized Earth Walls." *Journal of Geotechnical and Geoenvironmental Engineering*, 138(3), pp. 345–356.

Suzuki, K and Yanagisawa, E. (2006). "Principal Deviatoric Strain Increment Ratios for Sand Having Inherent Transverse Isotropy." *ASCE International Journal of Geomechanics*, Sept/Oct 2006, pp. 356-366.

Tatsuoka, F. (1976). "Stress-dilatancy relations of anisotropic sands in three dimensional stress condition." *Soils and Foundations*, 19(2), pp. 1-18.

Wan, R.G. and Guo, P.J. (2004). "Stress-dilatancy and fabric dependencies on sand behavior." *Journal of Engineering Mechanics*. 130(6), pp. 635-645.

Wanatowski, D. and Chu, J. (2008). "Stress-Strain Behavior of a Granular Fill Measured by a New Plane-Strain Apparatus." *Geotechnical Testing Journal*, 29(2), pp. 1-9.

Wang, Q., and Lade, P. V. (2001). "Shear banding in true triaxial tests and its effect on failure in sand." *Journal of Engineering Mechanics*, 127(8), pp. 754-761.

- Wood, D. M. (1990). *Soil behaviour and critical state soil mechanics*, Cambridge University Press, Cambridge, 462 pp.
- Xiao, Y., Liu, H., Chen, Y., and Chu, J. (2014a). ‘Influence of intermediate principal stress on the strength and dilatancy behavior of rockfill material.’ *Journal of Geotechnical and Geoenvironmental Engineering*, 140(11), 04014064.
- Xiao, Y., Liu, H., Chen, Y., and Jiang, J. (2014b). “Strength and deformation of rockfill material based on large-scale triaxial compression tests. I: Influences of Density and Pressure.” *Journal of Geotechnical and Geoenvironmental Engineering*, 10.1061/(ASCE)GT.1943-5606.0001176, 04014070.
- Xiao, Y., Liu, H., Ding, X., Chen, Y., Jiang, J., and Zhang, W. (2015). “Influence of Particle Breakage on Critical State Line of Rockfill Material.” *International Journal of Geomechanics*, 16(1), 04015031.
- Yamada, Y. and Ishihara, K. (1979). Anisotropic Deformation Characteristics of Sand under Three Dimensional Stress Conditions. *Soils Found.*, Vol. 19, No. 2, pp. 79–94.

**CHAPTER 6: FRICTIONAL RESISTANCE OF CLOSELY-SPACED
STEEL MSE WALL REINFORCEMENT STRIPS**

Andrew Strahler, M.S., E.I.T., James J. Walters M.S., E.I.T., and Armin W. Stuedlein,
PhD, P.E.

Journal of Geotechnical and Geoenvironmental Engineering

DOI: 10.1061/(ASCE)GT.1943-5606.0001492

1801 Alexander Bell Drive

Reston, VA 20191-4400

Submitted and Accepted

6.1 ABSTRACT

Frictional resistance between soil and steel reinforcements develops as a result of relative displacement at the soil-reinforcement interface and is typically characterized using interface shear or reinforcement pullout tests. The soil-reinforcement interaction between uniformly-graded soils and metal reinforcements has been well-characterized. However, the interface response of well-graded gravelly soils and ribbed steel strips is primarily based on lower-bound estimates of pullout resistance using databases of single isolated reinforcement pullout tests. Increases in horizontal stresses that develop in tall MSE walls are often accounted for in design by reducing the reinforcement spacing; however, the effect of possible frictional interference between closely spaced inextensible reinforcements has not been explored. Two reinforcement pullout apparatuses have been developed to study the soil-reinforcement interaction and effect of reinforcement proximity in a well-graded sandy gravel. A single strip pullout apparatus was developed to establish the baseline frictional resistance, comparable to typically-conducted pullout tests. The assessment of reinforcement strip interaction effects possible in closely-spaced reinforcements was evaluated using a multi-strip pullout apparatus. The effects of passive resistance at the front facing that alters the load-displacement response and contribute to epistemic uncertainty were mitigated using a well-characterized, soft boundary condition. Generally, the available resistance was observed to increase with increases in the localized stiffness, whereas the secant stiffness of the resistance-displacement response reduced with increases in localized stiffness. Current pullout resistance factor models are shown to be conservative and biased, and recently proposed, calibrated, exponential models more accurately capture the measured responses. Fitted isolated and confined strip models presented here should help practitioners estimate

the frictional resistance of ribbed steel strips in sandy gravel soils and incorporate increases resulting from closely-spaced reinforcements into design methodologies and numerical simulations.

6.2 INTRODUCTION

The use of MSE walls has proliferated since Vidal (1969) developed the modern concept of reinforced earth. Since the first application of reinforced earth in the United States in 1972, over 60,000 MSE walls have been constructed nationwide with increasing complexity, loading support, and height (Alzamora and Barrows 2007). The widespread implementation of MSE walls for the support of transportation infrastructure has stemmed from the high efficiency, low cost, and ease of construction associated with reinforced earth technologies (Anderson and Brabant 2005). Steel-reinforced MSE walls are constructed with reinforcement spacing that typically ranges between 600 and 750 mm vertically and 300 to 1100 mm horizontally. Construction of particularly tall MSE walls, defined here as having a height greater than 20 meters, and those in seismically active regions has necessitated the use of closely-spaced steel reinforcement strips (Stuedlein et al. 2010a and 2010b). For example, a 46 m high MSE wall described by Stuedlein et al. (2007, 2010a, 2010b, 2012) was constructed with vertical and horizontal reinforcement spacing as small as 240 and 180 mm (9.4 and 7.1 inches), respectively, to address seismic compound stability design considerations

Initial applications of reinforced soil walls used flat and relatively smooth reinforcement strips; however, experimental work showed that ribbed steel reinforcement strips provided improved response as a result of increased resistance provided by transverse ribs (Schlosser and Elias 1978; Christopher et al. 1990a, 1990b). The understanding of the load-displacement response of ribbed steel strips to date consists of direct shear interface tests (e.g. Irsyam and Hryciw 1991, Hryciw and Irsyam 1993, Dove and Jarrett 2002, Lings and Dietz 2005) and single strip pullout tests (e.g. Schlosser and Elias 1978, McKittrick 1978,

Christopher et al. 1990a, Christopher et al. 1990b, and Jayawickrama et al. 2014) to determine interface behavior. These tests have indicated that the transverse ribs increase mean effective stresses during shearing, extending the zone of shear strain mobilization further into the surrounding soil as compared to smooth strips (Hryciw and Irsyam 1993). Palmeira and Milligan (1989) showed that the frictional interference between closely-spaced steel mesh bearing members in grid-type reinforcements reduced the available pullout resistance significantly. However, design methodologies established to assess the frictional response of reinforcement strips for MSE wall design are based on isolated, single strip pullout tests; thus, the possible effect of constructive or deconstructive frictional interference or interaction of closely-spaced reinforcements is unknown, and warrants investigation.

This paper presents the results of a series of single and multi-strip pullout tests using ribbed steel strip reinforcements embedded in a well-graded gravelly soil. Vertical and horizontal reinforcement spacing were varied in a multi-strip pullout apparatus and the potential frictional interference effects on the load-displacement response were investigated. First, the stress-strain-strength characteristics of the well-graded gravelly soil is described, followed by the presentation of the experimental approach. The impact of pullout test boundary conditions on the test results is discussed. Thereafter, the role of overburden pressure and spacing on the secant stiffness and peak pullout resistance observed in the single and multi-strip tests is characterized. These experiments show that the initial stiffness decreases and the peak pullout resistance increases as the reinforcement spacing becomes smaller. The apparent friction coefficients derived from the pullout tests and calibrated design models appropriate for use with similar soils are presented. The experimental work presented here may serve as a guide to those planning the design or numerical simulation of

tall MSE walls in addition to illustrating the role of spacing on the development of pullout resistance of reinforcement strips.

6.3 APPARENT FRICTIONAL RESISTANCE

In general, pullout resistance of reinforcement strips is primarily of concern for the upper portions of MSE walls owing to the lower available effective overburden stresses and broader extent of the presumed active earth mass (Berg et al. 2009a, 2009b). However, an understanding of the frictional response of the soil-reinforcement strip interface as a function of relative shear displacement is necessary for calibration of appropriate numerical analyses of MSE walls at working and ultimate stresses, and pullout test data may provide such information. With regard to conventional design procedures, the available pullout resistance of a reinforcement embedded in a soil matrix, P_r , may be evaluated using:

$$P_r = f^* \sigma'_v A_s \quad (6.1)$$

where σ'_v is the vertical effective stress at the reinforcement depth, A_s is the area of steel in contact with the soil, and f^* is the apparent friction coefficient.

Default empirical estimates of f^* prescribed by the American Association of State Highway and Transportation Officials (AASHTO 2014) in the absence of soil-specific testing are given by:

$$f_0^* = 1.2 + \log(C_u) \leq 2.0 \quad (6.2)$$

at the top of the MSE wall, and reduces linearly with depth to $\tan(\phi')$ at a transitional depth, z_t , of 6 meters and below. In Eq. (6.2), C_u = the coefficient of uniformity of the soil and ϕ' = the friction angle of the entire soil mass. The AASHTO (2014) f^* model corresponds to the lower 95th percentile of a database that includes a broad range of soil gradations meeting AASHTO (2014) MSE wall backfill specifications (AASHTO 2014), and has been observed to be conservative for many soils (Bathurst et al. 2008, 2011, and Miyata and Bathurst 2012a). Miyata and Bathurst (2012b) used a database of laboratory and in-situ pullout tests conducted on a wide range of soils in Japan to show that there is no statistical justification for Eq. (2) and calibrated several models for estimating f^* using the functional form:

$$f^* = \frac{f_0^* - \tan(\mu_1)}{\exp(cz)} + \tan(\mu_1) \quad (6.3)$$

where z is the depth of fill, and f_0^* , μ_1 , c are fitting parameters. Statistical analyses performed by Miyata and Bathurst (2012a) showed that Eq. (6.3) adequately captures changes in f^* with changes in vertical effective stress and is more accurate than the functional forms of currently used f^* models when properly calibrated.

When backfill-specific test data are available, experimental f^* values can be determined by rearranging Eq. (6.1):

$$f^* = \frac{P_{max}}{\sigma'_v A_s} \quad (6.4)$$

where P_{max} is the observed peak frictional resistance measured in a pullout test. Miyata and Bathurst (2012b) noted that similar bias statistics are produced for in-situ and laboratory pullout testing results when using Eq (6.4). However, this approach does not address the

potential influence of reinforcement spacing on the actual available resistance. Since the reinforcement spacing, often expressed using the local stiffness in methods to estimate reinforcement loads at working stresses, S_{local} , affects the magnitude of reinforcement loads (Christopher et al. 1990a, Christopher et al. 1990b, Ehrlich and Mitchell 1994, Stuedlein et al. 2010b, Stuedlein et al. 2012, Allen and Bathurst 2015), the potential for the influence of reinforcement spacing on resistance seems possible. The local stiffness is given by:

$$S_{local} = \frac{E_r \cdot b \cdot t}{S_v \cdot S_h} \quad (6.5)$$

where E_r = the Young's modulus of the reinforcement, b is the width of the reinforcement, t is thickness of the reinforcement, S_v and S_h are the vertical and horizontal reinforcement spacing, respectively. The experimental work described subsequently investigates the magnitude and variation of observed and prescribed f^* with S_{local} .

6.4 EXPERIMENTAL PROGRAM

6.4.1. CHARACTERIZATION OF SOIL BACKFILL

Owing to its use in several tall MSE walls, the reinforced fill used in this study was Kanaskat gravel, a rounded to sub-rounded, well-graded sandy gravel quarried from a source in Kanaskat, WA. Modified Proctor curves developed according to ASTM D1557 method C (ASTM 2009) indicated that this gravel exhibits a maximum dry unit weight, $\gamma_{d,max}$, of approximately 22.4 kN/m³ at the optimum moisture content, w_{opt} , of 6.5%. A maximum void ratio, e_{max} , of 0.365 was established according to ASTM D4254 Method A (ASTM 2006a) and D4253 (ASTM 2006b), whereas the minimum void ratio, e_{min} , of 0.182 was estimated

from the modified Proctor tests. The grain size distribution was characterized by D_{10} , D_{50} and C_u equal to 0.22 mm, 6.0 mm, and 46, respectively. Walters (2013) describes additional details of the index properties of Kanaskat gravel.

Strahler et al. (2015) evaluated the strength and stress-dilatancy behavior of Kanaskat gravel in quasi- K_0 consolidated, pure shear, drained plane strain (PSK₀CD) tests and axisymmetric isotropically consolidated, drained (AICD) triaxial compression tests. Peak friction angles observed from the AICD specimens ranged from 54 to 42 degrees at effective consolidation stresses of 10 to 1000 kPa, respectively, whereas PSK₀CD specimens exhibited friction angles that ranged from approximately 65 to 57 degrees at mean effective consolidation stresses of 28 to 172 kPa. The peak friction and dilation angles derived from PSK₀CD tests were sufficiently described using constant trend functions (Figure 6.1). Constant volume friction angles, ϕ'_{cv} , for the AICD tests are presented in Figure 6.1, and are estimated equal to 40 degrees for PSK₀CD tests. Strahler et al. (2015) provides a complete description of the experimental program performed to evaluate the stiffness and strength of Kanaskat gravel.

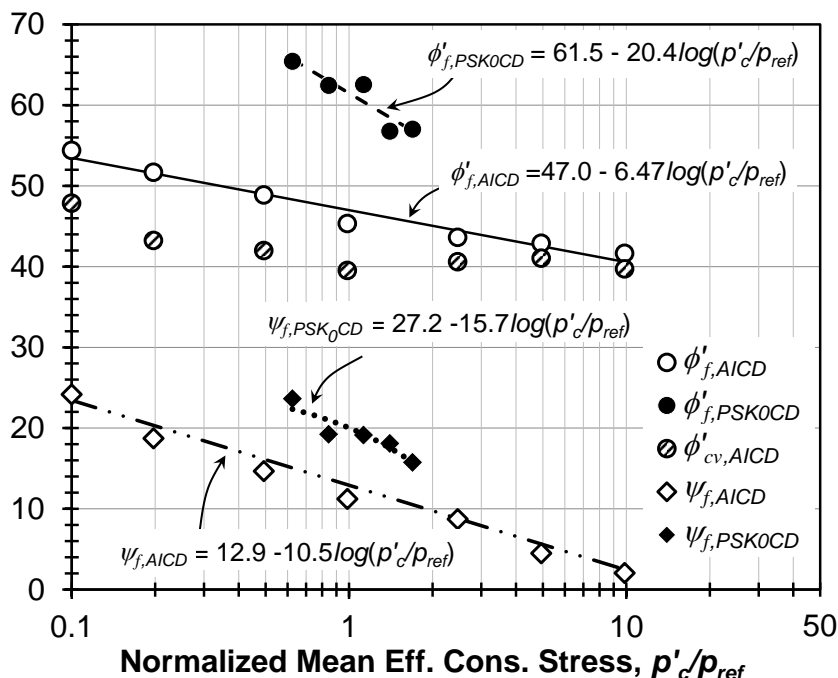


Figure 6.1. Friction and dilation angles at failure for Kanaskat gravel in AICD and PSK₀CD stress paths as a function of normalized mean effective confining pressure (data from Strahler et al. 2015).

6.4.2. SINGLE STRIP PULLOUT APPARATUS

A stiffened steel apparatus with internal (i.e., soil test specimen) dimensions of 356 mm × 456 mm × 2160 mm (H×W×L), presented in Figure 6.2, was constructed to investigate the soil-reinforcement strip interaction of single, isolated instrumented reinforcement strips in Kanaskat gravel. The ribbed, galvanized steel reinforcement test strips, originally fabricated for construction of the SeaTac International Airport third runway MSE walls (Stuedlein et al. 2010a, 2010b, 2012), were 6 mm thick, 50 mm wide, and included transverse trapezoidal ribs that protruded approximately 2 mm from both sides of the strip and were separated by an alternating distance of 40 and 125 mm. Four tensile test coupons fabricated from a reinforcement strip and tested in accordance with ASTM E8-15a (2011) indicated that a representative Young's modulus and ultimate yield stress for the reinforcement strips was

211 GPa and 530 MPa, respectively. Each reinforcement strip was set within the apparatus to achieve an embedment length, L_r , of 1.87 m, and protruded from the front steel face plate via a square, 101 mm wide opening as shown in Figure 6.3(a). The soil around the steel strip at the face of pullout box was restrained using a slotted, 6.6 mm thick neoprene rubber membrane characterized with a durometer hardness of 70A in accordance with ASTM D2240-05 (ASTM 2010) and a constrained elastic modulus, M , of 7.7 MPa. The opening geometry and rubber restraining membrane was designed to retain soil, but also allows for a near-zero stress condition within eight mean grain diameters above and below the reinforcement strips to mitigate potential passive earth pressures at the front face.

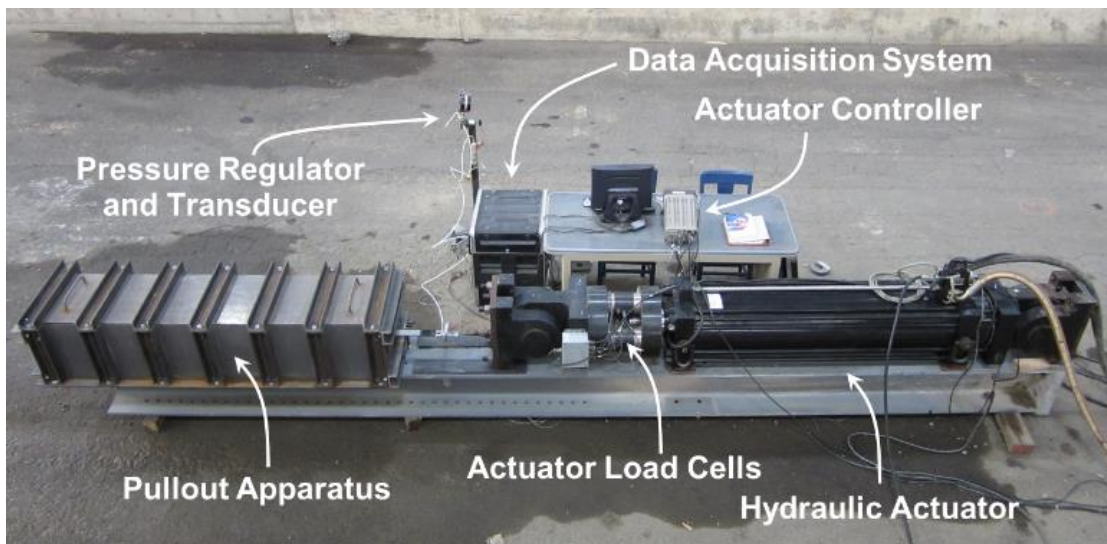


Figure 6.2. Single strip pullout testing apparatus.

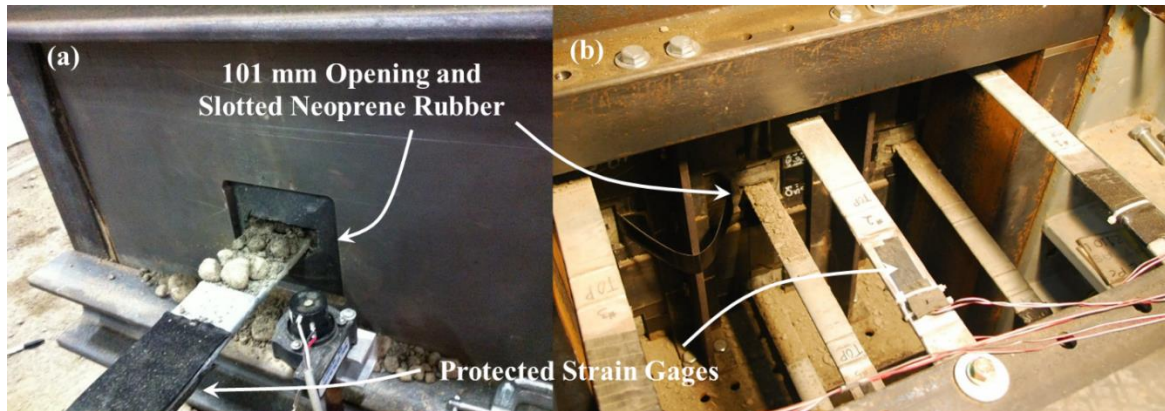


Figure 6.3. Stiffened steel face with 101 mm openings and slotted neoprene rubber membrane providing a soft boundary condition for the (a) single- and (b) multi-strip pullout apparatus.

Pullout tests were conducted by displacing the reinforcement strips at a rate of 1 mm/min. The displacement of the test strips was measured using a string potentiometer. The pullout resistance was measured using a load cell positioned between the actuator and the strip and verified using four strain gages (positioned in pairs on the top and bottom of each strip), shown in Figure 6.3(a). Vertical pressures ranging from 10 to 300 kPa were applied using a flexible rubber bladder positioned between the top of the soil specimen and the stiffened restraining plate, shown in Figure 6.2. Table 6.1 summarizes the single strip testing program and results, which are described subsequently in further detail below.

Table 6.1. Summary of isolated and fully confined pullout test results.

Test Designation	Relative Compaction, RC (%)	Vertical Effective Stress, σ'_v (kPa)	Initial Non-Slip Resistance, INSR (kN)	Secant Stiffness, k_{sec} (kN/mm)	Max. Pullout Force, P_{max}^d (kN)	Unit Frictional Resistance, f^*	Local Stiffness, S_{local} (MPa)	
Isolated, Single Strips	10-A	DNA	14	N/A	3.3	21.4	8.2	384
	50-A	DNA	61	N/A	7.7	61.1	5.3	384
	50-B	DNA	54	5.7	7.6	52.6	5.2	384
	50-C	DNA	54	0.9	5.9	44.3	4.4	384
	75-A	DNA	79	N/A	7.9	65.9	4.5	384
	100-A	DNA	104	11	10	81.9	4.2	384
	100-B	DNA	104	7.1	8.7	72.8	3.7	384
	100-C	DNA	104	7.5	9.5	74.9	3.8	384
	100-D	98	104	6	12.5	92.3	4.7	384
	100-E	95	104	7.4	10.4	81.7	4.2	384
	150-A	DNA	154	5.8	9.9	92.1	3.2	384
	150-B	99	154	7.6	7.9	76.4	2.7	384
	150-C	99	154	4.1	6.3	71.2	2.5	384
	150-D	95	154	9.2	10.1	79.8	2.8	384
	200-A	DNA	204	N/A	13.5	106.7	2.8	384
	250-A	99	254	8.2	10	92.7	2.0	384
	300-A ^b	DNA	304	7.5	16.4	N/A	N/A	384
Fully Confined Strips (Strip 5)	30A-66	99	47	N/A	4.3	53.6	6.1	2878
	30A-1212	DNA	47	N/A	7.5	76.4	8.7	676
	100A-44	98.5	117	N/A	6.3	91.5	4.2	5236
	100A-66	98.7	117	N/A	7.6	108.1	4.9	2878
	100A-88	100.4	117	N/A	7.2	110.5	5.1	1578
	100A-1010	100.1	117	N/A	7.3	108.7	5.0	989
	100B-1010	99.8	117	N/A	7.6	113.5	5.2	989
	100A-1212	98.7	117	N/A	8.1	103.5	4.7	676
	100A-2424 ^a	101.6	117	N/A	4.7	119.5	2.9	160
	200A-66	99.3	217	N/A	9.4	113.3	2.8	2878
	200A-1212	96.3	217	N/A	9.8	83.4	3.8	676

^a Multiple length test and embedment length = 1.75 m. ^d Corrected for front face boundary condition

^b Insufficient displacement.

DNA = Density not available

^c 5.3 kN added for length differences

6.4.3. *MULTI-STRIP PULLOUT APPARATUS*

In order to quantify potential frictional interaction of closely-spaced reinforcement strips, a second pullout apparatus was constructed to allow simultaneous testing of up to nine reinforcement strips as shown in Figures 6.3(b), 6.4, and 6.5. The multi-strip pullout apparatus consisted of two primary components: the pressurized, reinforced housing for the reinforced soil specimen and the reaction frame assembly. Soil specimens were compacted within the housing and measured 1520 mm in width, 1520 mm in height, and 1830 mm in length, corresponding to a volume of 4.25 m^3 , approximately 11 times larger than the single strip pullout tests. The design of the multi-strip pullout apparatus facilitated the experimental evaluation of different vertical and horizontal reinforcement spacing through the use of removable steel plates positioned at the front of the housing (shown in Figure D.1 of the supplemental appendix). The rubber-lined, reinforced, removable steel plates were constructed using the same 101 mm opening area as the single strip pullout apparatus so as to facilitate comparison of the two test series.

Compacted specimens were loaded using a pressurized flexible bladder placed within a 100 mm void space between the specimen and the restraining plate as shown in Figure 6.5. To minimize soil-steel wall interface friction along the side walls of the reinforced housing of the multi-strip test, two layers of lubricated plastic sheets were placed between the steel walls and soil specimen. The reinforcement strips were displaced at the rate of 1 mm/min and were measured using three string potentiometers attached to the stiffened steel housing and the 50 mm thick strip connection plate so that rotations, if any, could be quantified; however, none were observed. Multi-strip pullout tests were conducted with vertical effective overburden pressures ranging from 30 to 200 kPa. The vertical effective

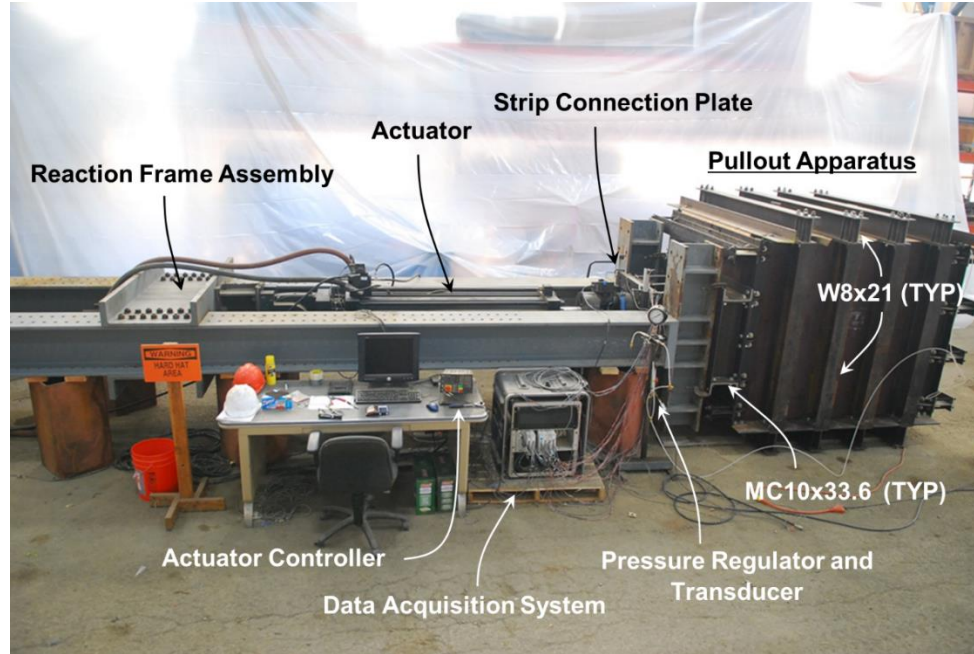


Figure 6.4. Multiple strip pullout test apparatus.

stresses presented in Table 6.1 have been increased by 4 and 17 kPa to account for geostatic stress gradients in the single and multi-strip specimens, respectively. Use of the multi-strip pullout box required embedded strip lengths of 1.75 m, slightly smaller than the length of the single strips (i.e., 1.87 m). Differences in the observed frictional resistance between strips of different lengths are corrected as discussed below.

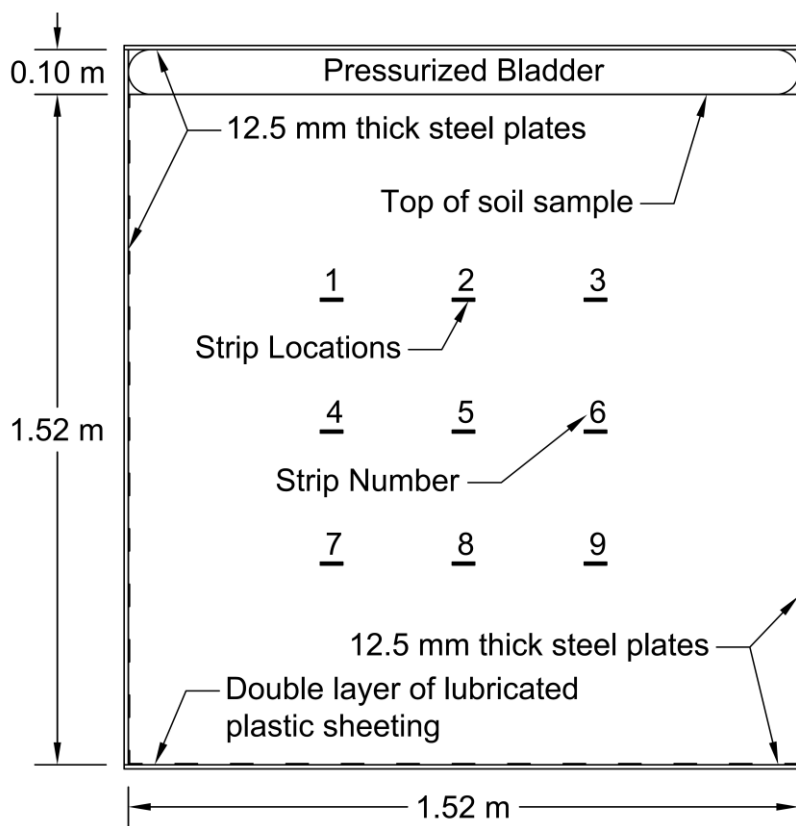


Figure 6.5. Cross section of the multi-strip pullout box with strip designations (reinforcement spacing of 305 mm shown).

6.4.4. SPECIMEN PREPARATION

Test specimens were compacted to achieve a minimum target relative density of 65 percent, equal to 95 percent of the maximum dry density to simulate conditions of pullout strips constructed in MSE walls. Some variability in the dry density of the well-graded sandy gravel due to the use of a relatively small vibratory plate-type compactor (owing to confined soil box) was observed and introduced some variability in the measured pullout response. However, the magnitude of variability would likely be less than or equal to that observed in-situ. Each lift of soil was conditioned prior to placement by raising the moisture content to the optimum water content, thoroughly mixed, and allowed to rest to help achieve moisture content uniformity. Dry densities of specimens were measured using nuclear densometer and

balloon density gage tests. Specimens were compacted using a Bomag BVP 18/45 vibratory plate compactor which provided a total force of 18.0 kN equal to a surcharge of 75 kPa. The repeatable, compaction protocol consisted of 10 passes on each lift to achieve 90 mm thick layers of soil at the target dry density in the single strip pullout apparatus. Balloon density gage (BDG) and nuclear densometer measurements performed on nine single strip test specimens were used to determine relative compaction, *RC*, of the reinforced soil. Results from the *RC* measurements indicated that the placement protocol consistently compacted the specimen to the target density specifications and was therefore used to build the remaining specimens. Relative compaction measurements were not used in the remaining tests to mitigate potential sample disturbance associated with balloon density gage testing.

Given the larger size of the multi-strip pullout box and the reduced potential for impact on the load displacement response, three BDG measurements were taken from each specimen, constituting a more thorough relative compaction sampling procedure. Lift thicknesses in the multi-strip pullout test apparatus were dictated by the reinforcement spacing to maintain the same interface characteristics between the strip and the reinforced soil. For example, a lift thickness of 101 mm was used for a vertical reinforcement spacing of 101 mm and a lift thickness of 127 mm was used for a vertical reinforcement spacing of 254 mm. A summary of the test results is presented in Table 6.1 and indicates that all tests presented here met density requirements with the exception of 30A-1212 which was assumed to meet density specifications because of the consistent compaction protocol.

6.4.5. EFFECT OF BOUNDARY CONDITIONS

Palmeira and Milligan (1989) showed that the resistance of welded wire mesh reinforcements subjected to tensile loads in a pullout test apparatus is influenced by the boundary conditions, particularly at the front face. Results from these tests indicated higher peak and residual pullout resistances result from higher interface friction angles, δ , at the front face. To assess the impact of the front face boundary developed for this study on the pullout resistance, one four-strip test with embedment lengths of 0.30, 0.61, 1.10, and 1.75 m was performed using an applied $\sigma'_v = 100$ kPa. The strips were spaced vertically and horizontally at 610 mm to minimize the potential for frictional interaction between strips. Measured peak resistances ranged from 5 to 70 kN and increased with increased strip embedment, as shown in Figure 6.6. A fitted linear trend, characterized by a slope, m , of 43.9 kN/m and an intercept, P_f , of -8.2 kN sufficiently captured the variation in peak resistance with embedment.

Increases in the pullout resistance reported by Palmeira and Milligan (1989) were attributed to increases in the mean effective stress stemming from wall friction-dependent passive pressures that form at the front face. These effects should be independent of strip length, and the additional resistance would be observed as a positive P_f in Figure 6.6. Conversely, a negative P_f such as that observed indicates that the mean effective stresses have been reduced to magnitudes below that expected to act on the reinforcement strip sufficiently away from the influence of the front face of

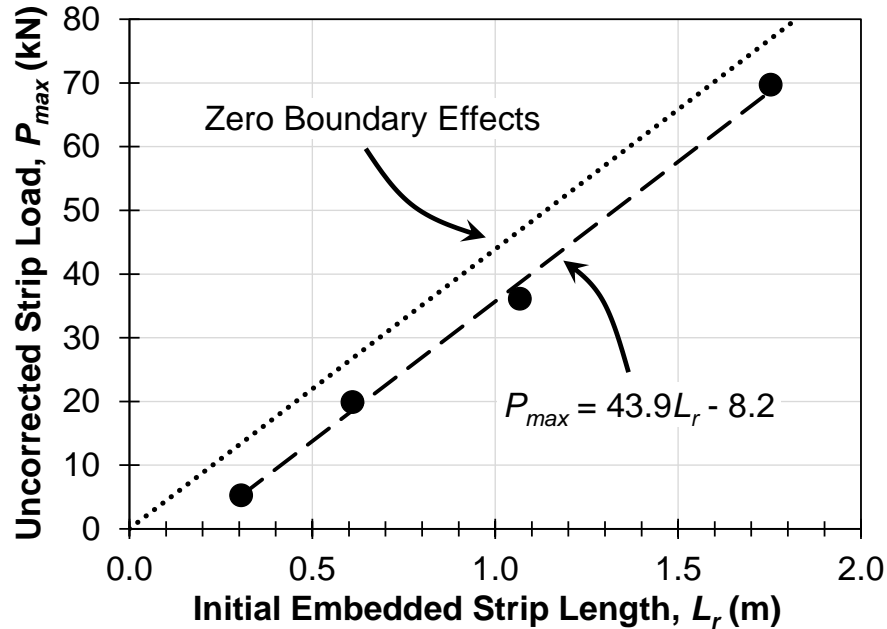


Figure 6.6. Influence of embedment length on the maximum pullout force of ribbed steel strips in Kanaskat gravel, $\sigma'_v = 100$ kPa.

the pullout apparatus. The influence of the boundary conditions at the front face can be evaluated in terms of a pullout apparatus facing bias, λ_f , given by:

$$\lambda_f = \frac{P_{max} + P_f}{P_{max}} \quad (6.6)$$

where a λ_f equal to one indicates no influence of the front face boundary. Biases greater than one and less than one correspond to increases and decreases, respectively, in the passive pressure at the front face. For the multi-strip pullout test 100A-2424 conducted herein where $P_{max} = 69.7$ kN for the full-length (i.e., 1.75 m) strip, $\lambda_f = 0.88$ indicates that measured reinforcement loads are approximately 12% smaller than what would be expected with zero front face boundary influence shown as a dotted line in Figure 6.6. Reinforcement loads

presented in Table 6.1 were corrected for the loss of resistance due to the front face boundary by dividing the measured pullout resistance by $\lambda_f = 0.88$.

6.5 SOIL REINFORCEMENT-INTERACTION OF ISOLATED AND CLOSELY-SPACED STRIPS

6.5.1. FRICTIONAL RESPONSE OF ISOLATED, SINGLE REINFORCEMENT STRIPS

Pullout loading tests of isolated and closely-spaced strips were conducted and interpreted with a view to the understanding of the front face boundary and its effect on the pullout resistance. An example pullout load-displacement curve for an isolated, single reinforcement strip (200-2), representative of those summarized in Table 6.1, is presented in Figure 6.7. Initially, the ribbed steel strip interface resists loading with zero displacements indicating that no relative shear displacement (e.g., slippage) occurred at the soil-strip interface. The load required to initiate slippage at the interface, the initial non-slip resistance (*INSR*), indicated in Figure 6.7(a) is representative of the static coefficient of friction at the interface (Schlosser and Elias 1978). The average *INSR* equaled 7 kN with a standard deviation of 3 kN; the variability did not appear to correlate with the applied vertical effective stress (Walters 2013). The significant amount of variability in the *INSR* is attributed to differences in *RC*, interface contact quality, and the location of larger particles with respect to the rib locations, but is not quantified herein.

After sufficient displacement, the *INSR* is exceeded and slippage occurs at the interface. Additional shearing resistance develops from particle rotation and soil dilation along the strip and at the ribs. At approximately 10 mm, the pullout response becomes dominated by erratic stick-slip hardening and softening as the ribs alternatively encounter, plow, and occasionally

crush the larger gravel particles in the surrounding soil (the latter phenomenon was observed following excavation of the test specimens). The stick-slip response occurred at large displacements and as such, no correlation to RC , confining pressure, or reinforcement spacing was

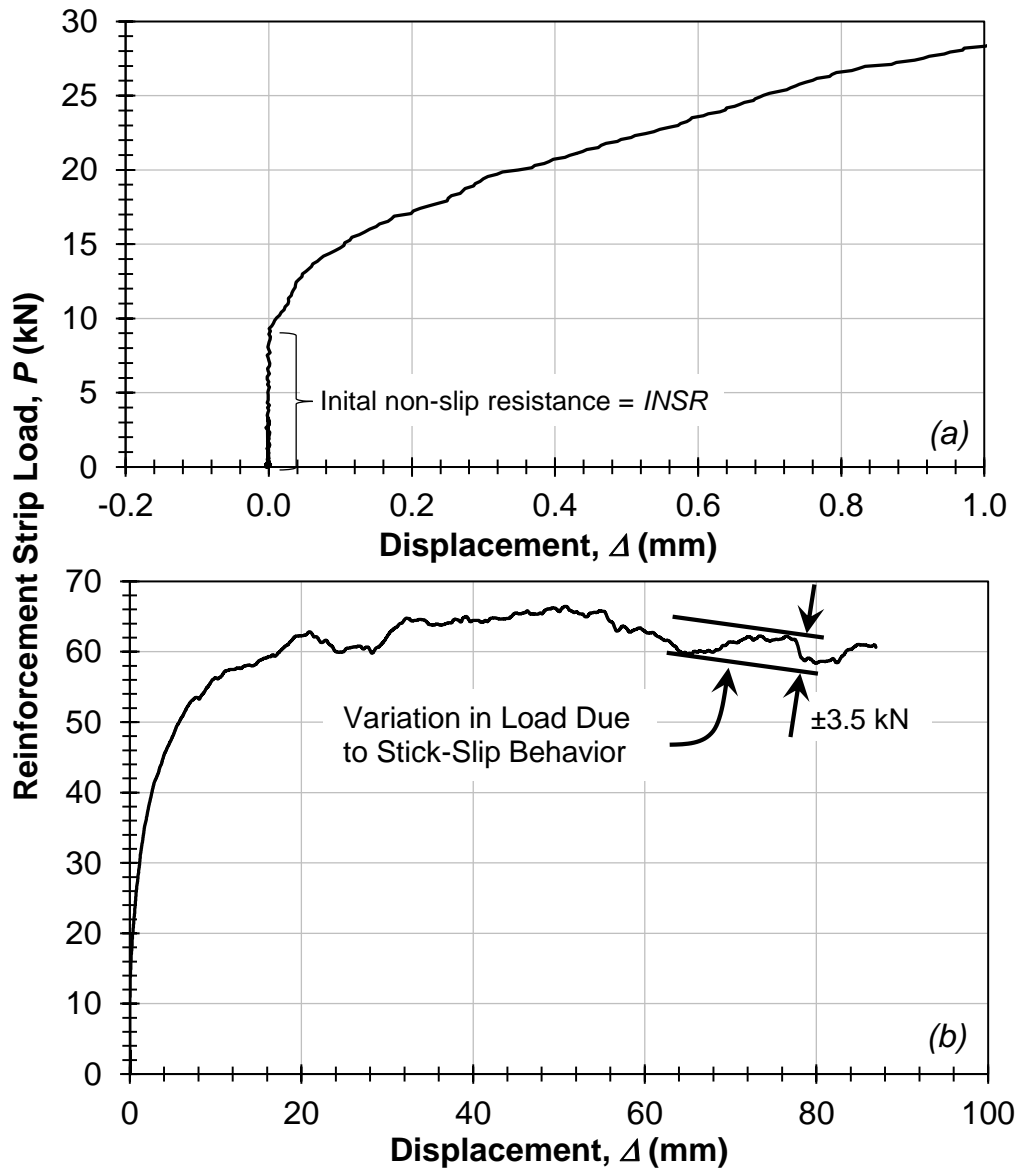


Figure 6.7. Apparent load versus strip displacement curve (a) at small displacements showing the initial non-slip resistance and (b) over full range of displacements for test 200-2.

observed. Rather, the erratic response was likely influenced by the proximity of larger particles to the reinforcement ribs. The variation in the measured load associated with the observed stick-slip behavior is on average ± 3.5 kN based on the test results shown in Figure 6.7 and Figures D.1 through D.11 in Appendix D. Thus, the peak load typically occurred between 20 and 60 mm of displacement for the isolated reinforcement strips and the onset of global softening started between 60 and 120 mm.

6.5.2. FRICTIONAL RESPONSE OF FULLY-CONFINED REINFORCEMENTS STRIPS

Typical multi-strip pullout load-displacement curves for ribbed steel strips are presented in Figure 6.8 for Test 100A-66, which was conducted at S_v and S_h equal to 150 mm corresponding to a S_{local} of 2880 MPa. The reinforcement strips were connected to a common steel plate (Figures 6.3 and 6.4), however individual strips experienced some seating and no *INSR* was observed. The initial portion of the load-displacement response of partially confined strips (strips 1 through 4, and 6 through 9), presented in Figures 6.8a and 5.8e, indicates a noticeable reduction in the stiffness, to about half of its initial value, at a displacement of about 2 mm. This reduction in stiffness was typically not observed for the fully confined strip (strip 5) presented in Figure 6.8(c) and Figures D.1 through D.11 in appendix D; rather, a gradual reduction in the stiffness was observed. This suggests that the stiffness of closely-spaced, fully-confined reinforcement strips may be influenced by the restraint of vertical and horizontal soil strains that are provided by the neighboring strips. Qualitatively, the larger displacement response of the partially- and fully-confined strips are similar to the isolated strip tests, and exhibit erratic load-displacement responses indicative of

stick-slip interface shear. However, strips 1, 3, 7, and 9 typically produced the smallest pullout resistances due to their positions in the corners of the 3 x 3 matrix. On average, strips 4 through 6 exhibited higher initial stiffness and peak pullout resistances

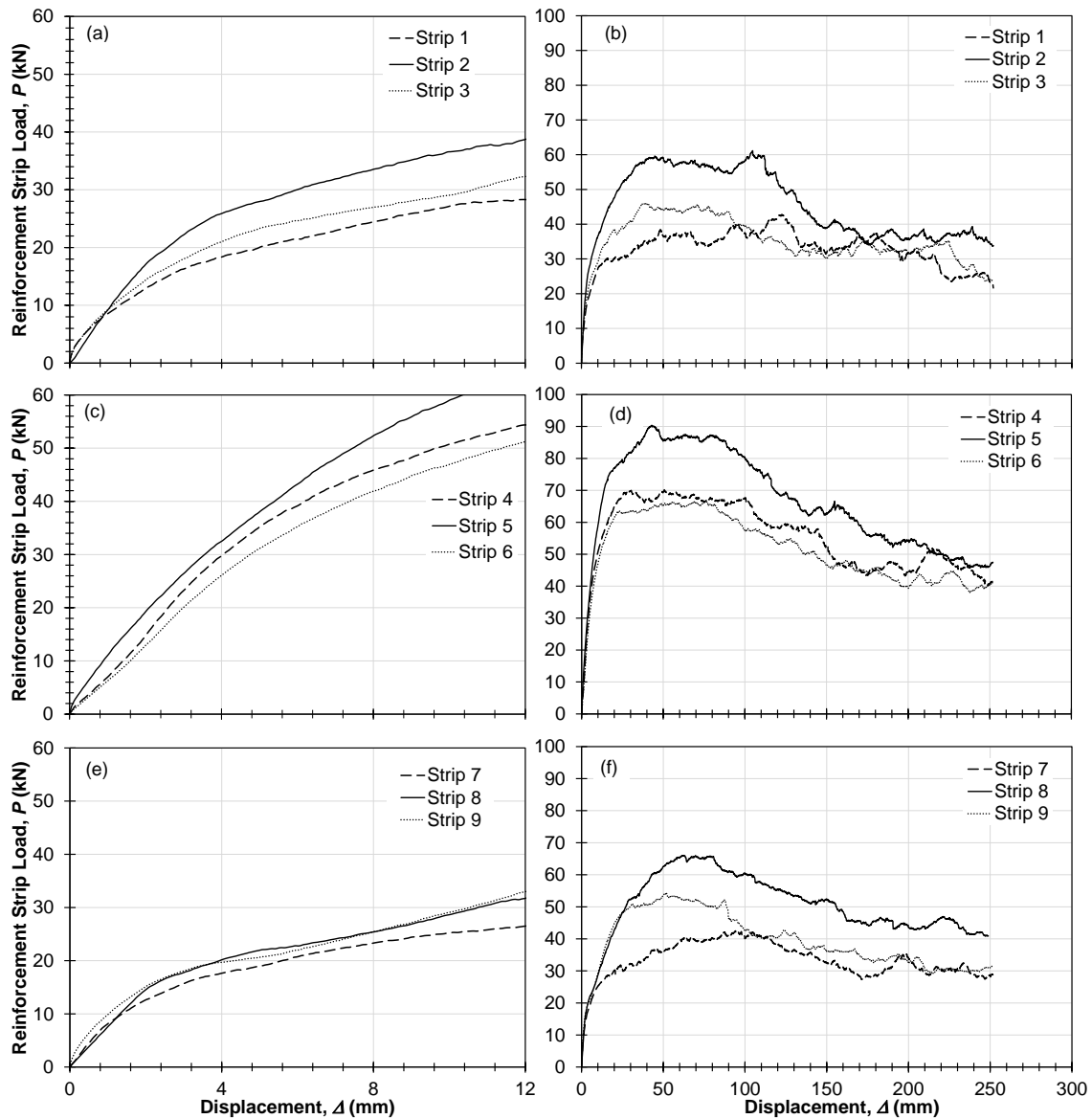


Figure 6.8. Typical load displacement behavior of the multiple strip pullout apparatus: (a), (c), (e) at small displacements and (b), (d), (f) over full range of displacements for test 100A-66 (Note: See Figure 4 for strip locations).

than those strips occupying the top and bottom rows, as shown in Figures 6.8(c) and D.1 through D.11 of appendix D. Of interest for design scenarios requiring assessment of pullout performance at large displacements (e.g., seismic loading), the magnitude of softening was largest for reinforcement strips in the middle row, and the center strip in particular.

Owing to its fully-confined position, the center strip was considered to represent a typical strip within a MSE wall; therefore, the performance of the center strip is of greatest interest in this study. The pullout resistance for the fully-confined strips presented in Table 1 has been corrected for both length differences and front face boundary effects. The reinforcement strips used in the single and multi-strip apparatus corresponded to L_r of 1.87 and 1.75 meters, respectively, resulting in an estimated difference in resistance of 5.3 kN according to Figure 6.6. Evaluation of length effects can be accomplished through the use of a length bias, λ_L , where P_f in Eq. (6.6) is replaced with the differential resistance stemming from length differences, P_L , given by:

$$\lambda_L = \frac{P_{\max} + P_L}{P_{\max}} \quad (6.7)$$

The corresponding λ_L is equal to 0.92 according to Eq. (6.7). Fully-confined strip P_{\max} presented in Table 6.1 have been corrected for the soft boundary condition at the front face and length differences by dividing the measured responses by the facing and length bias values.

6.5.3. PULLOUT RESPONSE AT WORKING STRESSES

Of interest to MSE wall designers is the load-displacement response of ribbed steel strips at small displacements, or working stresses, which can be sufficiently characterized using the secant stiffness. To evaluate the effect of reinforcement spacing on the initial stiffness, the secant stiffness at 5 mm displacement, k_{sec} , was calculated from each of the load-displacement curves. This magnitude of displacement corresponds to a condition where shear stresses along the strip are fully mobilized (Abramento and Whittle 1995, Bobet et al. 2007, Jayawickrama et al. 2014) and the behavior is minimally influenced by front boundary conditions. Measured single strip k_{sec} values ranged from 3.3 to 16.4 kN/mm and exhibited variation on the order of ± 4 kN/mm at a given overburden stress (Table 6.1, Figure 6.9a). The secant stiffness of single strips are separated by relative compaction where data is available and some variability in k_{sec} is attributed to the differences in RC . However, the spatial variability in relative compaction could not be separated from deviations associated with interface contact quality and random proximity of larger sized particles relative to the reinforcement ribs. Using the power law trend in Figure 6.9(a) representative single strip stiffness values of 6.3, 9.1, and 11.7 kN/mm were calculated for effective vertical pressures of 30, 100, and 200 kPa, respectively, and plotted in Figure 6.9(b) along with those corresponding to fully confined strips.

The secant stiffness for fully-confined strips at $\sigma'_v = 100$ kPa are presented in Figure 6.9(b) and indicate that k_{sec} decreases with increases in S_{local} . Superposition of propagating normal stresses that originate from adjacent strips in the soil mass produces higher soil strains at a given displacement, and subsequently results in smaller k_{sec} . A power law fitted

to k_{sec} and shown in Figure 6.9(b) appeared to capture the general trend in stiffness reduction, and similar trends in k_{sec} can be inferred for σ'_v of 30 and 200 kPa.

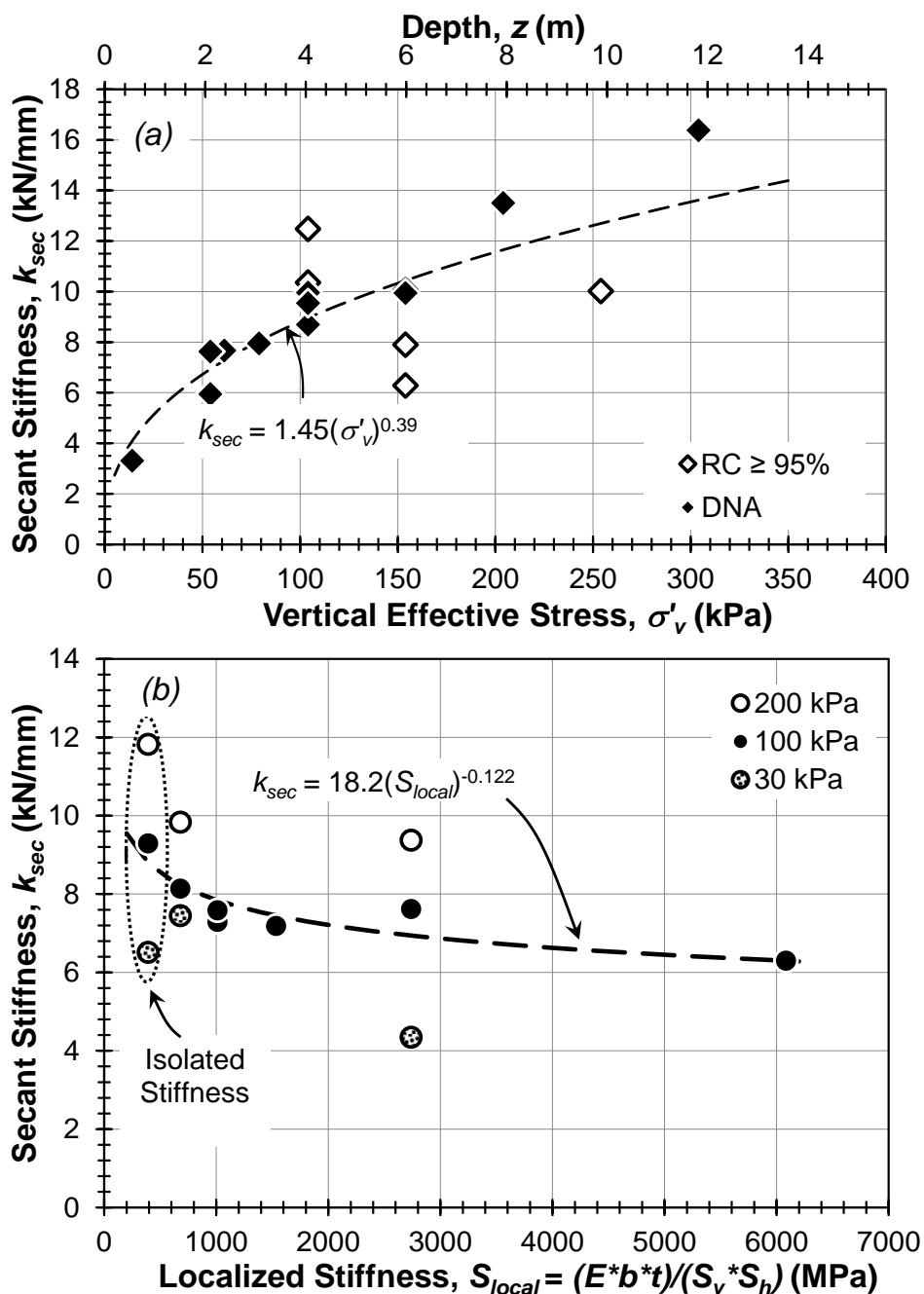


Figure 6.9. Secant stiffness at 5 mm of displacement as a function of normalized spacing ratio and vertical effective stress for (a) isolated and (b) fully-confined reinforcement strips (Note: DNA = Density Not Available).

6.5.4. ULTIMATE PULLOUT RESISTANCE OF ISOLATED SINGLE STRIPS

The ultimate pullout resistance, P_{max} , of isolated, single reinforcement strips, corrected for length differences and the front face boundary is presented in Figure 6.10(a) as a function of equivalent depth and effective vertical pressure. These data were used to develop a reference ultimate resistance relationship for isolated strips for comparison to the fully-confined strips. The ultimate pullout resistance of a single, isolated ribbed steel strip constructed in Kanaskat gravel may be approximated using:

$$P_{max} = \frac{\sigma'_v}{0.64 + 0.0078 \sigma'_v} \quad (6.8)$$

as shown in Figure 6.10(a). The baseline isolated resistance model is characterized with a coefficient of variability (*COV*) of 13%, greater than that due to the average variability associated with the observed stick slip response illustrated in Figure 6.7b (i.e., ± 3.5 kN or a *COV* of 5%). The majority of P_{max} lie outside of upper- and lower-bound curves that correspond to the variability associated with the stick-slip resistance, and indicate that the variability in the data and model is a result of multiple sources (e.g. measured stick-slip behavior, interface contact quality characteristics, variations in *RC*, and the random proximity of larger sized particles in relation to ribs). No reliable trend could be established between *RC* and corresponding P_{max} values due to the limited number of relative density measurements and the influence of other sources of variability on the measured response (Walters 2013). Variability associated with additional factors (e.g. quality of the interface contact, large particle location) could not be characterized with the current dataset.

Nonetheless, the variability reported here is much smaller than that associated with other pullout test results conducted in gravelly soils (e.g. McKittrick 1978, Miyata and Bathurst 2012a, Jayawickrama et al. 2014).

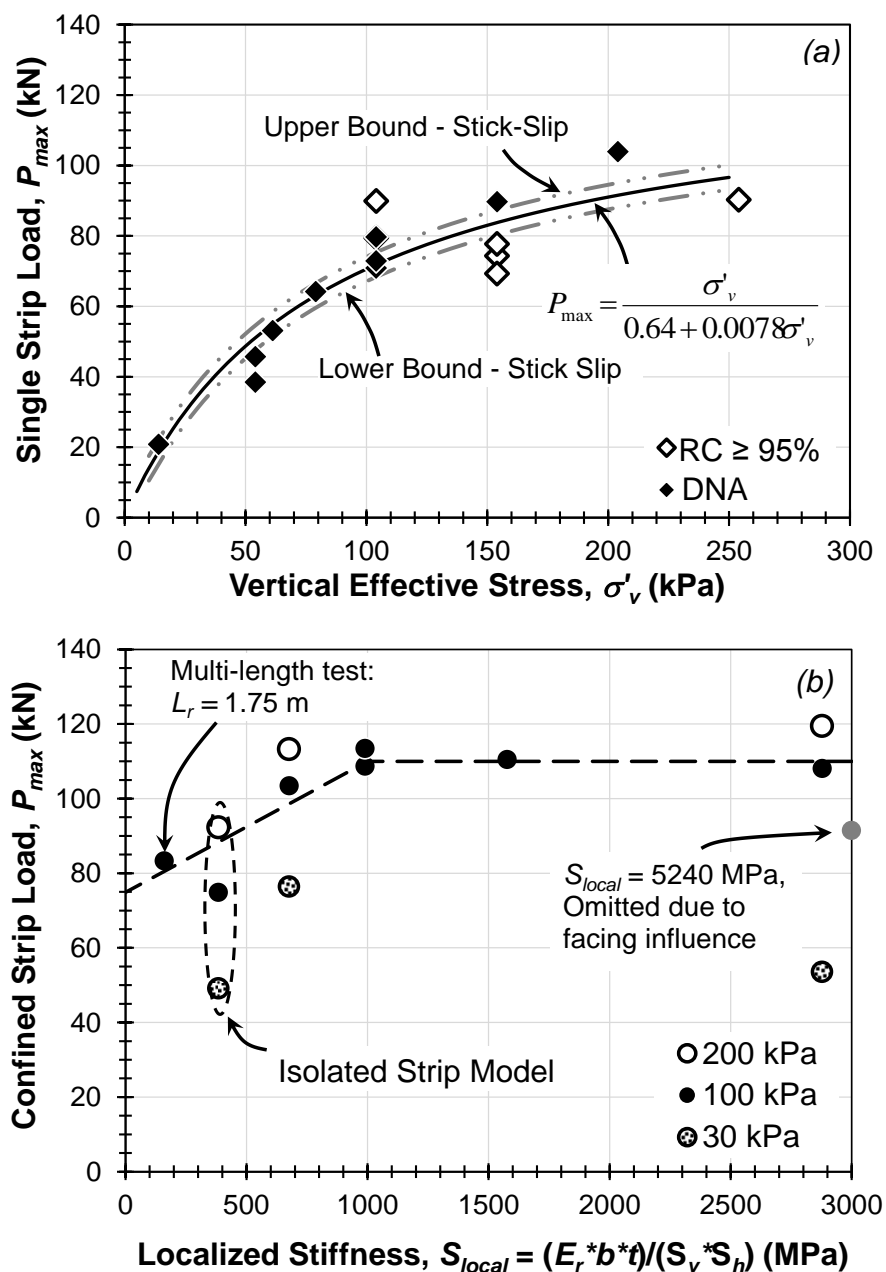


Figure 6.10. Peak apparent strip loads for (a) the single strip apparatus and (b) fully confined center strips adjusted for length differences and boundary condition effects. (Note: DNA = Density not available).

6.5.5. EFFECT OF SPACING ON ULTIMATE PULLOUT RESISTANCE OF FULLY- CONFINED STRIPS

The influence of reinforcement spacing on the behavior of ribbed steel reinforcement strips in Kanaskat gravel may be assessed by comparing P_{max} for fully-confined strips to variations in S_{local} (Figure 6.10b). The ultimate pullout resistance computed using Eq. (6.8) are also provided for an estimated S_{local} of 384 MPa, developed assuming that the S_v and S_h were equal to the height and width of the single strip pullout box, respectively. In general, with the exception of P_{max} at low σ'_v , the data indicates that as the S_{local} increases, P_{max} for fully-confined strips increases. The P_{max} for the fully-confined strips at σ'_v of 100 kPa and for $S_{local} = 2880$ MPa ($S_v = S_h = 152.4$ mm) is approximately 47% larger than that given by the isolated strip model at the same σ'_v . Similarly, the fully-confined P_{max} at $\sigma'_v = 200$ kPa are approximately 36% larger than the isolated strip model at the same σ'_v .

Two dimensional discrete numerical simulations (Wang et al. 2007) and laboratory interface tests (Irsyam and Hryciw 1991) have shown that shear strains propagate away from the interface during shearing and creates a zone of localization. The geometry of the strain localization zone is influenced by the surface roughness and rib geometry at the interface, but is generally considered to be semi-cylindrical and trapezoidal in shape. When the peak frictional response is attained, the extent of the trapezoidal zone of strain localization begins to reduce as the interface approaches a residual condition. Adjacent reinforcement strips that are positioned within the zone of strain localization experience an increase in the mean effective stress at the soil-strip interface, resulting in an increase in the available resistance as shown in Figure 6.10(b).

The multi-strip pullout test data shown in Figure 6.10 suggest that the effect of frictional interaction on pullout resistance is pressure-dependent due to suppression of soil dilation. Pullout test configurations associated with S_{local} equal or greater than about 600 MPa resulted in increases in P_{max} on the order of 33 and 10% when σ'_v increased from 30 to 100 kPa and 100 to 200 kPa, respectively. This is generally consistent with the reduction in shear strength parameters for Kanaskat gravel with log cycle of mean effective stress shown in Figure 6.1. The general trend of the increase in P_{max} for $\sigma'_v = 100$ kPa appeared best captured using a bilinear trend as shown in Figure 6.10(b). A single test at $S_{local} = 5240$ MPa was conducted to determine the response at very close spacing ($S_v = S_h = 114$ mm) and is plotted with a grayed marker in Figure 6.10(b). At this close spacing, the steel section that retains the soil around the strips was just 13 mm thick as a result of the 101 mm front face opening that was maintained for each test. The observed reduction in the P_{max} value is likely a product of the loss of lateral restraint and corresponding lateral effective stresses due to the soft front face; this test was therefore omitted from the bilinear trend.

6.5.6. APPARENT FRICTION COEFFICIENT FOR RIBBED STEEL STRIPS IN KANASKAT GRAVEL

Design pullout resistances, in terms of the apparent friction coefficient, for use with ribbed steel strips constructed in Kanaskat gravel or other soils with similar mineralogies, angularity, and gradation may be established from the pullout test data. The apparent friction coefficient f^* , for isolated, single strips were calculated using Eq. (6.4) and P_{max} corrected for length and front face boundary effects (Table 6.1). Accordingly, the length used for calculation of f^* for fully-confined strips was corrected to 1.87 m for comparison to the

isolated single strips. Figure 6.11(a) shows the resulting f^* values as a function of the applied vertical pressure and equivalent depth of fill. Measured single-strip f^* ranged from approximately 8.0 to 1.9 for σ'_v of 14 and 254 kPa, respectively, whereas f^* for fully-confined strips ranged from 8.7 to 2.7 at σ'_v of 47 and 217 kPa, respectively. The scatter in the isolated and fully-confined f^* is attributed to the erratic, stick-slip behavior and variations in specimen density, soil-strip interface contact quality, as discussed previously. Recommended design f^* , such as those derived from the AASHTO (2014) design model (Eq. 5.2) is presented in Figure 6.11(a) for comparison to the backfill-specific f^* .

Typically, a representative friction angle is chosen for use in Eq. 5.2 and is assumed constant with depth. However, this does not adequately represent soil behavior over the range of confining pressures that exist in many retaining walls and ignores the tendency of granular soils to approach a constant volume (or critical state) condition as confining stresses increase (Strahler et al. 2015). To incorporate the known soil mechanics into the AASHTO (2014) design framework, the PSK₀CD ϕ'_{cv} of 40 degrees was used to establish the recommended f^* values presented in Figure 6.11(a). The friction angles reported by Strahler et al. (2015) are high compared to typically reported values and AASHTO (2014) guidelines require that triaxial compression friction angles are capped at 40 degrees in design (Allen et al. 2001, Allen et al. 2004). In reality, the use of conservative strength parameters leads to the overestimation of reinforcement loads and underestimation of pullout resistance (Allen et al. 2001, Allen et al. 2004, Bathurst et al. 2009, Stuedlein et al. 2012), and therefore represents an inherent drawback associated with the use of Eq. (6.2) that can be mitigated using backfill-specific tests.

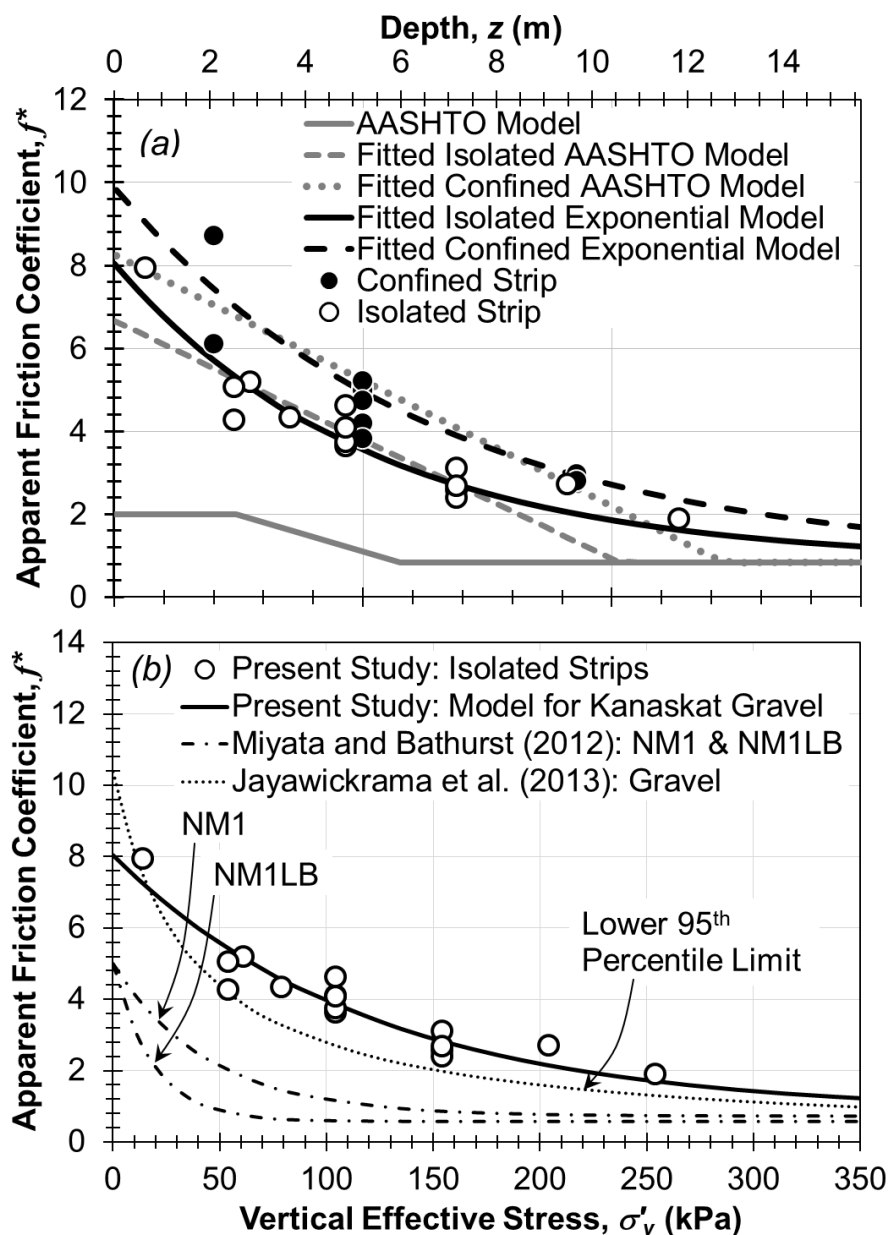


Figure 6.11. Fitted models for (a) single and multi-strip pullout tests presented here using Kanaskat gravel and (b) tests available in the literature. Note: NM1 and NM1LB correspond to New Model 1 and its lower bound, respectively, reported by Miyata and Bathurst (2012a).

The benefit of backfill-specific pullout tests are apparent in Figure 6.11 where the test results are compared to the AASHTO (2014) recommended f^* , particularly at shallower depths where “locked-in” stresses from compaction are most significant (Ehrlich and

Mitchell 1994; Stuedlein et al. 2010b, 2012). In order to estimate the pullout resistance for ribbed steel strips in Kanaskat gravel, and soils with similar gradations and angularity, the original AASHTO model (Eq. 5.2) has been empirically fit to single and multi-strip f^* . Fitting parameters f^*_0 and z_t were adjusted using ordinary least square regression techniques and ϕ' was held constant, set equal to $\tan(\phi'_{cv})$ with $\phi'_{cv} = 40$ degrees based on the backfill-specific plane strain tests reported by Strahler et al. (2015) to represent a constant volume condition. Fitted AASHTO (2014) models are presented in Figure 6.11(a) and fitting parameters are presented in Table 6.2. The ratio of the measured peak resistance to that predicted by the model (i.e., the bias) was used to check for stress dependencies in the models. The results of zero slope tests indicate that the original and fitted isolated AASHTO (2014) models depend on the vertical effective stress whereas the fitted confined model does not exhibit stress dependencies, at a significance level, α , of 0.05. The inconsistency in bias between the isolated and confined strip models suggests that the functional form of the AASHTO (2014) model is not particularly suited for modeling the pullout resistance of steel reinforcement strips given the data assessed herein.

The exponential model adopted by Miyata and Bathurst (2012a), presented as Eq. (6.3), overcomes drawbacks associated with the AASHTO (2014) and fitted AASHTO (2014) models (e.g. not continuous, not differentiable, stress dependent; Miyata and Bathurst 2012a). Additionally, Miyata and Bathurst (2012a) showed that there is no statistically significant difference between the in-situ and laboratory pullout resistance values. Thus, the exponential model was fitted to the single and confined f^* values using ordinary least square regression techniques. Although Eq. (6.3) was originally developed from pullout test results performed in Japan, the newly calibrated model accurately captures trends in the f^* response

of Kanaskat gravel as shown in Figure 6.11. The resulting fitting coefficients, f^*_o and c , for the isolated strip model are presented in Table 6.2; similar to the fitted AASHTO model, μ_I was held constant, set equal to $\tan(\phi'_{cv})$ with $\phi'_{cv} = 40$ degrees assuming that μ_I corresponded to constant volume sharing. Eq. (6.3) was fit to f^* determined from the confined reinforcement strip tests for S_{local} greater than 600 MPa, and produced fitting coefficients shown in Table 6.2. Similar to the isolated strip model, μ_I was held constant and equal to $\tan(\phi'_{cv})$, to produce a model that accurately captures f^* response over the ranges of stresses tested. The results of zero slope tests suggest that the fitted isolated and confined exponential models are independent of stress at a significance level, α , of 0.05.

Table 6.2. Summary of fitted AASHTO and New Model 1 (NM1) fitting parameters for Kanaskat gravel.

	AASHTO Fitted Model			NM1 - Fitted Model		
	z_t (m)	f^*_o	ϕ' (deg)	c	f^*_o	μ_I (deg)
Isolated strip	10.6	6.7	40	0.19	8.0	40
Confined strip	13.8	8.3	40	0.15	9.9	40

Figure 6.11(b) compares recently calibrated models of f^* for gravelly soils reported by Miyata and Bathurst (2012a) and Jayawickrama et al. (2014) to that appropriate for Kanaskat gravel. Jayawickrama et al. (2014) reported tests conducted on ribbed steel strips embedded in gravel backfill with similar characteristics as Kanaskat gravel ($C_u \approx 43$, $D_{50} \approx 10$ mm, sub-angular to sub-rounded) and presented a 95th percentile curve for use with allowable stress design procedures (shown in Figure 6.11b). The majority of the back-calculated f^* reported

by Jayawickrama et al. (2014) are significantly larger than that produced in this work. However, the experimental pullout apparatus used by Jayawickrama et al. (2014) employed rigid plates to apply vertical pressures and did not appear to provide sufficient controls for mitigating the passive earth pressures that are generated at the front face. Thus, the f^* back-calculated by Jayawickrama et al. (2014) could be artificially elevated, explaining the inverse correlation between the length of strip embedment and f^* that was reported, and may not represent the true soil-reinforcement strip interaction.

Conversely, Miyata and Bathurst (2012a) used a large database of Japanese pullout tests consisting of a combination of in-situ and laboratory tests, with various gravelly soil gradations to calibrate several different models. The New Model 1 (NM1) reported by Miyata and Bathurst (2012a) and presented in Figure 6.11(b), was calibrated using sandy gravels (GS) and gravelly sands (SG) as classified using the Public Works Research Center soil classification system (PWRC, 2003). The actual soil gradations were not provided, however, these soils are expected, on average, to be more uniformly graded than Kanaskat gravel based on the definitions established by the PWRC (2003). The database of tests used for calibration of New Model 1 consisted of a broad range of front facing conditions, soil gradations, and relative densities (80 to 102 percent of standard proctor density) that are observed in MSE wall construction in Japan (Miyata and Bathurst 2012b). As a result, f^* values computed using NM1 are specific to Japanese soils and construction methods, and are significantly less than the isolated, single strip Kanaskat f^* .

6.5.7. *DISCUSSION AND POTENTIAL DESIGN IMPLICATIONS*

Results from the isolated, single and multi-strip tests suggest that, although there is some observable scatter, reduction in the reinforcement spacing increases the available peak resistance but reduces the initial pullout stiffness. This behavior is attributed to overlapping zones of increased normal stresses and shearing strains that propagate away from the reinforcement strips. Initially, as the zones begin to overlap the stiffness reduces due to superposition of neighboring zones of stress. With further strip displacement, the increased normal stresses act to suppress dilation at the soil-strip interface and produce increases in the peak pullout resistance. The marked transition in stiffness of partially-confined reinforcement strips at small displacements (~ 2 mm) indicates the onset of slippage at the soil-strip interface, consistent with direct shear interface tests conducted by Hryciw and Irsyam (1993). In fully-confined strips, the transitional behavior is more gradual and suggests that the onset of slippage may be restrained by the frictional interference and/or confinement of surrounding strips.

The pullout resistance factors back-calculated from the experimental data appear to be poorly modeled by bilinear relationships that are implemented within certain national codes. Preferred models must be unbiased in addition to exhibiting low dispersion or variability about the design line. It was shown that the functional form of the pullout resistance factor model proposed by Miyata and Bathurst (2012a) provided an unbiased representation of the pullout resistance for the isolated and closely-spaced reinforcement strips in the sandy gravel soils evaluated herein.

Designers of typical MSE walls do not directly incorporate the frictional interference between closely-spaced reinforced strips because current empirical design procedures are

based on walls where the spacing is somewhat large (e.g. 600 to 750 mm). Based on the experimental P_{max} data presented in Figure 6.10, it appears that for reinforced soils with local stiffness greater than 1,000 MPa (250 mm spacing for the 6 mm thick reinforcements), further increase in P_{max} should not be anticipated. However, the data does not point to a definitive lower bound local stiffness at which increase in P_{max} no longer decreases, though the comparison of the isolated and confined-strip data suggest a possible lower bound local stiffness of about 500 MPa (360 mm spacing) where P_{max} no longer decreases. The results of this study do not point to definitive magnitude of local stiffness or reinforcement spacing where a transition in secant pullout stiffness occurs. Rather, a slowly decaying reduction in stiffness with decreases in spacing was observed (Figure 6.9).

The observations of the impact of local stiffness on pullout stiffness and ultimate resistance will be relevant for practitioners modeling the working stress and ultimate limit response for walls where large vertical overburden pressures and seismic loads may require small reinforcement spacing. The large geostatic stresses near the base of tall walls provides a condition where tensile failure in the strip can occur prior to pullout, and therefore interaction effects may be of most concern at working stresses where the steel strip response is largely controlled by the soil-reinforcement stiffness. The observed trends in pullout stiffness should help practitioners to more accurately predict reinforcement loads and wall deflections as a function of S_{local} , increasing the efficiency of constructed MSE walls, especially in design situations where reinforcement spacing less than about 360 mm are required.

The design of tall steel reinforced walls such as the 46 m tall MSE wall presented by Stuedlein et al. (2007, 2010a, 2010b, 2012) is commonly aided using numerical deformation

analyses. Recent investigations performed by Damians et al. (2013, 2015) have shown that numerical methods adequately predict the response of typical steel strip reinforced MSE walls and the trends presented here can be incorporated into future numerical models to improve the accuracy of working stress predictions of the performance of tall MSE walls.

6.6 CONCLUDING REMARKS

The popularity and proliferation of MSE walls in the U.S. has led to the design and construction of tall MSE walls that extend in height beyond those for which design procedures were developed (Stuedlein et al. 2012; Allen and Bathurst 2015). Increases in the magnitude of vertical overburden and lateral earth pressure in tall MSE walls has prompted designers to use closely-spaced reinforcements; yet, due consideration for the potential of frictional interaction between reinforcement strips has not been considered. In order to study the potential for frictional interference between closely spaced reinforcements, two pullout test apparatuses were designed and fabricated to study the load-displacement response of commonly used steel ribbed reinforcement strips. Both pullout systems were constructed with relatively soft front boundaries in order to mitigate the potential for artificially-elevated mean effective stresses resulting from passive earth pressure at the face. Single strip pullout test results were used to determine the fundamental behavior of an isolated strip and form the basis for a model that can be used to estimate the available resistance and initial stiffness of steel ribbed strips in well-graded sandy gravel similar to Kanaskat gravel. A multi-strip pullout test apparatus was used to characterize the frictional interference between closely-spaced and confined reinforcements. Results from the multi-strip tests indicate that the proximity of surrounding reinforcements may delay the onset of slippage at the soil-strip

interface due to potential increases in the mean effective stress, subsequently increasing the available resistance. However, the initial stiffness was observed to reduce with reductions in spacing. At higher confining stresses the interaction between reinforcement strips is less prominent due to reduced tendency for particles to dilate.

Comparisons between measured and predicted responses indicate that current AASHTO design methods are conservative and biased, especially at low confining stresses. An empirically modified version of the AASHTO design model is presented and adequately captures the peak pullout responses, but is biased for isolated strips. Following fitting to the experimental data, the exponential model proposed by Miyata and Bathurst (2012a) was found to accurately represent the trends in the pullout response. Incorporation of the trends in pullout responses reported here could lead to more efficiently-constructed MSE walls in scenarios where the reinforcement spacing is reduced to handle large overburden stresses, seismic forces, or prevent compound stability failure.

6.7 ACKNOWLEDGEMENTS

The study presented herein was supported by the National Science Foundation (Grant CMMI No. 1100903) under the direction of Dr. Richard Fragaszy, P.E.; the authors are grateful for this support. The authors thank FEI Testing & Inspection, Inc., for donating nuclear densometer tests, and Watson Asphalt, Inc. for donating the sandy gravel studied herein. The authors are grateful for the help of Chris Higgins, Thomas Miller, and Andre Barbosa, who kindly reviewed various structural design aspects of the pullout apparatuses.

6.8 REFERENCES

- American Association of State Highway and Transportation Officials (AASHTO). (2014). *AASHTO LRFD bridge design specifications*. 4th Edition, American Association of State, and Highway Transportation Officials, Washington, DC.
- Abramento, M., and Whittle, A. J. (1995). "Experimental evaluation of pullout analyses for planar reinforcements." *Journal of Geotechnical Engineering*, 121(6), pp. 486-492.
- Allen, T. M., Bathurst, R.J., Holtz, R.D., Walters, D., and Lee, W.F. (2004). "New method for prediction of loads in steel reinforced soil walls." *Journal of Geotechnical and Geoenvironmental Engineering*. 130(11), pp. 1109-1120.
- Allen, T. M., Christopher, B. R., Elias, V. and DiMaggio, J. A. (2001). "Development of the simplified method for internal stability design of mechanically stabilized earth (MSE) walls." *WSDOT Research Report WA-RD 513.1*.
- Allen, T.M. and Bathurst, R.J. (2015). "Improved Simplified Method for Prediction of Loads in Reinforced Soil Walls," *Journal of Geotechnical and Geoenvironmental Engineering*, 04015049.
- Alzamora, D., and Barrows, R.J. (2007). "Mechanically Stabilized Earth Walls on the Interstate Highway System, Thirty Years of Experience," *Research Pays Off*, TR News 249, Federal Highway Administration, U.S. Dept. of Transportation, pp. 32-33.
- American Society for Testing and Materials (ASTM). (2011). "Test Methods for Tension Testing of Metallic Materials." E8/E8M-15a, West Conshohocken, Pa.
- American Society for Testing and Materials (ASTM). (2010). "Standard Test Method for Rubber Property—Durometer Hardness." D2240-05, West Conshohocken, Pa.

- American Society for Testing and Materials (ASTM). (2009). "Test Methods for Laboratory Compaction Characteristics of Soil Using Modified Effort (56,000 ft-lbf/ft³ (2,700 kN-m/m³))." D1557-12e1, West Conshohocken, Pa.
- American Society for Testing and Materials (ASTM). (2006a). "Test Methods for Minimum Index Density and Unit Weight of Soils and Calculation of Relative Density." D4254-00, West Conshohocken, Pa.
- American Society for Testing and Materials (ASTM). (2006b). "*Test Methods for Maximum Index Density and Unit Weight of Soils Using a Vibratory Table.*" D4253-00, West Conshohocken, Pa.
- Anderson, P.L., and Brabant, K. (2005), "Increased Use of MSE Abutments," *Proceedings of the 22nd Annual International Bridge Conference*, Engineers' Society of Western Pennsylvania, Pittsburgh, PA, pp. 5-10.
- Bathurst, R.J., Nernheim, A., and Allen, T.M. (2008). "Comparison of measured and predicted loads using the Coherent Gravity Method for steel soil walls." *Ground Improvement*, 161(3), pp. 113-120.
- Bathurst R.J., Nernheim, A, and Allen, T.M. (2009). "Predicted Loads in Steel Reinforced Soil Walls Using the AASHTO Simplified Method." *Journal of Geotechnical and Geoenvironmental Engineering*, 135(2), pp. 177-184.
- Bathurst, R.J., Huang, B.Q., and Allen, T.M. (2011). "LRFD Calibration of Steel Reinforced Walls." *Geo-Frontiers 2011: Advances in Geotechnical Engineering*, Geotechnical Special Publication No. 211, ASCE, , Reston, VA, pp. 3429 to 3439.
- Berg, R. R., Christopher, B. R., and Samtani, N. C. (2009a)."Design of Mechanically Stabilized Earth Walls and Reinforced Soil Slopes." Report No. *FHWA-NHI-10-024*, Vol.

- I, National Highway Institute, Federal Highway Administration, U.S. DOT, Washington, DC. Berg, R. R., Christopher, B. R., and Samtani, N. C. (2009b). "Design of Mechanically Stabilized Earth Walls and Reinforced Soil Slopes." *No. FHWA-NHI-10-024*. Vol. II, National Highway Institute, Federal Highway Administration (FHWA), U.S. DOT, Washington, DC.
- Bobet, A., Lee, H. S., and Santagata, M. C. (2007). "Drained and undrained pullout capacity of a stiff inclusion in a saturated poroelastic matrix." *International journal for numerical and analytical methods in geomechanics*, 31(5), pp. 715-734.
- Christopher, B. R., Gill, S. A., Giroud, J. P., Juran, I., Mitchell, J. K., Schlosser, F., and Dunncliff, J. (1990a). *Reinforced soil structures Volume I. Design and construction guidelines*. Federal Highway Administration (FHWA), Washington, DC.
- Christopher, B. R., Gill, S. A., Giroud, J. P., Juran, I., Schlosser, F., and Dunncliff, J. (1990b). *Reinforced soil structures Volume II. Summary of research and systems information*. Federal Highway Administration (FHWA), Washington, DC.
- Damians, I., Bathurst, R., Josa, A., Lloret, A., and Albuquerque, P. (2013). "Vertical-Facing Loads in Steel-Reinforced Soil Walls." *Journal of Geotechnical and Geoenvironmental Engineering*, 139(9), pp. 1419–1432.
- Damians, I., Bathurst, R., Josa, A., and Lloret, A. (2015). "Numerical Analysis of an Instrumented Steel-Reinforced Soil Wall." *International Journal of Geomechanics*, 15(1), 04014037.
- Dove, J. E., and Jarrett, J. B. (2002). "Behavior of dilative sand interfaces in a geotribology framework". *Journal of Geotechnical and Geoenvironmental engineering*, 128(1), pp. 25-37.

- Ehrlich, M., and Mitchell, J. K. (1994). "Working Stress Design Method for Reinforced Soil Walls," *Journal of Geotechnical Engineering*, 120(4), pp. 625–645.
- Frost, J.D., Hebel, G.L., Evans, T.M., and DeJong, J.T. (2004). "Interface behavior of granular soils." *Proceedings, of the 9th ASCE Aerospace Division International Conference on Engineering, Construction and Operations in Challenging Environments*, ASCE, Reston, VA., pp. 7–10.
- Hryciw, R.D., and Irsyam, M. (1993). "Behavior of sand particles around rigid ribbed inclusions during shear," *Soils and Foundations*, 33(3), pp.1-13.
- Irsyam, M., and Hryciw, R. D. (1991). "Friction and passive resistance in soil reinforced by plane ribbed inclusions." *Géotechnique*, 41(4), pp. 485-498.
- Jayawickrama, P., Lawson, W., Wood, T., and Surles, J. (2014). "Pullout Resistance Factors for Steel MSE Reinforcements Embedded in Gravelly Backfill." *Journal of Geotechnical Geoenvironmental Engineering*, 10.1061/(ASCE)GT.1943-5606.0001192, 04014090.
- Lings, M. L. and Dietz, M. S. (2005). "The peak strength of sand-steel interfaces and the role of dilation." *Soils and Foundations* 46(6), pp.1–14.
- McKittrick, D.P. (1978). "Design, Construction, Technology and Performance of Reinforced Earth Structures," ASCE, Pittsburgh, pp. 596–617.
- Miyata, Y., and Bathurst, R. J. (2012a). "Analysis and calibration of default steel strip pullout models used in Japan." *Soils and Foundations* 52(3), 481-497.
- Miyata, Y., and Bathurst, R. J. (2012b). "Measured and predicted loads in steel strip reinforced $c - \phi$ soil walls in Japan." *Soils and Foundations*, 52(1), pp. 1-17.
- Palmeira, E.M., and Milligan, G. W. E. (1989). "Scale and other factors affecting the results of pull-out tests of grids buried in sand," *Géotechnique*, 39(3), pp. 511–542.

- PWRC, (2003). *Design Method, Construction Manual and Specifications for Steel Strip Reinforced Retaining Walls*, 3rd revised ed. Public Works Research Center (PWRC), Tsukuba, Ibaraki, Japan 302 pp. (in Japanese).
- Schlosser, F., and Elias, V. (1978). "Friction in reinforced earth," *Symposium on Earth Reinforcement at the ASCE Annual Convention*, ASCE, Reston, VA, April 27, 735–776.
- Strahler, A.W., Stuedlein, A.W., and Arduino, A. (2015). "Stress-Strain Response and Dilatancy of Sandy Gravel in Triaxial Compression and Plane Strain." *Journal of Geotechnical and Geoenvironmental Engineering*, *In Press*.
- Stuedlein, A. W., Allen, T. M., Holtz, R. D., and Christopher, B. R. (2012). "Assessment of Reinforcement Strains in Very Tall Mechanically Stabilized Earth Walls." *Journal of Geotechnical and Geoenvironmental Engineering*, 138(3), pp. 345–356.
- Stuedlein, A. W., Bailey, M. J., Lindquist, D. D., Sankey, J., and Neely, W. (2010a). "Design and Performance of a 46-m-High MSE Wall." *Journal of Geotechnical and Geoenvironmental Engineering*, 136(6), pp. 786–796.
- Stuedlein, A. W., Allen, T., Holtz, R., and Christopher, B. (2010b). Factors Affecting the Development of MSE Wall Reinforcement Strain. *ER2010: Earth Retention Conference 3*, ASCE, Reston, VA, pp. 502-511.
- Stuedlein, A. W., Mikkelsen, P. E., and Bailey, M. J. (2007). "Instrumentation and performance of the third runway north MSE wall at Seattle-Tacoma international airport." *7th International Symposium on Field Measurements in Geomechanics*, , Geotechnical Special Publication No. 175, ASCE, Reston, VA, pp. 1-14.
- Vidal, H. (1969). "The principle of reinforced earth," *Highway Research Record*, 282, pp. 1-16.

Walters, J.J. (2013). "Characterization of reinforced fill soil, soil-reinforcement interaction and global stability of very tall MSE walls." *MS Thesis*, Oregon State University, Corvallis, OR.

Wang, J., Gutierrez, M. S., and Dove, J. E. (2007). "Numerical studies of shear banding in interface shear tests using a new strain calculation method." *International Journal for Numerical and Analytical Methods in Geomechanics*, 31(12), pp. 1349-1366.

**CHAPTER 7: CALIBRATION AND NUMERICAL SIMULATIONS
OF TALL STEEL STRIP-REINFORCED MSE WALL**

Andrew Strahler, M.S., E.I.T., James J. Walters M.S., E.I.T., and Armin W. Stuedlein,
PhD, P.E.

Journal of Geotechnical and Geoenvironmental Engineering

1801 Alexander Bell Drive

Reston, VA 20191-4400

To Be Submitted

7.1 ABSTRACT

This paper describes the development of a tall complex numerical model that incorporates pressure dependent soil, panel-soil interaction, non-linear soil reinforcement interaction, facing rigidity, foundation stiffness, and compaction stresses to assess wall behavior. Performance measurements of the West MSE wall constructed as part of the third runway expansion of the Seattle Tacoma International Airport is used to validate the numerical model through an element specific parametric study. Measurements made during the construction of the West MSE wall are used to establish those factors within the model that most accurately simulates the observed wall performance. A second parametric study is conducted to evaluate the influence of boundary conditions on wall response are presented, focusing on impacts associated with tier height, tier offset, and wall height. Results from this parametric study are synthesized to establish a more thorough understanding of wall response, with specific emphasis on wall displacements and reinforcement strains. They indicate that complex multi-tiered walls are much more complicated than assumed in design approaches especially when pressure dependent soil behavior is incorporated.

7.2 INTRODUCTION

The construction and implementation of Mechanically Stabilized Earth (MSE) walls in the United States has experienced significant growth in recent years. This widespread increase in the use of reinforced earth technologies can be attributed to the relatively low cost, ease of construction, and high efficiency of MSE walls when compared to conventional retaining wall methods (Anderson and Brabant 2005). As a result, construction of tall walls (defined here as walls with a reinforced height greater than 20 m) and walls with complex geometry (e.g. multi-tiers, batter angles, and close reinforcement spacing) has increased even though the effect of these characteristics on general wall behavior at working stresses is not well understood. Available methods to predict reinforcement strains and the general deformed shape of MSE walls are empirically formulated from databases of single tier MSE walls less than 20 m tall (e.g. Allen et al. 2001, Allen et al. 2004, Christopher et al. 1990a, Christopher et al. 1990b, Berg et al. 2009a, Berg et al. 2009b). Liu (2014a), Liu and Won (2014b), and Liu and Yang (2015) provide recent alternatives to these approaches but are complicated and their predictive capabilities have only been verified against single tier MSE walls of typical height. Correspondingly, numerical simulations to estimate reinforcement loads and wall deformations greatly facilitate the assessment of design suitability. However, little information exists to help guide modelers for the soil-reinforcement interaction that can occur for reinforcements with close spacing. In an experimental study, Strahler et al. (2016) showed that the initial soil-reinforcement interface stiffness reduces and the ultimate pullout resistance increases with increases in the local reinforcement stiffness, S_{local} , given by (Christopher et al. 1990a, 1990b):

$$S_{local} = \frac{E_r b t}{S_v S_h} \quad (7.1)$$

where E_r , b , t , S_v , and S_h are the reinforcement modulus, width, thickness, vertical spacing, and horizontal spacing of the reinforcement, respectively. Stuedlein et al. (2010b) also showed that the local stiffness partially controls the rate of strain uptake in MSE reinforcements during construction. However, the impact of the observed soil-reinforcement interaction on global, working stress responses of tall MSE walls, such as their deformation mode and reinforcement load magnitude and distribution, have not been sufficiently explored.

The current study aims to provide practitioners with a better understanding of the working stress behavior of tall MSE walls during and after construction through the use of a calibrated numerical model that incorporates pressure dependent soil, panel-soil interaction, non-linear soil reinforcement interaction, facing rigidity, foundation stiffness, and compaction stresses. Selected elements (e.g. reinforcement-soil interface, facing-soil interface, soil constitutive response) were calibrated using high quality laboratory test. The performance of the West MSE wall constructed as part of the third runway expansion of the Seattle Tacoma International Airport (STIA) and reported by Stuedlein et al. (2010a, 2010b, and 2012) is used to validate the numerical model through an element specific parametric study. Measurements made during the construction of the West MSE wall are used to establish those factors within the model that most accurately simulates the observed wall performance. Results from a second parametric study conducted to assess the influence of boundary conditions on wall response are presented, focusing on impacts associated with tier

height, tier offset, and wall height. The synthesis of the results from the geometric parametric study are used to establish a more thorough understanding of wall response, with specific emphasis on wall displacements and reinforcement strains.

7.3 CRITICAL ASPECTS OF THE VALIDATION CASE HISTORY

The numerical simulations presented here are validated against data gathered from the performance of the West MSE wall constructed as part of STIA third runway project. The wall was constructed to raise the grade for the third runway to minimize the impact on adjacent wetlands, discussed in detail by Stuedlein et al. (2007, 2010a, and 2012). Figure 7.1 presents the cross-section of the West MSE wall at its tallest section. The West MSE wall is approximately 436 meters long, has four tiers with offsets of 2.4 m, and was constructed with an exposed and reinforced height of 41.9 and 46 m, respectively.. An additional 2H:1V embankment surcharge with a crest height of 4.5 m was constructed on top of the wall to achieve the required grade and was sloped at a negative 3% gradient to help direct surface runoff to drainage facilities. The wall construction performance was monitored with strain gages on the reinforcement strips, inclinometers and Sondex rings in the reinforced backfill, piezometers, and displacement monitoring points (DMPs) on the wall face at various cross-sections (Stuedlein et al. 2007, 2010a, and 2012). The reinforced fill used in the West MSE wall consisted of well-graded sandy Kanaskat gravel described in detail by Strahler et al. (2015) and met specific gradational criteria that was more restrictive than AASHTO (2002) minimum MSE wall requirements. The specifications for the retained fill was less restrictive, but was required to have a minimum direct shear friction angle of 35 degrees,

maximum particle size of 152 mm, and no more than 35% fines. Construction observations indicate that the embankment fill was of good quality with little fines content.

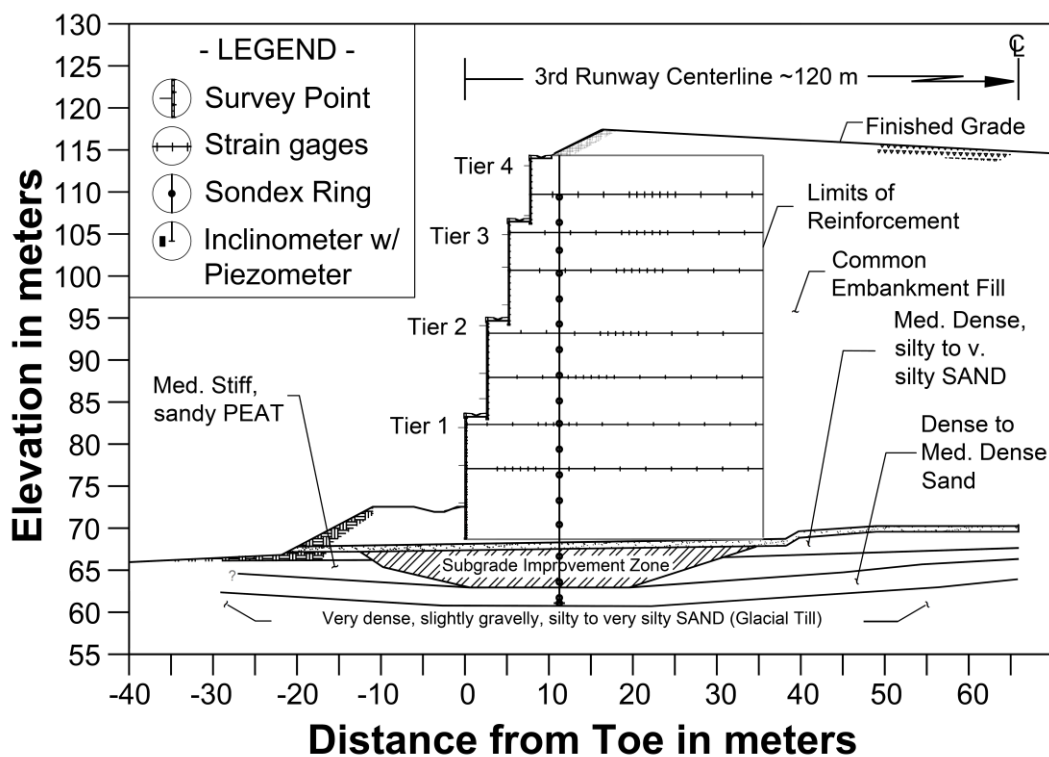


Figure 7.1. West MSE wall cross-section showing instrumentation locations.

The reinforcement used in the West MSE wall consisted of 6 mm by 50 mm ribbed steel strips with lengths that ranged from 28 to 35.4 m. Structural properties of the reinforcement strips are characterized by a Young's modulus, yield strength, and tensile failure strain of 211 GPa, 210 kN, and 0.28%, respectively (Walters 2013). Typical steel reinforced MSE walls are constructed with reinforcement spacing that range between 300 to 1,100 mm horizontally and 600 to 750 mm vertically. However, static and seismic considerations of compound stability dictated the relatively small horizontal and vertical reinforcement strip spacing (Stuedlein et al. 2010a), which ranged from 0.24 and 0.14 m at the base of the wall, to 0.78

and 0.74 m near the top, respectively. The close reinforcement spacing used in the design of the West MSE wall meant S_{local} was as high as 1,400 MPa, almost ten times greater than those used in the design of typical MSE walls. At such small spacing the proximity of surrounding reinforcements has an influence on reinforcement behavior (Stuedlein et al. 2010b, Strahler et al. 2016) which is not incorporated into design methods.

The performance of the West MSE wall has been described in detail by Stuedlein et al. (2010a, 2010b, 2012) including discussions of the reinforcement strain distributions, and lateral and vertical displacements at the wall face and within the reinforced fill. Notably, lateral displacements observed after completion of wall construction were 25% of that predicted by the empirically-based AASHTO (2002) procedure (Stuedlein et al. 2010a). The observed development of reinforcement strain during construction was found to be nonlinear and dependent on the local stiffness (Stuedlein et al. 2010b), which is not explicitly considered in the Simplified (Allen et al. 2001) and Coherent Gravity (Schlosser 1978) methods resulting in the under-prediction of reinforcement strains. Additionally, the strain distributions along the reinforcement were fairly uniform where not influenced by the reinforcement splices, and the location of peak strains were considered sufficiently bounded by the FHWA procedure (Elias et al. 2001) to estimate the zone of maximum stress (Stuedlein et al. 2012). However, comparison of reinforcement loads inferred from strain measurements following construction indicated that the Simplified and Coherent Gravity methods under-estimated reinforcement loads, whereas the Ehrlich and Mitchell (1994) and K-Stiffness methods (Allen et al. 2004) produced largely conservative estimates of reinforcement loads (Stuedlein et al. 2012). These observations were not considered surprising given the empirical basis for some methods which considered MSE walls with

typical heights (< 20 m) and local reinforcement stiffness (30 to 1000 MPa). The observations of lateral deformations and reinforcement strains in the West MSE wall suggested that the working response of tall MSE walls warranted additional study.

7.4 CALIBRATION OF ELEMENT SPECIFIC CONSTITUTIVE MODELS

7.4.1. GENERAL APPROACH

The two dimensional finite difference program FLAC version 7.0 (Itasca 2011) was used to model the plane strain response of the West MSE wall. The mesh of a representative cross-section of the West MSE wall is shown in Figure 7.2, with domain of 120 m in height and 175 m in width was considered sufficiently large to minimize the influence of the model boundary conditions. The modeled subsurface profile consists of five soil groups including the improved foundation zone directly beneath the reinforced soil zone. The mesh dimensions for the deep glacial till foundation soils were as large as 2.8 m, however, the typical mesh size in the foundation soils and reinforced and retained earth masses ranged from 0.2 to 0.4 m and were adjusted according to the reinforcement spacing. Bearing pads positioned between concrete facing panels were simulated using single beam elements that are attached to the wall face panels using hinged nodes. Interface elements were used to simulate the reinforced soil-panel and toe berm-panel interaction. An inset detailing the bearing pad panel connection and locations of interface elements is presented in Figure 7.2.

Previous studies of reinforced retaining walls have shown that most of the permanent deformation of MSE walls occurs during construction (Christopher et al. 1990a, Christopher et al. 1990b, Allen et al. 1992, Stuedlein 2010a). As a result, lift construction sequencing was used in MSE wall simulations to capture the development of deformations following

placement of the subsurface profile, (discussed in more detail below) drainage blanket, leveling pad, and first wall fascia panel. Initially, lateral and rotational displacements at the top of the panel were restrained to represent the bracing used during wall construction. The model was then stepped to equilibrium in small strain mode to initialize stresses at interfaces. Nodal locations and displacements were then updated by initiating the large strain mode and stepping to equilibrium again. Each lift of the MSE wall required the numerical placement of the reinforced and retained soil groups, the reinforcement elements, and then application of a small surcharge to simulate compaction. Following each lift, the model was stepped to equilibrium using the small and large strain mode, and the next lift placed and equilibrated until the top of the initial panel was reached. Lateral and rotational restraints at the top of the panel were removed followed by placement of the next restrained panel and corresponding bearing pad. The process was repeated for each panel until the top of the wall was reached.

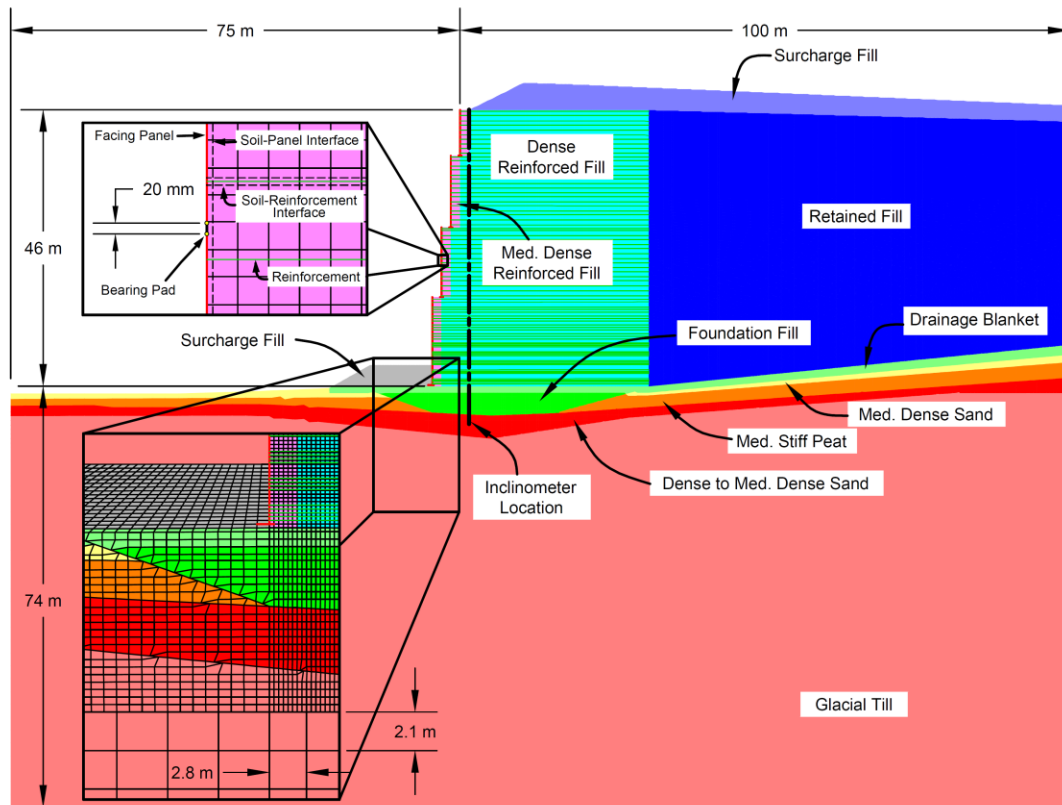


Figure 7.2. Mesh used for 2D FLAC simulations of the STIA West MSE wall.

The number of lifts per panel varied during simulation to accommodate changing reinforcement spacing but generally ranged between 0.2 and 0.6 m in thickness. The top of the west STIA MSE wall was reached after placing 110 soil lifts, 31 panels, and 77 reinforcement strips per the design drawings. The toe berm outside the base of the wall was placed in lift thicknesses that correspond to those in the wall. Reinforced soil-panel interface parameters were used to simulate the surcharge-panel interaction. After completion of each tier, concrete leveling pads represented by elastic beam elements were attached to the first panel of each subsequent tier. During construction of the West MSE wall, the measured vertical deformations indicated that global vertical strain in the reinforced soil mass was less than 1%. Four years after construction, the measured reinforcement strains ranged between

10 and 30% of yield stress (Stuedlein et al. 2012). Accordingly, the West MSE wall was considered to be operating under working stress conditions and the overall wall response was dictated by element responses at small strains. Efforts to capture the various element responses at these small strains are detailed below.

7.4.2. SUBSURFACE SOIL PROPERTIES

The stiffness of MSE wall foundations has been shown to significantly influence wall performance; for example, wall face settlements reduce with increasing foundation stiffness (Damians et al. 2012, 2016). Thus, effort was made to accurately represent the current state of stress and stiffness of the subsurface soils by simulating geological processes. Subsurface strata were placed sequentially and the model stepped to equilibrium after each layer was placed, including the subsurface excavation and replacement required for the West MSE wall construction. Subsurface soil constitutive responses were simulated using an elastic-plastic Mohr-Coulomb model. Representative subsurface strength properties were originally established based on results from an exploratory investigation program conducted during the initial design phase of the West MSE wall (Hart Crowser 2003). Specific foundation soil parameters established from the initial investigation were then adjusted to account for pressure dependencies and the plane strain stress path employed by FLAC. Changes in ϕ'_f and ψ_f resulting from changes in mean effective stress were represented by log-linear relationships of the form (Duncan et al. 1980):

$$\phi'_f = \phi'_0 - \Delta \phi' \log \left(\frac{P'_c}{P_{ref}} \right) \quad (7.2)$$

$$\psi_f = \psi_0 - \Delta\psi \log \left(\frac{p'_c}{p_{ref}} \right) \quad (7.3)$$

where ϕ'_0 and ψ_0 are friction and dilation angles at the reference pressure, p_{ref} (equal to 101.3 kPa), and $\Delta\phi'$, $\Delta\psi$ are the log-cycle change in friction and dilation angles with the mean effective consolidation stress, p'_c . Pressure dependent subsurface strength parameters presented in Table 7.1 for Equations (7.2) and (7.3) were developed by increasing the triaxial responses reported during the initial investigation by approximately 30% according to true-triaxial investigations reported by Strahler et al. (2015) and discussed in more detail below. Single, representative friction and dilation angles for use in the Mohr-Coulomb constitutive model were calculated at the mid-point of each soil layer directly beneath the reinforced soil mass. Since the focus of this study was on the response of the reinforced soil mass, further adjustments to stiffness of the drainage blanket and glacial were made during preliminary wall simulations to suitably capture the foundation performance during construction. The final, selected foundation soil model parameters are provided Table 7.1.

Table 7.1. Summary of Mohr-Coulomb soil properties.

Soil Layer	Unit Weight, γ (kN/m ³)	Bulk Modulus, K (MPa)	Shear Modulus, G (MPa)	Poisson's Ratio, ν	ϕ'_0 (deg)	$\Delta\phi'$ (deg)	ψ_0 (deg)	$\Delta\psi$ (deg)	Rep. Friction Angle, ϕ'_f (deg)	Rep. Dilation Angle, ψ_f (deg)
Embankment Fill	21.68	500	230	0.30	59	12	15	6	51	11
Drainage Blanket	21.50	36	8	0.40	52	12	9	6	43	5
Foundation Fill	21.50	150	70	0.30	59	12	15	6	49	10
Loose to Med. Dense Sand	20.02	120	40	0.35	42	8	4	4	36	1
Peat	17.62	95	20	0.40	20	0	0	0	20	0
Dense to Med. Dense Sand	20.82	3000	1000	0.35	46	8	11	4	39	7
Glacial Till	22.40	4000	1350	0.35	52	15	21	8	37	13

7.4.3. *ELEMENT PARAMETER UPDATING ROUTINES*

Current methods used in the design of MSE walls typically assume that friction angle and soil stiffness are independent of confining stress (Schlosser 1978, Ehrlich and Mitchell 1994, Elias et al. 2001, Allen et al. 2001). This assumption may be acceptable for use in MSE walls of typical heights (< 20 m); however, in tall walls where higher magnitudes in stresses develop, changes in the soil behavior are significant and are expected to influence on wall performance. Therefore, pressure dependent constitutive models were incorporated in the FLAC simulations to capture realistic soil-structure interaction. In each “step” in the simulation, which includes the mapping of nodal deformations and forces to strains and stresses and back again in the explicit integration scheme used by FLAC, the reinforced fill, retained fill, bearing pad, panel-soil interface, and reinforcement-soil interface constitutive models were updated to capture the change in model response with changes in p' . This approach required the calibration of the material elements used in the West MSE wall to incorporate changes in the p' , as described below.

7.4.4. *REINFORCED AND RETAINED SOIL PROPERTIES*

It is generally acknowledged that the behavior of MSE walls can be represented by a plane strain condition, even when reinforced by non-planar elements (Hatami and Bathurst 2005). However, the use of plain strain properties in MSE wall design is limited to a few methods (Schlosser et al. 1978, Ehrlich and Mitchell 1994) even though the friction angle and modulus of granular soils has been shown to be upwards of 33 and 225% greater (e.g. Cornforth 1964, Lee 1970, Marachi et al. 1981, Hatami and Bathurst 2005, Strahler et al.

2015) than that obtained in axisymmetric isotropically consolidated (AICD) triaxial specimens. The reinforced fill used in the construction of the West MSE wall consisted of a well-graded sandy gravel, termed Kanaskat gravel, which was the subject of an extensive true-triaxial laboratory investigation reported by Strahler et al. (2015). This investigation provided the basis for the calibration of the selected constitutive model, termed *Chsoil*, for the reinforced and retained fill. *Chsoil* is a shear and volumetric hardening/softening model rooted in incremental elasticity that uses the Mohr-Coulomb failure criterion and Rowe's stress-dilatancy theory to represent the soil response. The *Chsoil* model framework established within FLAC incorporates pressure-dependent Young's modulus, E , using a power law relationship given by (Janbu 1963):

$$E = E_{ref} p_{ref} \left(\frac{p'_c}{p_{ref}} \right)^m \quad (7.4)$$

where E_{ref} corresponds to the shear modulus at a reference pressure, p_{ref} , and m is a fitting coefficient. Schanz and Vermeer (1998) and Strahler et al. (2015) showed that m is relatively stress path independent, material specific, and equal to 0.56 for Kanaskat gravel. However, *Chsoil* does not update the strength and stiffness parameters during model simulation, as would be appropriate to model the construction of a fill wall. To overcome this drawback, a modified version of the *Chsoil* model was established by means of a user-defined model (UDM) where soil stiffness and strength parameters update with each simulation step. The modified *Chsoil* model calculates the current p' in each element during simulation and updates stiffness and strength parameters based on Equations (7.2), (7.3), and (7.4) where p'_c

is replaced with p' ; Appendix F provides the associated FISH and C++ code that was implemented.

Soil element tests were used to calibrate *Chsoil* against conventional AICD tests conducted by Strahler et al. (2015). Calibrated and measured experimental deviatoric stress and volumetric strain responses for Kanaskat gravel are provided in Figure 7.3 for p'_c ranging from 10 to 1,000 kPa; good agreement between the measured and simulated deviatoric stress response is observed. The comparison indicates that *Chsoil* emulates the observed hardening behavior with changes in confining pressure. Initial calibration attempts were not able to accurately capture the volumetric response over the entire range of stresses evaluated in Figure 7.3. Owing to the focus on working stresses in this work, subsequent calibration efforts focused on the response at small strains. The calibrated, modified *Chsoil* model produces fairly accurate global volumetric responses at axial strains smaller than about 2% over the range of pressures tested; however, it appears to over-predict the volumetric response at larger axial strains (Figures 7.3c and 7.3d). Fitted model parameters for the fitted *Chsoil* model are presented in Table 7.2 and are considered to represent a medium dense condition when used in some of the model simulations (discussed in later sections).

There is a significant body of work focused on the response of uniformly-graded granular soils in AICD and plane strain stress paths (e.g. Lee 1970, Marachi et al. 1981, Ramamurthy and Tokhi 1981, Peters and Lade 1988, Hanna 2001, Hatami and Bathurst 2005). However, the majority of this work has focused on the soil strength, with some discussions of stiffness by Lee (1970), and Hatami and Bathurst (2005).

Table 7.2. Summary of *Chsoil* constitutive model properties.

Stress Path and Density	Unit	Ref. Young's Modulus,						
	Weight, γ (kN/m ³)	E_{ref} (MPa)	Exponent, m	Poisson's Ratio, ν	ϕ_0' (deg)	$\Delta\phi'$ (deg)	ψ_0 (deg)	$\Delta\psi$ (deg)
Medium Dense AICD		16.0			47	7	27	11
Dense Plane Strain	23.86	41.8	0.56	0.26	65	19	42	15
Loose Plane Strain		10.0						
Loose Panel Zone		$0.55 E_{ref}$			52	6	20	11

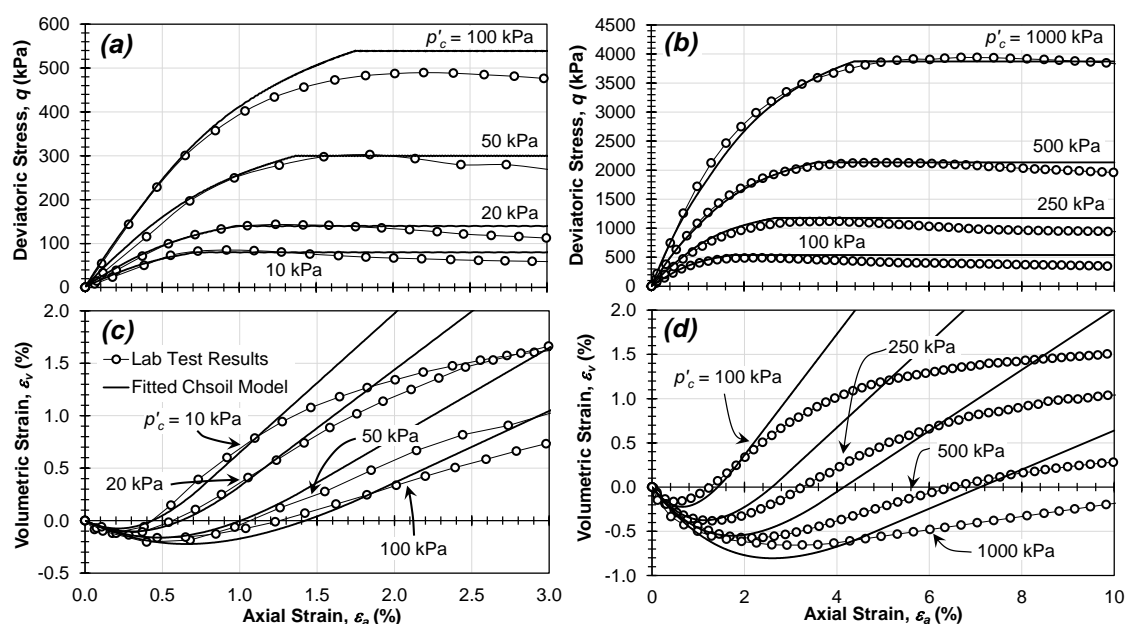


Figure 7.3. Comparison of observed triaxial test data and calibrated *Chsoil* constitutive model responses: (a) and (b) variation of deviatoric stress with axial strain, and (c) and (d) variation of volumetric strain with axial strain.

Generally, plane strain friction angles in uniform granular soils are considered to be 10-15% greater than those measured in AICD stress paths (Lee, 1970). However, pseudo-elastic stiffnesses exhibited increases ranging from 33% (Lee 1970) to 225% (Hatami and Bathurst 2005). Additional work conducted by Strahler et al. (2015) suggests that the stiffness of well-graded granular soils is 15 to 20% greater than that measured in uniform soils. Given

the high quality fill and stiff nature of the West MSE wall, the AICD E_{ref} (=16.0 MPa) was increased by 225% and 15% to account for plane strain stress path and gradational effects to represent a dense plane strain stiffness $E_{ref} = 41.8$ MPa for use in model simulations discussed in later sections.

Construction specifications for the West MSE wall required that compaction equipment was restricted to hand operated equipment within approximately 1.5 m of the wall face to minimize excessive facing displacements (Stuedlein et al. 2010a). The zone behind the panel facing was therefore modeled as a medium dense soil. AICD tests conducted on Kanaskat gravel by Walters (2013) showed that E_{ref} reduces up to 45% when relative density reduces. Hatami and Bathurst (2005) noted that reductions in the Young's modulus were on the order of 45% in the zone behind the wall facing of MSE walls. This information was used to guide the reduction of E_{ref} for the medium dense soil zones, which was taken as 55% of that for the compacted. Strength and dilatancy parameters for the medium dense soil near the wall facing panels were set to those reported by Walters (2013) for Kanaskat gravel at a relative density of 35% and are presented in Table 7.2.

7.4.5. PANEL BEAM ELEMENTS AND BEARING PAD RESPONSE

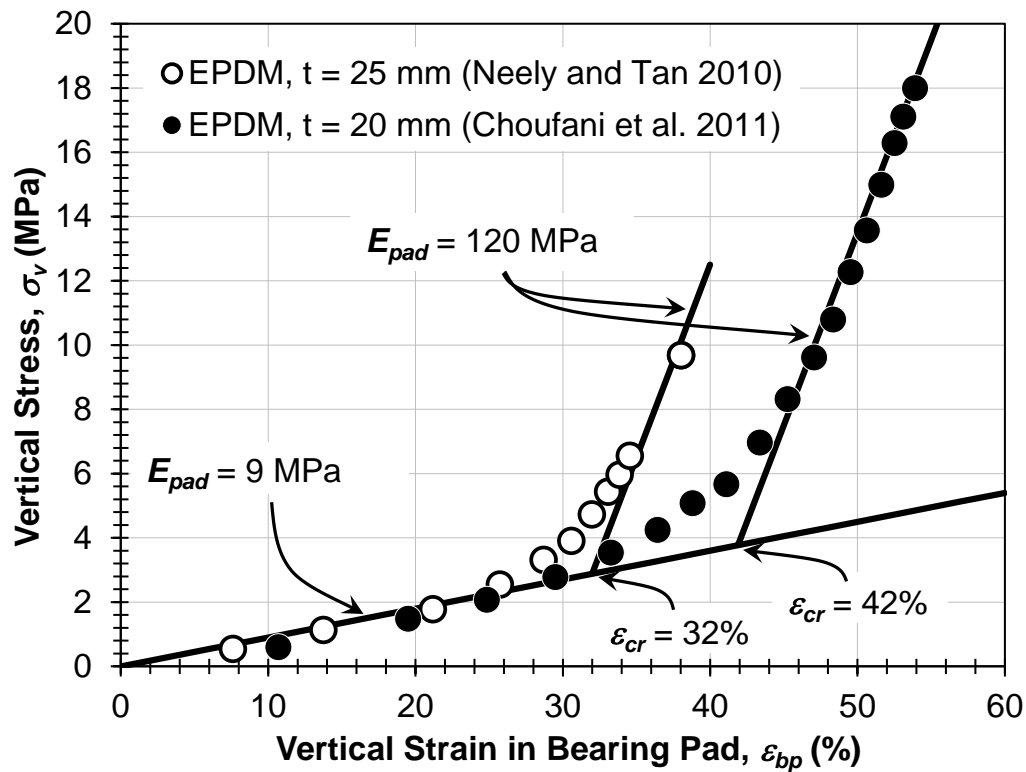
The 1.56 m tall cruciform concrete facing panels were simulated using seven elastic beam elements with properties presented in Table 7.3. Large vertical stresses at the base of the wall prompted designers to increase panel thickness from 152 to 178 mm in the first tier. Facing panels were separated from one another at horizontal joints by elastomeric bearing pads, which provided a compressible joint that can mitigate the potential for spalling and cracking of the panels (Damians et al. 2012). Correspondingly, the magnitude of the down

drag forces, wall deformations, and reinforcement strains depend on the compressibility of the bearing pads and the panel facing (Neely and Tan 2010, Damians et al. 2012). Damians et al. (2012) showed that the magnitude of reinforcement loads was not significantly influenced by the bearing pad stiffness, however local changes in the distribution of loads occurred, indicating the need to incorporate this behavior into the present study. The compressive behavior of bearing pads is nonlinear, exhibiting a convex hardening stress-strain relationship (Figure 7.4) that depends on the geometrical shape of the bearing pad and the stiffness of the base material (Neely and Tan 2010, Choufani et al. 2011, Damians et al. 2012). The bearing pads used in the construction of the West MSE wall were made of ethylene propylene dene monomer (EPDM), with thicknesses of 20 mm in Tiers 2 through 4 and 25 mm in Tier 1.

Damians et al. (2012) approximated actual EPDM bearing pad behavior using an average secant stiffness at 40 and 50 percent shear strain in their numerical analyses. However, increases and reductions in the bearing pad stiffness were not captured at higher and lower confining stresses, respectively. A more accurate approach proposed by Damians et al. (2014), uses a critical strain magnitude, ε_{cr} , to denote a transition in an assumed bilinear relationship. This approach was used here to capture the nonlinear response for the bearing representative laboratory stress-strain responses for 20 and 25 mm thick bearing pads, reported by Neely and Tan (2010) and Choufani et al. (2011), and indicated that a bilinear stress-strain relationship suitably captures the observed response for the range in strains anticipated.

Table 7.3. Summary of beam element modelling parameters.

Wall Tier	1	2 - 4
Facing Panel Thickness (mm)	178	140
Moment of Inertia, I_{beam} (m ⁴)	4.68e-4	2.27e-4
Area of Beam, A_{beam} (m ²)	0.178	0.140
Modulus of Beam, E_{beam} (MPa)	29,000	
Bearing Pad Thickness, t (mm)	25	20
Bearing Pad Critical Strain, ε_{cr} (%)	42	32
	$\varepsilon < \varepsilon_{cr}$	$\varepsilon \geq \varepsilon_{cr}$
Modulus of Pad, E_{pad} (MPa)	9	120
Pad Moment of Inertia, I_{pad} (m ⁴)	2.78E-06	
Area of Pad, A_{pad} (m ²)	0.02	

**Figure 7.4. Comparison of the fitted, bilinear bearing pad stress-strain responses to data reported by Neely and Tan (2010) and Choufani et al. (2011).**

The magnitudes of the critical strains used here were 32 and 42 percent, for the thickness of 25 and 20 mm, respectively. The bearing pad was modeled using single beam elements connected through hinges with zero rotational stiffness (Figure 7.2 inset). Scripts written using FISH codes, provided in Appendix F, were created to update the bearing pad stiffness every step of the simulation. Lateral displacements in the upper and lower nodes of the bearing pads were slaved to the corresponding, coincident wall panel nodes to prevent excessive lateral deformations at the connection. The bearing pad element parameters are summarized in Table 7.3.

7.4.6. CONCRETE-SOIL INTERFACE

Concrete-soil interfaces, such as those between the reinforced soil and the concrete wall facing panels, were simulated using the standard interface element. The element is formulated with linear-elastic shear and normal springs, tensile limits for simulation of gapping, and a shear slider to model an ultimate shearing resistance. The maximum shear resistance is defined using the Mohr-Coulomb failure criterion. Results from large-scale direct shear tests on fine to medium silica sand by Gomez et al. (2008) were used as a guide for the calibration of the soil-concrete interface model. The poorly-graded silica sand used by Gomez et al. (2008) had a d_{50} , of 0.55 mm, C_u , value of 1.8, and $\gamma_{d,max}$, equal to 17.5 kN/m³. Results from three triaxial tests on the silica sand compacted to a relative density of 92% at effective confining stresses of $15 < \sigma'_3 < 274$ kPa indicated that E_{ref} and m for use in Equation (3) of the uniform sand were 1.4 MPa and 0.63, respectively.

Peak triaxial friction angles for the uniform sand can be represented by Eqn. (2) where ϕ'_0 and $\Delta\phi'$ are 43.8 and 3.2 degrees, respectively, whereas the peak and residual concrete-

soil interface friction angles of 31 and 28 degrees, respectively, were reported by Gomez et al. (2008). Prior to the calibration of the interface element for Kanaskat gravel, a numerical model was required to show that the interface tests reported by Gomez et al. (2008) could be sufficiently reproduced. The numerical direct interface shear tests were simulated by imposing 25 mm of displacement and compared to the reported data as shown in Figure 7.5. Changes in the normal stiffness parameter, k_n , were found to have little influence on interface behavior and set equal to $1.0E^9$ kPa/m. This value is sufficiently large enough to prevent nodes from displacing through the interface. The shear stiffness, k_s , was varied as a function of confining stress and the behavior over the pressure range investigated can adequately be captured the observed interface shear response by a linear relationship, given by:

$$k_s = 1348 + 306 \left(\frac{\sigma'_n}{P_{ref}} \right) \quad (7.5)$$

where σ'_n is the effective normal stress acting on the interface. The reported interface friction, δ_i , and dilation angles, ξ_i , of 31 and 28 degrees, respectively, reported by Gomez et al. (2008) were found to adequately capture the peak shear stresses over the range of pressures reported, however, the interface element was not able to accurately represent the nonlinear, pre-failure shear stress and volumetric strains.

The interface model parameters were scaled to account for gradational differences between the Kanaskat gravel and the silica sand by determining the efficiency, e_{int} , of the concrete-silica sand interface. Interface efficiency is defined as the ratio of the interface parameter over the plane strain stress path parameter (e.g. $e_{int,\phi} = \delta'_i / \phi'_{ps}$). Plane strain friction angles for the concrete silica sand were established increasing triaxial friction angles

by 20%, consistent with plane strain tests on uniform sands by Marachi et al. (1981). Interface efficiencies based on Young's modulus, peak frictional, and peak dilational responses were 116%, 59%, and 16%, respectively. The concrete-Kanaskat gravel interface response was computed by multiplying the measured plane strain soil parameters by corresponding efficiencies. The resulting model parameters for the panel-soil interface are provided in Table 7.4. Use of FISH scripts allowed the pressure-dependent interface model to update k_s , δ'_i , and ξ_i at each step of simulation.

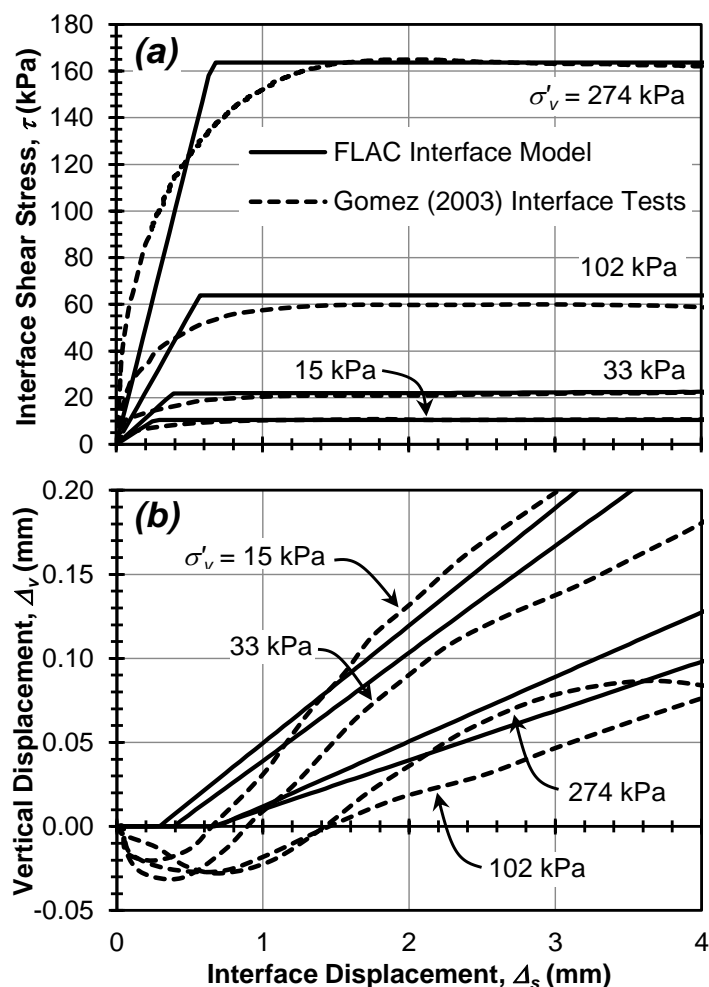


Figure 7.5. Comparison of sand-concrete interface response reported by Gomez to calibrated interface model used in the numerical simulations: (a) variation of shear stress with interface displacement, and (b) variation of vertical displacement with interface displacement (Note: $k_n = 1000$ MN/m/m).

Table 7.4. Summary of calibrated interface modelling parameters.

Interface Parameter	Density Sand (Gomez 2006)	Kanaskat Gravel
Ref. Interface Friction Angle, $\delta_{i,0}$ (deg)	31	36.3
Delta Interface Friction Angle, $\Delta\delta_i$	2.6	12
Ref. Interface Dilatation Angle, $\xi_{i,0}$ (deg)	2.2	1.9
Delta Interface Dilatation Angle, $\Delta\xi_i$	2.2	1.6

7.4.7. SOIL-REINFORCEMENT STRIP INTERFACE AND SPACING EFFECTS

The ribbed steel reinforcement strips were modeled using the strip element available in FLAC because it was specifically developed to simulate the behavior of thin reinforcement strips (Itasca 2011), and as such it does not sustain bending forces and the soil continuum can flow around the strip. The strip element simulates the pre-failure response using a shear stiffness parameter, $k_{s,strip}$, similar to the generic interface element. The modeling of the pullout response of reinforcement strips should be based on soil- and reinforcement-specific pullout tests, and when done, the strips are usually tested and simulated as isolated elements free from interaction effects from nearby elements. However, in tall walls, the spacing of reinforcement strips may become so close as to produce frictional interference (Strahler et al. 2016). Accordingly, the strip elements used in this study were calibrated against single and multi-strip pullout test results in Kanaskat gravel reported by Strahler et al. (2016). Representative single, isolated pullout test results at a vertical effective stress, σ'_v , of 50, 100, and 200 kPa provided in Figure 7.6 indicate that the interface resistance is nonlinear. To sufficiently capture the soil-reinforcement strip response, the shear stiffness for isolated strips, $k_{s,iso}$, was modified to establish the tri-linear response shown in Figure 7.6. At

accumulated interface shear displacements, u_{shear} , less than 0.3 mm, the isolated interface stiffness parameter, $k_{s,iso} = 29$ MN/m/m to capture the initial response. At larger shear displacements, ($u_{shear} > 0.3$ mm), the pullout response was modeled using a pressure-dependent power law, provided in Table 7.5, to replicate the pullout response for isolated strips reported by Strahler et al. (2016).

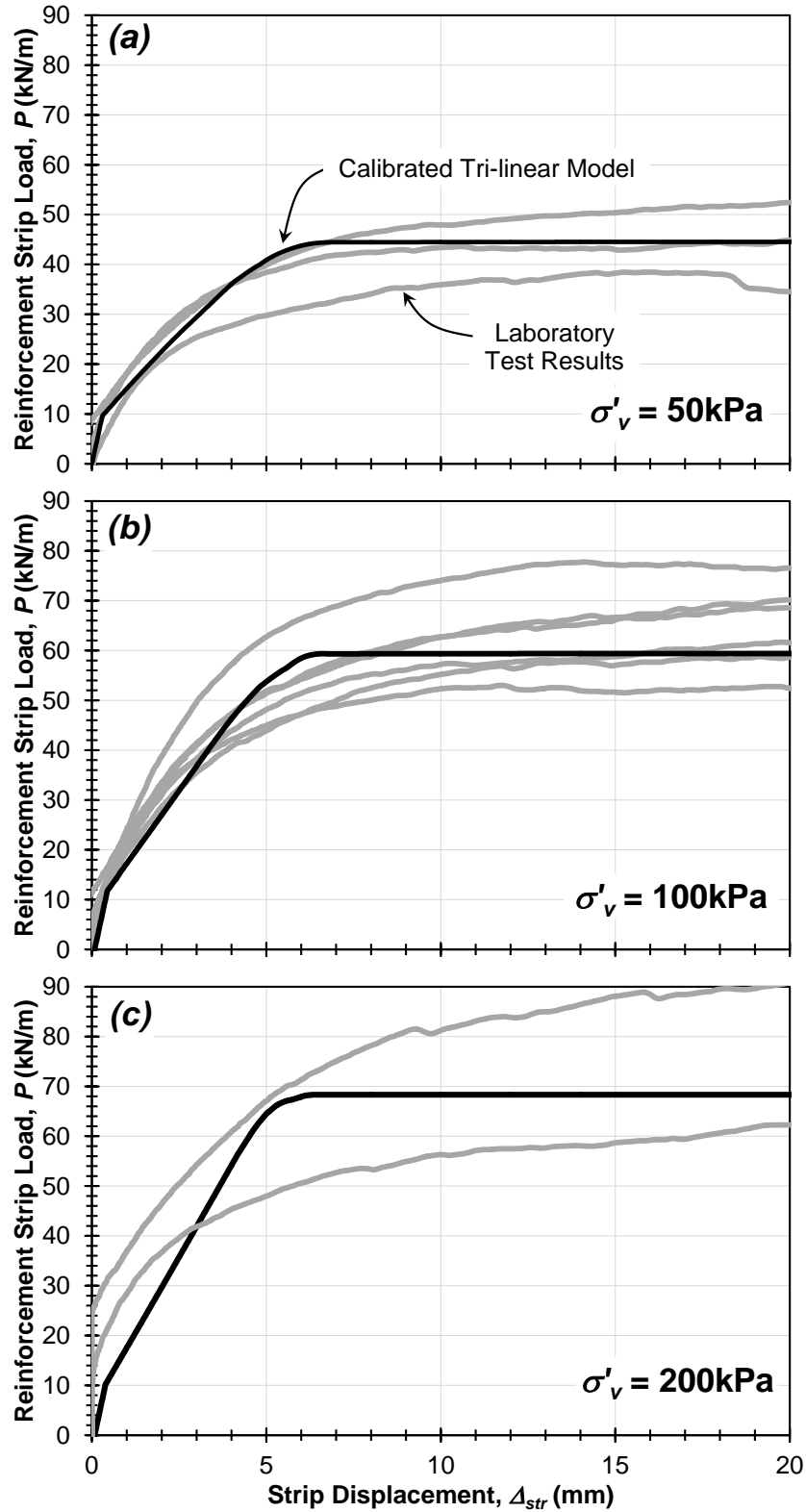


Figure 7.6. Comparison of calibrated and measured pullout resistance of ribbed steel strips in dense Kanaskat gravel at $\sigma'_v =$ (a) 50 kPa, (b) 100 kPa, and (c) 200 kPa.

Table 7.5. Summary of FLAC strip interface element properties.

Accumulated Shear Displacement, u_{shear} (mm)	$\underline{u_{shear} < 0.3}$	$\underline{u_{shear} \geq 0.3}$
Isolated Shear Stiffness Parameter, $k_{s,iso}$ (MN/m/m)	29.0	$6.1 \left(\frac{\sigma'_n}{p_{ref}} \right)^{0.39}$
Strip Confinement Condition	<u>Isolated</u>	<u>Confined</u>
Ref. Unit Frictional Res., f_0^*	6.67	8.30
Trans. Conf. Stress, σ'_t (kPa)	250	330
Ref. Unit Frictional Res., f_l^*	$\tan(\phi'_{cv}) = 0.84$	

An experimental program of multi-strip pullout tests results reported by Strahler et al. (2016) indicated that increased confinement at smaller spacing resulted in decreased interface stiffness and increased ultimate pullout resistance. Efforts to incorporate changes in the soil-reinforcement interaction stemming from closely-spaced reinforcement were incorporated using a stiffness ratio, k_{rat} , defined as the ratio of the confined strip stiffness, $k_{s,conf}$, to $k_{s,iso}$ that is smaller than or equal to one. Based on the experimental work reported by Strahler et al. (2016), the effect of confinement on reduced interface shear stiffness was incorporated into the numerical model using the product of $k_{s,iso}$ and the k_{rat} given by the trend in the stiffness ratio:

$$k_{rat} = 2.1(S_{local})^{-0.12} \leq 1 \quad (7.6)$$

The strip element in FLAC is capable of modeling pullout and tensile rupture of the strip through the specification of unit frictional resistances, f^* , and a tensile failure strain, ε_f , respectively. The tensile failure strain was established based on tensile tests of coupons machined from the reinforcement strips used in the West MSE wall and conducted by Walters (2013); ε_f was determined equal to 2.75%. The unit frictional resistance has been

shown to be dependent on pressure (Schlosser and Elias 1978) and local stiffness (Strahler et al. 2016), and this dependency was incorporated into the numerical simulations using a bilinear relationship similar to that specified by AASHTO (2010). The f^* model is greatest at the top of the wall, f^*_{o} , and reduces linearly to a transitional confining stress, σ'_t , where f^* becomes independent of stress and equal to f^*_l . An extensive laboratory program to investigate the influence of reinforcement spacing on the pullout response conducted by Strahler et al. (2016) indicated that the available resistance increased with increases in S_{local} up to 1,000 MPa. However, at $S_{local} > 1,000$ MPa, no additional increase was observed. Therefore, the numerical models performed in this study incorporated reinforcement spacing effects by selecting the corresponding isolated and confined, calibrated f^* models developed by Strahler et al. (2016) and quantified in Table 7.5 as a function of S_{local} .

7.5 MODEL VALIDATION AND PARAMETRIC EVALUATION OF THE WEST MSE WALL

A parametric study was conducted using the various calibrated wall elements to assess the influence of the retained and reinforced fill soil parameters, applied compaction stresses, and reinforcement strip interface stiffness on the simulated wall performance. A baseline model was established with dense soil parameters and individual factors were adjusted to determine the impact on wall response. Table 7.6 summarizes the individual factors, defined previously in Tables 7.1 through 7.5, that were investigated in this parametric study. Results from the parametric study are compared against measurements of lateral and vertical displacements and axial reinforcement strains at the end-of-construction (EOC) to validate

the accuracy of the numerical model and inform a subsequent parametric study conducted to evaluate the performance associated with variations in selected design variables.

Table 7.6. Element-level parametric study of the simulated West MSE wall performance. Note: baseline model parameters indicated by bold text.

	Compaction Stress σ'_{com} (kPa)	Reinforcement Strip Interaction Effects	Retained Fill	Reinforced Fill
<i>Condition</i>	0	Confined Strip	Dense Chsoil	Dense Chsoil
<i>evaluated</i>	10	Isolated Strip	M. Dense Chsoil	M. Dense Chsoil
<i>for each</i>	20		Dense Mohr-Coulomb	Loose Chsoil
<i>factor</i>			Loose Chsoil	

7.5.1. MEASURED RESPONSES AND THE BASELINE MODEL

Construction of the West MSE wall occurred over a 13 month period with vertical and horizontal displacements measured at the wall face and inclinometer installations, and reinforcement strains measured at numerous locations and stages of wall construction as described by Stuedlein et al. (2010a). Unfortunately, no measurements of vertical and horizontal displacement in the inclinometer casing were made after the construction of Tier 4. As a result, the lateral, Δ_{in} , and vertical displacements, s_{inc} , measured at the inclinometer installation presented in Figures 7, 8, and 10 correspond to the completion of Tier 4. Figures 7, 8, and 10 also present the lateral panel displacements, Δ_{DMP} , panel settlements, s_{DMP} , and peak axial strip strains, $\varepsilon_{m, str}$, measured at the tallest section of the West MSE wall at EOC. The peak lateral panel displacement, $\Delta_{DMP, max}$, measured at EOC was approximately 90 mm (Figure 7.7a) and occurred around the mid-height of the wall (El. = 93 m). At lower elevations, Δ_{DMP} were relatively independent of wall height whereas reductions were observed at elevations greater than 93 m. In addition to wall face displacements, strains in

the reinforcements were integrated and added to lateral displacements at the base, following the method outlined by Stuedlein et al. (2007 and 2010a), producing an estimate of wall face displacement, Δ_{str} at EOC. Lateral displacements estimated by this approach are smaller than those measured at the facing and exhibit much less variation.

The baseline model was developed using the plane strain soil parameters for the reinforced and retained embankment fills as presented in Table 7.2; this corresponds to the “dense” parametric condition as summarized in Table 7.6. Generally, the baseline model simulation produced smaller horizontal and vertical facing displacements, on the order of 63 and 70 mm, respectively, than those measured at EOC (Figures 7a and 7b), but generally had a similar distribution. The departure in agreement was not observed at the simulated inclinometer location, where s_{in} and Δ_{inc} were over- and under-estimated by only 33 and 5% on average, respectively (Figures 7d and 7e). Peak axial strains predicted by the baseline model, smoothed over a 1.5 m averaging window, exhibited a uniform distribution similar to that measured but were 7% greater on average with the maximum $\varepsilon_{m, str}$ occurring at an elevation of 89 m. In general, the baseline model over-estimates the measured strains and under-estimates the lateral and vertical wall face displacements. Efforts to adjust specific element parameters and create a model that more accurately represents measured responses are discussed subsequently.

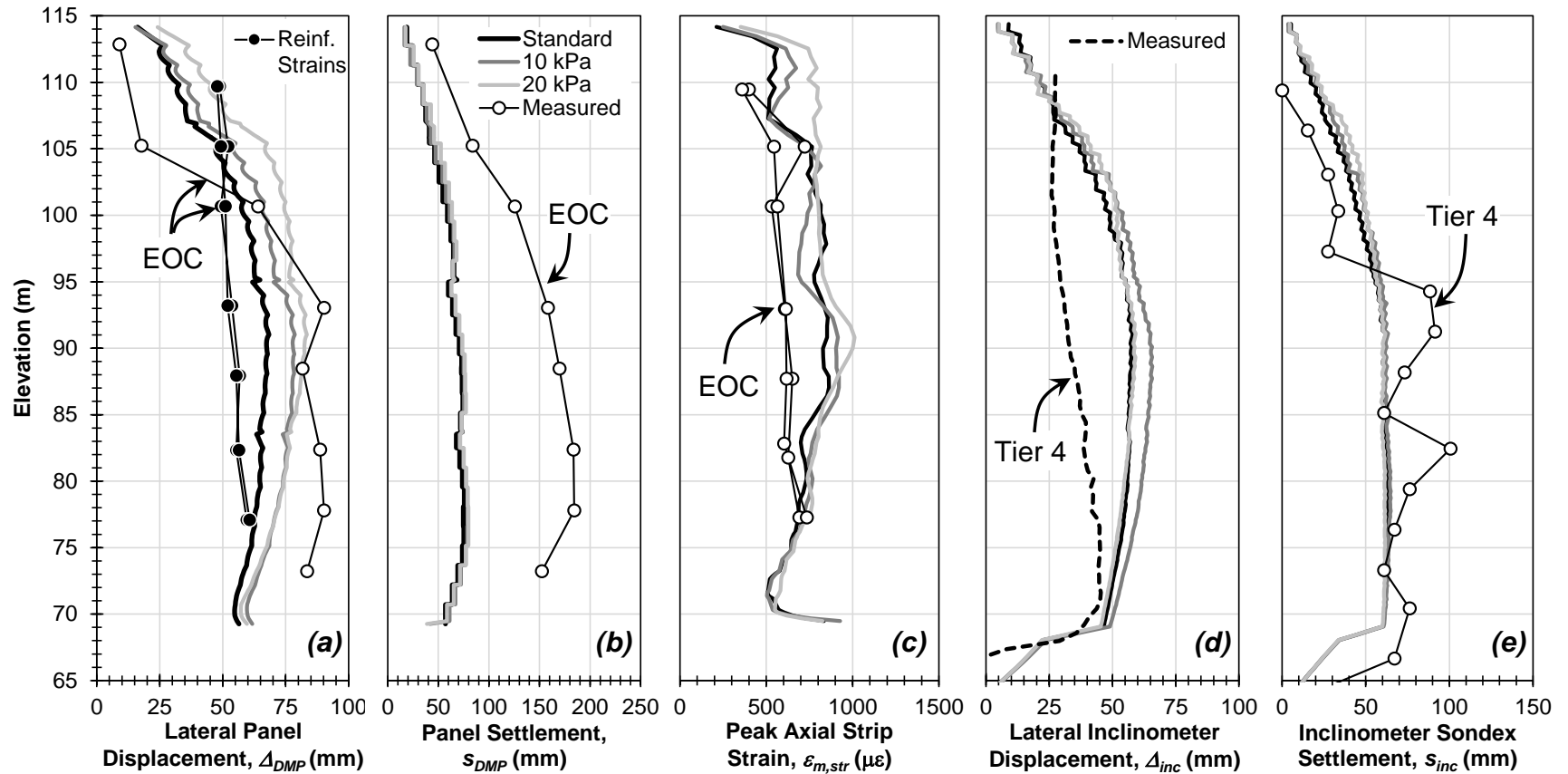


Figure 7.7. Influence of compaction stresses on (a) lateral and (b) vertical panel displacement, (c) peak axial strip strains measured at EOC, (d) lateral and (e) vertical inclinometer displacement measured at completion of Tier 4.

7.5.2. INFLUENCE OF COMPACTION STRESSES

Compaction equipment used to construct MSE walls are considered to increase vertical stresses in the reinforced soil mass, increasing axial strains, lateral, and vertical displacements during erection (Ehrlich and Mitchell 1994, Ehrlich and Mitchell 1995, Ehrlich et al. 2012, and Liu 2014). They are often not considered in numerical MSE wall models, however, there is a small body of work that suggests they have an influence on lateral displacements of geo-synthetic reinforced walls (Hatami and Bathurst 2005, 2006; Huang et al 2009, Liu 2014). Compaction stresses of 10 and 20 kPa were evaluated numerically by using uniform vertical surcharge stresses at each lift. These were selected based on precedent established by Hatami and Bathurst (2005), among others, who reported that a uniform surcharge on the order of 8 kPa was sufficient to represent stresses induced by vibratory compactors. Compaction stresses were not applied within 1.5 meters of the wall face, consistent with construction specifications.

A compaction stress of 10 kPa increased s_{DMP} and s_{in} by 15% (Figures 7a and 7d) while only increasing Δ_{DMP} and s_{in} by 5%, on average relative to the baseline model (Figures 7b and 7e), with little to no change in the overall distribution of Δ_{DMP} . However, when compaction stresses were increased to 20 kPa, Δ_{DMP} increased to 21% greater than the baseline model with greater displacements developing in the upper half of the wall. Peak axial strains in the reinforcement strips were also increased by 11 and 20% on average relative to the baseline model with compaction stresses of 10 and 20 kPa, respectively. Increases in peak axial strains in the 20 kPa simulation were focused in the upper half of the wall, similar to the lateral wall face displacement distribution. Relative to the baseline

model, the incorporation of 10 kPa in compaction stresses appears to produce the most accurate response in Δ_{DMP} , though at the expense of accuracy in Δ_{inc} and $\varepsilon_{m,str}$.

7.5.3. INFLUENCE OF RETAINED EMBANKMENT STIFFNESS

The stiffness of the retained soil has been shown to influence the general deformed shape of the reinforced soil mass (e.g. Boyle 1995, Liu and Yang 2015). Reductions in the retained soil stiffness are considered to increase horizontal pressures at the back of the reinforced soil mass and subsequently increase lateral displacements. To evaluate the influence of retained soil stiffness on the baseline model, models with loose, medium dense, and dense embankment fills were simulated. A loose retained fill E_{ref} of 10 MPa presented in Table 7.2 was selected based on plane strain stiffnesses reported by Strahler et al. (2016a). Changes in simulated wall response stemming from variations in the retained embankment stiffness, presented in Figure 7.8, indicate that vertical displacements are generally independent of retained fill stiffness (Figure 7.8b and 8e) with relatively good agreement between measured and simulated s_{inc} . However, reductions in the retained fill stiffness of 75% (i.e., the “loose” condition) resulted in increases in the simulated Δ_{DMP} and Δ_{inc} on the order of 50% over the baseline. When the retained fill stiffness was reduced by 62% (to model the “medium dense” condition), Δ_{DMP} , Δ_{inc} , and $\varepsilon_{m,str}$ increased 15% on average, as compared to the baseline. In order to compare the effect of constitutive response of the retained fill on wall performance, a simulation was conducted using an elasto-plastic Mohr-Coulomb constitutive model.

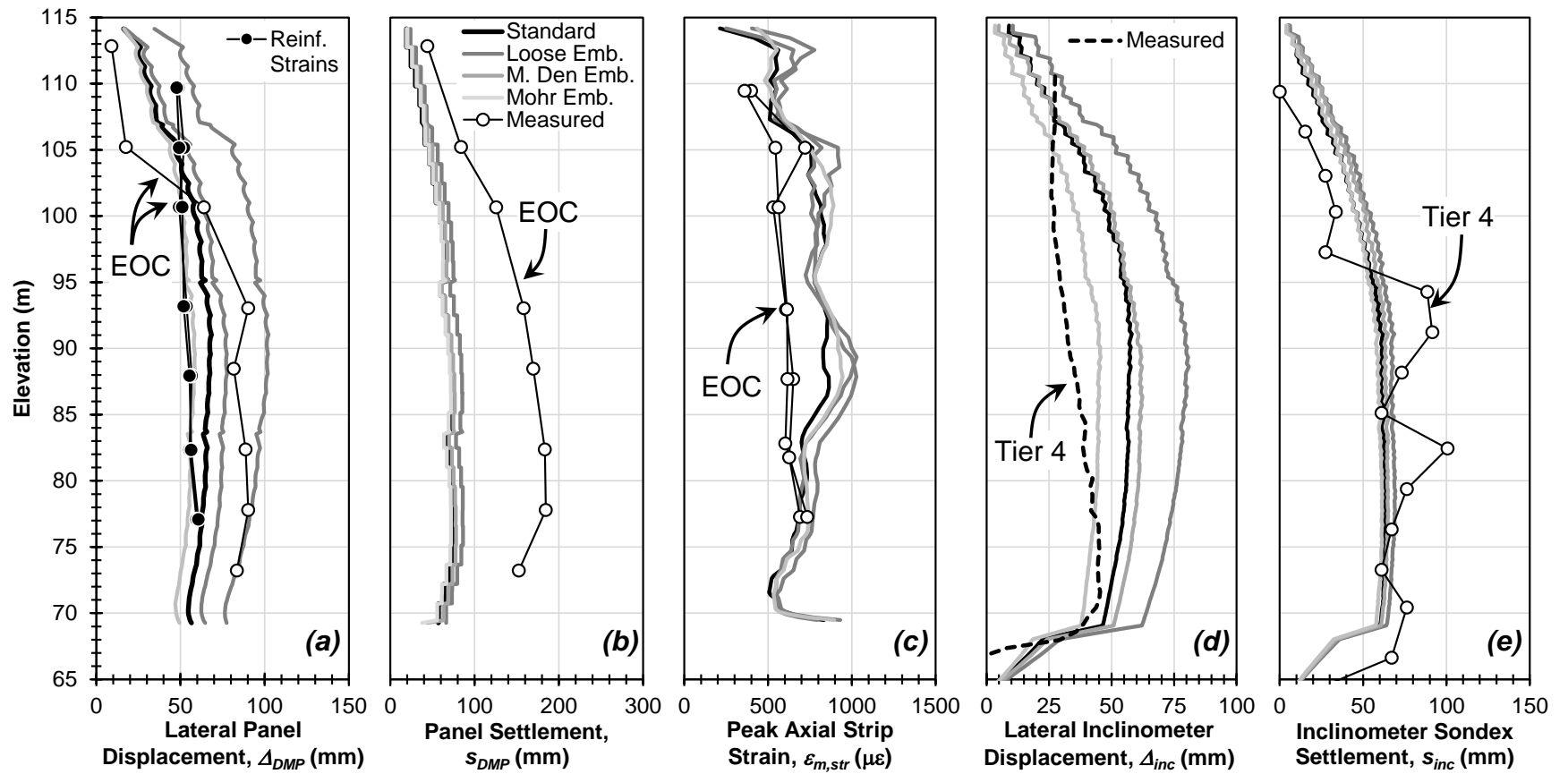


Figure 7.8. Influence of retained embankment stiffness on (a) lateral and (b) vertical panel displacement, (c) peak axial strip strains measured at EOC, (d) lateral and (e) vertical inclinometer displacement measured at completion of Tier 4.

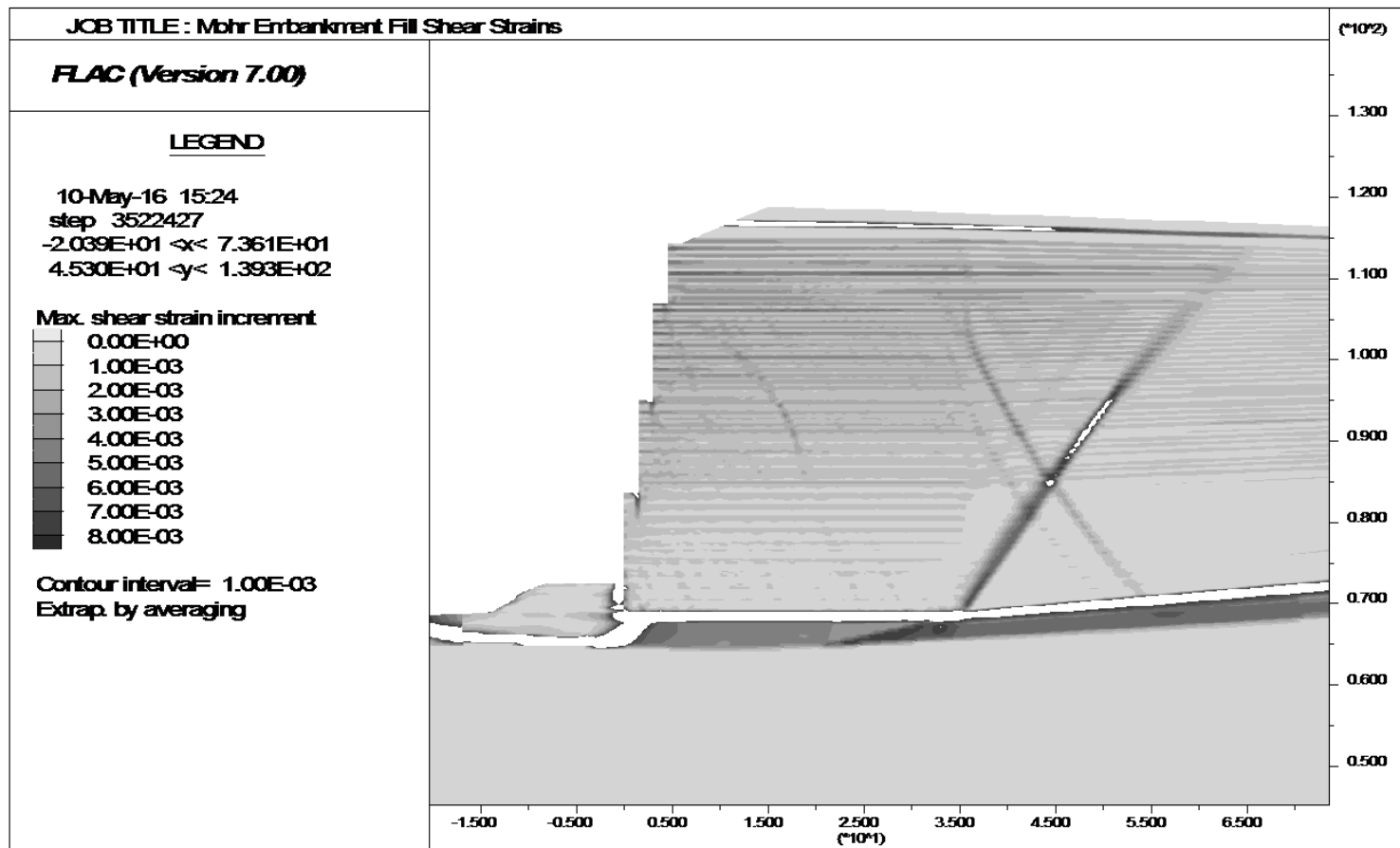


Figure 7.9. Accumulated shear strain increments at EOC in the dense Mohr embankment fill numerical model.

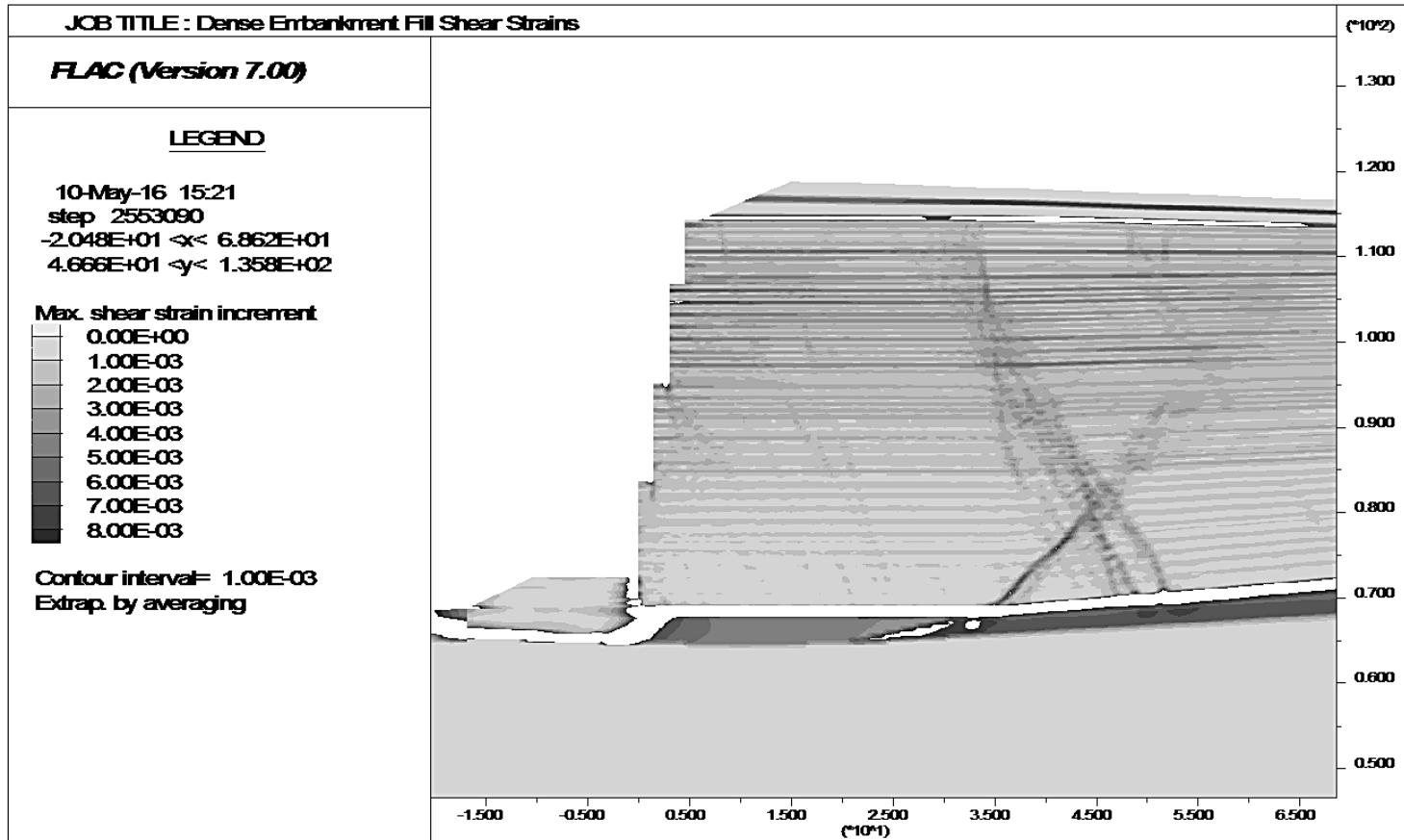


Figure 7.10. Accumulated shear strain increments at EOC in the dense *Chsoil* embankment fill numerical model.

Strength and stiffness parameters in the Mohr-Coulomb model are presented in Table 1 and were selected to represent a very stiff embankment. Figure 8 indicates that although there are smaller lateral displacements resulting from the elasto-plastic constitutive model, there is little discernible difference in the wall performance. However, Figure 9 suggests that the use of the elasto-plastic Mohr-Coulomb model will result in the development of two distinct, conjugate localized zones of accumulated shear strain. Similar zones are produced in the *Chsoil* model (Figure 10), however, the accumulated shear strains are dispersed over a larger area and are approximately 20 to 40% smaller in the upper half of the wall. As a result, displacements, stresses, and strains are more evenly distributed in the retained embankment and distinct, localized wedge shaped regions of shearing strains did not form. The use of the *Chsoil* model is therefore preferred for modeling the retained fill.

7.5.4. INFLUENCE OF REINFORCED FILL AND STRIP INTERFACE STIFFNESS

It is apparent from the previous discussion that applied stresses have a significant influence on the behavior of the reinforced fill mass, however, it has also been shown that its stiffness also impacts its response (Boyle 1995, Liu 2014). Increases in the reinforcement fill stiffness are expected to reduce strains in the reinforcement and lateral displacements. To evaluate the influence of the reinforced fill stiffness on the baseline model, the wall construction was simulated using stiffness that represent the dense, medium dense, and loose states in the same manner as the retained fill (Table 6). The wall performance presented in Figure 11 indicate that reductions in the reinforced fill modulus generally produce a softer response, with increased peak axial reinforcement strains, lateral, and vertical displacements. Lateral displacements (Δ_{DMP} and Δ_{inc}) and settlements (y_{DMP} and y_{inc}) increased by as much

as 57 and 81%, respectively, over the baseline model when E_{ref} was reduced from 41.8 to 10.0 MPa (i.e. "loose condition). The largest lateral displacements and peak axial strains occurred at its mid-height and the distribution as expected from observations of the performance of large fills (Charles 2008)

Simulated wall displacements are much less than predictions based on common methods (Christopher et al. 1990a, Christopher et al. 1990b) which are on the order of 780 mm and almost 9 greater than observed. The back-calculated shear modulus based on these predicted displacements, assuming a purely elastic body following Boyle (1995) vary depending on the retained fill stiffness but ranged from 4.5 and 7.0 MPa for inextensible reinforcements. The average composite shear modulus, G_{com} , for the West MSE wall reinforced soil mass was 173 MPa, which is 39 and 24 times stiffer than that back-calculated, respectively. Therefore it is not surprising that simulations incorporating more appropriate stiffness parameters are able to more accurately represent the observed performance. Relative to the baseline model, the medium dense condition appears to produce the most accurate response in Δ_{DMP} and s_{inc} though at the expense of accuracy in Δ_{inc} .

Interestingly, unexpected increases in simulated Δ_{DMP} and $\varepsilon_{m, str}$ occurred in the lower half of the wall when $k_{s, iso}$ was used in the simulation. This likely resulted from the stiffer reinforced mass at the base of the wall that was able to resist translational shear stresses. In effect, the less stiff, confined strip model allows translational shear strains at the base of the wall that counteract horizontal displacements in the reinforced soil mass.

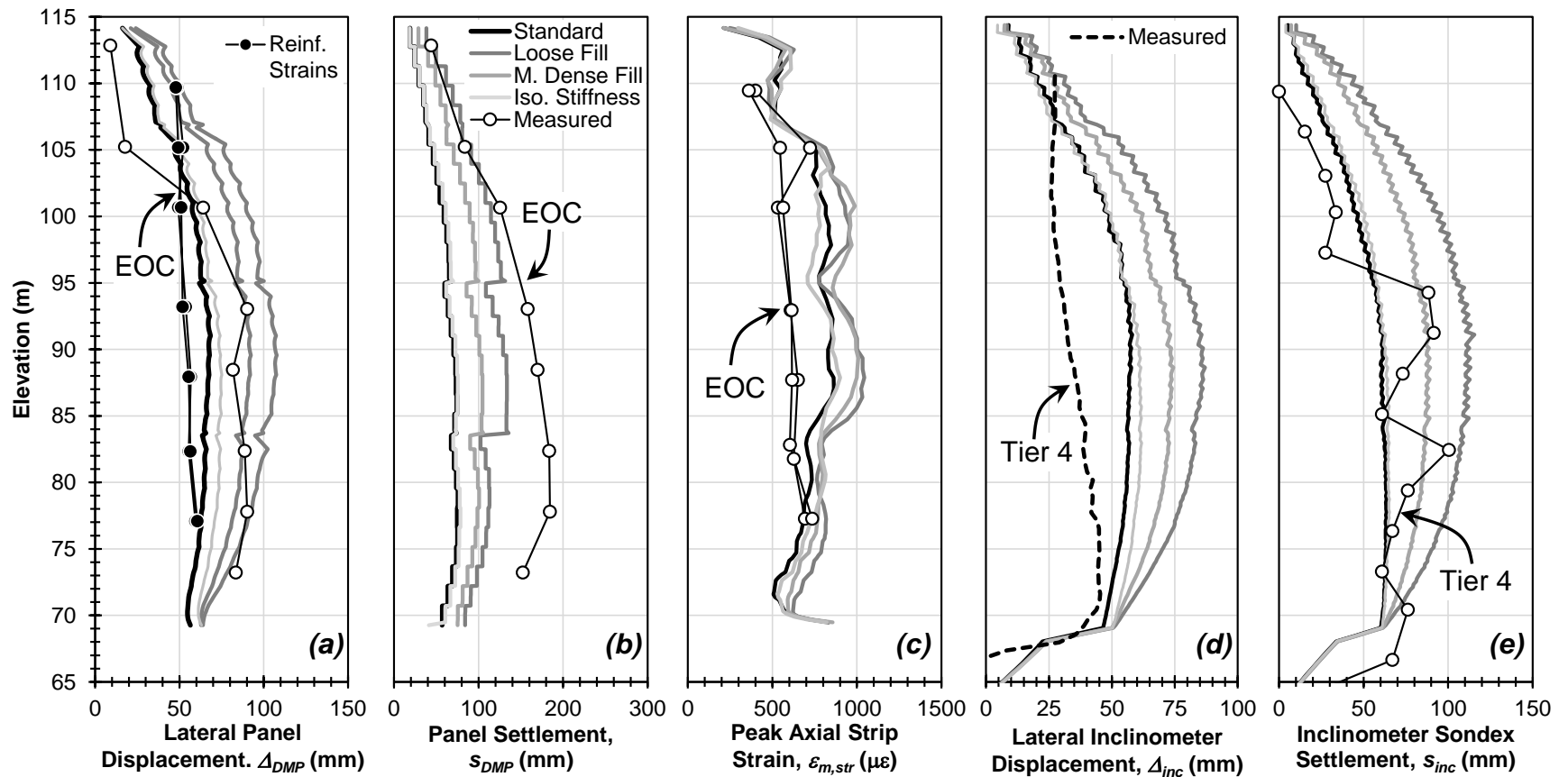


Figure 7.11. Influence of reinforcement interface and reinforced fill stiffness on (a) lateral and (b) vertical panel displacement, (c) peak axial strip strains measured at EOC, (d) lateral and (e) vertical inclinometer displacement measured at completion of Tier 4.

7.5.5. SIMULATION OF CONSTRUCTION SEQUENCING USING THE REPRESENTATIVE MSE WALL MODEL ANALYSIS

In general, the West MSE wall model provided markedly better estimates of wall displacements at EOC than those from current approximation methods. However, the majority of deformations in the reinforced mass develop during wall construction (Hatami and Bathurst 2005) and comparisons between measured and simulated responses at different stages of wall placement will yield a more thorough calibration approach. To assess wall performance during construction, a final representative model was selected based on the previous parametric study. It was found that reinforced and retained fills modelled in the medium dense condition with no compaction stresses, and the confined strip interface stiffness produced the most accurate estimates of wall behavior. The following section compares the representative West MSE wall model at different stages of construction to available measured responses to assess simulation performance.

7.5.5.1. Wall Displacements

Measured and representative model responses at EOC and completion of Tiers 3 and 4 indicated that there is relatively good agreement between s_{inc} , and Δ_{DMP} during wall construction (Figure 12). However, much like the baseline model Δ_{inc} and s_{DMP} are over- and under-estimated, respectively. Some of the discrepancy between measured and simulated Δ_{inc} can be attributed to the rapid construction of the West MSE wall. After completion of Tier 4 approximately 150 days elapsed before placement of the surcharge fill and during this time Δ_{DMP} on the order of 20 mm were observed (Stuedlein et al. 2010a). Therefore, additional movements stemming from creep and stress mobilization were not

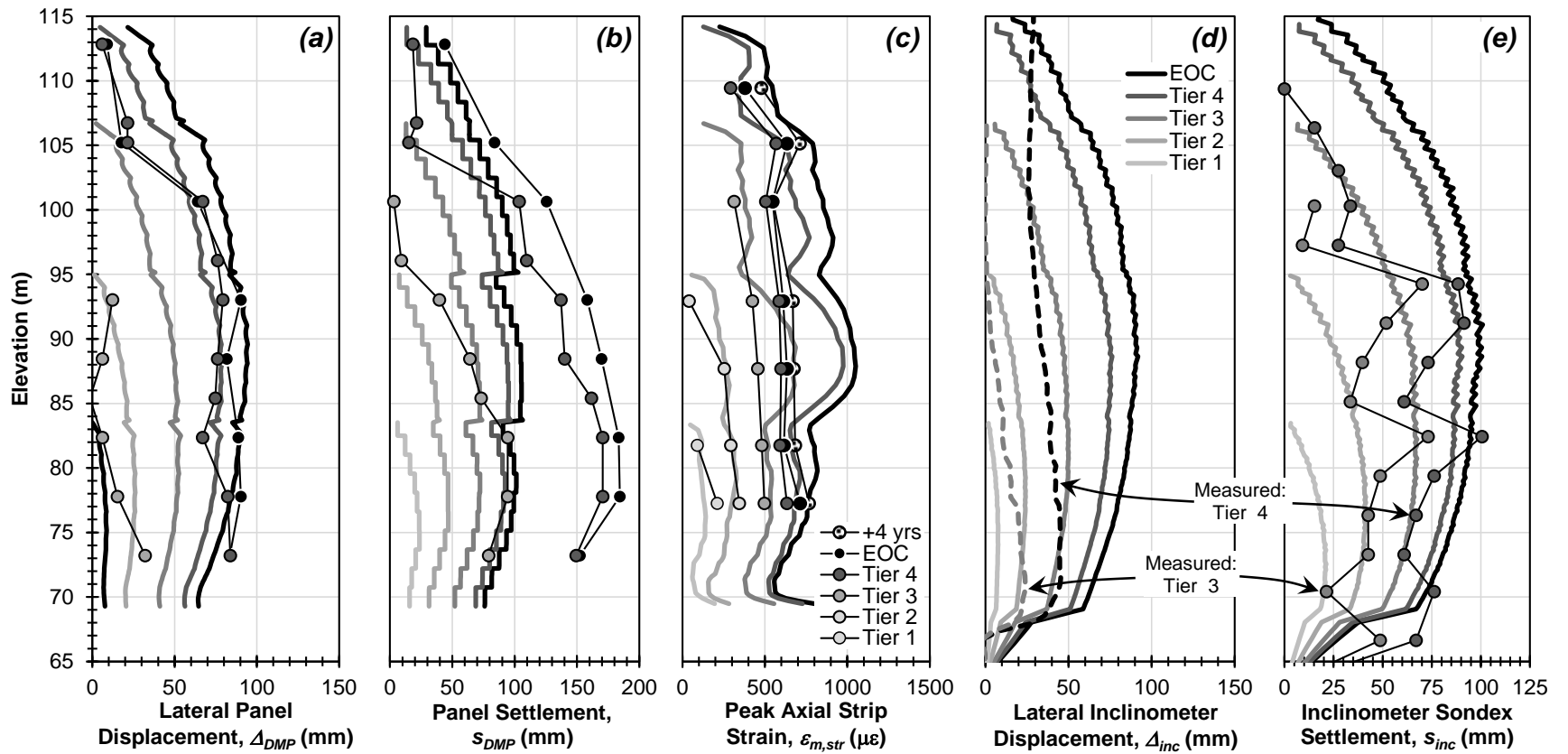


Figure 7.12. Influence of reinforcement interface and reinforced fill stiffness on (a) lateral and (b) vertical panel displacement, (c) peak axial strip strains, (d) lateral and (e) vertical inclinometer displacement measured at various times during construction.

captured in inclinometer measurements taken at completion of Tier 4 as discussed previously. This could explain the relatively good agreement between Δ_{DMP} taken at EOC and Tier 4, and discrepancies between simulated and measured inclinometer responses. Nonetheless, the simulated wall deformations presented in Figures 12(a, b, d, and e) are considered to accurately represent the MSE wall deformation response throughout construction.

7.5.5.2. Reinforcement Strain Distributions

Axial strain distributions measured along the length of reinforcement at EOC and completion of Tiers 1 through 4 are presented in Figure 7.13 and have been averaged at each elevation for clarity. Additional strain gage readings taken approximately 4 years after EOC are also included for comparison, indicating that stress mobilization and creep raised reinforcement strains by 10% on average. Local observed minima stem from increases in the reinforcement cross section at splice plates which resulted in lateral bearing forces at those locations (Stuedlein et al. 2010a, 2012). Reinforcement splices were not included into the numerical model and therefore similar reductions were not observed. Nonetheless, observed strain distributions are fairly uniform with larger strains developing near the wall face. Simulated reinforcement strains exhibited similar uniform distributions with peak responses generally occurring within 10 to 15 m of the wall face. Local deviations in simulated axial strains stem from the modified *Chsoil* constitutive model that increase localized shearing strains and is considered to be the result of the implemented pressure dependent response. Nonetheless, simulated $\varepsilon_{m,str}$ generally occur at locations closer to the wall face than predicted by the FHWA zone of maximum stress approach (Stuedlein et al. 2012) with the exception of Tier 1

where fairly good agreement occurs (Figure 7.13). Peak axial reinforcement strains at each elevation presented in Figure 7.12(c) indicate that the representative model tends to overestimate axial strains by 20 to 25% on average in the later stages of wall construction also noted in Figures 7.13(b) through 13(e). However, exceptional agreement is found between simulated and measured responses during early stages of construction. Axial strains within 2 meters of the wall face exhibit sharp reductions as a result of the looser zone of soil, producing strains at the facing-reinforcement connection similar to those measured in Tiers 1 and 2. At higher elevations (Tiers 3 and 4) strains at the connection are significantly larger than those measured. This behavior is attributed to the linear approach taken to adjust the loose soil parameters where the reference modulus was 55% of the denser soil. At lower confining pressures, differences in the modulus are much less pronounced than at higher confining stresses, resulting in less pronounced reductions in axial strip strain. The larger increase in axial strain at the facing in Figure 7.13(b) is partially attributed to an increase in vertical and lateral pressures stemming from the leveling pad for Tier 1 positioned just above.

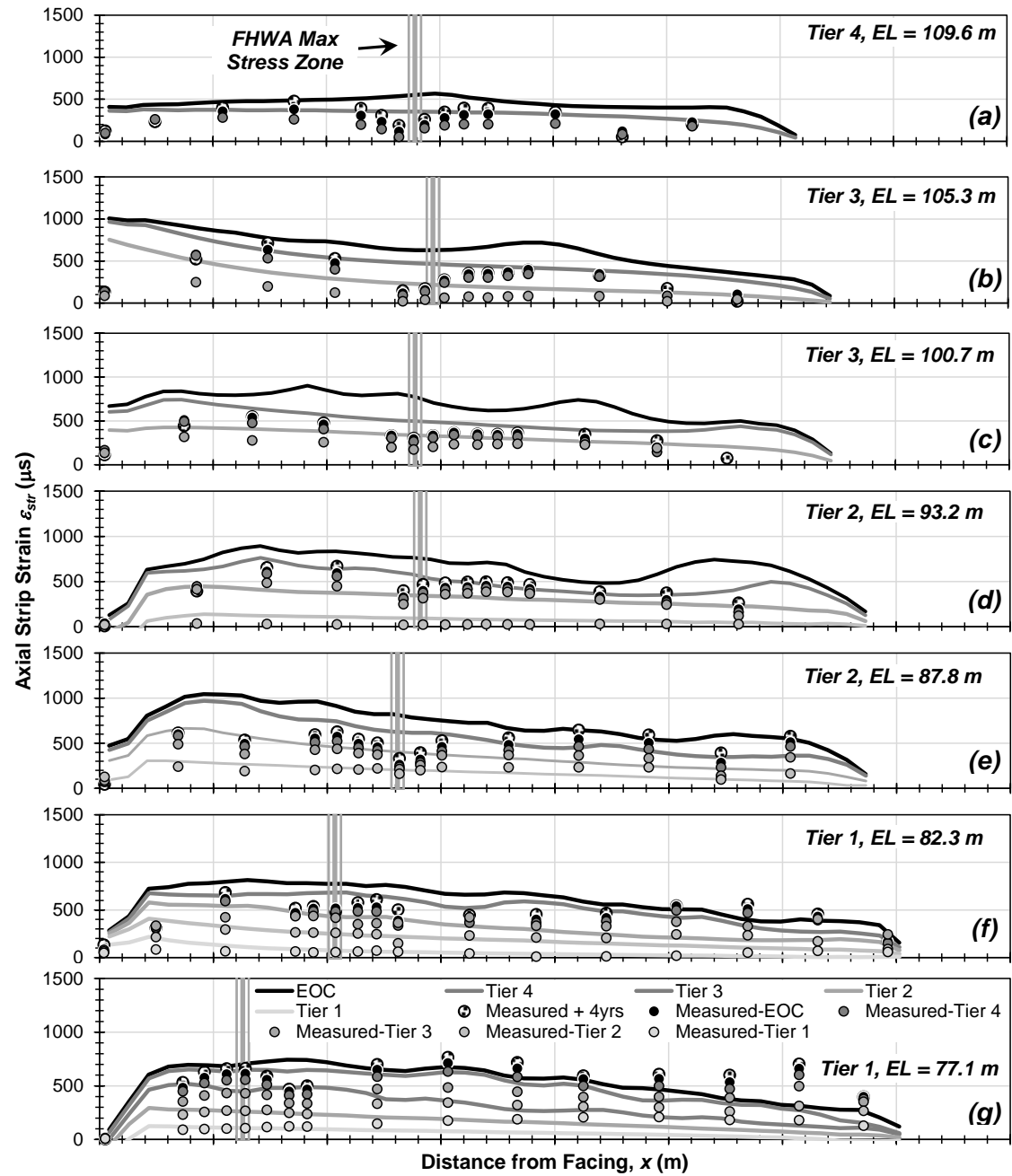


Figure 7.13. Measured and representative axial strain distributions along reinforcements at instrumented elevations (a through g) during completion of different stages of construction.

7.5.5.3. Overturning Stresses

The coherent gravity (Schlosser 1978) and Ehrlich and Mitchell (1994) internal stability design approaches assume that the reinforced soil mass is rigid enough for retained lateral earth pressures to induce vertical stresses that are larger than a geostatic condition. However, inclusion of overturning stresses at the base of the reinforced soil mass has been the focus of some debate. Basal vertical stresses measured in a database of steel and geo-synthetically reinforced MSE walls reported by Allen et al. (2001) are generally 40% less than geostatic conditions immediately behind the wall face, followed by increases to a peak condition 40% greater than geostatic stresses, σ'_{geo} , on average. Vertical stresses then reduce to σ'_{geo} approximately 80% of the reinforcement length behind the wall face. Simulated basal vertical stresses, σ'_{yy} , in the representative West MSE wall during construction presented in Figure 7.14 can be characterized by a similar behavior and have been normalized by geostatic stresses, $\sigma'_{geo} = \gamma z$, where z was taken as the actual height at each point including surcharge. At completion of Tier 1, vertical stresses directly behind the wall face are less than a geostatic condition as a result of down drag forces being transmitted to the front facing and to the leveling pad. At later stages of the construction, subsequent increases in vertical stresses are due to down drag forces induced by leveling pads in Tiers 2 through 4 and soil arching (Damians et al. 2014). Vertical stresses reduce to a geostatic condition approximately 14 m behind the wall face which is consistent with that expected from stage two soil arching (Handy 1985). Reductions in vertical stresses greater than 20 m from the wall face are considered to stem from displacements in the foundation, owing to the non-linear dimensions of the excavated and replaced fill.

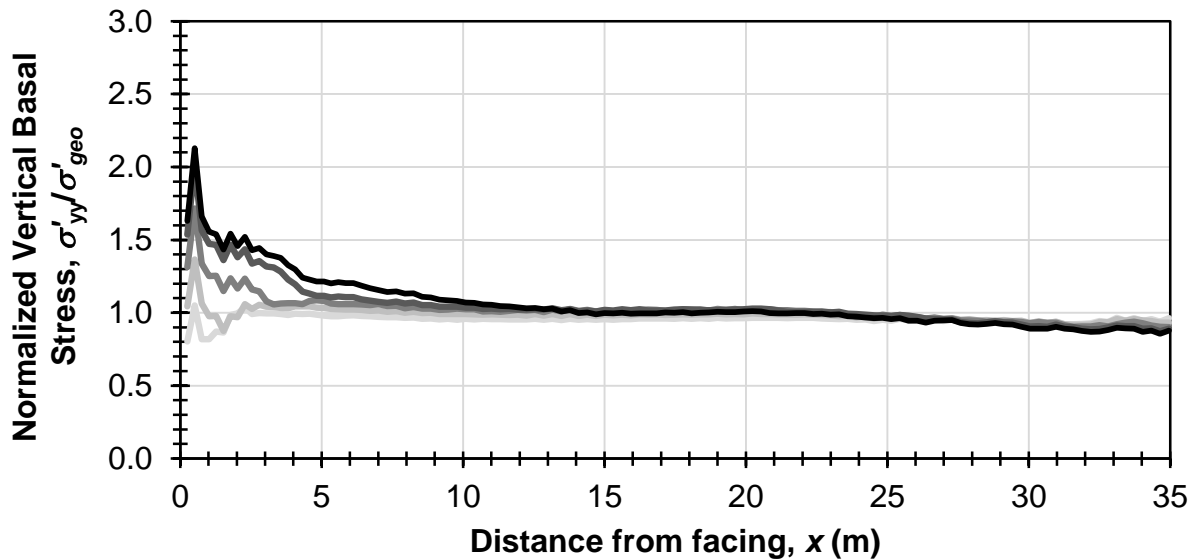


Figure 7.14. Variations in normalized vertical stresses at completion of different stages in the representative West MSE wall model (Note: a smoothing function with 2 m interval was used to reduce scatter).

7.6 GEOMETRIC PARAMETRIC STUDY

Impacts on wall response associated with geometric effects (e.g. number of tiers, tier offsets, and non-uniform reinforcement spacing) are not well understood and current approaches rely on limit equilibrium methods (Leshchinsky and Han 2004, Wright 2005) and numerical simulations of a short 6 m tall reinforced mass (Ho and Rowe 1996). Currently, the FHWA (Elias et al. 2001) specifies that multi-tiered MSE walls with equivalent batter angles, β , less than 70 degrees be designed using limit equilibrium methods. For walls with β greater than 70 degrees, FHWA requires lateral earth pressure approaches for design, even though no fundamental difference has been acknowledged. There are significant differences between assumptions in the two methods (e.g. reinforcement strain distributions, shape and location of failure surface) that have not been validated against working stress behavior of tall MSE walls and could lead to un-conservative estimates of wall response. To evaluate the

assumption of a change in wall behavior at a β of 70 degrees and tier effects on wall response, the geometry of the representative West wall model, discussed previously, was altered to create a generic model where parameters could easily be manipulated. Constitutive element parameters in soil-reinforcement interfaces, the reinforced, and retained soil masses, were not altered, however, the subsurface profile was changed to represent a stiff elastic medium ($G = 1,350$ GPa). Toe surcharge was not included in the simulation and the 0.5% slope in the overburden surcharge was flattened to zero. The generic model was modified to simulate wall heights of 20 and 50 m for a series of tier, offset, and reinforcement configurations outlined in Table 7.7. Up to six tiers with offsets as high as 12% of H representing β ranging from 90 to 59 degrees (presented in Table 7.8) were simulated by changing the geometry of the generic model. Reinforcement lengths were maintained at $0.7H$ in every tier in accordance with AASHTO specifications.

Table 7.7. Summary of geometric parametric study.

Parameter	Test Values
Reinforcement Gradation	Stiff, Med. Stiff, Flexible
Wall Heights (m)	20, 50
Number of Tiers, N	0, 1, 4, 6
Tier Offsets (%)	0, 1, 2, 4, 8, 12

Table 7.8. Number of tiers and tier offsets evaluated in the geometric parametric study and equivalent batter angles.

No. of Tiers, N	Equivalent Batter Angle, β (deg)				
	Offset at Each Tier* (%)				
	0	2	4	6	12
1	90				
4		86.6	83.2	79.8	
6		84.3	78.7	73.3	59.0

*As a percentage of H

Tall MSE wall design is often accompanied with reductions in reinforcement spacing to mitigate increases in lateral earth pressures. As a result, reinforcement spacing in tall MSE walls is non-uniform, with larger spacing near the top of the wall. However, investigations into impacts of reinforcement spacing gradients on wall response are limited to numerical simulations of short 6 m tall walls (Ho and Rowe 1996). Work conducted by Strahler et al. (2016) has shown that at small local stiffness, reinforcement proximity does influence soil-strip response and is ignored in wall design. To evaluate the impact of reinforcement stiffness gradients and proximity, three distributions of S_{local} , representing stiff, medium stiff, and flexible conditions (Figure 7.15a), were established based on those observed in three prominent case histories. The stiff and medium stiff distributions were developed by fitting exponential trends to the S_{local} used in the construction of the West and North MSE walls constructed as part of the STIA third runway project discussed previously (Stuedlein et al. 2007, 2010a, 2010b, 2012) and can be characterized as having S_{global} of 502 and 247 MPa, respectively, and the trend representing the flexible distribution was roughly selected to represent a conservative estimate of S_{local} observed in the 17 m tall wall reported by Runser et al. (2001) presented in Figure 7.15(a) and is characterized with an S_{global} of 84 MPa. Vertical reinforcement spacing in the generic model was equal to 0.50 m over the entire height of the wall and S_{local} distributions were incorporated by adjusting S_h according to Figure 7.15(b). Each simulation is identified by the respective reinforcement distribution, number of tiers, tier offset, and height based on the outlined in Figure 7.15. Results from the parametric study are used to establish a recommended design approach to estimate reinforcement loads, their location along the reinforcement, facing settlements, and lateral displacements. Efforts to interpret wall behavior are discussed below.

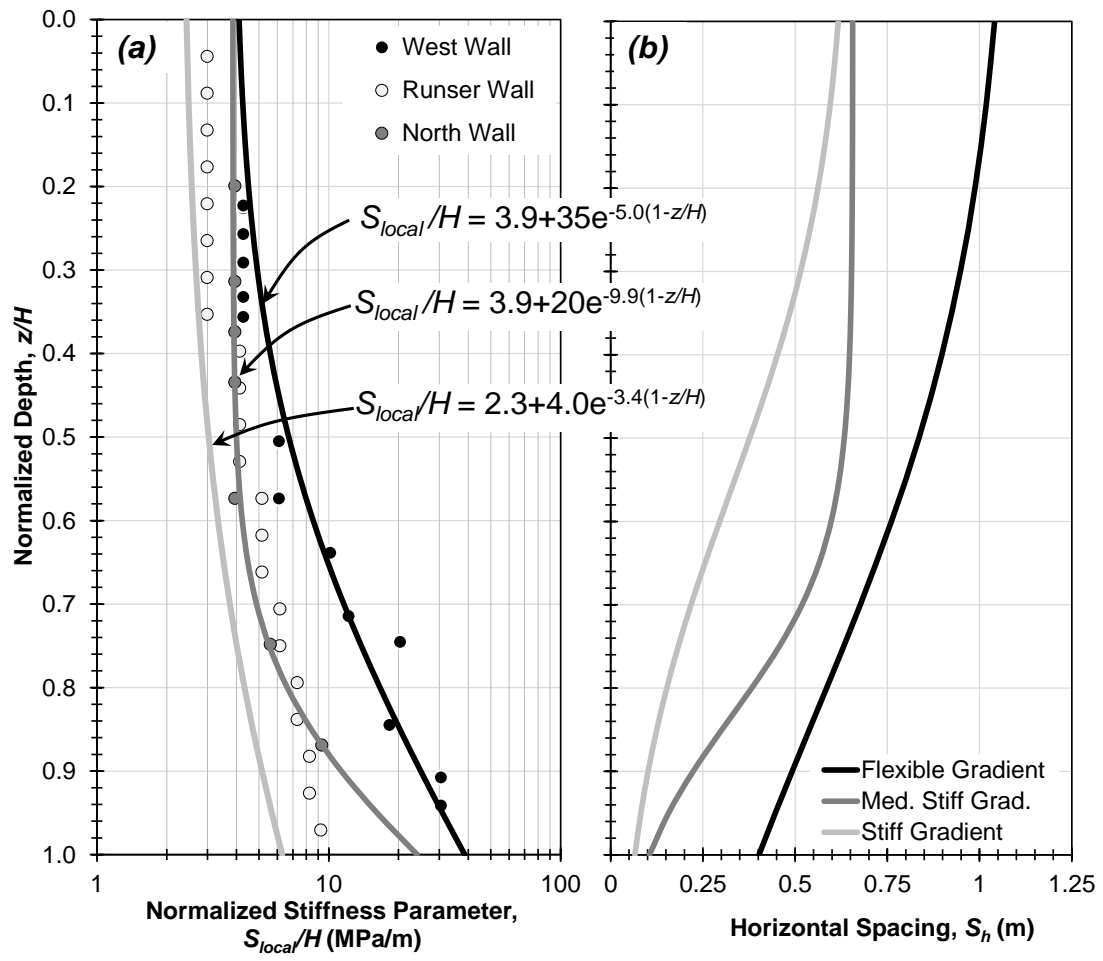
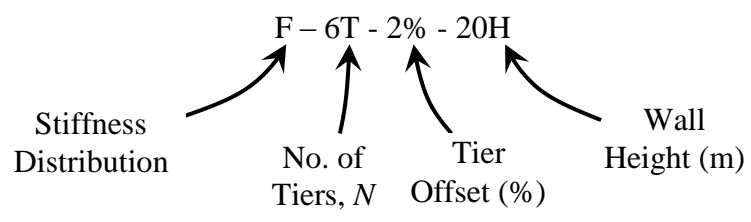


Figure 7.15. Variation in (a) normalized local stiffness and (b) horizontal spacing in the generic model. (Note: $S_v = 0.50$ m)

Figure 7.16. Test designation based on wall geometry and reinforcement spacing distribution.



7.6.1. WALL DEFORMATIONS

Impacts on wall response stemming from changing wall geometry were evaluated by adjusting the number of tiers in the wall fascia, the offset between each tier were taken as a percentage of overall wall height according to Tables 7.7 and 7.8, discussed previously. In general, wall deformations exhibited similar distributions with peak displacements occurring near mid-height. Wall deformations at EOC for a representative 50 m tall 6 tiered wall with flexible reinforcement gradients are presented in Figure 7.17 and 7.18. Localized deviations in the data at uniform intervals indicate tier and panel locations. Facing settlements in the representative 50 m tall walls were generally less than $0.24\%H$ on average with the largest values occurring in single tier models and reducing with batter angle. The sharp increase in face settlement at an approximate elevation of 15 m in the medium stiff simulation (Figure 7.17b) is considered to be the depth at which the bearing pad critical strain was exceeded during wall construction. As a result, facing stiffness below this depth is 13 times greater, producing much less settlement. This behavior is more prominent in the medium stiff reinforcement condition below this depth due to increases in local stiffness near the base of the wall (Figure 7.15) that were not incorporated into the flexible and stiff models.

Lateral displacement magnitudes in the representative 6 tiered 50 m simulations presented in Figure 7.18 were less consistent with changes in reinforcement stiffness and batter angle. Stiff and flexible walls in the single tier condition ($\beta = 90$ degrees) produced Δ_x as high as $0.10\%H$, however, Δ_x increased significantly when β was reduced to 84 degrees. Subsequent reductions in β produced reductions in lateral displacements that generally trended toward the single tier condition in the both the stiff and flexible conditions.

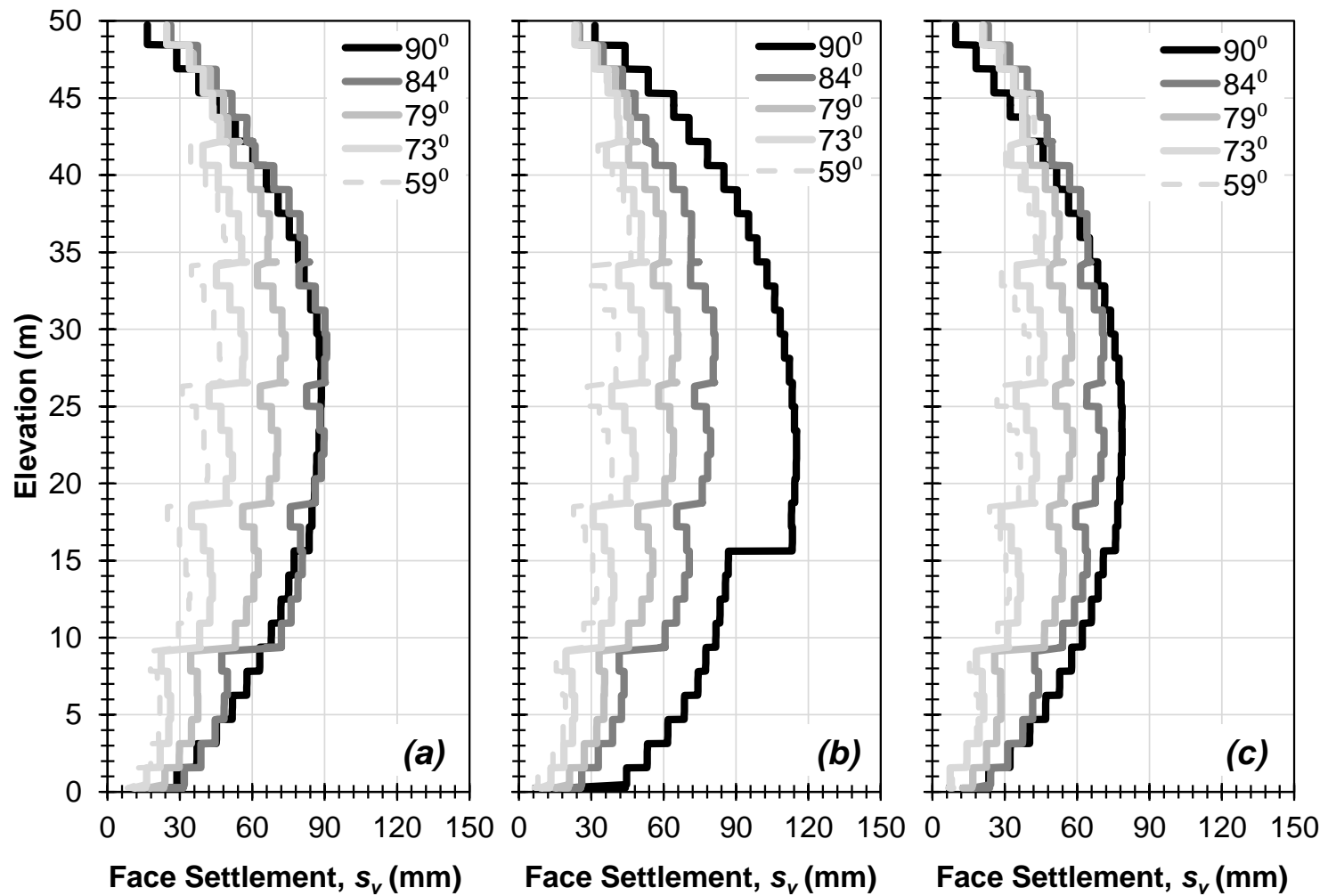


Figure 7.17. Normalized face settlement for a 6 tiered 50 m tall wall with (a) flexible, (b) medium stiff, and (c) stiff reinforcement distributions for various batter angles.

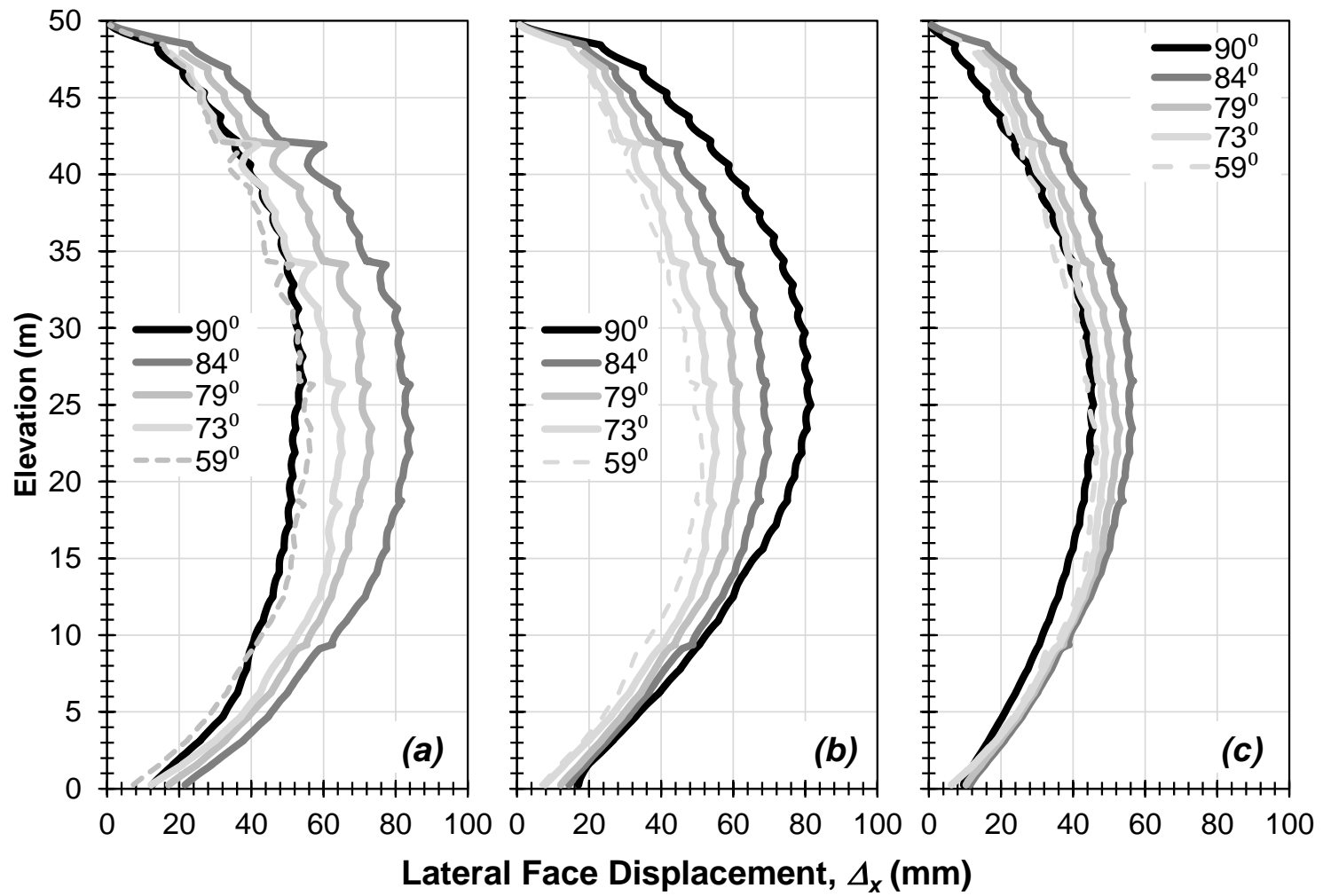


Figure 7.18. Normalized lateral face displacement for a 6 tiered 50 m tall wall with (a) flexible, (b) medium stiff, and (c) stiff reinforcement distributions as a function of batter angle

This behavior is most prominent in the flexible wall condition where increases in lateral displacements are as high as 88% stemming from increases in horizontal stresses at the back of the wall facing due to induced leveling pad vertical stresses. Upon further investigation, the single tier model in the flexible condition was found to exhibit a zone of excessive shearing strains in the lower 15 m of the wall extending at a 56 degree angle from the horizontal that initiated during placement of the second to last panel. The occurrence of this zone indicates that there may be sufficient lateral movement in the wall to initiate an active condition. Conversely, zones of excessive shear strains did not develop in the stiff and medium stiff single tier reinforcement conditions suggesting that reinforcement spacing was small enough to sufficiently prevent an active state from developing. Interestingly, only reductions in Δ_x occurred with reductions in batter angle in the medium stiff condition presented in Figures 7.17 and 7.18. This behavior is attributed to significant reductions in reinforcement spacing near the base of the wall, prevents movement near the toe (Figure 7.15b) resulting in higher lateral stresses and displacements in the upper portion of the wall.

Peak lateral displacements and vertical settlements for all wall configurations have been normalized by H and plotted against equivalent batter angle in Figures 7.19 and 7.20, respectively. In general, normalized peak lateral displacements were 40% greater than those in 20 m walls indicating that wall behavior is pressure dependent and increases with increases in β . Simulation responses in single tier walls can be attributed to changes in the state of lateral earth pressures in the reinforced soil mass, changes in the local stress distribution discussed previously. However, additional influences are associated with increases in vertical stresses directly beneath the leveling pad. Simulations with leveling

pads positioned greater than 2 m behind the wall face, exhibited vertical zones of excessive shearing strains ($> 1\%$) extending to the base of the tier below it presented in Appendix F.

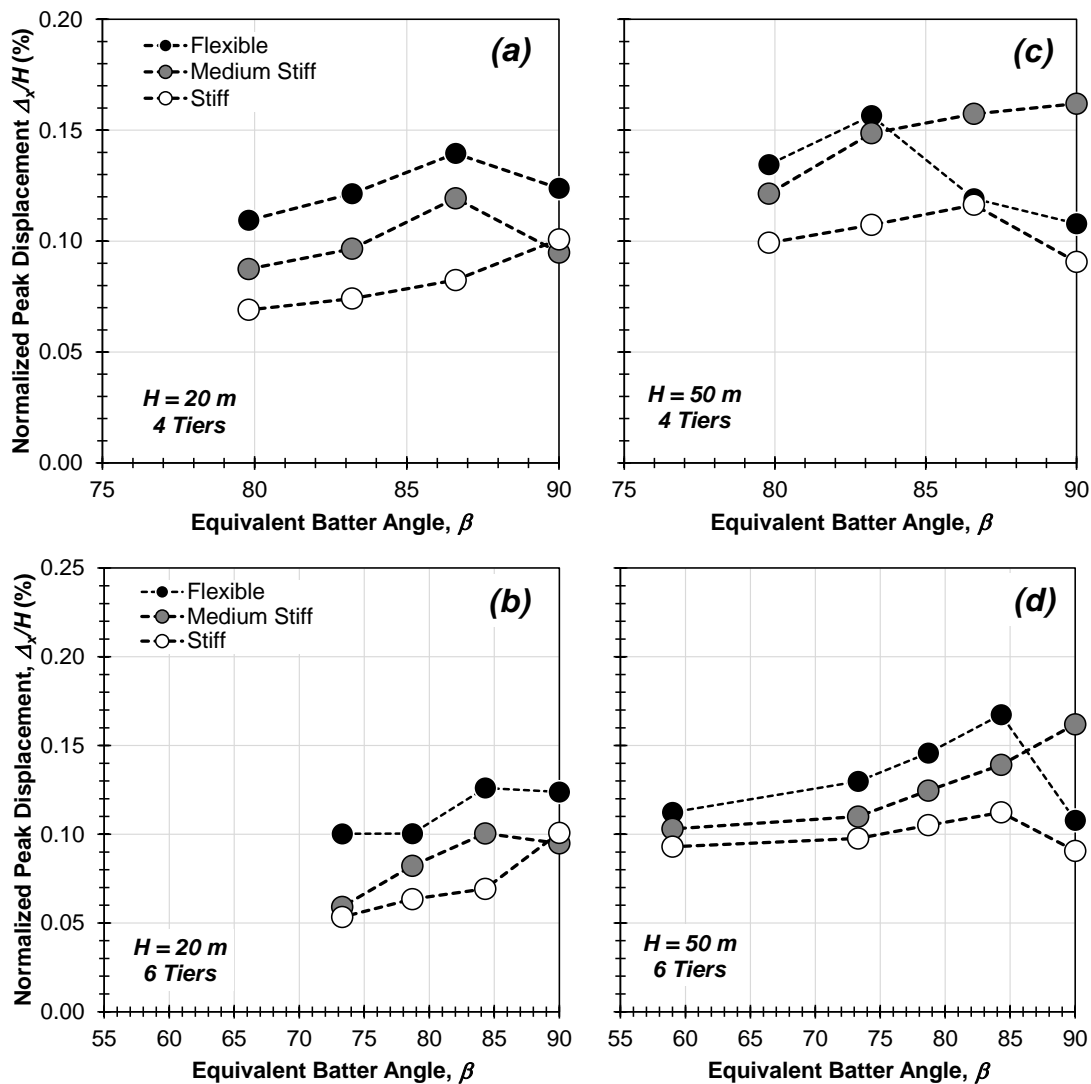


Figure 7.19. Normalized peak lateral displacement versus wall batter angle for (a and b) 20 m and (c and d) 50 m tall wall simulations with 4 and 6 tiers.

This behavior is the result of leveling pad stresses being transferred into the soil mass and subsequent outward movement of the supporting tier, resulting in localized increases in shearing strains and corresponding facing displacement and settlement. Trends in the 6 tier

50 m tall wall behavior presented in Figure 7.19(d) and Figure 7.20(d) suggest that the influence of leveling pad stresses does not significantly influence wall deformations below a β of 73 degrees. This suggests that the 70 degree cutoff specified by the FHWA design method has some merit and warrants further investigation.

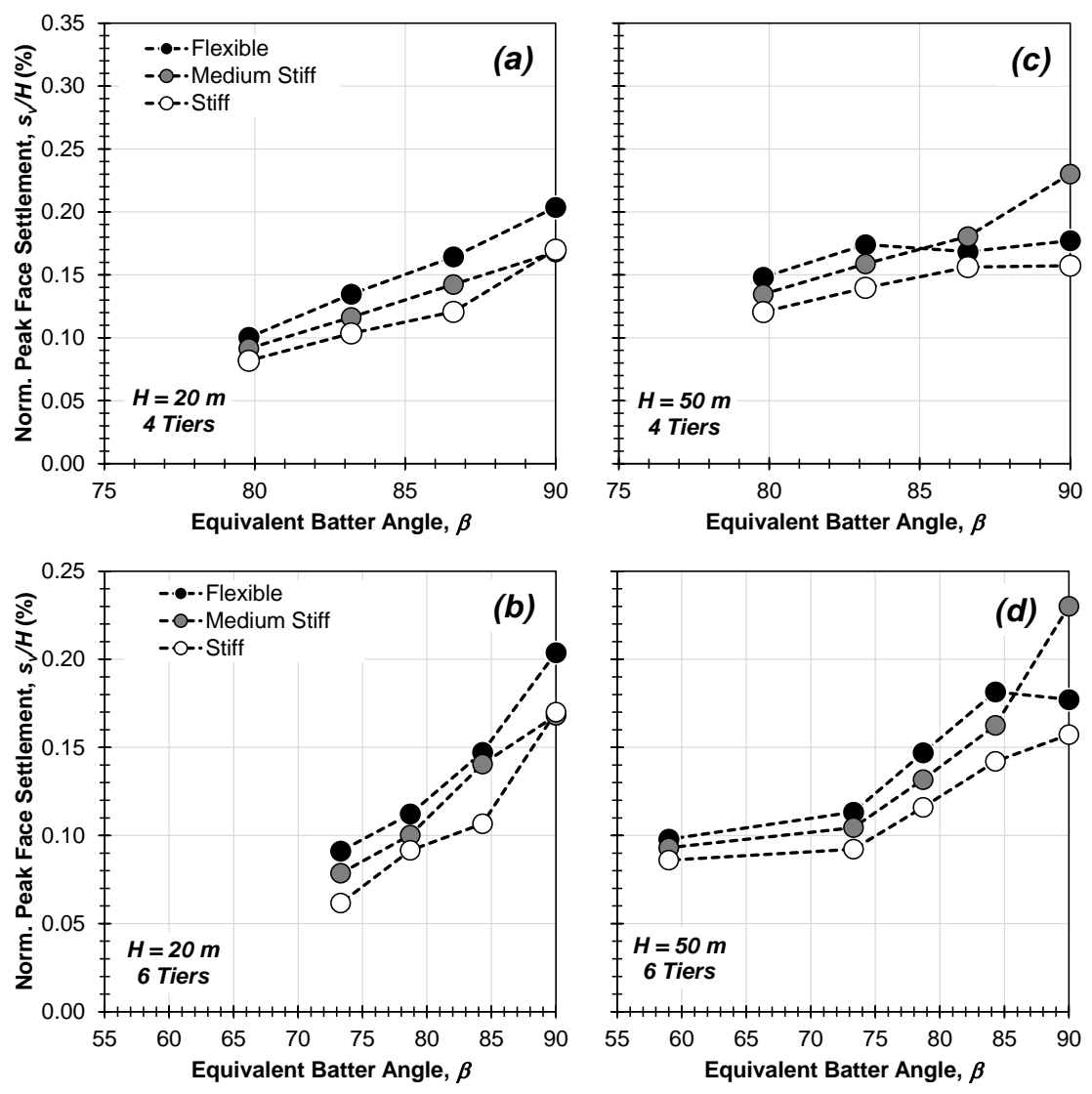


Figure 7.20. Normalized peak face settlement versus wall batter angle for (a, b, c) 20 m and (d, e, f) 50 m tall wall simulations with 4 and 6 tiers.

7.6.2. REINFORCEMENT STRAINS

Current design methods generally assume that peak reinforcement strains coincide with an assumed failure surface, (Elias et al. 2001) and pseudo-active and at-rest earth pressures are determined from an empirical database of typical MSE walls. Reinforcement strains in model simulations were fairly uniform along the length of the reinforcement in every simulation. Peak reinforcement strain distributions for the representative flexible 50 m tall wall discussed previously are presented in Figure 7.21 and indicate that maximum strains generally occur in the lower half of the wall, reducing in magnitude, and increasing in deviations with reductions in batter angle. Generally, peak shear strains exhibited similar trends to those observed in peak lateral displacements, with the exception of the flexible wall where marked increases occurred in the zone of excessive shearing strains. Locations of peak reinforcement strains along the reinforcement for the representative 50 m tall flexible wall are presented in Figure 7.22 and have been corrected for wall batter angle, $x_{p,\beta}$. Generally, $x_{p,\beta}$, exhibit some variation but are sufficiently bracketed by the FHWA design approach. However, there is remarkable agreement between the single tiered wall and the FHWA approximation in the bottom 15 m of the wall consistent with the assumption of an active state.

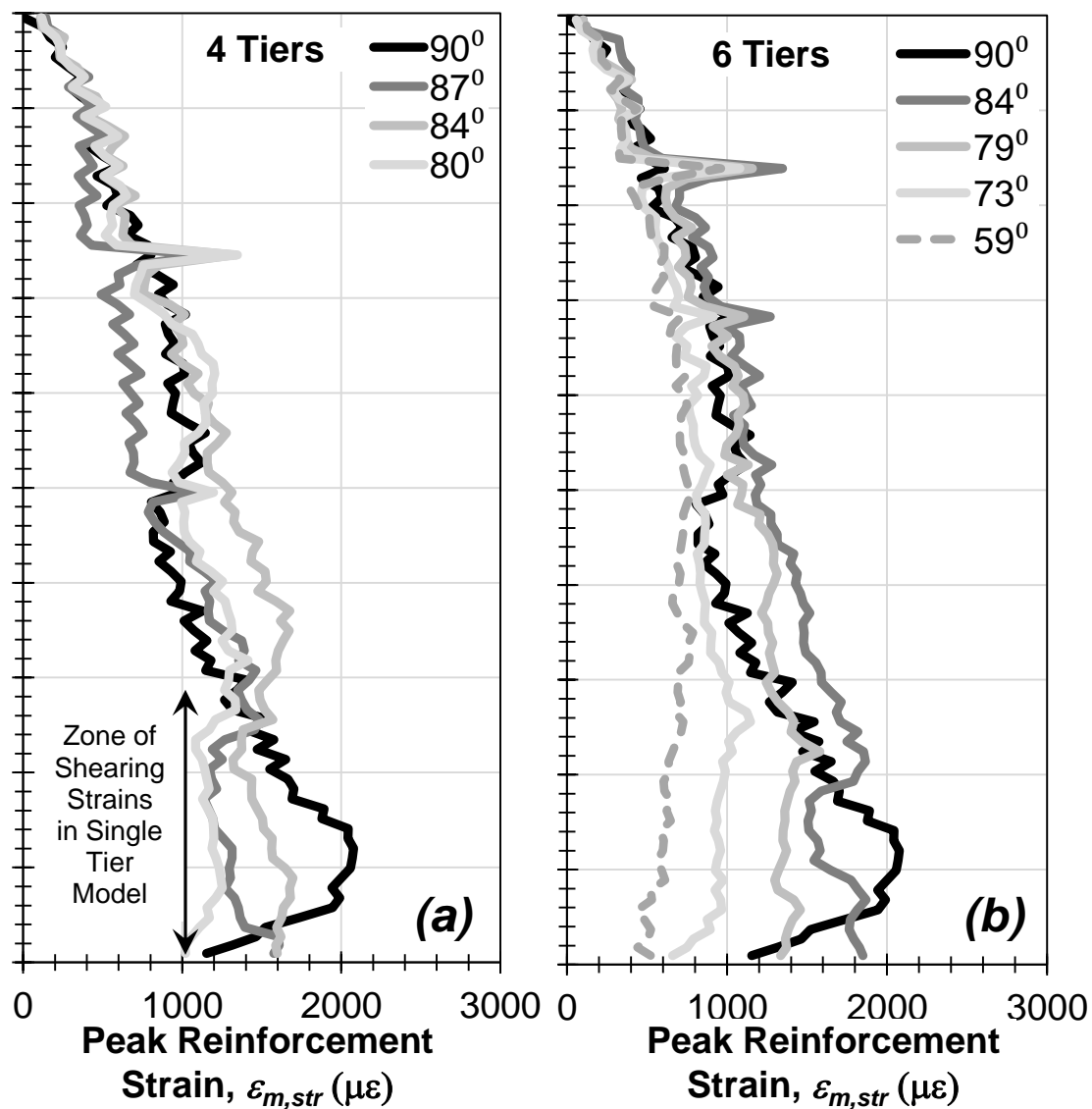


Figure 7.21. Peak reinforcement strain for (a) 4 and (b) 6 tiered 50 m tall walls with flexible strip distributions.

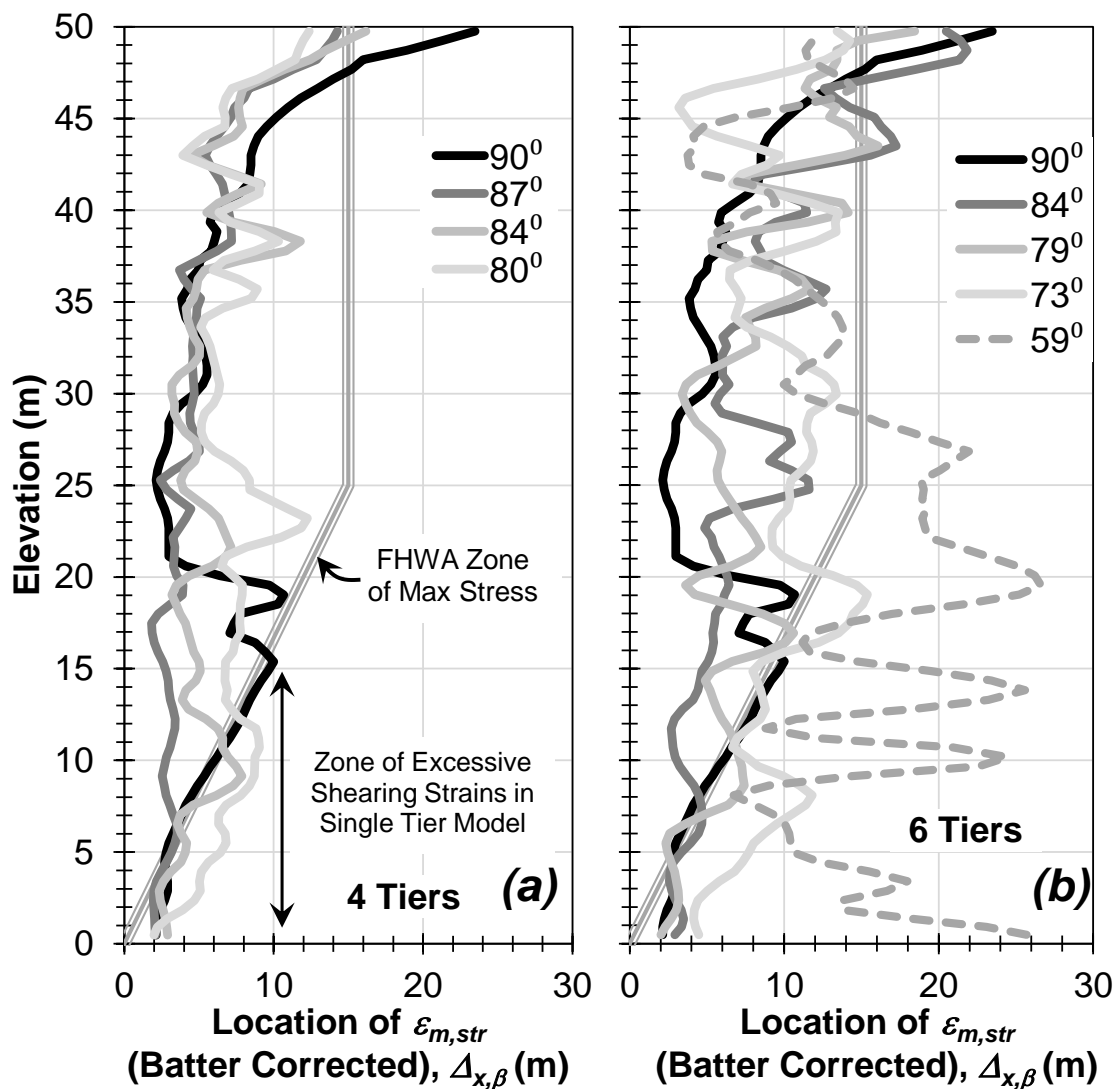


Figure 7.22. Location of peak strain corrected for batter angle effects for (a) 4 and (b) 6 tiered 50 m tall flexible walls (Note: data has been smoothed using a 2 m interval).

To evaluate the influence of wall height, reinforcement gradients, and tier effects, maximum reinforcement strains in each simulated wall configuration have been normalized to account for differences in wall height using a reinforcement strain factor, Γ , which is indicative of the amount of stresses that develop in the reinforcement, relative to vertical stresses and is given by:

$$\Gamma = \frac{\varepsilon_{str} E_r}{\gamma H} \quad (7.6)$$

Reinforcement strain factors for each wall configuration are presented in Figure 7.23 and range between 0.1 and 0.7 and are generally 70% larger in the 20 m walls. Additionally, changes in batter angle has significant effects on Γ in 20 m and 50 m tall walls with increases as high as 0.35 and 0.2, respectively, when β is increased by 31 degrees. These results indicate that reinforcement strains in small walls are greater than those expected in tall walls in relation to the wall height, suggesting that general MSE wall response is pressure dependent. Reinforcement strain factors predicted by the FHWA and Coherent Gravity approaches are generally independent of reinforcement spacing and estimates based on wall geometry provided in Figure 7.23 are most accurately represented by the stiff and medium stiff conditions in 20 m and 50 m tall walls, respectively. Trends in the 6 tiered 50 m tall wall reinforcement strain (Figure 7.23d) suggest that at smaller batter angles ($\beta < 73$ degrees) Γ becomes insensitive to β , indicating that leveling pad stresses are sufficiently far enough from the face to influence horizontal stresses. As a result, the 70 degree cutoff established by the FHWA does have some merit, although further research is required to fully understand the response.

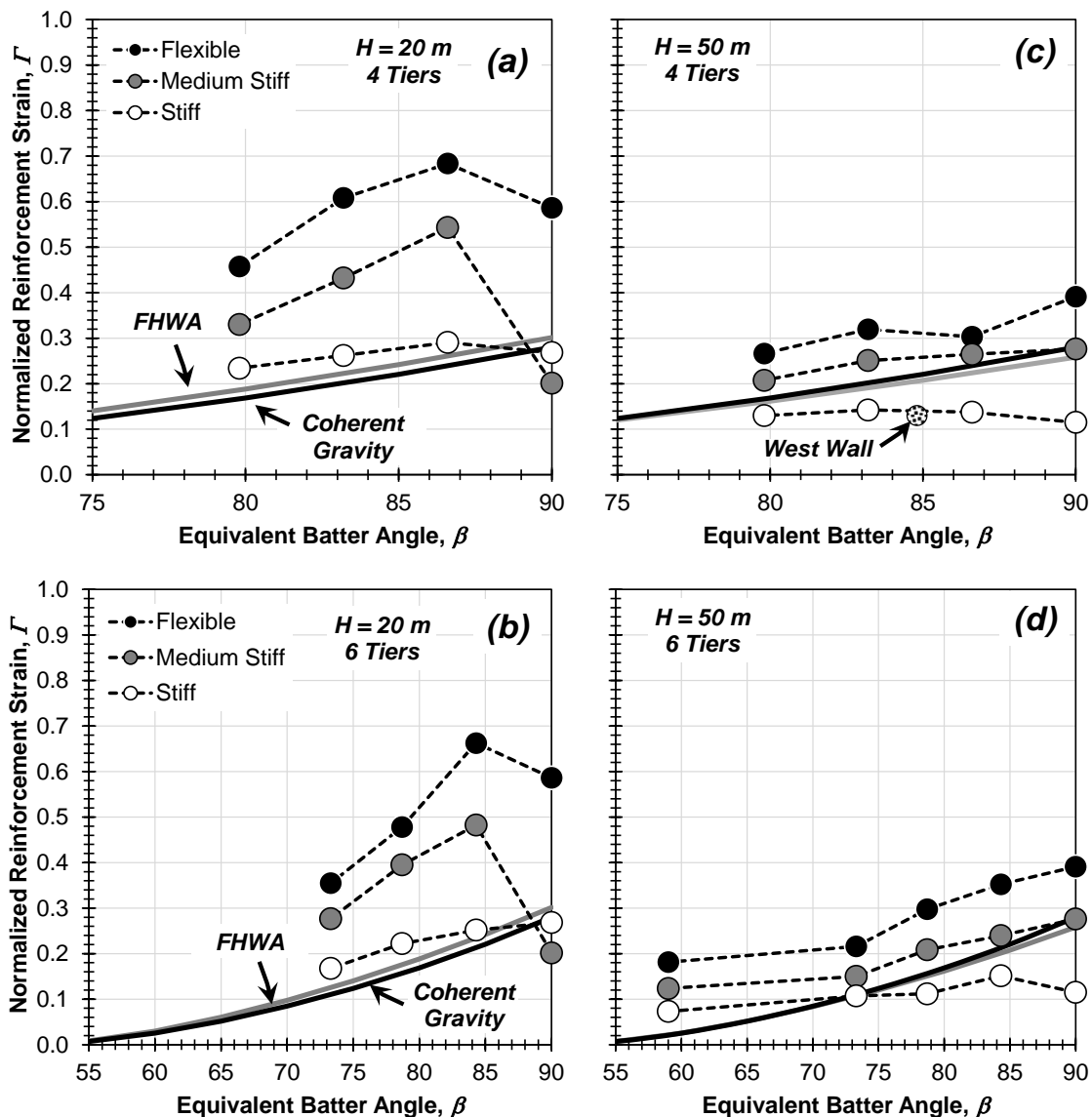


Figure 7.23. Normalized reinforcement strain parameter versus wall batter angle for (a and b) 20 m and (c and d) 50 m tall wall simulations with 4 and 6 tiers.

7.7 CONCLUDING REMARKS

The current study provides practitioners with a better understanding of complex wall response by using calibrated element specific parameters to develop a tall multi-tiered MSE wall numerical model that incorporates pressure dependent soil response in the framework provided by FLAC. The model was subjected to an element specific parametric study to

assess the influence of compaction stresses, soil stiffness, and soil-strip reinforcement interface stiffness on wall behavior. Simulated model responses were validated against measurements made during the construction of the West MSE wall and a final representative model was used to conduct a second parametric study focusing on impacts associated with wall geometry. Tier heights, tier offsets, and global wall heights were altered to assess changes in wall deformations and reinforcement strains.

Results from this research indicate that the working stress response of tall MSE walls during and after construction is adequately predicted by properly calibrated numerical models. Facing settlements are largely influenced by the stiffness reinforced soil and rigidity of bearing pads located between panels. Lateral wall displacements are significantly influenced by the distribution and magnitude of the local reinforcement stiffness and are generally smallest in the single tier geometry. This contradicts simulations of typical walls, in which reductions in batter angle reduced lateral displacements. Accumulated shear strains in the reinforced soil mass exhibited zones of excessive shearing stemming from initiation of an active state and tier effects associated with the pressure dependent stiffness of soil. The location of peak strains along the reinforcements are generally much closer to the wall face than those estimated by current methods whereas the magnitude of reinforcement strain generally reduces with reduction in batter angle. Trends in the deformation reinforcement strain response of 20 m and 50 m tall walls suggest that the 70 degree cutoff between lateral earth pressure and limit equilibrium design methods defined by the FHWA does have some merit. Although further research is required to fully understand this behavior, results from the research here provides novel insights into the response of complex multi-tiered MSE walls.

7.8 ACKNOWLEDGEMENTS

The study presented herein was supported by the National Science Foundation (Grant CMMI No. 1100903) under the direction of Dr. Richard Fragaszy, P.E.; the authors are grateful for this support. Any opinions, findings, and conclusions expressed in this study are those of the writers and do not necessarily reflect the views of the National Science Foundation. The authors would like to thank Dr. Richard Bathurst and Dr. Mathew Gibson for helpful discussions of this work.

7.9 REFERENCES

- AASHTO. (2010). *AASHTO LRFD bridge design specifications*. 3rd Edition, American Association of State, and Highway Transportation Officials, Washington, DC.
- Abramento, M., and Whittle, A. J. (1995). "Experimental evaluation of pullout analyses for planar reinforcements." *Journal of geotechnical engineering*, 121(6), 486-492.
- Allen, T. M., Christopher, B.R., and Holtz, R.D., (1992), "Performance of a 12.6 m High Geotextile Wall in Seattle, Washington", *Geosynthetic Reinforced Soil Retaining Walls*, J. T. H. Wu (editor), Balkema, Rotterdam, pp. 81-100.
- Allen, T. M., Bathurst, R. J., Holtz, R. D., Lee, W. F., and Walters, D. (2004). "New method for prediction of loads in steel reinforced soil walls." *Journal of Geotechnical and Geoenvironmental Engineering*, 130(11), pp. 1109-1120.
- Allen, T.M. and Bathurst, R.J. (2015) "Improved Simplified Method for Prediction of Loads in Reinforced Soil Walls," *Journal of Geotechnical and Geoenvironmental Engineering*, 04015049.
- Anderson, P.L., and Brabant, K. (2005). "Increased Use of MSE Abutments," *Proceedings of the 22nd Annual International Bridge Conference*, Pittsburgh, PA, pp. 5-10.
- Boyle, S. R., (1995), *Deformation Prediction of Geosynthetic Reinforced Soil Retaining Walls*, Ph.D. Dissertation, University of Washington, pp. 391.
- Bathurst, R. J., and Hatami, K. (1998). "Seismic response analysis of a geosynthetic-reinforced soil retaining wall." *Geosynthetics International*, 5(1-2), pp. 127-166.
- Bathurst, R.J., Huang, B.Q., and Allen, T.M. (2011). "LRFD Calibration of Steel Reinforced Walls." *Proceedings of the Geo-Frontiers 2011 conference*, March 13-16, 2011, Dallas, Texas| d 20110000. American Society of Civil Engineers, 2011.
- Berg, R. R., Christopher, B. R., and Samtani, N. C. (2009a)."Design of Mechanically Stabilized Earth Walls and Reinforced Soil Slopes–Volume I" (No. FHWA-NHI-10-025).
- Berg, R. R., Christopher, B. R., and Samtani, N. C. (2009b)."Design of Mechanically Stabilized Earth Walls and Reinforced Soil Slopes–Volume II" (No. FHWA-NHI-10-025).

- Charles, J. A. (2008). "The engineering behaviour of fill materials: the use, misuse and disuse of case histories." *Géotechnique*, 58(7), pp. 541-570.
- Choufani, C., Wu, P., Gagnon, G., and Macintosh, M. (2011). "A precast faced mechanical stabilized earth solution for a 20 metre high mining crusher wall with various technical and site challenges." *Proc., 2011 Pan-Am Canadian Geotechnical Conf.*, Canadian Geotechnical Society, Richmond, British Columbia, Canada.
- Christopher, B. R., Gill, S. A., Giroud, J. P., Juran, I., Mitchell, J. K., Schlosser, F., and Dunncliff, J. (1990a). *Reinforced soil structures Volume I. Design and construction guidelines*. Federal Highway Administration, Washington, DC.
- Christopher, B. R., Gill, S. A., Giroud, J. P., Juran, I., Schlosser, F., and Dunncliff, J. (1990b). *Reinforced soil structures Volume II. Summary of research and systems information*. Federal Highway Administration, Washington, DC.
- Cornforth, D. H. (1964). "Some experiments on the influence of strain conditions on the strength of sand." *Geotechnique*, 14(2), 143-167.
- Damians, I. P., Bathurst, R. J., Josa, A., Lloret, A., and Albuquerque, P. J. R. (2012). "Vertical-facing loads in steel-reinforced soil walls." *Journal of Geotechnical and Geoenvironmental Engineering*, 139(9), pp. 1419-1432.
- Damians, I.P., Bathurst, R.J., Josa, A. and Lloret, A., (2014). "Numerical analysis of an instrumented steel-reinforced soil wall." *International Journal of Geomechanics*, 15(1), p.04014037.
- Damians, I.P., Bathurst, R.J., Lloret, A. and Josa, A., (2016). "Vertical Facing Panel-Joint Gap Analysis for Steel-Reinforced Soil Walls." *International Journal of Geomechanics*, p.04015103.
- Duncan J.M., Byrne, P., Wong, K.S. and Mabry, P., (1980), "Strength, Stress-Strain and Bulk Modulus Parameters for Finite Element Analyses of Stresses and Movements in Soil Masses", *Geotechnical Engineering Report No. UCB/GT/80-01*, University of California, Berkeley, pp. 70.
- Ehrlich, M., and Mitchell, J. K. (1994). "Working Stress Design Method for Reinforced Soil Walls," *Journal of Geotechnical Engineering*, 120(4), pp. 625-645.

- Ehrlich, M., Mitchell, J.K., 1995. "Working stress design method for reinforced soil walls closure." *Journal of Geotechnical Engineering*, ASCE 121 (11), pp. 820-821.
- Ehrlich, M., Mirmoradi, S. H., and Saramago, R. P. (2012). "Evaluation of the effect of compaction on the behavior of geosynthetic-reinforced soil walls." *Geotextiles and Geomembranes*, 34, pp. 108-115.
- Elias, V., and Christopher, B.R., and Berg, R. R., 2001, Mechanically Stabilized Earth Walls and Reinforced Soil Slopes - Design and Construction Guidelines, No. FHWA-NHI-00-043, Federal Highway Administration.
- Gomez, J. E., Filz, G. M., Ebeling, R. M., and Dove, J. E. (2008). "Sand-to-concrete interface response to complex load paths in a large displacement shear box." *Geotechnical Testing Journal*, 31(4), pp. 534.
- Handy, R. L. (1985). "The arch in soil arching." *Journal of Geotechnical Engineering*, 111(3), pp. 302-318.
- Hanna, A. (2001). "Determination of plane-strain shear strength of sand from the results of triaxial tests." *Canadian geotechnical journal*, 38(6), pp. 1231-1240.
- Hart Crowser, Inc. (2003). "Seismic design summary report, third runway embankment, Sea-Tac International Airport, SeaTac, Washington." *Engineering Rep.*, prepared for HNTB.
- Hatami, K., and Bathurst, R. J. (2005). "Development and verification of a numerical model for the analysis of geosynthetic-reinforced soil segmental walls under working stress conditions." *Canadian Geotechnical Journal*, 42(4), pp. 1066-1085.
- Hatami, K., and Bathurst, R. J. (2006). "Numerical model for reinforced soil segmental walls under surcharge loading." *Journal of Geotechnical and Geoenvironmental engineering*, 132(6), pp. 673-684.
- Helwany, S. M. B., Reardon, G., and Wu, J. T. H. (1999). "Effects of backfill on the performance of GRS retaining walls." *Geotextiles and Geomembranes*, 17(1), pp. 1-16.
- Ho, S. K., and Rowe, R. K. (1996). "Effect of wall geometry on the behaviour of reinforced soil walls." *Geotextiles and Geomembranes*, 14(10), pp. 521-541.

- Huang, B., Bathurst, R. J., and Hatami, K. (2009). "Numerical study of reinforced soil segmental walls using three different constitutive soil models." *Journal of Geotechnical and Geoenvironmental engineering*, 135(10), pp. 1486-1498.
- Itasca (2011) Itasca Consulting Group. FLAC Version 4.0 User's Guide.
- Janbu, N. (1963). "Soil compressibility as determined by oedometer and triaxial Test." *Proceedings of the European Conference on Soil Mechanics And Foundation Engineering*, 1, pp. 19-25.
- Lee, K. L. (1970). "Comparison of plane strain and triaxial tests on sand." *Journal of the Soil Mechanics and Foundations Division*, 96(3), pp. 901-923.
- Leshchinsky, D. and Han, J. (2004). "Geosynthetic Reinforced Multitiered Walls." *J. Geotech. Geoenviron. Eng.*, 130(12), pp. 1225-1235.
- Liu, H., and Won, M. S. (2014). "Stress dilatancy and reinforcement load of vertical-reinforced soil composite: Analytical method." *Journal of Engineering Mechanics*, 140(3), pp. 630-639.
- Liu, H., and Yang, G. (2015). "Analytical method for the lateral displacements of steel-reinforced soil walls on stiff foundations with incremental panel facings." *Géotechnique*, 65(9), pp. 728-739.
- Marachi, N., Duncan, J., Chan, C., and Seed, H. (1981). "Plane-strain testing of sand." *Laboratory shear strength of soils*, ASTM STP 740, R. N. Yong and F. C. Townsend, eds., ASTM, West Conshohocken, Pa., pp. 294-302.
- McKittrick, D.P. (1978). "Design, Construction, Technology and Performance of Reinforced Earth Structures," ASCE, Pittsburgh, pp. 596-617.
- Miyata, Y., and Bathurst, R. J. (2012). "Measured and predicted loads in steel strip reinforced $c - \phi$ soil walls in Japan." *Soils and Foundations*, 52(1), pp. 1-17.
- Neely, W. J., and Tan, S. L. (2010). "Effects of second-order design factors on the behavior of MSE walls." *Proceedings Earth Retention Conference*, ASCE, Reston, VA., 3, pp. 522-530.

- Palmeira, E.M., and Milligan, G. W. E. (1989). "Scale and other factors affecting the results of pull-out tests of grids buried in sand," *Géotechnique*, 39(3), pp. 511–542.
- Peters, J., Lade, P., and Bro, A. (1988). "Shear band formation in triaxial and plane strain tests." *Advanced triaxial testing of soil and rock, ASTM STP 977*, R. Donaghe, R. Chaney, and M. Silver, eds., ASTM, West Conshohocken, Pa., pp. 604–627.
- Ramamurthy, T., and Tokhi, V. K. (1981). "Relation of triaxial and plane strain strengths." *Proceedings of Int. Conf. on Soil Mechanics and Foundation Engineering*, Rotterdam, The Netherlands: Balkema. 1, pp. 755-758.
- Rowe, R. K., and Ho, S. K. (1998). "Horizontal deformation in reinforced soil walls." *Canadian Geotechnical Journal*, 35(2), pp. 312-327.
- Schanz, T., and Vermeer, P. A. (1998). "On the stiffness of sands." *Géotechnique*, 48, pp. 383-387.
- Schlosser, F., and Elias, V. (1978). "Friction in reinforced earth," *Symposium on Earth Reinforcement at the ASCE Annual Convention*, April 27, pp. 735–776.
- Strahler, A.W., Stuedlein, A.W., and Arduino, A. (2015). "Stress-Strain Response and Dilatancy of Sandy Gravel in Triaxial Compression and Plane Strain." *Journal of Geotechnical and Geoenvironmental Engineering*, pp. 04015098.
- Strahler, A. W., Walters, J. J., and Stuedlein, A. W. (2016). "Frictional Resistance of Closely Spaced Steel Reinforcement Strips Used in MSE Walls." *Journal of Geotechnical and Geoenvironmental Engineering*, pp. 04016030.
- Stuedlein, A. W., Mikkelsen, P. E., and Bailey, M. J. (2007). "Instrumentation and performance of the third runway north MSE wall at Seattle-Tacoma international airport." *7th International Symposium on Field Measurements in Geomechanics, FMGM 2007, September 24, 2007 - September 27, 2007*, Geotechnical Special Publication, American Society of Civil Engineers, pp. 26.
- Stuedlein, A. W., Bailey, M. J., Lindquist, D. D., Sankey, J., and Neely, W. (2010a). "Design and Performance of a 46-m-High MSE Wall." *Journal of Geotechnical and Geoenvironmental Engineering*, 136(6), pp. 786–796.

Stuedlein, A. W., Allen, T., Holtz, R., and Christopher, B. (2010b). "Factors Affecting the Development of MSE Wall Reinforcement Strain." *Earth Retention Conference 3*, pp. 502-511.

Stuedlein, A. W., Allen, T. M., Holtz, R. D., and Christopher, B. R. (2012). "Assessment of Reinforcement Strains in Very Tall Mechanically Stabilized Earth Walls." *Journal of Geotechnical and Geoenvironmental Engineering*, 138(3), pp. 345–356.

Walters, J.J. (2013). "Characterization of reinforced fill soil, soil-reinforcement interaction and global stability of very tall MSE walls." *MS Thesis*, Oregon State University, Corvallis, OR.

Wright, S. G. (2005). "Design guidelines for multi-tiered MSE walls." *No. FHWA/TX-05/0-4485-2*, pp. 118.

CHAPTER 8: SUMMARY, CONCLUSIONS, AND PROPOSED FUTURE WORK

8.1 SUMMARY

The research presented in this dissertation addresses significant shortcomings associated with the current state of practice of the design of MSE walls and studies the underlying factors contributing to reinforcement loads and wall deformations. A literature review was conducted to identify limitations in the currently recommended MSE wall design methodologies and investigate the manner in which soil behavior, soil-structure interaction, and geometrical constraints is presently considered in practice with specific emphasis given to tall walls.

Due to the importance of fundamental soil behavior in geotechnical design, differences between well-graded gravelly soils commonly used in practice and poorly graded laboratory sands require attention. To reduce the evident gap in information, Chapters 4 and 5 detailed an experimental program that was conducted to study the three dimensional stiffness, strength, and stress-dilatancy of a well-graded Kanaskat gravel in axisymmetric, isotropically consolidated drained (AICD) triaxial, cubical pure shear quasi- K_0 consolidated drained (PS K_0 CD) plane strain, triaxial compression (TC), simple shear (SS), and triaxial extension (TE) stress path tests over a wide range of confining stresses. Initial stiffnesses, peak friction and dilation angles are presented and a discussion is provided regarding the geometrical constraints of the cubical testing device. Comparisons in terms of failure surfaces and stress-dilatancy behavior were made to well established theoretical formulations. Results from the testing program indicated that the stress-dilatancy behavior of Kanaskat gravel may differ from that of uniform sands but can be calibrated to account for discrepancies.

Increases in the magnitude of vertical overburden and lateral earth pressure in tall MSE walls has prompted designers to use closely-spaced reinforcements; yet, due consideration for the potential of frictional interaction between reinforcement strips have not been considered. Chapter 6 investigated the influence of reinforcement spacing on the load-displacement response of ribbed steel strip reinforcements compacted in Kanaskat gravel. Single strip pullout test results were used to determine the fundamental behavior of an isolated strip and form the basis for a model that can be used to estimate the available resistance and initial stiffness of steel ribbed strips in well-graded sandy gravel similar to Kanaskat gravel. Similarly, results from available pullout tests in the literature were used to establish a gravel specific resistance model for use with a wider range of soils. A multi-strip pullout test apparatus, was used to characterize the frictional interference between closely-spaced and confined reinforcements. Both pullout systems were constructed with a relatively soft front boundary condition in order to mitigate the potential for heightened mean effective stresses resulting from passive earth pressure at the face.

The work conducted in Chapters 4, 5, and 6 provide the foundation for the proposed research presented in Chapter 7 which seeks to provide a more thorough understanding of MSE wall behavior by refining the understanding of reinforced soil technology. Results from Chapters 4, 5, and 6 were used to calibrate element specific models in an explicit finite difference framework that aided in developing a tall MSE wall numerical model. Calibration and validation of the numerical model was accomplished through comparisons with measurements taken during and after construction of the West STIA MSE wall. The framework established by the tall MSE numerical model guided two parametric studies to reduce the evident gap in MSE wall behavior.

8.2 SUMMARY AND CONCLUSIONS

The following points outline the major findings and conclusions of the work discussed in Chapters 4 through 7.

8.2.1. *STRESS-STRAIN RESPONSE AND DILATANCY OF SANDY GRAVEL IN TRIAXIAL COMPRESSION AND PLANE STRAIN*

The majority of geotechnical stress-dilatancy investigations have focused on uniform sands, however, very little information of this kind exists for well-graded gravelly soils. Pertinent questions regarding the stiffness, strength, and volumetric response of these soils in plane strain remain to be answered. To reduce the evident gap in information, an experimental program was conducted to study the stiffness, strength, and stress-dilatancy of a well-graded Kanaskat gravel over a wide range of confining stresses. Significant findings of this manuscript include:

1. The initial stiffness of PSK₀CD specimens was much less than AICD specimens, which is attributed to the influence of non-zero intermediate principal strains during shearing.
2. It appears that the plane strain friction angle of Kanaskat gravel at failure is significantly larger than for AICD specimens sheared in triaxial compression, and is generally on the order of 33 percent.
3. Geometrical constraints imposed by the cubical triaxial device impacted the measured volumetric response and inhibited free shear band formation. Resulting in the development of two incipient shear bands forming in PSK₀CD tests,

requiring careful interpretation of volumetric responses for estimation of the dilation angle.

4. The Matsuoka-Nakai failure criterion was found to under-predict the observed failure envelope, whereas the Lade-Duncan failure criterion was found to adequately predict the measured PSK_0CD response at failure.
5. Bolton's (1986) original correlation appears to adequately estimate the dilatancy well-graded gravelly soils in a triaxial compression stress path over the range in pressures investigated; however, it may not be appropriate for soils loaded in a plane strain stress path.

8.2.2. *THREE-DIMENSIONAL STRESS-STRAIN RESPONSE AND STRESS-DILATANCY OF WELL-GRADED GRAVEL*

The three dimensional stress-strain response of granular soils has predominantly focused on uniformly-graded sands. However, the 3-D behavior of these soils do not accurately model well-graded fill soils commonly used in construction. Pertinent questions regarding the stiffness, strength, and stress-dilatancy were investigated through a series of drained true-triaxial tests on specimens of well-graded Kanaskat gravel. Tests were conducted on the triaxial compression (TC), simple shear (SS), and triaxial extension (TE) constant mean effective stress paths at three different confining stresses. The results from the laboratory investigation suggest that the three dimensional stress-dilatancy and frictional responses differs from that of uniform soils. However, the theories developed based on uniformly graded soils can sufficiently estimate this soil response, once properly calibrated. Pertinent findings from this research include:

1. The secant shear modulus at an initial stage of shearing was found to be dependent on stress path; TC specimens produced a shear modulus 30% larger than TE specimens, on average. However, the stiffness at larger strains was found to be relatively independent of stress path and the fitted power laws adequately capture the pressure-dependent stiffness.
2. The development of multiple shear bands was inferred from deviations in principal face displacements in the cubical device and failure was defined as
3. Friction and dilation angles at failure were observed to be as high as 33% larger in the SS and PS stress paths than in TC, greater than expected for uniform granular soils based on previously reported experimental data.
4. New parameters for Bolton's (1986) stress dilatancy approximation can be used to approximate the 3-D stress dilatancy response of Kanaskat gravel, which allows estimation of greater dilatancy than implied for uniformly-graded soils.
5. A modified, pressure-dependent version of the Matsuoka-Nakai failure criterion is used to incorporate the stress dependent nature of granular soils. However, the Lade Duncan failure criterion was found to most accurately capture the measured responses at failure and fitting parameters are presented for its use in forward modeling.

8.2.3. FRICTIONAL RESISTANCE OF CLOSELY-SPACED STEEL MSE WALL REINFORCEMENT STRIPS

Increased confining stresses that develop in tall MSE walls are often accounted for by reducing reinforcement spacing even though very little work has focused on the effect of

frictional interference between closely spaced inextensible reinforcements. The soil-reinforcement interaction of uniformly-graded soils and steel strips has been well characterized, little data exists for the interface response of ribbed steel strips that are commonly specified in MSE wall construction. A series of single and multi-strip pullout tests were performed to study the potential for frictional interference between closely spaced ribbed steel strips using two newly developed pullout test apparatuses with a unique front soft boundary condition. The significant findings include:

1. Single strip pullout test results were used to basis for a model that can be used to estimate the available resistance and initial stiffness of steel ribbed strips in well-graded sandy gravel similar to Kanaskat gravel.
2. Results from available pullout tests in the literature were used to establish a gravel specific resistance model for use with a wider range of soils.
3. Results from the multi-strip tests indicate that the proximity of surrounding reinforcements delays the formation of a shear zone in the soil adjacent to the strip, subsequently increasing the available resistance but also reducing the initial stiffness.
4. At higher confining stresses the interaction between reinforcing strips is less prominent due to the reduced tendency for particles to dilate. This behavior suggests that incorporating trends discussed here could produce more efficient designs in scenarios where the reinforcement spacing near the top of the wall is reduced (e.g. large surcharge placed on the wall or high dynamic forces).
5. Both pullout boxes were constructed with a relatively soft front boundary condition in order to mitigate the potential for heightened mean effective stresses resulting from passive earth pressure at the face.

8.2.4. NUMERICAL MODELLING OF TALL MSE WALLS

The current study provides practitioners with a better understanding of complex wall response by using calibrated element specific parameters to develop a tall multi-tiered MSE wall numerical model that incorporates pressure dependent soil response in the framework provided by FLAC. The model was subjected to an element specific parametric study to assess the influence of compaction stresses, soil stiffness, and soil-strip reinforcement interface stiffness on wall behavior. Simulated model responses were validated against measurements made during the construction of the West MSE wall and a final representative model was used to conduct a second parametric study focusing on impacts associated with wall geometry. Tier heights, tier offsets, and global wall heights were altered to assess changes in wall deformations and reinforcement strains. Significant conclusions from this work include:

1. Facing settlements are largely influenced by the stiffness reinforced soil and rigidity of bearing pads located between panels.
2. Lateral wall displacements are significantly influenced by the distribution and magnitude of the local reinforcement stiffness and are generally smallest in the single tier geometry. This contradicts simulations of typical walls, in which reductions in batter angle reduced lateral displacements.
3. Accumulated shear strains in the reinforced soil mass exhibited zones of excessive shearing stemming from initiation of an active state and tier effects associated with the pressure dependent stiffness of soil.
4. The location of peak strains along the reinforcements are generally much closer to the wall face than those estimated by current methods.

5. The equivalent batter angle cutoff of 70 degrees between limit equilibrium and lateral earth pressure design approaches does have some merit however, further research is required to fully understand the behavior.

8.3 PROPOSED FUTURE WORK

This research investigated the three dimensional behavior of a well graded gravelly soil, interference effects associated with closely spaced reinforcements, and behavior of tall numerically stabilized earth walls. All of these efforts have resulted in useful information that can be used by the practicing engineer to better understand soil behavior, steel strip pullout response, and tall MSE wall behavior. Nevertheless, there are several areas in which further study could be performed in order to better understand MSE wall behavior:

1. Conduct additional true-triaxial tests in various cyclic and static 3-D stress paths to further assess the stress-dilatancy response of a well-graded gravelly fill.
2. Perform additional multi-strip pullout tests to investigate independent influences of vertical and horizontal reinforcement spacing. In addition, further pullout tests could be conducted to fully characterize the influence of soft front boundary condition.
3. Expand the range of batter angles investigated in the geometric parametric study to produce a more thorough understanding of tier effects, tier offsets, and general MSE wall behavior in relation to the 70 degree cutoff established by the FHWA.

COMPLETE LIST OF REFERENCES

- AASHTO. (2010). *AASHTO LRFD bridge design specifications*. 3rd Edition, American Association of State, and Highway Transportation Officials, Washington, DC.
- Abelev, A. V., and Lade, P. V. (2003). Effects of cross-anisotropy on three-dimensional behavior of sand. I: Stress-strain behavior and shear banding. *Journal of Engineering Mechanics*, 129(2), pp. 160–166.
- Abramento, M., and Whittle, A. J. (1995). “Experimental evaluation of pullout analyses for planar reinforcements.” *Journal of geotechnical engineering*, 121(6), 486-492.
- Allen, T. M., Bathurst, R. J., Holtz, R. D., Lee, W. F., and Walters, D. (2004). “New method for prediction of loads in steel reinforced soil walls.” *Journal of Geotechnical and Geoenvironmental Engineering*, 130(11), pp. 1109-1120.
- Allen, T. M., Christopher, B. R., Elias, V. and DiMaggio, J. A. (2001). “Development of the simplified method for internal stability design of mechanically stabilized earth (MSE) walls.” *WSDOT Research Report WA-RD 513.1*.
- Allen, T. M., Christopher, B.R., and Holtz, R.D., (1992), "Performance of a 12.6 m High Geotextile Wall in Seattle, Washington", *Geosynthetic Reinforced Soil Retaining Walls*, J. T. H. Wu (editor), Balkema, Rotterdam, pp. 81-100.
- Allen, T.M. and Bathurst, R.J. (2015) “Improved Simplified Method for Prediction of Loads in Reinforced Soil Walls,” *Journal of Geotechnical and Geoenvironmental Engineering*, 04015049.

- Alshibli, K.A., Batiste, S.N., and Sture, S. (2003). Strain Localization in Sand: Plane Strain versus Triaxial Compression. *Journal of Geotechnical and Geoenvironmental Engineering*, 129(6), pp. 483-494.
- Alzamora, D., and Barrows, R.J. (2007). “Mechanically Stabilized Earth Walls on the Interstate Highway System, Thirty Years of Experience,” *Research Pays Off*, TR News 249, Federal Highway Administration, U.S. Dept. of Transportation, pp. 32-33.
- American Association of State Highway and Transportation Officials (AASHTO). (2014). *AASHTO LRFD bridge design specifications*. 4th Edition, American Association of State, and Highway Transportation Officials, Washington, DC.
- American Society for Testing and Materials (ASTM). (2006). “Test methods for minimum index density and unit weight of soils and calculation of relative density.” *ASTM D4254-06*, West Conshohocken, PA.
- American Society for Testing and Materials (ASTM). (2009). “Test Methods for Laboratory Compaction Characteristics of Soil Using Modified Effort (56,000 ft-lbf/ft³ (2,700 kN-m/m³)).” D1557-12e1, West Conshohocken, Pa.
- American Society for Testing and Materials (ASTM). (2010). “Standard Test Method for Rubber Property—Durometer Hardness.” D2240-05, West Conshohocken, Pa.
- American Society for Testing and Materials (ASTM). (2011). “Test Methods for Tension Testing of Metallic Materials.” E8/E8M-15a, West Conshohocken, Pa.
- American Society for Testing and Materials (ASTM). (2011). “Test Method for Consolidated Drained Triaxial Compression Test for Soils. Standard”, *ASTM D71881-11*, West Conshohocken, PA.

- American Society for Testing and Materials (ASTM). (2012). "Standard Test Methods for Laboratory Compaction Characteristics of Soil Using Modified Effort (56,000 ft-lbf/ft³ (2,700 kN-m/m³))." *ASTM D1557-12*, West Conshohocken, PA.
- Anderson, P.L., and Brabant, K. (2005). "Increased Use of MSE Abutments," *Proceedings of the 22nd Annual International Bridge Conference*, Pittsburgh, PA, pp. 5-10.
- Arthur, J.R.F. (1988) Cubical Devices: Versatility and Constraints. *Advanced Triaxial Testing of Soil and Rock, ASTM 977*, Robert T. Donaghe, Ronald C. Chaney, and Marshal L. Silver, Eds., American Society of Testing Materials, Philadelphia, pp. 743-765.
- Arthur, J.R.F. and Assadi, A. (1977). Ruptured Sand Sheared in Plane Strain. *Proceedings, Ninth International Conference on Soil Mechanics and Foundation Engineering*, Tokyo, 1, pp.19-22.
- Bardet, J.P. (1991). Orientation of shear bands in frictional soils. *Journal of Engineering Mechanics*, 117(7), 1466-1485.
- Bathurst R.J., Nernheim, A, and Allen, T.M. (2009). "Predicted Loads in Steel Reinforced Soil Walls Using the AASHTO Simplified Method." *Journal of Geotechnical and Geoenvironmental Engineering*, 135(2), pp. 177-184.
- Bathurst, R. J., and Hatami, K. (1998). "Seismic response analysis of a geosynthetic-reinforced soil retaining wall." *Geosynthetics International*, 5(1-2), pp. 127-166.
- Bathurst, R.J., Huang, B.Q., and Allen, T.M. (2011). "LRFD Calibration of Steel Reinforced Walls." *Proceedings of the Geo-Frontiers 2011 conference*, March 13-16, 2011, Dallas, Texas| d 20110000. American Society of Civil Engineers, 2011.

- Bathurst, R.J., Nernheim, A., and Allen, T.M. (2008). "Comparison of measured and predicted loads using the Coherent Gravity Method for steel soil walls." *Ground Improvement*, 161(3), pp. 113-120.
- Berg, R. R., Christopher, B. R., and Samtani, N. C. (2009a)."Design of Mechanically Stabilized Earth Walls and Reinforced Soil Slopes–Volume I" (No. FHWA-NHI-10-025).
- Berg, R. R., Christopher, B. R., and Samtani, N. C. (2009a)."Design of Mechanically Stabilized Earth Walls and Reinforced Soil Slopes." Report No. *FHWA-NHI-10-024*, Vol. I, National Highway Institute, Federal Highway Administration, U.S. DOT, Washington, DC.
- Berg, R. R., Christopher, B. R., and Samtani, N. C. (2009b)."Design of Mechanically Stabilized Earth Walls and Reinforced Soil Slopes." No. *FHWA-NHI-10-024*. Vol. II, National Highway Institute, Federal Highway Administration (FHWA), U.S. DOT, Washington, DC.
- Biggerstaff, D.C. (2010). Analysis of the effects of the Intermediate Principal Stress on the Behavior of Gravel with a 9.5 inch True Triaxial Apparatus. *MS Thesis*, University of Washington, Seattle, WA.
- Bishop, A.W. (1954). Correspondence on "Shear characteristics of a saturated silt, measured in triaxial compression." *Géotechnique*, 4(1), pp. 43-45.
- Black, D.K., and Lee, K.L. (1973). Saturating laboratory samples by back pressure. *Journal of the Soil Mechanics and Foundation Division, ASCE*, 99(1), 75-93.
- Bobet, A., Lee, H. S., and Santagata, M. C. (2007). "Drained and undrained pullout capacity of a stiff inclusion in a saturated poroelastic matrix." *International journal for numerical and analytical methods in geomechanics*, 31(5), pp. 715-734.

- Bolton, M.D. (1986). "The strength and dilatancy of sands." *Géotechnique*, 36(1), pp. 65-78.
- Bolton, M.D. (1987). "Closure of 'The strength and dilatancy of sands' by Tatsuoka, F." *Géotechnique*, 37(2), pp. 219-226.
- Boyle, S. R., (1995), *Deformation Prediction of Geosynthetic Reinforced Soil Retaining Walls*, Ph.D. Dissertation, University of Washington, pp. 391.
- Chakraborty, T. and Salgado, R. (2010). "Dilatancy and Shear Strength of Sand at Low Confining Pressures." *Journal of Geotechnical and Geoenvironmental Engineering*, 136(3), pp. 527-532.
- Chang, C.S. and Yin, Z.Y. (2010). Modeling Stress-Dilatancy for Sand under Compression and Extension Loading Conditions. *Journal of Engineering Mechanics*, 136(6), pp. 777-786.
- Charles, J. A. (2008). "The engineering behaviour of fill materials: the use, misuse and disuse of case histories." *Géotechnique*, 58(7), pp. 541-570.
- Charles, J.A. and Watts, K.S. (1980). The influence of confining pressure on the shear strength of compacted rockfill. *Géotechnique*, 30(4), pp. 353-367.
- Choi, C. H. (2004). "Physical and mathematical modeling of coarse-grained soils." *Ph.D. thesis*, Univ. of Washington, Seattle.
- Choi, C., Arduino, P., and Harney, M.D. (2008). "Development of a True Triaxial Apparatus for Sands and Gravels." *Geotechnical Testing Journal*, 31(1), pp. 1-13.
- Choufani, C., Wu, P., Gagnon, G., and Macintosh, M. (2011). "A precast faced mechanical stabilized earth solution for a 20 metre high mining crusher wall with various technical

and site challenges.” *Proc., 2011 Pan-Am Canadian Geotechnical Conf.*, Canadian Geotechnical Society, Richmond, British Columbia, Canada.

Christopher, B. R., Gill, S. A., Giroud, J. P., Juran, I., Mitchell, J. K., Schlosser, F., and Dunicliff, J. (1990a). *Reinforced soil structures Volume I. Design and construction guidelines*. Federal Highway Administration, Washington, DC.

Christopher, B. R., Gill, S. A., Giroud, J. P., Juran, I., Schlosser, F., and Dunicliff, J. (1990b). *Reinforced soil structures Volume II. Summary of research and systems information*. Federal Highway Administration, Washington, DC.

Chu, J. (1994). “Study on the stress-dilatancy behavior of sand by strain path testing.” *Proc. Pre-failure Deformation of Geomaterials*, Shibuya, Malachi and Miura, Eds., Rotterdam, pp. 365-370.

Colliat-Dangus, J.L., Desrues, J., and Foray, P. (1988). Triaxial testing of granular soil under elevated cell pressure. *Advanced triaxial testing of soil and rock*. Edited by R.T. Donaghe, R.C. Chaney, and M.L. Silver. American Society for Testing and Materials, Special Technical Publication STP 977, pp. 290–310.

Cornforth, D. H. (1964). “Some experiments on the influence of strain conditions on the strength of sand.” *Geotechnique*, 14(2), 143-167.

Damians, I. P., Bathurst, R. J., Josa, A., Lloret, A., and Albuquerque, P. J. R. (2012). “Vertical-facing loads in steel-reinforced soil walls.” *Journal of Geotechnical and Geoenvironmental Engineering*, 139(9), pp. 1419-1432.

- Damians, I., Bathurst, R., Josa, A., and Lloret, A. (2015). “Numerical Analysis of an Instrumented Steel-Reinforced Soil Wall.” *International Journal of Geomechanics*, 15(1), 04014037.
- Damians, I., Bathurst, R., Josa, A., Lloret, A., and Albuquerque, P. (2013). “Vertical-Facing Loads in Steel-Reinforced Soil Walls.” *Journal of Geotechnical and Geoenvironmental Engineering*, 139(9), pp. 1419–1432.
- Damians, I.P., Bathurst, R.J., Josa, A. and Lloret, A., (2014). “Numerical analysis of an instrumented steel-reinforced soil wall.” *International Journal of Geomechanics*, 15(1), p.04014037.
- Damians, I.P., Bathurst, R.J., Lloret, A. and Josa, A., (2016). “Vertical Facing Panel-Joint Gap Analysis for Steel-Reinforced Soil Walls.” *International Journal of Geomechanics*, p.04015103.
- De Josselin de Jong, G. (1976). Rowe’s stress-dilatancy relation based on friction. *Géotechnique*, 26(3), pp. 527-534.
- Desrues, J., and Chambon, R. (2002). “Shear band analysis and shear moduli calibration.” *International Journal of Solids and Structures*, 39(13), pp. 3757-3776.
- Dove, J. E., and Jarrett, J. B. (2002). “Behavior of dilative sand interfaces in a geotribology framework”. *Journal of Geotechnical and Geoenvironmental engineering*, 128(1), pp. 25-37.
- Duncan J.M., Byrne, P., Wong, K.S. and Mabry, P., (1980), “Strength, Stress-Strain and Bulk Modulus Parameters for Finite Element Analyses of Stresses and Movements in Soil Masses”, *Geotechnical Engineering Report No. UCB/GT/80-01*, University of California, Berkeley, pp. 70.

- Ehrlich, M., and Mitchell, J. K. (1994). "Working Stress Design Method for Reinforced Soil Walls," *Journal of Geotechnical Engineering*, 120(4), pp. 625–645.
- Ehrlich, M., Mirmoradi, S. H., and Saramago, R. P. (2012). "Evaluation of the effect of compaction on the behavior of geosynthetic-reinforced soil walls." *Geotextiles and Geomembranes*, 34, pp. 108-115.
- Ehrlich, M., Mitchell, J.K., (1995). "Closure of working stress design method for reinforced soil walls." *Journal of Geotechnical Engineering*, ASCE 121 (11), pp. 820-821.
- Elias, V., and Christopher, B.R., and Berg, R. R., 2001, Mechanically Stabilized Earth Walls and Reinforced Soil Slopes - Design and Construction Guidelines, No. FHWA-NHI-00-043, Federal Highway Administration.
- Evans, T.M., and Frost, J.D. (2010). "Multi-scale investigation of shear bands in sand: Physical and numerical experiments." *International Journal for Numerical and Analytical Methods in Geomechanics*, 34(15), pp. 1634-1650.
- Finn, W.D.L., Wade, N.H., and Lee, K.L. (1967). "Volume changes in triaxial and plane strain tests." *Journal of the Soil Mechanics and Foundation Division*, ASCE, 93(SM6), pp. 297-308.
- Frost, J.D., Hebel, G.L., Evans, T.M., and DeJong, J.T. (2004). "Interface behavior of granular soils." *Proceedings, of the 9th ASCE Aerospace Division International Conference on Engineering, Construction and Operations in Challenging Environments*, ASCE, Reston, VA., pp. 7–10.

- Frydman, S., Talesnick, M., Nawatha, H., and Schwartz, K. (2007). "Stress-dilation of undisturbed sand samples in drained and undrained triaxial shear." *Soils and Foundations*, 47(1), pp. 27-32.
- Gomez, J. E., Filz, G. M., Ebeling, R. M., and Dove, J. E. (2008). "Sand-to-concrete interface response to complex load paths in a large displacement shear box." *Geotechnical Testing Journal*, 31(4), pp. 534.
- Green, G. E., (1972), "Strength and Deformation of Sand Measured in an Independent Stress Control Cell." *Proceedings of the Roscoe Memorial Symposium: Stress Strain Behaviour of Soils*, R. H. G. Parry, Ed., G.T. Foulis & Co. Ltd., Oxfordshire, England, pp 752.
- Green, G.E. (1971). "Strength and deformation of sand measured in an independent stress control cell." *Stress-strain behavior of soils. Proc. Roscoe Memorial Symposium*, pp. 285-323.
- Handy, R. L. (1985). "The arch in soil arching." *Journal of Geotechnical Engineering*, 111(3), pp. 302-318.
- Hanna, A. (2001). "Determination of plane-strain shear strength of sand from the results of triaxial tests." *Canadian geotechnical journal*, 38(6), pp. 1231-1240.
- Hart Crowser, Inc. (2003). "Seismic design summary report, third runway embankment, Sea-Tac International Airport, SeaTac, Washington." *Engineering Rep.*, prepared for HNTB.
- Hatami, K., and Bathurst, R. J. (2005). "Development and verification of a numerical model for the analysis of geosynthetic-reinforced soil segmental walls under working stress conditions." *Canadian Geotechnical Journal*, 42(4), pp. 1066-1085.

- Hatami, K., and Bathurst, R. J. (2006). "Numerical model for reinforced soil segmental walls under surcharge loading." *Journal of Geotechnical and Geoenvironmental engineering*, 132(6), pp. 673-684.
- Helwany, S. M. B., Reardon, G., and Wu, J. T. H. (1999). "Effects of backfill on the performance of GRS retaining walls." *Geotextiles and Geomembranes*, 17(1), pp. 1-16.
- Ho, S. K., and Rowe, R. K. (1996). "Effect of wall geometry on the behaviour of reinforced soil walls." *Geotextiles and Geomembranes*, 14(10), pp. 521-541.
- Holtz, W.G. and Gibbs, J. (1956). "Triaxial shear tests on pervious gravelly soils." *Journal of Soil Mech. Found. Div. ASCE*, 82(1), pp. 1-22.
- Hoopes, O.T. (2007). Experimental Study with a 9.5-in. True-Triaxial Apparatus: Phase Transformation Surface Mapping and PID Strain-Control. *MS Thesis*, University of Washington, Seattle, WA.
- Horne, M.R. (1965). The behavior of an assembly of rotund, rigid, cohesionless Particles. *Proc. Of the Royal Society of London. Series A, Mathematical and Physical Sciences*, 286(1404), pp. 79-97.
- Houlsby, G.T. (1991). "How the dilatancy of soils affects their behavior. Invited Theme Lecture", *Proceedings of the Tenth European Conference on Soil Mechanics and Foundation Engineering*, Florence, May 27-30, 4, pp. 1189-1202.
- Hryciw, R.D., and Irsyam, M. (1993). "Behavior of sand particles around rigid ribbed inclusions during shear," *Soils and Foundations*, 33(3), pp.1-13.

- Huang, B., Bathurst, R. J., and Hatami, K. (2009). "Numerical study of reinforced soil segmental walls using three different constitutive soil models." *Journal of Geotechnical and Geoenvironmental engineering*, 135(10), pp. 1486-1498.
- Irsyam, M., and Hryciw, R. D. (1991). "Friction and passive resistance in soil reinforced by plane ribbed inclusions." *Géotechnique*, 41(4), pp. 485-498.
- Itasca (2011) Itasca Consulting Group. FLAC Version 4.0 User's Guide.
- Janbu, N. (1963). "Soil compressibility as determined by oedometer and triaxial Test." *Proceedings of the European Conference on Soil Mechanics And Foundation Engineering*, 1, pp. 19-25.
- Jayawickrama, P., Lawson, W., Wood, T., and Surles, J. (2014). "Pullout Resistance Factors for Steel MSE Reinforcements Embedded in Gravelly Backfill." *Journal of Geotechnical Geoenvironmental Engineering*, 10.1061/(ASCE)GT.1943-5606.0001192, 04014090.
- Jewell, R.A., and Wroth, C.P. (1987). Direct Shear Tests on Reinforced Sand. *Géotechnique*, 37(1), pp. 53-68.
- Kjellman, W., (1936). Report on an Apparatus for Consummate Investigation of the Mechanical Properties of Soils, *Proceedings of the First International Conference on Soil Mechanics and Foundation Engineering*, Vol. 2, A. Casagrande, P. C. Rutledge, and J. D. Watson, Ed., Harvard University, Cambridge, MA, pp. 16–20.
- Krumbein, W. C. and Sloss, L. L. (1963). *Stratigraphy and sedimentation*, 2nd Ed., Freeman and Company, San Francisco.

- Kulhawy, F.H., and Mayne, P.W. (1990). *Manual on Estimating Soil Properties for Foundations*, Final Report, Project 1493-6, EL-6800, Electric Power Research Institute, Palo Alto, CA.
- Lade, P. V. (2008). "Failure criterion for cross-anisotropic soils." *Journal of Geotechnical and Geoenvironmental engineering*, 134(1), pp. 117-124.
- Lade, P. V., (1978). "Cubical Triaxial Apparatus for Soil Testing." *Geotechnical Testing Journal*, Vol. 1, No. 2, pp. 93-101.
- Lade, P. V., and Abelev, A. V. (2003). "Effects of cross anisotropy on three-dimensional behavior of sand. II: Volume change behavior and failure." *Journal of Engineering Mechanics*, 129(2), pp. 167-174.
- Lade, P. V., and Abelev, A. V. (2003). Effects of cross anisotropy on three-dimensional behavior of sand. II: Volume change behavior and failure. *Journal of Engineering Mechanics*, 129(2), pp. 167-174.
- Lade, P. V., and Duncan, J. M. (1975). "Elastoplastic stress-strain theory for cohesionless soil." *Journal of the Geotechnical Engineering Division*, 101(10), pp. 1037-1053.
- Lade, P. V., and Wang, Q. (2001). "Analysis of shear banding in true triaxial tests on sand." *Journal of Engineering Mechanics*, 127(8), pp. 762-768.
- Lade, P.V. and Duncan, J.M. (1973). "Cubical triaxial tests on cohesionless soils." *Journal of Soil Mechanics and Foundations Division*, 99(SM10), 793-812.
- Lee, K.L. (1970) Comparison of plane strain and triaxial tests on sand. *Journal of the Soil Mechanics and Foundation Division*, 96(SM3), pp. 901-923.

- Lee, K.L. and Seed, H.B. (1967). Drained Strength Characteristics of Sands. *Journal of the Soil Mechanics and Foundation Division*, November, 93(SM6), pp. 117-141.
- Leshchinsky, D. and Han, J. (2004). "Geosynthetic Reinforced Multitiered Walls." *J. Geotechnical and Geo-environmental. Eng.*, 130(12), pp. 1225-1235.
- Lings, M. L. and Dietz, M. S. (2005). "The peak strength of sand-steel interfaces and the role of dilation." *Soils and Foundations* 46(6), pp.1–14.
- Liu, H., and Won, M. S. (2014). "Stress dilatancy and reinforcement load of vertical-reinforced soil composite: Analytical method." *Journal of Engineering Mechanics*, 140(3), pp. 630-639.
- Liu, H., and Yang, G. (2015). "Analytical method for the lateral displacements of steel-reinforced soil walls on stiff foundations with incremental panel facings." *Géotechnique*, 65(9), pp. 728-739.
- Maqbool, S. and Koseki, J. (2007). Large-Scale Plane Strain Compression Tests on Compacted Gravel. *Pakistan Journal of Engineering and Applied Science*, 1, pp. 40-60.
- Marachi, N., Duncan, J., Chan, C., and Seed, H. (1981). "Plane-strain testing of sand." *Laboratory shear strength of soils*, ASTM STP 740, R. N. Yong and F. C. Townsend, eds., ASTM, West Conshohocken, Pa., pp. 294–302.
- Marachi, N.D., Chan, C.K., and Seed, H.B. (1972). "Evaluation of properties of rockfill materials." *Journal of Soil Mechanics and Foundations Division ASCE*, 98(SM1), pp. 95-114.
- Marsal, R.J. (1967). "Large scale testing of rockfill materials." *Journal of Soil Mechanics and Foundations Division ASCE*, 93(SM2), pp. 27-44.

- Matsuoka, H. and Liu, S. (1998). "Simplified direct shear test on granular materials and its application to rockfill materials." *Soils and Foundations*, 38(4), pp. 275-284.
- Matsuoka, H. and Nakai, T. (1974). "Stress-Deformation and Strength Characteristics of Soil under Three Different Principal Stresses." *Proc. JSCE*, Vol. 232, pp. 59-70.
- Matsuoka, H., Hoshikawa, T., and Ueno, K. (1990). "A general failure criterion and stress-strain relation for granular materials to metals." *Soils and Foundations*, 30(2), pp.119-127.
- Matsuoka, H., Liu, S., Sun, D., and Nishikata, U. (2001). "Development of a new in situ direct shear test." *Geotechnical Testing Journal*, 24(1), pp. 92-101.
- Matsuoka, H., Sun, D., Kogane, A., Fukuzawa, N., and Ichihara, W. (2002). "Stress-Strain Behaviour of Unsaturated Soil in True Triaxial Tests." *Canadian Geotechnical Journal*, 39(3), pp. 608–619.
- McKittrick, D.P. (1978). "Design, Construction, Technology and Performance of Reinforced Earth Structures," ASCE, Pittsburgh, pp. 596–617.
- Mitchell, J.K., and Soga, K. (2005). *Fundamentals of Soil Behavior*, John Wiley and Sons, Inc., New York.
- Miyata, Y., and Bathurst, R. J. (2012a). "Analysis and calibration of default steel strip pullout models used in Japan." *Soils and Foundations* 52(3), 481-497.
- Miyata, Y., and Bathurst, R. J. (2012b). "Measured and predicted loads in steel strip reinforced $c - \phi$ soil walls in Japan." *Soils and Foundations*, 52(1), pp. 1-17.
- Palmeira, E.M., and Milligan, G. W. E. (1989). "Scale and other factors affecting the results of pull-out tests of grids buried in sand," *Géotechnique*, 39(3), pp. 511–542.

- Neely, W. J., and Tan, S. L. (2010). "Effects of second-order design factors on the behavior of MSE walls." *Proceedings Earth Retention Conference*, ASCE, Reston, VA., 3, pp. 522-530.
- Newland, P.L. and Allely, B.H. (1957). Volume Changes in Drained Triaxial Tests on Granular Materials. *Géotechnique*, 7(1), pp. 17-34.
- Palmeira, E.M., and Milligan, G. W. E. (1989). "Scale and other factors affecting the results of pull-out tests of grids buried in sand," *Géotechnique*, 39(3), pp. 511–542.
- Panda, B.C. and Ghosh, A.K. (2000). "Influence of Grain Size Distribution on Dilatancy of Sand." *Journal of the Institution of Engineers*, 81(2), pp. 68-70.
- Penman, A.D.M. (1953). "Shear characteristics of a saturated silt." *Géotechnique*, 3(8), pp. 312-328.
- Peters, J., Lade, P., and Bro, A. (1988). "Shear band formation in triaxial and plane strain tests." *Advanced triaxial testing of soil and rock*, ASTM STP 977, R. Donaghe, R. Chaney, and M. Silver, eds., ASTM, West Conshohocken, Pa., pp. 604–627.
- Poorooshasb, H.B. and Roscoe, K.H. (1961). "The correlation of the results of shear tests with varying degrees of dilatation." *Proc. 5th International Conference on Soil Mechanics*, 1, pp. 297-304.
- Powers, M.C. (1953). "A New Roundness Scale for Sedimentary Particles. *Journal of Sedimentary Petrology*." 23(2), pp. 117-119.
- Public Works Research Center (PWRC), (2003). *Design Method, Construction Manual and Specifications for Steel Strip Reinforced Retaining Walls*, 3rd revised ed., Tsukuba, Ibaraki, Japan 302 pp. (in Japanese).

- Ramamurthy, T. and Tokhi, V.K. (1981). "Relation of Triaxial and Plane Strain Strengths." *Proc. of the International Conference on Soil Mechanics and Foundation Engineering*, 1, pp. 755-758.
- Ramamurthy, T., and Tokhi, V. K. (1981). "Relation of triaxial and plane strain strengths." *Proceedings of Int. Conf. on Soil Mechanics and Foundation Engineering*, Rotterdam, The Netherlands: Balkema. 1, pp. 755-758.
- Reades, D.W. and Green, G.E. (1976). Independent stress control and triaxial extension tests on sand. *Géotechnique*, 26(4), pp. 551-576.
- Reynolds, O. (1885). The Dilating of Media Composed of Rigid Particles in Contact. *Philosophical Magazine*. December.
- Rowe, P.W. (1962). The Stress-dilatancy Relations for static Equilibrium of an Assembly of Particles in Contact. *Proc. R. Soc.*, 269A, pp. 500-527.
- Rowe, P.W. (1969). "The relation between the shear strength of sands in triaxial compression, plane strain, and direct shear." *Géotechnique*, 19(1), pp. 75-86.
- Rowe, P.W., Barden, L., and Lee, I.K. (1964) "Energy Components during the Triaxial Cell and Direct Shear Tests." *Géotechnique*, 14(3), September.
- Rowe, R. K., and Ho, S. K. (1998). "Horizontal deformation in reinforced soil walls." *Canadian Geotechnical Journal*, 35(2), pp. 312-327.
- Russell, A., and Khalili, N. (2005). "A bounding surface plasticity model for sands exhibiting particle crushing." *Canadian Geotechnical Journal*, 41, pp. 1179-1192.
- Salgado, R., Bandini, P., and Karim, A. (2000). "Shear Strength and Stiffness of Silty Sand." *Journal of Geotechnical and Geoenvironmental Engineering*, 126(5), pp. 451-462.

- Schanz, T. and Vermeer, P.A. (1996). "Angles of friction and dilatancy of sand." *Géotechnique*, 46(1), pp. 145-151.
- Schanz, T. and Vermeer, P.A. (1998). "On the stiffness of sands. Special issue on Pre-failure Deformation Behaviour of Geomaterials." *Géotechnique*, pp. 383-387.
- Schlosser, F., and Elias, V. (1978). "Friction in reinforced earth," *Symposium on Earth Reinforcement at the ASCE Annual Convention*, April 27, pp. 735-776.
- Shapiro, S. and Yamamuro, J.A. (2003). "Effects of Silt on Three-Dimensional Stress-Strain Behavior of Loose Sand." *Journal of Geotechnical and Geoenvironmental Engineering*, 129(1), pp. 1-11.
- Skermer, N. A. and Hillis, S. F. (1970). "Gradation and shear characteristics of four cohesionless soils." *Canadian Geotechnical Journal*, 7, pp. 62-68.
- Strahler, A. W., Walters, J. J., and Stuedlein, A. W. (2016). "Frictional Resistance of Closely Spaced Steel Reinforcement Strips Used in MSE Walls." *Journal of Geotechnical and Geoenvironmental Engineering*, pp. 04016030.
- Strahler, A.W., Stuedlein, A.W., and Arduino, A. (2015). "Stress-Strain Response and Dilatancy of Sandy Gravel in Triaxial Compression and Plane Strain." *Journal of Geotechnical and Geoenvironmental Engineering*, pp. 04015098.
- Stuedlein, A. W., Allen, T. M., Holtz, R. D., and Christopher, B. R. (2012). "Assessment of Reinforcement Strains in Very Tall Mechanically Stabilized Earth Walls." *Journal of Geotechnical and Geoenvironmental Engineering*, 138(3), pp. 345-356.

- Stuedlein, A. W., Bailey, M. J., Lindquist, D. D., Sankey, J., and Neely, W. (2010a). "Design and Performance of a 46-m-High MSE Wall." *Journal of Geotechnical and Geoenvironmental Engineering*, 136(6), pp. 786–796.
- Stuedlein, A. W., Allen, T., Holtz, R., and Christopher, B. (2010b). "Factors Affecting the Development of MSE Wall Reinforcement Strain." *Earth Retention Conference 3*, pp. 502-511.
- Stuedlein, A. W., Mikkelsen, P. E., and Bailey, M. J. (2007). "Instrumentation and performance of the third runway north MSE wall at Seattle-Tacoma international airport." *7th International Symposium on Field Measurements in Geomechanics, FMGM 2007, September 24, 2007 - September 27, 2007*, Geotechnical Special Publication, American Society of Civil Engineers, pp. 26.
- Suzuki, K and Yanagisawa, E. (2006). "Principal Deviatoric Strain Increment Ratios for Sand Having Inherent Transverse Isotropy." *ASCE International Journal of Geomechanics*, Sept/Oct 2006, pp. 356-366.
- Tatsuoka, F. (1976). "Stress-dilatancy relations of anisotropic sands in three dimensional stress condition." *Soils and Foundations*, 19(2), pp. 1-18.
- Tatsuoka, F. (1987). "Discussion of 'The strength and dilatancy of sands' by Bolton, 1986." *Géotechnique*, 37(2), 219–226.
- Terzaghi, K., Peck, R.B., and Mesri, G. (1996). *Soil in engineering practice*, 3rd Edn. London: Wiley.
- Tatsuoka, F., Sakamoto, M., and Kawamura, T. (1986). "Strength and deformation characteristics of sand in plane strain compression at extremely low pressures." *Soils and Foundations*, 26(1), pp. 65-84.

- Taylor, D.W. (1948). *Fundamentals of Soil Mechanics*. New York: J. Wiley and Sons.
- Vardoulakis, I. (1980). "Shear band inclination and shear modulus of sand in biaxial tests." *Int. Journal for Numerical and Analytical Methods in Geomechanics*, 4, 103-119.
- Vidal, H. (1969). "The principle of reinforced earth," *Highway Research Record*, 282, pp. 1-16.
- Walters, J.J. (2013). "Characterization of reinforced fill soil, soil-reinforcement interaction and global stability of very tall MSE walls." *MS Thesis*, Oregon State University, Corvallis, OR.
- Wan, R.G. and Guo, P.J. (2004). "Stress-dilatancy and fabric dependencies on sand behavior." *Journal of Engineering Mechanics*. 130(6), pp. 635-645.
- Wanatowski, D. and Chu, J. (2008). "Stress-Strain Behavior of a Granular Fill Measured by a New Plane-Strain Apparatus." *Geotechnical Testing Journal*, 29(2), pp. 1-9.
- Wang, J., Gutierrez, M. S., and Dove, J. E. (2007). "Numerical studies of shear banding in interface shear tests using a new strain calculation method." *International Journal for Numerical and Analytical Methods in Geomechanics*, 31(12), pp. 1349-1366.
- Wang, Q., and Lade, P. V. (2001). "Shear banding in true triaxial tests and its effect on failure in sand." *Journal of Engineering Mechanics*, 127(8), pp. 754-761.
- Wood, D. M. (1990). *Soil behaviour and critical state soil mechanics*, Cambridge University Press, Cambridge, 462 pp.
- Wood, D.M., and Maeda, K. (2008). "Changing grading of soil: effect on critical states." *Acta Geotechnica*, 3(1), pp. 3-14.

- Wright, S. G. (2005). "Design guidelines for multi-tiered MSE walls." No. *FHWA/TX-05/0-4485-2*, pp. 118.
- Xiao, Y., Liu, H., Chen, Y., and Chu, J. (2014a). "Influence of intermediate principal stress on the strength and dilatancy behavior of rockfill material." *Journal of Geotechnical and Geoenvironmental Engineering*, 140(11), 04014064.
- Xiao, Y., Liu, H., Chen, Y., and Jiang, J. (2014b). "Strength and deformation of rockfill material based on large-scale triaxial compression tests. I: Influences of Density and Pressure." *Journal of Geotechnical and Geoenvironmental Engineering*, 10.1061/(ASCE)GT.1943-5606.0001176, 04014070.
- Xiao, Y., Liu, H., Ding, X., Chen, Y., Jiang, J., and Zhang, W. (2015). "Influence of Particle Breakage on Critical State Line of Rockfill Material." *International Journal of Geomechanics*, 16(1), 04015031.
- Yamada, Y. and Ishihara, K. (1979). Anisotropic Deformation Characteristics of Sand under Three Dimensional Stress Conditions. *Soils Found.*, Vol. 19, No. 2, pp. 79–94.
- Zhao, H.F., Zhang, L.M., and Chang, D.S. (2013). Behavior of Coarse Widely Graded Soils under Low Confining Pressures. *Journal Geotechnical and Geoenvironmental Engineering*, 139(1), pp. 35-48.
- Zienciewicz, O.C. Humpheson, C. and Lewis, R.W. (1975). Associated and Non-Associated Visco-Plasticity and Plasticity in Soil Mechanics, *Géotechnique*, Vol. 25, 4, pp. 671-689.

APPENDIX A: RESULTS FROM PSK₀CD TESTS

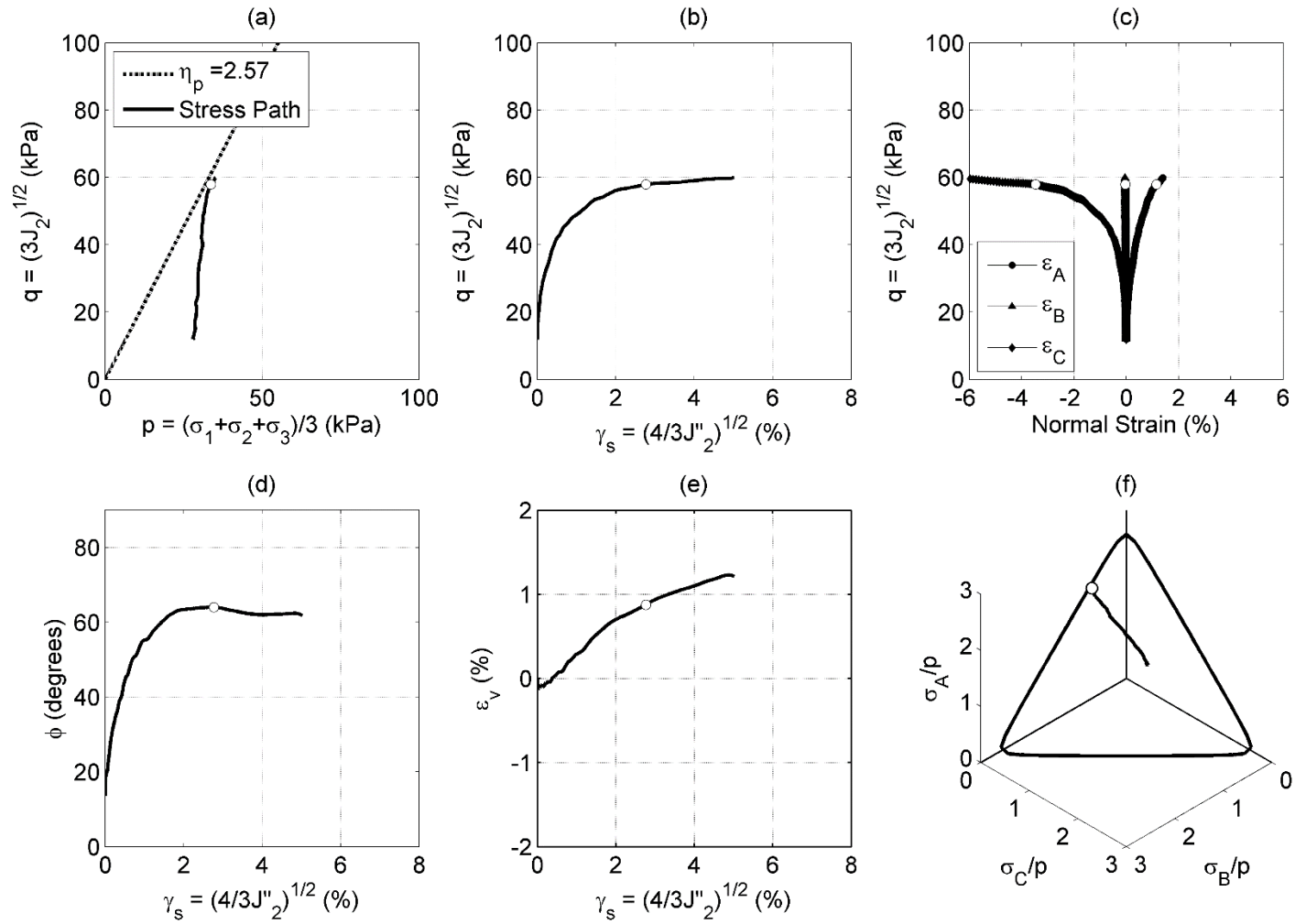


Figure A.1. Results from PSK₀CD test at $p'_0 = 28$ kPa on Kanaskat gravel: (a) stress path, (b) deviatoric stress versus shear strain, (c) deviatoric stress versus normal strain in principal stress directions, (d) friction angle versus shear strain, (e) burette volumetric strain measurement, (f) normalized 3-D stress path. (Note: white marker denotes failure)

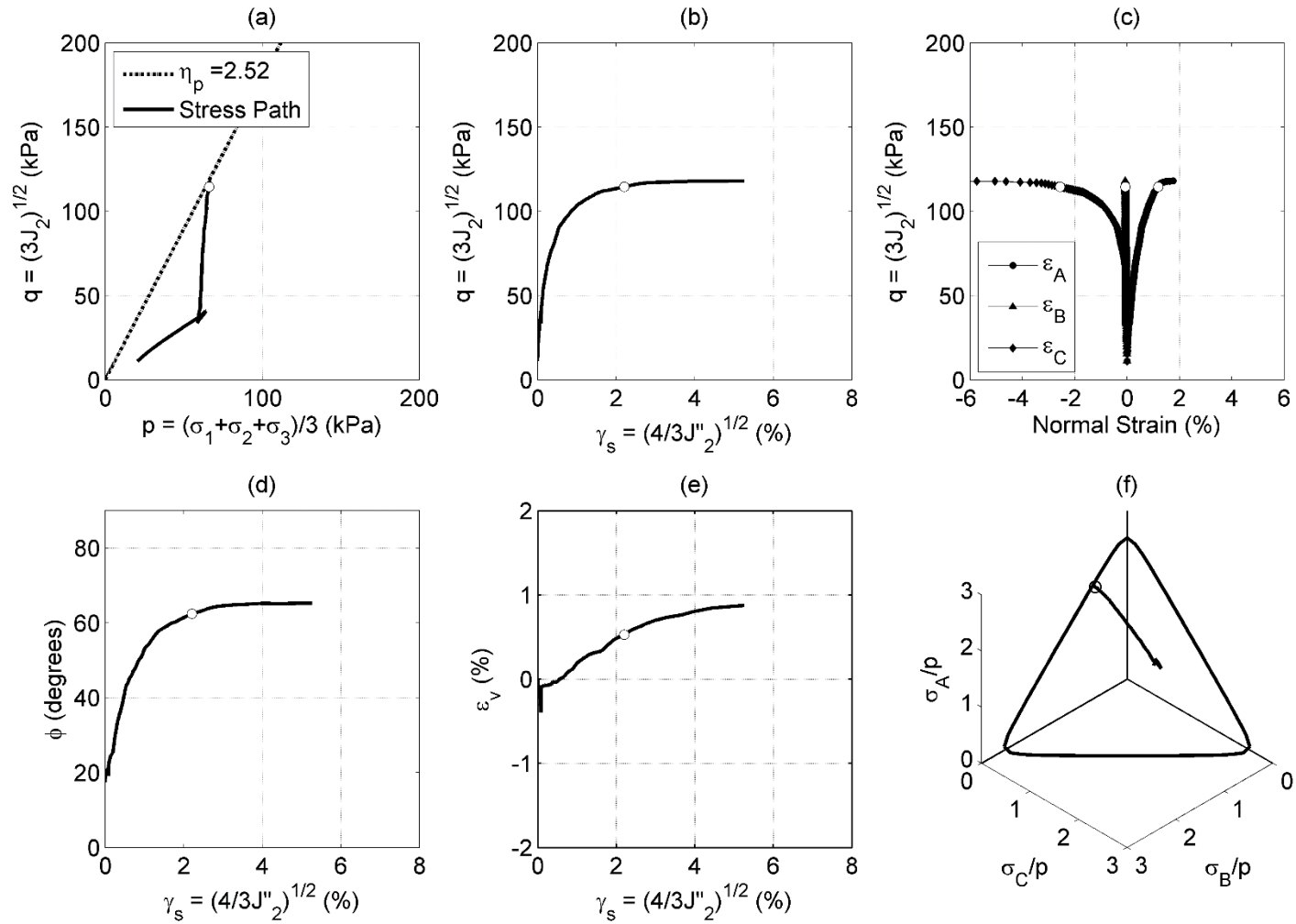


Figure A.2. Results from PSK₀CD test at $p'_0 = 63$ kPa on Kanaskat gravel1: (a) stress path, (b) deviatoric stress versus shear strain, (c) deviatoric stress versus normal strain in principal stress directions, (d) friction angle versus shear strain, (e) burette volumetric strain measurement, (f) normalized 3-D stress path. (Note: white marker denotes failure)

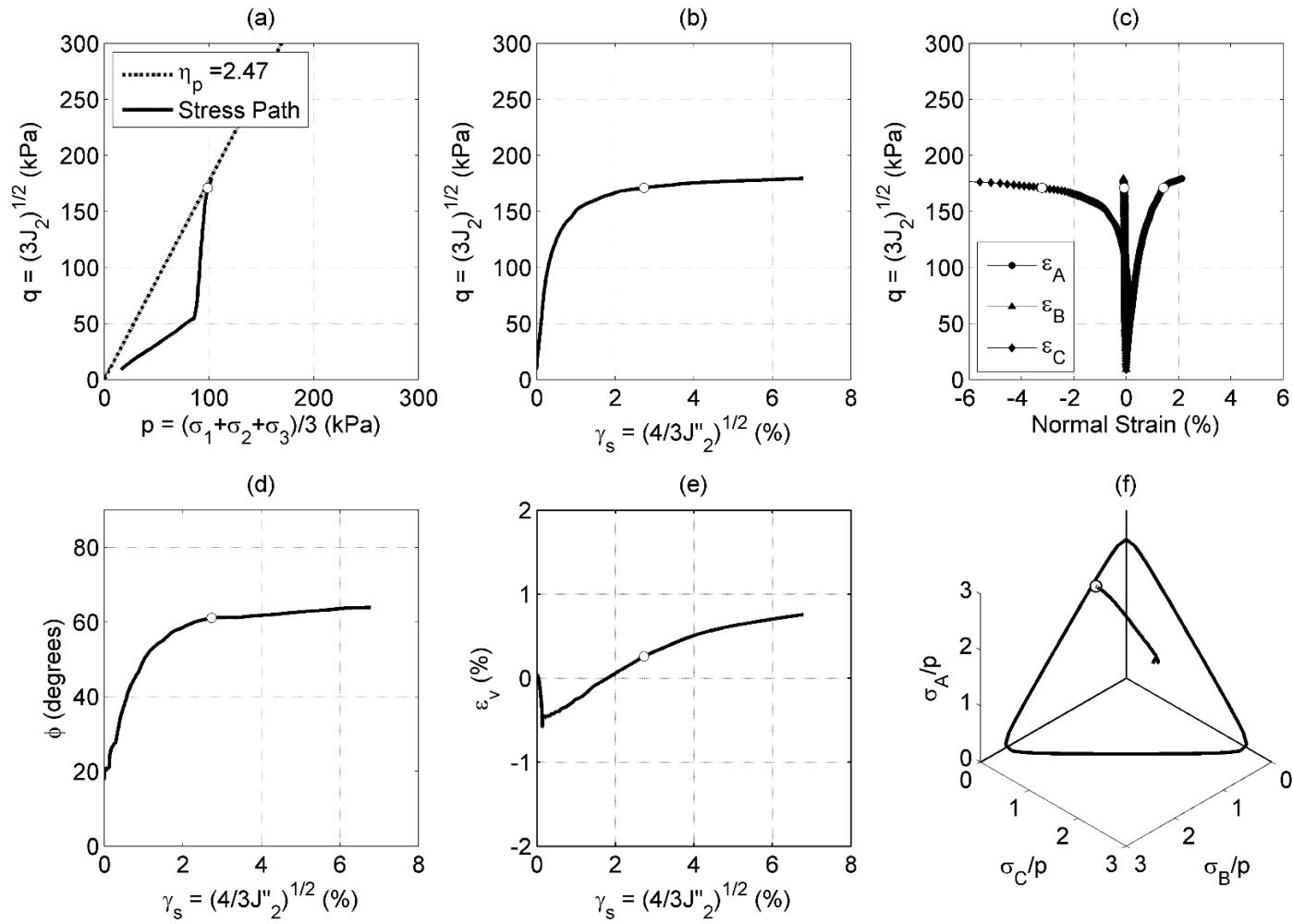


Figure A.3. Results from PSK₀CD test at $p'_0 = 86$ kPa on Kanaskat gravel: (a) stress path, (b) deviatoric stress versus shear strain, (c) deviatoric stress versus normal strain in principal stress directions, (d) friction angle versus shear strain, (e) burette volumetric strain measurement, (f) normalized 3-D stress path. (Note: white marker denotes failure)

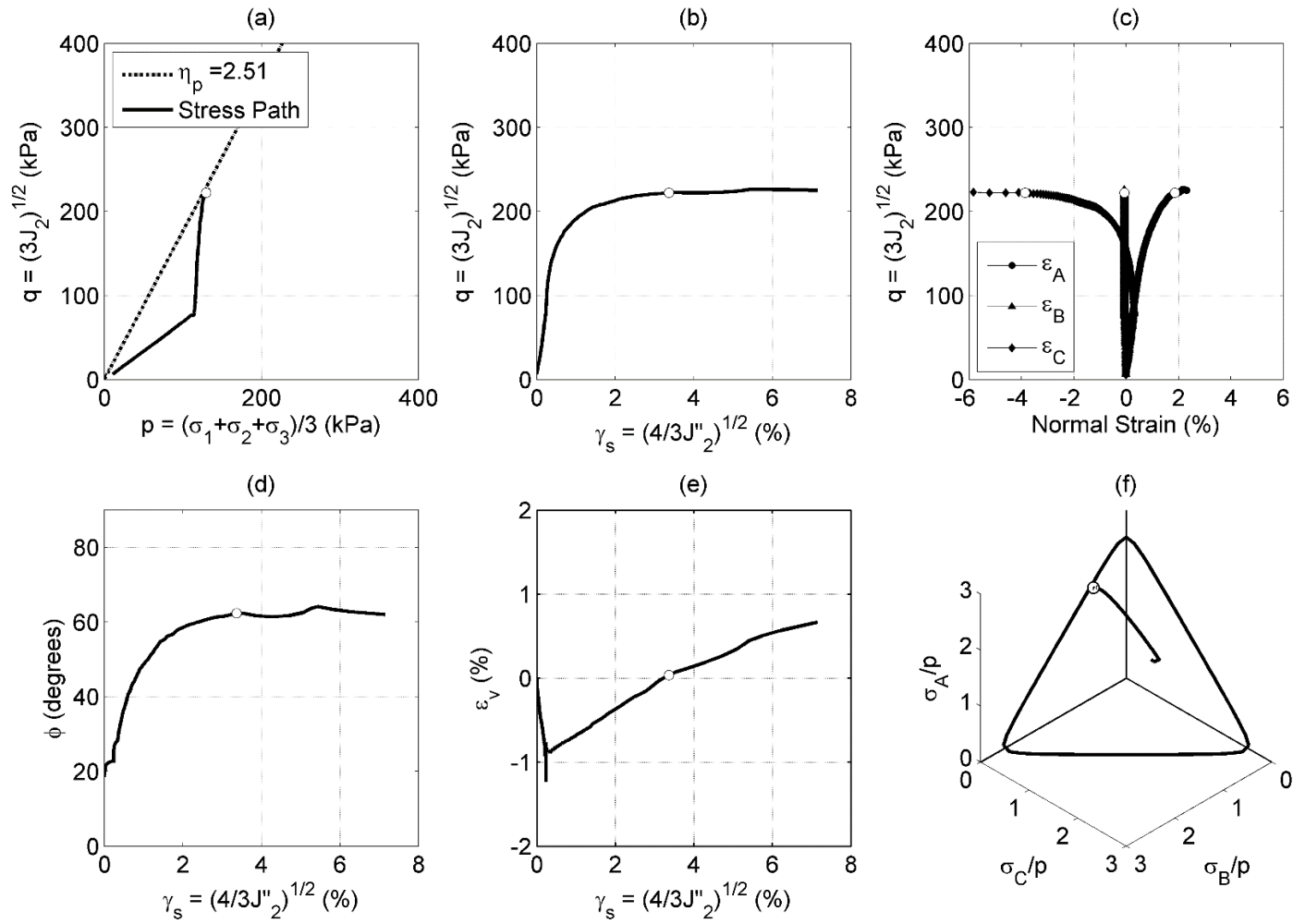


Figure A.4. Results from PSK₀CD test at $p'_0 = 114$ kPa on Kanaskat grave1: (a) stress path, (b) deviatoric stress versus shear strain, (c) deviatoric stress versus normal strain in principal stress directions, (d) friction angle versus shear strain, (e) burette volumetric strain measurement, (f) normalized 3-D stress path. (Note: white marker denotes failure)

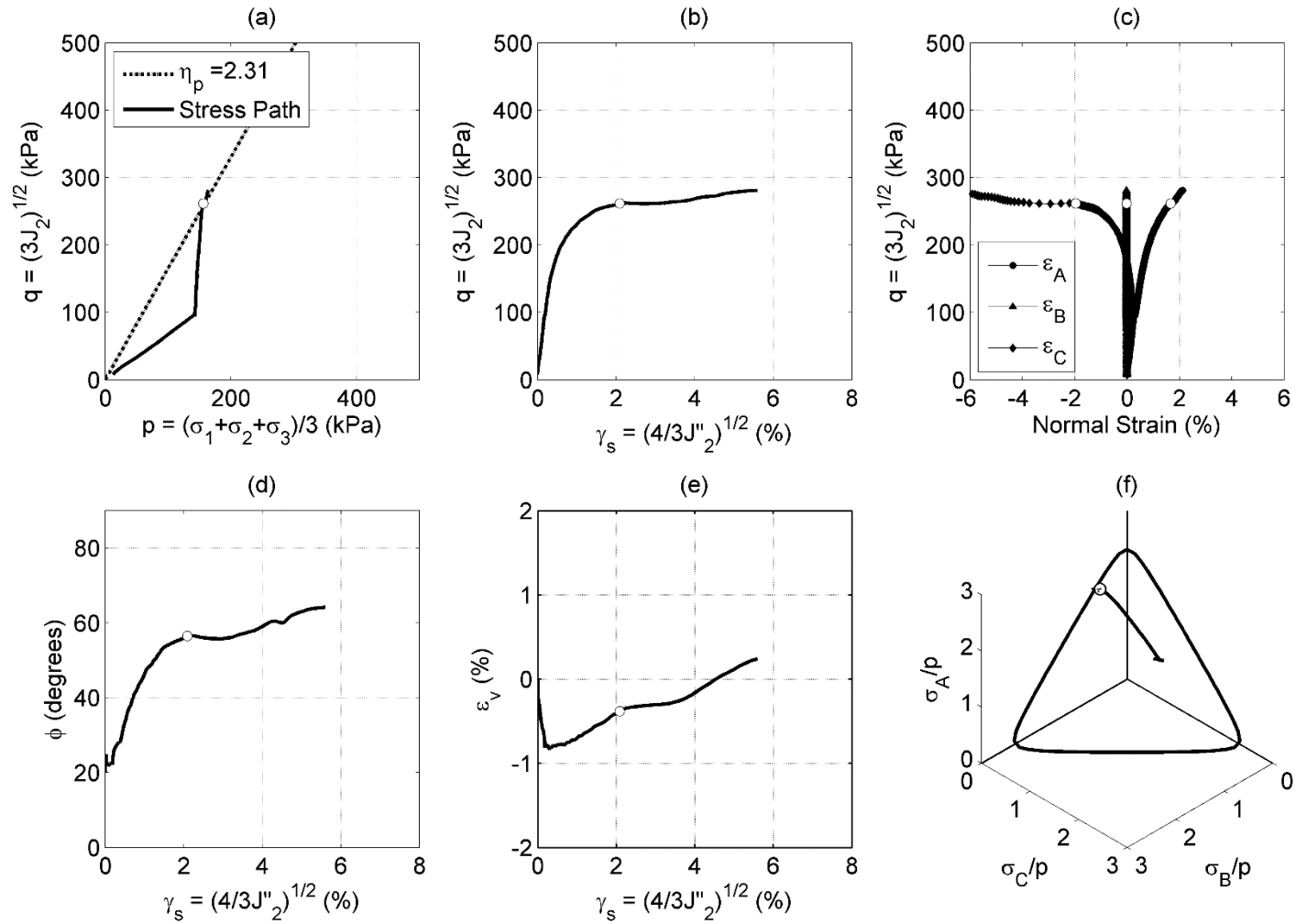


Figure A.5. Results from PSK₀CD test at $p'_0 = 147$ kPa on Kanaskat gravel1: (a) stress path, (b) deviatoric stress versus shear strain, (c) deviatoric stress versus normal strain in principal stress directions, (d) friction angle versus shear strain, (e) burette volumetric strain measurement, (f) normalized 3-D stress path. (Note: white marker denotes failure)

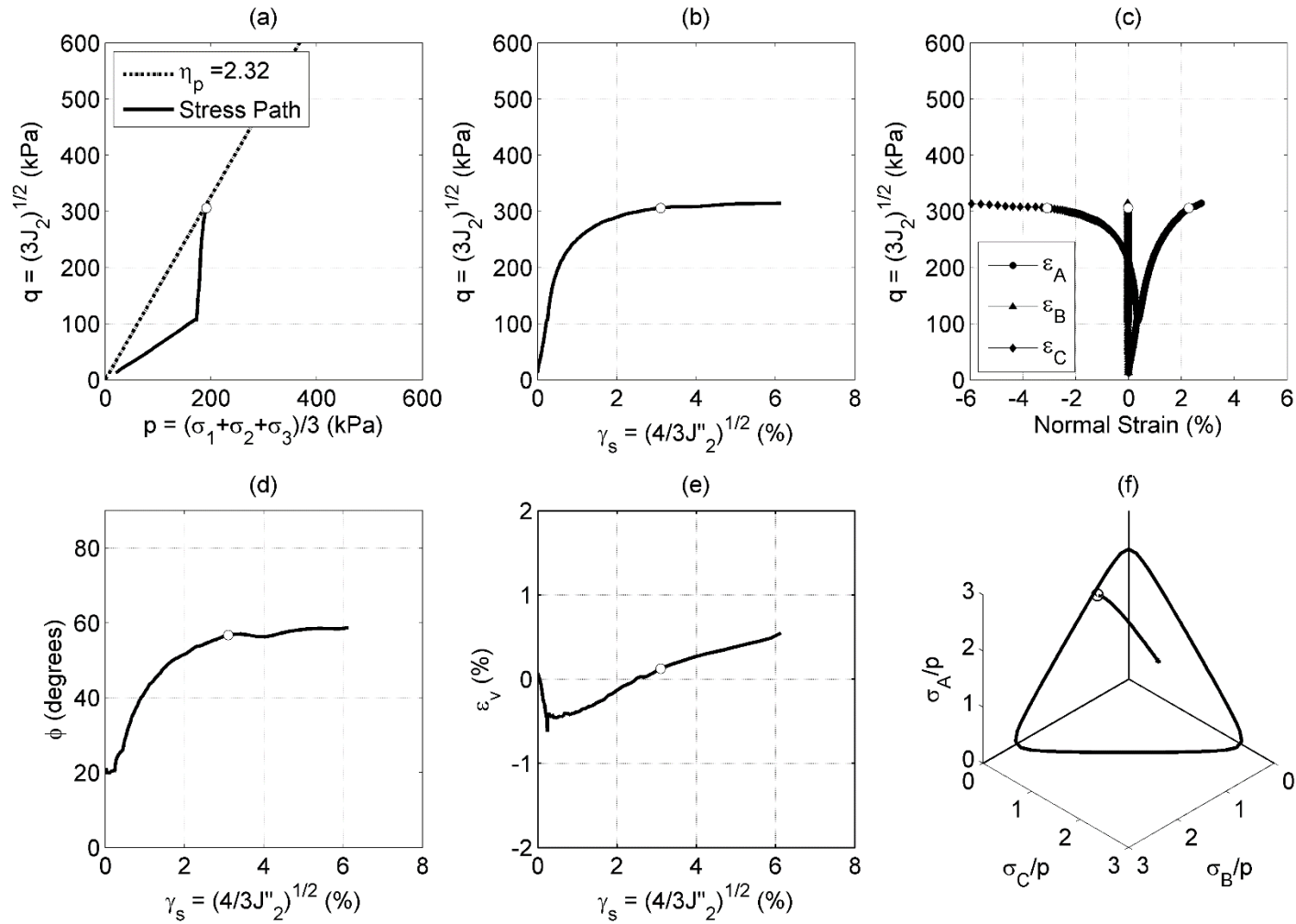


Figure A.6. Results from PSK₀CD test at $p'_0 = 172$ kPa on Kanaskat gravel1: (a) stress path, (b) deviatoric stress versus shear strain, (c) deviatoric stress versus normal strain in principal stress directions, (d) friction angle versus shear strain, (e) burette volumetric strain measurement, (f) normalized 3-D stress path. (Note: white marker denotes failure)

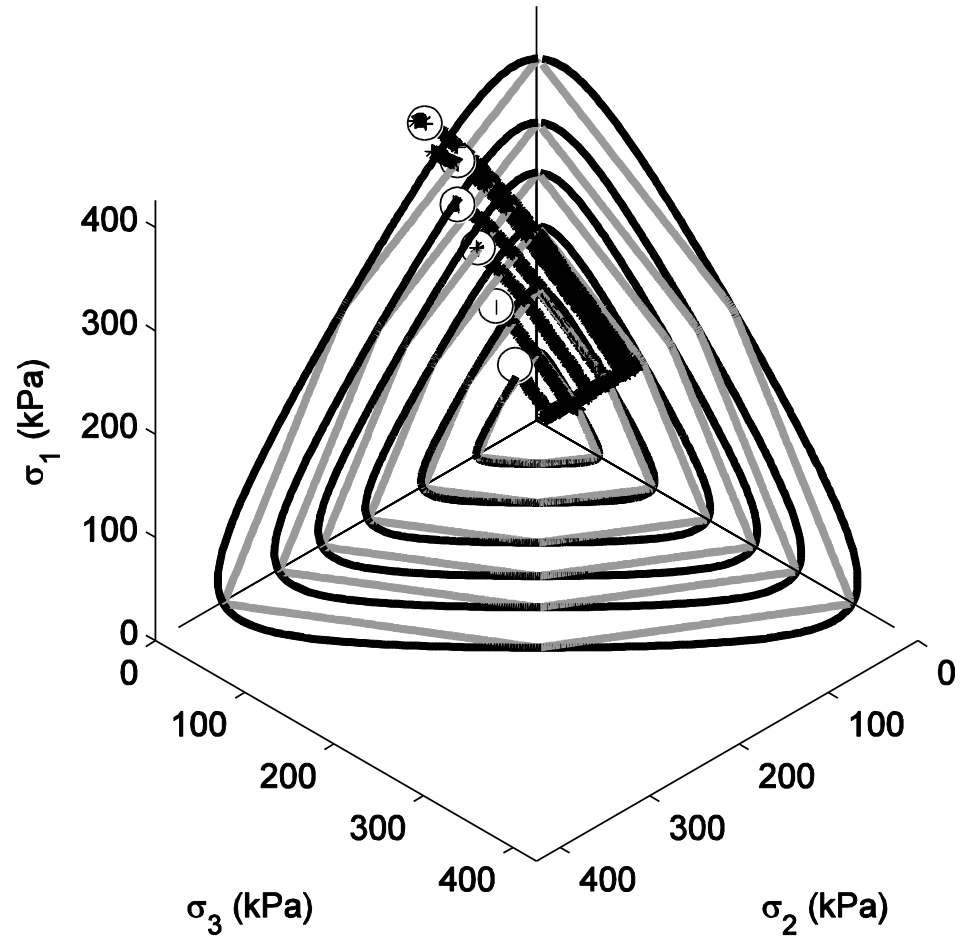


Figure A.7. Three dimensional stress path responses for all PSK₀CD tests compared to the Mohr-Coulomb (in grey) and Matsuoka Nakai (in black) failure surfaces. (Note: white marker denotes failure)

APPENDIX B: RESULTS FROM TC, TE, AND SS TESTS

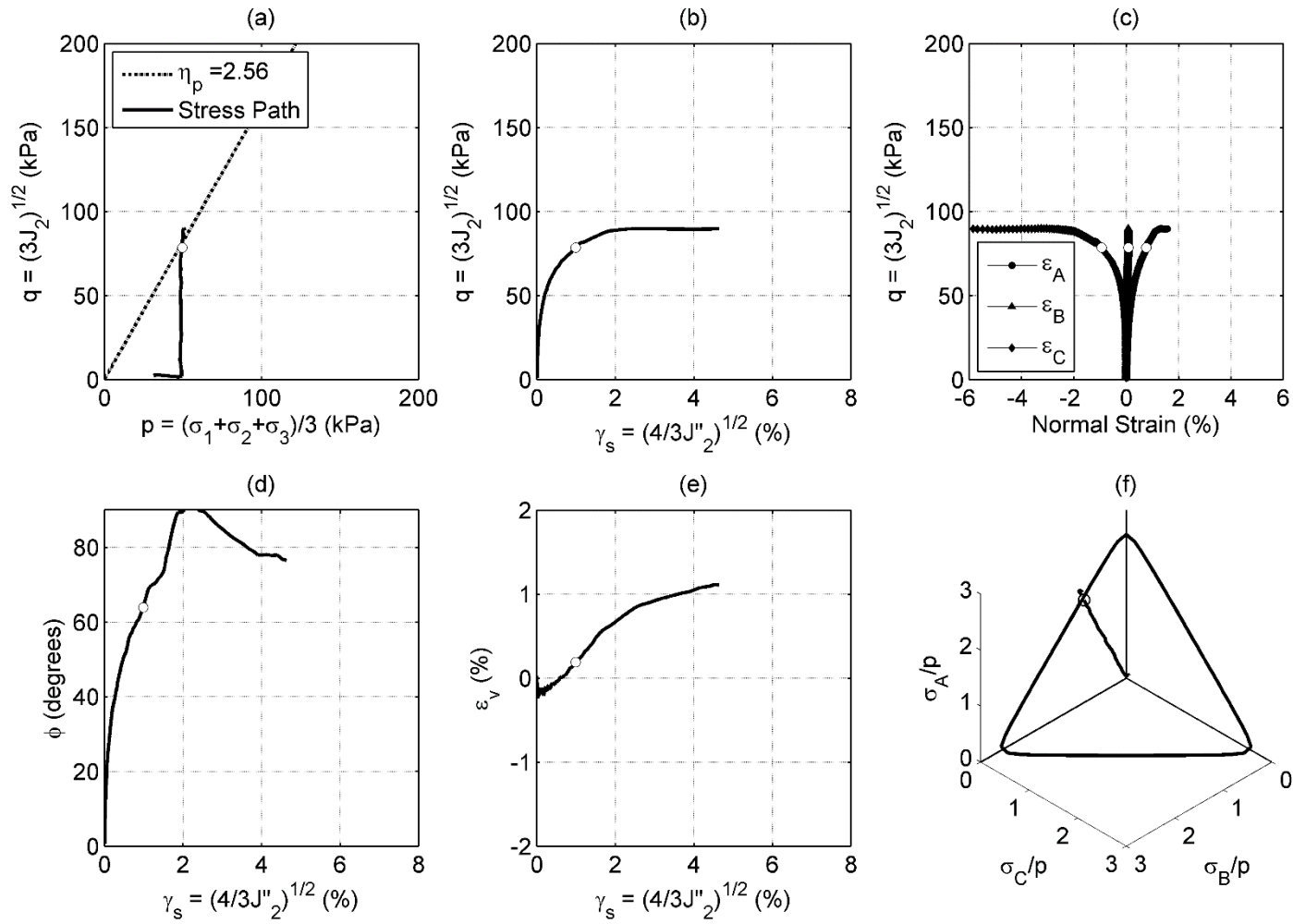


Figure B.1. Results from SS test at $p'_c = 49$ kPa on Kanaskat gravel1: (a) stress path, (b) deviatoric stress versus shear strain, (c) deviatoric stress versus normal strain in principal stress directions, (d) friction angle versus shear strain, (e) burette volumetric strain measurement, (f) normalized 3-D stress path. (Note: white marker denotes failure.)

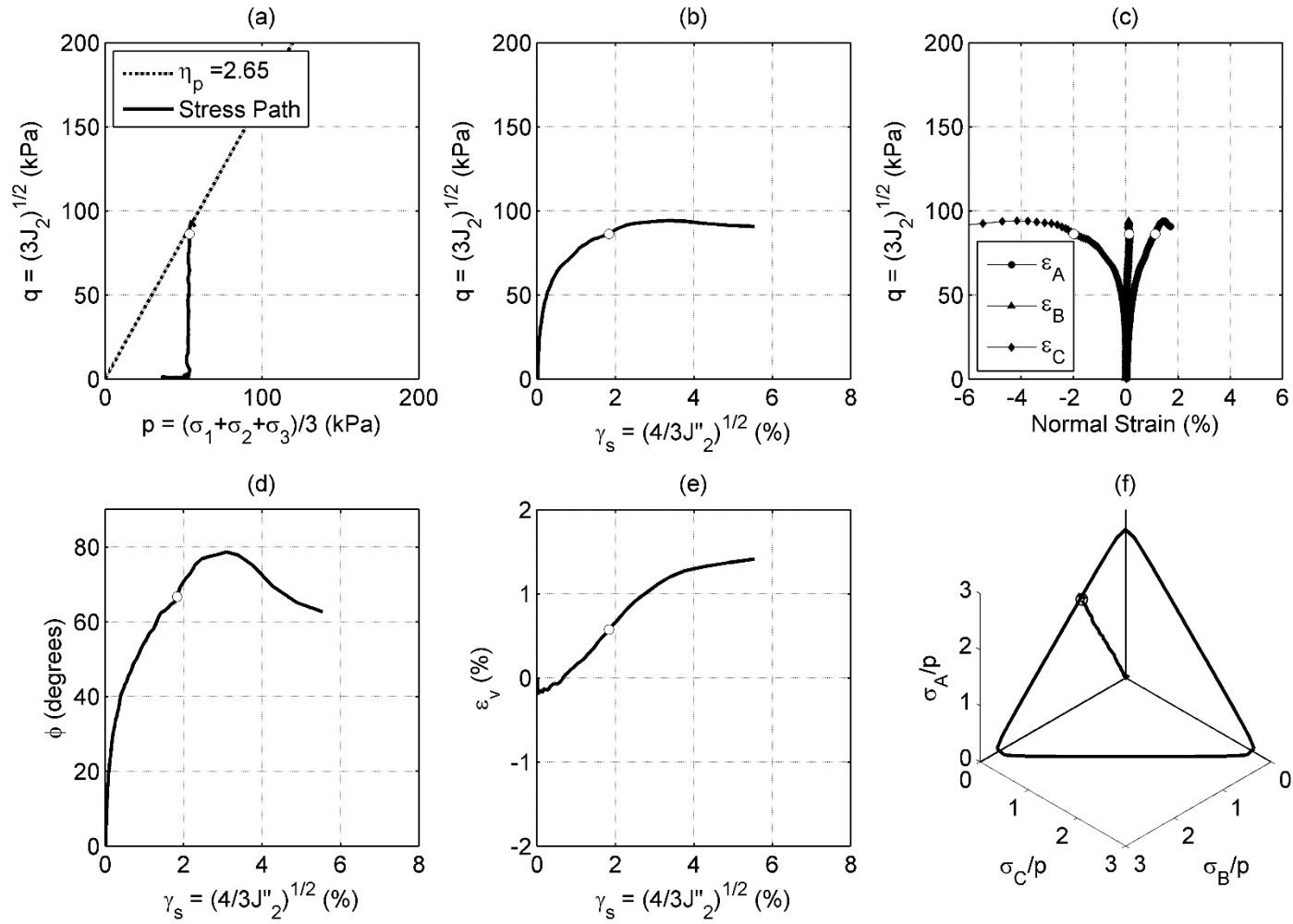


Figure B.2. Results from SS test at $p'_0 = 54$ kPa on Kanaskat grave1: (a) stress path, (b) deviatoric stress versus shear strain, (c) deviatoric stress versus normal strain in principal stress directions, (d) friction angle versus shear strain, (e) burette volumetric strain measurement, (f) normalized 3-D stress path. (Note: white marker denotes failure.)

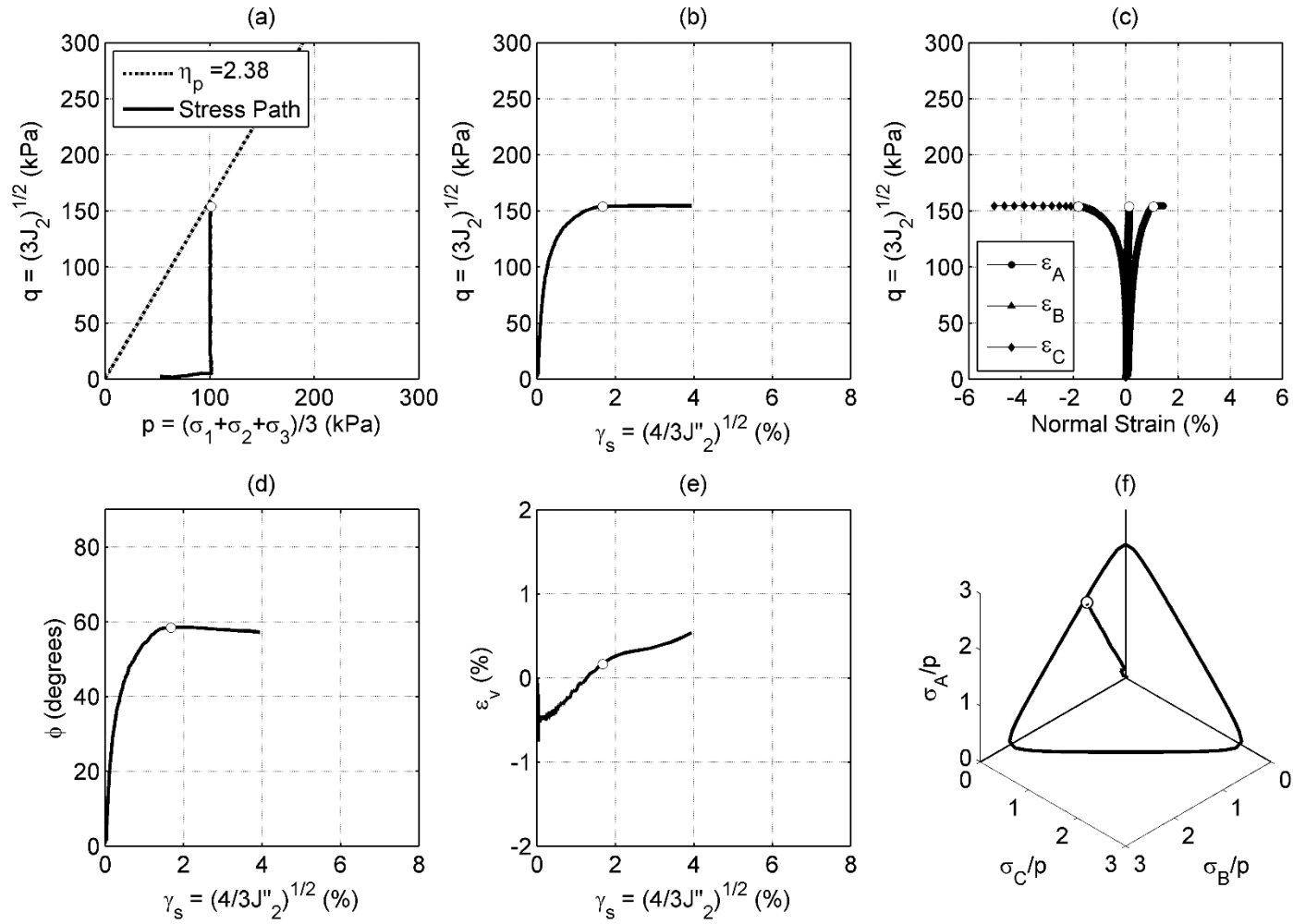


Figure B.3. Results from SS test at $p'_0 = 101$ kPa on Kanaskat gravel1: (a) stress path, (b) deviatoric stress versus shear strain, (c) deviatoric stress versus normal strain in principal stress directions, (d) friction angle versus shear strain, (e) burette volumetric strain measurement, (f) normalized 3-D stress path. (Note: white marker denotes failure.)

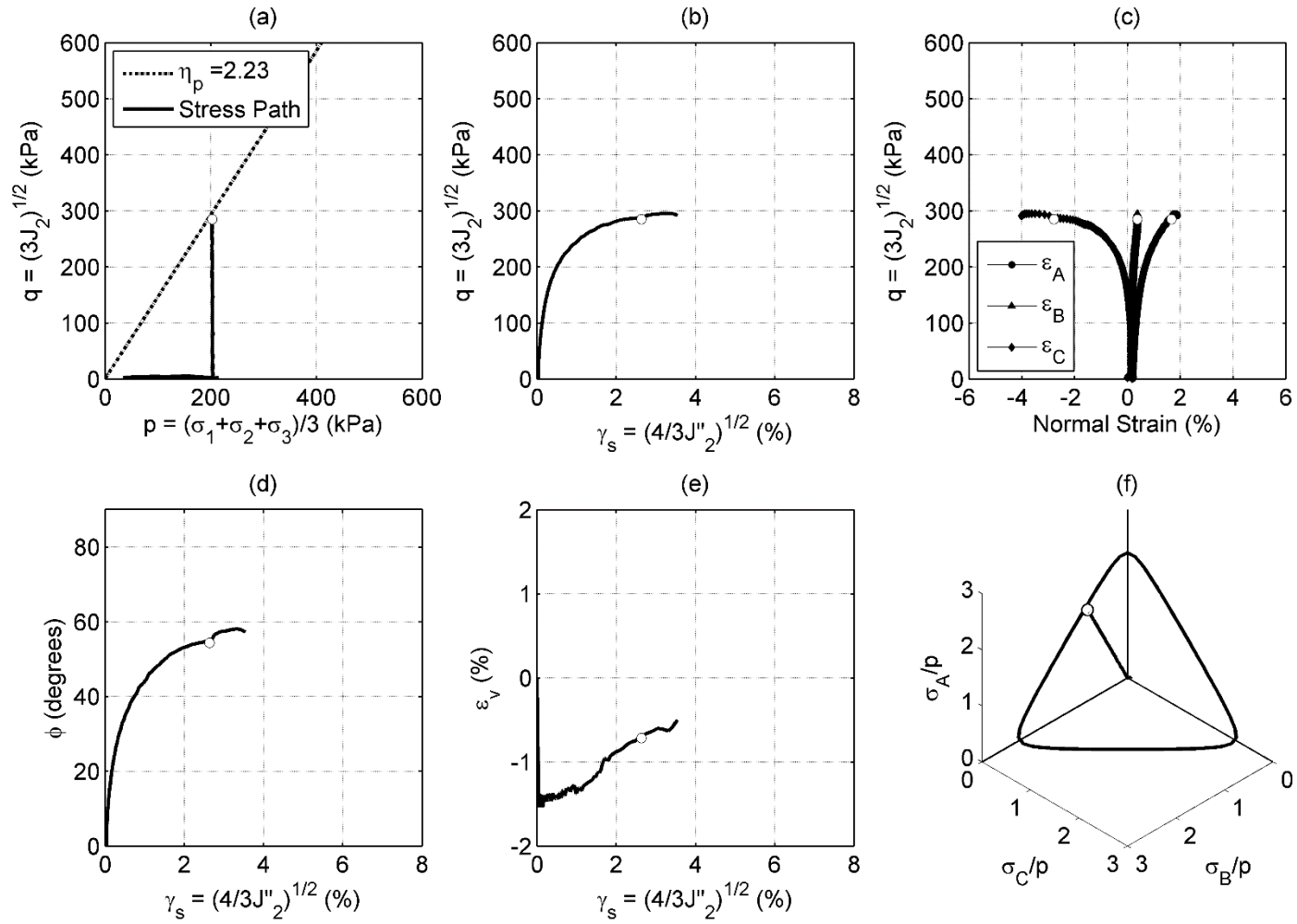


Figure B.4. Results from SS test at $p'_0 = 204$ kPa on Kanaskat gravel1: (a) stress path, (b) deviatoric stress versus shear strain, (c) deviatoric stress versus normal strain in principal stress directions, (d) friction angle versus shear strain, (e) burette volumetric strain measurement, (f) normalized 3-D stress path. (Note: white marker denotes failure.)

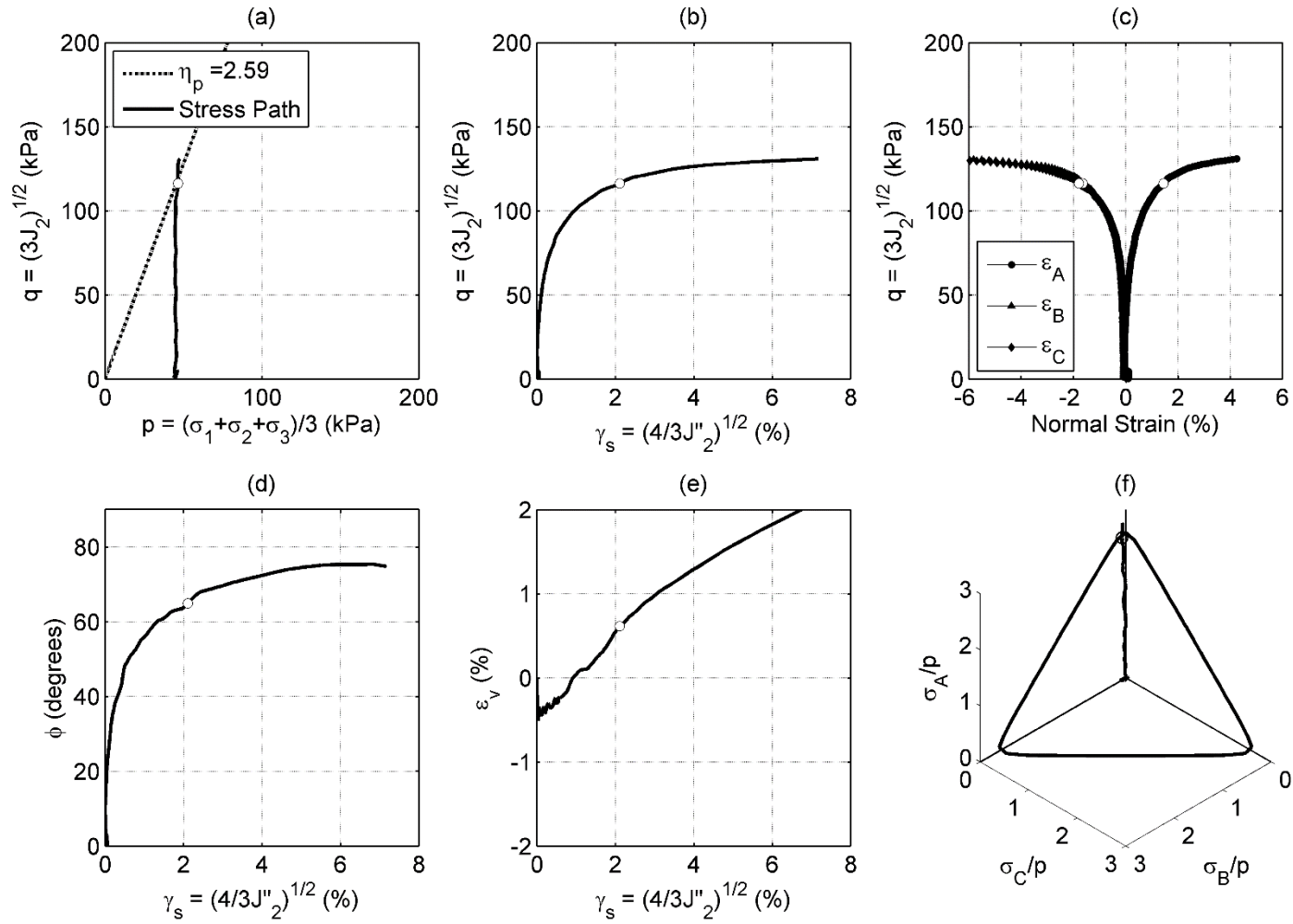


Figure B.5. Results from TC test at $p'_0 = 46$ kPa on Kanaskat grave1: (a) stress path, (b) deviatoric stress versus shear strain, (c) deviatoric stress versus normal strain in principal stress directions, (d) friction angle versus shear strain, (e) burette volumetric strain measurement, (f) normalized 3-D stress path. (Note: white marker denotes failure.)

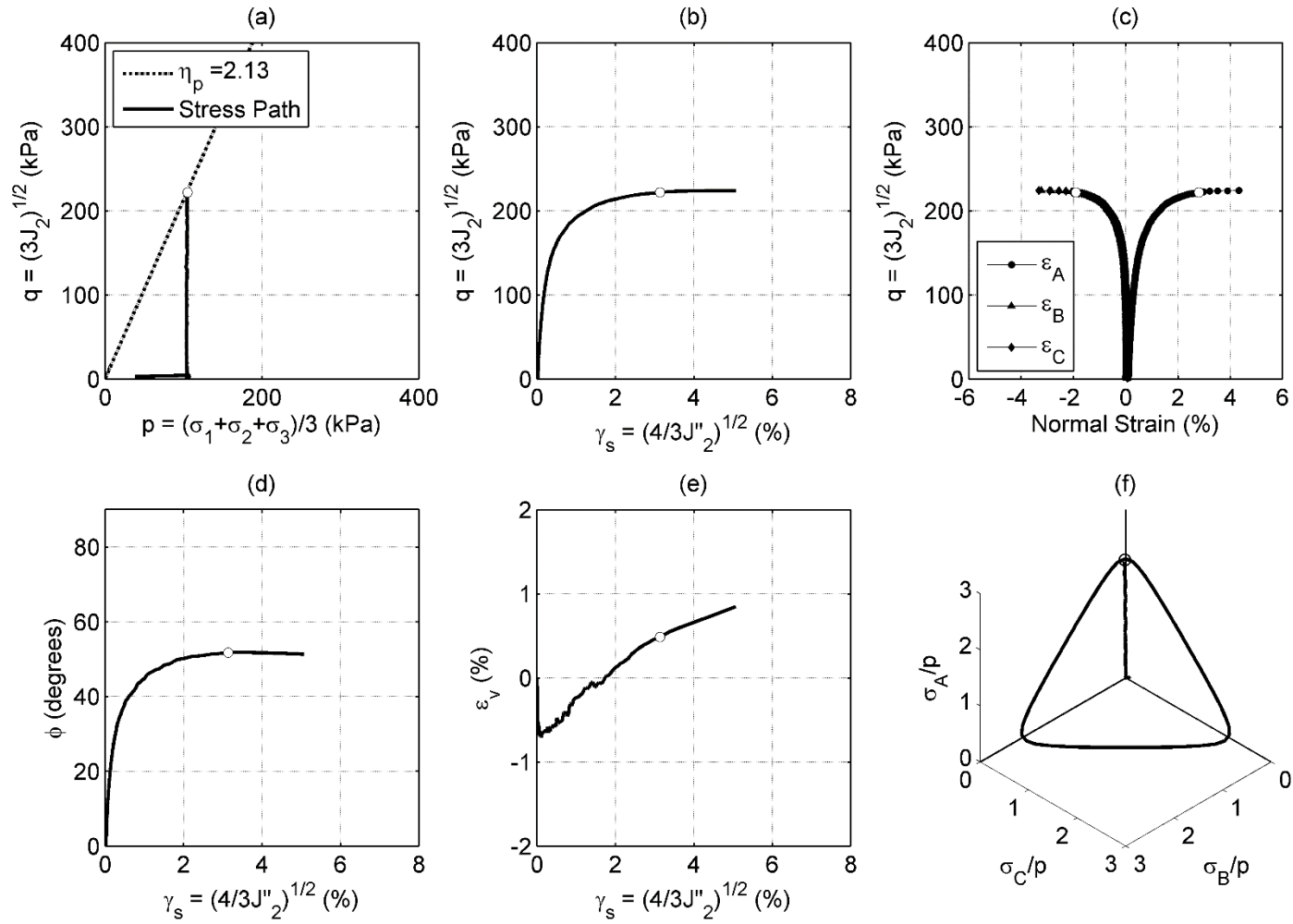


Figure B.6. Results from TC test at $p'_0 = 106$ kPa on Kanaskat gravel1: (a) stress path, (b) deviatoric stress versus shear strain, (c) deviatoric stress versus normal strain in principal stress directions, (d) friction angle versus shear strain, (e) burette volumetric strain measurement, (f) normalized 3-D stress path. (Note: white marker denotes failure.)

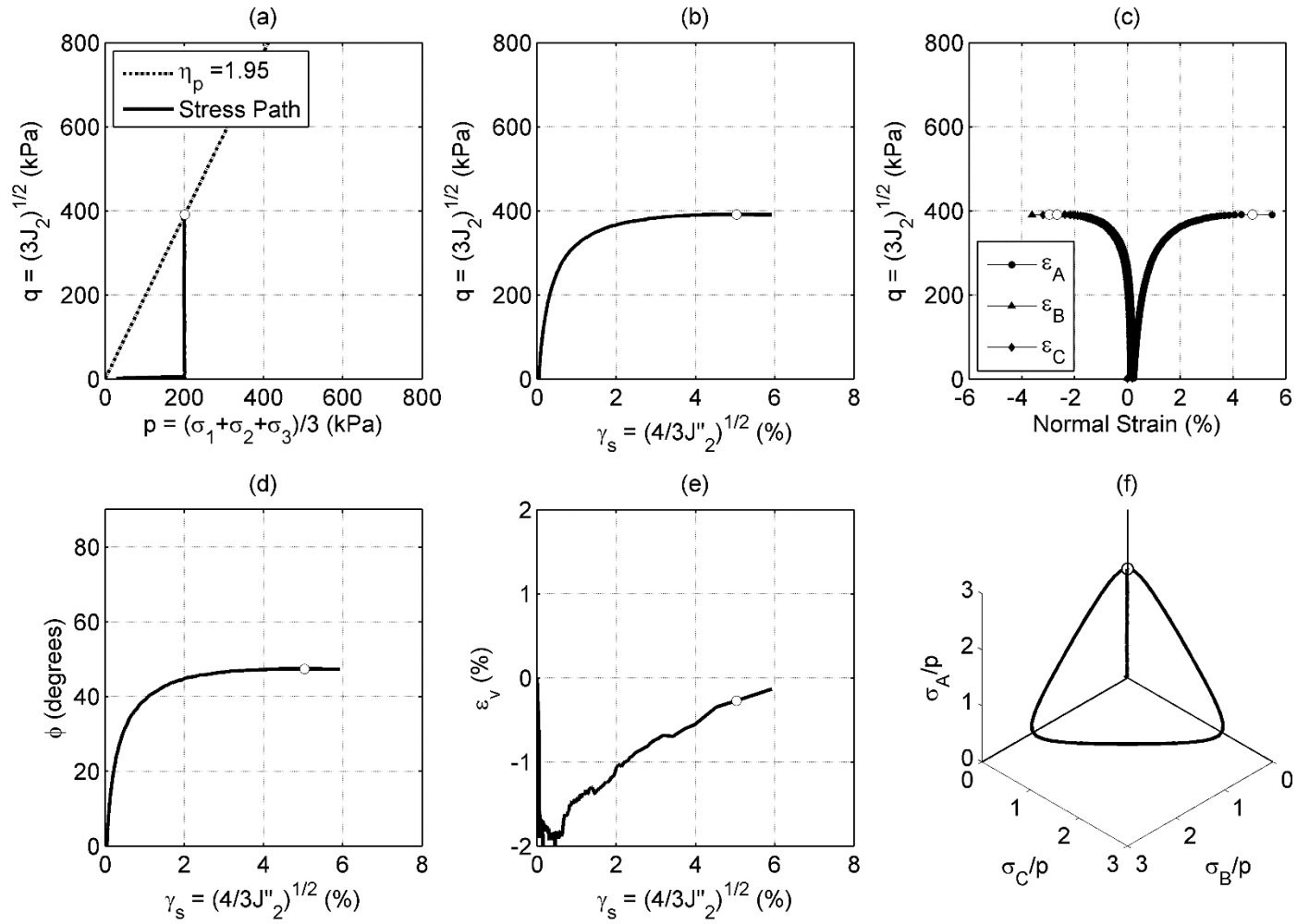


Figure B.7. Results from TC test at $p'_0 = 201$ kPa on Kanaskat gravel1: (a) stress path, (b) deviatoric stress versus shear strain, (c) deviatoric stress versus normal strain in principal stress directions, (d) friction angle versus shear strain, (e) burette volumetric strain measurement, (f) normalized 3-D stress path. (Note: white marker denotes failure.)

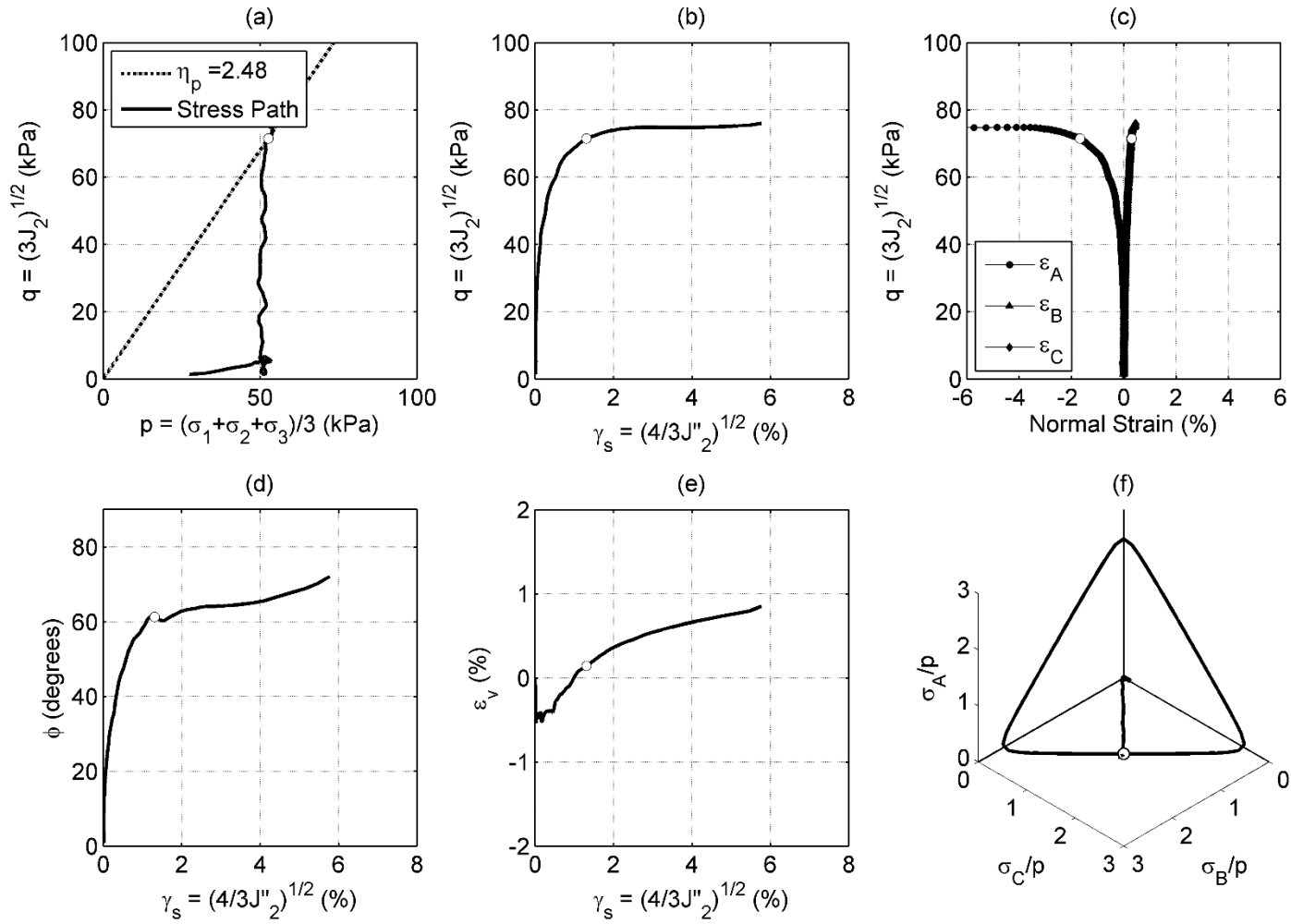


Figure B.8. Results from TE test at $p'_0 = 52$ kPa on Kanaskat grave1: (a) stress path, (b) deviatoric stress versus shear strain, (c) deviatoric stress versus normal strain in principal stress directions, (d) friction angle versus shear strain, (e) burette volumetric strain measurement, (f) normalized 3-D stress path. (Note: white marker denotes failure.)

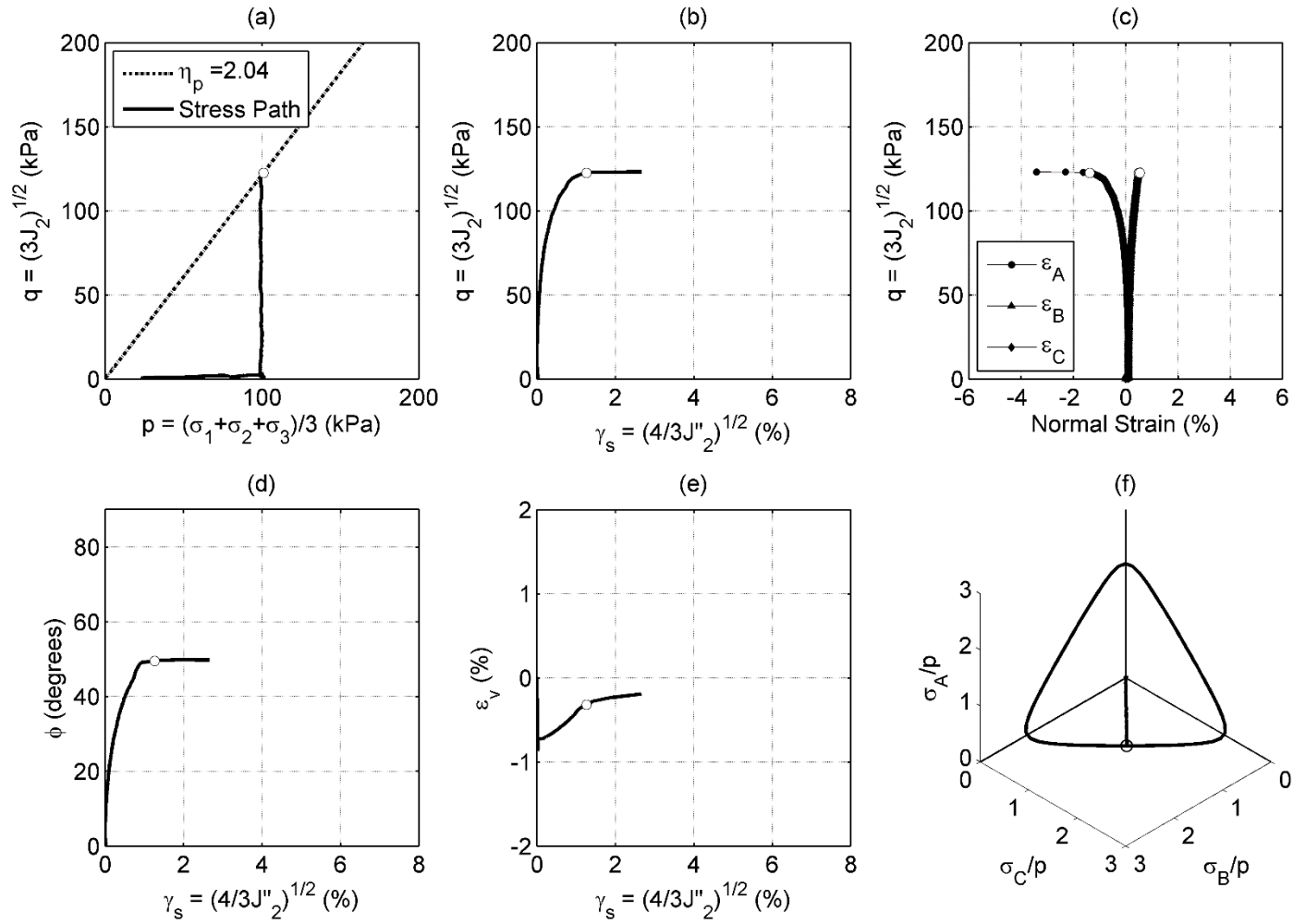


Figure B.9. Results from TE test at $p'_0 = 98$ kPa on Kanaskat grave1: (a) stress path, (b) deviatoric stress versus shear strain, (c) deviatoric stress versus normal strain in principal stress directions, (d) friction angle versus shear strain, (e) burette volumetric strain measurement, (f) normalized 3-D stress path. (Note: white marker denotes failure.)

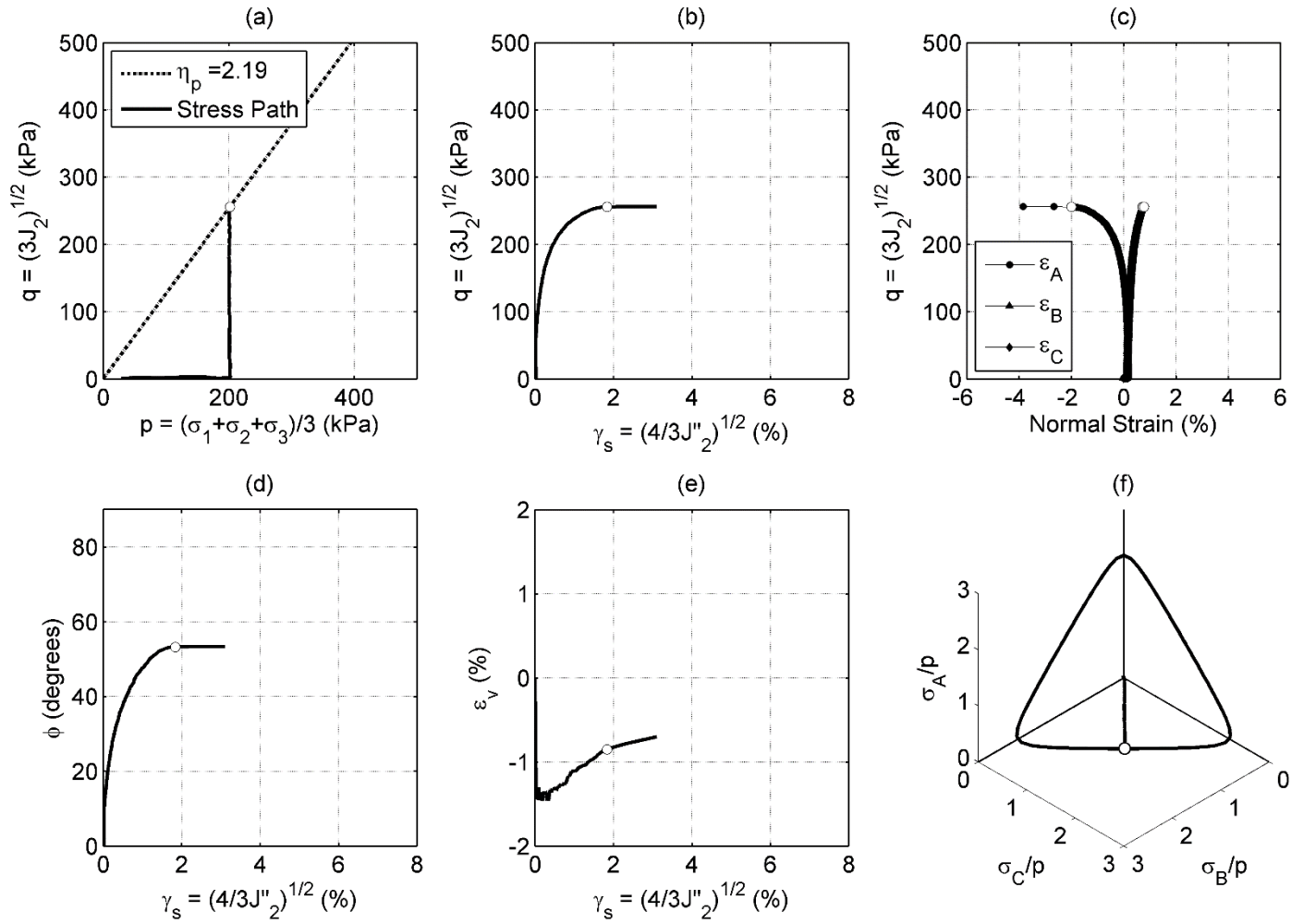


Figure B.10. Results from TE test at $p'_0 = 202$ kPa on Kanaskat grave1: (a) stress path, (b) deviatoric stress versus shear strain, (c) deviatoric stress versus normal strain in principal stress directions, (d) friction angle versus shear strain, (e) burette volumetric strain measurement, (f) normalized 3-D stress path. (Note: white marker denotes failure.)

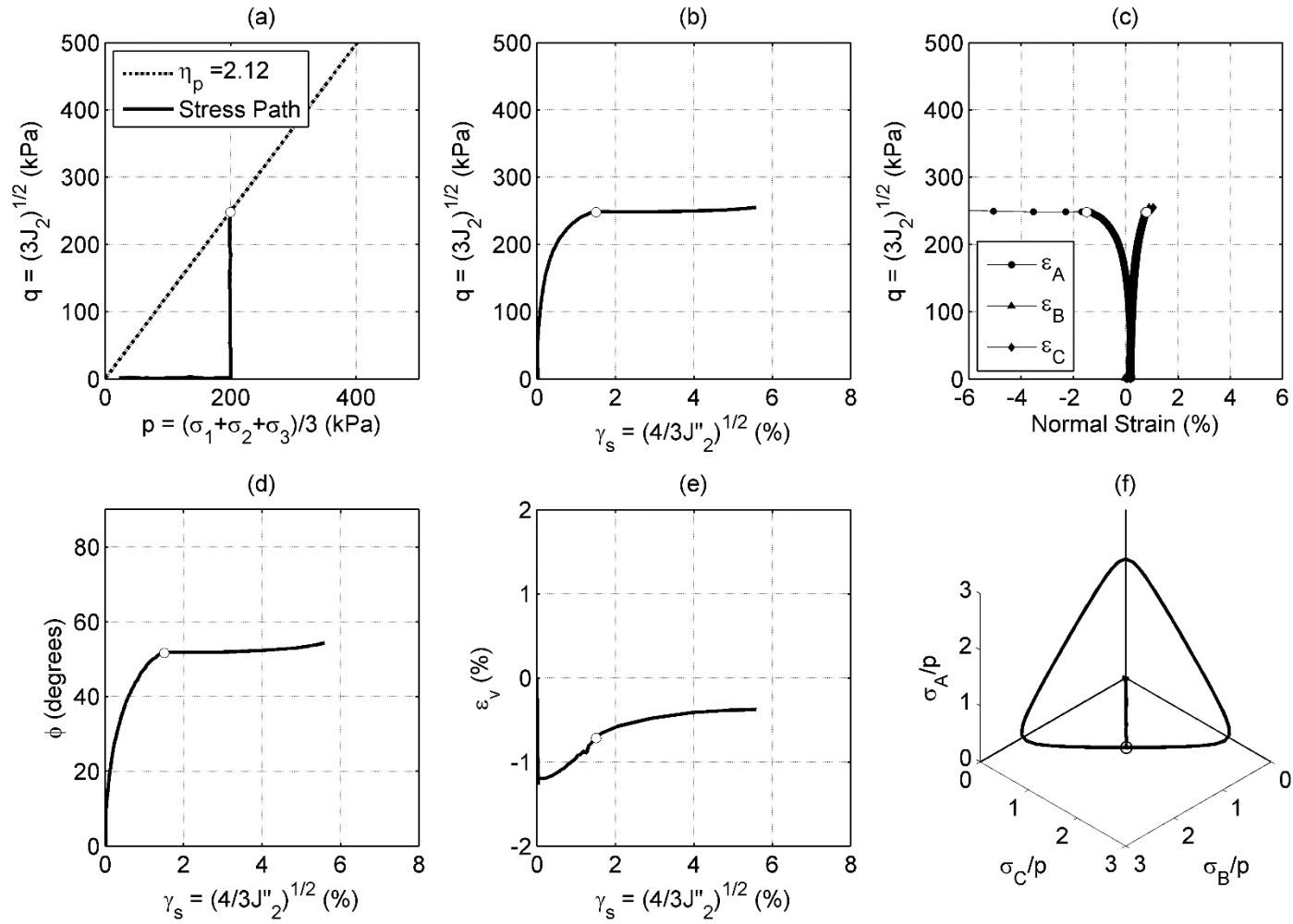


Figure B.11. Results from TE test at $p'_0 = 200$ kPa on Kanaskat grave1: (a) stress path, (b) deviatoric stress versus shear strain, (c) deviatoric stress versus normal strain in principal stress directions, (d) friction angle versus shear strain, (e) burette volumetric strain measurement, (f) normalized 3-D stress path. (Note: white marker denotes failure.)

APPENDIX C: DESIGN OF THE MULTI-STRIP PULLOUT BOX

Part 1: Design Calculations and Procedures

Part 2: Shop Drawings and 3-D renderings

Part 3: Supplemental appendix for Chapter 5.

PART 1: DESIGN CALCULATIONS AND PROCEDURES

Pages: 291 – 313

BIG BOX STRUCTURAL DESIGN

A large steel box (5' x 5' x 6.6') is to be constructed to facilitate multiple inclusion pull out tests on steel reinforcement in a well graded gravelly soil. The Big Box Design (BBD) will be completed using ASD design requirements. Preliminary drawings for the BBD are attached. The box will be pressurized with 300 kPa using a large bladder positioned at the top of the box.

$$h := 5\text{ft} \quad w := 5\text{ft} \quad P_{\text{bladder}} := 300\text{kPa} = 43.5\cdot\text{psi}$$

The expected horizontal soil pressure is calculating using an expected friction angle:

$$\phi := 50\text{deg} \quad \gamma_{\text{soil}} := 145\text{pcf} \quad K_a := 45\text{deg} - \frac{\phi}{2} = 0.3$$

$$P_{\text{weight}} := h \cdot \gamma_{\text{soil}} = 5\cdot\text{psi} \quad P_{\text{horsoil}} := K_a \cdot h \cdot \gamma_{\text{soil}} = 2\cdot\text{psi}$$

As a result the design pressure for the top and bottom of the box is:

$$P_{\text{top}} := P_{\text{bladder}} = 43.5\cdot\text{psi} \quad P_{\text{bottom}} := P_{\text{top}} + P_{\text{weight}} = 48.5\cdot\text{psi}$$

Design using the largest of these two pressures (for conservatism):

$$P_{\text{design}} := \max(P_{\text{top}}, P_{\text{bottom}}) = 48.5\cdot\text{psi}$$

To minimize the amount of reinforcement required the thickness of the plate containing the soil was chosen to be 1/2" thick.

$$t_p := 0.5\text{in}$$

For all steel:

$$F_y := 36\text{ksi} \quad F_u := 58\text{ksi} \quad E := 29000\text{ksi}$$

1.0 Design support spacing based on rigid plate flexure:

$$\Omega_b := 1.67$$

$$b := 60\text{in}$$

$$w := P_{\text{design}} \cdot b = 2912.8 \cdot \frac{\text{lb}}{\text{in}} \quad I_{\text{plate}} := \frac{b \cdot t_p^3}{12} = 0.625 \cdot \text{in}^4 \quad y := \frac{t_p}{2}$$

$$M_n := \frac{F_y \cdot I_{\text{plate}}}{y} = 90 \cdot \text{kip} \cdot \text{in} \quad \frac{M_n}{\Omega_b} = 53.9 \cdot \text{kip} \cdot \text{in}$$

Try:

$$s_{fl} := 12\text{in} \quad M_{\text{app}} := \frac{w \cdot s_{fl}^2}{8} = 52.4 \cdot \text{kip} \cdot \text{in}$$

$$M_{\text{app}} \leq \frac{M_n}{\Omega_b} = 1$$

Therefore flange to flange distance must be limited to 12".

2.0 Size top support beam for flexure and shear

2.0 Size top support beam for flexure:

$$\Omega_b := 1.67$$

$$L := 60 \text{ in}$$

Assume flange width: $b_f := 6 \text{ in}$

Center to center spacing: $s_c := s_{fl} + b_f = 18 \text{ in}$

$$w := P_{\text{design}} \cdot s_c = 0.87 \cdot \frac{\text{kip}}{\text{in}} \quad M_{\text{app}} := \frac{w \cdot L^2}{8} = 393.2 \cdot \text{kip} \cdot \text{in}$$

Assume: $Z_{\text{req}} := \frac{M_{\text{app}} \cdot \Omega_b}{F_y} = 18.2 \cdot \text{in}^3$

Try W8 x 21

$$Z_x := 20.4 \text{ in}^3 \quad r_y := 1.26 \text{ in} \quad b_f := 5.27 \text{ in} \quad s_{fl} := s_{fl} + b_f = 17.27 \text{ in}$$

$$A_g := 6.16 \text{ in}^2 \quad I := 75.3 \text{ in}^4 \quad t_f := 0.400 \text{ in} \quad t_w := 0.250 \text{ in} \quad d := 8.28 \text{ in}$$

$$T := 6.25 \text{ in}$$

$$w := P_{\text{design}} \cdot s_c = 0.84 \cdot \frac{\text{kip}}{\text{in}} \quad M_{\text{app}} := \frac{w \cdot L^2}{8} = 377.3 \cdot \text{kip} \cdot \text{in}$$

$$M_n := F_y \cdot Z_x = 734.4 \cdot \text{kip} \cdot \text{in} \quad \frac{M_n}{\Omega_b} = 439.8 \cdot \text{kip} \cdot \text{in} \quad M_{\text{app}} \leq \frac{M_n}{\Omega_b} = 1$$

W8 x 21 works in flexure

Check lateral torsion buckling

$$L_p := 1.76 \cdot r_y \cdot \sqrt{\frac{E}{F_y}} = 62.9 \text{ in} \quad L_b := L \quad L_b \leq L_p = 1$$

Therefore ok.

Size top support beam for tension:

Assume design pressure acts in horizontal and vertical pressure. In reality this pressure is reduced by K_a in the horizontal direction but will maintain for conservatism.

$$w = 838.4 \frac{\text{lbf}}{\text{in}} \quad L := 64 \text{ in} \quad \Omega_t := 1.67 \quad P_n := F_y \cdot A_g = 221.8 \cdot \text{kip}$$

$$P_{\text{app}} := w \cdot \frac{L}{2} = 26.8 \cdot \text{kip}$$

$$\frac{P_n}{\Omega_t} = 132.8 \cdot \text{kip}$$

$$P_{\text{app}} \leq \frac{P_n}{\Omega_t} = 1$$

Therefore ok.

Size top support beam for bending and tension:

$$P_r := P_{\text{app}} = 26.8 \cdot \text{kip} \quad M_r := M_{\text{app}} = 377.3 \cdot \text{kip} \cdot \text{in}$$

$$P_c := \frac{P_n}{\Omega_t} = 132.8 \cdot \text{kip} \quad M_c := \frac{M_n}{\Omega_b} = 439.8 \cdot \text{kip} \cdot \text{in} \quad \frac{P_r}{P_c} = 0.202$$

$$Z := \begin{cases} \left[\frac{P_r}{P_c} + \frac{8}{9} \left(\frac{M_r}{M_c} \right) \right] & \text{if } \frac{P_r}{P_c} \geq 0.2 \\ \frac{P_r}{2P_c} + \left(\frac{M_r}{M_c} \right) & \text{if } \frac{P_r}{P_c} < 0.2 \end{cases}$$

$$Z \leq 1 = 1$$

Therefore ok.

Check deflection

$$w = 838.4 \frac{\text{lbf}}{\text{in}} \quad L := 60 \text{ in}$$

$$\Delta_{\text{all}} := \frac{L}{580} = 0.103 \text{ in}$$

$$\Delta_{\text{max}} := \frac{5 \cdot w \cdot L^4}{384 \cdot E \cdot I} = 0.065 \text{ in}$$

$$\Delta_{\text{max}} \leq \Delta_{\text{all}} = 1$$

Therefore ok.

2.1 Size top support beam for shear:

$$w = 838.4 \frac{\text{lbf}}{\text{in}} \quad V_{\text{app}} := \frac{w \cdot L}{2} = 25.15 \cdot \text{kip} \quad A_g = 6.2 \text{ in}^2 \quad \Omega_v := 1.50$$

$$A_w := d \cdot t_w \quad C_v := 1.0 \quad \frac{T}{t_w} = 25 \quad 2.24 \cdot \sqrt{\frac{E}{F_y}} = 63.6$$

$$V_n := 0.6 \cdot F_y \cdot A_w \cdot C_v = 44.7 \cdot \text{kip}$$

$$\frac{V_n}{\Omega_v} = 29.8 \cdot \text{kip}$$

$$V_{\text{app}} \leq \frac{V_n}{\Omega_v} = 1$$

TOP SUPPORT BEAM SUMMARY

W8X21 $s_c = 17.27 \text{ in}$ Must be less than this

This beam size and spacing to be used through out the rest of the box as the main support (i.e. the rear section of the box and sides).

2.0 Size top support beam for flexure and shear

3.0 W-section connection design

3.0 Design W-section connection of the side support beams to top beams

Bolts will transfer the vertical load from the top beams through a 1/2" plate to to the side beams. The bolts should be checked for shear forces produced from the horizontal pressures. The plate will be welded to the top and bottom of the side W-sections.

W8 x 21

$$Z_x := 20.4 \text{ in}^3 \quad r_{yy} := 1.26 \text{ in} \quad b_x := 5.27 \text{ in} \quad s_{fl} := s_{fl} + b_f = 17.27 \text{ in}$$

$$A_x := 6.16 \text{ in}^2 \quad I_x := 75.3 \text{ in}^4 \quad t_c := 0.400 \text{ in} \quad t_{ww} := 0.250 \text{ in} \quad d := 8.28 \text{ in}$$

$$T := 6.25 \text{ in}$$

Bolts connecting W-section to plate - Tension

$$w = 0.838 \cdot \frac{\text{kip}}{\text{in}} \quad L := 60 \text{ in} \quad R_{appt} := w \cdot \frac{L}{2} = 25.2 \cdot \text{kip}$$

Try 1 bolt on each side of the web $n := 4$

$$r_{appt} := \frac{R_{appt}}{n} = 6.3 \cdot \text{kip} \quad d_b := \frac{7}{8} \text{ in}$$

$$A_b := 0.60 \text{ in}^2$$

Available tensile strength: A325 N S 7/8" bolt

$$r_c := 40.6 \text{ kip}$$

$$r_{appt} \leq r_c = 1$$

Min Spacing: $s_{min} := 2.667 \cdot d_b = 2.33 \text{ in}$ Therefore ok.

Bolts connecting W-section to plate - Shear

$$w = 0.838 \cdot \frac{\text{kip}}{\text{in}} \quad L := 60 \text{ in} \quad R_{appv} := w \cdot \frac{L}{2} = 25.2 \cdot \text{kip}$$

Try 1 bolt on each side of the web

$$r_{appv} := \frac{R_{appv}}{n} = 6.3 \cdot \text{kip}$$

Available shear strength: A325 N S 7/8" bolt

$$r_{cc} := 21.6 \text{ kip} \quad R_c := r_c \cdot n = 86.4 \cdot \text{kip}$$

$$\Omega := 2.00$$

$$r_{appv} \leq r_c = 1$$

Therefore ok.

Bolts connecting W-section to plate - Combined Shearing and Tension

$$F_{nt} := 90 \text{ ksi} \quad F_{nv} := 48 \text{ ksi} \quad \Omega_{vt} := 2.00$$

$$f_v := \frac{r_{appv}}{A_b} = 10.5 \cdot \text{ksi} \quad r_{appt} = 6.3 \cdot \text{kip}$$

$$F'_{nt} := 1.3 \cdot F_{nt} - \frac{\Omega_{vt} \cdot F_{nt}}{F_{nv}} \cdot f_v = 77.8 \cdot \text{ksi} \quad F'_{nt} \leq F_{nv} = 0$$

$$r_n := F'_{nt} \cdot A_b = 46.7 \cdot \text{kip} \quad \frac{r_n}{\Omega_{vt}} = 23.4 \cdot \text{kip}$$

$$r_{appt} \leq \frac{r_n}{\Omega_{vt}} = 1$$

Therefore ok.

Bolts connecting W-section to plate - Bearing strength in flange section

Distance from edge of beam to bolt

$$L_c := 1.8425 \text{ in} \quad \Omega := 2.00 \quad s_w := 3.5 \text{ in}$$

$$R_{n1} := 1.5 \cdot L_c \cdot t_f \cdot F_u = 64.1 \cdot \text{kip} \quad R_{n2} := 3.0 \cdot d_b \cdot t_f \cdot F_u = 60.9 \cdot \text{kip}$$

$$R_n := \min(R_{n1}, R_{n2})$$

$$\frac{R_n}{\Omega} = 30.5 \cdot \text{kip}$$

$$r_{appv} \leq \frac{R_n}{\Omega_t} = 1$$

Therefore ok.

Min Spacing: $s_{min} := 2.667 \cdot d_b = 2.33 \text{ in}$

Min Edge Distance: $L_{cmin} := 1.5 \text{ in}$

Bolts are not slip critical.

Bolts connecting W-section to plate - Flange local bending

$$R_{nw} := 6.25 \cdot t_f^2 \cdot F_y = 36 \cdot \text{kip} \quad 0.15 \cdot b_f = 0.8 \text{ in} \quad \Omega_f := 1.67$$

$10 \cdot t_f = 4 \text{ in}$ Bolts must be 5 in from the end of the beam.

$$\frac{R_n}{\Omega_f} = 21.6 \cdot \text{kip}$$

$$\frac{R_{appt}}{\frac{n}{2}} = 12.6 \cdot \text{kip}$$

$$\frac{R_{appt}}{\left(\frac{n}{2}\right)} \leq \frac{R_n}{\Omega_f} = 1$$

Therefore ok.

Bolts connecting W-section to plate - Web local yielding

$$F_{yw} := F_y \quad k := 0.700 \text{ in} \quad N := 4.375 \text{ in} \quad \Omega_w := 1.50$$

$$R_{ww} := (2.5 \cdot k + N) \cdot F_{yw} \cdot t_w = 55.1 \cdot \text{kip}$$

$$\frac{R_n}{\Omega_w} = 36.8 \cdot \text{kip} \quad R_{appt} = 25.2 \cdot \text{kip}$$

$$R_{appt} \leq \frac{R_n}{\Omega_w} = 1$$

Therefore ok.

Plate to W-section - Weld Design

Design weld for tension:

Length of weld: $l_1 := b_f - t_w$

$$F_{E70} := 70 \text{ ksi} \quad D := 5 \text{ in} \quad l_w := 2 \cdot (l_1) \quad \Omega_{weld} := 2.00$$

$$R_{ww} := 0.6 \cdot F_{E70} \cdot \frac{\sqrt{2}}{2} \cdot \frac{D}{16} \cdot l_w = 93.2 \cdot \text{kip}$$

$$\frac{R_n}{\Omega_{weld}} = 46.6 \cdot \text{kip}$$

$$r_{appt} < \frac{R_n}{\Omega_{weld}} = 1$$

$$t_f = 0.4 \text{ in}$$

Check base metal thickness: Therefore ok

$$t_{\min} := \frac{0.6 \cdot F_{E70} \cdot \frac{\sqrt{2}}{2} \cdot \frac{D}{16}}{0.6 F_u} = 0.267 \text{ in}$$

$$t_{\min} \leq t_f = 1$$

4.0 Rear angle connection design

4.0 Design angle connection of the rear support beams to sides

An angle will be used to connect the rear support to the sides of the box. It is likely that a stiffener will be necessary at the W section connection.

Bolts connecting angle to plate - Shear

Assume that all the shear from each rear support is taken up by bolts located directly across from it on the angle.

$$w = 0.838 \cdot \frac{\text{kip}}{\text{in}} \quad L := 60\text{in} \quad R_{\text{appv}} := w \cdot \frac{L}{2} = 25.2 \cdot \text{kip}$$

1 bolt on each side of the stiffener.

$$n := 2 \quad r_{\text{appv}} := \frac{R_{\text{appv}}}{n} = 12.6 \cdot \text{kip} \quad d_b := \frac{7}{8}\text{in} \quad A_b := 0.601\text{in}^2$$

Available shear strength: A325 N S 3/4" bolt

$$r_{\text{av}} := 15.9\text{kip} \quad R_c := r_c \cdot n = 31.8 \cdot \text{kip}$$

$$\Omega := 2.00$$

$$r_{\text{appv}} \leq r_c = 1$$

Therefore ok.

Bolts connecting angle to plate - Tension

The angle will supply a moment and subsequent tension in the bolt depending on distance from the center of moment.

Try: L6 x 3 1/2 x 1/2

Workable gages for legs:

$$\Omega := 2.00$$

$$W_{G6} := 3.5\text{in}$$

$$W_{G3.5} := 2\text{in}$$

Use these for moment arm calculations

$$R_{\text{appt}} := \frac{R_{\text{appv}} \cdot W_{G3.5}}{W_{G6}} = 14.4 \cdot \text{kip} \quad r_{\text{appt}} := \frac{R_{\text{appt}}}{n} = 7.2 \cdot \text{kip}$$

Available tensile strength: A325 N S 7/8" bolt

$$r_{\text{av}} := 29.8\text{kip}$$

$$r_{\text{appt}} \leq r_c = 1$$

Min Spacing:

$$s_{\text{min}} := 2.667 \cdot d_b = 2.33\text{in}$$

Therefore ok.

Bolts connecting angle to plate - Combined Shearing and Tension

$$F_u := 90 \text{ ksi} \quad F_y := 48 \text{ ksi} \quad \Omega := 2.00$$

$$f_t := \frac{r_{\text{appt}}}{A_b} = 20.9 \text{ ksi} \quad r_{\text{appt}} = 7.2 \text{ kip}$$

$$F'_t := 1.3 \cdot F_{nt} - \frac{\Omega \cdot F_{nt}}{F_{nv}} \cdot f_v = 38.5 \text{ ksi} \quad F'_{nt} \leq F_{nv} = 1$$

$$r'_t := F'_t \cdot A_b = 23.2 \text{ kip} \quad \frac{r_n}{\Omega_t} = 13.9 \text{ kip} \quad r_{\text{appt}} \leq \frac{r_n}{\Omega_t} = 1$$

Therefore ok.

Bolts connecting angle to plate - Edge distance and bearing on plate

$$L_{\text{min}} := W_{G6} - \frac{d_b}{2} = 3.06 \text{ in} \quad \Omega := 2.00$$

$$R_{n1} := 1.5 \cdot L_c \cdot t_p \cdot F_u = 133.2 \text{ kip} \quad R_{n2} := 3.0 \cdot d_b \cdot t_p \cdot F_u = 76.1 \text{ kip}$$

$$R_n := \min(R_{n1}, R_{n2})$$

$$\frac{R_n}{\Omega} = 38.1 \text{ kip} \quad r_{\text{appt}} \leq \frac{R_n}{\Omega_t} = 1$$

Therefore ok.

Min Spacing: $s_{\text{min}} := 2.667 \cdot d_b = 2.33 \text{ in}$

Min Edge Distance: $L_{\text{min}} := 1.5 \text{ in}$

Bolts are not slip critical.

Bolts connecting angle to W-section - Tension

$$\Omega_t = 1.67$$

$$R_{\text{appw}} := R_{\text{appv}} = 25.2 \text{ kip} \quad r_{\text{appt}} := \frac{R_{\text{appt}}}{n} = 12.6 \text{ kip}$$

Available tensile strength: A325 N S 7/8" bolt

$$r_c := 27.1 \text{ kip} \quad r_{\text{appt}} \leq r_c = 1$$

Therefore ok.

Bolts connecting angle to W-section - Web local yielding

$$F_y := F_y \quad k := 0.859 \text{ in} \quad N := 3.5 \text{ in} \quad \Omega_w := 1.50$$

$$R_w := (2.5 \cdot k + N) \cdot F_{yw} \cdot t_w = 50.8 \cdot \text{kip}$$

$$\frac{R_n}{\Omega_w} = 33.9 \cdot \text{kip} \quad R_{appt} = 25.2 \cdot \text{kip}$$

$$R_{appt} \leq \frac{R_n}{\Omega_w} = 1$$

Therefore ok.

Angle to W-section - Stiffener Sizing

$$t_1 := 0.5 \text{ in} \quad \Omega_m := 1.67$$

$$M_{app} := R_{appt} \cdot W_{G3.5} = 50.3 \cdot \text{kip} \cdot \text{in}$$

$$A_1 := s_c \cdot t_1 = 8.6 \text{ in}^2 \quad I_{angle} := \frac{s_c \cdot t_1^3}{12} = 0.18 \text{ in}^4$$

$$M_{angle} := \frac{F_y \cdot I_{angle}}{\frac{t_1}{2}} = 25.9 \cdot \text{kip} \cdot \text{in}$$

$$\frac{M_{angle}}{\Omega_m} = 15.5 \cdot \text{kip} \cdot \text{in}$$

$$M_{app} < \frac{M_{angle}}{\Omega_m} = 0$$

Therefore need stiffeners.

Design stiffeners and welds for required additional moment.

$$M_{stiff} := M_{app} - M_{angle} = 24.4 \cdot \text{kip} \cdot \text{in} \quad F_{req} := \frac{M_{stiff}}{W_{G3.5}} = 12.2 \cdot \text{kip}$$

Stiffener is at an angle to the applied moment. The equivalent forces must be resolved.

$$\theta := \text{atan}\left(\frac{W_{G3.5}}{W_{G6}}\right) = 29.7 \cdot \text{deg} \quad F_{resultant} := \frac{F_{req}}{\sin(90 \text{ deg} - \theta)} = 14.1 \cdot \text{kip}$$

$$\text{Design stiffener for tension} \quad \Omega_t := 1.67 \quad A_g := t_p \cdot (W_{G3.5} \cdot \sin(90 \text{ deg} - \theta)) = 0.87 \text{ in}^2$$

$$P_n := F_y \cdot A_g = 31.3 \cdot \text{kip}$$

$$\frac{P_n}{\Omega_t} = 18.7 \cdot \text{kip}$$

$$F_{resultant} < \frac{P_n}{\Omega_t} = 1$$

Therefore stiffener thickness ok

Angle to W-section - Stiffener Weld Design

Design weld for tension:

$$F_{E70} := 70 \text{ ksi} \quad D := 4 \quad l := 2 \cdot W_{G3.5} \quad \Omega_{\text{weld}} := 2.00$$

$$R_n := 0.6 \cdot F_{E70} \cdot \frac{\sqrt{2}}{2} \cdot \frac{D \cdot \text{in}}{16} \cdot 1 = 29.7 \cdot \text{kip}$$

$$\frac{R_n}{\Omega_{\text{weld}}} = 14.8 \cdot \text{kip}$$

$$F_{\text{req}} < \frac{R_n}{\Omega_{\text{weld}}} = 1$$

Therefore ok

5.0 Front channel design

5.0 Design front face sections

$$\Omega_b = 1.67$$

$$L := 60\text{in} \quad \text{Tributary Area:} \quad w_s := 21.8\text{in} \quad A := w_s \cdot L = 1308\text{in}^2$$

$$w := P_{\text{design}} \cdot w_s = 1.06 \cdot \frac{\text{kip}}{\text{in}} \quad M_{\text{app}} := \frac{w \cdot L^2}{8} = 476.2 \cdot \text{kip} \cdot \text{in}$$

Assume:

$$Z_{\text{req}} := \frac{M_{\text{app}} \cdot \Omega_b}{F_y} = 22.1 \cdot \text{in}^3$$

Try MC10 x 25

$$d := 10\text{in} \quad Z_x := 26.2\text{in}^3 \quad b_x := 3.41\text{in} \quad r_x := 0.993\text{in} \quad I_x := 139\text{in}^4$$

$$t_w := 0.380\text{in} \quad T := 7.375\text{in} \quad A_w := d \cdot t_w$$

Yielding

$$M_{\text{app}} := \frac{w \cdot L^2}{8} = 476.2 \cdot \text{kip} \cdot \text{in}$$

$$M_n := F_y \cdot Z_x = 943.2 \cdot \text{kip} \cdot \text{in} \quad \frac{M_n}{\Omega_b} = 564.8 \cdot \text{kip} \cdot \text{in}$$

$$M_{\text{app}} \leq \frac{M_n}{\Omega_b} = 1$$

MC10 x 25 works in flexure

Check lateral torsion buckling

$$L_p := 1.76 \cdot r_y \cdot \sqrt{\frac{E}{F_y}} = 49.6\text{in} \quad L_r := 23.5\text{in}$$

$$L_b \leq L_p = 1$$

Therefore ok.

Check deflection

$$w = 1058.3 \cdot \frac{\text{lb}}{\text{in}} \quad L := 68\text{in}$$

$$\Delta_{\text{all}} := \frac{L}{580} = 0.117\text{in}$$

$$\Delta_{\text{max}} := \frac{5 \cdot w \cdot L^4}{384 \cdot E \cdot I} = 0.073\text{in}$$

$$\Delta_{\text{max}} \leq \Delta_{\text{all}} = 1$$

Therefore ok.

Nominal shear strength

Load applied to the front face channels will sum up to estimated load applied through the actuator.

$$P_{\text{total}} := 250\text{kip} \quad L_{\text{chan}} := 68\text{in}$$

To design the channel facing that transfers the load to the reaction frame, the 250 kips is assumed to be evenly distributed over the length of the channel.

$$w := \frac{P_{\text{total}}}{2L_{\text{chan}}} = 1.84 \cdot \frac{\text{kip}}{\text{in}}$$

The distance between the reaction frame is approximately:

$$d_{\text{react}} := 48\text{in}$$

$$V_{\text{app}} := \frac{w \cdot L_{\text{chan}}}{2} = 62.5 \cdot \text{kip}$$

$$V_c := 49.1\text{kip}$$

$$V_{\text{app}} < V_c = 0$$

Therefore need to increase section or
add stiffeners

Increase section

Try MC 10 X 33.6

$$V_c := 74.4\text{kip}$$

$$V_{\text{app}} < V_c = 1$$

6.0 Rear angle connection design

6.0 Design angle connection of the rear support beams to sides

An angle will be used to connect the front channel support to the sides of the box. It is likely that a stiffener will be necessary at the connection.

Bolts connecting angle to plate - Shear

Assume that all the shear from each support is taken up by bolts located directly across from it on the angle.

$$w := P_{design} \cdot s_c = 0.84 \cdot \frac{\text{kip}}{\text{in}} \quad L := 60\text{in} \quad R_{appv} := w \cdot \frac{L}{2} = 25.2 \cdot \text{kip}$$

$$n := 2$$

$$r_{appv} := \frac{R_{appv}}{n} = 12.6 \cdot \text{kip}$$

$$d_b := \frac{7}{8} \text{in}$$

$$\Omega := 2.00$$

Available shear strength: A325 N S 7/8" bolt

$$r_n := 14.4 \text{kip} \quad R_n := r_n \cdot n = 28.8 \cdot \text{kip}$$

$$r_{appv} \leq r_n = 1$$

Therefore ok.

Bolts connecting angle to plate - Tension

The angle will supply a moment and subsequent tension in the bolt depending on distance from the center of moment.

Try: L6 x 31/2 x 1/2

Workable gages for legs:

$$\Omega := 2.00$$

$$W_{G6} := 3.5\text{in}$$

$$W_{G3.5} := 2\text{in}$$

Use these for moment arm calculations

$$R_{appt} := \frac{R_{appv} \cdot W_{G3.5}}{W_{G6}} = 14.4 \cdot \text{kip}$$

$$r_{appt} := \frac{R_{appt}}{n} = 7.2 \cdot \text{kip}$$

Available tensile strength: A325 N S 7/8" bolt

$$r_n := 27.1 \text{kip}$$

$$r_{appt} \leq r_n = 1$$

Therefore ok.

Min Spacing: $s_{min} := 2.667 \cdot d_b = 2.33 \text{in}$

Bolts connecting angle to plate - Combined Shearing and Tension

$$A_b := 0.60 \text{ in}^2 \quad F_u := 90 \text{ ksi} \quad F_y := 48 \text{ ksi} \quad \Omega := 2.00$$

$$f_v := \frac{r_{\text{appt}}}{A_b} = 20.9 \cdot \text{ksi} \quad r_{\text{appt}} = 7.2 \cdot \text{kip}$$

$$F'_v := 1.3 \cdot F_{nt} - \frac{\Omega \cdot F_{nt}}{F_{nv}} \cdot f_v = 38.5 \cdot \text{ksi} \quad F'_{nt} \leq F_{nv} = 1$$

$$R_n := F'_{nt} \cdot A_b = 23.2 \cdot \text{kip} \quad \frac{R_n}{\Omega_t} = 13.9 \cdot \text{kip} \quad r_{\text{appt}} \leq \frac{R_n}{\Omega_t} = 1$$

Therefore ok.

Bolts connecting angle to plate - Edge distance and bearing on plate

$$L_c := W_{G6} - \frac{d_b}{2} = 3.06 \text{ in} \quad \Omega := 2.00$$

$$R_{n1} := 1.5 \cdot L_c \cdot t_p \cdot F_u = 133.2 \cdot \text{kip} \quad R_{n2} := 3.0 \cdot d_b \cdot t_p \cdot F_u = 76.1 \cdot \text{kip}$$

$$R_n := \min(R_{n1}, R_{n2})$$

$$\frac{R_n}{\Omega} = 38.1 \cdot \text{kip} \quad r_{\text{appt}} \leq \frac{R_n}{\Omega} = 1$$

Therefore ok.

Min Spacing: $s_{\text{min}} := 2.667 \cdot d_b = 2.33 \text{ in}$

Min Edge Distance: $L_{\text{min}} := 1.5 \text{ in}$

Bolts are not slip critical.

Bolts connecting angle to W-section - Tension

$$\Omega_t = 1.67$$

$$R_{\text{appt}} := R_{\text{appv}} = 25.2 \cdot \text{kip} \quad r_{\text{appt}} := \frac{R_{\text{appt}}}{n} = 12.6 \cdot \text{kip}$$

Available tensile strength: A325 N S 7/8" bolt

$$r_c := 27.1 \text{ kip} \quad r_{\text{appt}} \leq r_c = 1$$

Therefore ok.

Bolts connecting angle to W-section - Web local yielding

$$F_n := F_y \quad k := 0.859 \text{ in} \quad N := 3.5 \text{ in} \quad \Omega_w := 1.50$$

$$R_n := (2.5 \cdot k + N) \cdot F_{yw} \cdot t_w = 77.3 \cdot \text{kip}$$

$$\frac{R_n}{\Omega_w} = 51.5 \cdot \text{kip} \quad R_{\text{appt}} = 25.2 \cdot \text{kip}$$

$$R_{\text{appt}} \leq \frac{R_n}{\Omega_w} = 1$$

Therefore ok.

Angle to W-section - Stiffener Sizing

$$t_l := 0.5 \text{ in} \quad \Omega_m := 1.67$$

$$M_{\text{app}} := R_{\text{appt}} \cdot W_{G3.5} = 50.3 \cdot \text{kip} \cdot \text{in}$$

$$A_l := s_c \cdot t_l = 8.6 \text{ in}^2 \quad I_{\text{angle}} := \frac{s_c \cdot t_l^3}{12} = 0.18 \text{ in}^4$$

$$M_{\text{angle}} := \frac{F_y \cdot I_{\text{angle}}}{\frac{t_l}{2}} = 25.9 \cdot \text{kip} \cdot \text{in}$$

$$\frac{M_{\text{angle}}}{\Omega_m} = 15.5 \cdot \text{kip} \cdot \text{in}$$

$$M_{\text{app}} < \frac{M_{\text{angle}}}{\Omega_m} = 0$$

Therefore need stiffeners.

Design stiffeners and welds for required additional moment.

$$M_{\text{stiff}} := M_{\text{app}} - M_{\text{angle}} = 24.4 \cdot \text{kip} \cdot \text{in} \quad F_{\text{req}} := \frac{M_{\text{stiff}}}{W_{G3.5}} = 12.2 \cdot \text{kip}$$

Stiffener is at an angle to the applied moment. The equivalent forces must be resolved.

$$\theta := \text{atan} \left(\frac{W_{G3.5}}{W_{G6}} \right) = 29.7 \cdot \text{deg} \quad F_{\text{resultant}} := \frac{F_{\text{req}}}{\sin(90 \text{ deg} - \theta)} = 14.1 \cdot \text{kip}$$

$$\text{Design stiffener for tension} \quad \Omega_t := 1.67 \quad A_g := t_p \cdot (W_{G3.5} \cdot \sin(90 \text{ deg} - \theta)) = 0.87 \text{ in}^2$$

$$P_n := F_y \cdot A_g = 31.3 \cdot \text{kip}$$

$$\frac{P_n}{\Omega_t} = 18.7 \cdot \text{kip}$$

$$F_{\text{resultant}} < \frac{P_n}{\Omega_t} = 1$$

Therefore stiffener
thickness ok

Angle to W-section - Stiffener Weld Design

Design weld for tension:

$$F_{E70} := 70 \text{ ksi} \quad D := 8 \quad l := 2 \cdot W_{G3.5} \quad \Omega_{\text{weld}} := 2.00$$

$$R_n := 0.6 \cdot F_{E70} \cdot \frac{\sqrt{2}}{2} \cdot \frac{D \cdot \text{in}}{16} \cdot l = 59.4 \cdot \text{kip}$$

$$\frac{R_n}{\Omega_{\text{weld}}} = 29.7 \cdot \text{kip}$$

$$F_{\text{req}} < \frac{R_n}{\Omega_{\text{weld}}} = 1$$

Therefore ok

▲ 6.0 Rear angle connection design

7.0 Connection Plate

7.0 Design connection plate from actuator to strips

$$t_p := 2.5 \text{ in} \quad F_y = 36 \text{ ksi} \quad P := 80 \text{ kip} \quad \Omega_b = 1.67$$

$$d := 7 \text{ in} \quad M_{app} := P \cdot d = 560 \cdot \text{kip} \cdot \text{in} \quad b := 28 \text{ in} \quad h := t_p \quad I := \frac{b \cdot h^3}{12} = 36.5 \text{ in}^4$$

$$M_{max} := \frac{F_y \cdot I}{\frac{t_p}{2}} = 1050 \cdot \text{kip} \cdot \text{in} \quad \frac{M_n}{\Omega_b} = 628.7 \cdot \text{kip} \cdot \text{in}$$

Bolts connecting angle to plate - Tension

L 4 X 2 X 5/8

$$P := 20 \text{ kip} \quad L := 28 \text{ in} \quad w := 3 \cdot \frac{P}{L} = 2.1 \cdot \frac{\text{kip}}{\text{in}}$$

$$R_{appt} := w \cdot \frac{L}{2} = 30 \cdot \text{kip}$$

3 bolts into plate

$$r_{appt} := \frac{R_{appt}}{n} = 5 \cdot \text{kip}$$

$$n := 6$$

$$d_b := \frac{5}{8} \text{ in}$$

$$\Omega := 2.00$$

Available tensile strength: A325 5/8" bolt

$$r_c := 13.8 \text{ kip} \quad R_c := r_c \cdot n = 82.8 \cdot \text{kip}$$

$$r_{appt} \leq r_c = 1$$

Therefore ok.

Bolts connecting angle to strips - Shear

$$P := 20 \text{ kip}$$

$$d_b := \frac{5}{8} \text{ in}$$

Available shear strength: A325 N D 5/8" bolt

$$r_c := 14.7 \text{ kip}$$

$$P \leq r_c = 0$$

Increase bolt size.

Available shear strength: A325 N D 3/4" bolt

$$r_c := 21.1 \text{ kip}$$

$$d_b := \frac{3}{4} \text{ in}$$

$$P \leq r_c = 1$$

Therefore ok.

Bolts connecting angle to strip - Edge distance and bearing on angle

$$L_3 := 3 \text{ in} \quad W_{G3} := 2 \text{ in} \quad W_{G2} := \frac{7}{8} \text{ in} \quad i := 2 \quad \Omega := 2.00$$

$$t_p := \frac{5}{8} \text{ in} \quad L_c := L_3 - W_{G3} - \frac{d_b}{2} = 0.62 \text{ in}$$

$$R_{n1} := 1.5 \cdot L_c \cdot t_p \cdot F_u = 34 \cdot \text{kip} \quad R_{n2} := 3.0 \cdot d_b \cdot t_p \cdot F_u = 81.6 \cdot \text{kip}$$

$$R_n := \min(R_{n1}, R_{n2})$$

$$P = 20 \cdot \text{kip} \quad \frac{i \cdot R_n}{\Omega} = 34 \cdot \text{kip}$$

$$P \leq \frac{i R_n}{\Omega} = 1$$

Therefore ok.

$$\text{Min Spacing: } s_{min} := 2.667 \cdot d_b = 2 \text{ in}$$

7.0 Connection Plate

8.0 Pullout zone reinforcement

8.0 Flexure

$$s := 300\text{mm} \quad L := 28\text{in} \quad \sigma_{\text{design}} := 60\text{psi}$$

$$w := \sigma_{\text{design}} \cdot s = 0.7 \cdot \frac{\text{kip}}{\text{in}}$$

$$V_{\text{app}} := \frac{w \cdot L}{2} = 9.9 \cdot \text{kip} \quad M_{\text{app}} := \frac{w \cdot L^2}{8} = 69.4 \cdot \text{kip} \cdot \text{in}$$

$$Z_{\text{req}} := \frac{M_{\text{app}} \cdot \Omega_b}{F_y} = 3.2 \cdot \text{in}^3$$

Try WT 6 X 11

$$Z_x := 4.63 \cdot \text{in}^3 \quad r_{yy} := 0.847\text{in} \quad b_f := 4.03\text{in}$$

$$A_g := 3.24 \cdot \text{in}^2 \quad I_x := 11.7 \cdot \text{in}^4 \quad t_f := 0.425\text{in} \quad t_w := 0.260\text{in} \quad d := 6.16\text{in}$$

$$M_{\text{app}} := \frac{w \cdot L^2}{8} = 69.4 \cdot \text{kip} \cdot \text{in}$$

$$M_n := F_y \cdot Z_x = 166.7 \cdot \text{kip} \cdot \text{in} \quad \frac{M_n}{\Omega_b} = 99.8 \cdot \text{kip} \cdot \text{in} \quad M_{\text{app}} \leq \frac{M_n}{\Omega_b} = 1$$

WT6 x 11 works in
flexure

8.1 Shear

$$w = 708.7 \cdot \frac{\text{lbf}}{\text{in}} \quad V_{\text{app}} := \frac{w \cdot L}{2} = 9.92 \cdot \text{kip} \quad A_g = 3.2 \cdot \text{in}^2 \quad \Omega_w := 1.50$$

$$A_w := d \cdot t_w \quad C_w := 1.0 \quad \frac{T}{t_w} = 28.4 \quad 2.24 \cdot \sqrt{\frac{E}{F_y}} = 63.6$$

$$V_n := 0.6 \cdot F_y \cdot A_w \cdot C_w = 34.6 \cdot \text{kip} \quad \frac{V_n}{\Omega_v} = 23.1 \cdot \text{kip} \quad V_{\text{app}} \leq \frac{V_n}{\Omega_v} = 1$$

Plate to WT-section - Weld Design

Design weld for shear:

Length of weld: $L_w := b_f - t_w$

$$F_{E70} := 70 \text{ ksi} \quad D := 5 \text{ in} \quad L := 2 \cdot (L_1) \quad \Omega_{\text{weld}} := 2.00$$

$$R_n := 0.6 \cdot F_{E70} \cdot \frac{\sqrt{2}}{2} \cdot \frac{D}{16} \cdot L = 70 \cdot \text{kip}$$

$$\frac{R_n}{\Omega_{\text{weld}}} = 35 \cdot \text{kip}$$

$$V_{\text{app}} < \frac{R_n}{\Omega_{\text{weld}}} = 1$$

$$t_f = 0.425 \text{ in}$$

Check base metal thickness: Therefore ok

$$t_{\text{min}} := \frac{0.6 \cdot F_{E70} \cdot \frac{\sqrt{2}}{2} \cdot \frac{D}{16}}{0.6 F_u} = 0.267 \text{ in}$$

$$t_{\text{min}} \leq t_f = 1$$

Bolts connecting angle to plate - Shear

Assume that all the shear from each support is taken up by bolts located directly across from it on the angle.

$$v_{\text{app}} := \frac{V_{\text{app}}}{n} = 1.7 \cdot \text{kip} \quad n := 2$$

$$d_b := \frac{5}{8} \text{ in} \quad \Omega := 2.00$$

Available shear strength: A325 N S 5/8" bolt

$$r_c := 7.36 \text{ kip} \quad R_c := r_c \cdot n = 14.7 \cdot \text{kip}$$

$$v_{\text{app}} \leq r_c = 1$$

Therefore ok.

Bolts connecting angle to strip - Edge distance and bearing on angle

$$t_p := \frac{4}{8} \text{ in} \quad L_w := \frac{d - t_f}{2} = 2.9 \text{ in} \quad i_w := 1$$

$$R_{n1} := 1.5 \cdot L_c \cdot t_p \cdot F_u = 124.7 \cdot \text{kip} \quad R_{n2} := 3.0 \cdot d_b \cdot t_p \cdot F_u = 54.4 \cdot \text{kip}$$

$$R_n := \min(R_{n1}, R_{n2})$$

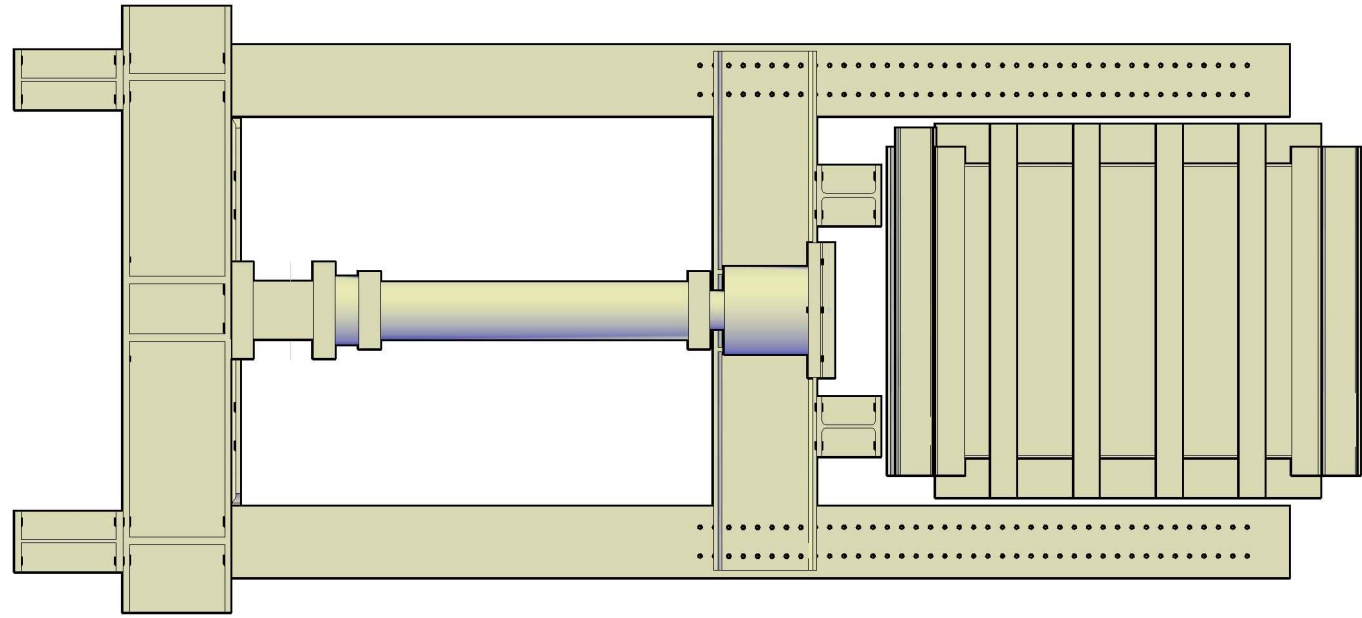
$$\frac{i \cdot R_n}{\Omega} = 27.2 \cdot \text{kip}$$

$$v_{\text{app}} \leq \frac{i \cdot R_n}{\Omega} = 1$$

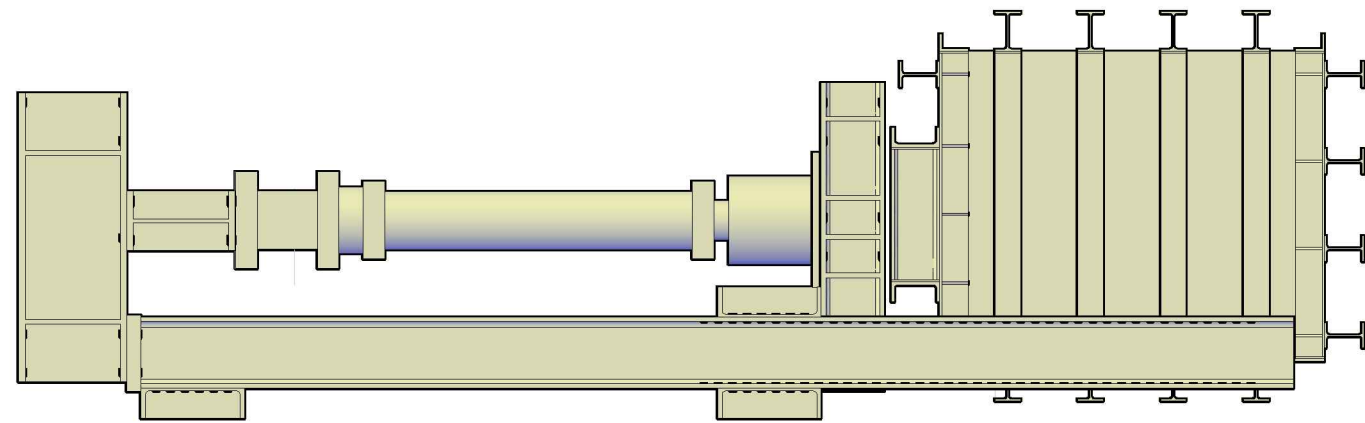
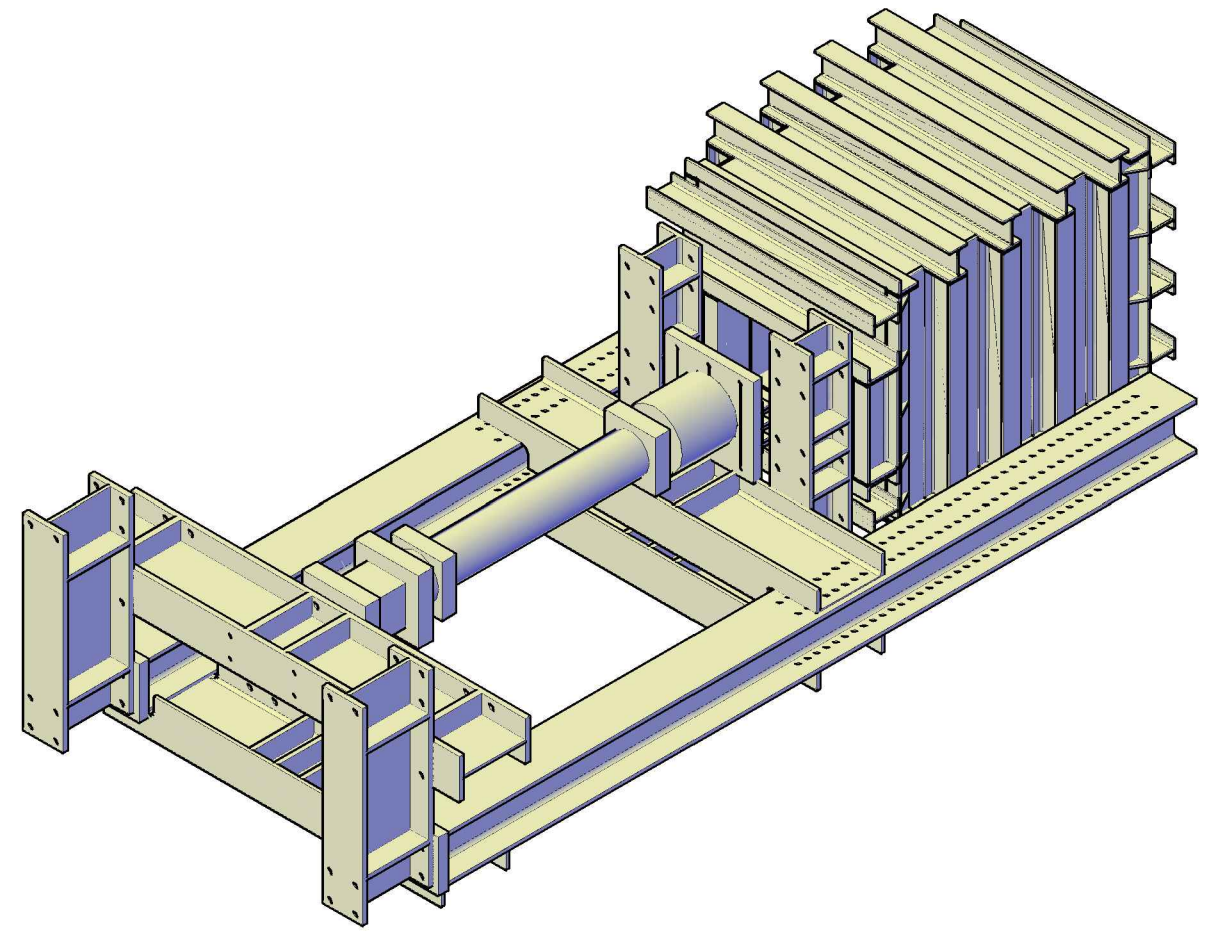
Therefore ok.

PART 2: SHOP DRAWINGS AND 3D RENDERINGS

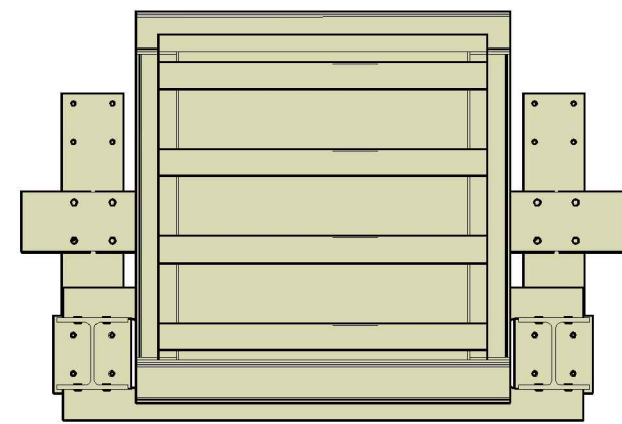
Pages: 314 – 337



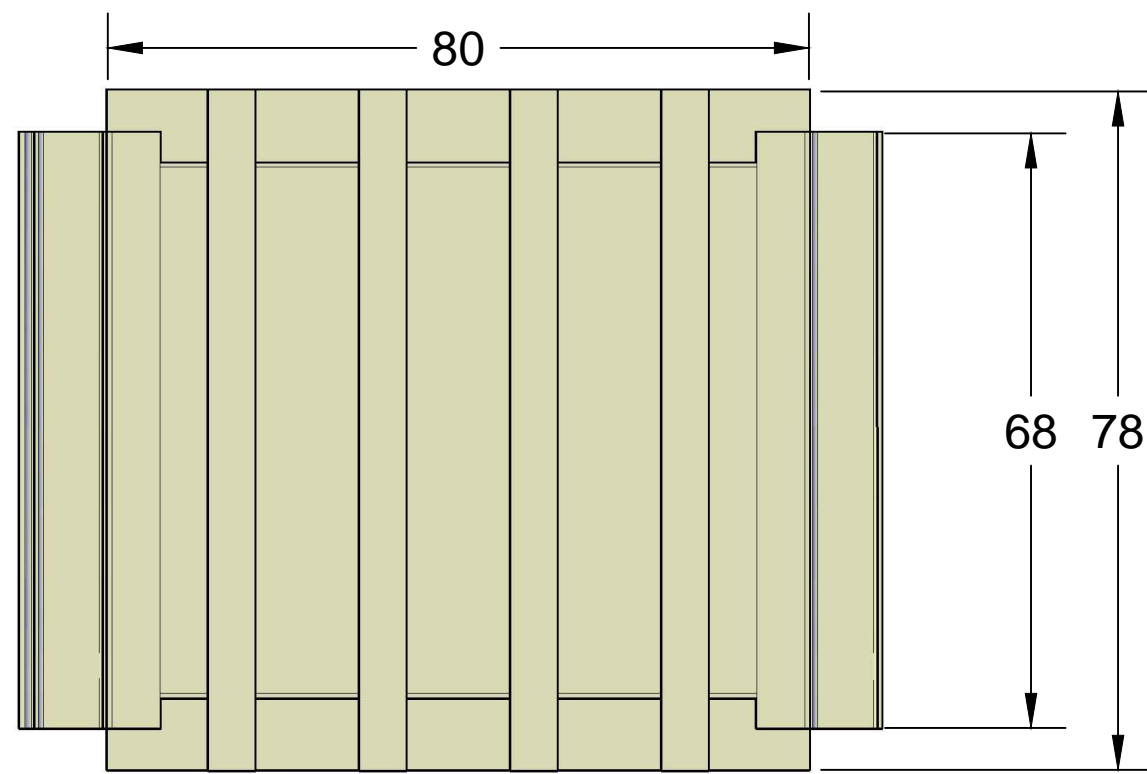
PLAN VIEW



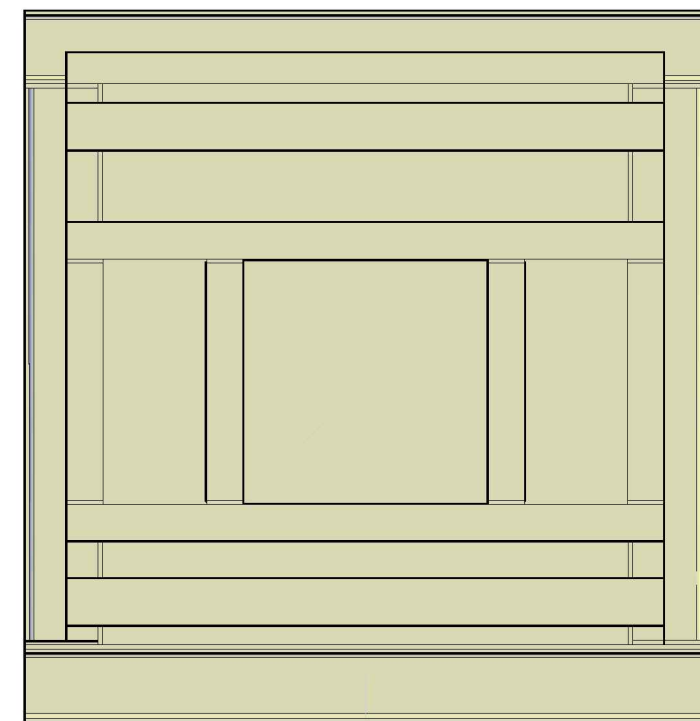
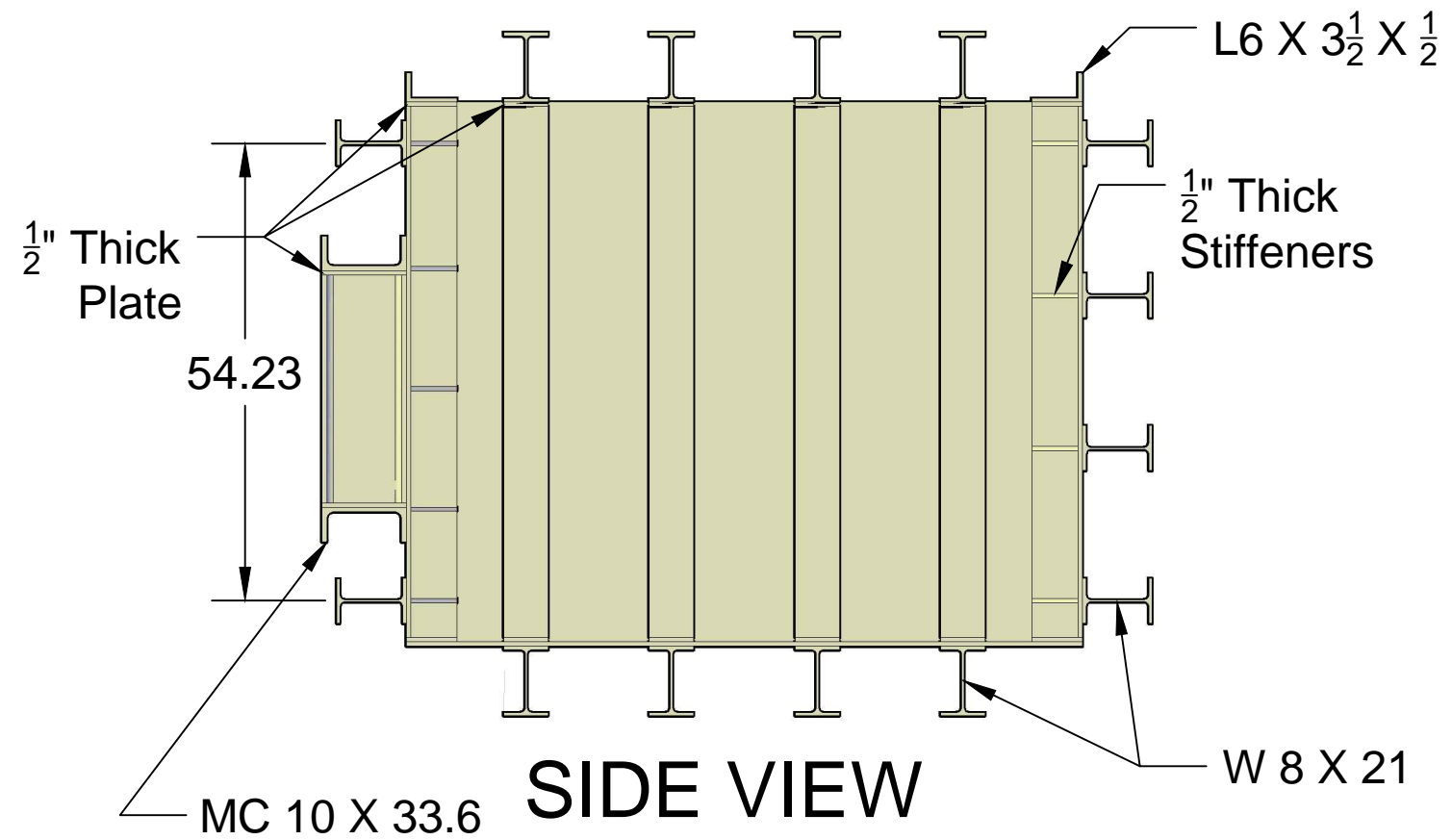
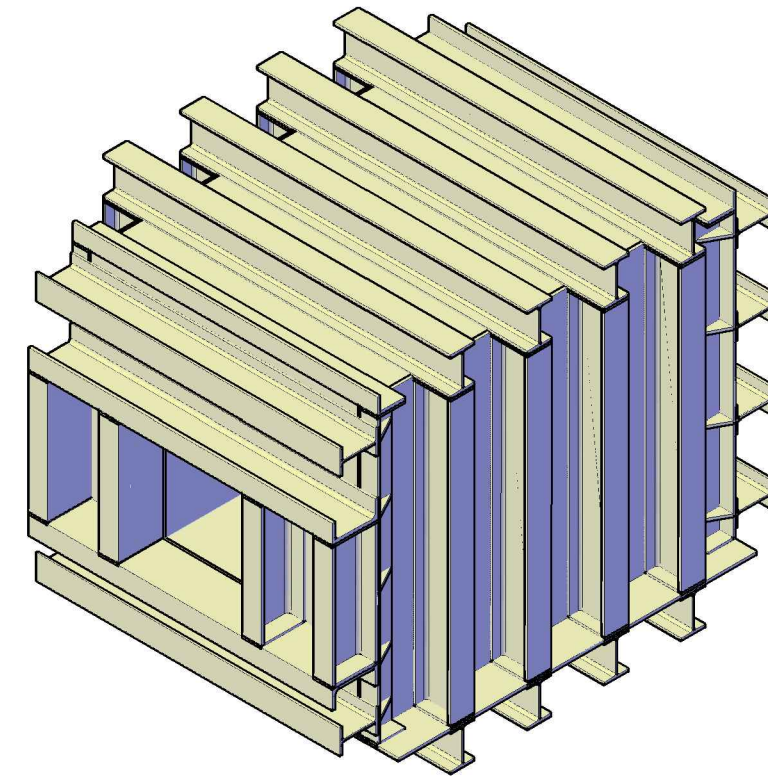
SIDE VIEW



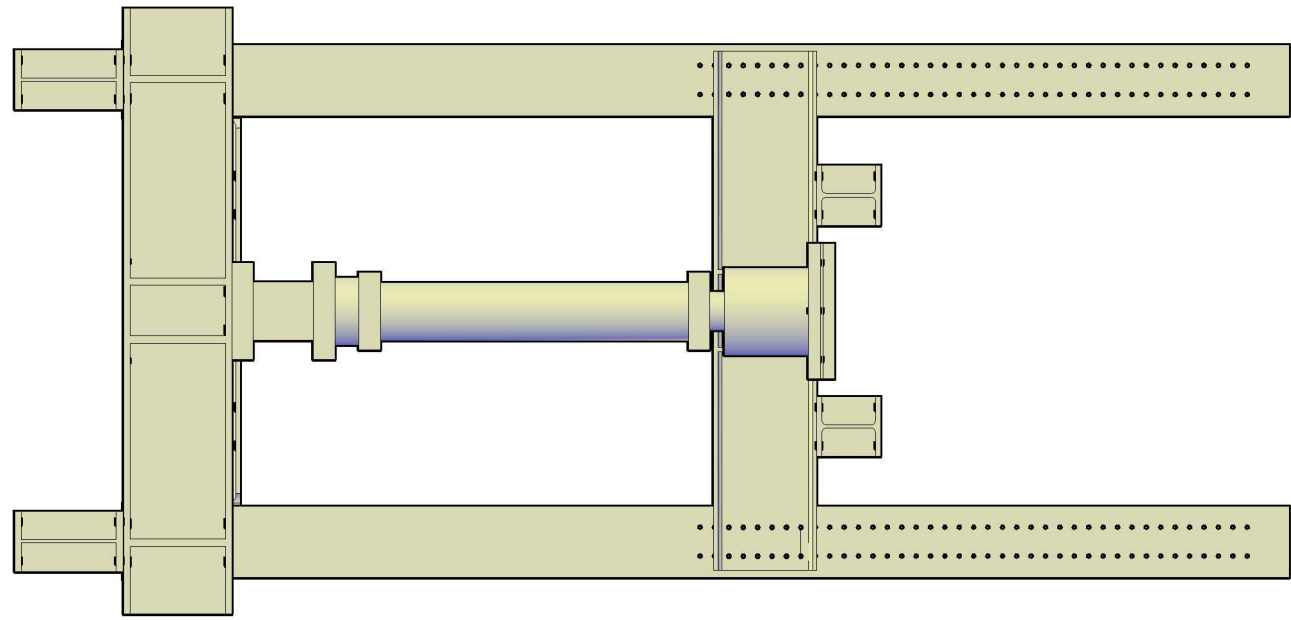
FRONT VIEW



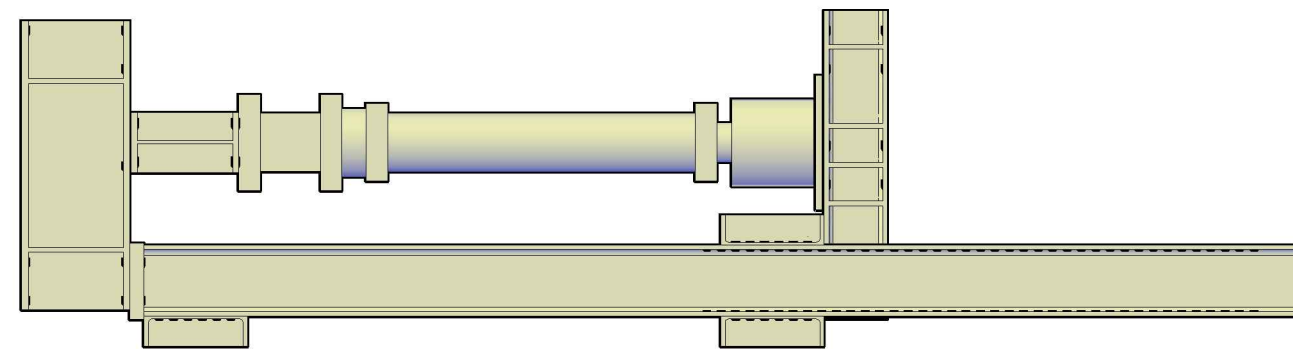
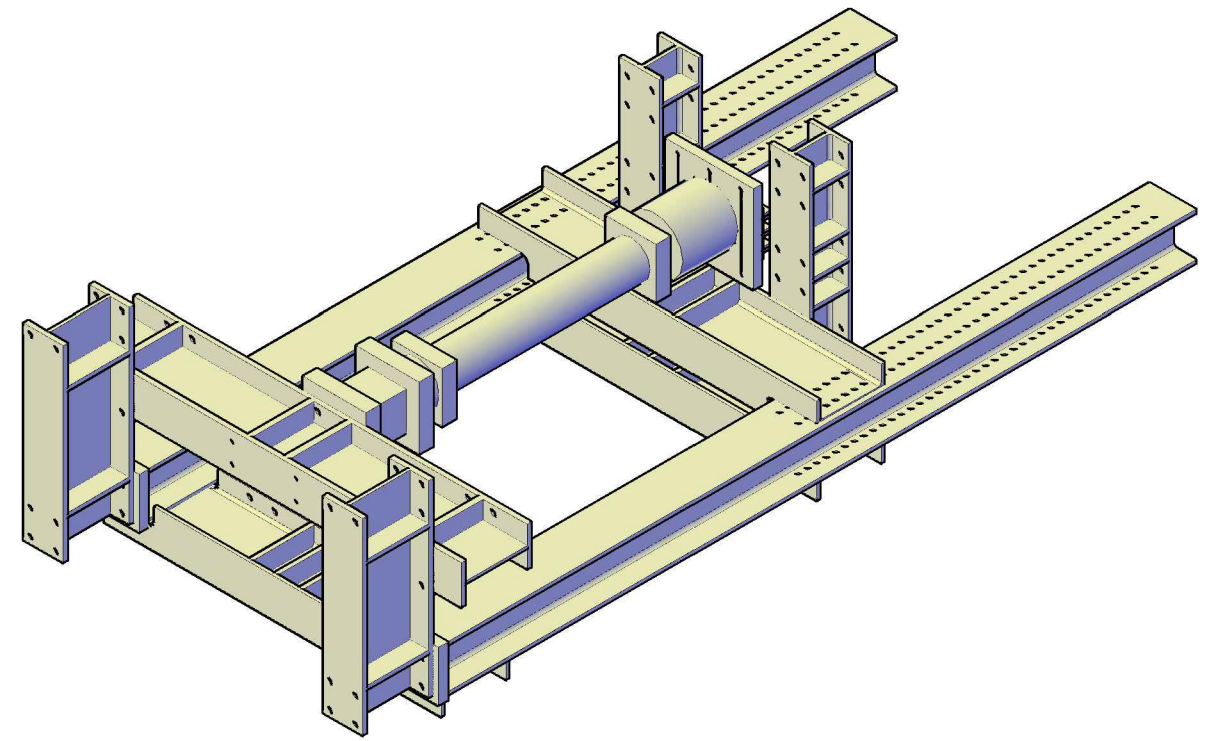
PLAN VIEW



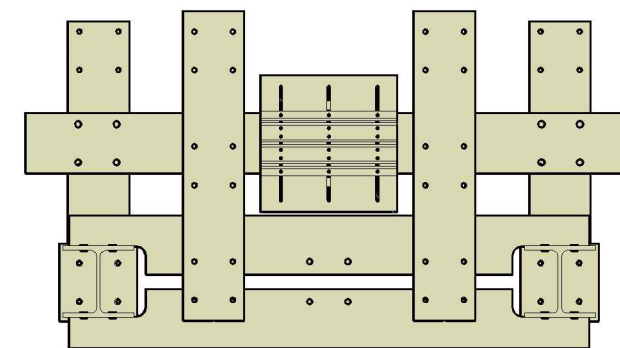
FRONT VIEW



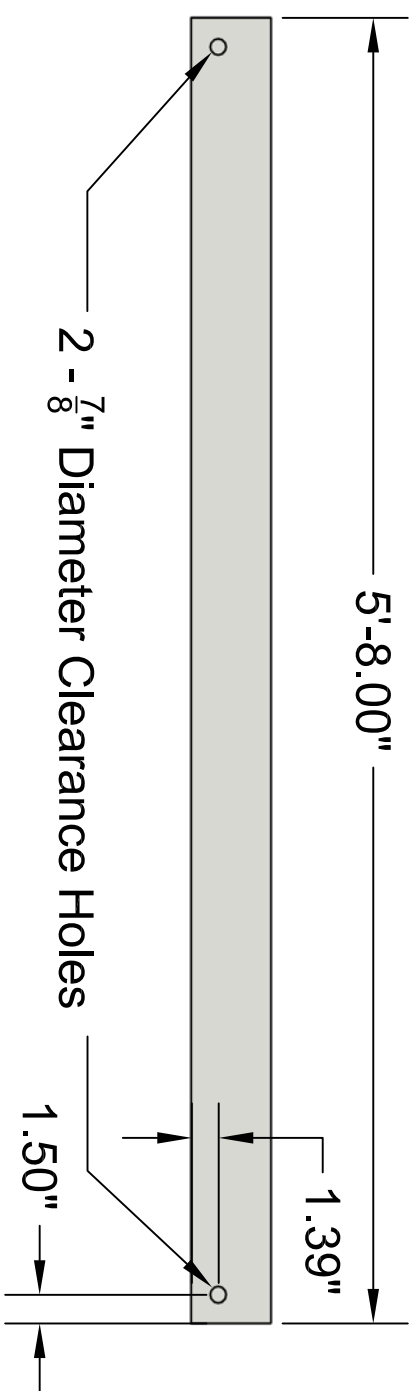
PLAN VIEW



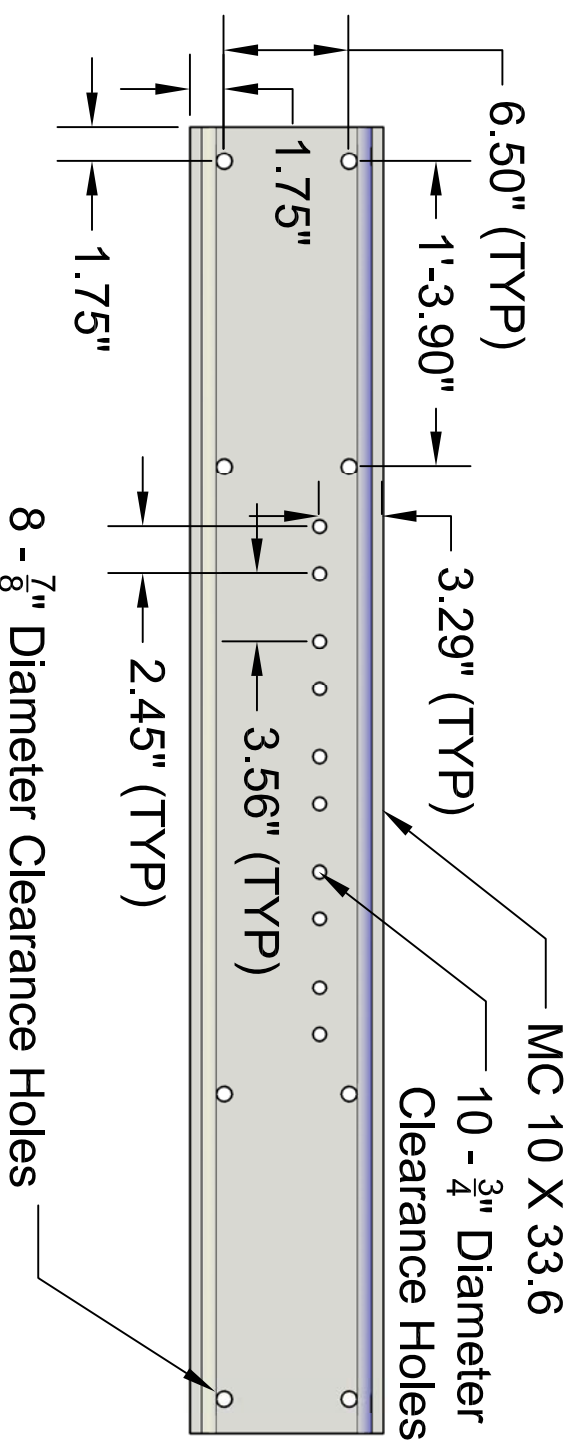
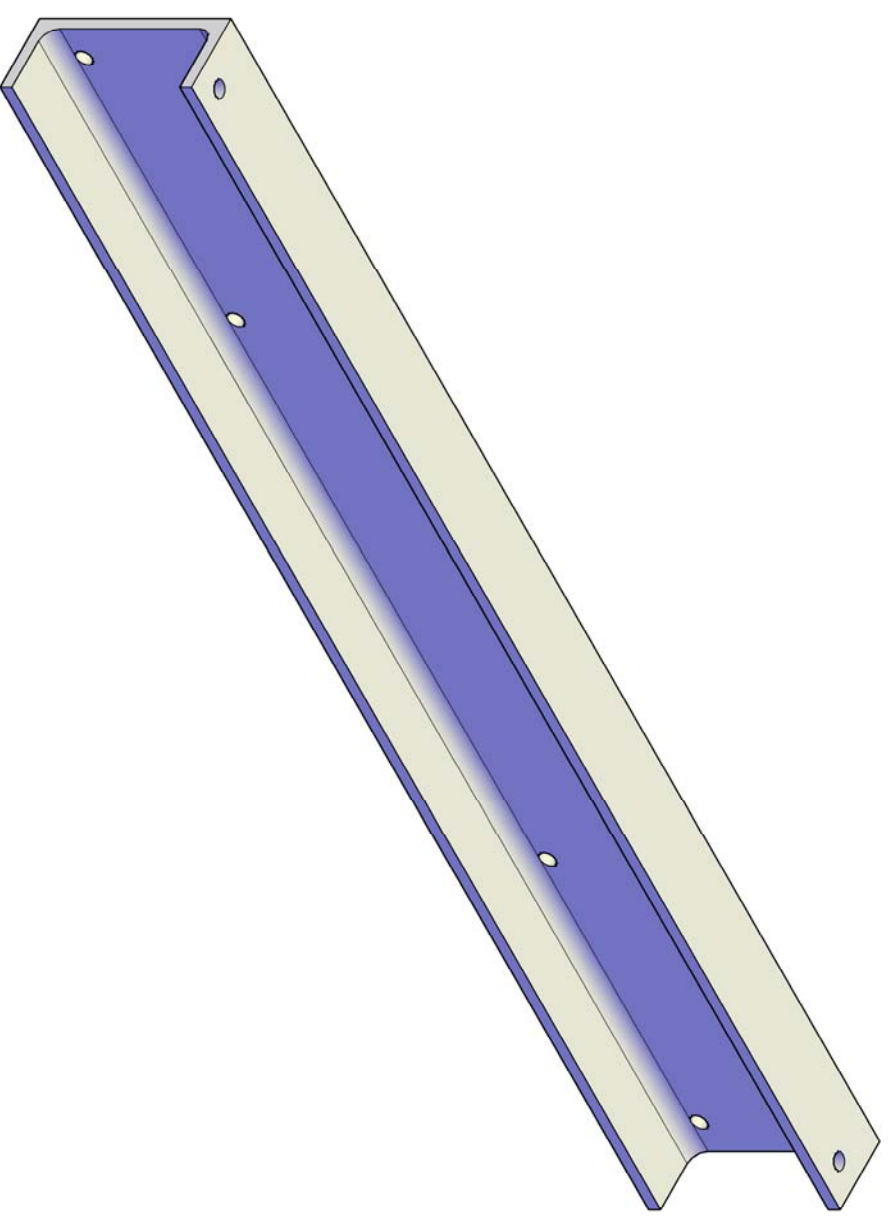
SIDE VIEW



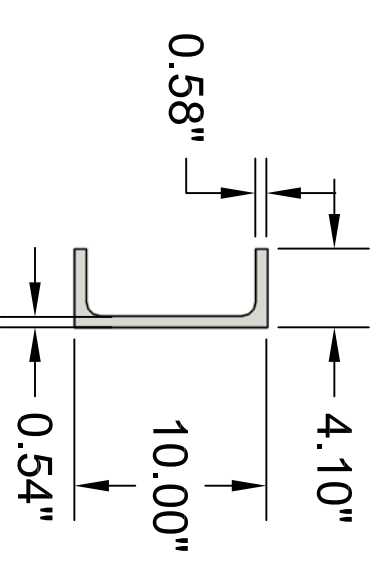
FRONT VIEW



TOP VIEW



FRONT VIEW

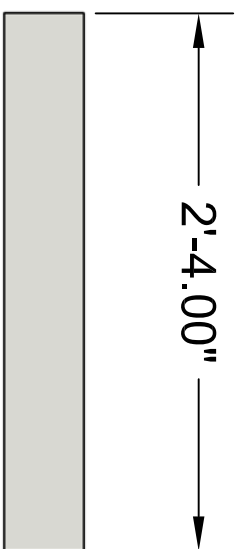


SIDE VIEW

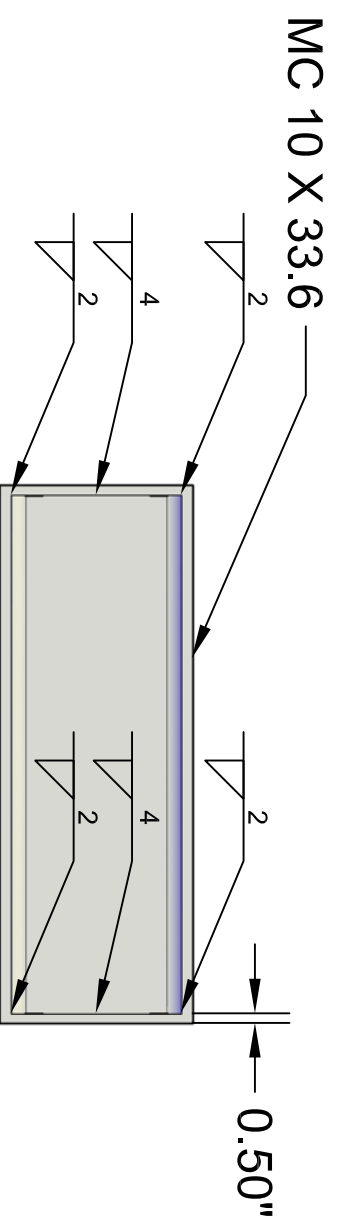
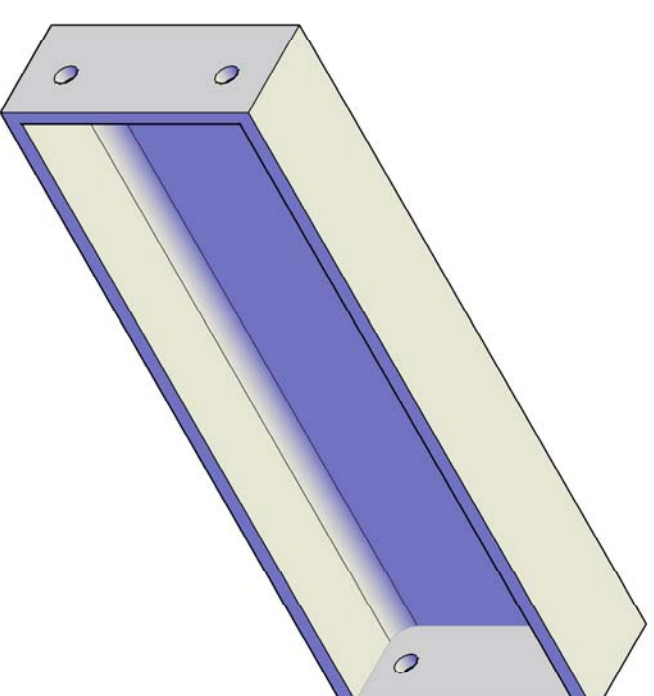
Part ID: Main Face Channel

Drawn by: AWS
Project: Multiple Pull-out Box

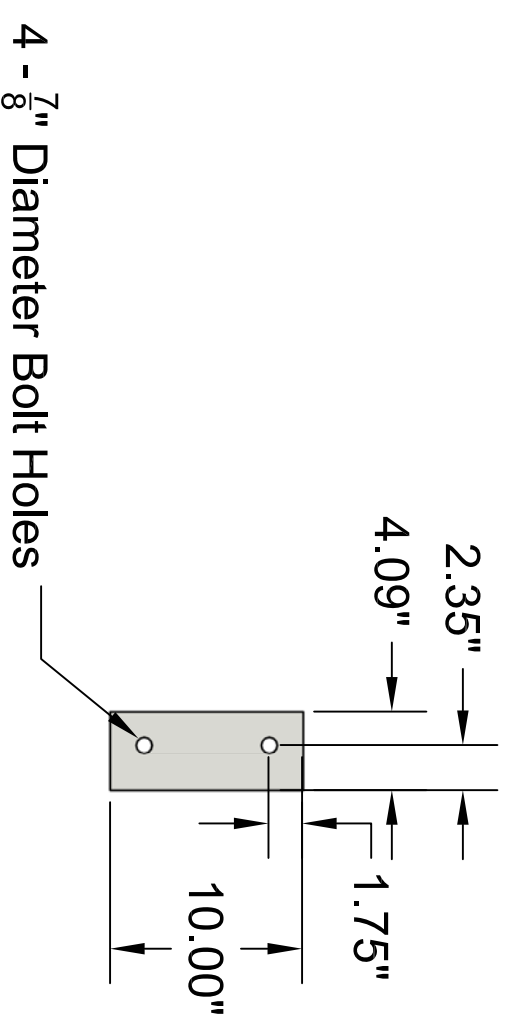
Date: 11/18/12
Quantity: 2



TOP VIEW



FRONT VIEW

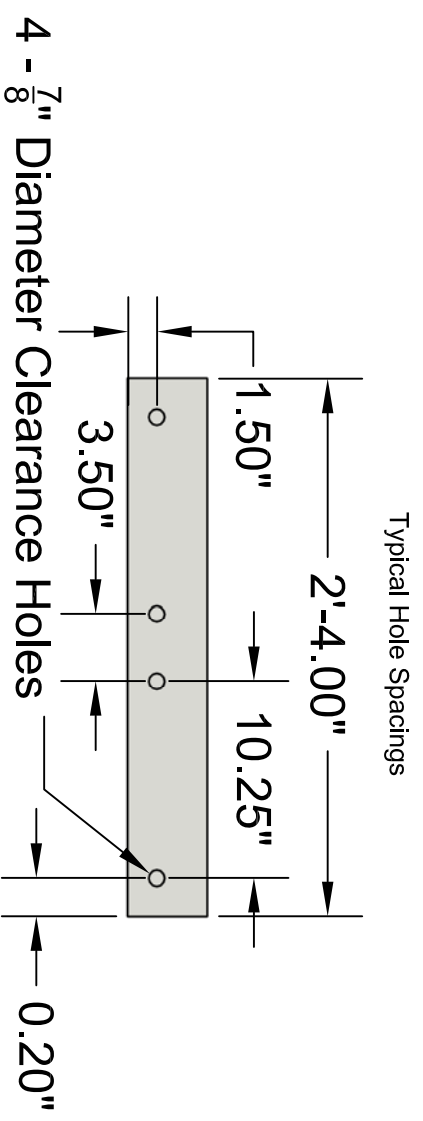


SIDE VIEW

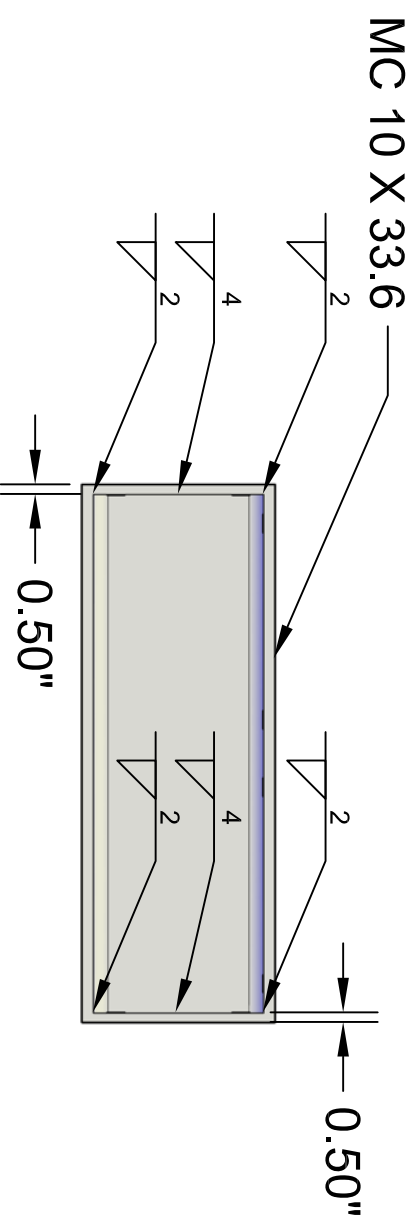
Part ID: Support Face Channel1

Drawn by: AWS
Project: Multiple Pull-out Box

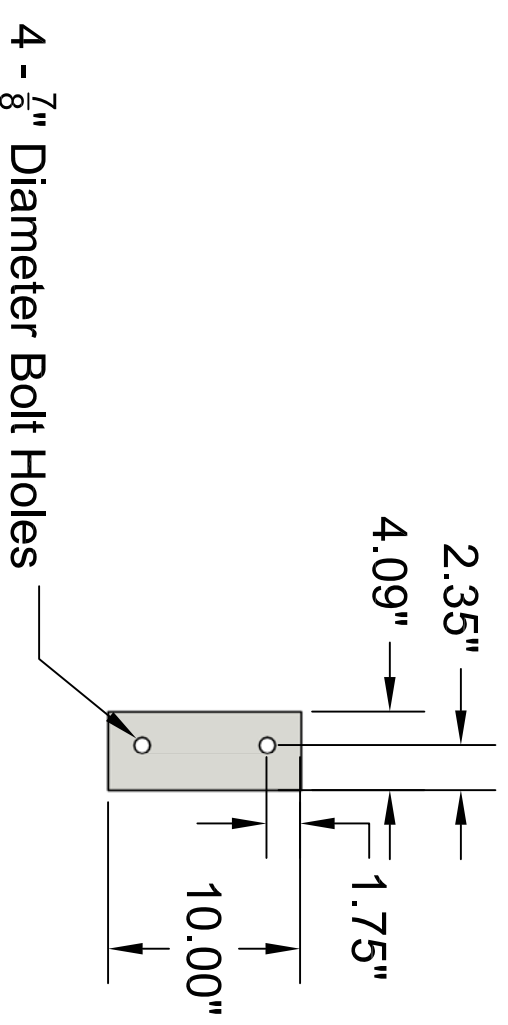
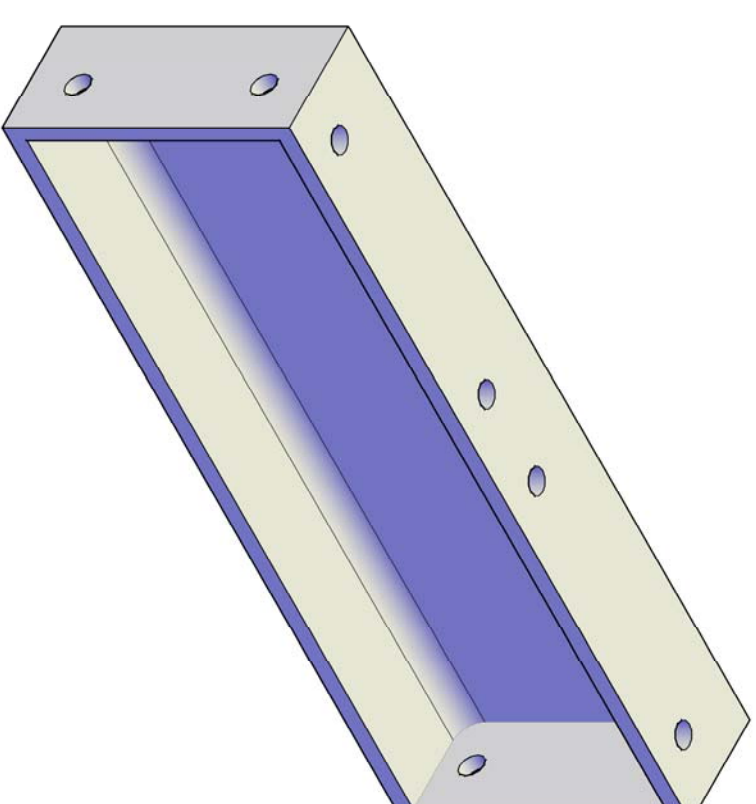
Date: 11/18/12
Quantity: 2



TOP VIEW



FRONT VIEW

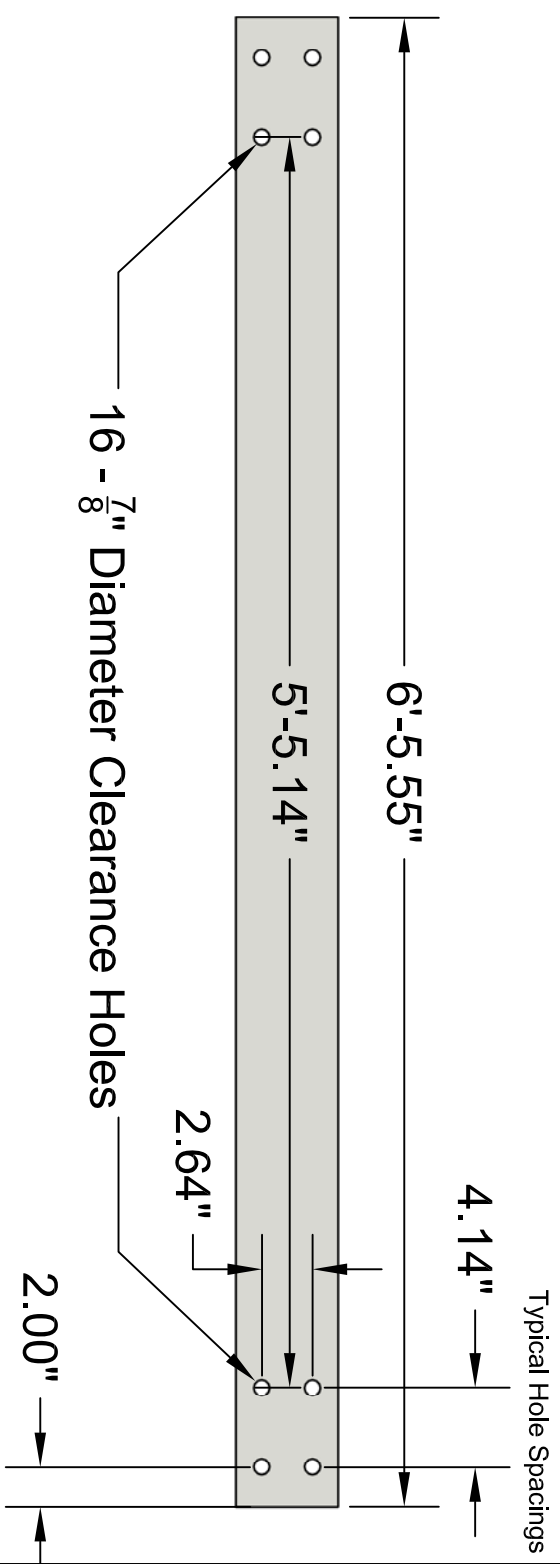


SIDE VIEW

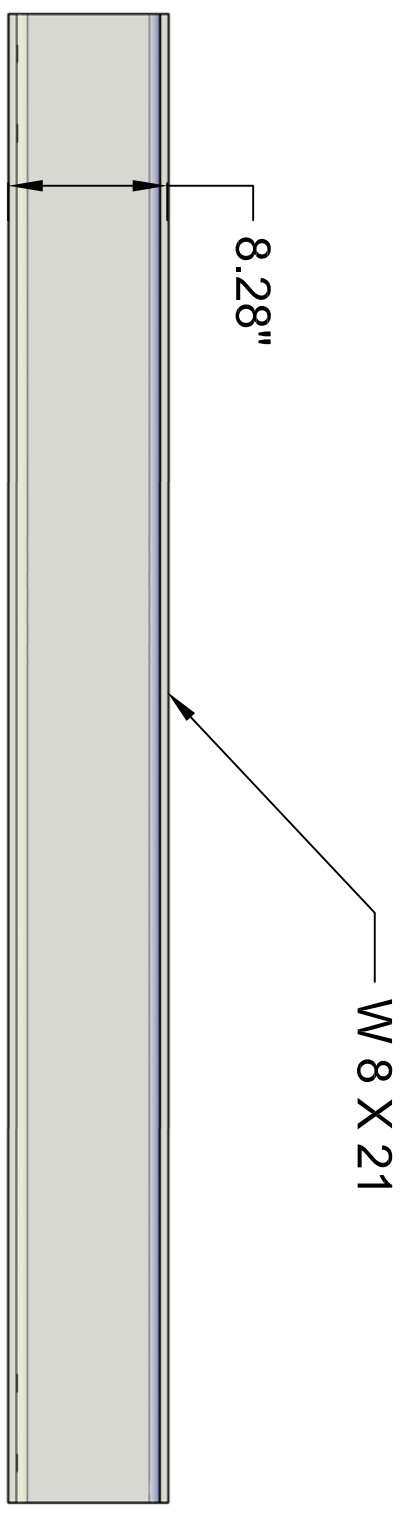
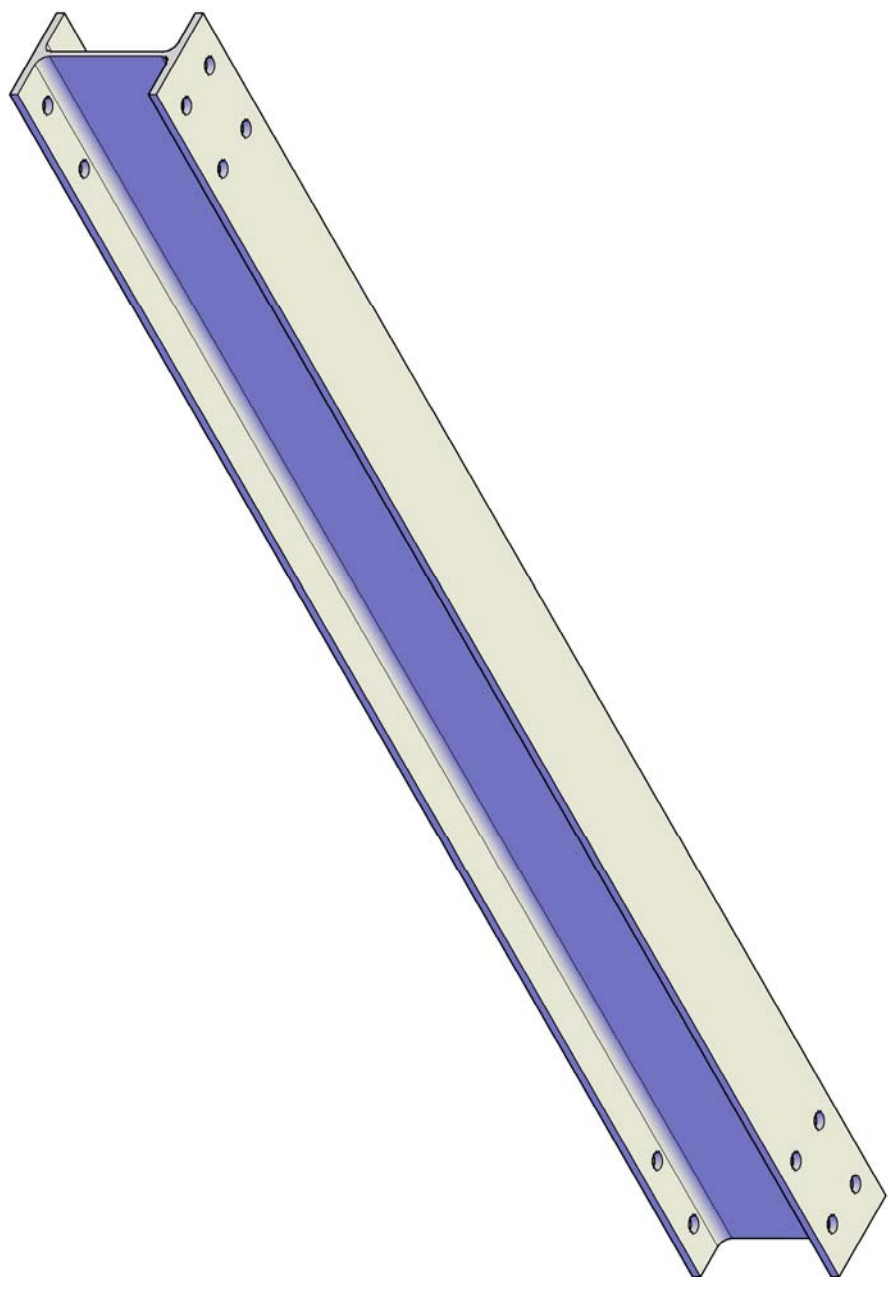
Part ID: Support Face Channel2

Drawn by: AWS
Project: Multiple Pull-out Box

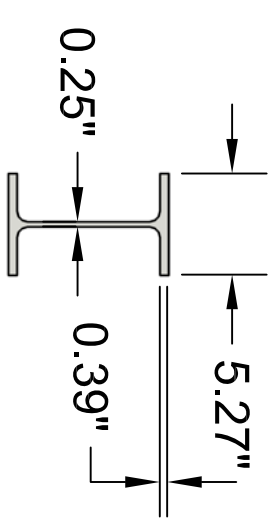
Date: 11/18/12
Quantity: 2



TOP VIEW



FRONT VIEW



SIDE VIEW

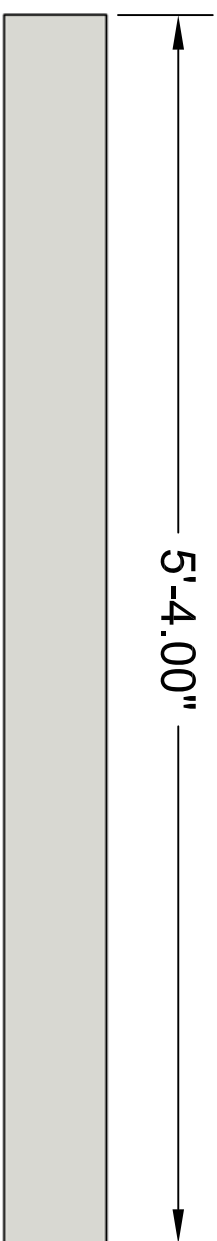
Part ID: Top Support Beam

Drawn by: AWS

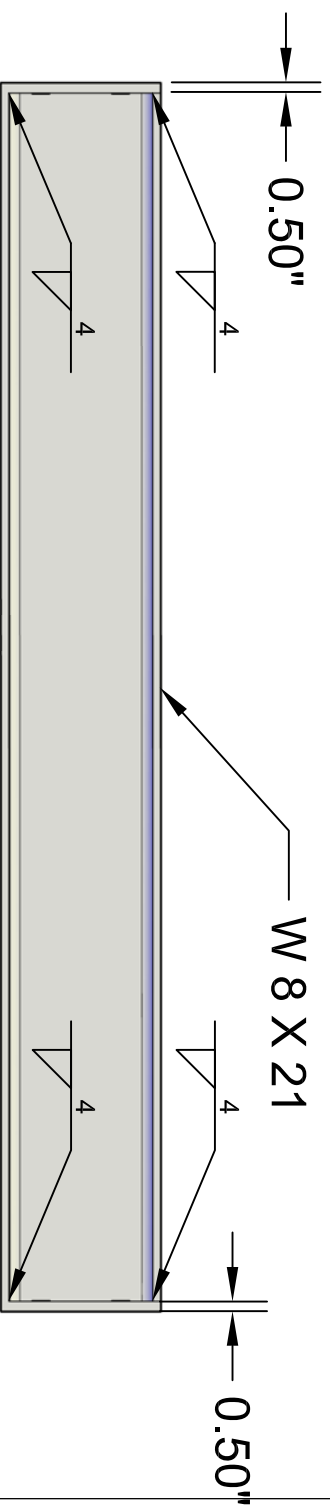
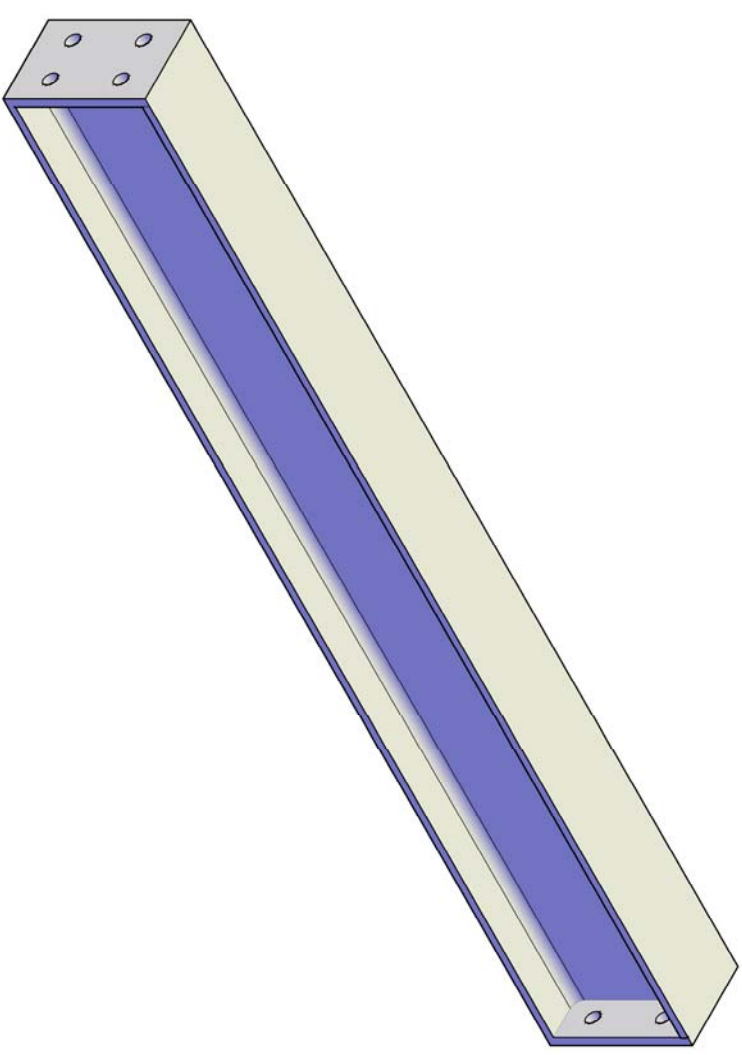
Date: 11/18/12

Project: Multiple Pull-out Box

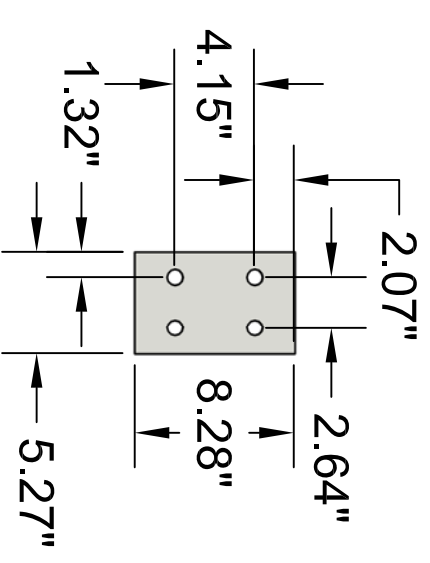
Quantity: 8



TOP VIEW



FRONT VIEW

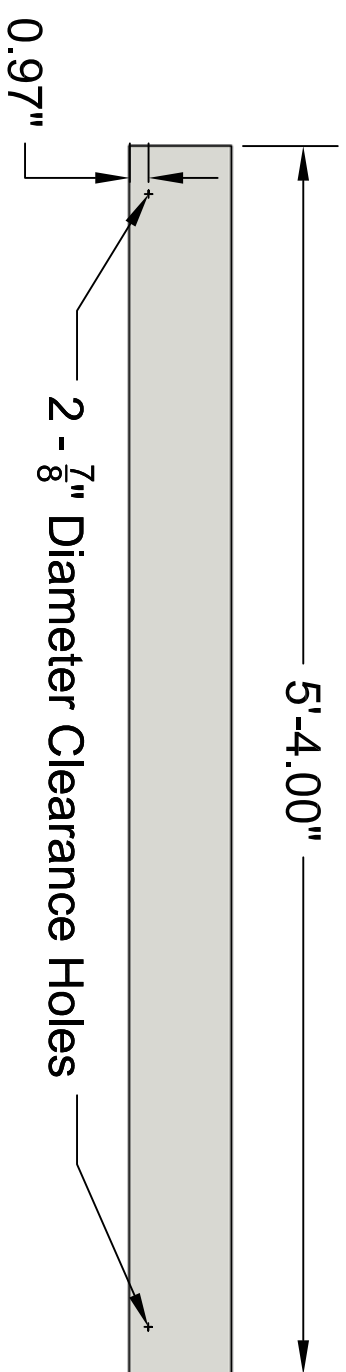


SIDE VIEW

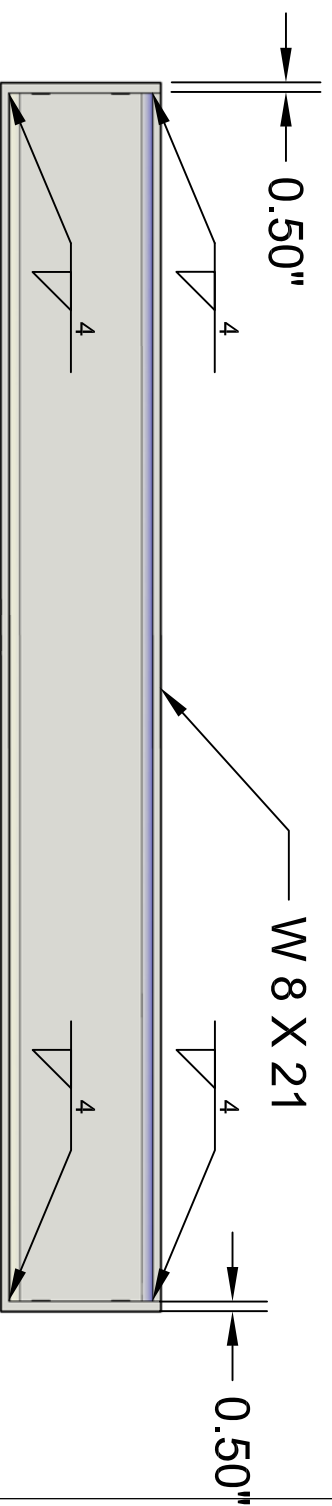
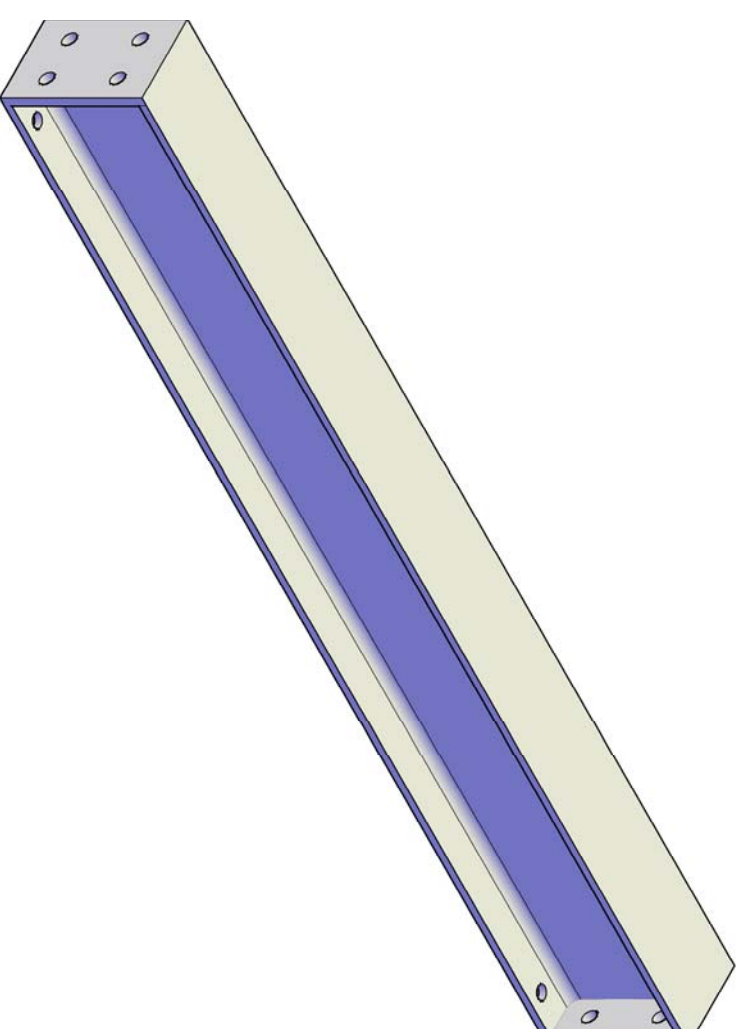
Part ID: Side Support Beam

Drawn by: AWS
Project: Multiple Pull-out Box

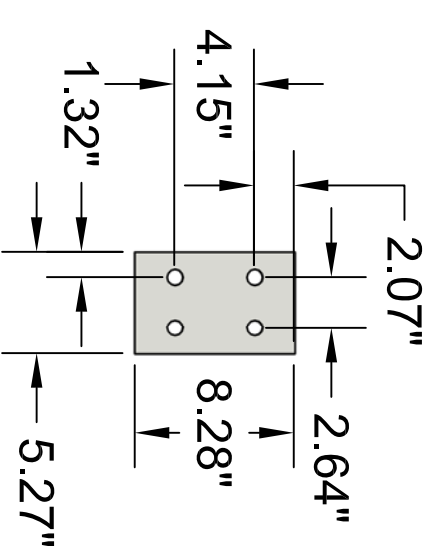
Date: 11/18/12
Quantity: 4



TOP VIEW



FRONT VIEW

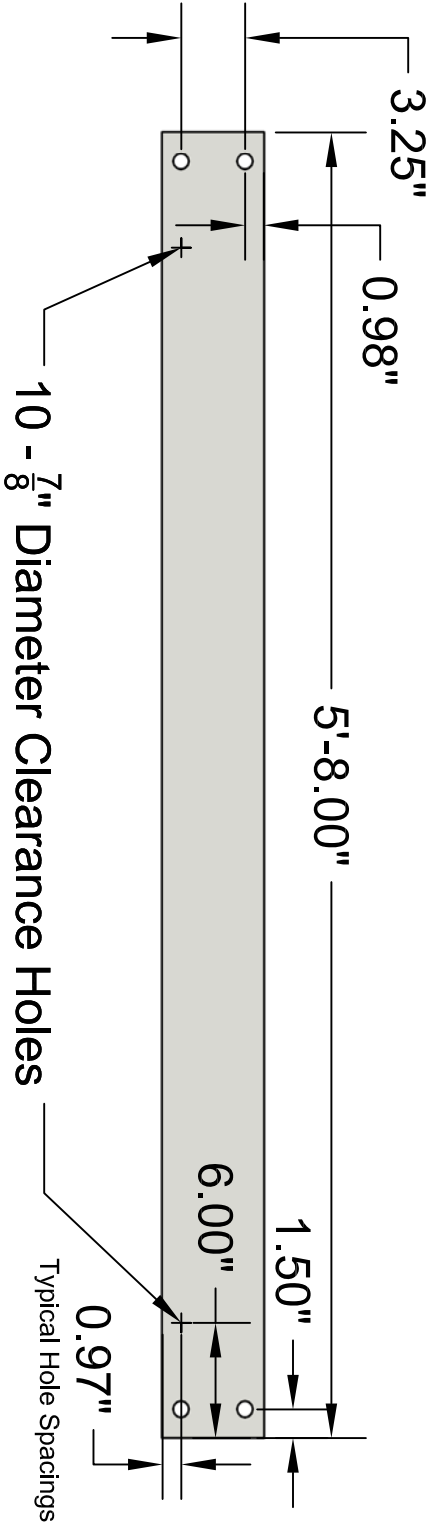


SIDE VIEW

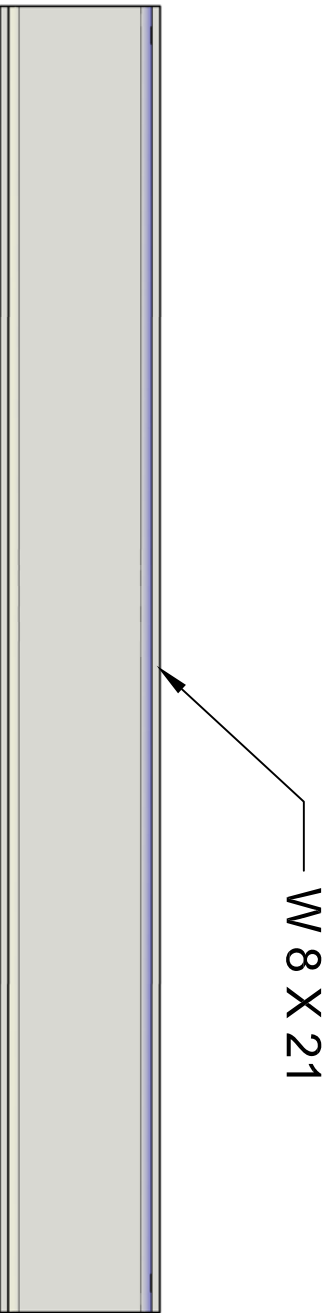
Part ID: Side Support Beam

Drawn by: AWS
Project: Multiple Pull-out Box

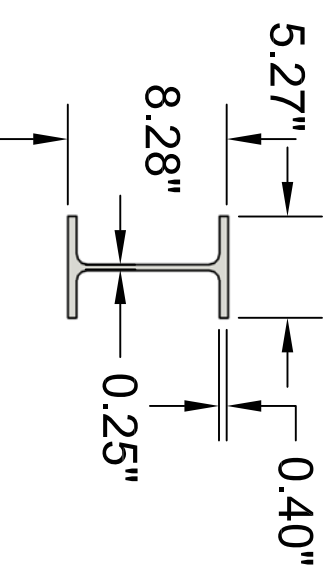
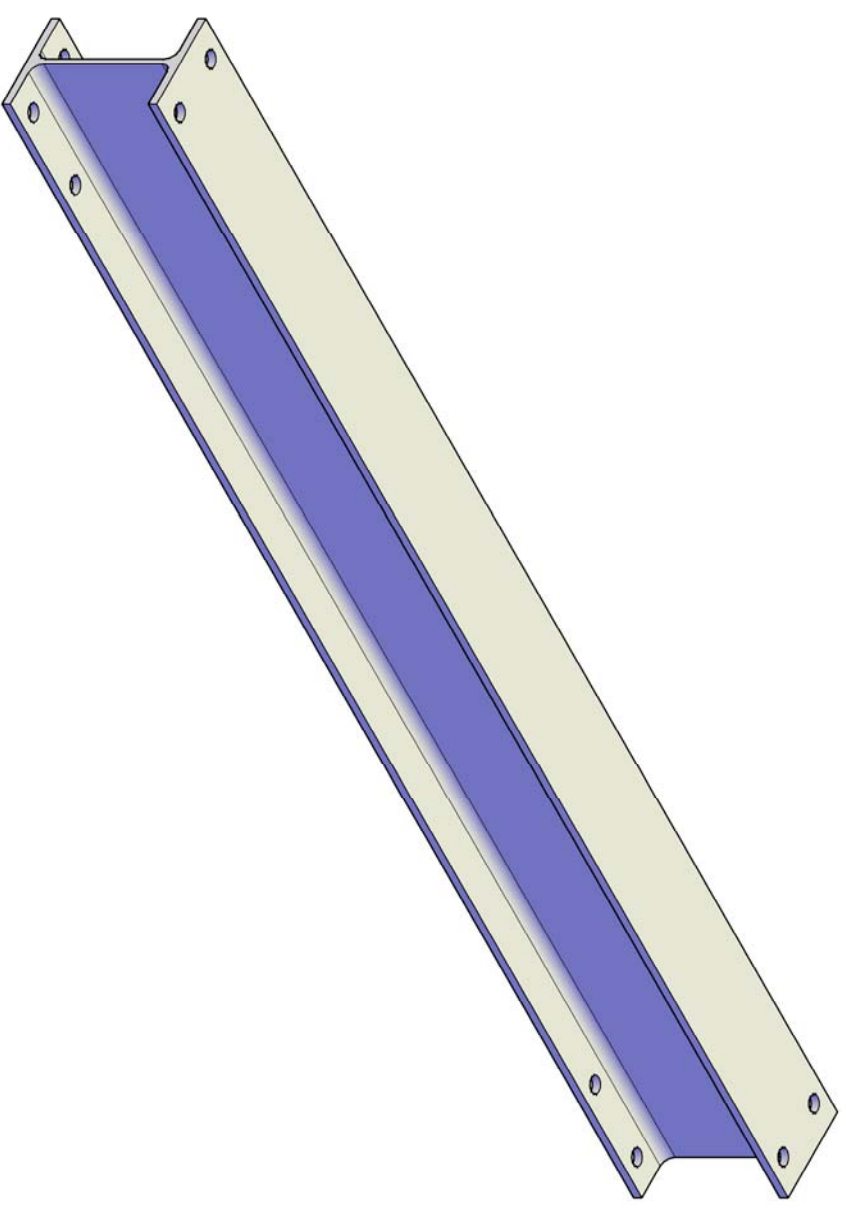
Date: 11/18/12
Quantity: 4



TOP VIEW



FRONT VIEW

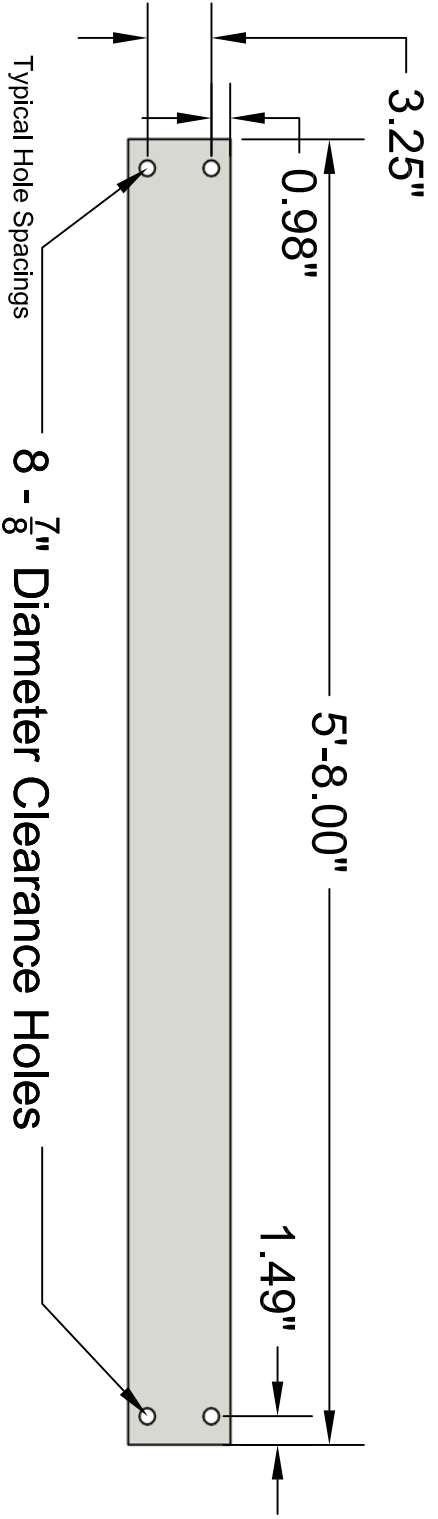


SIDE VIEW

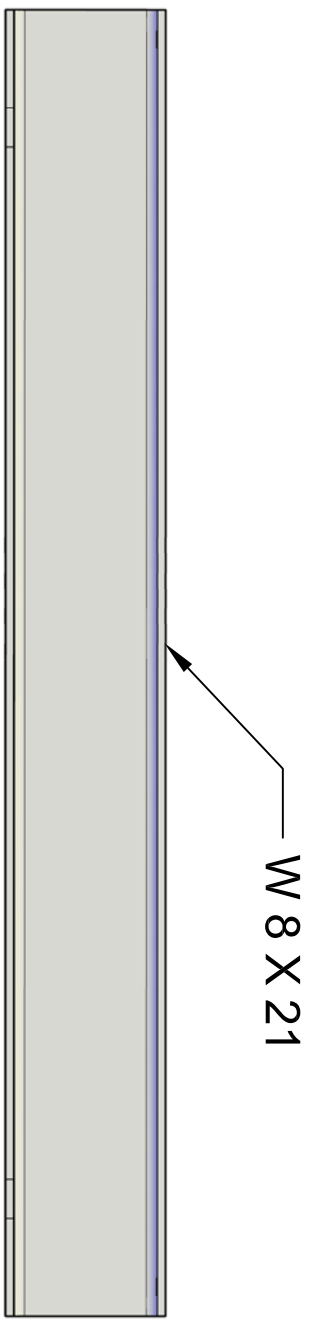
Part ID: Rear Support Beam 1

Drawn by: AWS
Project: Multiple Pull-out Box

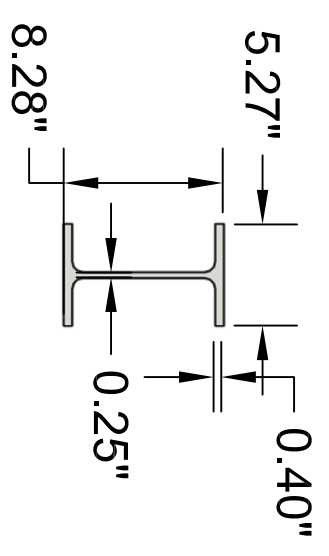
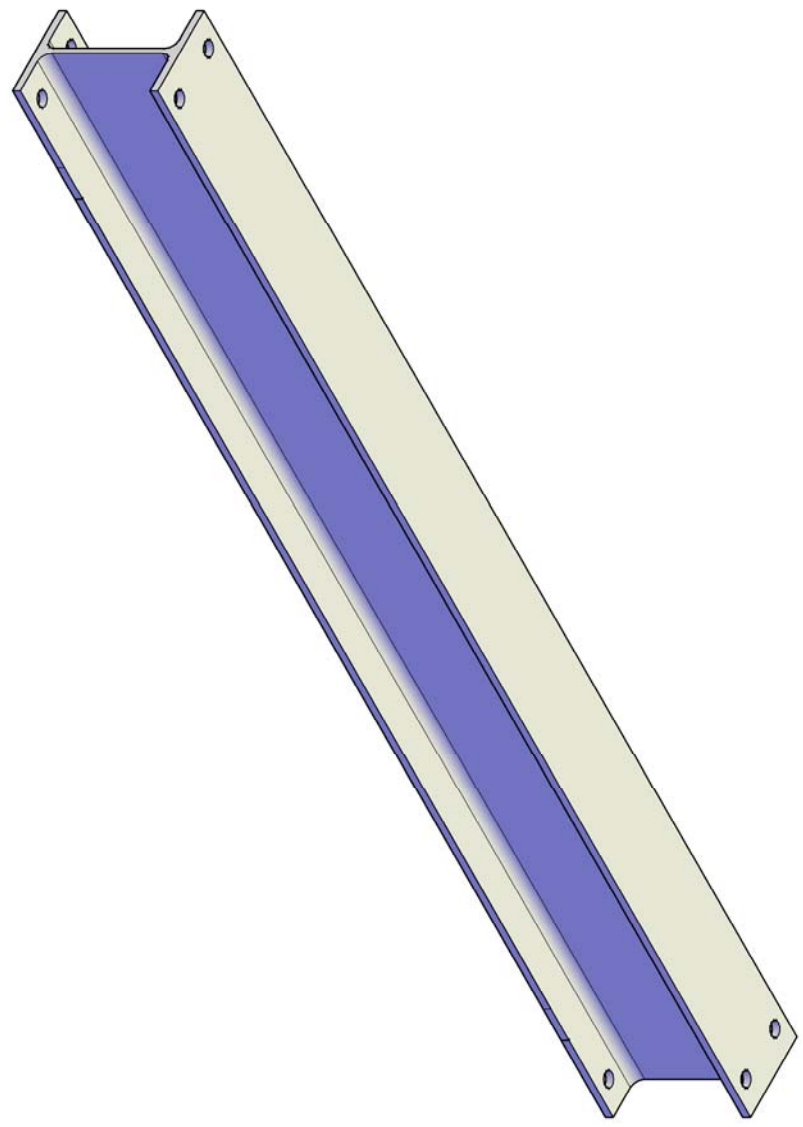
Date: 11/18/12
Quantity: 4



TOP VIEW



FRONT VIEW



SIDE VIEW

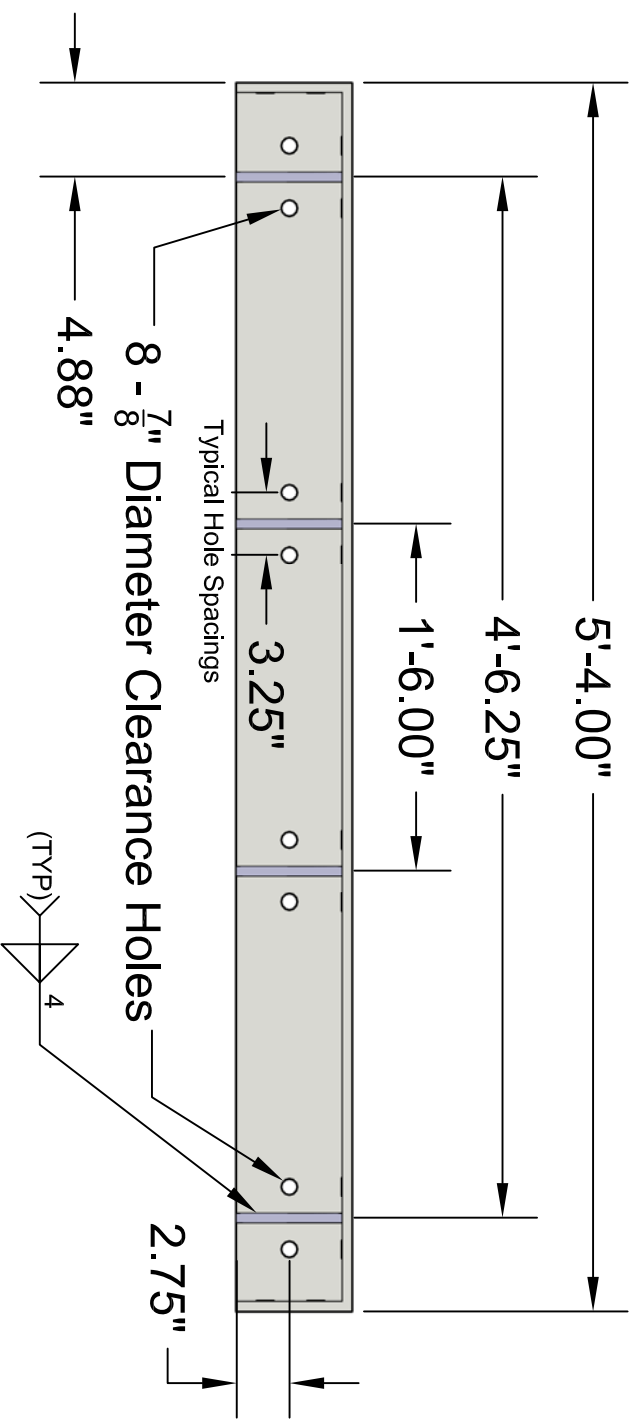
Part ID: Rear Support Beam

Drawn by: AWS

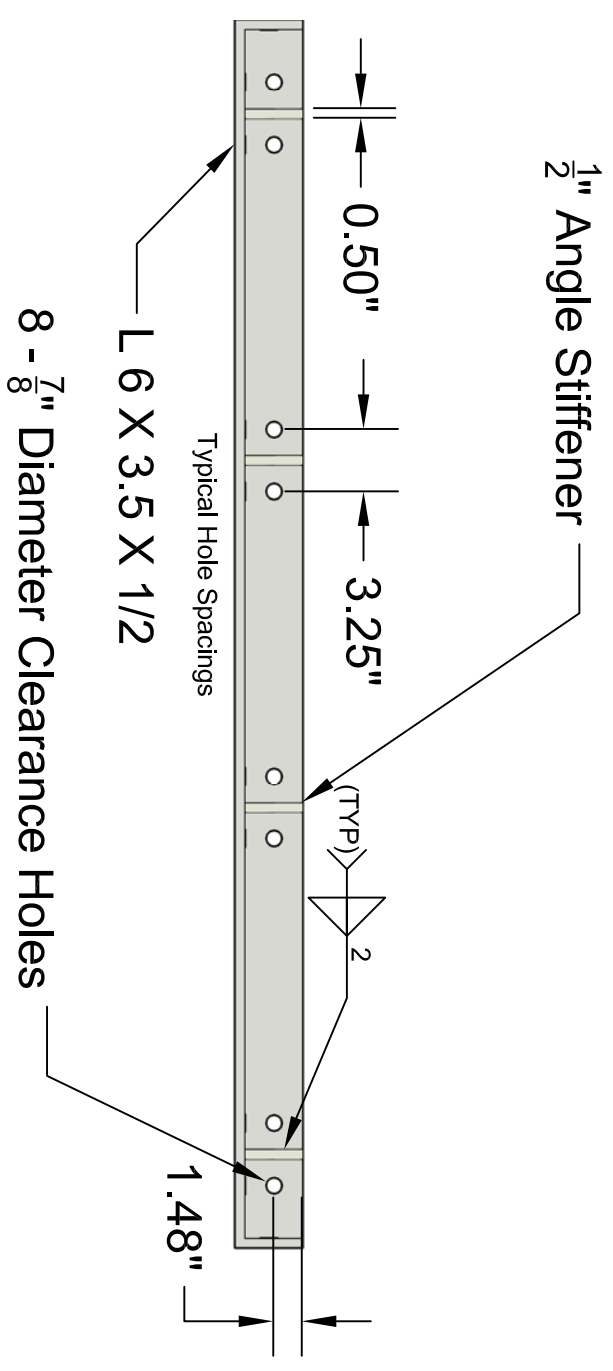
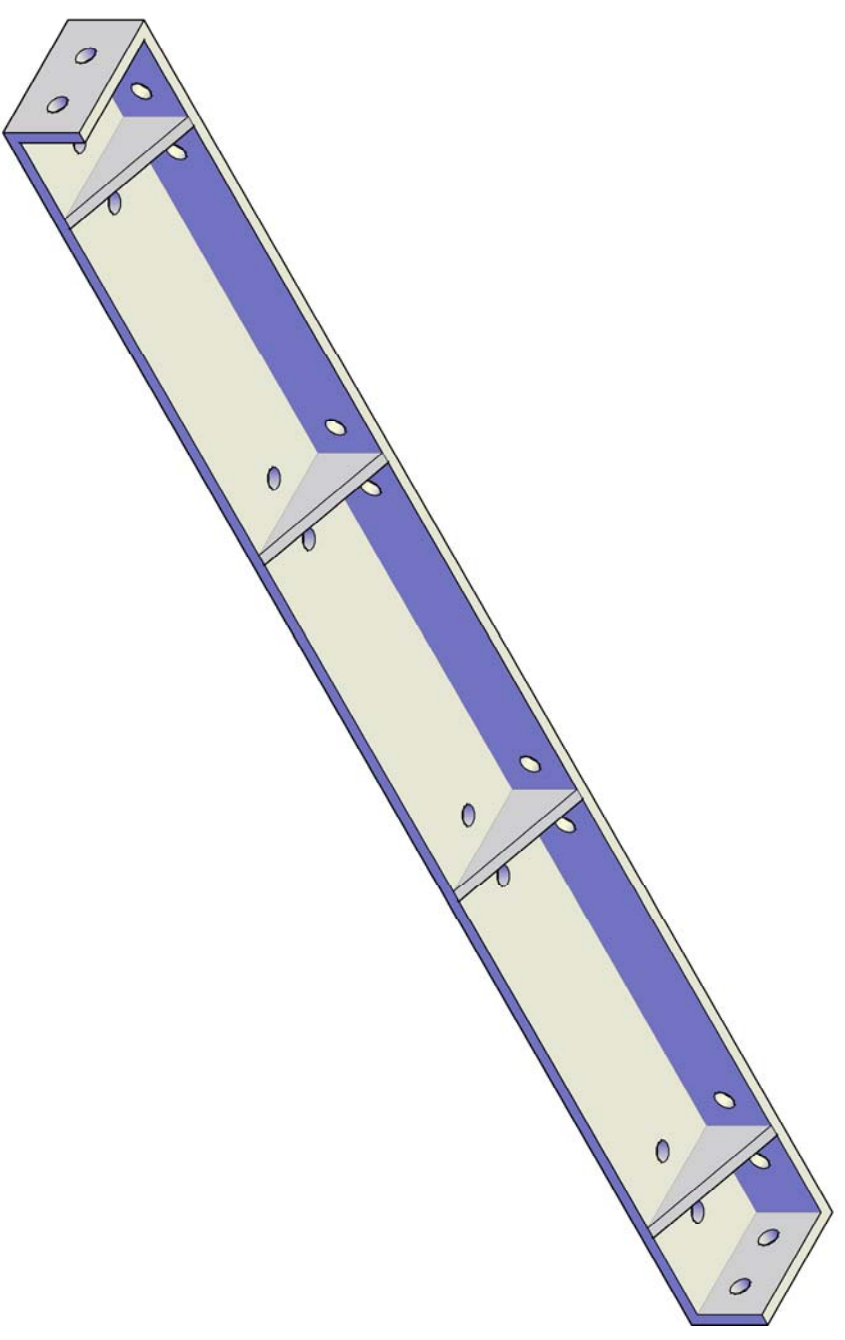
Date: 11/18/12

Project: Multiple Pull-out Box

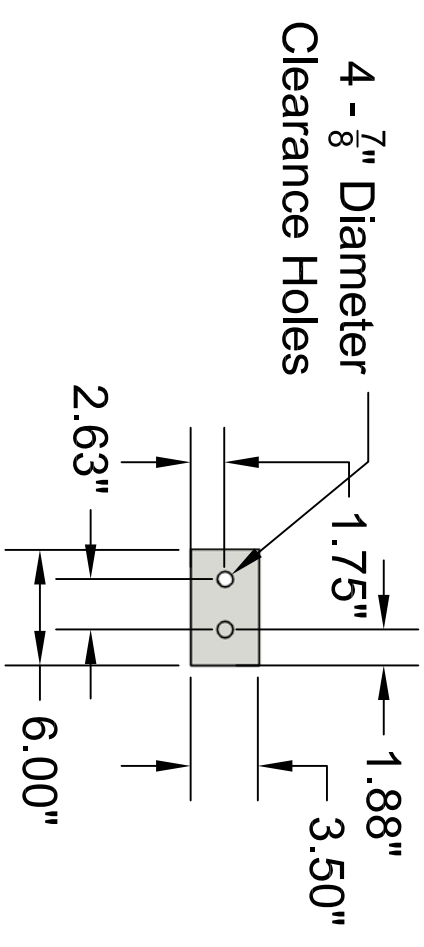
Quantity: 2



TOP VIEW



FRONT VIEW



SIDE VIEW

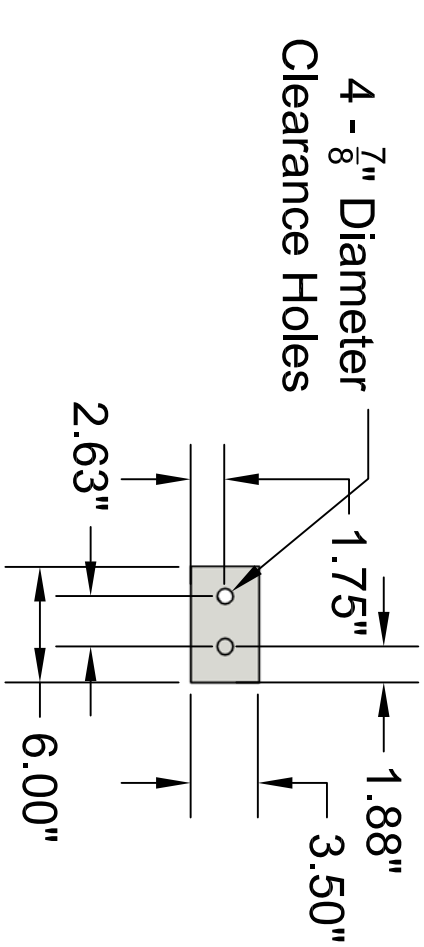
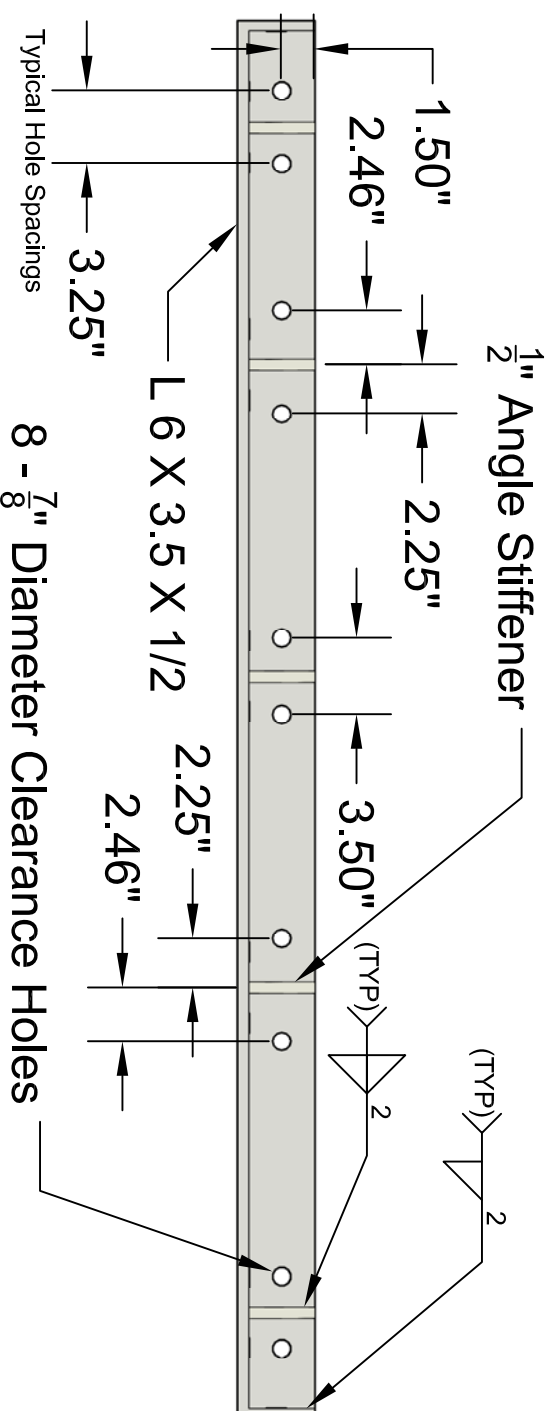
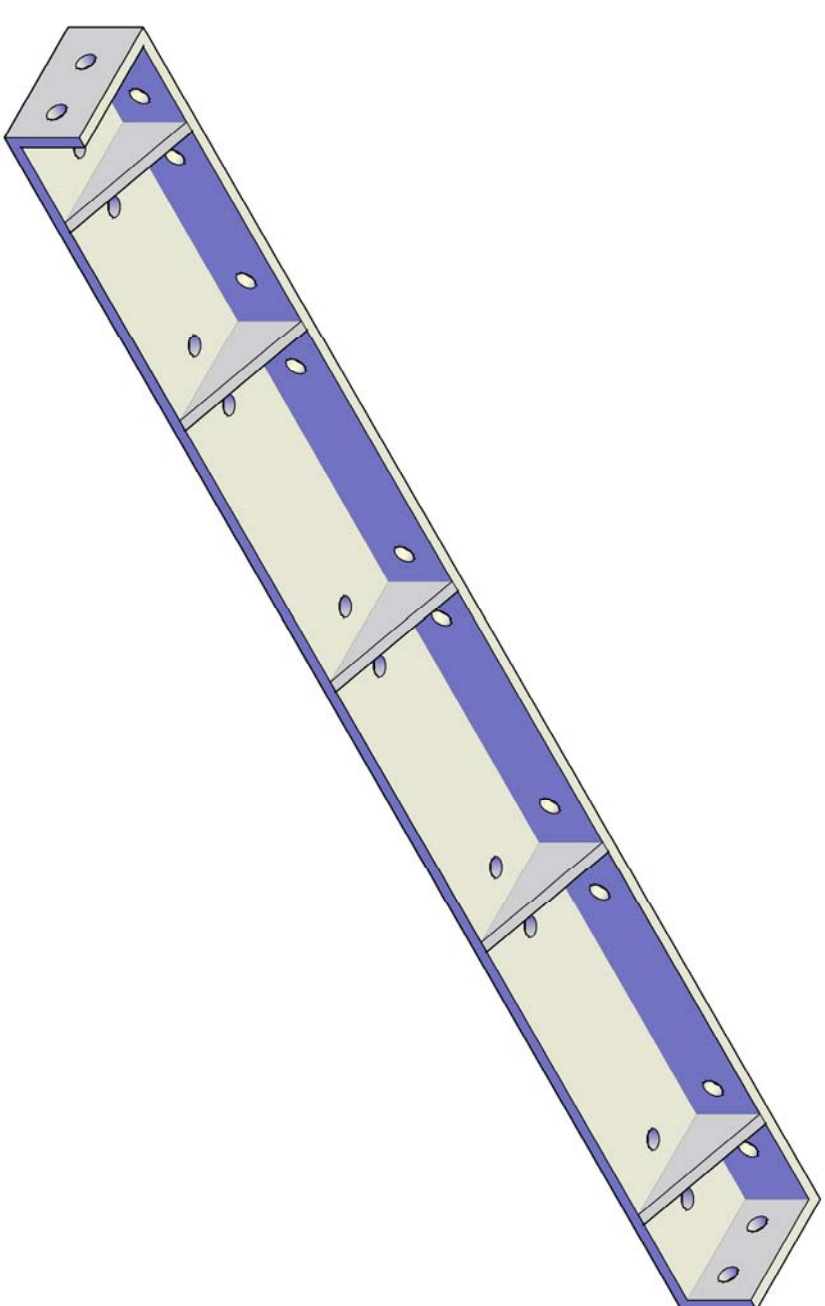
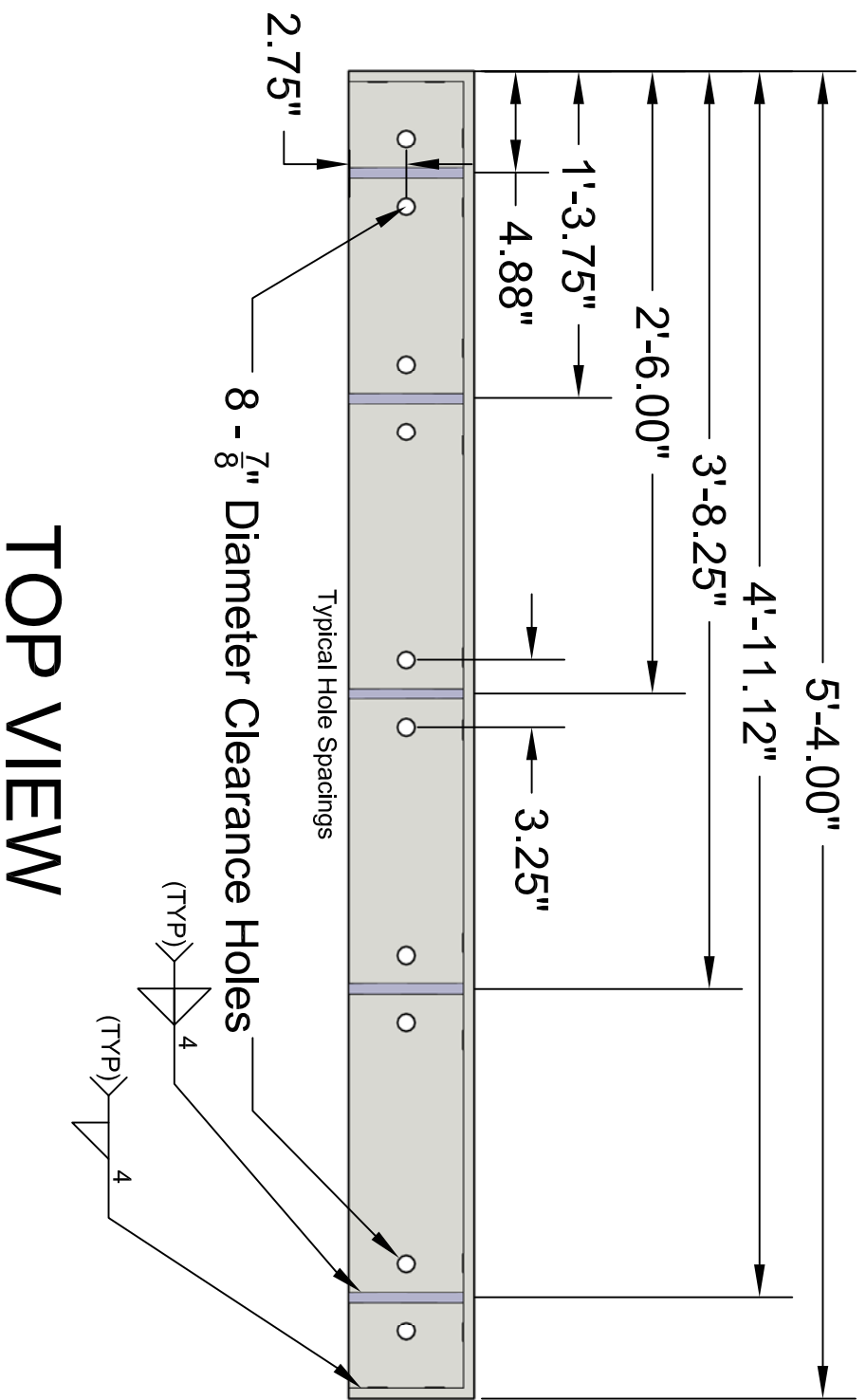
Part ID: Rear Support Angle

Drawn by: AWS

Date: 11/18/12

Project: Multiple Pull-out Box

Quantity: 2

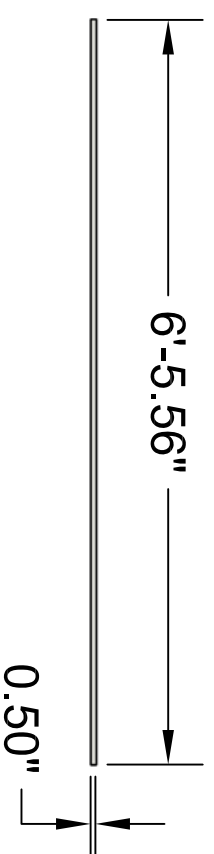
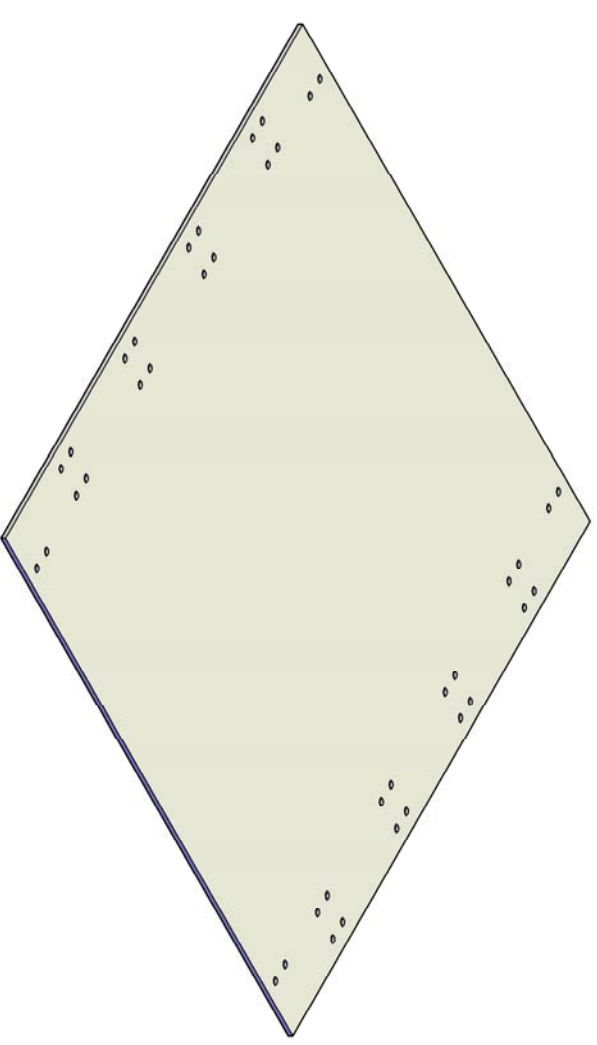
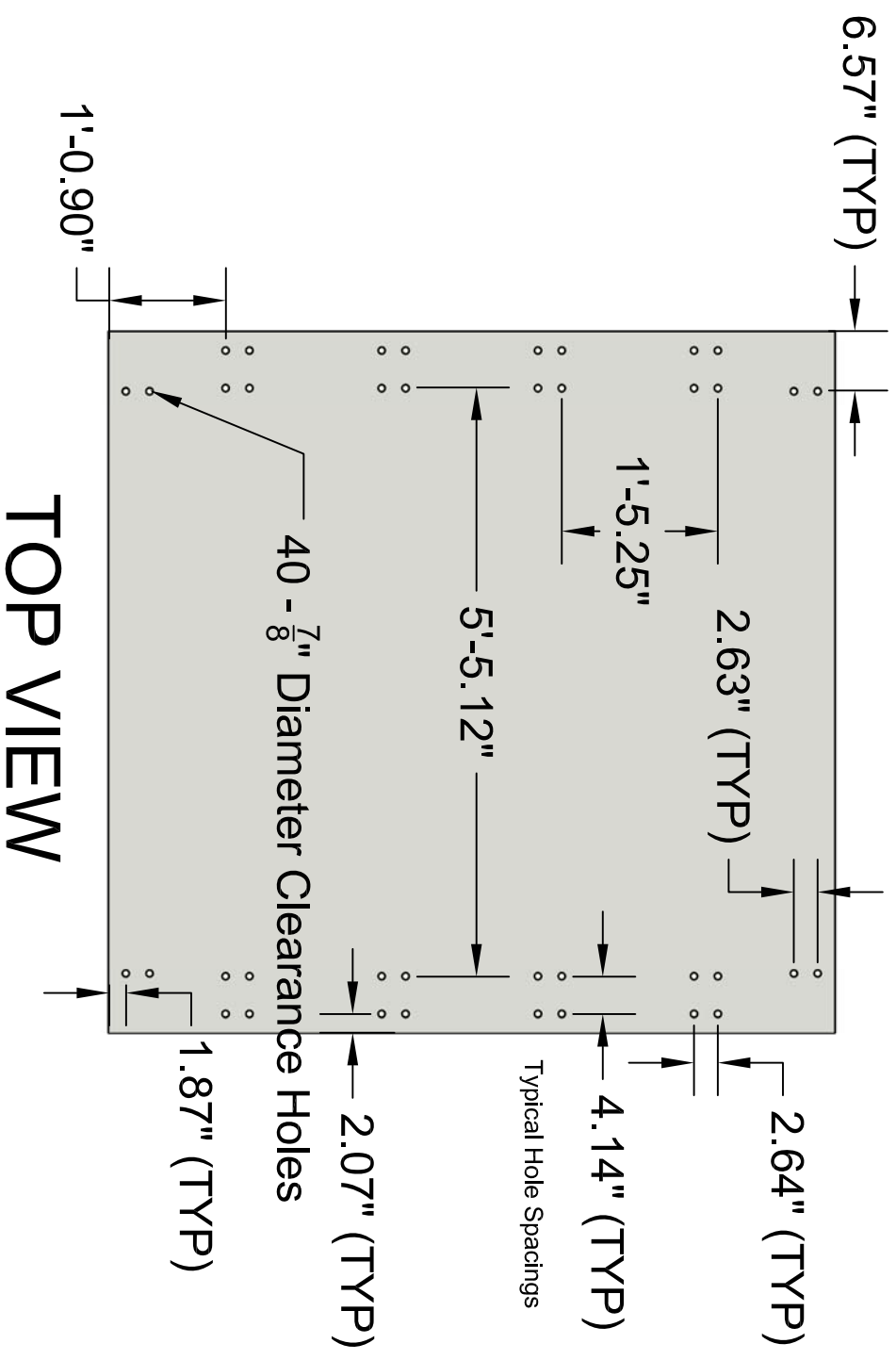


FRONT VIEW

SIDE VIEW

Part ID: Front Support Angle

Drawn by: AWS	Date: 11/18/12
Project: Multiple Pull-out Box	Quantity: 2



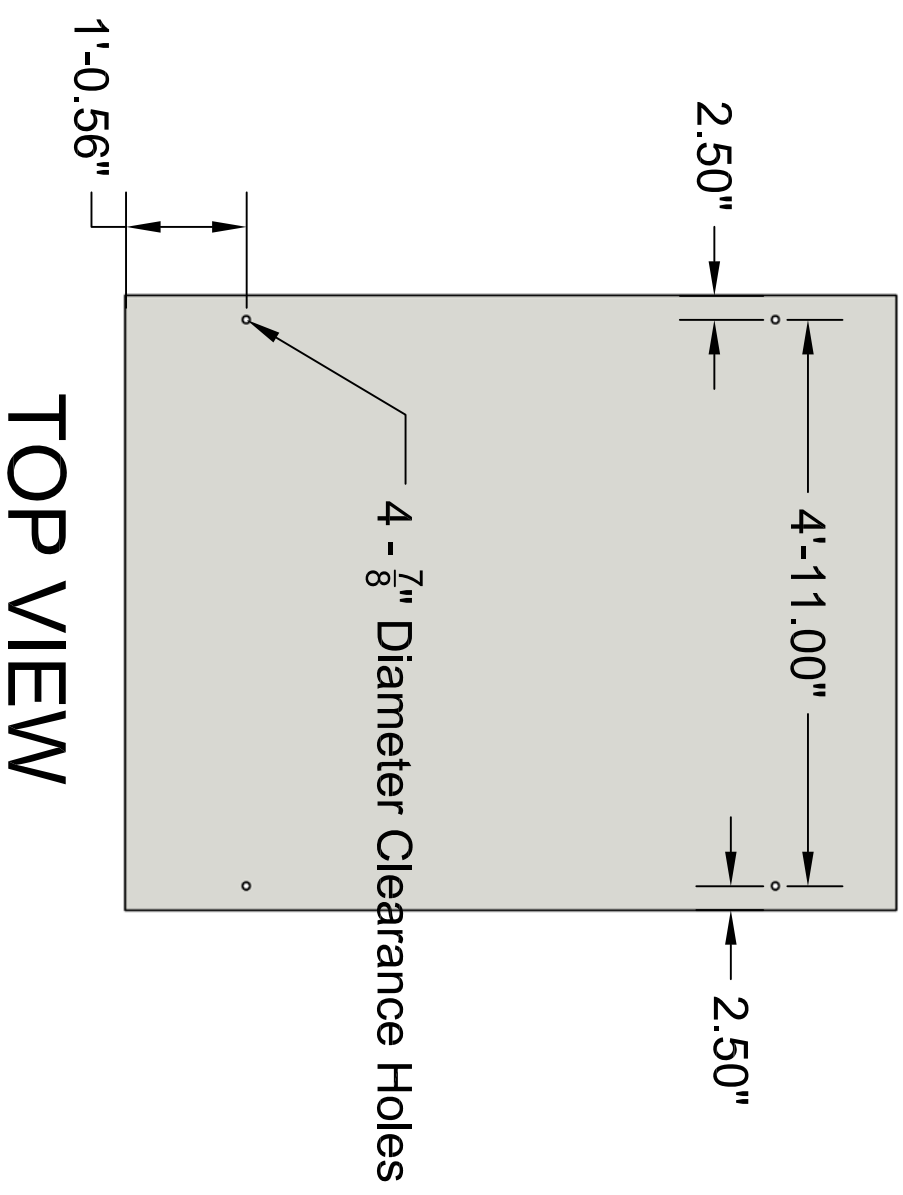
Part ID: Base Plate

Drawn by: AWS

Project: Multiple Pull-out Box

Date: 11/18/12

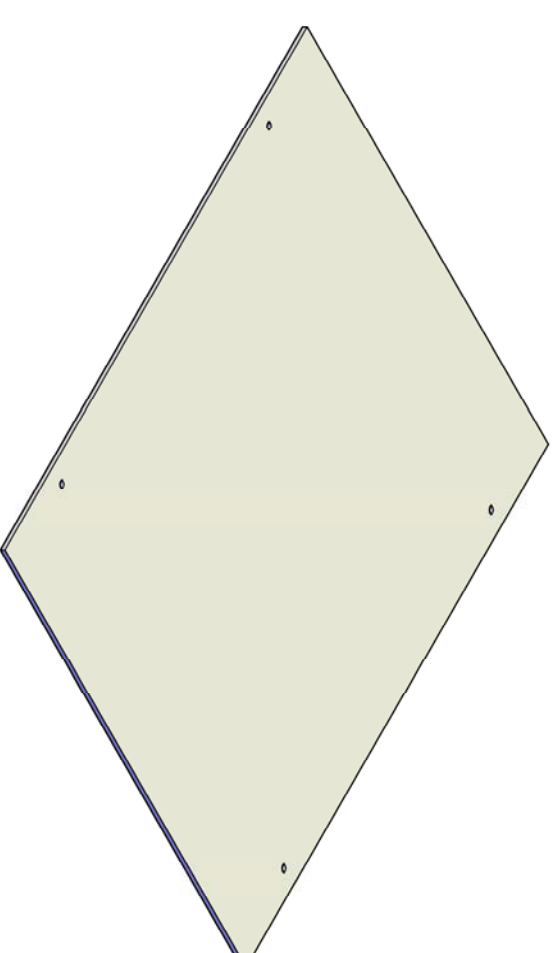
Quantity: 1



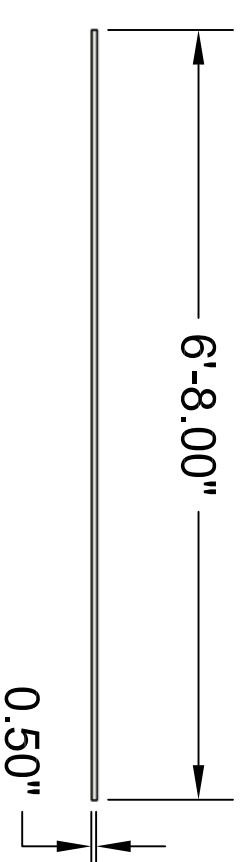
TOP VIEW



FRONT VIEW



SIDE VIEW



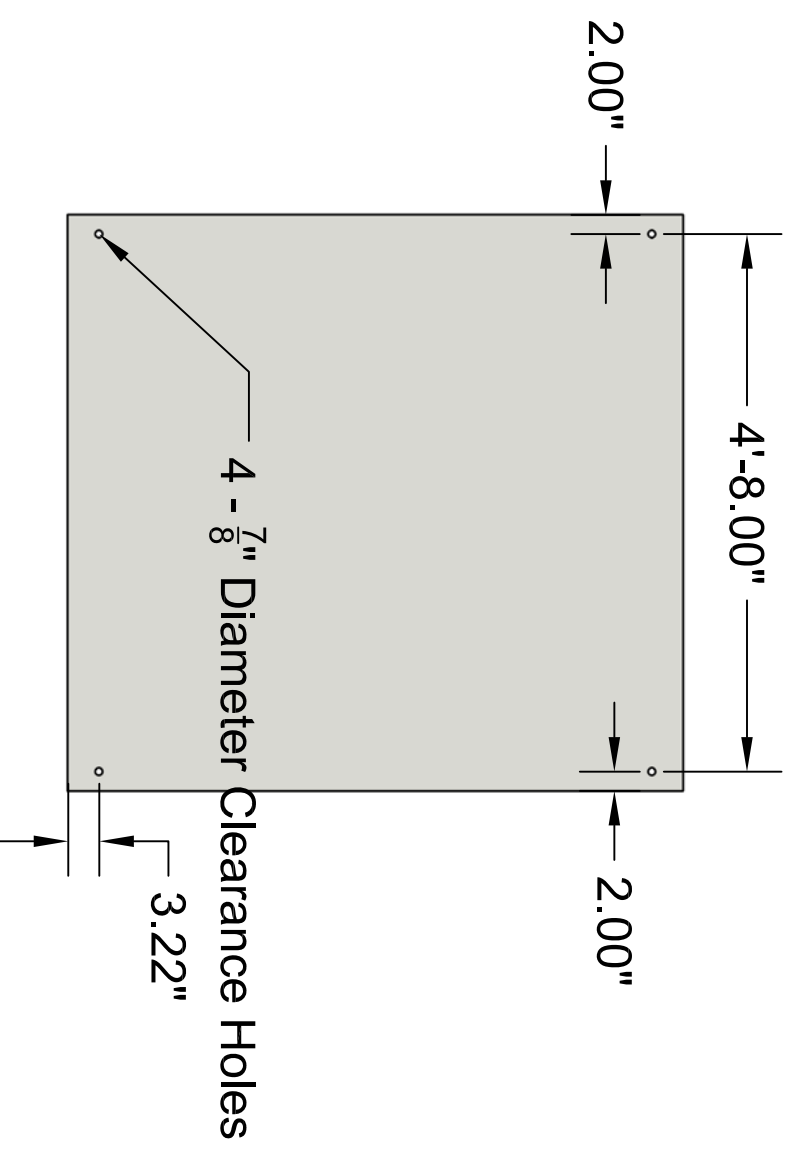
Part ID: Side Plate

Drawn by: AWS

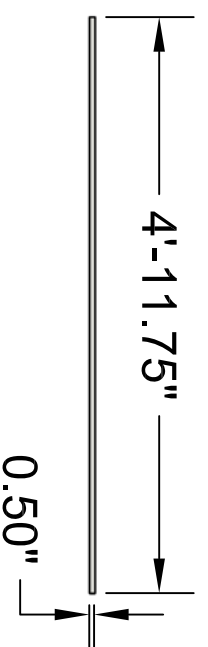
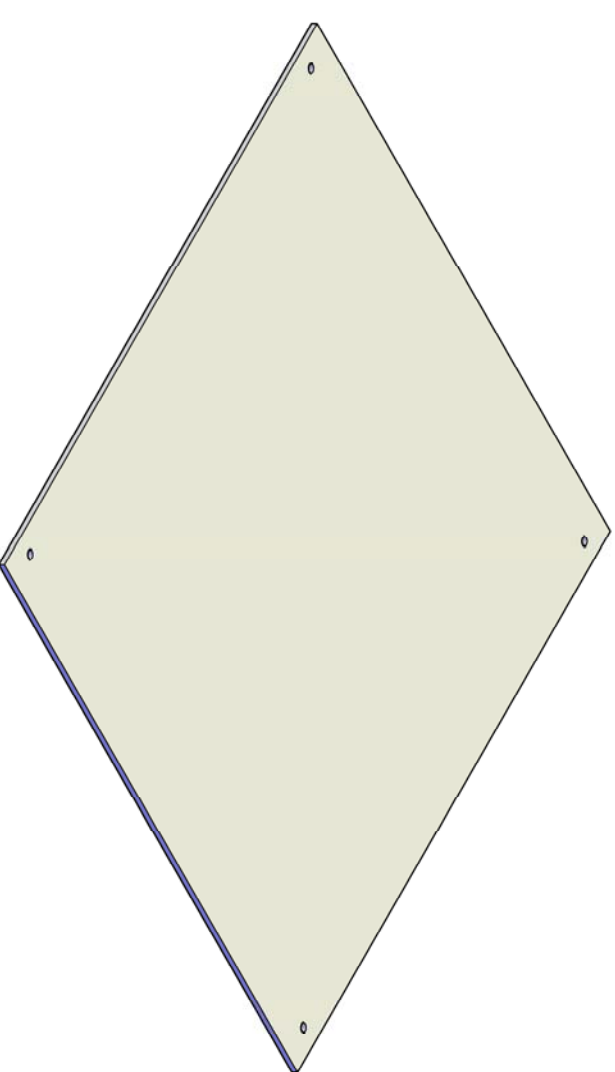
Date: 11/18/12

Project: Multiple Pull-out Box

Quantity: 2



TOP VIEW



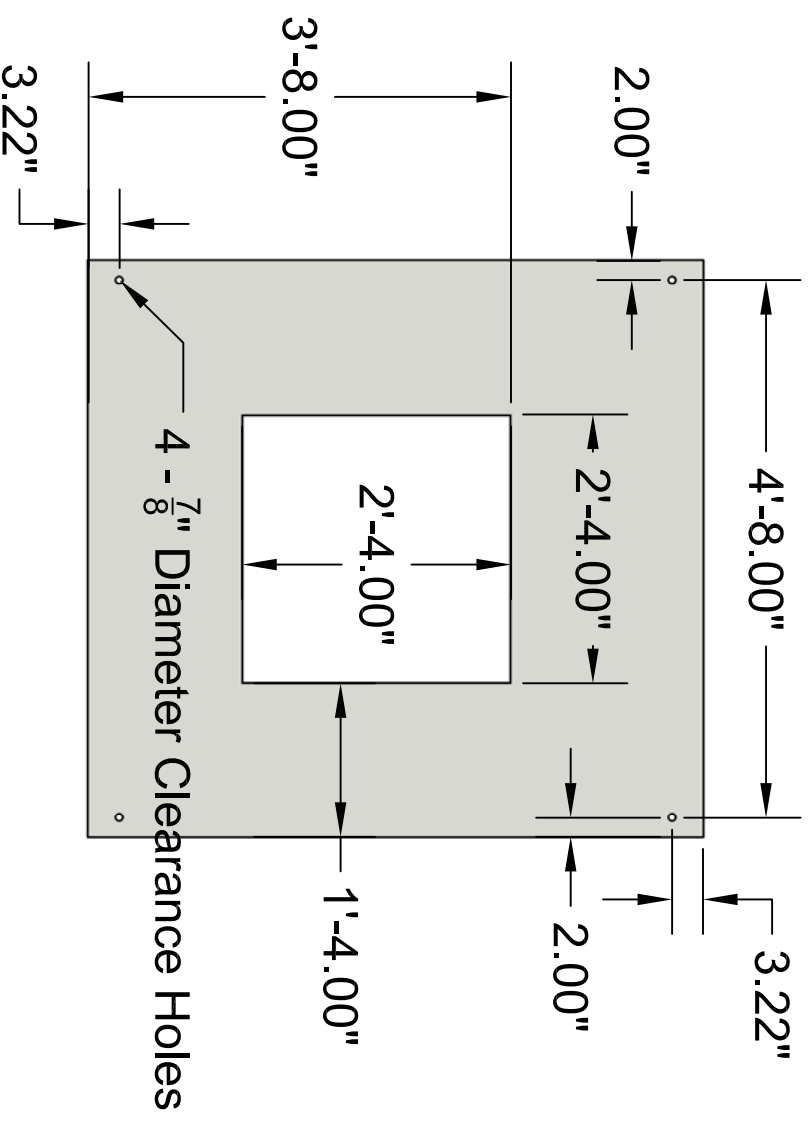
FRONT VIEW

SIDE VIEW

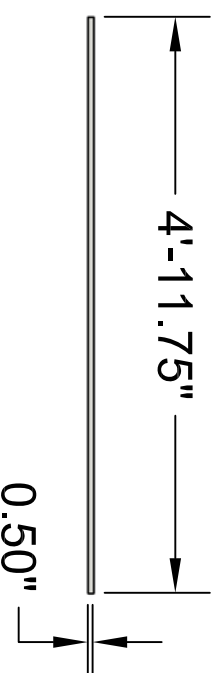
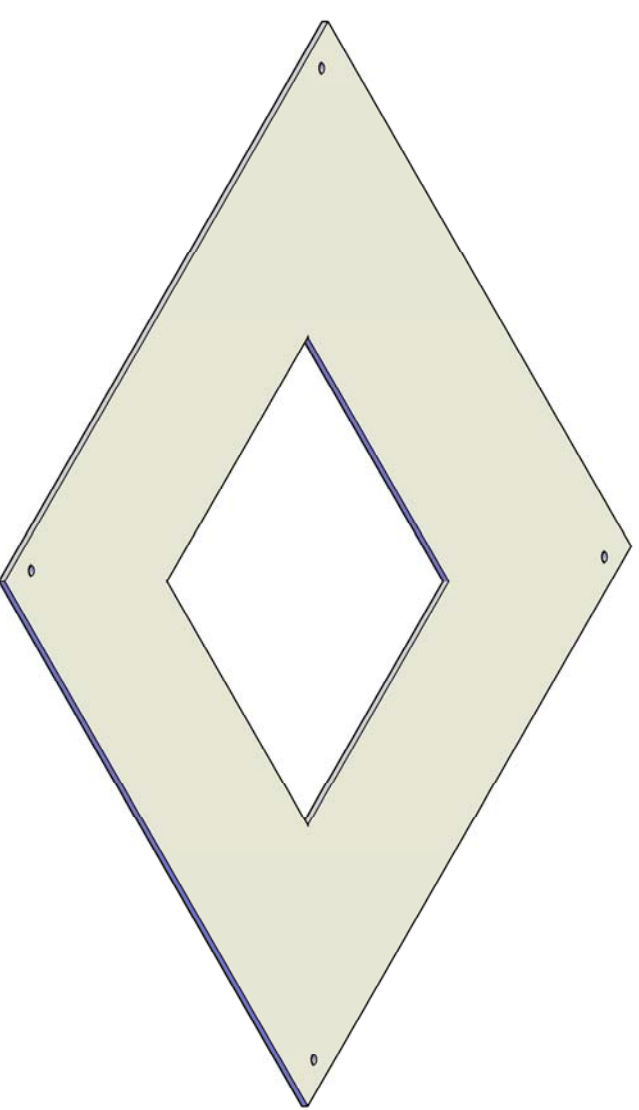
Part ID: Rear Plate

Drawn by: AWS
Project: Multiple Pull-out Box

Date: 11/18/12
Quantity: 1



TOP VIEW



FRONT VIEW

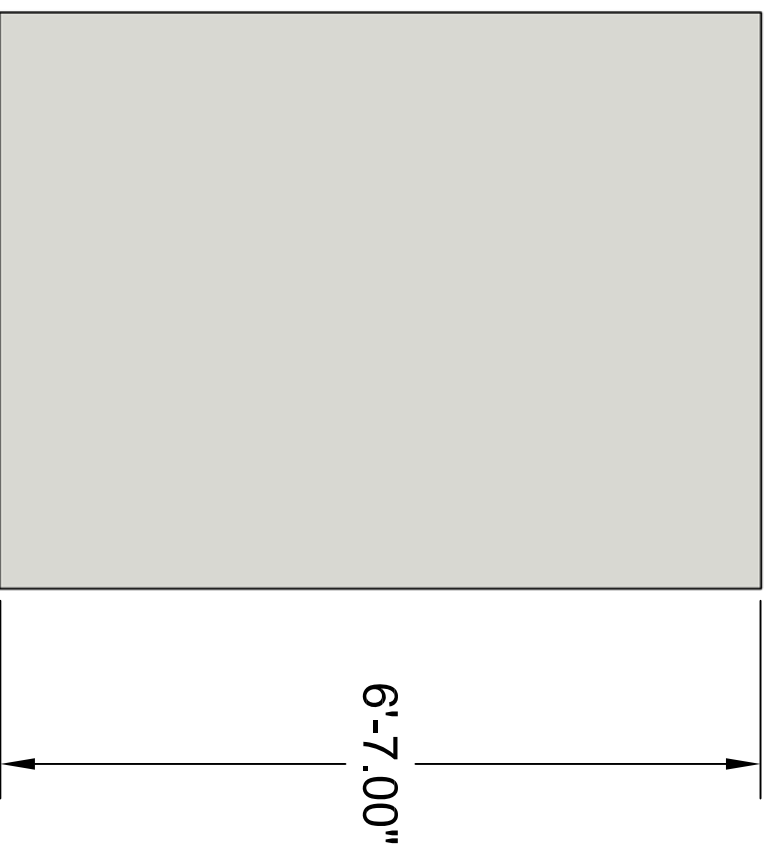


SIDE VIEW

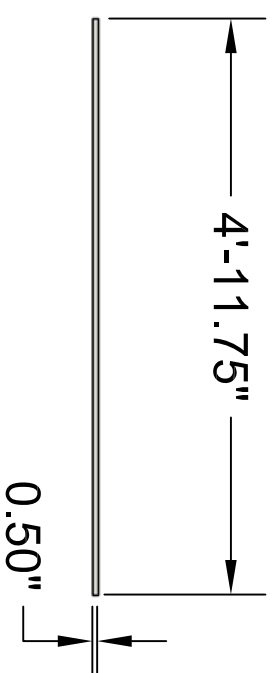
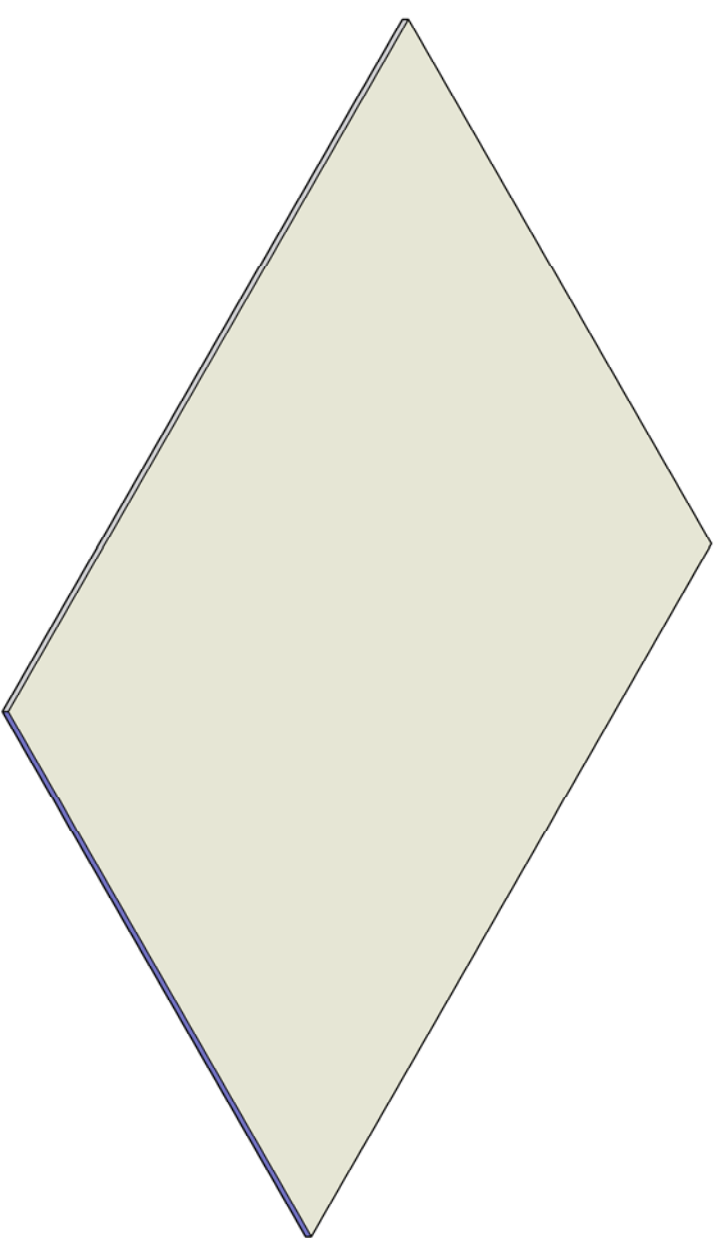
Part ID: Front Plate

Drawn by: AWS
Project: Multiple Pull-out Box

Date: 11/18/12
Quantity: 1



TOP VIEW



FRONT VIEW



SIDE VIEW

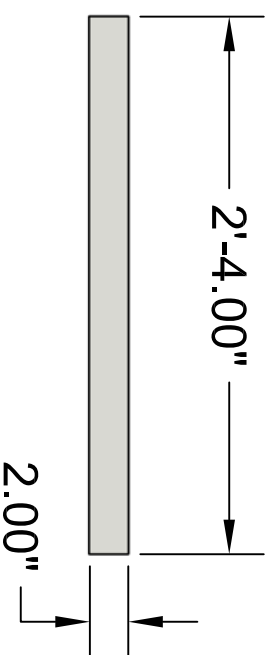
Part ID: Top Plate

Drawn by: AWS

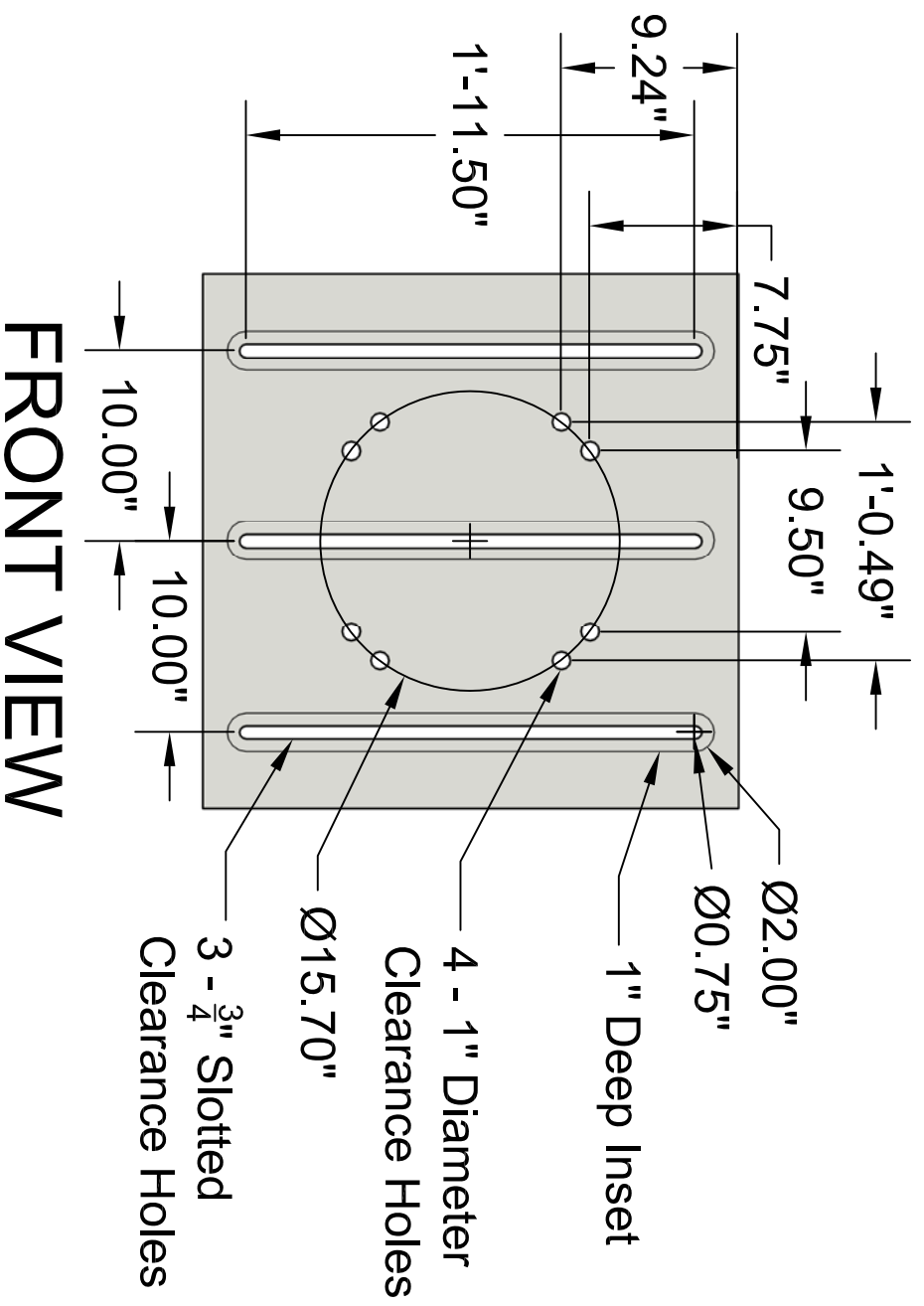
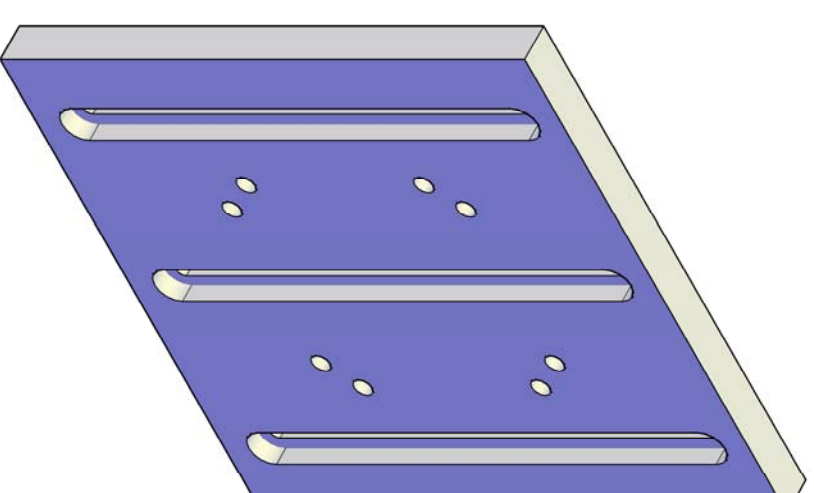
Date: 11/18/12

Project: Multiple Pull-out Box

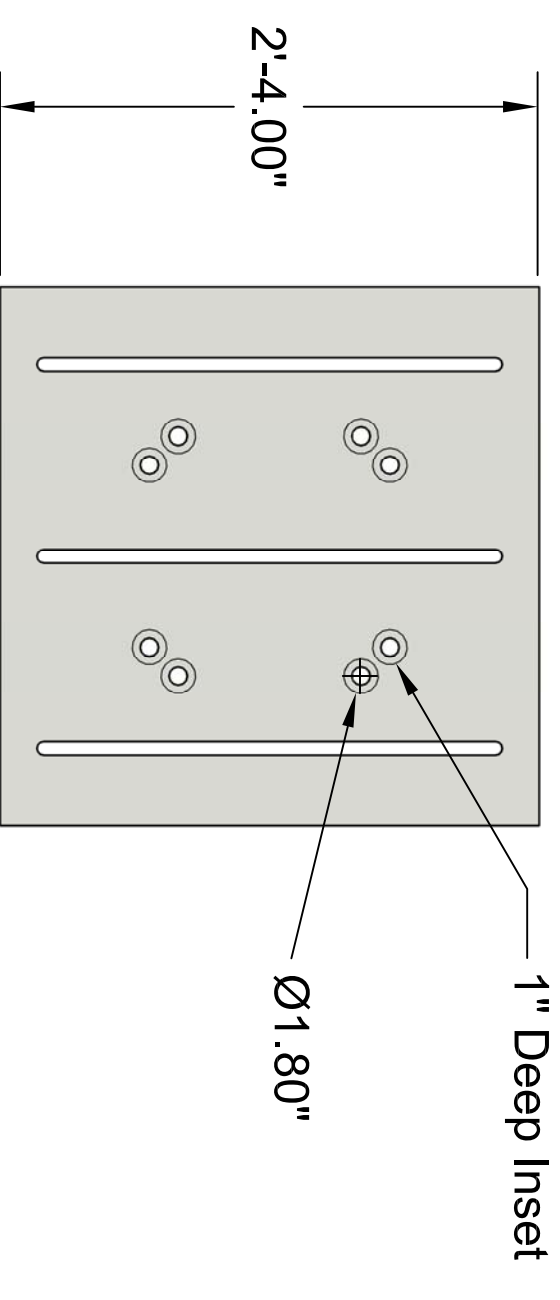
Quantity: 1



TOP VIEW



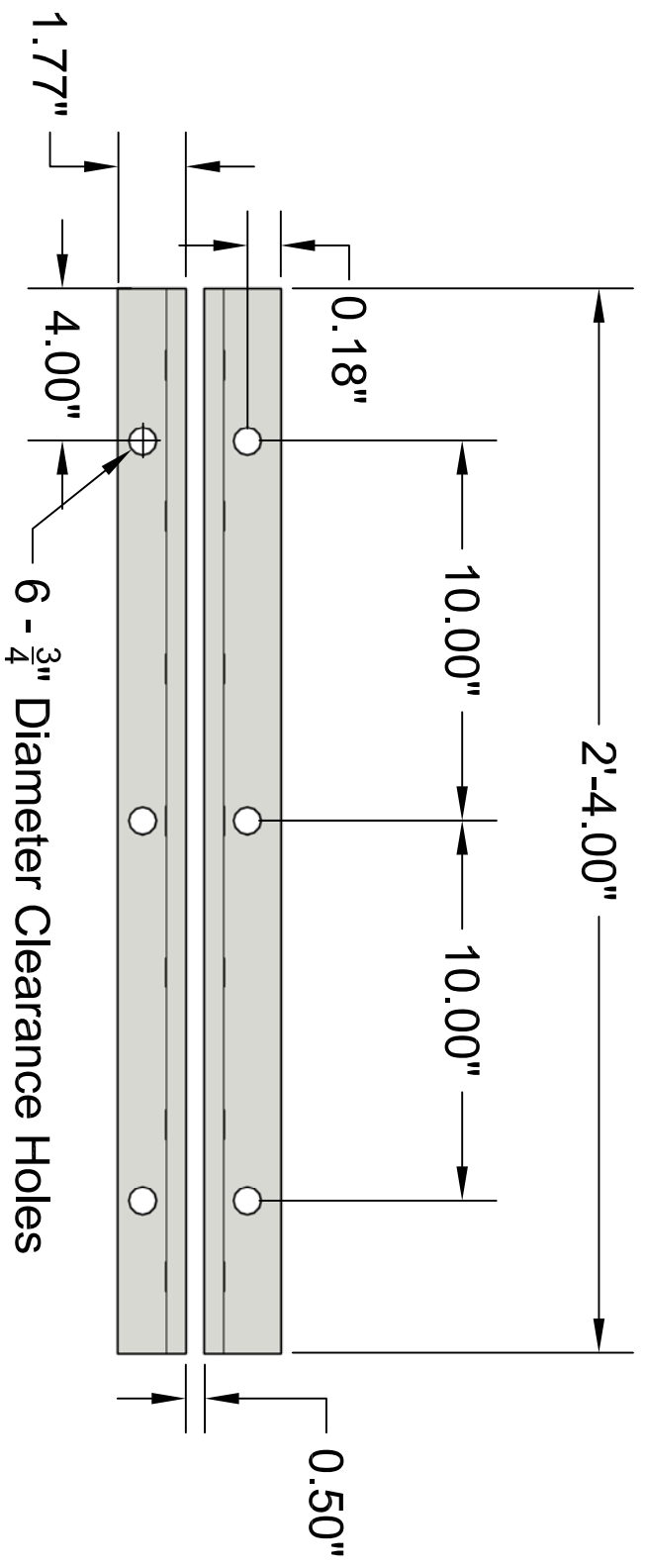
FRONT VIEW



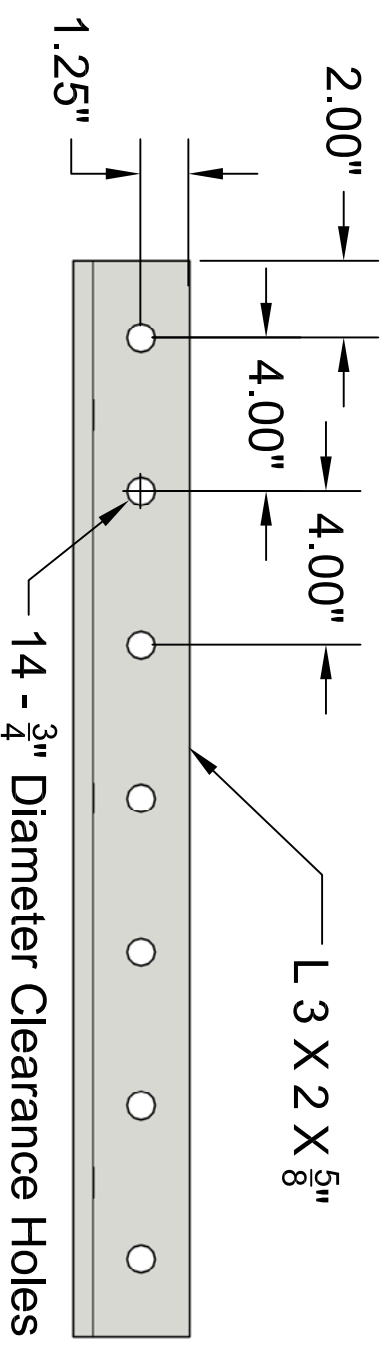
BACK VIEW

Part ID: Connection Plate 1

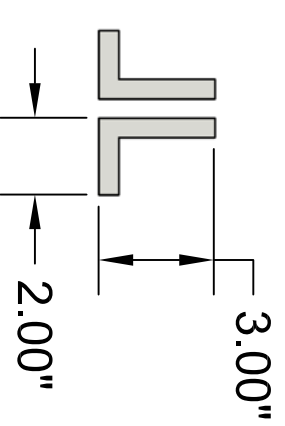
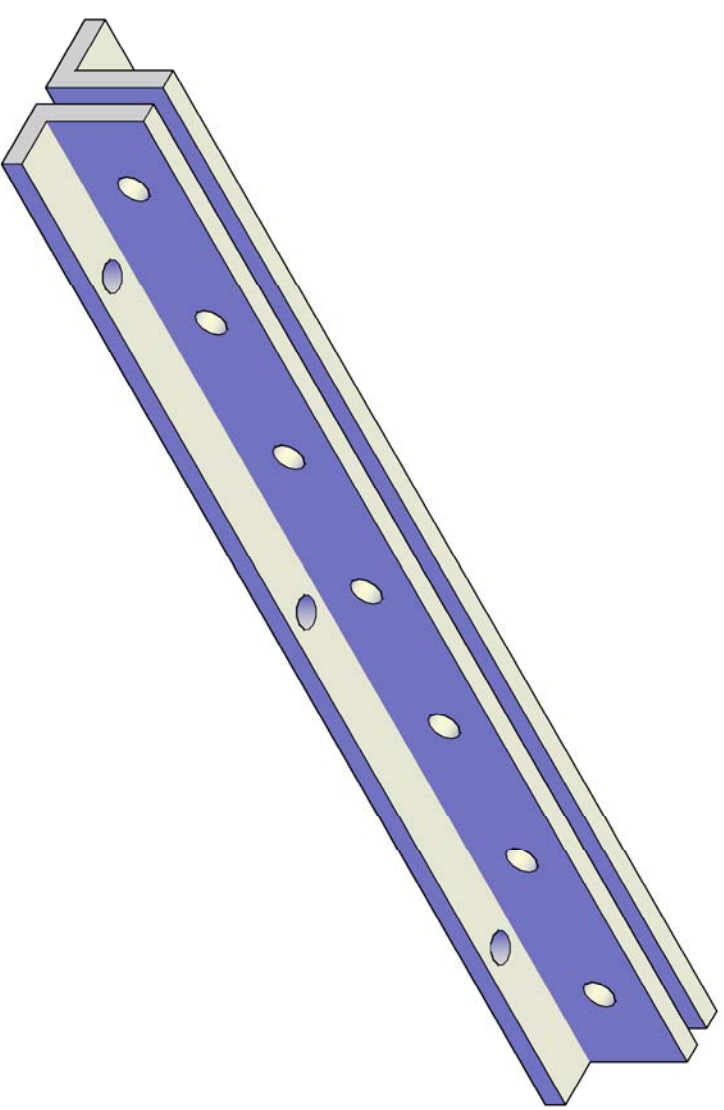
Drawn by: AWS	Date: 11/18/12
Project: Multiple Pull-out Box	Quantity: 1



TOP VIEW



FRONT VIEW

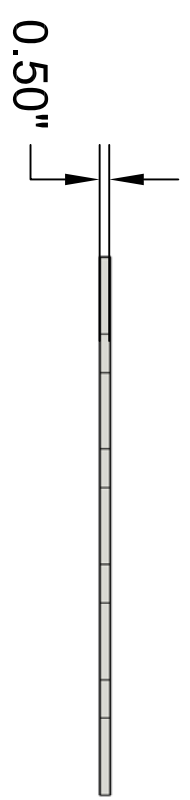
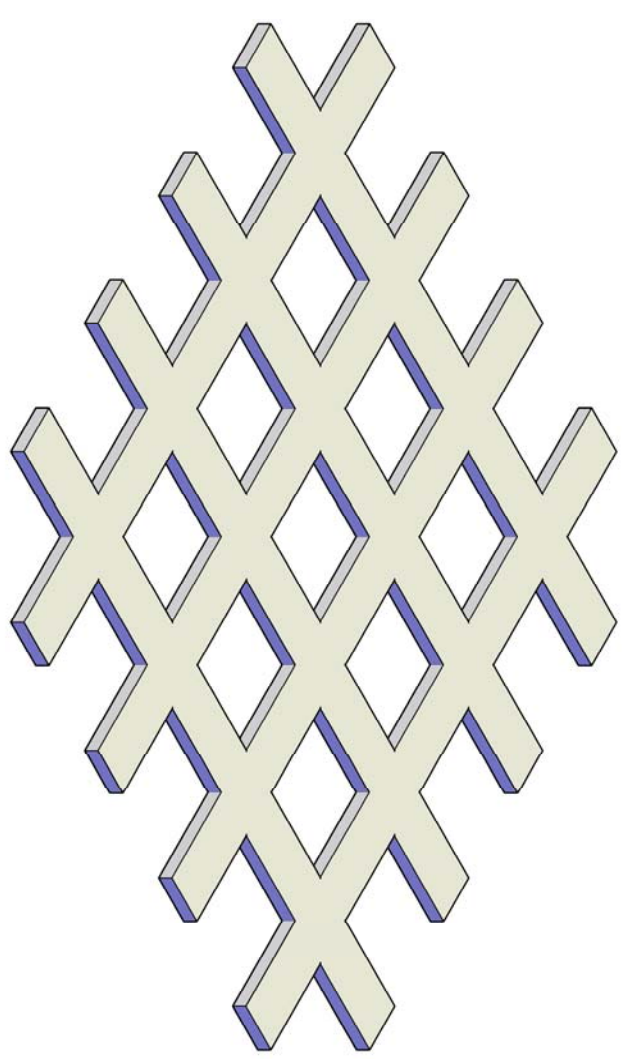
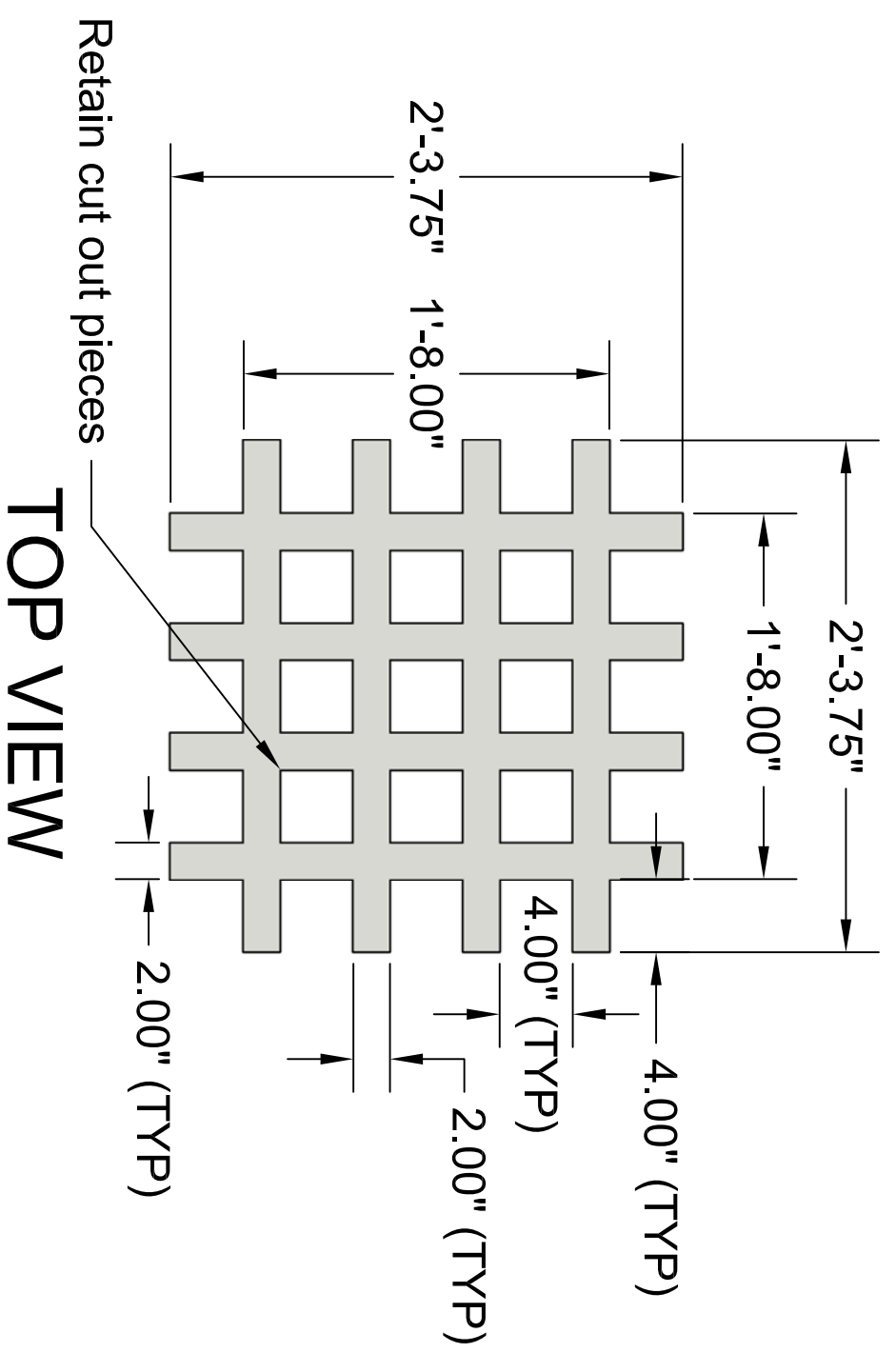


SIDE VIEW

Part ID: Connection Angle

Drawn by: AWS
Project: Multiple Pull-out Box

Date: 11/18/12
Quantity: 3



FRONT VIEW

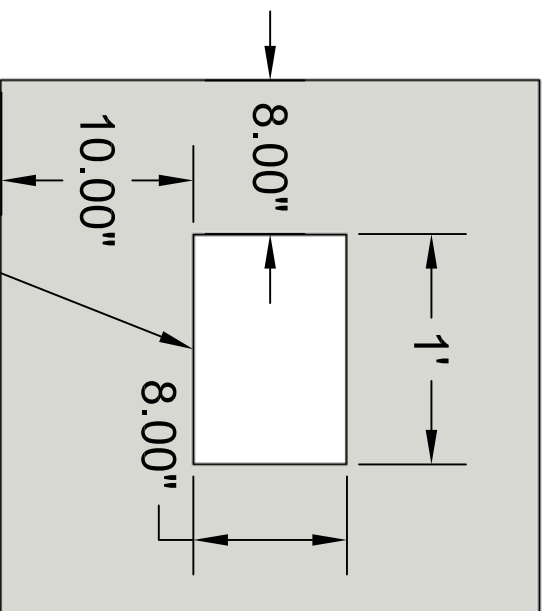
SIDE VIEW



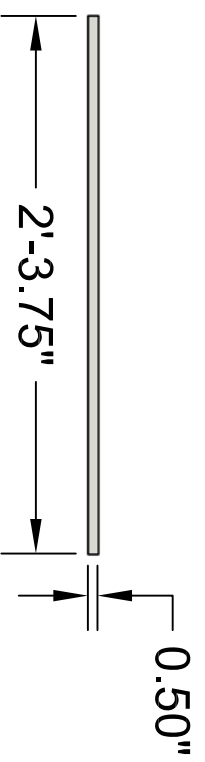
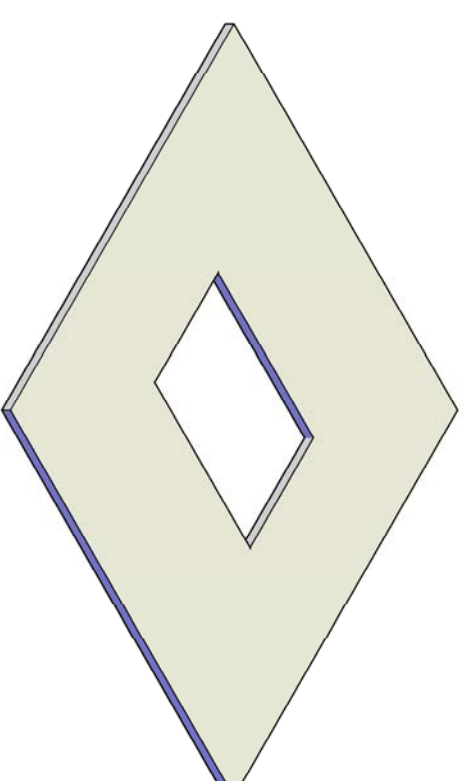
Part ID: Pull-out Plate 1

Drawn by: AWS
Project: Multiple Pull-out Box

Date: 11/20/12
Quantity: 1



TOP VIEW



FRONT VIEW

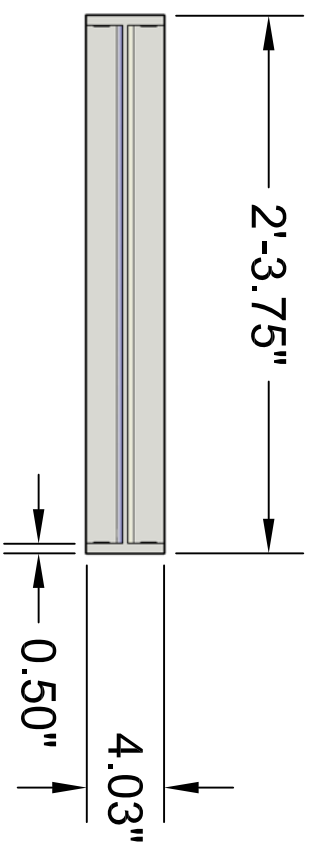


SIDE VIEW

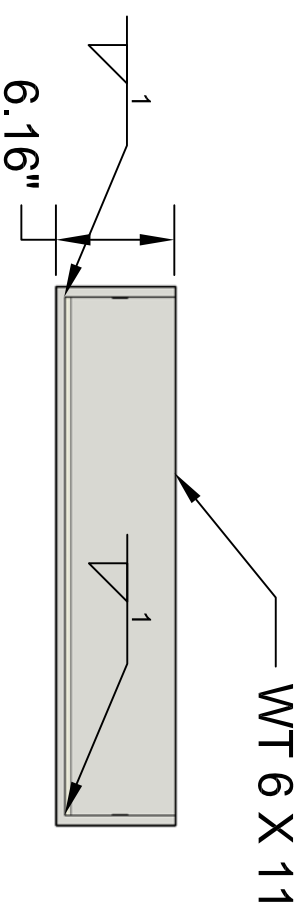
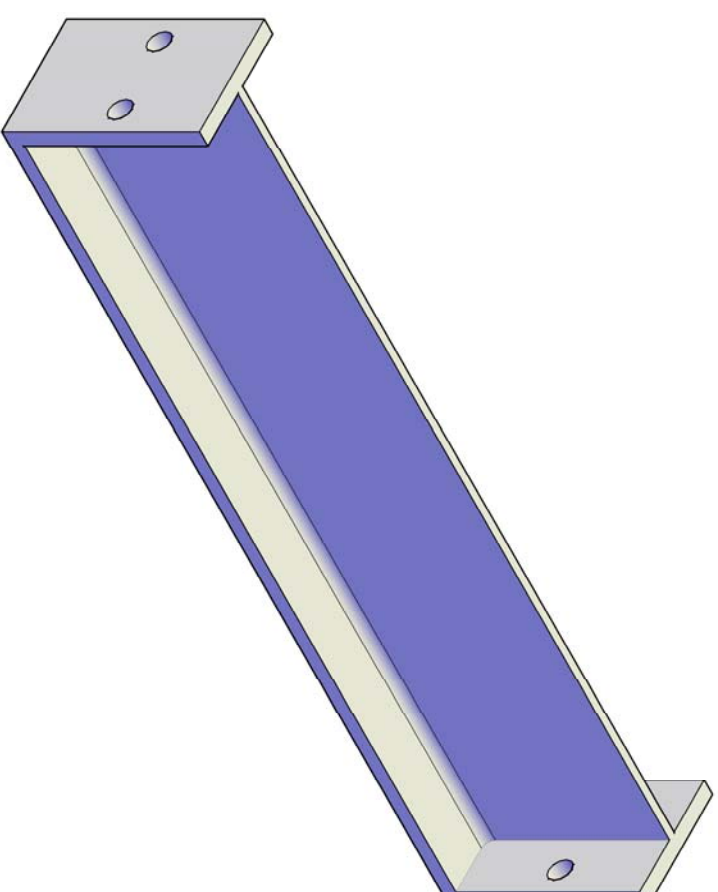
Part ID: Pull-out Plate 2

Drawn by: AWS
Project: Multiple Pull-out Box

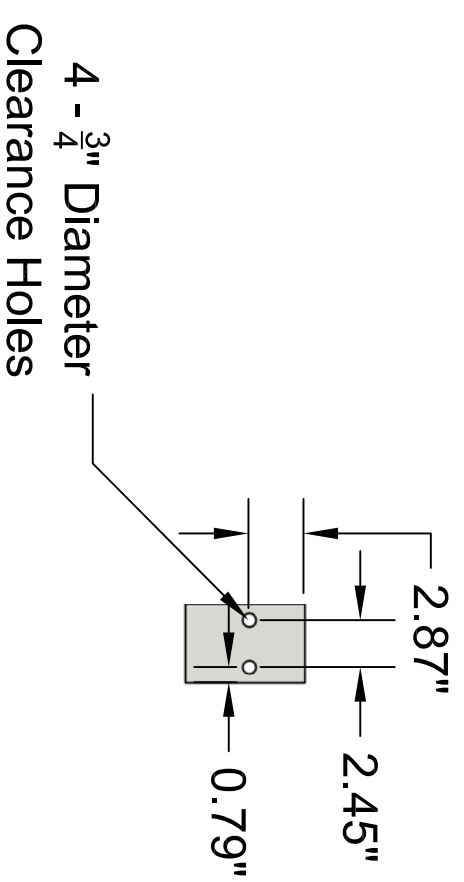
Date: 11/20/12
Quantity: 1



TOP VIEW



FRONT VIEW



SIDE VIEW

Part ID: Pull-out Reinforcement

Drawn by: AWS
Project: Multiple Pull-out Box

Date: 11/20/12
Quantity: 3

PART 3: SUPPLEMENTAL APPENDIX FOR CHAPTER 5

Pages: 338 – 340

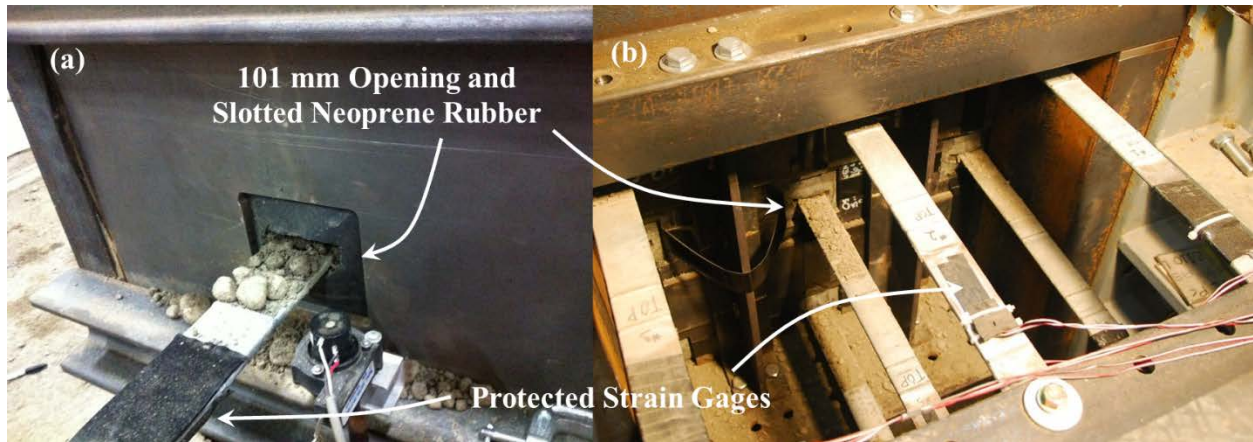
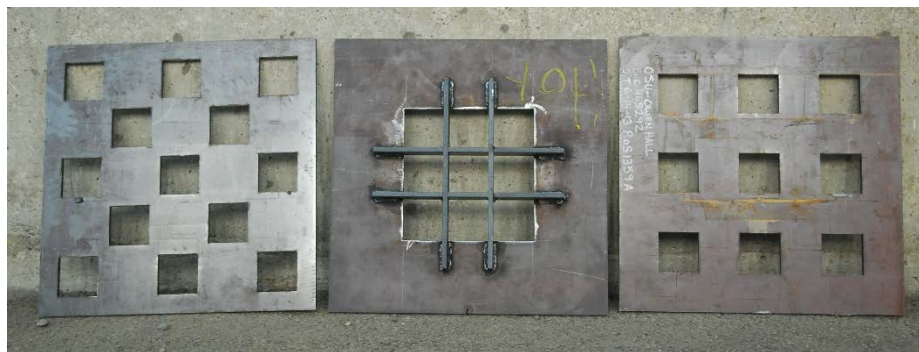


Figure B.5.S1. Stiffened steel face with 101 mm openings and slotted neoprene rubber membrane providing a soft boundary condition for the (a) single- and (b) multi-strip pullout apparatus.



**Figure B.5.S2. Interchangeable steel plates that represent different reinforcement spacing
(Note: 101 mm opening maintained in each plate).**

**APPENDIX D: LOAD-DISPLACEMENT RESPONSE FROM MULTI-
STRIP PULLOUT TESTS**

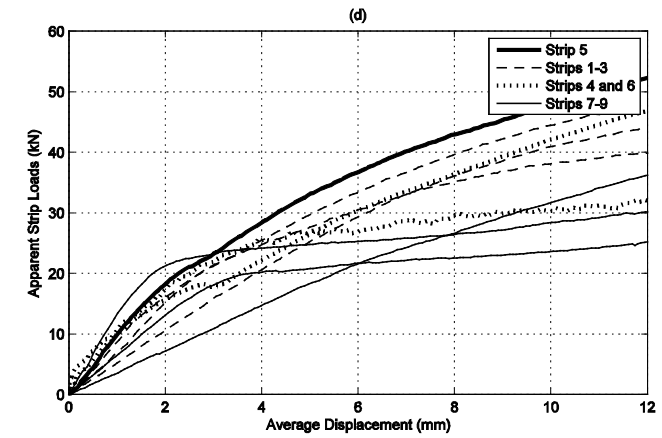
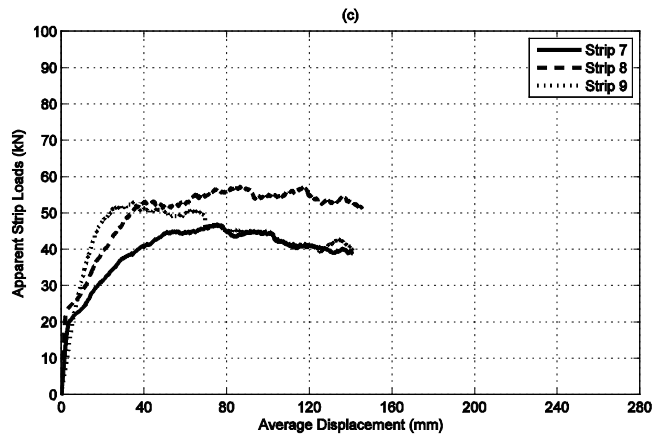
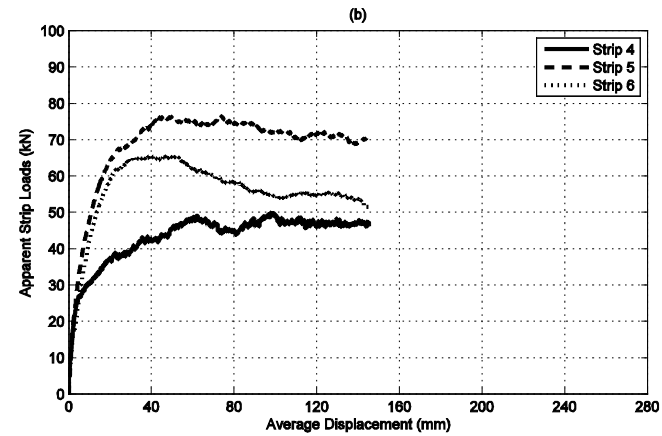
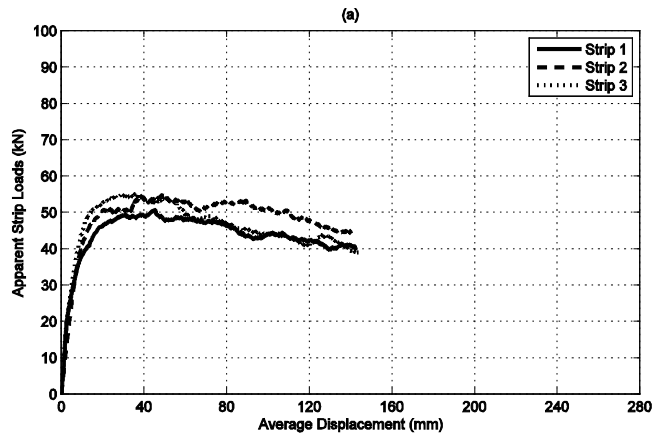


Figure D.1. Multi-strip pullout test results for 100A-44: (a) strips 1-3, (b) strips 4-6, (c) strips 7-9, (c) strips 1-9 at small displacements.

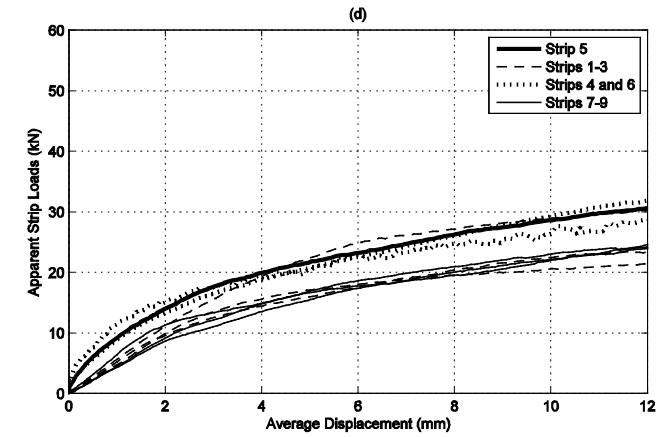
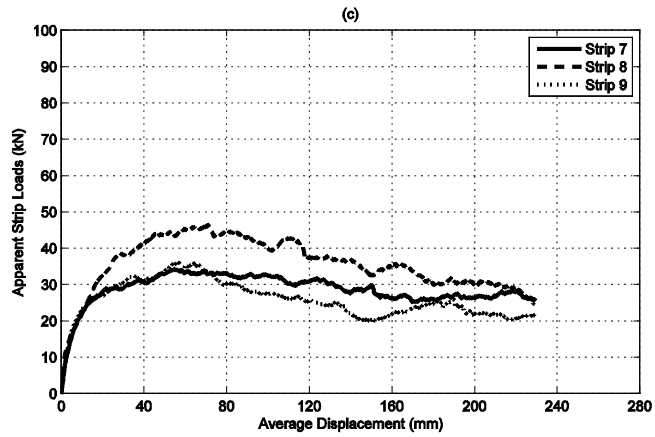
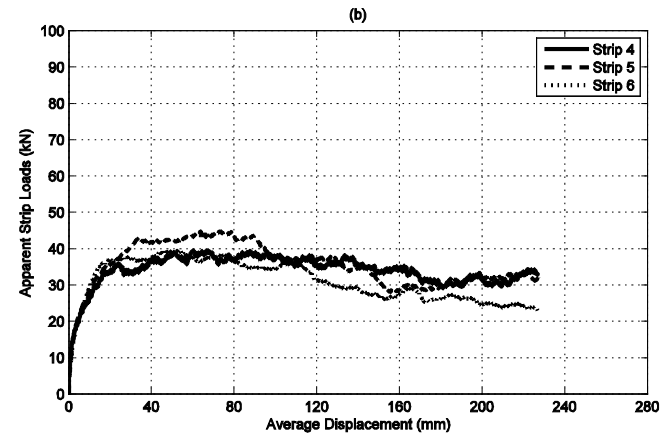
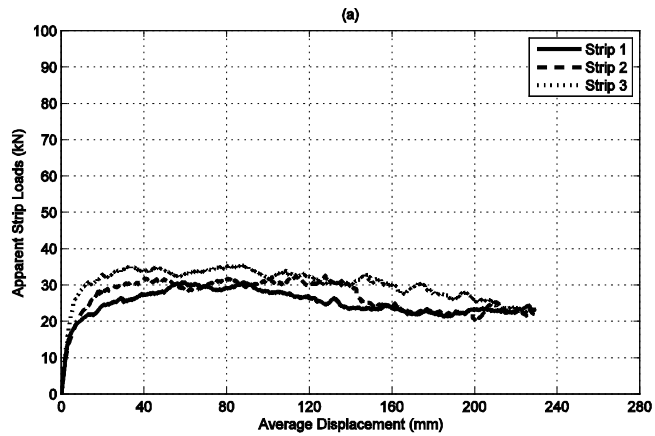


Figure D.2. Multi-strip pullout test results for 30A-66: (a) strips 1-3, (b) strips 4-6, (c) strips 7-9, (d) strips 1-9 at small displacements.

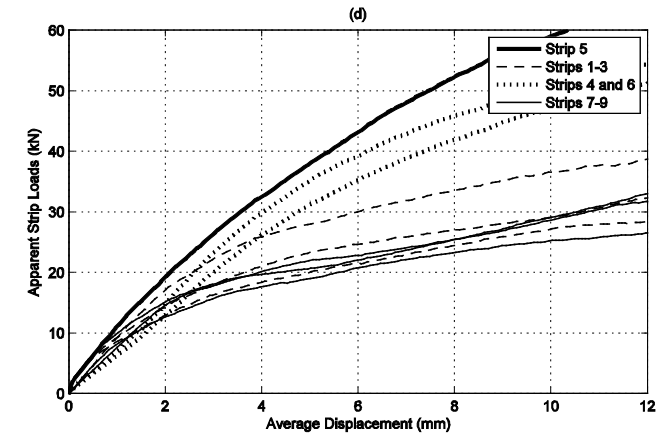
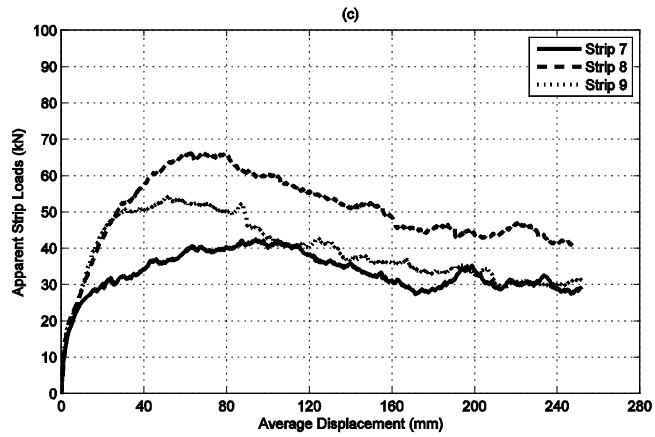
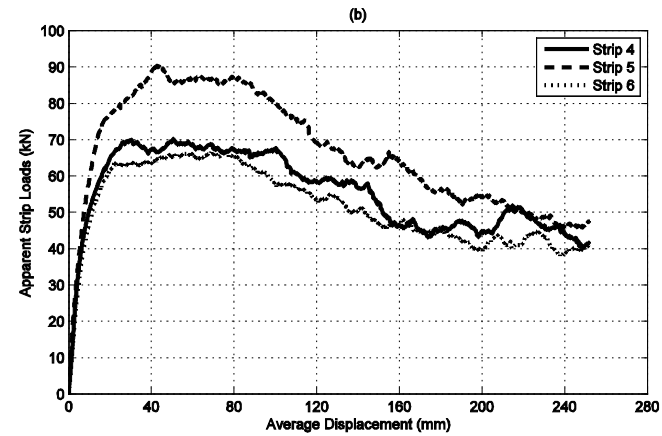
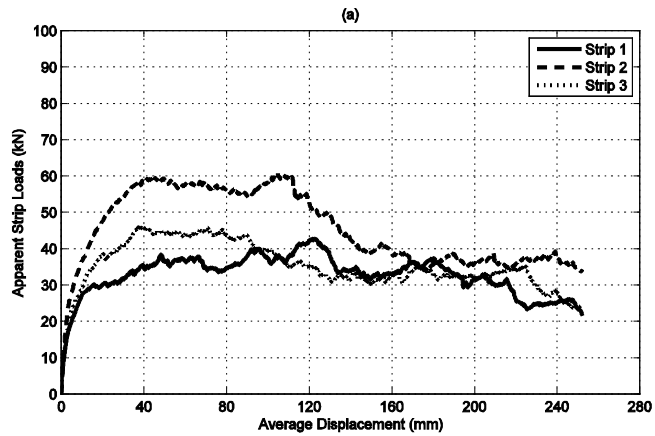


Figure D.3. Multi-strip pullout test results for 100B-66: (a) strips 1-3, (b) strips 4-6, (c) strips 7-9, (c) strips 1-9 at small displacements.

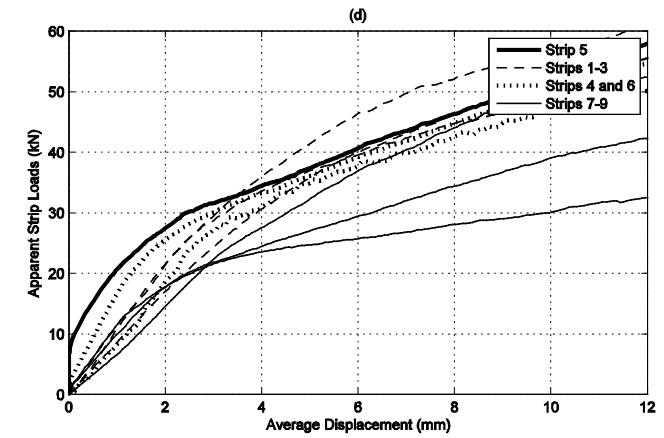
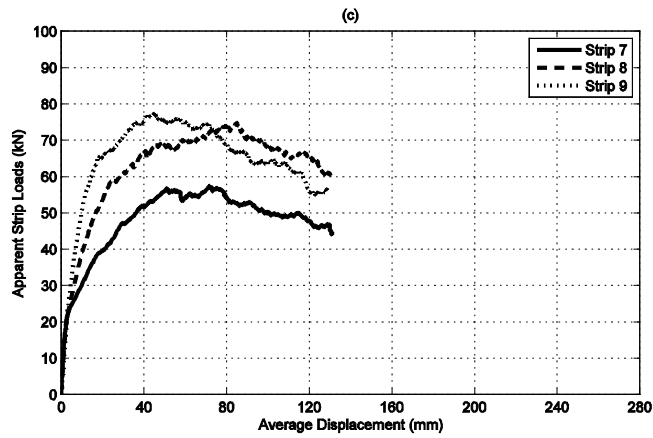
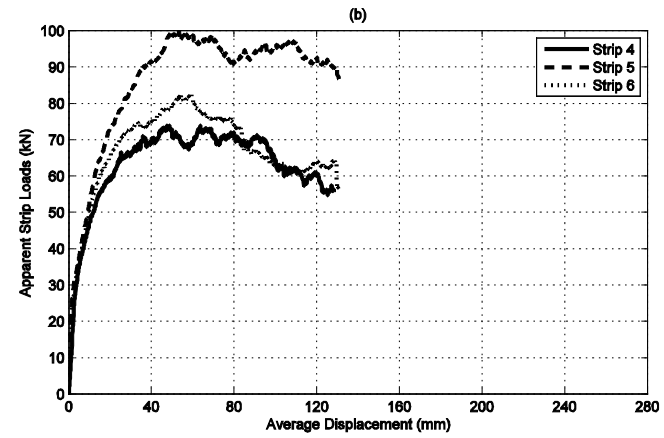
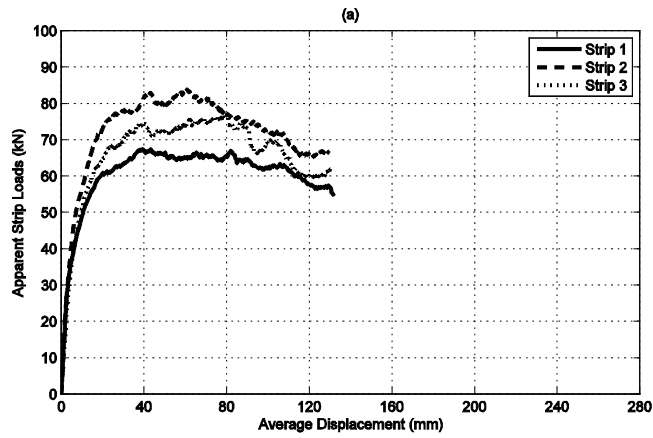


Figure D.4. Multi-strip pullout test results for 200A-66: (a) strips 1-3, (b) strips 4-6, (c) strips 7-9, (c) strips 1-9 at small displacements.

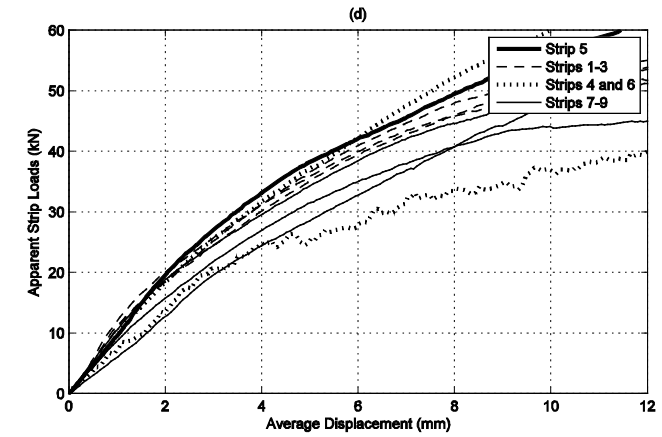
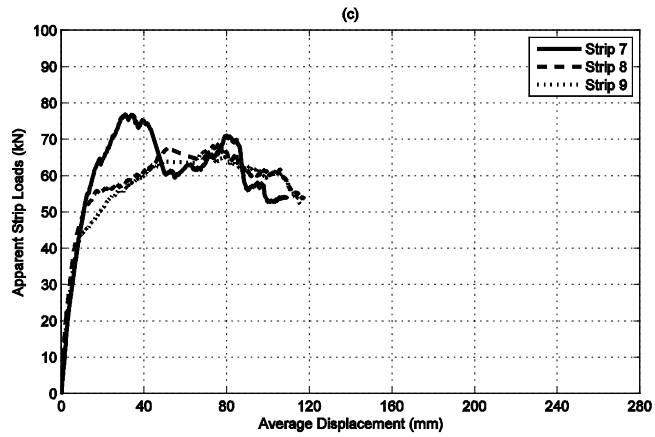
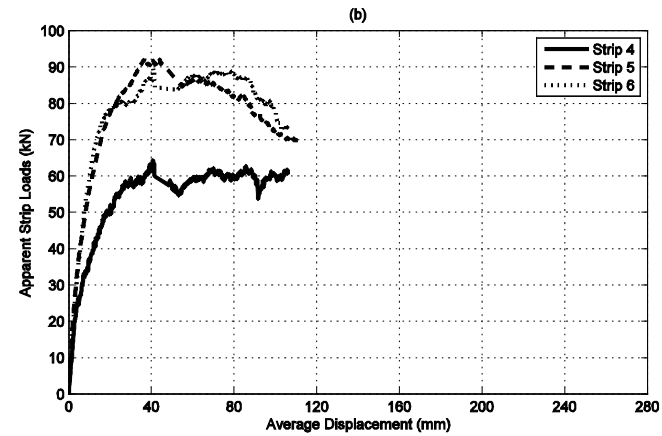
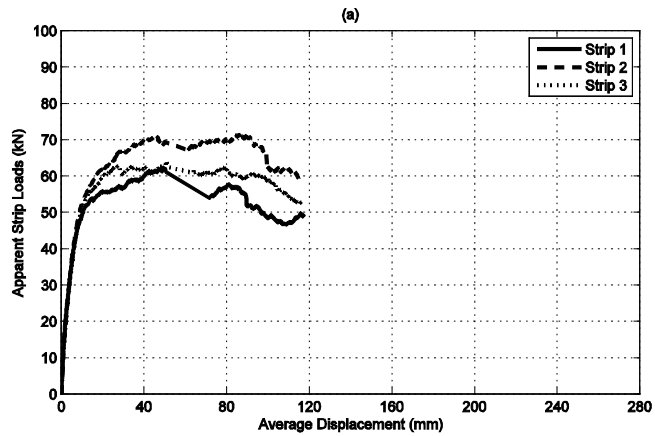


Figure D.5. Multi-strip pullout test results for 100A-88: (a) strips 1-3, (b) strips 4-6, (c) strips 7-9, (c) strips 1-9 at small displacements.

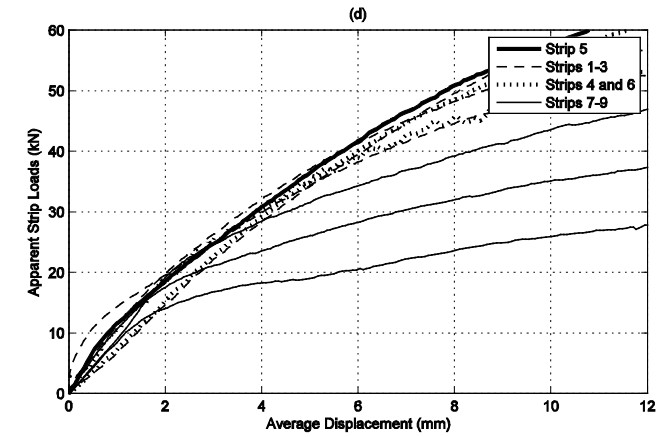
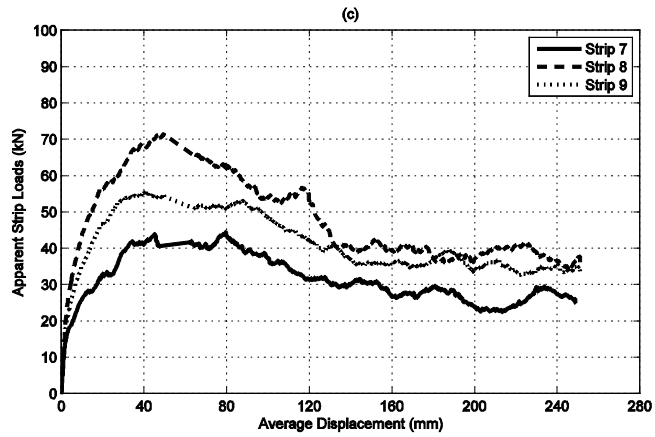
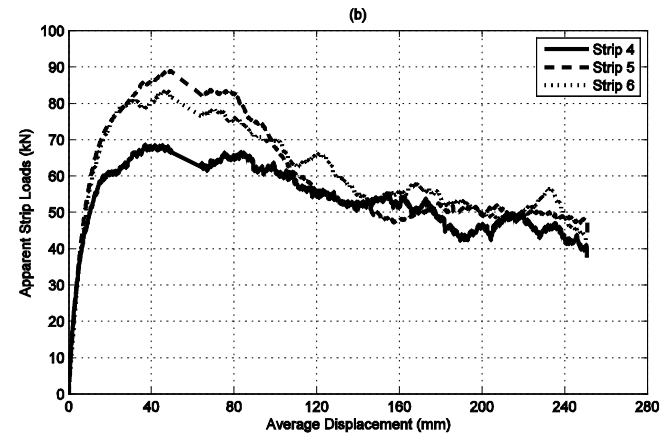
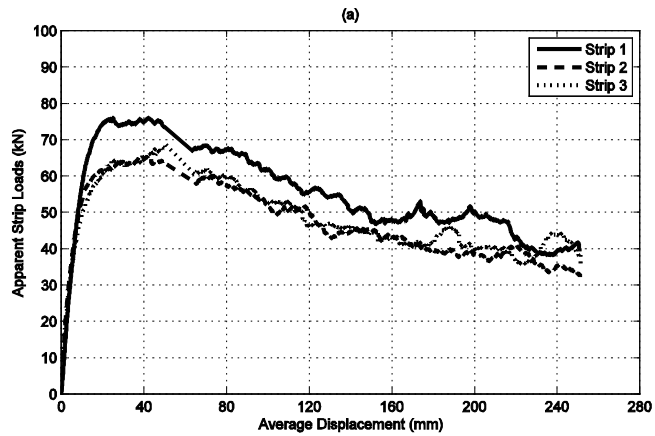


Figure D.6. Multi-strip pullout test results for 100A-1010: (a) strips 1-3, (b) strips 4-6, (c) strips 7-9, (c) strips 1-9 at small displacements.

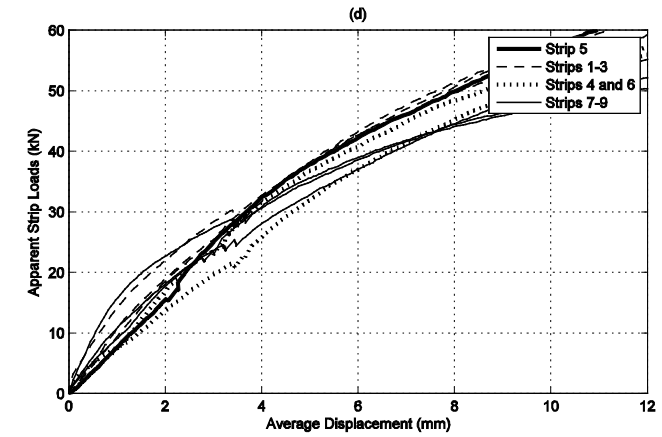
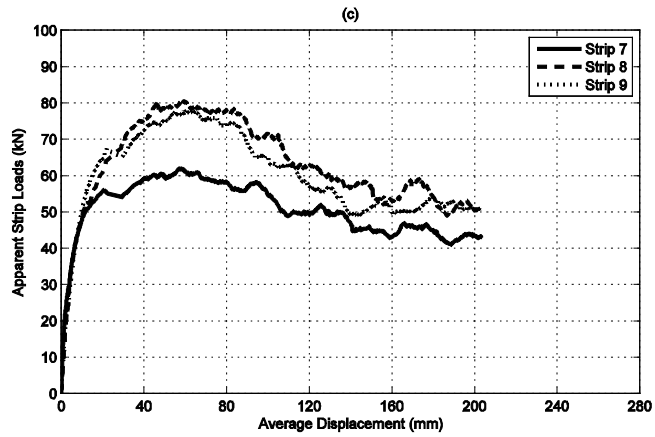
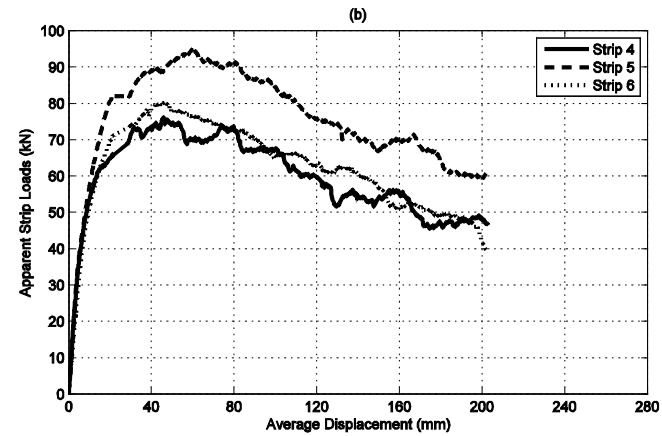
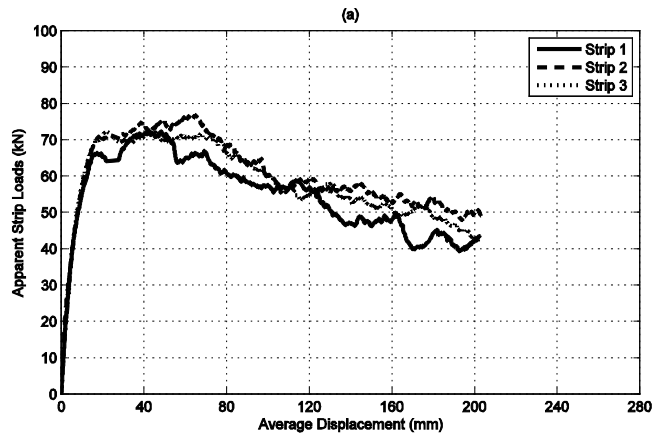


Figure D.7. Multi-strip pullout test results for 100B-1010: (a) strips 1-3, (b) strips 4-6, (c) strips 7-9, (c) strips 1-9 at small displacements.

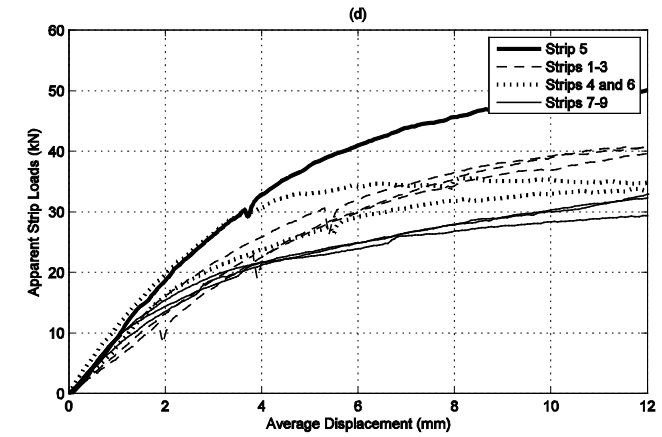
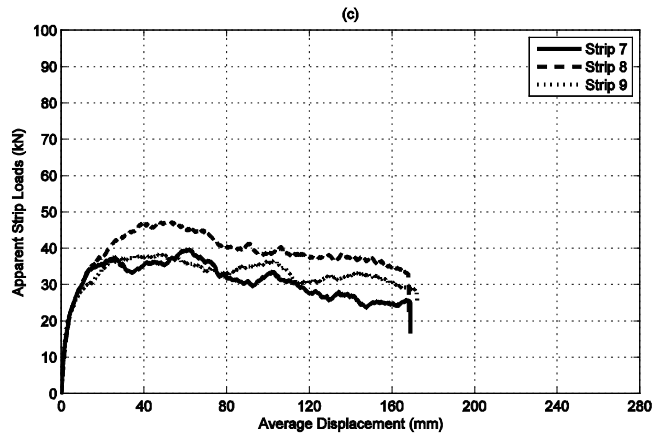
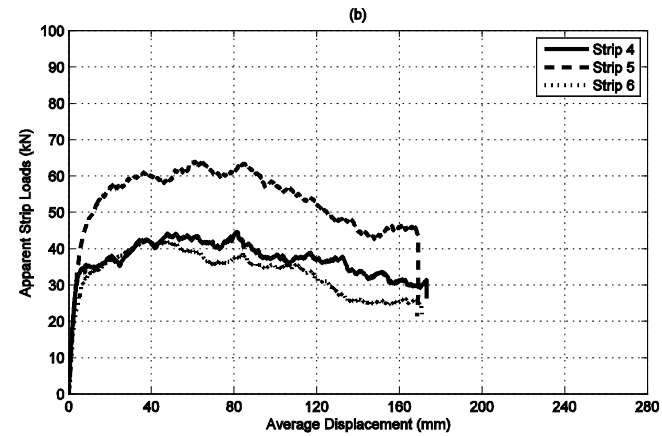
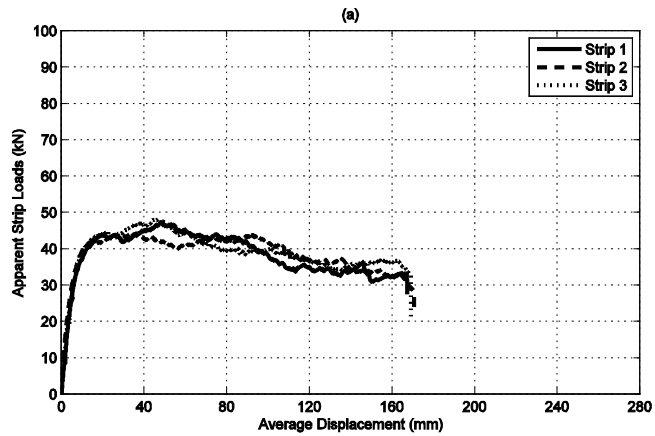


Figure D.8. Multi-strip pullout test results for 30A-1212: (a) strips 1-3, (b) strips 4-6, (c) strips 7-9, (c) strips 1-9 at small displacements.

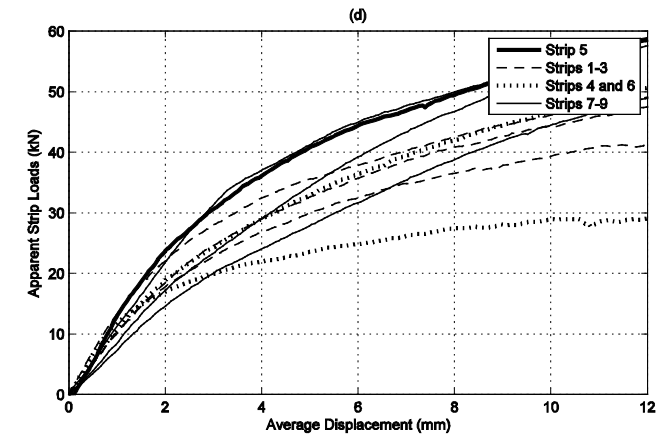
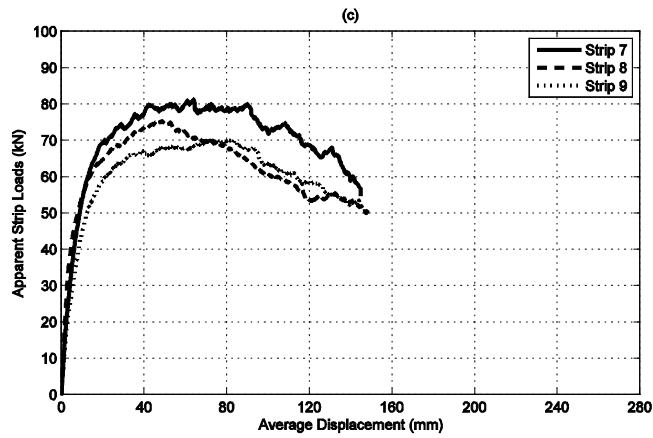
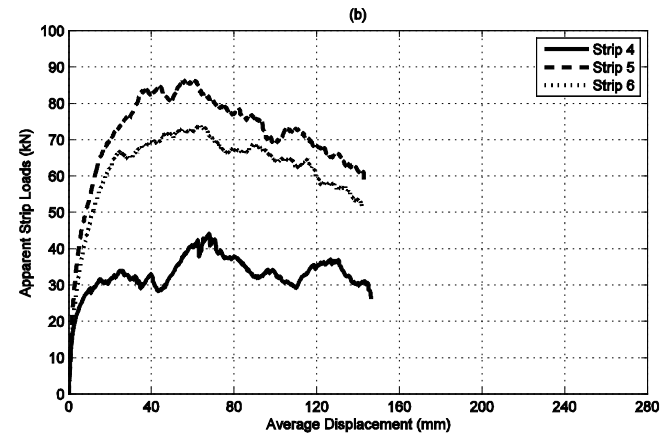
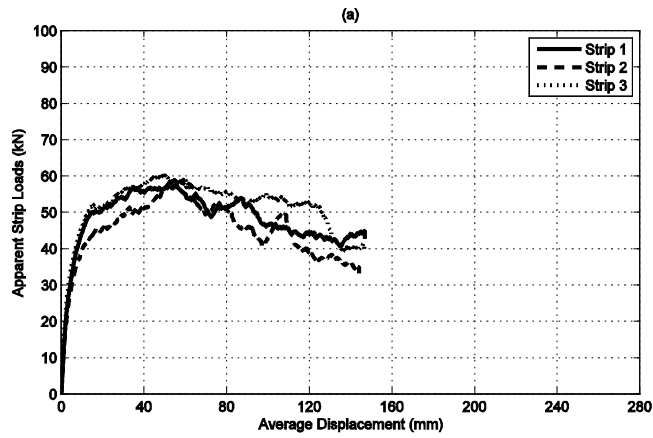


Figure D.9. Multi-strip pullout test results for 100A-1212: (a) strips 1-3, (b) strips 4-6, (c) strips 7-9, (c) strips 1-9 at small displacements.

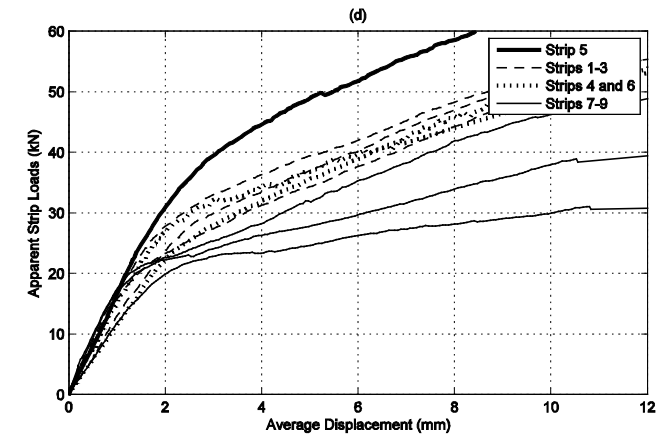
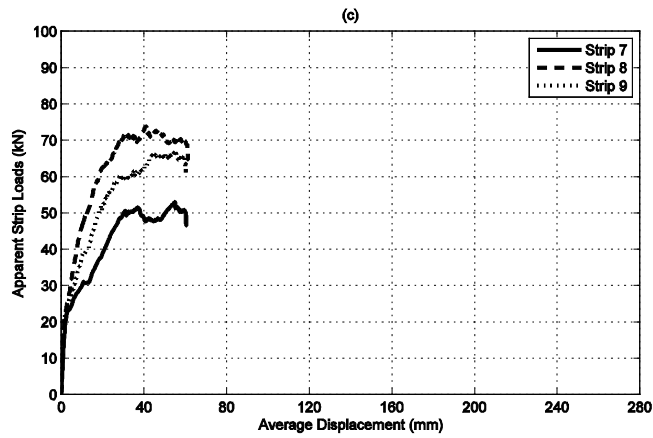
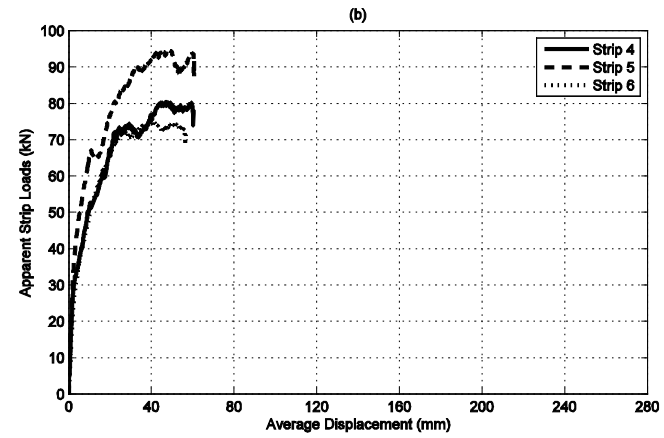
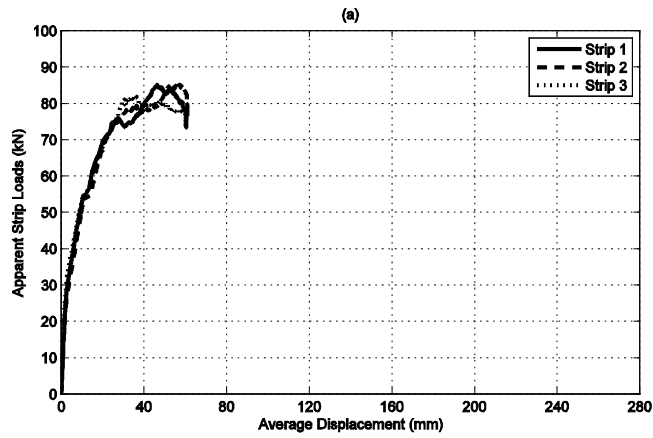


Figure D.10. Multi-strip pullout test results for 200A-1212: (a) strips 1-3, (b) strips 4-6, (c) strips 7-9, (c) strips 1-9 at small displacements.

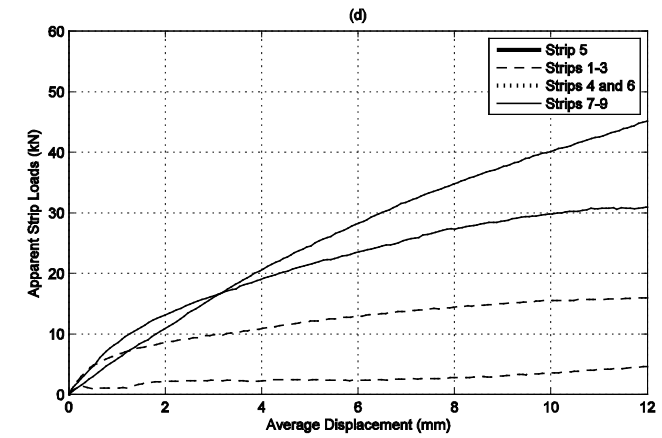
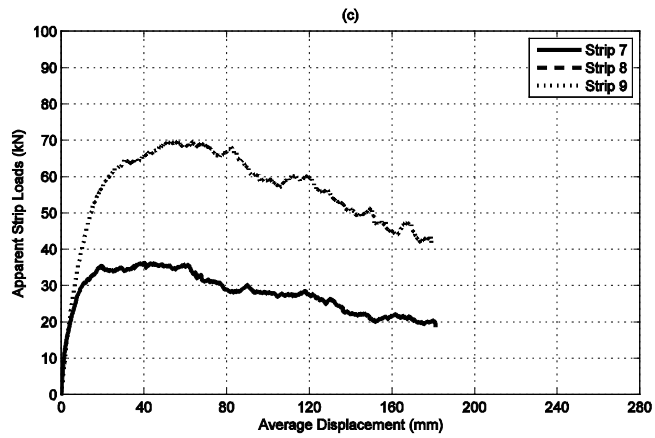
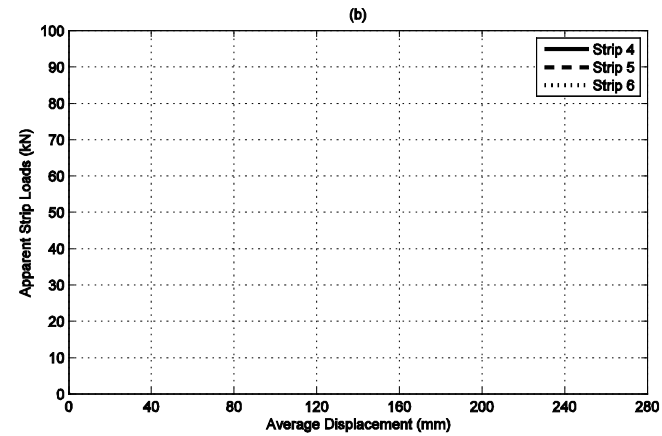
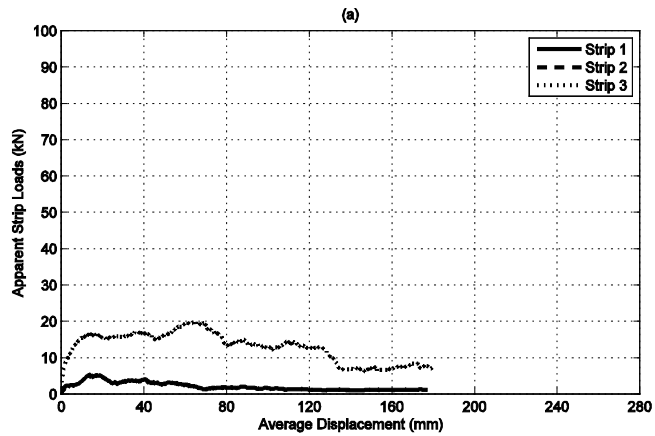


Figure D.11. Multi-strip pullout test results for 100A-2424: (a) strips 1-3, (b) strips 4-6, (c) strips 7-9, (c) strips 1-9 at small displacements.

**APPENDIX E: FISH AND C++ CODES USED TO UPDATE MEAN
EFFECTIVE STRESS AND ELEMENT PARAMETERS IN
NUMERICAL SIMULATIONS**

E.1 C++ UDM - MODIFIED CHSOIL

Header File: modelHardSoil.cpp

```

#pragma once

#include "../models/src/conmodel.h"

namespace models {
class ModelCHSoil : public ConstitutiveModel {
public:
    // Creators
    ModelCHSoil();
    virtual String      getName() const { return(L"chsoil"); }
    virtual String      getFullName() const { return(L"CHSoil"); }
    virtual UInt        getMinorVersion() const;
    virtual String      getProperties() const;
    virtual String      getStates() const;
    virtual Variant     getProperty(UInt index) const;
    virtual void        setProperty(UInt ul,const Variant &p,UInt restoreVersion) ;
    virtual ModelCHSoil *clone() const { return(NEW("ModelCHSoil")
ModelCHSoil()); }
    virtual Double      getConfinedModulus() const;// { return(bulk_ + shear_*4.0/3.0); }
    virtual Double      getShearModulus() const { return(shear_); }
    virtual Double      getBulkModulus() const { return(bulk_); }
    virtual void        copy(const ConstitutiveModel *mod);
    virtual void        initialize(UByte dim,State *s);
    virtual void        run(UByte dim,State *s);
    // Optional
    //virtual Bool      supportsHystereticDamping() const { return(true);}
    //void              HDampInit(const Double dHMult);
    //virtual Double    getStressStrengthRatio(const SymTensor &st) const;
    //virtual void      scaleProperties(const Double &scale,const std::vector<UInt>
&props);
    //virtual Bool      supportsStressStrengthRatio() const { return(true); }
    //virtual Bool      supportsPropertyScaling() const { return(true); }

private:
    Double
bulkr_,shearr_,bulk_,shear_,youngr_,poisson_,cohesion_,friction_,dilation_,fricv_;
    Double pref_,pini_,m_,n_,rf_,fricf_,tension_,shp_,thp_,dilf_;
    Double e1_,e2_,g2_,nph_,csn_,sc1_,sc2_,sc3_,sf1_,sf3_,bisc_;
    Double rmps_,sinr_,sincv_;
    UInt   ctab_,dtab_,ttab_,dilaw_,psp_;
    void   *ictab_,*idtab_,*ittab_;

```

```

    Double cmul_;
};
}

```

C++ File: modelHardSoil.cpp

```

#include "C:\Program Files
(x86)\Itasca\FLAC700\Exe32\plugins\models\HardSoilProject\HardSoil\modelHardSoil.h"
#include "C:\Program Files
(x86)\Itasca\FLAC700\Exe32\plugins\models\HardSoilProject\HardSoil\models/src/state.h"
#include "C:\Program Files
(x86)\Itasca\FLAC700\Exe32\plugins\models\HardSoilProject\HardSoil\models/src/convert.
h"
#include "C:\Program Files
(x86)\Itasca\FLAC700\Exe32\plugins\models\HardSoilProject\HardSoil\version.txt"
#include <algorithm>
#include <limits>

#ifdef HARDSOIL_EXPORTS
int __stdcall DllMain(void *, unsigned, void *) {
    return 1;
}

extern "C" EXPORT_TAG const char *getName() {

#ifdef MODELDEBUG
    return("modelHardSoild");
#else
    return("modelHardSoil");
#endif
}

extern "C" EXPORT_TAG unsigned getMajorVersion() {
    return MAJOR_VERSION;
}

extern "C" EXPORT_TAG unsigned getMinorVersion() {
    return (MINOR_VERSION);
}

extern "C" EXPORT_TAG void *createInstance() {

```

```

    models::ModelHardSoil *m = NEWC(models::ModelHardSoil());
    return((void *)m);
}
#endif // HardSoil_EXPORTS

namespace models {
    //variables used by all model objects. Hence only one copy is maintained for all objects
    static const double d4d3 = 4.0 / 3.0;
    static const double d1d3 = 1.0 / 3.0;
    static const double d2d3 = 2.0 / 3.0;
    static const double dPi = 3.141592653589793238462643383279502884197169399;
    static const double dDegRad = dPi/180.0;

    // Plasticity Indicators
    static const unsigned long mShearNow = 0x01; /* state logic */
    static const unsigned long mTensionNow = 0x02;
    static const unsigned long mShearPast = 0x04;
    static const unsigned long mTensionPast = 0x08;

    ModelHardSoil::ModelHardSoil()
        : bulkr_(0.0),shearr_(0.0),
          bulk_(0.0),shear_(0.0),youngr_(0.0),poisson_(0.0),
          cohesion_(0.0),friction_(0.0),dilation_(0.0),fricv_(0.0),
          pref_(0.0),p_ini(0.0),m_(0.0),n_(0.0),rf_(0.0),fricf_(0.0),
          tension_(0.0),shp_(0.0),thp_(0.0),dilf_(0.0),ctab_(0),
          dtab_(0),ttab_(0),dilaw_(1),e1_(0.0),e2_(0.0),g2_(0.0),nph_(0.0),
          csn_(0.0),sc1_(0.0),sc2_(0.0),sc3_(0.0),sf1_(0.0),
          sf3_(0.0),bisc_(0.0),ictab_(0),idtab_(0),
          ittab_(0),sinr_(0.0),sincv_(0.0),psp_(0),cmul_(1.0),mean_p(0.0),
          dphi_(0.0),phi0_(0.0),dpsi_(0.0),psi0_(0.0),frilim_(0.0)
    {
    }

    String ModelHardSoil::getProperties(void) const {
        return (L"bulk_ref,shear_ref,young_ref,poisson,"
            L"p_ref,p_ini,m_K,n_G,R_f,fricf,friction,cohesion,"
            L"dilf,dilation,tension,ctable,dtable,ttable,"
            L"dilaw,es_plastic,et_plastic,bulk_mod,shear_mod,"
            L"fricv,psp,cohesion_mul,meanp,d_phi,phi_0,d_psi,psi_0,fri_lim");
    }

    UInt ModelHardSoil::getMinorVersion() const {
        return(MINOR_VERSION);
    }
}

```

```

String ModelHardSoil::getStates() const {
    return L"shear-n,tension-n,shear-p,tension-p";
}

double ModelHardSoil::getConfinedModulus() const
{
    double bulk,shear;
    bulk = bulk_;
    shear = shearr_;
    if (!bulk || !shear)
    {

        //mean_p = std::abs(s->stnS_.getTrace()/3.0);
        bulk = bulkr_ * pref_ * std::pow (p_ini/pref_,m_);
        shear = shearr_ * pref_ * std::pow (p_ini/pref_,n_);
        double dval = 2.0*shear/3.0;
        bulk = bulk < dval ? dval : bulk; // nu > 0
        dval = 49.66*shear;
        bulk = bulk > dval ? dval : bulk; // nu < 0.49
    }
    return(bulk + shear*4.0/3.0);
}

Variant ModelHardSoil::getProperty(UInt ul) const {
    switch (ul)
    {
        case 1: return(bulkr_);
        case 2: return(shearr_);
        case 3:
            {
                double young;
                getYPfromBS(bulkr_,shearr_,&young,0);
                return(young);
            }
            break;
        case 4:
            {
                double poisson;
                getYPfromBS(bulkr_,shearr_,0,&poisson);
                return(poisson);
            }
            break;
        case 5: return(pref_);
        case 6: return(p_ini);
        case 7: return(m_);
    }
}

```

```

case 8: return(n_);
case 9: return(rf_);
case 10: return(fricf_);
case 11: return(friction_);
case 12: return(cohesion_);
case 13: return(dilf_);
case 14: return(dilation_);
case 15: return(tension_);
case 16: return(ctab_);
case 17: return(dtab_);
case 18: return(ttab_);
case 19: return(dilaw_);
case 20: return(shp_);
case 21: return(thp_);
case 22: return(bulk_);
case 23: return(shear_);
    case 24: return(fricv_);
case 25: return(psp_);
    case 26: return(cmul_);
    case 27: return(mean_p);
    case 28: return(dphi_);
    case 29: return(phi0_);
    case 30: return(dpsi_);
    case 31: return(psi0_);
    case 32: return(frilim_);
}
return(0.0);
}

void ModelHardSoil::setProperty(UInt ul,const Variant &p,UInt restoreVersion) {
    ConstitutiveModel::setProperty(ul,p,restoreVersion);
    switch (ul)
    {
        case 1: bulkr_ = p.toDouble(); break;
        case 2: shearr_ = p.toDouble(); break;
        case 3:
            {
                getYPfromBS(bulkr_,shearr_,&youngr_,&poisson_);
                youngr_ = p.toDouble();
                if (!restoreVersion) getBSfromYP(youngr_,poisson_,&bulkr_,&shearr_);
                break;
            }
        case 4:
            {
                getYPfromBS(bulkr_,shearr_,&youngr_,&poisson_);
                poisson_ = p.toDouble();
            }
    }
}

```

```

        if (!restoreVersion) getBSfromYP(youngr_,poisson_,&bulkr_,&shearr_);
            break;
        }
case 5: pref_    = p.toDouble(); break;
case 6: p_ini   = p.toDouble(); break;
case 7: m_     = p.toDouble(); break;
case 8: n_     = p.toDouble(); break;
case 9: rf_    = p.toDouble(); break;
case 10: fricf_ = p.toDouble(); break;
case 11: friction_ = p.toDouble(); break;
case 12: cohesion_ = p.toDouble(); break;
case 13: dilf_  = p.toDouble(); break;
case 14: dilation_ = p.toDouble(); break;
case 15: tension_ = p.toDouble(); break;
case 16: ctab_  = p.toInt();   break;
case 17: dtab_  = p.toInt();   break;
case 18: ttab_  = p.toInt();   break;
case 19: dilaw_ = p.toInt();   break;
case 20: shp_   = p.toDouble(); break;
case 21: thp_   = p.toDouble(); break;
case 22: bulk_  = p.toDouble(); break;
case 23: shear_ = p.toDouble(); break;
    case 24: fricv_ = p.toDouble(); break;
    case 25: psp_   = p.toInt();   break;
    case 26: cmul_  = p.toDouble(); break;
    case 27: mean_p = p.toDouble(); break;
    case 28: dphi_  = p.toDouble(); break;
    case 29: phi0_  = p.toDouble(); break;
    case 30: dpsi_  = p.toDouble(); break;
    case 31: psi0_  = p.toDouble(); break;
    case 32: frilim_ = p.toDouble(); break;
    }
}

void ModelHardSoil::copy(const ConstitutiveModel *cm) {
    ConstitutiveModel::copy(cm);
    const ModelHardSoil *mm = dynamic_cast<const ModelHardSoil *>(cm);
    if (!mm) throw std::runtime_error("Internal error: constitutive model dynamic cast
failed.");
    bulkr_ = mm->bulkr_;
    shearr_ = mm->shearr_;
    youngr_ = mm->youngr_;
    poisson_ = mm->poisson_;
    pref_ = mm->pref_;
    p_ini = mm->p_ini;
    m_ = mm->m_;
}

```

```

n_      = mm->n_;
rf_     = mm->rf_;
fricf_  = mm->fricf_;
friction_ = mm->friction_;
cohesion_ = mm->cohesion_;
dilf_   = mm->dilf_;
dilation_ = mm->dilation_;
tension_ = mm->tension_;
shp_    = mm->shp_;
thp_    = mm->thp_;
bulk_   = mm->bulk_;
shear_  = mm->shear_;
  fricv_ = mm->fricv_;
  dilaw_ = mm->dilaw_;
psp_    = mm->psp_;
  cmul_  = mm->cmul_;
  mean_p = mm->mean_p;
  dphi_  = mm->dphi_;
  phi0_  = mm->phi0_;
  dpsi_  = mm->dpsi_;
  psi0_  = mm->psi0_;
  frilim_ = mm->frilim_;
}

void ModelHardSoil::initialize(UByte dim,State *s) {
  ConstitutiveModel::initialize(dim,s);

  if (pref_ < 0.0) pref_ = -pref_;
  if (pref_ == 0.0) pref_ = 100.0;           // default value is 100
  if (p_ini <= 0.0) p_ini = pref_ * 0.005; //
  if (rf_ <= 0.0) rf_ = 0.1;               // dRef
  if (rf_ > 1.0) rf_ = 1.0;                // dRef
  m_ = m_ > 1.0 ? 1.0 : m_;
  n_ = n_ > 1.0 ? 1.0 : n_;

  bulk_ = bulkr_ * pref_ * std::pow (mean_p/pref_,m_);
  shear_ = shearr_ * pref_ * std::pow (mean_p/pref_,n_);
  double dval = 2.0*shear_/3.0;
  bulk_ = bulk_ < dval ? dval : bulk_; // nu > 0
  dval = 49.66*shear_;
  bulk_ = bulk_ > dval ? dval : bulk_; // nu < 0.49

  s->modulus_changed_=true;

  e1_ = bulk_ + d4d3 * shear_;

```

```

e2_ = bulk_ - d2d3 * shear_;
g2_ = 2.0 * shear_;

if (ctab_||dtab_||ttab_) {
    if (ctab_) ictab_ = s->getTableIndexFromID(ctab_);
    if (dtab_) idtab_ = s->getTableIndexFromID(dtab_);
    if (ttab_) ittab_ = s->getTableIndexFromID(ttab_);
}
mean_p = std::abs(s->stnS_.getTrace()/3.0);
mean_p = mean_p < p_ini ? p_ini : mean_p;
mean_p = mean_p > 1000000000.0 ? 1000000000.0 : mean_p;

fricf_ = phi0_-dphi_*std::log10(mean_p/pref_);// MODIFICATION
dilf_ = psi0_-dpsi_*std::log10(mean_p/pref_);
fricf_ = fricv_ > fricf_ ? fricv_ : fricf_;
fricf_ = fricf_ > frilim_ ? frilim_ : fricf_;
friction_ = friction_ < fricf_ ? friction_ : fricf_;
dilf_ = dilf_ > fricf_ ? fricf_ : dilf_;
if (!dilaw_ && !idtab_) dilation_ = dilf_;
dilation_ = dilation_ > friction_ ? friction_ : dilation_;

sinr_ = std::sin(fricf_ * dDegRad) / rf_;
double dRSinphi = std::sin(friction_ * dDegRad);
shp_ = (mean_p / shear_) * sinr_ * (1.0/(1.0-dRSinphi/sinr_) - 1.0); // gamma_p
nph_ = (1.0 + dRSinphi) / (1.0 - dRSinphi);
csn_ = 2.0 * cohesion_ * sqrt(nph_);
if (friction_) {
    double dApex = cohesion_ * std::cos(friction_ * dDegRad) / dRSinphi;
    tension_ = tension_ < dApex ? tension_ : dApex;
}
double dRSinpsi = std::sin(dilation_ * dDegRad);
rnps_ = (1.0 + dRSinpsi) / (1.0 - dRSinpsi);

double dRa = e1_ - rnps_ * e2_;
double dRb = e2_ - rnps_ * e1_;
double dRd = dRa - dRb * nph_;
sc1_ = dRa / dRd;
sc3_ = dRb / dRd;
sc2_ = e2_ * (1.0 - rnps_) / dRd;
sf1_ = 1.0 / dRd;
sf3_ = -rnps_ / dRd;
bisc_ = std::sqrt(1.0 + nph_ * nph_) + nph_;

if (dilaw_== 1) {

    sincv_ = std::sin(fricv_ * dDegRad);

```

```

    }
    else if (dilaw_ == 2) {
        if (friction_ < fricv_){
            dilation_ = 0.0;
        }
        else {
            dilation_ = std::min(dilf_,friction_);
            dilation_ = dilf_ > friction_ ? friction_ : dilf_;
        }
    }
}

```

```

static const int Dqs = 0;
static const int Dqt = 1;
void ModelHardSoil::run(UByte dim, State *s) {
    ConstitutiveModel::run(dim,s);
    /* --- plasticity indicator: */
    /* store 'now' info. as 'past' and turn 'now' info off ---*/
    if (s->state_ & mShearNow) s->state_ |= mShearPast;
    s->state_ &= ~mShearNow;
    if (s->state_ & mTensionNow) s->state_ |= mTensionPast;
    s->state_ &= ~mTensionNow;
    int iPlas = 0;
    // --- hardening/softening:initialize stacks to calculate hardening parameters for zone -
--
    if (!s->sub_zone_) {
        s->working_[Dqs] = 0.0;
        s->working_[Dqt] = 0.0;
    }
    // --- trial elastic stresses ---
    s->stnS_.rs11() += (s->stnE_.s22() + s->stnE_.s33()) * e2_ + s->stnE_.s11() * e1_;
    s->stnS_.rs22() += (s->stnE_.s11() + s->stnE_.s33()) * e2_ + s->stnE_.s22() * e1_;
    s->stnS_.rs33() += (s->stnE_.s11() + s->stnE_.s22()) * e2_ + s->stnE_.s33() * e1_;
    s->stnS_.rs12() += s->stnE_.s12() * g2_;
    s->stnS_.rs13() += s->stnE_.s13() * g2_;
    s->stnS_.rs23() += s->stnE_.s23() * g2_;

    // --- calculate and sort principal stresses and principal directions ---
    SymTensorInfo info;
    DVect3 prin = s->stnS_.getEigenInfo(&info);
    mean_p = std::abs(s->stnS_.getTrace()/3.0);
    mean_p = mean_p < p_ini ? p_ini : mean_p;
    mean_p = mean_p > 1000000000.0 ? 1000000000.0 : mean_p;

    // --- Update Friction Angles and Establish Mohr-Coulomb failure criterion ---

```

```

fricf_ = phi0_-dphi_*std::log10(mean_p/pref_);
dilf_ = psi0_-dpsi_*std::log10(mean_p/pref_);
fricf_ = fricv_ > fricf_ ? fricv_ : fricf_;
fricf_ = fricf_ > frilim_ ? frilim_ : fricf_;
friction_ = friction_ < fricf_ ? friction_ : fricf_;
dilf_ = dilf_ > fricf_ ? fricf_ : dilf_;
if (!dilaw_ && !ldtab_) dilation_ = dilf_;
dilation_ = dilation_ > friction_ ? friction_ : dilation_;

sinr_ = std::sin(fricf_ * dDegRad) / rf_;
double dRSinphi = std::sin(friction_ * dDegRad);
shp_ = (mean_p / shear_) * sinr_ * (1.0/(1.0-dRSinphi/sinr_) - 1.0); // gamma_p
nph_ = (1.0 + dRSinphi) / (1.0 - dRSinphi);
csn_ = 2.0 * cohesion_ * sqrt(nph_);

double $fsh = prin.x() - nph_ * prin.z() + csn_;
// --- Tensile failure criteria ---
double $alamth = tension_ - prin.z();
double $pdivh = -$alamth + (prin.x() - nph_ * tension_ + csn_) * bisc_;

bulk_ = bulkr_ * pref_ * std::pow (mean_p/pref_,m_);
shear_ = shearr_ * pref_ * std::pow (mean_p/pref_,n_);
double dval = 2.0*shear_/3.0;
bulk_ = bulk_ < dval ? dval : bulk_; // nu > 0
dval = 49.66*shear_;
bulk_ = bulk_ > dval ? dval : bulk_; // nu < 0.49

e1_ = bulk_ + d4d3 * shear_;
e2_ = bulk_ - d2d3 * shear_;
g2_ = 2.0 * shear_;

double dRSinpsi = std::sin(dilation_ * dDegRad);
rnps_ = (1.0 + dRSinpsi) / (1.0 - dRSinpsi);

double dRa = e1_ - rnps_ * e2_;
double dRb = e2_ - rnps_ * e1_;
double dRd = dRa - dRb * nph_;
sc1_ = dRa / dRd;
sc3_ = dRb / dRd;
sc2_ = e2_ * (1.0 - rnps_) / dRd;
sf1_ = 1.0 / dRd;
sf3_ = -rnps_ / dRd;
bisc_ = std::sqrt(1.0 + nph_ * nph_) + nph_;

```

```

// --- tests for failure
if ($fsh < 0.0 && $pdivh < 0.0) {
  iPlas = 1;
  // --- shear failure: correction to principal stresses ---
  s->state_ |= mShearNow;
  prin.rx() -= $fsh * sc1_;
  prin.ry() -= $fsh * sc2_;
  prin.rz() -= $fsh * sc3_;
} else if ($salamth < 0.0 && $pdivh > 0.0) {
  iPlas = 2;
  // --- tension failure: correction to principal stresses ---
  s->state_ |= mTensionNow;
  double dTco = e2_ * $salamth / e1_;
  prin.rx() += dTco;
  prin.ry() += dTco;
  prin.rz() = tension_;
}
if (iPlas != 0)
{
  double smelas3 = s->stnS_.s11() + s->stnS_.s22() + s->stnS_.s33();
  s->stnS_ = info.resolve(prin); // Transform back to reference frame
  s->viscous_ = false; // Inhibit stiffness-damping terms
  s->mean_plastic_stress_change_ = (smelas3 - s->stnS_.s11() - s->stnS_.s22() - s-
>stnS_.s33()) / 3.0;
  s->modulus_changed_ = true;
  // --- hardening parameter accumulation ---
  if (iPlas == 1)
  {
    // --- shear parameter ---
    double dDe1p = $fsh * sf1_;
    double dDe3p = $fsh * sf3_;
    if (psp_ == 0)
    {
      double dDepa = d1d3 * (dDe1p + dDe3p);
      dDe1p -= dDepa;
      dDe3p -= dDepa;
      s->working_[Dqs] += std::sqrt(0.5 *
(dDe1p*dDe1p+dDepa*dDepa+dDe3p*dDe3p)) * s->getSubZoneVolume();
    }
    else
    {
      s->working_[Dqs] += fabs(dDe1p - dDe3p)*s-
>getSubZoneVolume();
    }
  }
  if (iPlas == 2)

```

```

{
  // ---          tensile parameter ---
  double dAux = $alamth / e1_;
  if (dAux < 0.) dAux = -dAux;
  s->working_[Dqt] += dAux * s->getSubZoneVolume();
}
}
else
{
  s->viscous_ = true; // allow viscous strains
}
// --- plastic parameter incrementation and properties update ---

if (s->sub_zone_==s->total_sub_zones_-1) {
  double dAux = 1.0 / s->getZoneVolume();
  if (s->overlay_==2) dAux *= 0.5;
  shp_ += s->working_[Dqs] * dAux; // Tensile Strains
  thp_ += s->working_[Dqt] * dAux; // Shear Strains
  //pini_ = mean_p; // Mean Effective Stress
  if (s->working_[Dqs] > 0.0) {
    // update cohesion
    if (ictab_) cohesion_ = s->getYFromX(ictab_,shp_) * cmul_;

    double dsinphi = sinr_*(1.0 - 1.0 / (1.0 + shp_ * shear_ / (sinr_ * mean_p)));
    friction_ = std::asin(dsinphi) / dDegRad; // arsin in degree

    if (dilaw_ == 1) {
      //sincv_ = std::sin(fricv_ * dDegRad);
      dRa = std::sin(fricf_ * dDegRad);
      dRb = std::sin(dilf_ * dDegRad);
      double sincv_rowe = (dRa - dRb)/(1.0 - dRa * dRb);
      double dsinphi = std::sin(friction_ * dDegRad);
      double dsinpsi = (dsinphi - sincv_rowe)/(1. - dsinphi * sincv_rowe);
      dilation_ = std::asin(dsinpsi) / dDegRad; // arsin in degree
      dilation_ = dilation_ > friction_ ? friction_ : dilation_;
    }
    else if (dilaw_ == 2) {
      if (friction_ < fricv_){
        dilation_ = 0.0;
      }
      else {
        dilation_ = std::min(dilf_,friction_);
        dilation_ = dilf_ > friction_ ? friction_ : dilf_;
      }
    }
  }
}
else

```


E.2 FISH CODE - STRIP INTERFACE STIFFNESS

```

; Strip Stiffness Parameters
def k_sec
  if _Disp < _Displim
    _ksec = 2.9e7*_krat
  else
    _ksec = (1.0*(_xval)^0.391)*1000000;
    _ksec = min(2.9e7,_ksec)*_krat
  end_if
end

def adjust_stripK
  while_stepping
  ip=imem(str_pnt+$ksnode)
  loop while ip # 0
    if imem(ip+$kndcod2) = 7 then
      if imem(ip+$kndadd) # 0 then
        _xval = fmem(ip+$kndep)
        _xval = abs(fmem(ip+$kndep))*0.001
        _xval = max(1.0,_xval)
        _Disp = abs(fmem(ip+$kndus))
        ipadd = imem(ip+$kndtad)
        _propID = imem(ipadd+$ktypid)
        _Displim = 0.0003
        _krat = table(800,_propID)
        k_sec
      end_if
      pip = imem(ip+$kndtad)
      fmem(pip+$ktypstkb) = _ksec
    end_if
    ip = imem(ip)
  end_loop
end

```

E.3 FISH CODE - SOIL-PANEL INTERFACE

```

def Update_param
  _nst = max(1.0,abs(nstav))/1000.0
  _ks = (1350000.0*_nst+31130000.0); KAN
  _ks = max(1.0e7,_ks)
  _kn = 1.0e9

  _DSfri1 = 36.3-12.0*log(_nst/101.4); KAN
  _DSfri = min(70.0,_DSfri1)

```

```

_DSdil1 = 1.9-1.6*log(_nst/101.4); KAN
_DSdil = max(-1.0, _DSdil1)
_DSdilt = tan(_DSdil*3.1415/180)
end

def adjust_intK
  whilestepping
    sstav = 0.0
    nstav = 0.0
    ncon = 0
    jlen = 0.0
    pnt = int_pnt
    loop while pnt # 0
      pa = imem(pnt+$kicapt)
      loop while pa # 0
        sstav = sstav + fmem(pa+$kidfs)
        nstav = nstav + fmem(pa+$kidfn)
        jlen = jlen + fmem(pa+$kidlen)
        pa = imem(pa)
        Update_param
        fmem(pnt+$kicfri) = _DSfri
        fmem(pnt+$kicdil) = _DSdilt
        fmem(pnt+$kickn) = _kn
        fmem(pnt+$kicks) = _ks
      end_loop
      pa = imem(pnt+$kicbpt)
      loop while pa # 0
        ncon = ncon + 1
        sstav = sstav + fmem(pa+$kidfs)
        nstav = nstav + fmem(pa+$kidfn)
        jlen = jlen + fmem(pa+$kidlen)
        pa = imem(pa)
        Update_param
        fmem(pnt+$kicfri) = _DSfri
        fmem(pnt+$kicdil) = _DSdilt
        fmem(pnt+$kickn) = _kn
        fmem(pnt+$kicks) = _ks
      end_loop
      pnt = imem(pnt)
      if ncon # 0
        sstav = sstav / jlen
        nstav = nstav / jlen
      endif
    end_loop
  end
end

```

E.4 FISH CODE - BEARING PAD MODULUS

```

call str.fin

def elast_upd_4
  _axstr = max(0.10,_axstr)
  if _axstr < 32.
    _elast = 9000000.0
  else
    _elast = 120000000.0
  end_if
end

def elast_upd_13
  _axstr = max(0.10,_axstr)
  if _axstr < 42.
    _elast = 9000000.0
  else
    _elast = 120000000.0
  end_if
end

def Upd_elast
  while_stepping
  ip=imem(str_pnt+$ksels)
  loop while ip # 0
    if imem(ip+$kelcod) = 1
      if imem(ip+$keltyp) <= 1011
        if imem(ip+$keltyp) > 1002
          _axstr = abs(fmem(ip+$skeleax)*100)
          ;set new elasticity value
          elast_upd_4
          ;step through properties and update
          pip = imem(ip+$keltad)
          fmem(pip+$ktype) = _elast
        end_if
      end_if
      if imem(ip+$keltyp) > 1012
        if imem(ip+$keltyp) < 1050
          _axstr = abs(fmem(ip+$skeleax)*100)
          ;set new elasticity value
          elast_upd_13
          ;step through properties and update
          pip = imem(ip+$keltad)
          fmem(pip+$ktype) = _elast
        end_if
      end_if
    end_if
  end
end

```

```
                end_if
            end_if
            ip = imem(ip)
        end_loop
    end
```

**APPENDIX F: PLOTS FROM THE GEOMETRIC PARAMETRIC
STUDY OF TALL MSE WALLS**

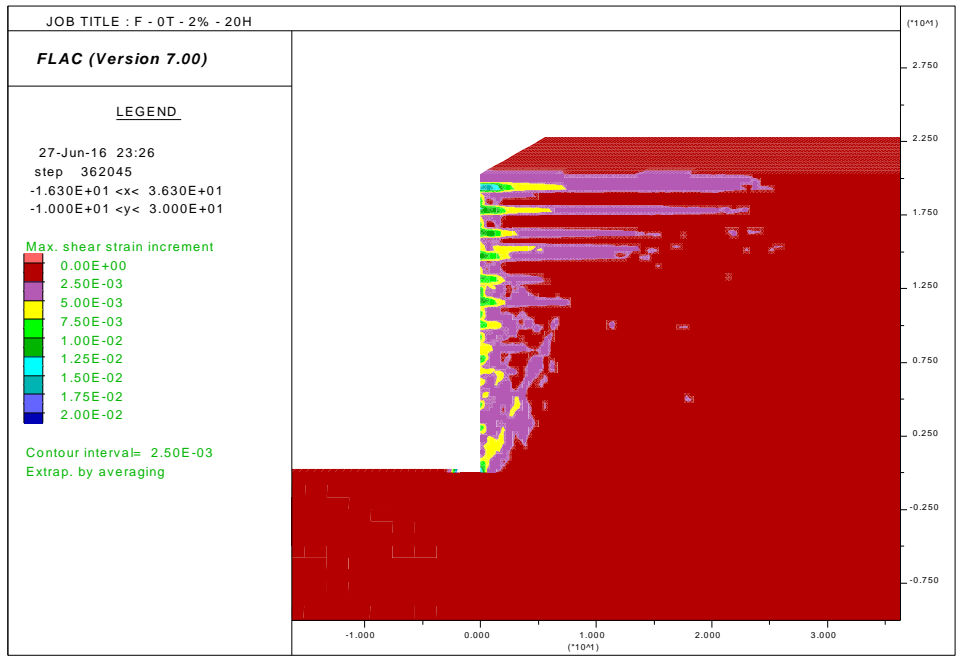


Figure F.1. FLAC model results showing shear strains for F – 1T – 0% - 20H.

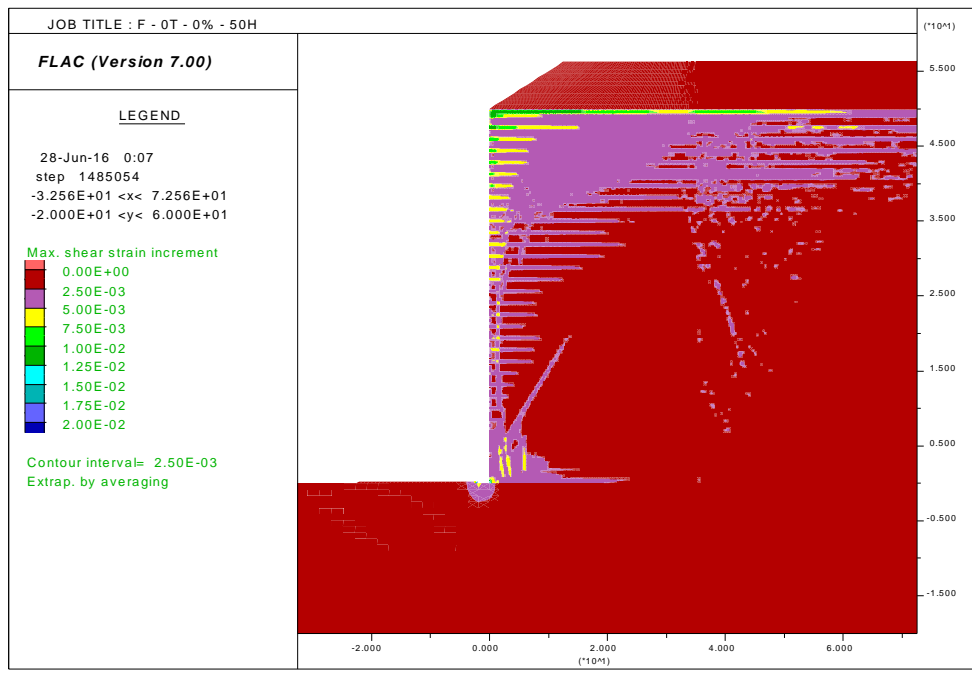


Figure F.2. FLAC model results showing shear strains for F – 1T – 0% - 50H.

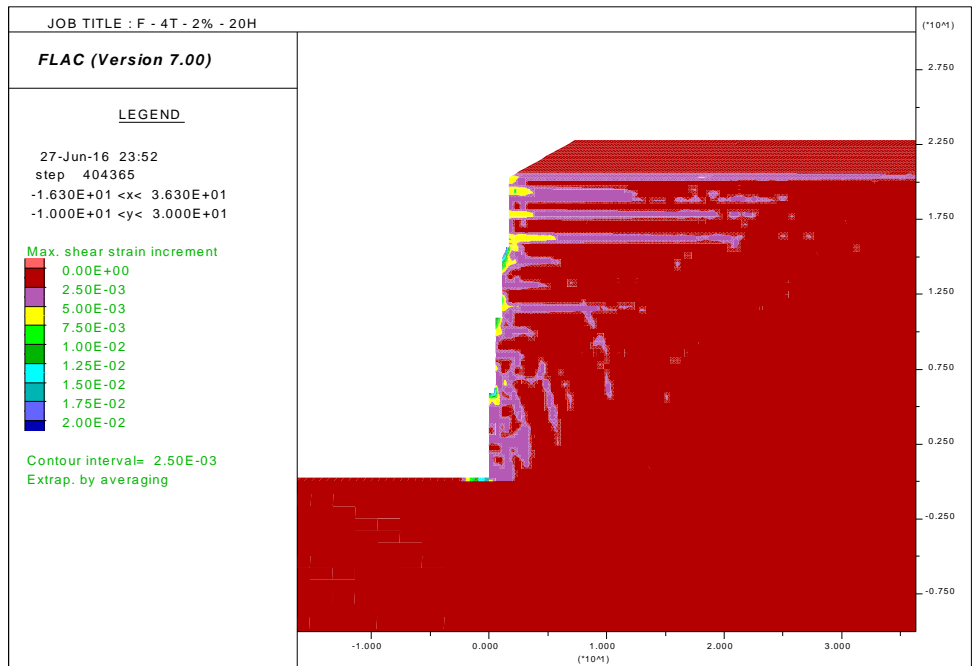


Figure F.3. FLAC model results showing shear strains for F – 4T – 2% - 20H.

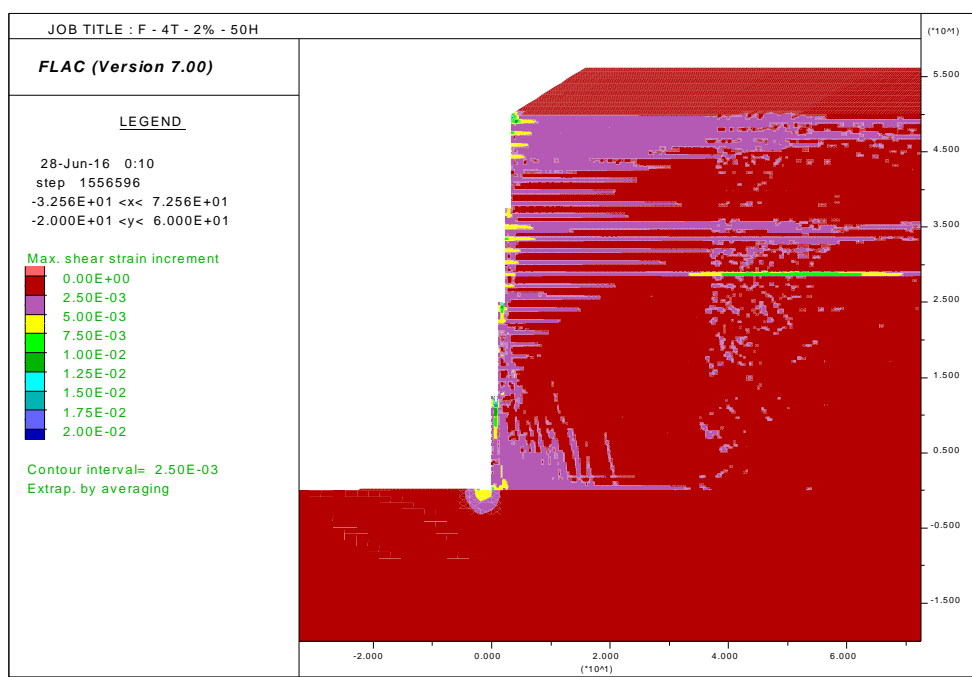


Figure F.4. FLAC model results showing shear strains for F – 4T – 2% - 50H.

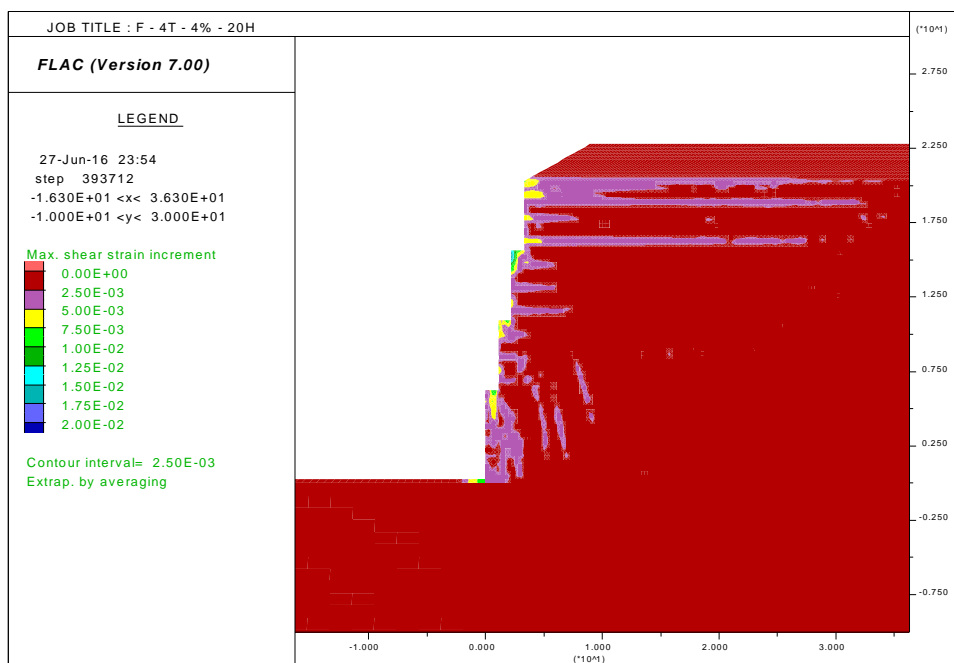


Figure F.5. FLAC model results showing shear strains for F – 4T – 4% - 20H.

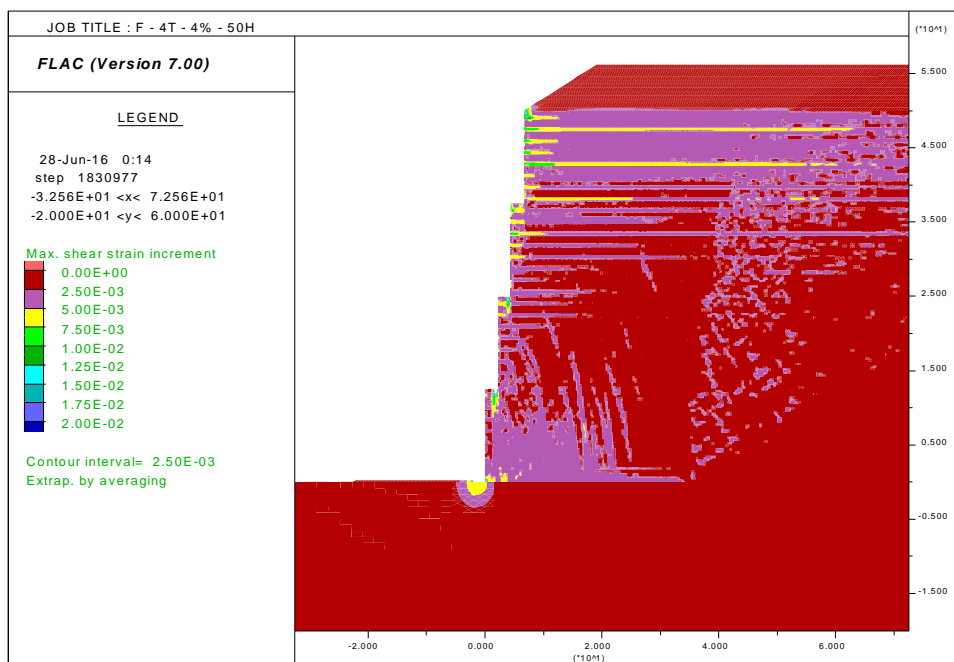


Figure F.6. FLAC model results showing shear strains for F – 4T – 4% - 50H.

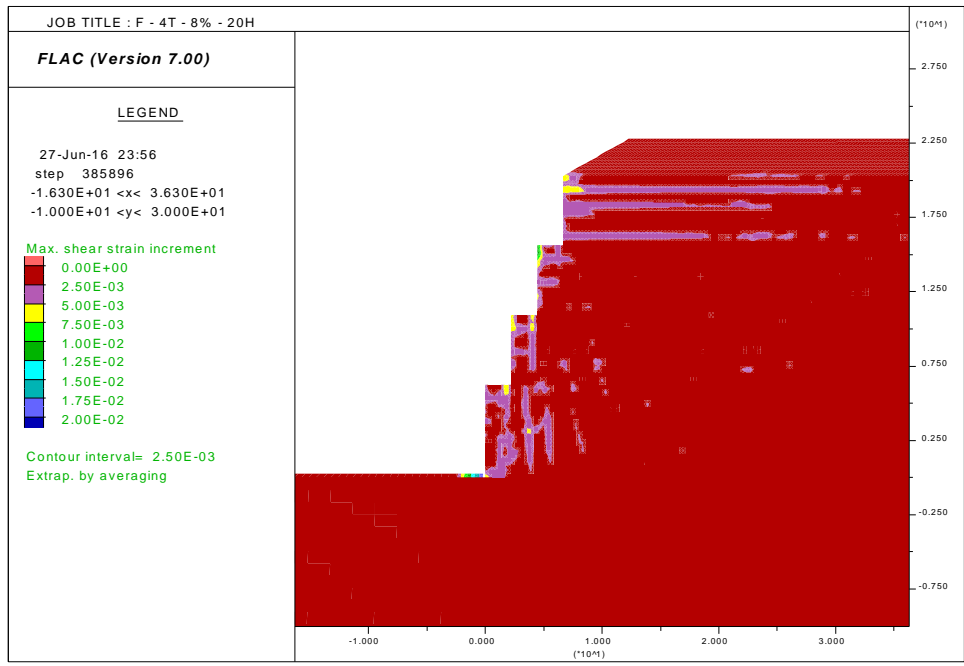


Figure F.7. FLAC model results showing shear strains for F – 4T – 8% - 20H.

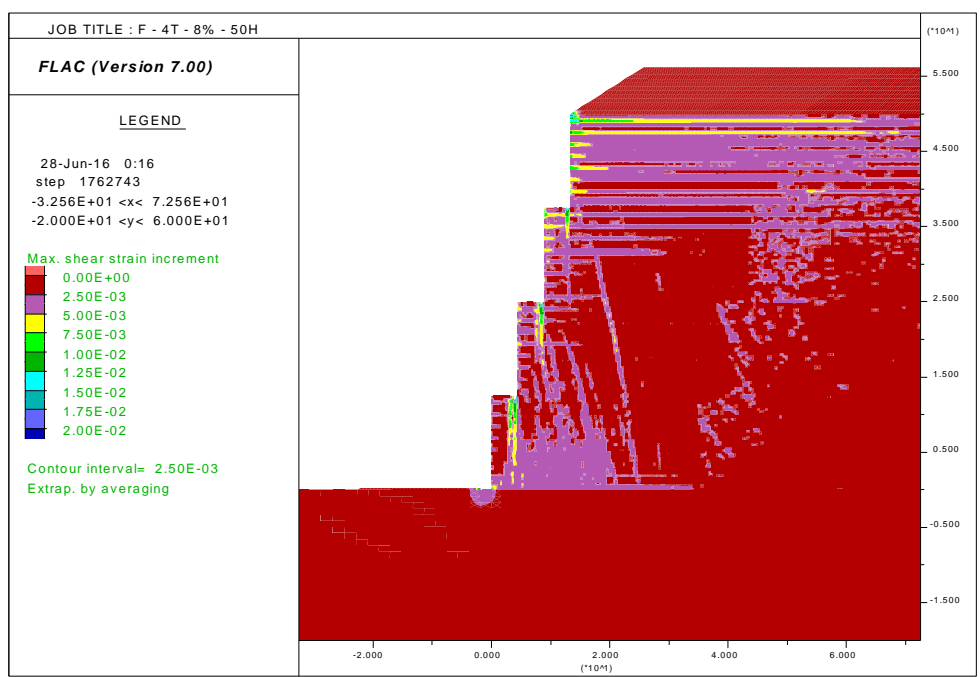


Figure F.8. FLAC model results showing shear strains for F – 4T – 8% - 50H.

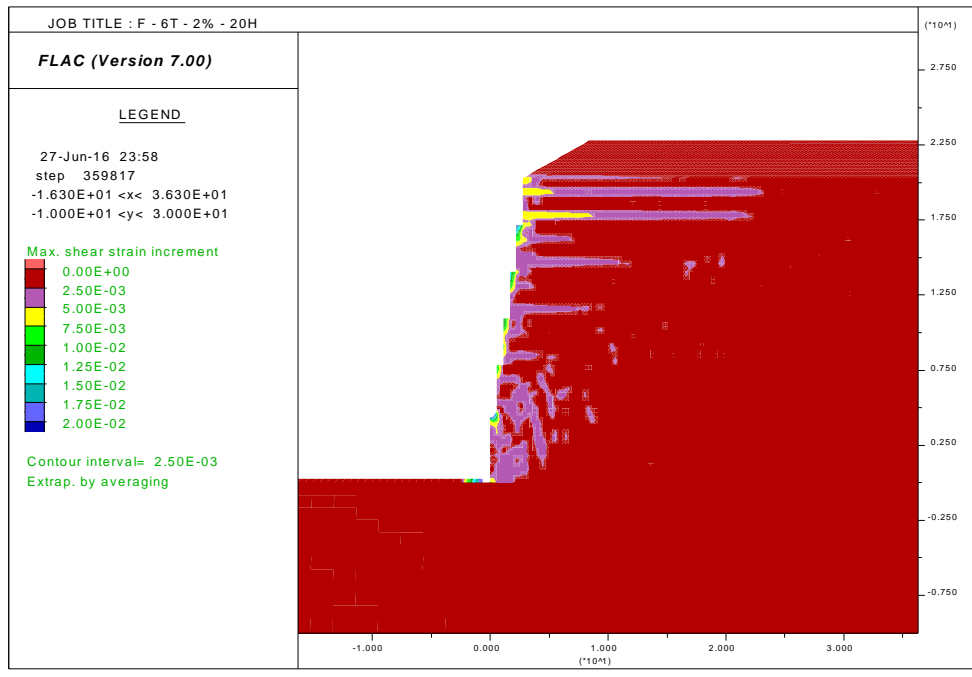


Figure F.9. FLAC model results showing shear strains for F – 6T – 2% - 20H.

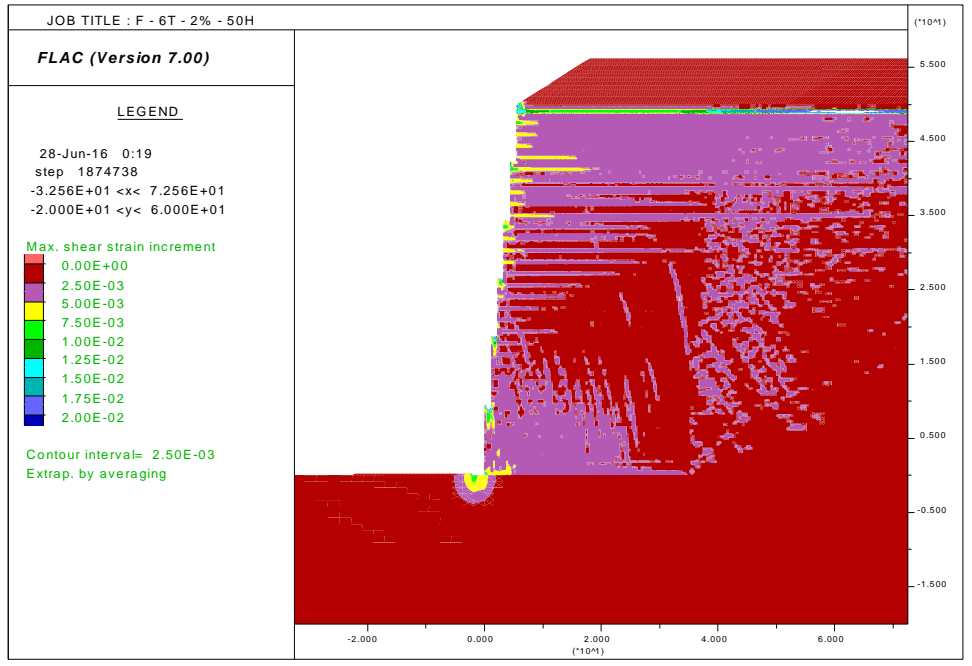


Figure F.10. FLAC model results showing shear strains for F – 6T – 2% - 50H.

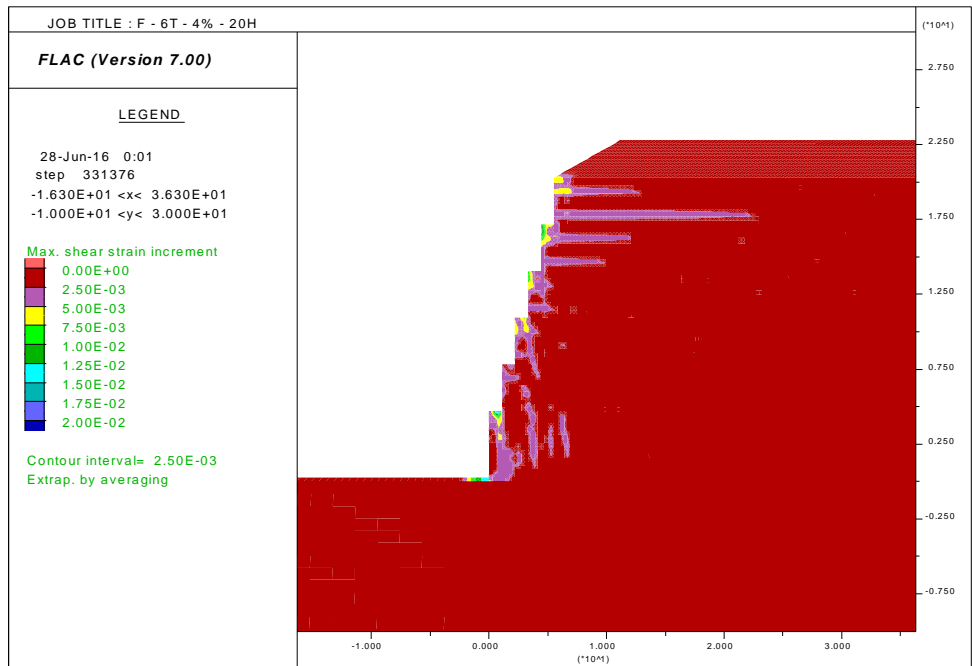


Figure F.11. FLAC model results showing shear strains for F – 6T – 4% - 20H.

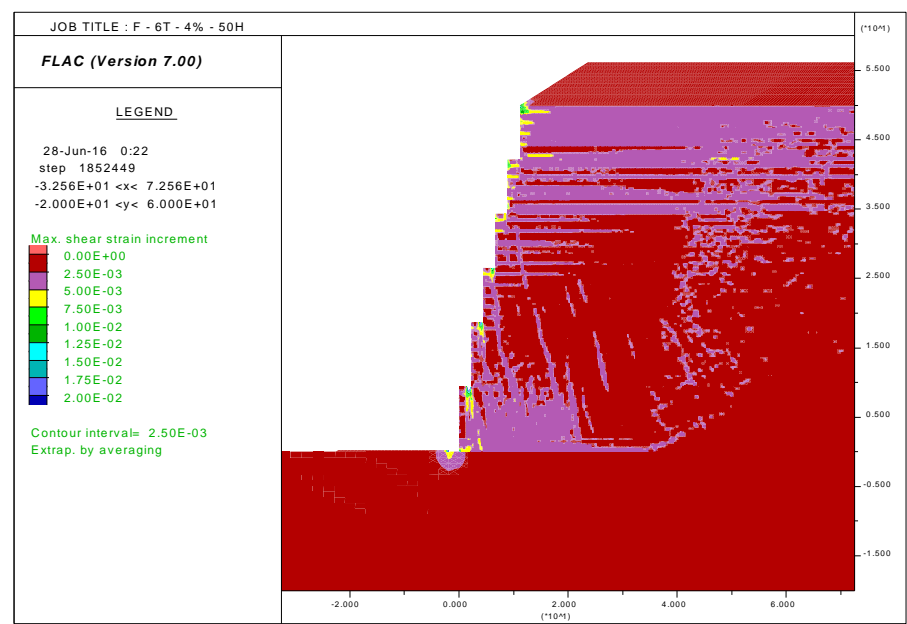


Figure F.12. FLAC model results showing shear strains for F – 6T – 4% - 50H.

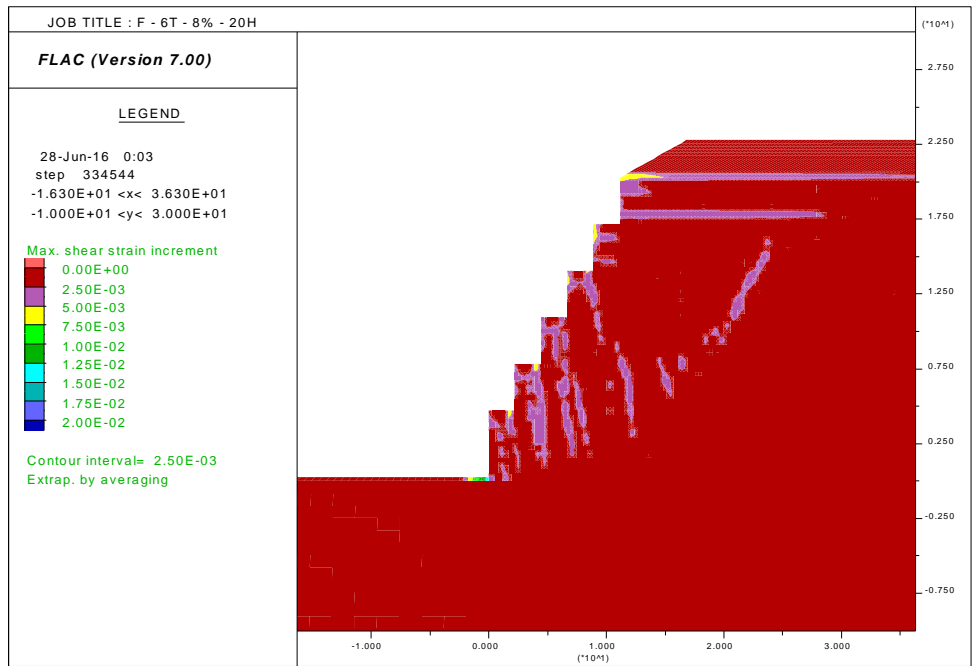


Figure F.13. FLAC model results showing shear strains for F – 6T – 8% - 20H.

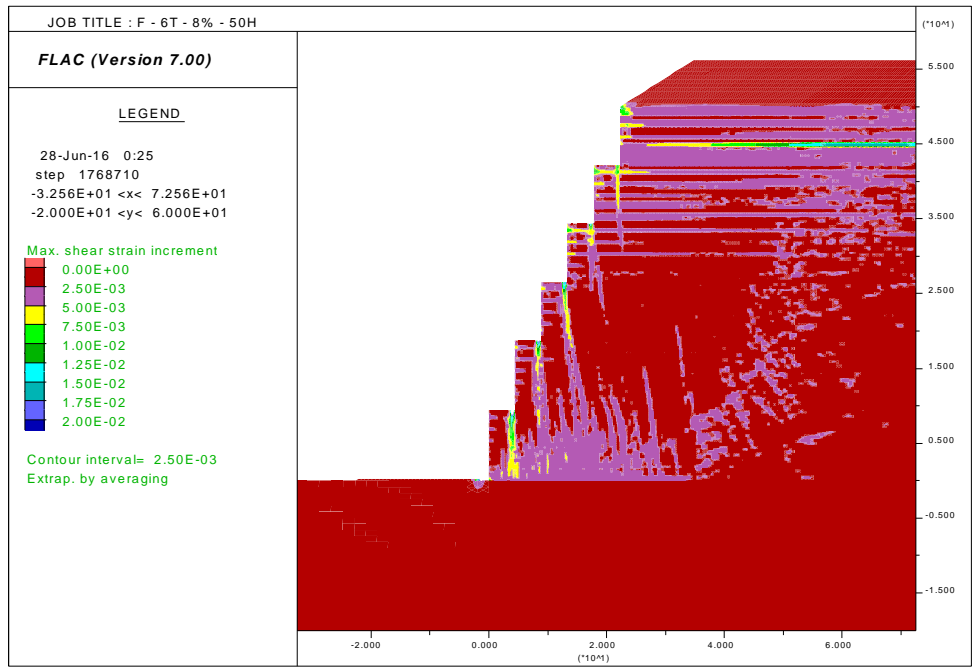


Figure F.14. FLAC model results showing shear strains for F – 6T – 8% - 50H.

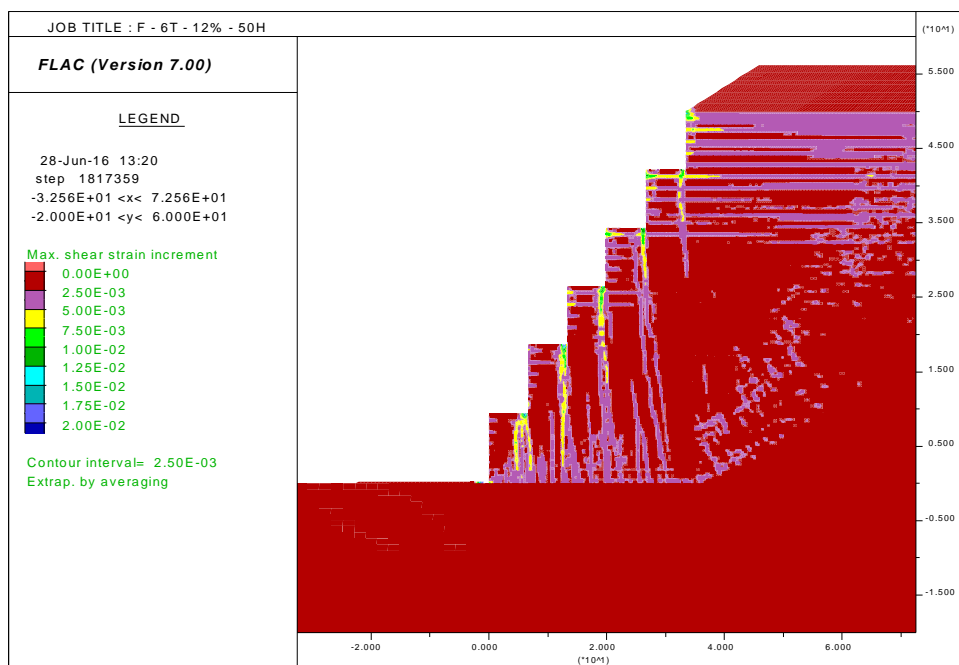


Figure F.15. FLAC model results showing shear strains for F – 6T – 12% - 50H.

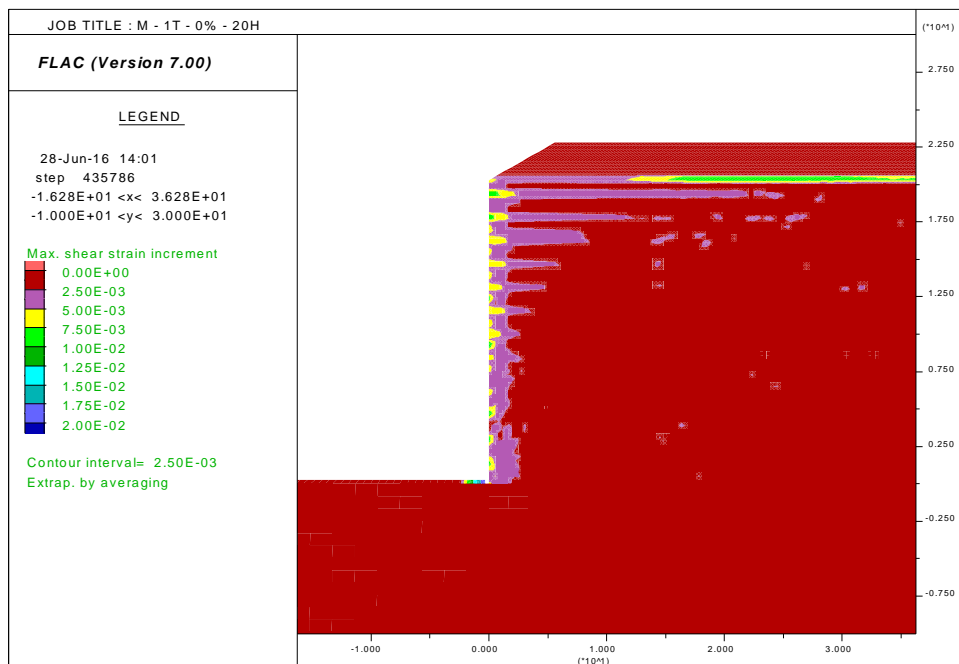


Figure F.16. FLAC model results showing shear strains for M – 1T – 0% - 20H.

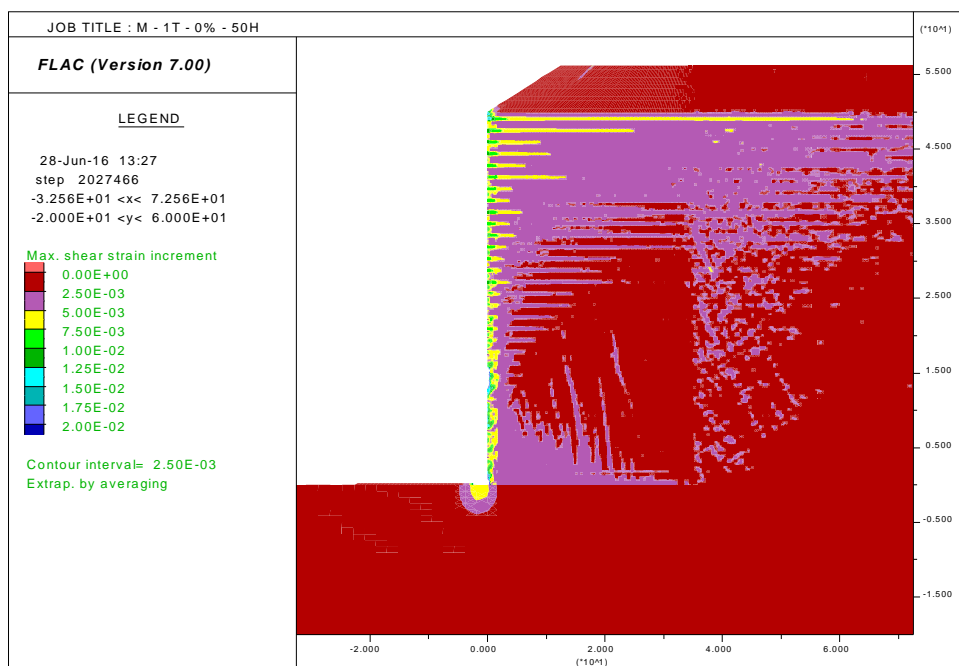


Figure F.17. FLAC model results showing shear strains for M – 1T – 0% - 50H.

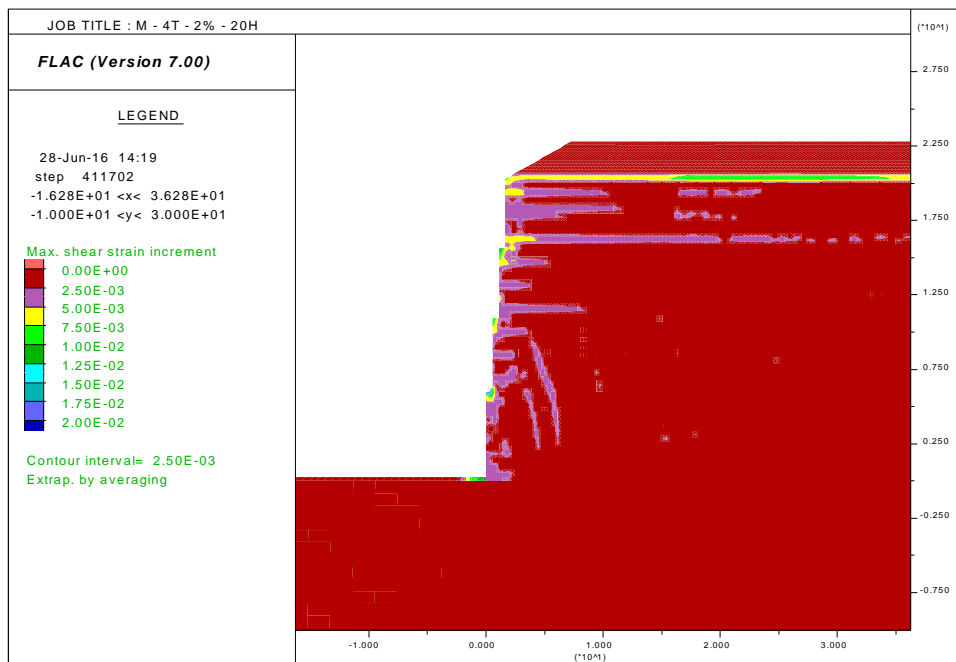


Figure F.18. FLAC model results showing shear strains for M – 4T – 2% - 20H.

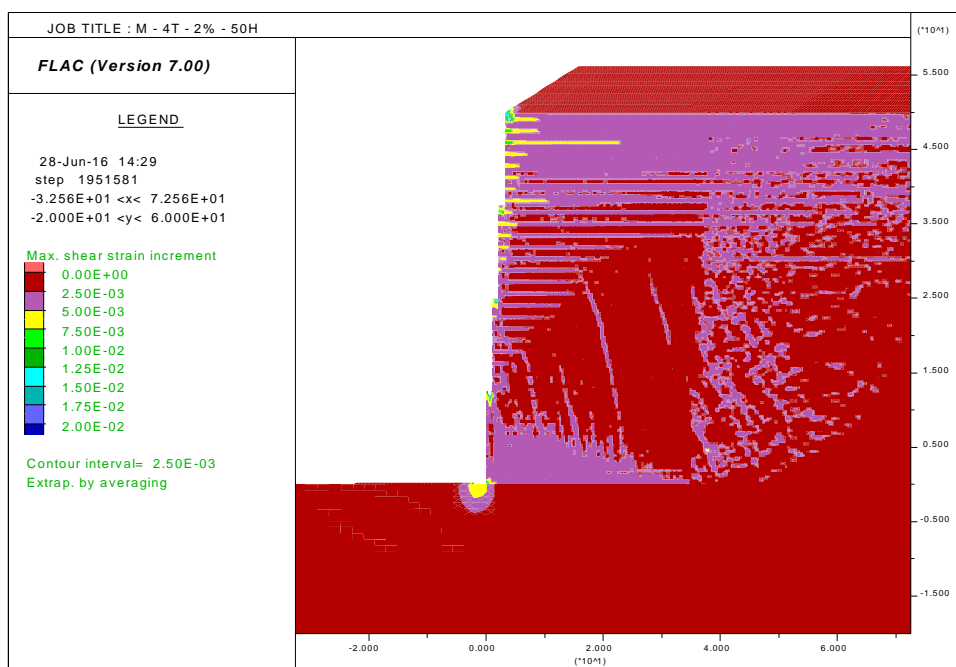


Figure F.19. FLAC model results showing shear strains for M – 4T – 2% - 50H.

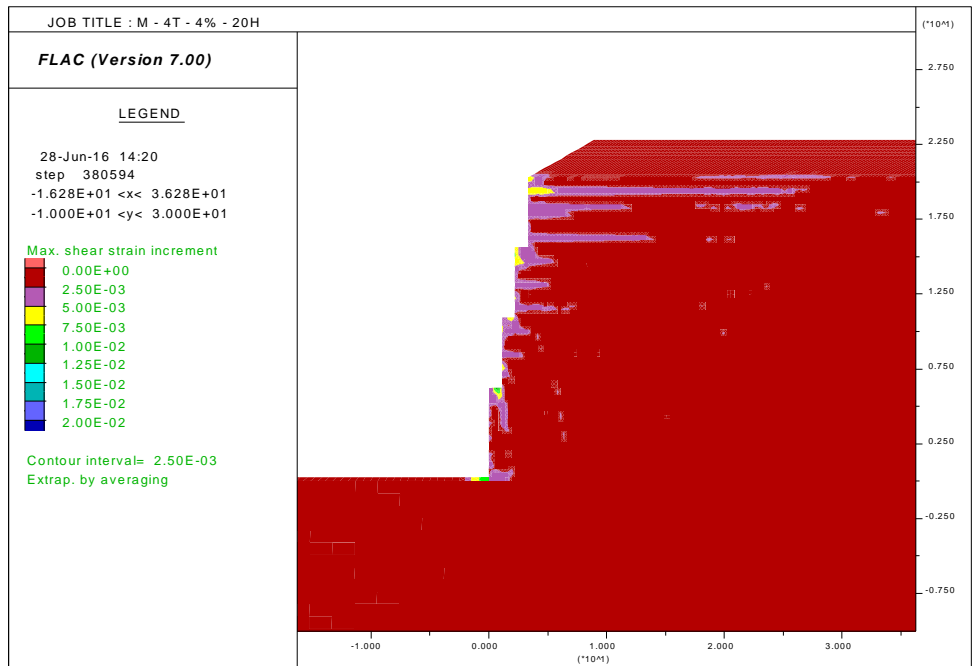


Figure F.20. FLAC model results showing shear strains for M – 4T – 4% - 20H.

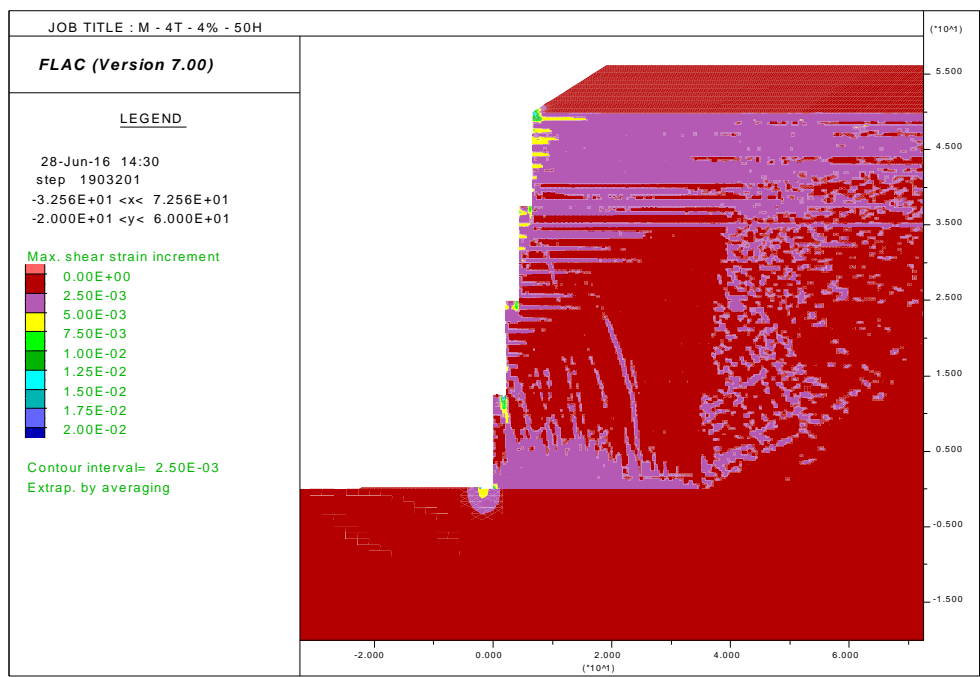


Figure F.21. FLAC model results showing shear strains for M – 4T – 4% - 50H.

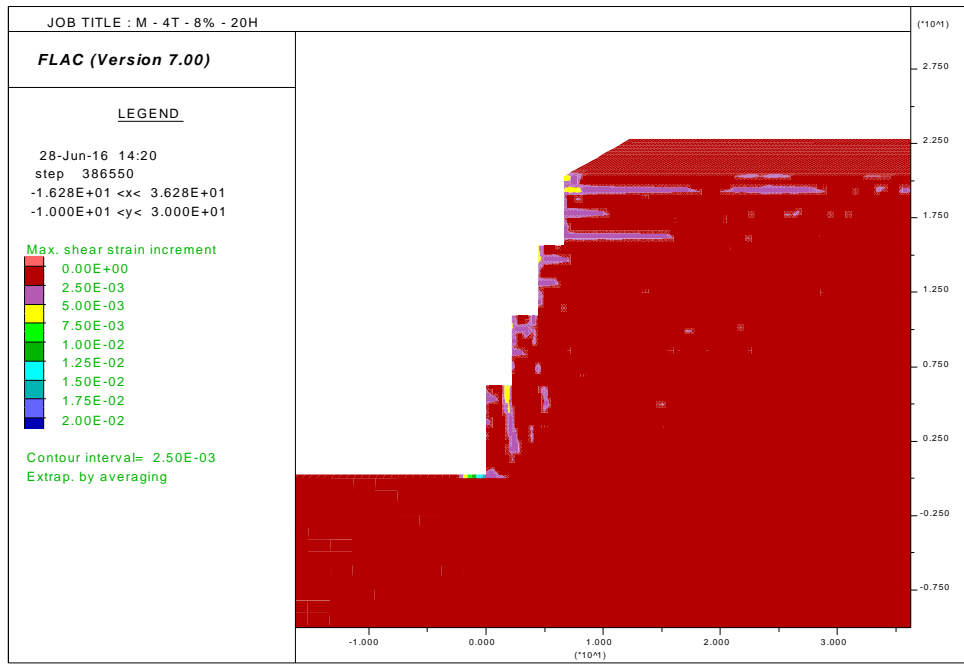


Figure F.22. FLAC model results showing shear strains for M – 4T – 8% - 20H.

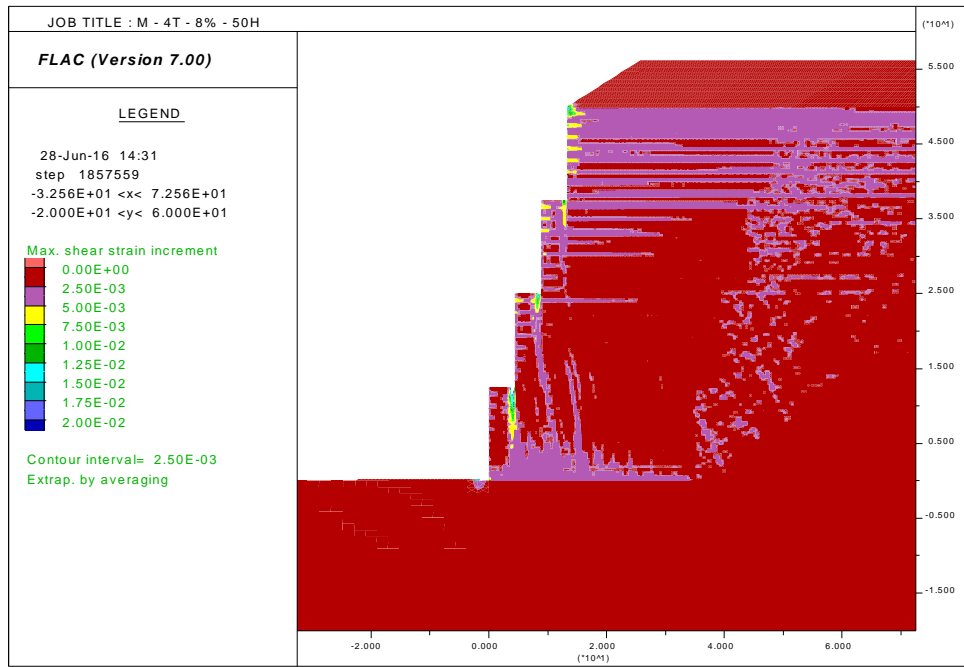


Figure F.23. FLAC model results showing shear strains for M – 4T – 8% - 50H.

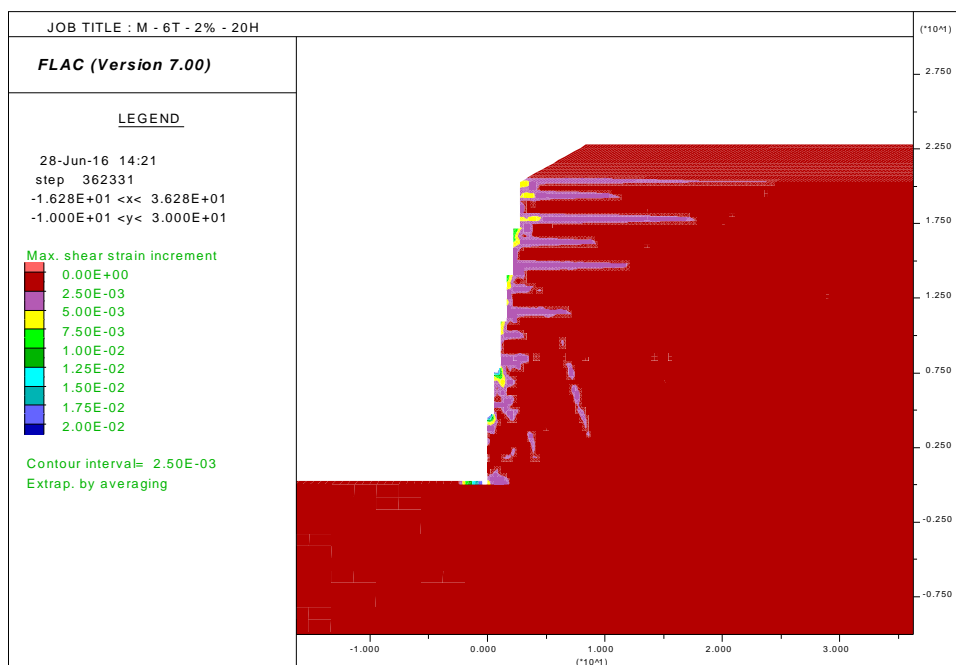


Figure F.24. FLAC model results showing shear strains for M – 6T – 2% - 20H.

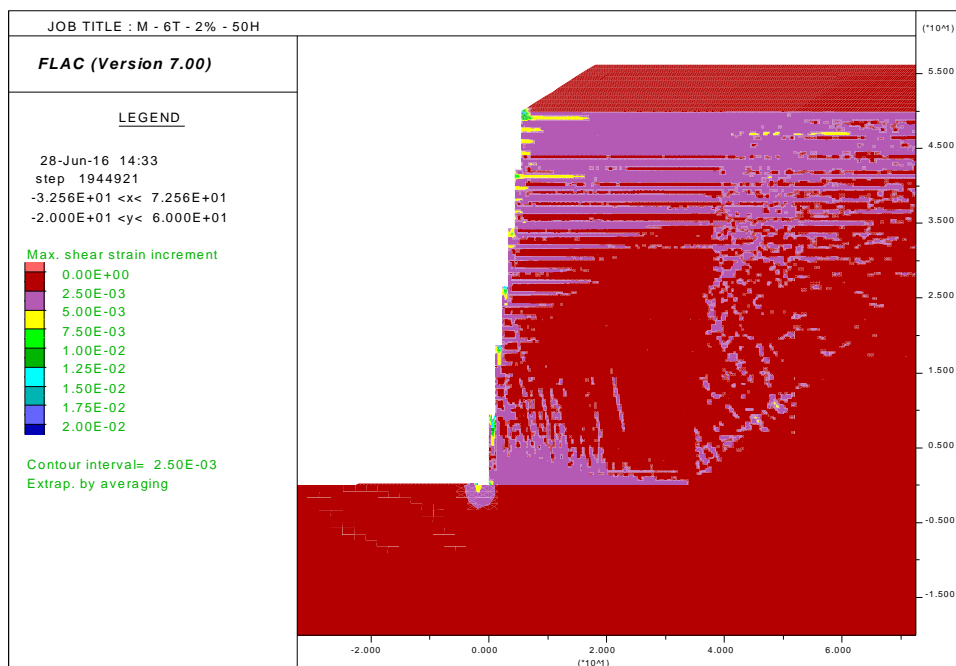


Figure F.25. FLAC model results showing shear strains for M – 6T – 2% - 50H.

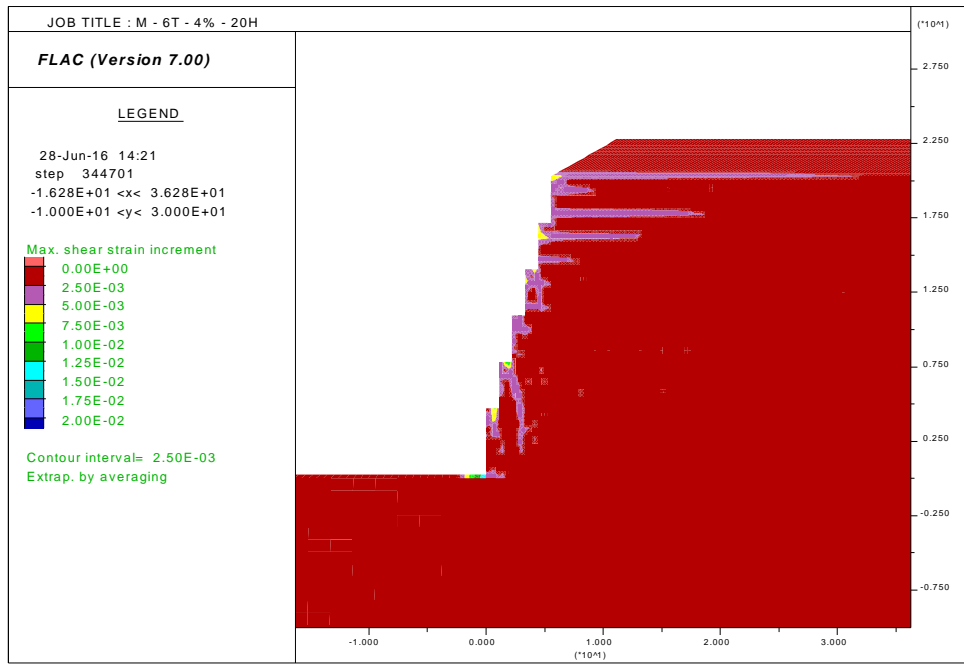


Figure F.26. FLAC model results showing shear strains for M – 6T – 4% - 20H.

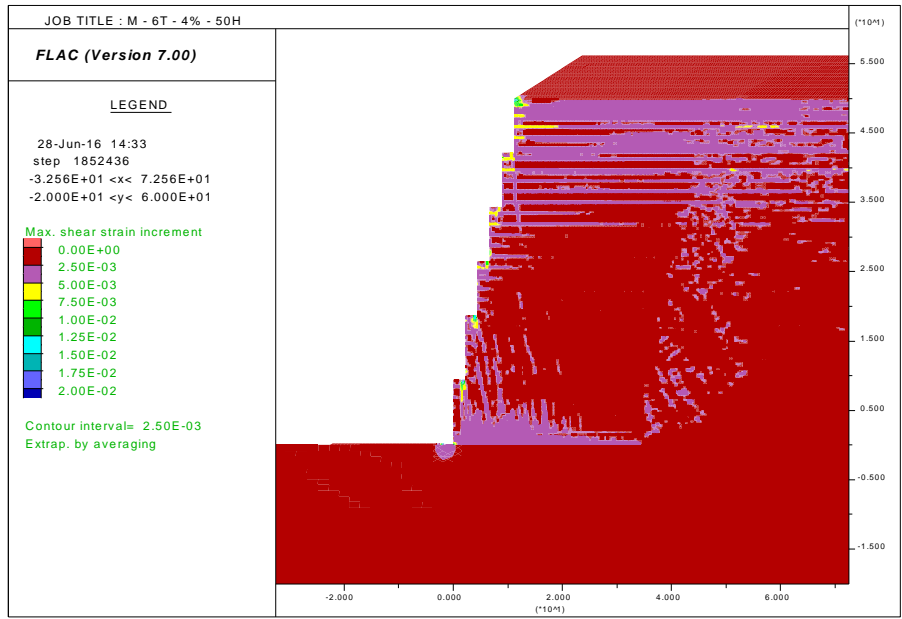


Figure F.27. FLAC model results showing shear strains for M – 6T – 4% - 50H.

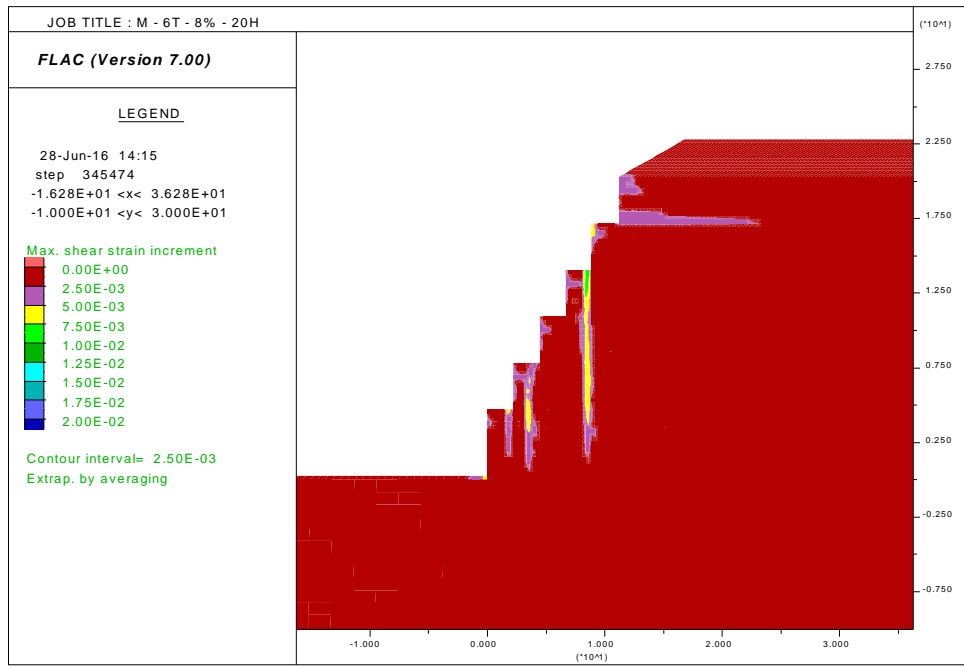


Figure F.28. FLAC model results showing shear strains for M – 6T – 8% - 20H.

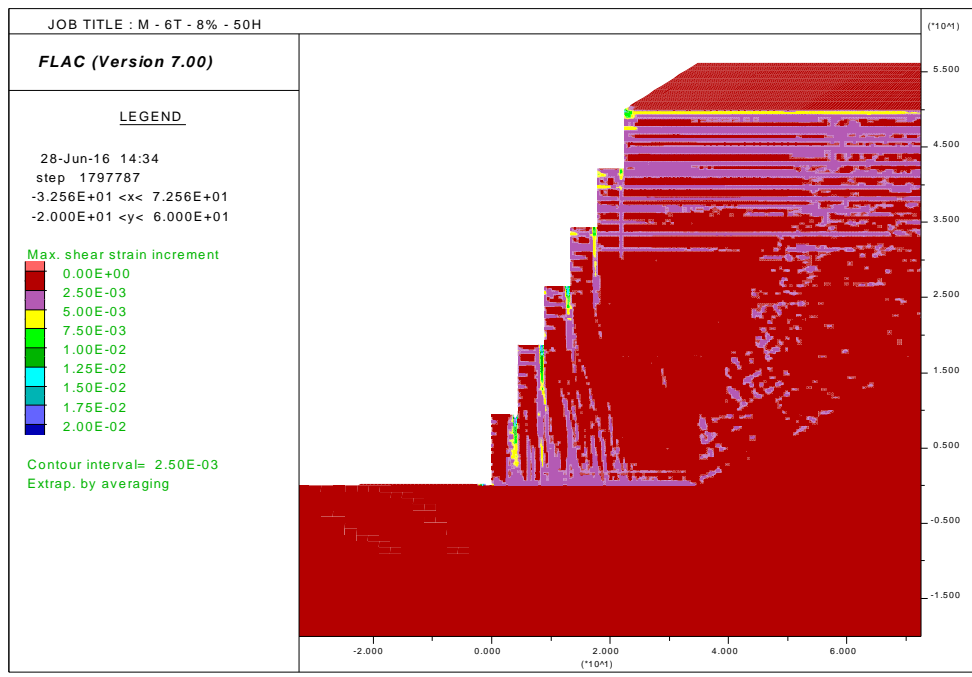


Figure F.29. FLAC model results showing shear strains for M – 6T – 8% - 50H.

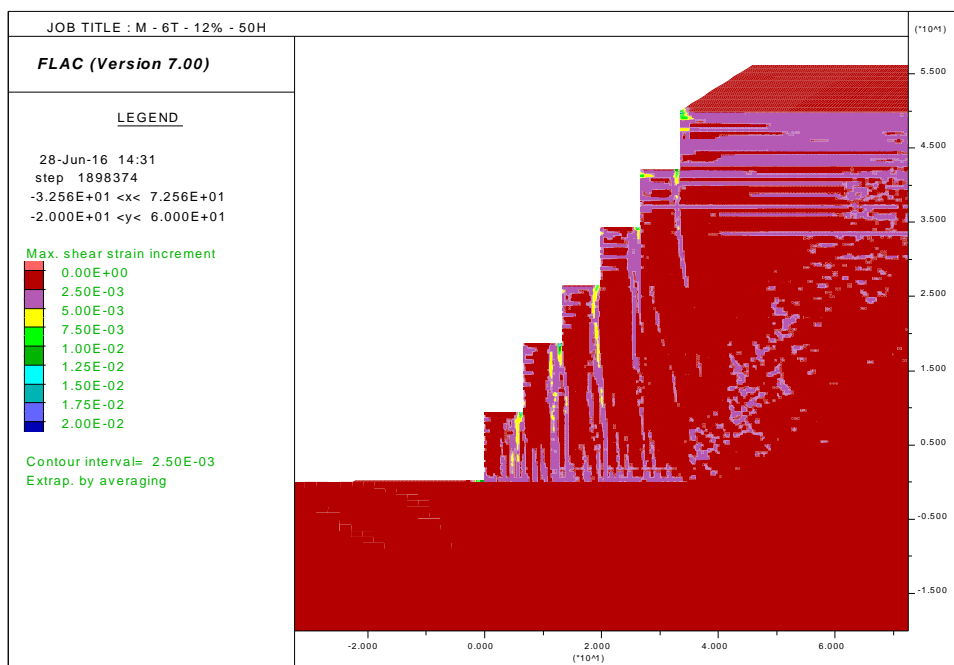


Figure F.30. FLAC model results showing shear strains for M – 6T – 12% - 50H.

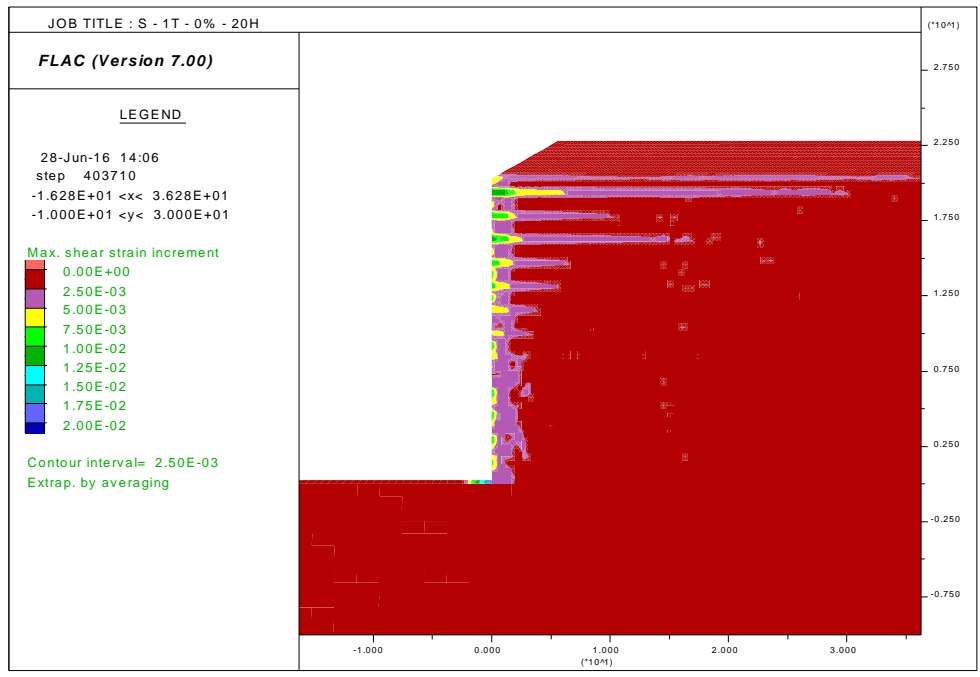


Figure F.31. FLAC model results showing shear strains for S – 1T – 0% - 20H.

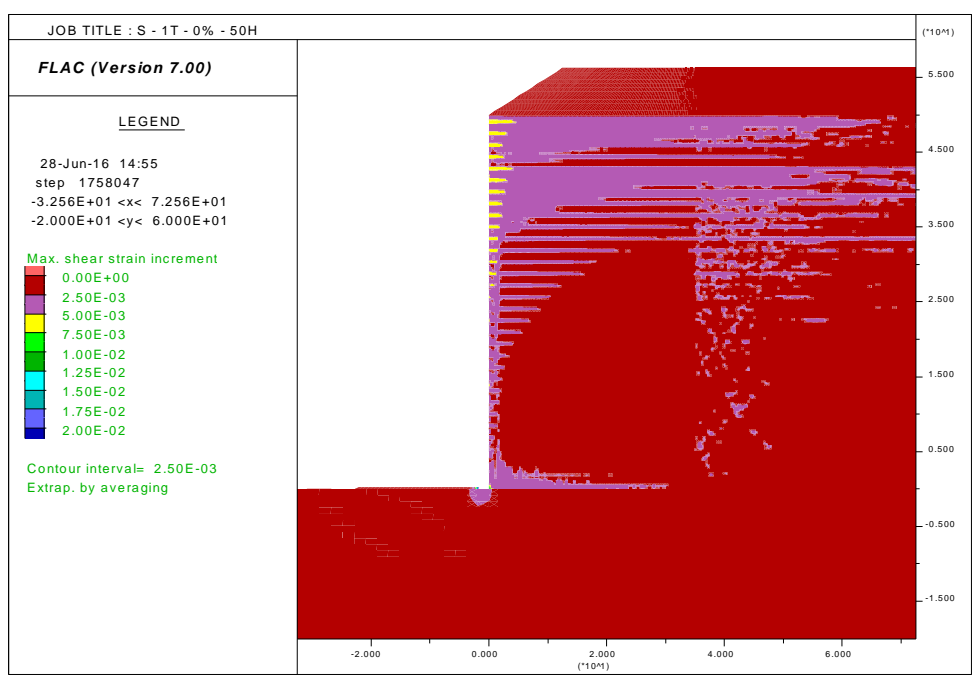


Figure F.32. FLAC model results showing shear strains for S – 1T – 0% - 50H.

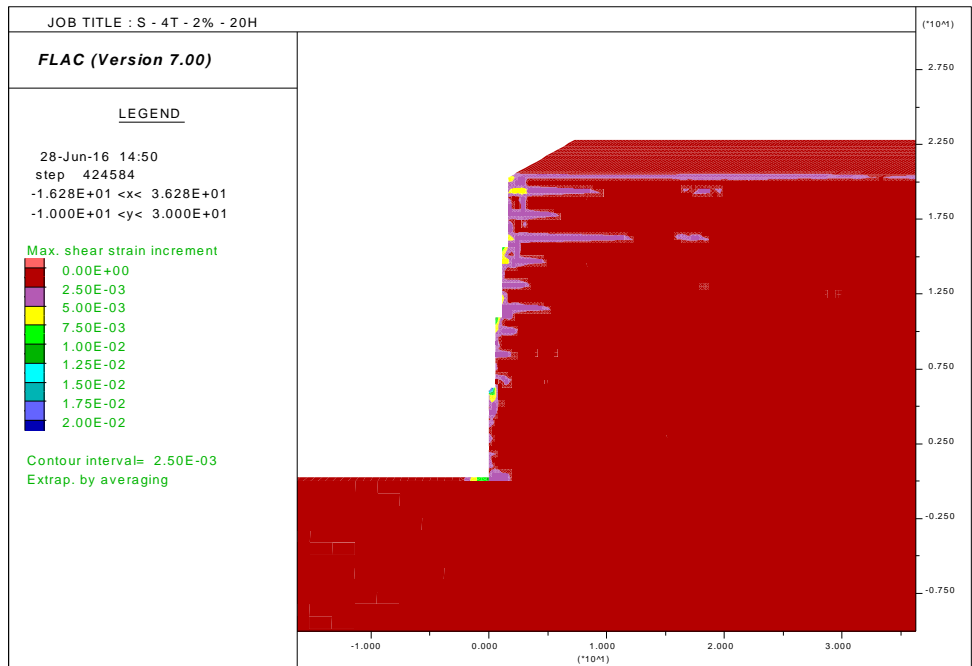


Figure F.33. FLAC model results showing shear strains for S – 4T – 2% - 20H.

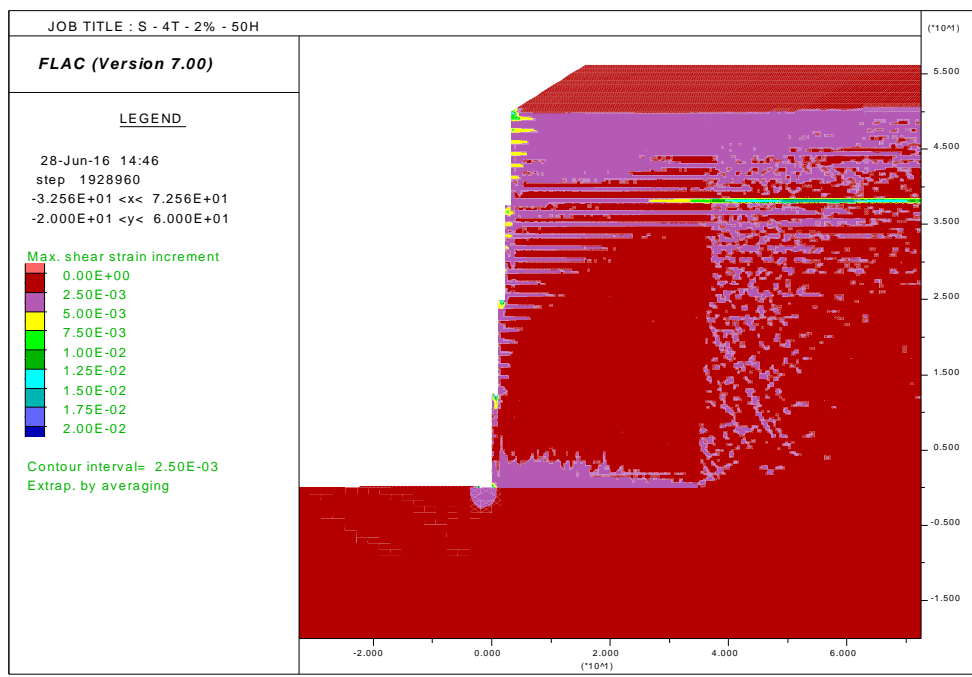


Figure F.34. FLAC model results showing shear strains for S – 4T – 2% - 50H.

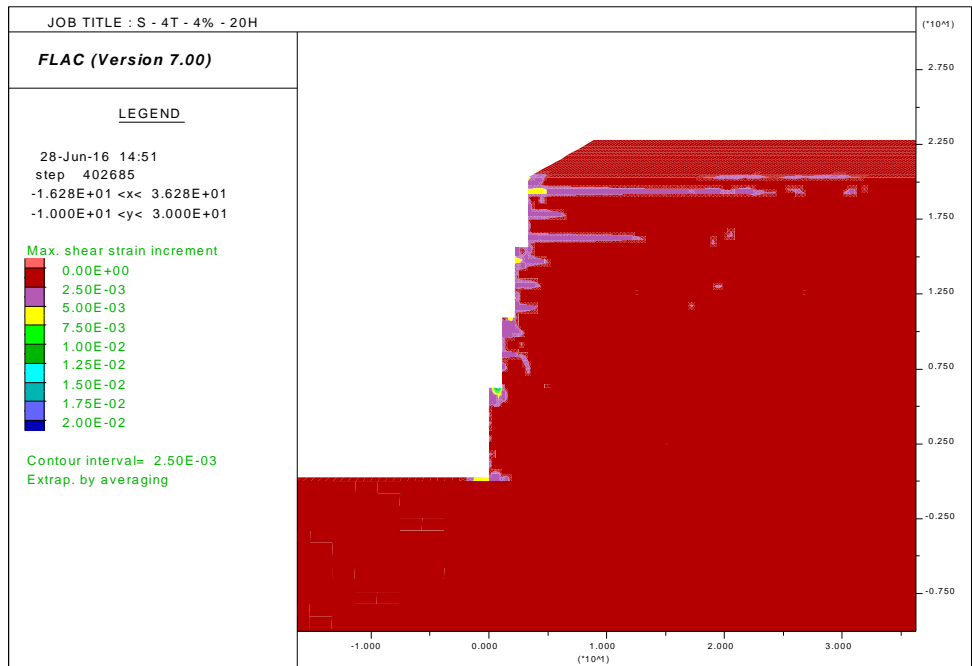


Figure F.35. FLAC model results showing shear strains for S – 4T – 4% - 20H.

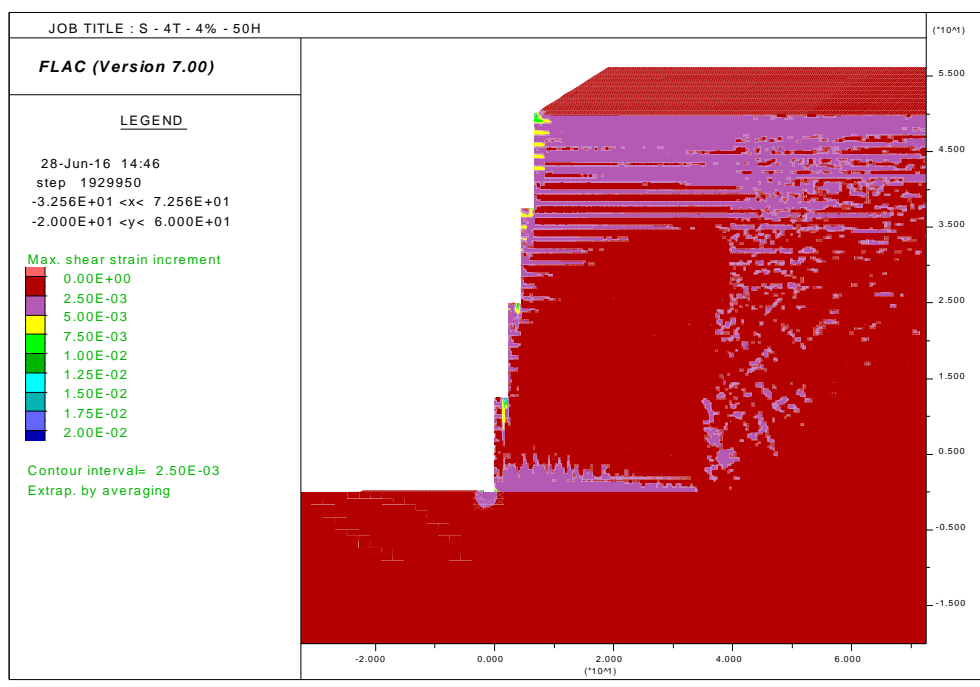


Figure F.36. FLAC model results showing shear strains for S – 4T – 4% - 50H.

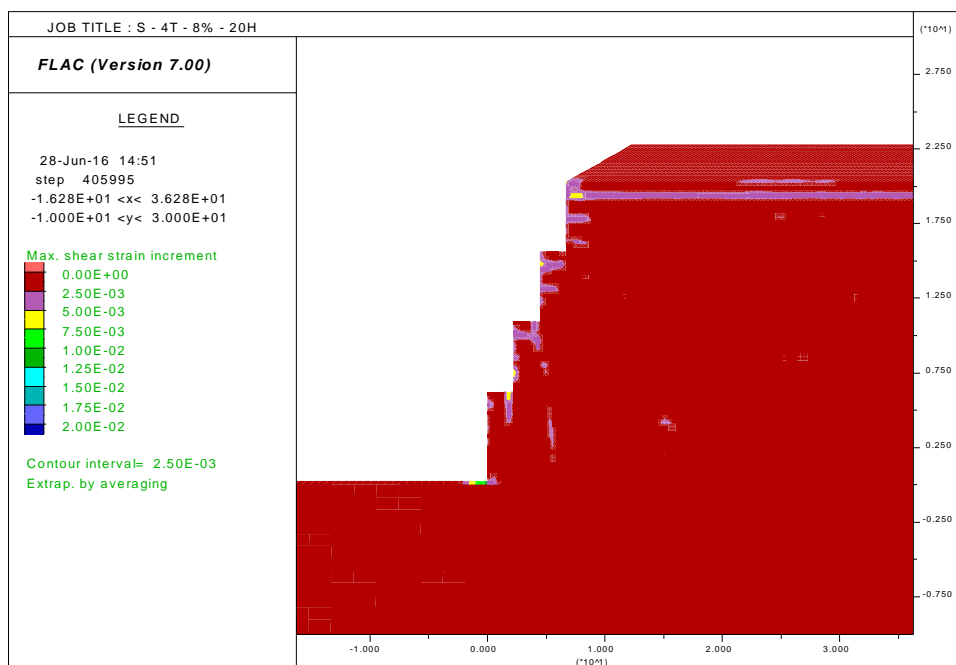


Figure F.37. FLAC model results showing shear strains for S – 4T – 8% - 20H.

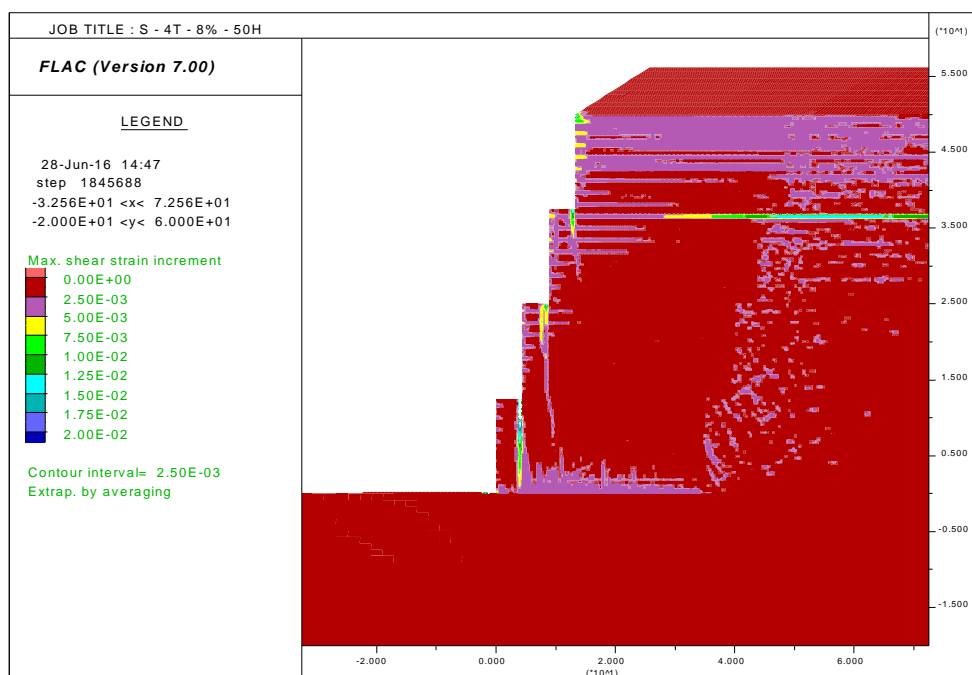


Figure F.38. FLAC model results showing shear strains for S – 4T – 8% - 50H.

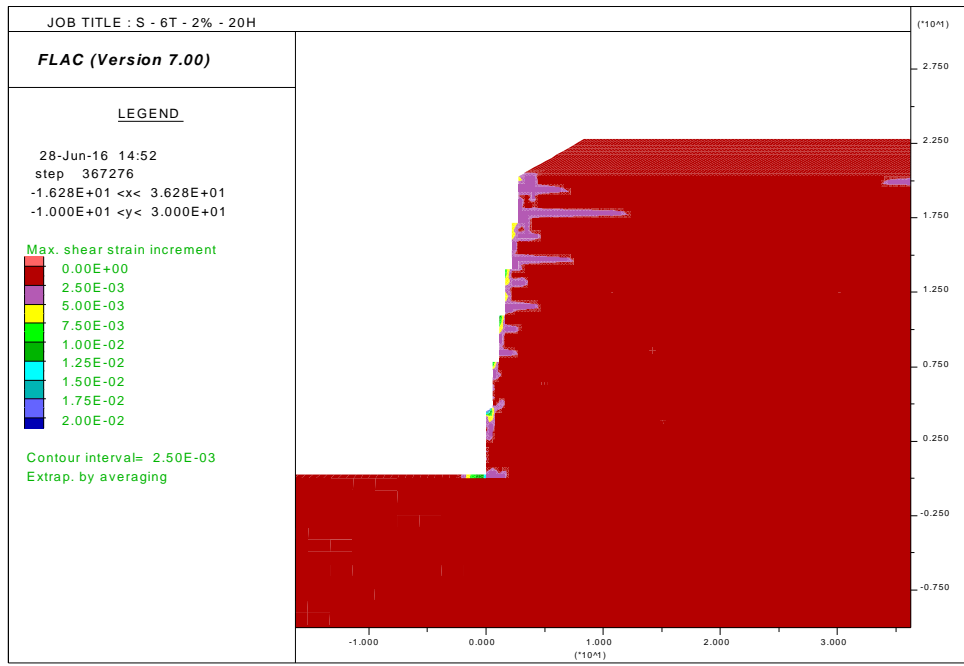


Figure F.39. FLAC model results showing shear strains for S – 6T – 2% - 20H.

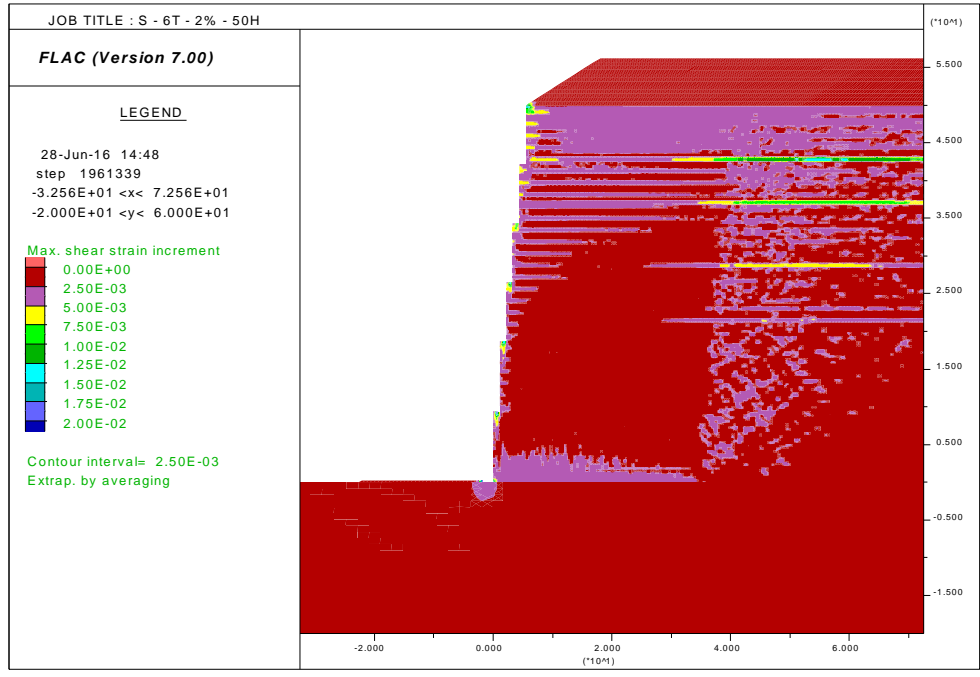


Figure F.40. FLAC model results showing shear strains for S – 6T – 2% - 50H.

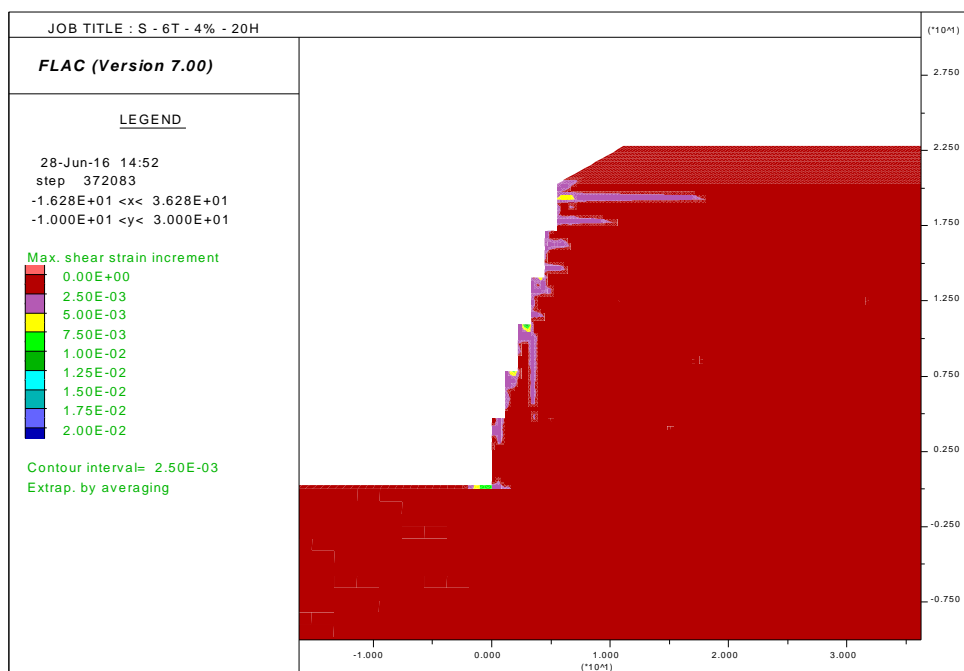


Figure F.41. FLAC model results showing shear strains for S – 6T – 4% - 20H.

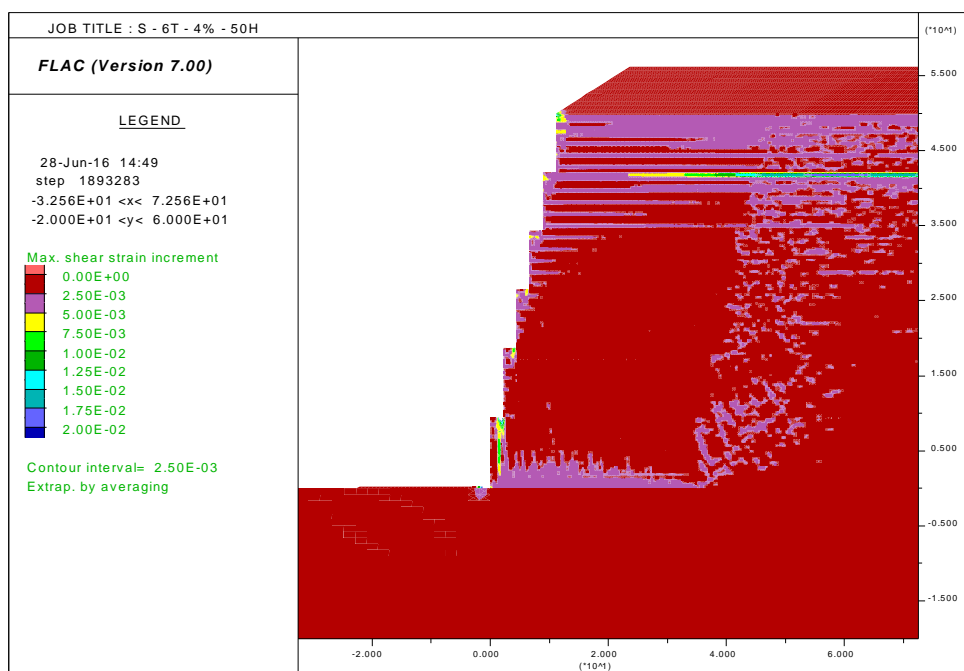


Figure F.42. FLAC model results showing shear strains for S – 6T – 4% - 50H.

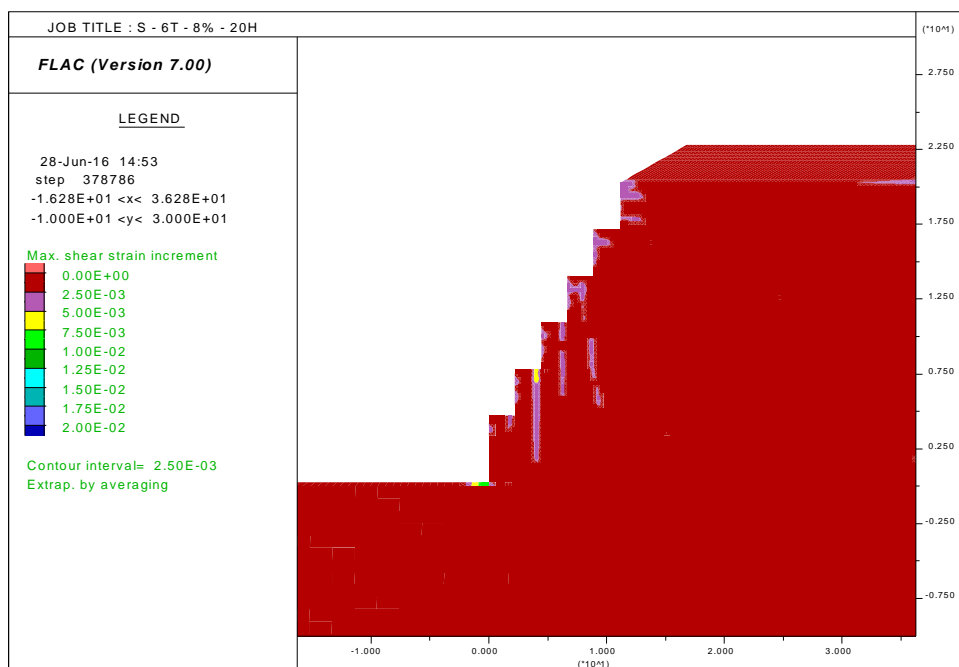


Figure F.43. FLAC model results showing shear strains for S – 6T – 8% - 20H.

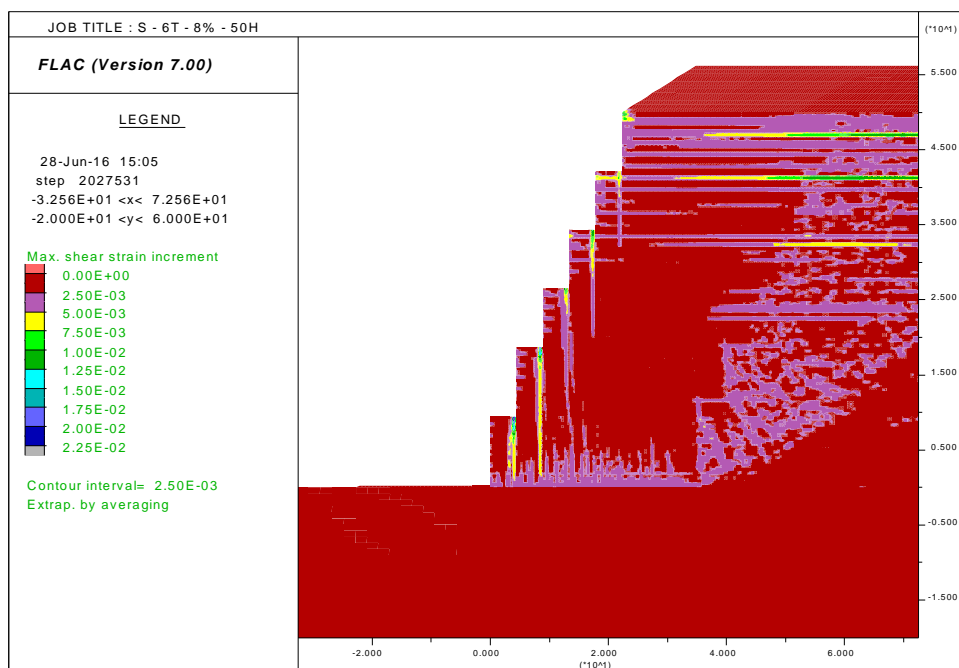


Figure F.44. FLAC model results showing shear strains for S – 6T – 8% - 50H.

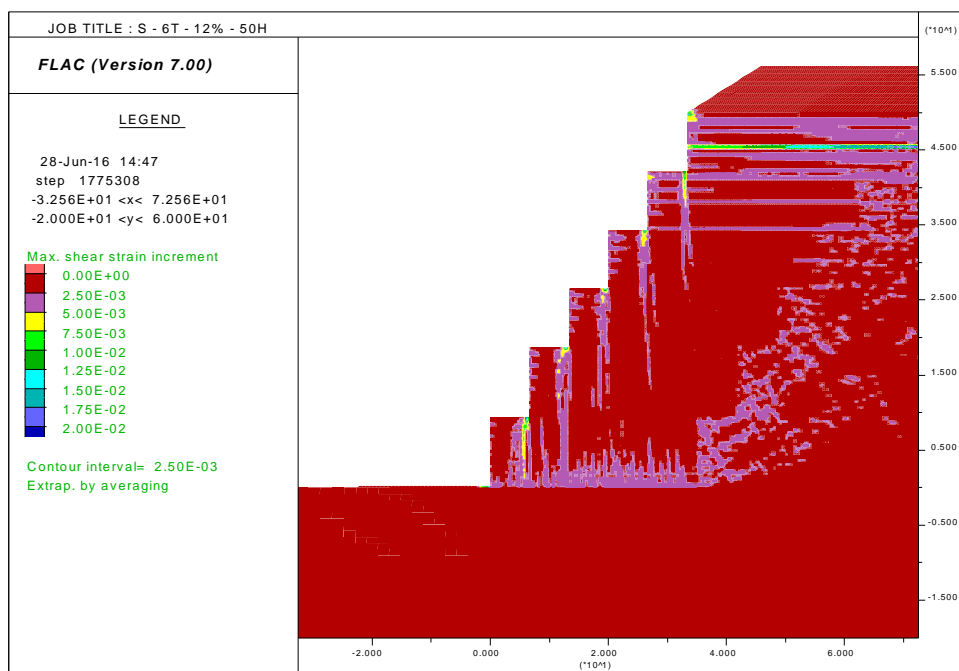


Figure F.45. FLAC model results showing shear strains for S – 6T – 12% - 50H.